EMERGING ADVANCES IN BIO-NANO ENGINEERED APPROACHES TOWARD INTELLIGENT NANOMEDICINE

EDITED BY: Gang Liu, Wei Tao and Lin Mei

PUBLISHED IN: Frontiers in Bioengineering and Biotechnology and
Frontiers in Molecular Biosciences

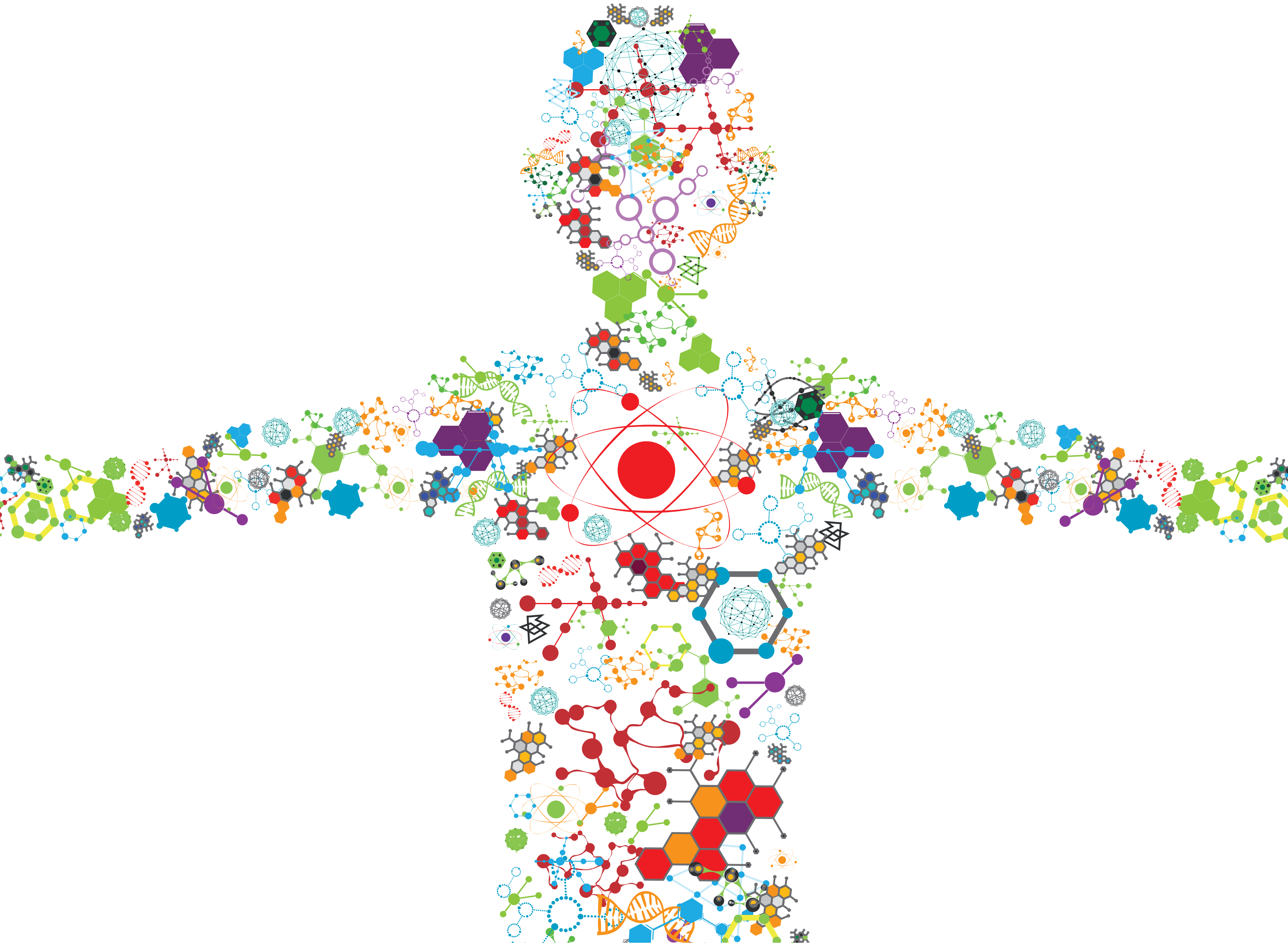

frontiers Research Topics

ISSN 1664-8714
ISBN 978-2-88971-052-2
DOI 10.3389/978-2-88971-052-2

About Frontiers

Frontiers is more than just an open-access publisher of scholarly articles: it is a pioneering approach to the world of academia, radically improving the way scholarly research is managed. The grand vision of Frontiers is a world where all people have an equal opportunity to seek, share and generate knowledge. Frontiers provides immediate and permanent online open access to all its publications, but this alone is not enough to realize our grand goals.

Frontiers Journal Series

The Frontiers Journal Series is a multi-tier and interdisciplinary set of open-access, online journals, promising a paradigm shift from the current review, selection and dissemination processes in academic publishing. All Frontiers journals are driven by researchers for researchers; therefore, they constitute a service to the scholarly community. At the same time, the Frontiers Journal Series operates on a revolutionary invention, the tiered publishing system, initially addressing specific communities of scholars, and gradually climbing up to broader public understanding, thus serving the interests of the lay society, too.

Dedication to Quality

Each Frontiers article is a landmark of the highest quality, thanks to genuinely collaborative interactions between authors and review editors, who include some of the world's best academicians. Research must be certified by peers before entering a stream of knowledge that may eventually reach the public - and shape society; therefore, Frontiers only applies the most rigorous and unbiased reviews.
Frontiers revolutionizes research publishing by freely delivering the most outstanding research, evaluated with no bias from both the academic and social point of view. By applying the most advanced information technologies, Frontiers is catapulting scholarly publishing into a new generation.

What are Frontiers Research Topics?

Frontiers Research Topics are very popular trademarks of the Frontiers Journals Series: they are collections of at least ten articles, all centered on a particular subject. With their unique mix of varied contributions from Original Research to Review Articles, Frontiers Research Topics unify the most influential researchers, the latest key findings and historical advances in a hot research area! Find out more on how to host your own Frontiers Research Topic or contribute to one as an author by contacting the Frontiers Editorial Office: frontiersin.org/about/contact

EMERGING ADVANCES IN BIO-NANO ENGINEERED APPROACHES TOWARD INTELLIGENT NANOMEDICINE

Topic Editors:
Gang Liu, Xiamen University, China
Wei Tao, Harvard Medical School, United States
Lin Mei, Sun Yat-Sen University, China

Citation: Liu, G., Tao, W., Mei, L., eds. (2021). Emerging Advances in Bio-Nano Engineered Approaches Toward Intelligent Nanomedicine.
Lausanne: Frontiers Media SA. doi: 10.3389/978-2-88971-052-2

Table of Contents

05 ***Editorial: Emerging Advances in Bio-Nano Engineered Approaches Toward Intelligent Nanomedicine***
Junqing Wang, Lin Mei, Wei Tao and Gang Liu

08 ***β-Elemene Reverses the Resistance of p53-Deficient Colorectal Cancer Cells to 5-Fluorouracil by Inducing Pro-death Autophagy and Cyclin D3-Dependent Cycle Arrest***
Ruonan Zhang, Ting Pan, Yu Xiang, Mingming Zhang, Jiao Feng, Shuiping Liu, Ting Duan, Peng Chen, Bingtao Zhai, Xiaying Chen, Wengang Wang, Bi Chen, Xuemeng Han, Liuxi Chen, Lili Yan, Ting Jin, Ying Liu, Guohua Li, Xingxing Huang, Wenzheng Zhang, Yitian Sun, Qiujie Li, Qin Zhang, Lvjia Zhuo, Tian Xie, Qibiao Wu and Xinbing Sui

21 ***Differently Charged Super-Paramagnetic Iron Oxide Nanoparticles Preferentially Induced M1-Like Phenotype of Macrophages***
Wenyue Zhang, Shuwen Cao, Shunung Liang, Chee Hwee Tan, Baoming Luo, Xiaoding Xu and Phei Er Saw

31 ***Nanotechnology in Chronic Pain Relief***
Jing Chen, Teng Jin and Hua Zhang

37 ***Energy Conversion-Based Nanotherapy for Rheumatoid Arthritis Treatment***
Pingping Wang, Ao Li, Luodan Yu, Yu Chen and Di Xu

53 ***Lipidation Approaches Potentiate Adjuvant-Pulsed Immune Surveillance: A Design Rationale for Cancer Nanovaccine***
Junqing Wang, Harshal Zope, Mohammad Ariful Islam, Jamie Rice, Sage Dodman, Kevin Lipert, Yunhan Chen, Bruce R. Zetter and Jinjun Shi

62 ***Zinc Ion-Stabilized Aptamer-Targeted Black Phosphorus Nanosheets for Enhanced Photothermal/Chemotherapy Against Prostate Cancer***
Li Gao, Ruobing Teng, Sen Zhang, Yun Zhou, Miaomiao Luo, Youqiang Fang, Lei Lei and Bo Ge

75 ***A Spellbinding Interplay Between Biological Barcoding and Nanotechnology***
Shehla Munir, Sarfraz Ahmed, Muhammad Ibrahim, Muhammad Khalid and Suvash Chandra Ojha

92 ***Drug-Loaded Lipid-Coated Hybrid Organic-Inorganic "Stealth" Nanoparticles for Cancer Therapy***
Xue Li, Giuseppina Salzano, Jingwen Qiu, Mathilde Menard, Kristian Berg, Theodossis Theodossiou, Catherine Ladavière and Ruxandra Gref

104 ***Recent Advances in Self-Exciting Photodynamic Therapy***
Nicholas Thomas Blum, Yifan Zhang, Junle Qu, Jing Lin and Peng Huang

123 ***Exosomes as a Novel Approach to Reverse Osteoporosis: A Review of the Literature***
Xudong Xie, Yuan Xiong, Adriana C. Panayi, Liangcong Hu, Wu Zhou, Hang Xue, Ze Lin, Lang Chen, Chenchen Yan, Bobin Mi and Guohui Liu

133 ***Injecting Immunosuppressive M2 Macrophages Alleviates the Symptoms of Periodontitis in Mice***
Yibin Miao, Liuting He, Xiaoyu Qi and Xiaoping Lin

143 ***Mesenchymal-Stem-Cell–Derived Extracellular Vesicles Mitigate Trained Immunity in the Brain***
Yiwei Feng, Min Guo, Hongchen Zhao, Sida Han, Qiang Dong and Mei Cui

153 ***Rutin-Loaded Silver Nanoparticles With Antithrombotic Function***
Haitao Wu, Manlin Su, Hui Jin, Xinyu Li, Puyu Wang, Jingxiao Chen and Jinghua Chen

164 ***BSA-Stabilized Mesoporous Organosilica Nanoparticles Reversed Chemotherapy Resistance of Anaplastic Thyroid Cancer by Increasing Drug Uptake and Reducing Cellular Efflux***
Xiao Han, Xiaoquan Xu, Yuxia Tang, Feipeng Zhu, Ying Tian, Wei Liu, Doudou He, Guangming Lu, Yunfei Gu and Shouju Wang

172 ***Baicalin Induces Apoptosis and Suppresses the Cell Cycle Progression of Lung Cancer Cells Through Downregulating Akt/mTOR Signaling Pathway***
Xinbing Sui, Xuemeng Han, Peng Chen, Qibiao Wu, Jiao Feng, Ting Duan, Xiaying Chen, Ting Pan, Lili Yan, Ting Jin, Yu Xiang, Quan Gao, Chengyong Wen, Weirui Ma, Wencheng Liu, Ruonan Zhang, Bi Chen, Mingming Zhang, Zuyi Yang, Na Kong, Tian Xie and Xia Ding

181 ***Formation Mechanism and Biomedical Applications of Protease-Manipulated Peptide Assemblies***
Tianyue Jiang, Chendan Liu, Xiao Xu, Bingfang He and Ran Mo

frontiers in Bioengineering and Biotechnology

EDITORIAL
published: 24 May 2021
doi: 10.3389/fbioe.2021.703227

Editorial: Emerging Advances in Bio-Nano Engineered Approaches Toward Intelligent Nanomedicine

Junqing Wang[1], Lin Mei[2]*, Wei Tao[3]* and Gang Liu[4]**

[1] School of Pharmaceutical Sciences (Shenzhen), Sun Yat-sen University, Shenzhen, China, [2] Tianjin Key Laboratory of Biomedical Materials, Key Laboratory of Biomaterials and Nanotechnology for Cancer Immunotherapy, Institute of Biomedical Engineering, Chinese Academy of Medical Sciences, Peking Union Medical College, Tianjin, China, [3] Center for Nanomedicine, Brigham and Women's Hospital and Harvard Medical School, Boston, MA, United States, [4] State Key Laboratory of Molecular Vaccinology and Molecular Diagnostics, Center for Molecular Imaging and Translational Medicine, School of Public Health, Xiamen University, Xiamen, China

Keywords: drug delivery, nanomedicine, bio-nano, nanovaccines, auto-PDT, SPIONs, exosomes, nanoMOFs

Editorial on the Research Topic

Emerging Advances in Bio-Nano Engineered Approaches Toward Intelligent Nanomedicine

Edited and reviewed by:
Gianni Ciofani,
Italian Institute of Technology (IIT), Italy

****Correspondence:***
Junqing Wang
wangjunqing@mail.sysu.edu.cn
Lin Mei
meilin@bme.pumc.edu.cn
Wei Tao
wtao@bwh.harvard.edu
Gang Liu
gangliu.cmitm@xmu.edu.cn

Specialty section:
This article was submitted to Nanobiotechnology, a section of the journal Frontiers in Bioengineering and Biotechnology

Received: *30 April 2021*
Accepted: *04 May 2021*
Published: *24 May 2021*

Citation:
Wang J, Mei L, Tao W and Liu G (2021) Editorial: Emerging Advances in Bio-Nano Engineered Approaches Toward Intelligent Nanomedicine. Front. Bioeng. Biotechnol. 9:703227. doi: 10.3389/fbioe.2021.703227

In the past two decades, nanomedicine has made tremendous progress in the fields of diagnosis, treatment, and prevention of diseases. With the continuous deepening of the knowledge in nanobiology, nanomedicine has rapidly evolved from the early stage of classic functional nanoparticles (e.g., liposomes, iron oxide nanoparticles, semiconductor/graphene quantum dots, colloidal gold nanoparticles, etc.) to a variety of bio-nano fusion systems with the "intelligent" use of nano-biological effects. This paradigm shift will bring about fundamental changes in drug delivery strategies (Zhang et al., 2018), companion diagnostics (Cai et al., 2018; Liu et al., 2021), synchronous therapy (Shi et al., 2020), as well as in the way of manipulating bio-nano interactions for medical applications (Tao et al., 2019). In this Research Topic, we present six representative original articles highlighting the recent research advances in design and concepts of novel bio-nano engineered approaches that cover multiple applications, including polymer-lipid hybrid nanovaccine for anti-tumor therapy, differently charged super-paramagnetic iron oxide nanoparticles (SPIONs) for M2 to M1 macrophages polarization, immuno-inert nanoMOFs for cancer therapy, self-driven photodynamic therapy (PDT), exosomes-based osteoporosis therapy, and nanomedicine for chronic pain relief.

Wang et al. described an effective prophylactic anti-cancer nanovaccine approached by co-encapsulation of lipidated TLR7/8 agonists and ovalbumin-derived peptide (SIINFEKL) in core-shell polymer–lipid hybrid nanoparticles (PLNs). This research attempts to address the major limitations of conventional vaccine formulation, including the poor tolerability profile of adjuvants, instability of peptide antigens, insufficient cellular uptake, rapid diffusion from post-injection, and systemic adverse effects. They have demonstrated that lipidation of adjuvant and peptide epitope following PLN encapsulation can largely improve anti-tumor immune responses and achieve desired *in vivo* prophylactic efficacy. In comparison to aluminum-contained vaccine formulation, PLN vaccine exhibited minimally systemic exposure, enhanced encapsulation efficacy, persistent antigen-presenting cellular uptake, and prolonged immune surveillance effect. The integration of lipidation modification and the PLN approach developed by the authors could be an important concept to direct the future success of anti-cancer nanovaccines.

Understanding the interactions between biological systems and nanoscale entities play a crucial role in the development of the biomedical application of nanomedicine (Liu et al., 2021). In this research topic, Zhang et al. presented a hypothesis that differently charged SPIONs would exhibit variable abilities to induce the conversion of the macrophage phenotype. The authors designed three different charged SPIONs (i.e., S+ positive, SN neutral, and S– negative) and investigated their intrinsic re-polarization effect on tumor-associated macrophages (TAMs), as well as their influence on tumor growth rate. They found that both S+ and S– could effectively reprogram TAMs from an M2 to an M1 phenotype at cellular level. This is possibly due to their high cellular uptake. To further study the *in vivo* antitumor activity, the authors co-injected the TAMs (pre-treated with SPIONs) with the tumor cells to establish a tumor xenograft. The tumor growth was significantly attenuated by S+ and S–, but S– exhibited enhanced cytotoxicity at higher concentrations. They concluded that S+ may be considered for further clinical anti-tumoral evaluation.

In another original work, Li et al. designed a "stealth" nanoMOFs for safe and efficient anti-cancer therapy. They engineered the MIL-100(Fe) nanoMOF via a step approach. Initially, the drug molecules (Gem-MP) were loaded into the pores and on the surfaces of the nanoMOF through the impregnation in aqueous solutions; then, the Gem-MP-loaded nanoMOF was further modified by the surface coating of DOPC and DSPE-PEG 2000 in alcoholic solution. This work showed that the PEGylation of drug-loaded MIL-100(Fe) can not only influence the drug release rate but also regulate the degradation process. The authors showed that PEGylation of NanoMOFs can significantly reduce the human serum albumin adsorption, macrophage uptake, and exhibited notable *in vitro* anticancer activity. However, a further *in vivo* study is encouraged to explore their therapeutic potential.

In a review article, Xie et al. highlighted the important role of exosomes in the pathogenesis of age-related osteoporosis. They initially introduced the basic characteristics of exosomes, followed by the discussion of regulatory pathways in mesenchymal stem cells (MSCs) differentiation mediated by exosomes. Then, they summarized the recent findings regarding osteoblast proliferation and osteoclastogenesis effects stimulated by exosomes. They also pointed out the negative regulatory effects of exosomes on osteoclast differentiation. In the end, the authors commented on the opportunities and challenges of clinical translation on utilizing exosomes for treating osteoporosis. In another mini-review, Chen et al. briefly introduced the latest nanotechnological approaches for managing chronic pain. The application of Liposomes, PLGA nanoparticles, carbon-based, and other inorganic nanomaterials for the targeted/non-targeted neuropathic pain relief were highlighted. Moreover, the authors provided a detailed discussion in considerations of nanomaterial design for chronic pain relief and exemplified future strategies that can be explored, such as oral, inhalation, sprayable nanomaterials, electrical stimulation, microneedles, targeted delivery, etc. In another mini-review, Blum et al. introduced the concept of self-exciting photodynamic therapy (auto-PDT) to overcome the major limitation of conventional PDT, which is the insufficient tissue penetration depth of light. The auto-PDT nanoplatforms can drive the PDT process without the presence of an external light source. However, these platforms are usually designed in response to oxidative chemical excitation in the manner of chemiluminescence or Cherenkov luminescence (radiological excitation). The authors critically reviewed the design strategies, mechanisms of excitation, and the therapeutic effect of auto-PDT nanoplatforms with state-of-the-art researches. In addition, the authors also provided a detailed discussion of the recent studies of auto-PDT nanotherapeutics concerning design strategy, challenges, and themes in their synthesis and application.

Overall, this collection of articles contributes to the research topic with innovative designs and concepts in intelligent nanomedicine. The bio-nano engineered approach is not only the key strategy to overcome the intrinsic limitations of nanomaterials but also opening doors to new opportunities for patients. The fast pace and emerging breakthroughs in bio-nanotechnology will motivate and inspire both research and industry to accelerate these interdisciplinary translations to clinical applications.

AUTHOR CONTRIBUTIONS

All authors listed have made a substantial, direct and intellectual contribution to the work, and approved it for publication.

FUNDING

This work was financially supported in part by the National Natural Science Foundation of China (82001887, 81925019, and U1705281), the Major State Basic Research Development Program of China (2017YFA0205201), and the Program for New Century Excellent Talents in University, China (NCET-13-0502). JW was also supported by a grant from the Hundred Talents Program (75110-18841227) from Sun Yat-sen University and the Guangdong Basic and Applied Basic Research Foundation (2019A1515110326).

ACKNOWLEDGMENTS

We thank the support of the National Natural Science Foundation of China.

REFERENCES

Cai, W., Wang, J., Liu, H., Chen, W., Wang, J., Du, L., et al. (2018). Gold nanorods@metal-organic framework core-shell nanostructure as contrast agent for photoacoustic imaging and its biocompatibility. *J. Alloys Compds* 748, 193–198. doi: 10.1016/j.jallcom.2018.03.133

Liu, Y., Wang, J., Xiong, Q., Hornburg, D., Tao, W., and Farokhzad, O.C. (2021). Nano–bio interactions in cancer: from therapeutics delivery to early detection. *Acc. Chem. Res.* 54, 291–301. doi: 10.1021/acs.accounts.0c00413

Shi, Y., Wang, J., Liu, J., Lin, G., Xie, F., Pang, X., et al. (2020). Oxidative stress-driven DR5 upregulation restores TRAIL/Apo2L sensitivity induced by iron oxide nanoparticles in colorectal cancer. *Biomaterials* 233:119753. doi: 10.1016/j.biomaterials.2019.119753

Tao, W., Wang, J., Parak, W.J., Farokhzad, O.C., and Shi, J. (2019). Nanobuffering of pH-responsive polymers: a known but sometimes overlooked phenomenon and its biological applications. *ACS Nano* 13, 4876–4882. doi: 10.1021/acsnano.9b01696

Zhang, P., Wang, J., Chen, H., Zhao, L., Chen, B., Chu, C., et al. (2018). Tumor microenvironment-responsive ultrasmall nanodrug generators with enhanced tumor delivery and penetration. *J. Am. Chem. Soc.* 140, 14980–14989. doi: 10.1021/jacs.8b09396

Conflict of Interest: The authors declare that the research was conducted in the absence of any commercial or financial relationships that could be construed as a potential conflict of interest.

frontiers
in Bioengineering and Biotechnology

ORIGINAL RESEARCH
published: 08 May 2020
doi: 10.3389/fbioe.2020.00378

β-Elemene Reverses the Resistance of p53-Deficient Colorectal Cancer Cells to 5-Fluorouracil by Inducing Pro-death Autophagy and Cyclin D3-Dependent Cycle Arrest

Ruonan Zhang[1,2,3], Ting Pan[1,2], Yu Xiang[1,2], Mingming Zhang[1,2], Jiao Feng[1,2], Shuiping Liu[1,2], Ting Duan[1,2], Peng Chen[1,2], Bingtao Zhai[1,2], Xiaying Chen[1,2], Wengang Wang[1,2], Bi Chen[1,2,3], Xuemeng Han[1,2], Liuxi Chen[1,2], Lili Yan[1,2], Ting Jin[1,2], Ying Liu[4], Guohua Li[1,2], Xingxing Huang[1,2], Wenzheng Zhang[1,2], Yitian Sun[1,2], Qiujie Li[1,2], Qin Zhang[1,2], Lvjia Zhuo[1,2], Tian Xie[1,2], Qibiao Wu[3]* and Xinbing Sui[1,2,3]**

[1] Department of Medical Oncology, Holistic Integrative Pharmacy Institutes, The Affiliated Hospital of Hangzhou Normal University, College of Medicine, Hangzhou Normal University, Hangzhou, China, [2] Key Laboratory of Elemene Class Anti-Cancer Chinese Medicine of Zhejiang Province and Engineering Laboratory of Development and Application of Traditional Chinese Medicine from Zhejiang Province, Hangzhou Normal University, Hangzhou, China, [3] State Key Laboratory of Quality Research in Chinese Medicines, Faculty of Chinese Medicine, Macau University of Science and Technology, Macau, China, [4] Department of Medical Oncology, Sir Run Run Shaw Hospital, Zhejiang University, Hangzhou, China

OPEN ACCESS

Edited by:
Gang Liu,
Xiamen University, China

Reviewed by:
Wei Li,
First Affiliated Hospital of Soochow University, China
Qinghua Yao,
Zhejiang Cancer Hospital, China
Deqiang Wang,
Affiliated Hospital of Jiangsu University, China

****Correspondence:***
Tian Xie
drxiet@aliyun.com
Qibiao Wu
qbwu@must.edu.mo
Xinbing Sui
hzzju@zju.edu.cn

Specialty section:
This article was submitted to Nanobiotechnology, a section of the journal Frontiers in Bioengineering and Biotechnology

Received: *12 March 2020*
Accepted: *06 April 2020*
Published: *08 May 2020*

Citation:
Zhang R, Pan T, Xiang Y, Zhang M, Feng J, Liu S, Duan T, Chen P, Zhai B, Chen X, Wang W, Chen B, Han X, Chen L, Yan L, Jin T, Liu Y, Li G, Huang X, Zhang W, Sun Y, Li Q, Zhang Q, Zhuo L, Xie T, Wu Q and Sui X (2020) β-Elemene Reverses the Resistance of p53-Deficient Colorectal Cancer Cells to 5-Fluorouracil by Inducing Pro-death Autophagy and Cyclin D3-Dependent Cycle Arrest. Front. Bioeng. Biotechnol. 8:378. doi: 10.3389/fbioe.2020.00378

Objective: Colorectal cancer is a malignant tumor of the digestive system with high morbidity and mortality. 5-fluorouracil remains a widely used chemotherapeutic drug in the treatment of advanced colorectal cancer, but chemotherapy drugs are prone to develop drug resistance, p53 deletion or mutation is an important reason for the resistance of colorectal cancer cells to 5-fluorouracil. β-elemene has been proved to have the potential of reverse chemotherapy drug resistance, but the mechanism is unknown. This study aimed to investigate the effect of β-elemene to 5-fluorouracil in drug-resistant p53-deficient colorectal cancer cells HCT116p53$^{-/-}$, and determine the possible molecular mechanism of β-elemene to reverse 5-fluorouracil resistance.

Methods: The effect of β-elemene on HCT116p53$^{-/-}$ cell activity was detected by Cell counting Kit-8. Cell proliferation was detected by monoclonal plate. The apoptosis was detected by flow cytometry and western blot. The autophagy was detected by western blot, immunofluorescence and transmission electron microscope. Determine the role of Cyclin-related protein Cyclin D3 in β-elemene reversing the resistance of HCT116p53$^{-/-}$ to 5-fluorouracil was detected by overexpression of Cyclin D3. The effect of β-elemene on the tumorigenic ability of p53-deficient colorectal cancer cells was detected establishing HCT116p53$^{-/-}$ all line xenograft model.

Results: For p53 wildtype colorectal cancer cells, β-elemene could augment the sensitivity of 5-fluorouracil, for p53-deficient colorectal cancer cells, β-elemene significantly inhibited cell proliferation in a concentration-dependent manner, and reversed the resistance of HCT116p$53^{-/-}$ to 5-fluorouracil by inducing pro-death autophagy and Cyclin D3-dependent cycle arrest.

Conclusion: β-elemene enhances the sensitivity of p53 wild-type cells to 5-fluorouracil, β-elemene can reverse the resistance of HCT116p$53^{-/-}$ to 5-fluorouracil by inducing pro-death autophagy and Cyclin D3-dependent cycle arrest in p53-deficient colorectal cancer,which will provide a new method for the treatment of p53 deletion colorectal cancer patients.

Keywords: colorectal cancer, p53, β-elemene, 5-fluorouracil, autophagy, cell cycle, drug resistance

INTRODUCTION

Cancer is one of the most serious public health problems in the world and has become a major killer of human health. According to the results of cancer data published in 2020 (Siegel et al., 2020), it is estimated that there will be 147,950 new cancer cases worldwide in 2020, and the incidence of colon cancer is 8.5%, ranking third, with 53,200 cancer deaths, and the death rate of colon cancer will be 9%, ranking third. Statistics of cancer data in China showed that (Chen W. et al., 2016) the incidence of colon cancer in men accounts for 10.98%, the incidence of women accounts for 7.92%, ranks third; male mortality accounts for 9.17%, female mortality accounts for 6.05%, ranks fifth.

Colorectal cancer is a malignant gastrointestinal tumor with very high morbidity and mortality. Due to the lack of early symptoms, most patients with colorectal cancer are advanced when diagnosed, and their prognosis is poor. And because the incidence of colorectal cancer is increasing year by year, it has brought tremendous mental and economic pressure to society. Current treatments include surgery, radiotherapy, chemotherapy, molecular targeted therapy, immunotherapy, and traditional Chinese medicine. Chemotherapy is a routine treatment for patients with advanced colorectal cancer. At present, the commonly used chemotherapy regimens in the clinic include FOLFIRI regimen for the combination therapy of aflibercept + fluorouracil, Leucovorin, and Irinotecan (Chau et al., 2020); mFOLFOX7 regimen combining Oxaliplatin, calcium folate and fluorouracil (Li et al., 2014); FOLFOX regimen combination with monoclonal antibodies (Raimondi et al., 2019). Fluorouracil drugs represented by 5-fluorouracil (5-Fu) are the first choice for the treatment of advanced colorectal cancer.

5-Fu plays an anti-tumor role by inhibiting thymidine adenylate synthase activity, preventing methylation of deoxythymidylate, and impairing DNA synthesis and repairing ability (Saif and Diasio, 2016). The efficacy of 5-Fu is usually limited by its resistance, and its resistance mechanisms include primary and secondary resistance. Increased transcription and translation levels of thymidine phosphorylase are the main causes of primary 5-Fu resistance. At present, there is no clear explanation of the molecular mechanism of secondary resistance to 5-Fu. The resistance mechanisms that have been reported in the literature mainly include the following: (1) The loss of thymidine kinase (TK) activity that catalyzes the metabolism of 5-Fu to an active effective product results in 5-Fu resistance (Sakamoto et al., 2015); (2) Dihydropyrimidine dehydrogenase (DPD) is mainly used to catalyze the catabolism of 5-Fu, and its enhanced activity causes 5-Fu to break down in large quantities, making it difficult to achieve effective drug concentrations for treating tumors (Fidai et al., 2018); (3) Lack of reduced folic acid substrate; (4) Mutations of tumor suppressor genes such as p53 (Dominijanni and Gmeiner, 2018); (5) Abnormal activation of signaling pathways such as Ras and Akt (Zong et al., 2019); (6) Related to DNA repair Mutation or deletion. The above molecular mechanism can make tumor cells resistant to 5-Fu and affect the therapeutic effect. Therefore, the enhancement of 5-Fu sensitivity is a research hotspot and needs to be further explored.

In recent years, there have been many therapeutic drugs for colorectal cancer. Fluorouracil drugs represented by 5-Fu are the cornerstone of colorectal cancer chemotherapy (Gajjar et al., 2018). During the treatment of recurrent tumors, stubborn tumor cells will produce chemotherapy. Drug resistance will greatly reduce the efficacy of chemotherapy drugs. Therefore, drug resistance has become a major problem that needs to be urgently addressed in clinical tumor treatment (Shamekhi et al., 2019), and how to reverse the resistance of 5-Fu has also become the focus of research.

It is reported that p53 as a tumor suppressor protein can control 5-Fu catabolism through the expression of the key rate-limiting enzyme of pyrimidine-degrading dihydropyrimidine dehydrogenase (DPYD). When p53 is mutated or deleted, 5-Fu catabolism is out of control to make cells resistant to drugs (Gokare et al., 2017). According to the distribution of p53 mutations in cancer worldwide[1], it is known that the p53 mutation rate of colorectal cancer is 60%, ranking second in the p53 mutation rate of all cancers. Among all gene mutations in colorectal cancer, the p53 mutation rate is second only to allophycocyanin (APC). p53 can regulate a variety of physiological processes and inhibit tumor cell growth and reproduction (Gao et al., 2020), so it is of great significance to study the relationship between p53 mutations and colorectal cancer.

The mechanisms by which 5-Fu acts on p53 and participates in cellular processes are as follows: 5-Fu directly acts on p53: (1) p53 can inhibit the expression of IKB kinase (IKBK). IKBK participates in the intracellular immune response caused by cytokines, inhibits the phosphorylation of inhibitory protein (IκB), and inhibits the activation of NF-κB, thus inhibits cell survival; (2) p53 inhibits intracellular phosphatidylinositol kinase

---

[1] http://www.genecards.org

(PI3K) expression, or activates AMP-dependent protein kinase (AMPK), thereby inhibiting mammalian target of rapamycin (mTOR) expression and causing autophagy in tumor cells (Petroni et al., 2020); (3) p53 can promote cell apoptosis by activating members of the cysteine-containing aspartic proteolytic enzyme (caspase) family, B lymphoma-2 gene (Bcl-2), and other apoptosis-related proteins; (4) p53 can also directly acts on p21, inhibiting the expression of cycle-related proteins and causing cell cycle arrest (Sun et al., 2019). 5-Fu also can indirectly acts on p53:(1) 5-Fu indirectly acts on p53 by activating mitogen-activated protein kinase (MAPK), c-Jun amino terminal kinase (JNK), etc., causing apoptosis, autophagy, and cycle arrest; (2) 5-Fu causes DNA damage, p53 expression is affected by proteins related to DNA repair, causing apoptosis, autophagy and cycle arrest (Hafner et al., 2019).

Elemene (1-methyl-1-vinyl-2,4-diisopropenyl-cyclohexane) is a natural compound, and it has been found in more than 50 different plants, including warm turmeric, earthy wood, etc. Elemene has three isomers α, β, γ-elemene. β-elemene is the most active ingredient in the treatment of various cancers, accounting for 85% of the total (Yao et al., 2008; Wu et al., 2009; Sun et al., 2016).

Modern pharmacological studies have shown that β-elemene can inhibit many types of cancer by regulating multiple signaling pathways and targeting genes or proteins without causing serious side effects (Lee et al., 2012). β-elemene used to be treated with variety of cancers, including lung cancer (Li et al., 2011), esophageal cancer (Chen X. et al., 2016), breast cancer (Guan et al., 2014), gastric cancer (Imanishi et al., 2019), liver cancer (Zhai et al., 2018), melanoma cancer (Shi et al., 2015), ovarian cancer (Li et al., 2013b), can also cross the blood-brain barrier to treat gliomas (Feng et al., 2017). Its main antitumor mechanisms include inhibition of tumor cell proliferation, elimination of tumor cells, induction of apoptosis and differentiation, induction of autophagy, induction of cell cycle arrest, inhibition of tumor metastasis and immune regulation (Chen et al., 2017; Satyavarapu et al., 2018; Zhang et al., 2018).

In vitro research and clinical practice also proved that β-elemene can reverse the resistance of tumor cells to a variety of anticancer drugs (Mu et al., 2016) including chemotherapeutics, tyrosine kinase inhibitor gefitinib, etc. However, the target of β-elemene and the effect of reversing the resistance to 5-Fu in p53-deficient colorectal cancer in clinical treatment have not been reported.

As many tumors develop resistance to conventional chemotherapy and radiotherapy soon after treatment, even at the beginning of treatment, this has become one of the main reasons for the failure of tumor treatment. The strategy of western medicine in overcoming tumor resistance is to replace with new antitumor drugs. As a result, new resistance or even multidrug resistance is easy to be produced, and Chinese medicine has incomparable advantages in overcoming antitumor resistance. Therefore, studying the role of β-elemene in reversing 5-Fu resistance and clarifying its target and molecular mechanism has particularly important clinical significance, which will provide important theoretical basis and treatment strategies for the treatment of p53-deficient colorectal cancer patients.

MATERIALS AND METHODS

Cell Lines and Culture Methods

The human colorectal cancer lines HCT116p53$^{+/+}$ and HCT116p53$^{-/-}$ were a gift from Mr. Liu Jiang, Hangzhou Normal University. The cells were cultured in McCoy's 5A medium (GENOM, GNM16600, China), supplemented with 10% heat-inactivated fetal bovine serum at 37°C with 5% CO_2 and 95% humidity, and the culture medium was usually changed every 2 days. The fetal bovine serum was purchased from Corille (184590, Australia).

Antibodies and Chemicals

Anti-GAPDH (#5174) antibody and p21 (#2947), p27 (#3686) were purchased from Cell Signaling Technology (CST). Anti-p53 (sc-126) antibody was obtained from Santa Cruz. Autophagy marker LC3B (#3868) and Beclin-1 (#3738) was purchased from CST. Apoptosis marker Active caspase-3 (BS7004) was obtained from Bioworld, Cleaved PARP (#5625) was purchased from CST. Cell cycle protein CDK2 (#2546), CDK4 (#12790), CDK6 (#3136), Cyclin D3 (#2936) were purchased from CST. Anti-rabbit IgG, HRP-linked Antibody (#7074) and Anti-mouse IgG, HRP-linked Antibody (#7076) were also obtained from CST.

β-elemene was obtained from LKT lab (E4418, purity ≥98%), β-elemene was dissolved in ethanol (02483, Supelco). 5-Fluorouracil (HY-90006), Bafilomycin A1 (HY-100558) and Hydroxychloroquine (HCQ) (HY-B1370) were purchased from MCE. Ampicillin (A8180) was obtained from Solarbio. Kanamycin (K8020) was obtained from Solarbio. *Trans*5α Chemically Competent Cell (CD201-01) was purchased from Transgene. LB Broth (L1010) was obtained from Solarbio. LB agar (L1015) was obtained from Solarbio. AxyPrep Plasmid Miniprep Kit (AP-MN-P-250G) was purchased from Axygen. pCMV6-Entry Tagged Cloning Vector (PS100001) and Cyclin D3 plasmid (RC227101) were obtained from Origene. pMRX-IP-GFP-LC3-RFP-LC3ΔG (#84572) was purchased from addgene. Lipofectamine^{TM} 2000 Transfection Reagent (11668019) and ProLong® Gold Antifade Reagent (P10144) were purchased from Thermo Fisher Scientific. DAPI (C0065) was purchased from Solarbio.

Cell Proliferation and Viability Assays

Cell viability was evaluated using the Cell Counting Kit-8 (CCK-8) (LJ621, Dojindo, Japan) according to the manufacturer's instructions. HCT116p53$^{+/+}$ and HCT116p53$^{-/-}$ cells were seeded in 96-well flat bottom microtiter plates at a density of 5,000 cells per well. Incubated overnight, add 100 μl of media containing different concentrations of β-elemene, and incubate in the incubator for 24, 48, and 72 h. After incubation, aspirate the medium from the 96-well plate and add the medium mixed with CCK8 (medium: CCK8 = 10: 1) Continue to incubate for 4 h at 37℃. After 4 h, stop the culture. The optical density values were determined at least in triplicate against a reagent blank at a reference wavelength of 450 nm using a spectrophotometer microplate reader. The experiment was repeated three times.

Clone Formation Assays

HCT116p53$^{+/+}$ and HCT116p53$^{-/-}$ cells were seeded in 10 cm dish at a density of 1,000 cells per well, and then culture them in a cell incubator at 37℃, 5% CO_2 and saturated humidity. When the clone can be seen under the microscope, add the medium containing different drugs (control, 5-Fu, β-elemene, 5-Fu + β-elemene), change the new culture medium once every 3 days, and continue to culture for 2 weeks. When visible macroscopic clones appear, the culture is terminated. The supernatant was discarded and carefully washed twice with PBS. Fix with 4% formaldehyde for 15 min. Then remove the fixing solution, add an appropriate amount of 0.25% crystal violet staining solution, dye for 15–20 min, then slowly wash away the staining solution with running water, and air dry. Invert the plate and overlay a grid of transparencies and count the clones directly with the naked eye, or count more than 50 cells with a microscope (low magnification). The experiment was repeated three times.

Cell Apoptosis Assays

Flow cytometry was used to detect apoptosis induced by 5-Fu, β-elemene, and 5-Fu + β-elemene. Using the Annexin V-FITC/PI Apoptosis Detection Kit (556547) from BD in the United States, each operation step is strictly performed according to the instructions. HCT116p53$^{+/+}$ and HCT116p53$^{-/-}$ cells were seeded in 6 cm dish at a density of 5×10^5 cells per well, and then culture them in a cell incubator at 37℃, 5% CO_2 and saturated humidity. Incubated overnight, add different treatment group media (control, 5-Fu, β-elemene, 5-Fu + β-elemene) for 24 h, collect all cell culture fluids and cells, centrifuge at 800 *g* for 5 min and remove the supernatant. Wash the cells with cold PBS, centrifuge, discard the supernatant, then resuspend the cells by adding 1 ml of 1 × binding buffer, and adjust the cell concentration to 10^6 cells/ml. Add 100 μl (10^5 cells) of cell suspension to the flow tube, add 5 μl FITC-Annexin V and 5 μl PI to each flow tube. Mix the cells with the staining agent, and leave it in the dark for 15 min at room temperature. Then add 400 μl of 1 × binding buffer to each flow tube, and test it on the machine. Annexin V-FITC shows green fluorescence and PI shows red fluorescence. The experiment was repeated three times.

Cell Transfection

The Lipofectamine^{TM} 2000 Transfection Reagent (11668019) was used to transfect the HCT116 p53$^{-/-}$ cells. Transfection was performed according to the manufacturer's instructions. HCT116 p53$^{-/-}$ cells were seeded in 6 cm dish at a density of 5×10^5 cells per well. Incubated overnight, the cell fusion degree reached 70–80%. Add 50 μl OPTI-MEM to two 1.5 ml EP tubes, add 3 μg plasmid to one tube, 9 μl Lipofectamine 2000 to one tube, and add OPTI-MEM containing Lipofectamine 2000 to OPTI-MEM with plasmid. After mixing, leave it at room temperature for 5 min, then add it dropwise to the culture well and shake gently, mix it in the incubator and incubate for 6 h, then change to complete medium and continue to culture.

Western Blot

HCT116p53$^{+/+}$ and HCT116p53$^{-/-}$ cells were seeded in 6 cm dish at a density of 6×10^5 cells per well. Incubated overnight, add different treatment group media (control, 5-Fu, β-elemene, 5-Fu + β-elemene) for 24 h. Cells were harvested and lysed using the RIPA buffer (P0013B, Beyotime) in the presence of a phenylmethyl sulfonylfluoride (PMSF) (#8553, CST). Protein concentration was determined using the BCA Protein Assay Kit (P0009, Beyotime). Equivalent amounts of protein were resolved and mixed with 5× SDS-PAGE protein sample buffer (P0015, Beyotime), electrophoresed in SDS-PAGE, transferred to PVDF membranes (Merck Millipore, Billerica, MA, United States). The blotted membranes were blocked with 5% skim milk for 1 h and incubated with primary antibodies overnight at 4℃. Day 2, washed with TBST (CW0043S, CWBIO), then incubated with suitable HRP-conjugated second antibodies and subjected to enhanced chemiluminescent staining using an ECL detection system (Bio-Rad). All experiments were conducted in triplicate.

Immunofluorescence Assay

For immunofluorescence assays, 3×10^5 cells were seeded into 6-well plates with coverslips, transiently transfected the plasmid with RFP-GFP-LC3B into HCT116p53$^{-/-}$ cells for 48 h, and treated with control, 5-Fu, β-elemene, and 5-Fu + β-elemene for 24 h. Then the cells were fixed in 4% paraformaldehyde, washed with PBS and stained with 0.05% DAPI for 15 min. Finally, washed with PBS and mounted with anti-fluorescent quencher (ProLong® Gold Antifade Reagent). Images were obtained with the laser scanning confocal microscope (Nikon, Japan).

Transmission Electron Microscopy

HCT116p53$^{+/+}$ and HCT116p53$^{-/-}$ cells were seeded in 6 cm dish at a density of 6×10^5 cells per well. Incubated overnight, add different treatment group media (control, 5-Fu, β-elemene, 5-Fu + β-elemene, Bafilomycin A1, 5-Fu + β-elemene+ Bafilomycin A1) for 24 h. Collected cells and fixed with 2.5% glutaraldehyde, then dehydrated, embedded, sectioned, stained, and finally observed for autophagic vacuole using a Transmission electron microscopy (TEM).

Animal Experiments

Eighteen female nude mice of 6-week-old BALB/c thymus deletion weighing about 20 g were purchased. Nude mice were randomly divided into six groups: control group, 5-Fu group, β-elemene group, HCQ group, 5-Fu + β-elemene group, and 5-Fu + β-elemene + HCQ group. 10^6/100 μl of the cell suspension was inoculated under the skin of the nude mice. On the third day of vaccination, the nude mice in the control group were injected intraperitoneally with PBS daily. The 5-Fu group was intraperitoneally injected with 20 mg/kg/2d 5-Fu. The β-elemene group was intraperitoneally injected with 100 mg/kg/d β-elemene. The HCQ group intraperitoneally injected 60 mg/kg/d HCQ. The 5-Fu + β-elemene group was intraperitoneally injected with 20 mg/kg/2d 5-Fu and 100 mg/kg/d β-elemene. HCQ group intraperitoneally injected 60 mg/kg/d HCQ. 5-Fu + β-elemene + HCQ group intraperitoneally injected 20 mg/kg/2d 5-Fu and 100 mg/kg/d β-elemene and 60 mg/kg/d HCQ. Record daily, and measure the long and short diameters of the tumor every 3 days. Tumor volume = (shortest diameter)^2 × longest diameter × 0.5. On the 24th day after vaccination, all nude mice were sacrificed by cervical dislocation, with time as the abscissa and tumor volume as the ordinate to make growth curves.

Statistical Analysis

Data are expressed as means ± SD of three independent experiments. Statistical analysis was performed using Prism 7.0 GraphPad Software. The significance of differences between groups was determined using t-test. A *p*-value <0.05 was considered statistically significant.

RESULTS

5-Fu and β-Elemene Inhibit Proliferation of Colorectal Cancer Cells

Previous literature has confirmed that p53-deficient colorectal cancer cells HCT116p53$^{-/-}$ are resistant to 5-Fu (Sui et al., 2014). So we investigated the sensitivity of 5-Fu in HCT116p53$^{+/+}$ and HCT116p53$^{-/-}$ cells. The two cells were treated with various concentrations of 5-Fu for 24 h and the cell viability was assessed by the CCK-8. The results showed that 5-Fu inhibits cell proliferation in HCT116p53$^{+/+}$ cells in a dose-dependent manner. HCT116p53$^{+/+}$ cells were highly sensitive to 5-Fu, but very few dying cells emerged in HCT116p53$^{-/-}$ cells after 5-Fu treatment ($^{***}p < 0.001$), indicating that HCT116p53$^{-/-}$ cells may be insensitive or resistant to 5-Fu (**Figure 1A**). The 24 h IC$_{50}$ of 5-Fu for HCT116p53$^{+/+}$ cells was 23.39 μM, so we used 20 μM 5-Fu in HCT116p53$^{+/+}$ cells and HCT116p53$^{-/-}$ cells for 24 h in subsequent experiments.

To study the effect of β-elemene on the proliferation of HCT116p53$^{+/+}$ and HCT116p53$^{-/-}$ cells, the cells were treated with various concentrations of β-elemene for 24, 48, and 72 h, the cell inhibited rates were assessed by the CCK-8 (**Figure 1A**). The results showed that β-elemene inhibit cell proliferation in a dose-dependent manner. As the concentration of β-elemene increased, the inhibition rates of HCT116p53$^{+/+}$ cells was increased. The IC$_{50}$ of 24, 48, and 72 h were 42.20, 39.17, and 38.27 μg/ml, respectively. HCT116p53$^{-/-}$ cells also had a concentration and time dependence on β-elemene. As the concentration and time of β-elemene increased, the inhibition rates on HCT116p53$^{-/-}$ cells was increased. The IC$_{50}$ of the HCT116p53$^{-/-}$ cells at 24, 48, and 72 h were 71.75, 14.88, and 9.40 μg/ml, respectively. Consequently, we used 40 μg/ml β-elemene in HCT116p53$^{+/+}$ cells and HCT116p53$^{-/-}$ cells for 24 h in subsequent experiments.

Combination of 5-Fu and β-Elemene Can Increase the Sensitivity of HCT116p53$^{+/+}$ Cells to 5-Fu and Reverse the Resistance of HCT116p53$^{-/-}$ Cells to 5-Fu

To investigate the effect of β-elemene on the sensitivity of 5-Fu to HCT116p53$^{-/-}$ cells and HCT116p53$^{+/+}$ cells, we performed a clone formation assays to detect cell proliferation. Every cell line divided into four groups: control group, 5-Fu group, β-elemene group, 5-Fu + β-elemene group (**Figure 1B**). The results showed that both 5-Fu and β-elemene can inhibit the proliferation of HCT116p53$^{+/+}$ cells, while the inhibition effect of 5-Fu + β-elemene is more obvious. This may indicate that the sensitivity of 5-Fu is enhanced by β-elemene. For HCT116p53$^{-/-}$ cells, 5-Fu has little effect on the proliferation of cells, but β-elemene can inhibit clone formation of HCT116p53$^{-/-}$ cells. The combination of 5-Fu and β-elemene can significantly inhibit the reproduction of HCT116p53$^{-/-}$ and reduce the colony formation rates. This may indicate that β-elemene reversed 5-Fu resistance.

To further investigate whether β-elemene can enhance the sensitivity of 5-Fu to HCT116p53$^{-/-}$ cells and reverse the resistance of 5-Fu to p53-deficient colorectal cancer cells, we used flow cytometry to detect the apoptosis rates of cells (**Figure 1C**). The results showed that HCT116p53$^{-/-}$ cells were not sensitive to 5-Fu, and cells have little apoptosis in the 5-Fu group. More cells apoptosis in β-elemene group, but it was not obvious compared with the control group. A large number of cells died in the 5-Fu + β-elemene group, and apoptosis was significantly higher than control group ($^{*}p < 0.05$), indicating that β-elemene can reverse the resistance of 5-Fu to p53-deficient colorectal cancer cells. For HCT116p53$^{+/+}$ cells, both 5-Fu and β-elemene can cause apoptosis ($^{*}p < 0.05$). And the apoptosis of the 5-Fu + β-elemene group was significantly higher than the control group ($^{**}p < 0.01$), indicating that β-elemene can increase the sensitivity of 5-Fu.

β-Elemene Reverses the Resistance of HCT116p53$^{-/-}$ Cells to 5-Fu by Inducing Pro-death Autophagy

To determine how β-elemene reverse the resistance of HCT116p53$^{-/-}$ cells to 5-Fu, the HCT116p53$^{+/+}$ cells and HCT116p53$^{-/-}$ cells were treated with 5-Fu, β-elemene, and 5-Fu + β-elemene for 24 h, and then the protein was extracted for Western blot. The results showed that LC3B, an autophagy marker protein, was significantly increased in β-elemene group and 5-Fu + β-elemene group in HCT116p53$^{-/-}$ cells (**Figure 2A**). Besides, the autophagy protein Beclin-1 showed the same result. However, there was no change in autophagy protein in HCT116p53$^{+/+}$ cells, indicating that there was no autophagy in HCT116p53$^{+/+}$ cells. In HCT116p53$^{-/-}$ cells, Active caspase-3, an apoptosis protein, was increased in β-elemene group and 5-Fu + β-elemene group, indicating that β-elemene increased apoptosis by promoting autophagy of HCT116p53$^{-/-}$ cells.

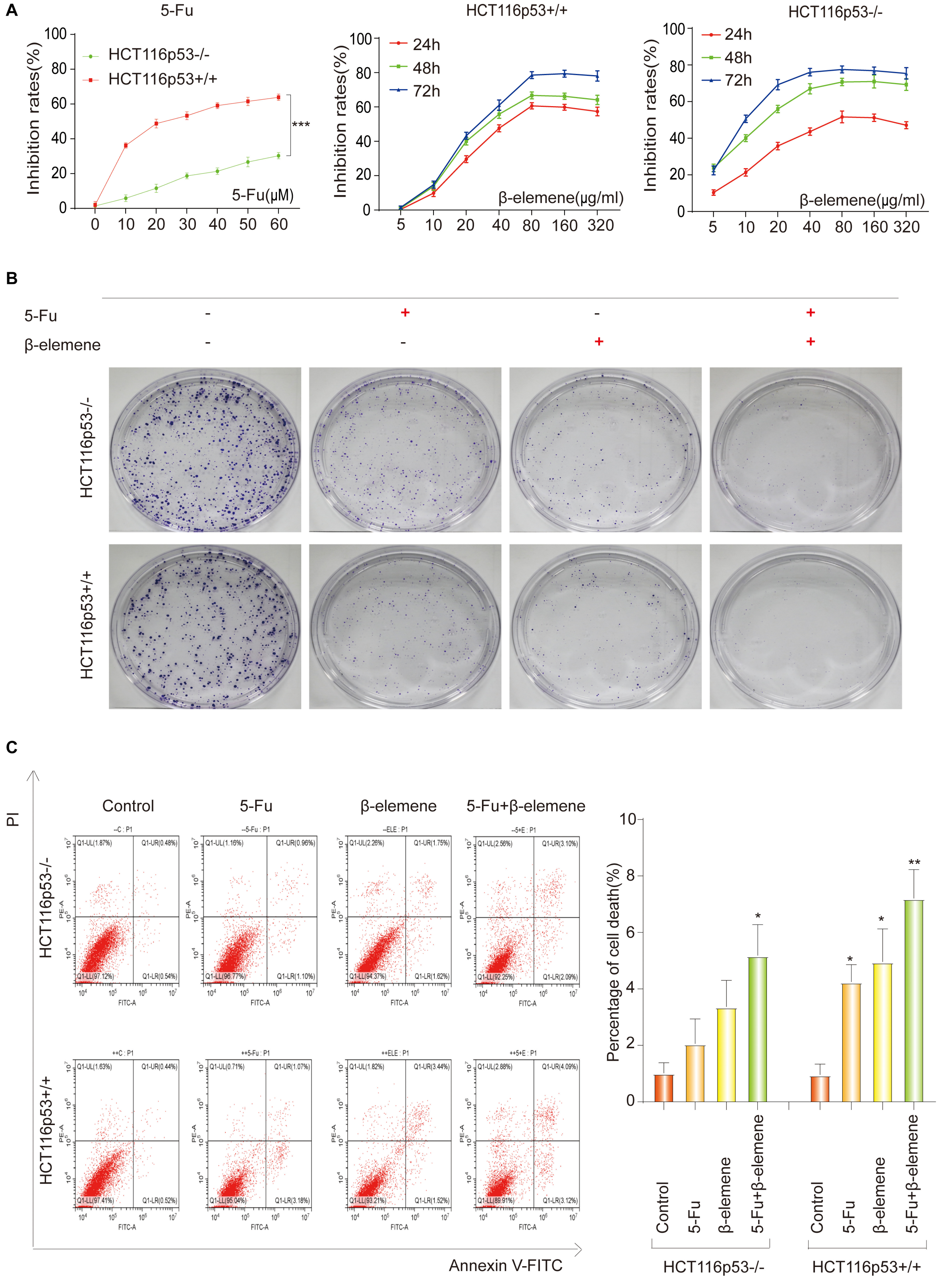

FIGURE 1 | 5-Fu and β-elemene inhibits proliferation of colorectal cancer cells. **(A)** HCT116p53 $^{+/+}$ and HCT116p53$^{-/-}$ cells were treated with different concentrations of 5-Fu for 24 h, or treated with β-elemene for 24, 48, and 72 h, the cell viability was examined by CCK8; **(B)** the cell proliferation was detected by a clone formation assays; **(C)** the apoptosis rate of cells was examined by flow cytometry. (*$p < 0.05$, **$p < 0.01$, $n = 3$).

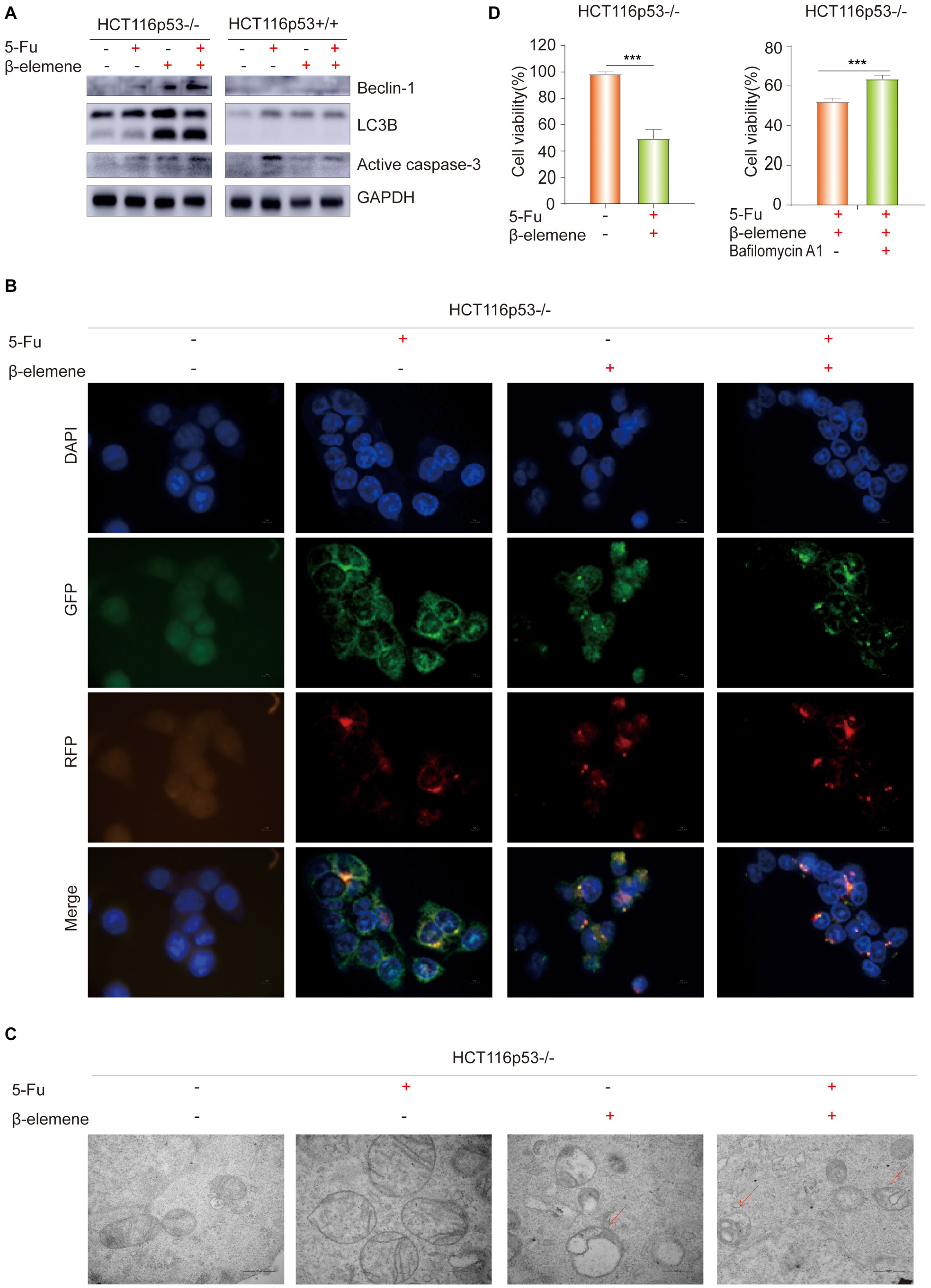

FIGURE 2 | β-elemene reverse the resistance of HCT116p53$^{-/-}$ cells to 5-Fu by inducing pro-death autophagy. **(A)** HCT116p53$^{+/+}$ and HCT116p53$^{-/-}$ cells were treated with control, 5-Fu, β-elemene, 5-Fu + β-elemene, the protein expression of LC3B, Beclin-1, and Active caspase-3 were examined by Western blot; **(B)** HCT116p53$^{-/-}$ cells were treated with control, 5-Fu, β-elemene, 5-Fu + β-elemene, the autophagy flow was observed by immunofluorescence, red arrow indicates autolysosomes; **(C)** HCT116p53$^{-/-}$ cells were treated with control, 5-Fu, β-elemene, 5-Fu + β-elemene, the occurrence of autophagy was observed by transmission electron microscope; **(D)** HCT116p53$^{-/-}$ cells were treated with 5-Fu + β-elemene, 5-Fu + β-elemene + Bafilomycin A1, the cell viability was examined by CCK8. (***$p < 0.001$, $n = 3$).

LC3B is a hallmark protein of autophagy. Through immunofluorescence-labeled LC3B, the localization of LC3B in cells can be observed under a fluorescence microscope. The amount of LC3BII can reflect the autophagy activity of cells, the number of autophagy particles indicates the degree of autophagy (Kaizuka et al., 2016). Increased autophagy caused by β-elemene was further confirmed by immunofluorescence (IF) staining, we transiently transfected the plasmid with RFP-GFP-LC3B into HCT116p53$^{-/-}$ cells, and treated with 5-Fu, β-elemene, and 5-Fu + β-elemene. The IF staining data revealed that there were no autophagy particles in the control group and 5-Fu group, autophagy particles were increased in the β-elemene group and 5-Fu + β-elemene group, and red fluorescence enhancement in the 5-Fu +β-elemene group, which proved that β-elemene promoted autophagy in HCT116p53$^{-/-}$ (**Figure 2B**).

Observing the formation and number of autophagosomes with a transmission electron microscope (TEM) is the most commonly used method for measuring autophagy (Levy et al., 2017). Phagocytic vesicles are characterized by a crescent or goblet-shaped, double-layered or multi-layered membrane with a tendency to surround cytoplasmic components. Autophagosomes is characterized by a vacuole-like structure with double or multilayer membranes, which contain cytoplasmic components such as mitochondria, endoplasmic reticulum, and ribosomes. Autophagosome are characterized by a monolayer membrane and cytoplasmic components that have been degraded (Amaravadi et al., 2019). To better observe the occurrence of autophagy, TEM was performed after the cells were treated with control, 5-Fu, β-elemene, 5-Fu + β-elemene (**Figure 2C**). It was observed that the mitochondrial bilayer membrane structure in the control group and 5-Fu group was intact, indicating that there was no autophagy. The mitochondrial structure in the β-elemene group and 5-Fu + β-elemene group was destroyed. Red arrow indicates the fusion of autophagosomes and lysosomes. The number of Autophagolysosomes increased in the 5-Fu + β-elemene group, indicating that β-elemene can induce autophagy in HCT116p53$^{-/-}$ cells and increase the formation of autophagosome.

To verify the type of autophagy induced by β-elemene in HCT116p53$^{-/-}$ cells, we performed a CCK-8 assay on HCT116p53$^{-/-}$ cells (**Figure 2D**). The results showed that 5-Fu + β-elemene can significantly reduced the activity of HCT116p53$^{-/-}$ cells ($^{***}p < 0.001$). Then we added autophagy inhibitor Bafilomycin A1 (20 nM) to HCT116p53$^{-/-}$ cells, compared with the 5-Fu + β-elemene group, the cell activity of 5-Fu + β-elemene+ Bafilomycin A1 group was significantly increased ($^{***}p < 0.001$), indicating that β-elemene induced pro-death autophagy in HCT116p53$^{-/-}$ cells.

β-Elemene Reverses the Resistance of HCT116p53$^{-/-}$ Cells to 5-Fu by Inducing Cyclin D3-Dependent Cycle Arrest

As everyone knows that p53 directly activates p21, which can inhibit the cell cycle-related protein such as Cyclin D and CDK4/6, leading to G1 phase cell arrest (Cayrol et al., 1998). Cyclin D3 can directly combine with CDK4/CDK6 to form a complex and promote the cell cycle process. Therefore, we speculated that β-elemene can inhibit cell growth by inhibiting the cell cycle process. To verify this view, Western blot was used to detect cell cycle-related proteins. The results showed that the expression of Cleaved PARP protein was increased in β-elemene group and 5-Fu + β-elemene group, indicating that β-elemene increased the apoptosis of HCT116p53$^{-/-}$ cells and reverse 5-Fu resistance. The expression of CDK2/4/6 and Cyclin D3, which are related to G1 phase proteins, were decreased in β-elemene group and 5-Fu + β-elemene group, indicating that β-elemene can inhibit the expression of G1 phase proteins and cause cycle arrest (**Figure 3A**).

Effect of Overexpression of Cyclin D3 on β-Elemene Reverses the Resistance of HCT116p53$^{-/-}$ Cells to 5-Fu

The above results showed that β-elemene induced cell cycle arrest. In the β-elemene group and 5-Fu + β-elemene group, the expression of the cell cycle-related protein Cyclin D3 was significantly reduced than the control group. Because Cyclin D forms a complex with CDK4/6, which can lead to G1 phase arrest. Therefore, we supposed that the cell cycle arrest caused by β-elemene is related to Cyclin D3. To verify this guess, we transiently transfected the Cyclin D3 plasmid and the empty plasmid into HCT116p53$^{-/-}$ cells, respectively. After transfection, they were divided into control group and 5-Fu + β-elemene group. Western blot results showed that overexpressing Cyclin D3 increased the expression of Cyclin D3 protein and CDK6 protein, while the expression of Cyclin D3 protein and CDK6 protein were reduced by treated with 5-Fu + β-elemene (**Figure 3B**). CCK8 results showed that compared with the transfection of empty plasmid, overexpression of Cyclin D3 can increase the sensitivity of 5-Fu ($^{**}p < 0.01$), and also increased the activity of cells in β-elemene group, but it was not obvious. Overexpression of Cyclin D3 can also significantly increased the activity of cells in the 5-Fu + β-elemene group ($^{**}p < 0.01$), indicating that β-elemene can reverse the resistance of HCT116p53$^{-/-}$ cells to 5-Fu by inhibiting the expression of Cyclin D3 (**Figure 3C**).

Effect of β-Elemene Combined With 5-Fu on Tumorigenicity of HCT116p53$^{-/-}$ Cells *in vivo*

To investigate the effect of 5-Fu + β-elemene on tumorigenicity of tumor cells in vivo, we established HCT116p53$^{-/-}$ all line xenograft model, which was randomly divided into six groups: control group, 5-Fu group, β-elemene group, HCQ group, 5-Fu + β-elemene group, and 5-Fu + β-elemene + HCQ group. At the end of the experiment, the tumor tissue was taken and photographed. The results showed that the tumor in the control group was completely uncontrolled and grew wildly. In the HCQ group, there has no effect on tumor growth. In the 5-Fu group and β-elemene group, the tumor volume was suppressed, while the tumor volume suppression rates was lower. In the 5-Fu + β-elemene group, tumor volume was

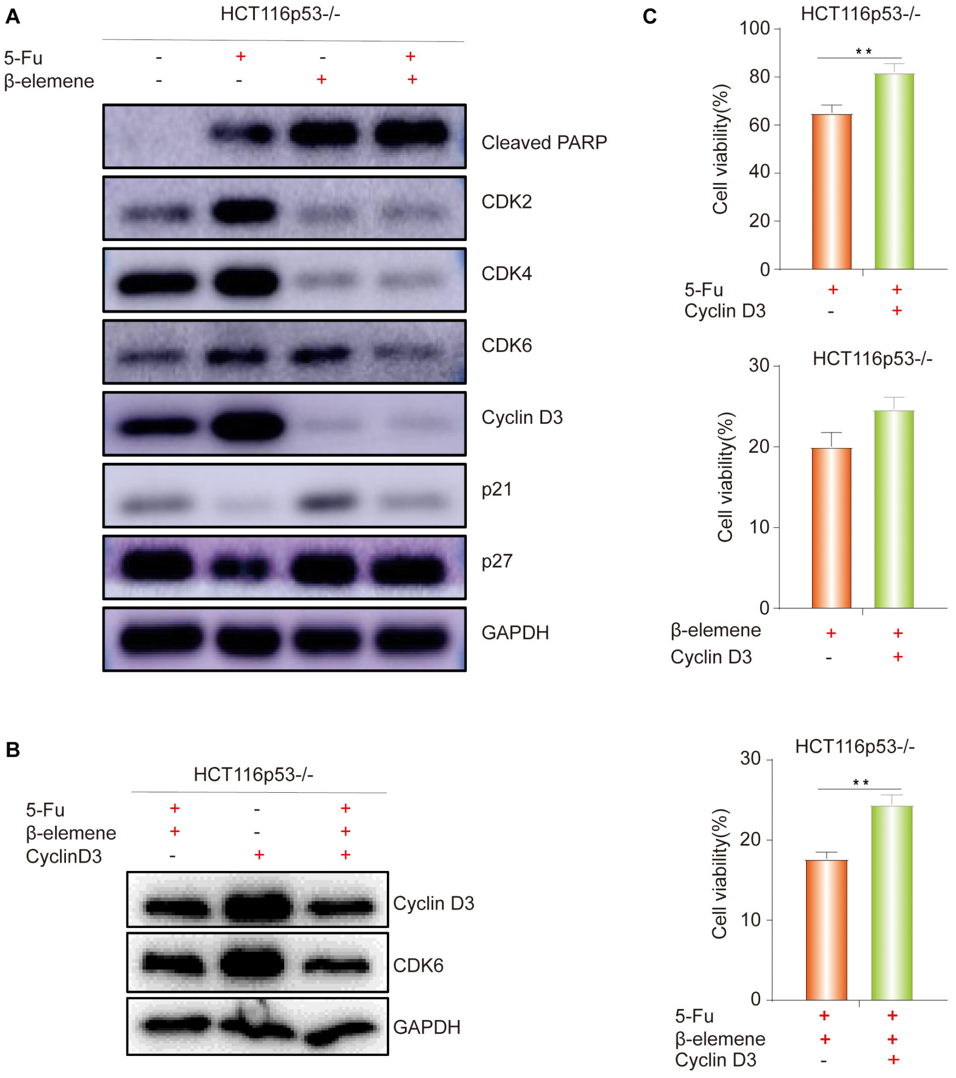

FIGURE 3 | β-elemene reverse the resistance of HCT116p53$^{-/-}$ cells to 5-Fu by inducing Cyclin D3- dependent cycle arrest. **(A)** HCT116p53$^{-/-}$ cells were treated with control, 5-Fu, β-elemene, 5-Fu + β-elemene, the expression of cell cycle-related proteins were examined by Western blot; **(B)** HCT116p53$^{-/-}$ cells were treated with 5-Fu + β-elemene, Cyclin-D3, 5-Fu + β-elemene + Cyclin D3, the protein expression of Cyclin D3 and CDK6 were examined by Western blot; **(C)** Overexpression Cyclin D3 of HCT116p53$^{-/-}$ cells and treated with 5-Fu, β-elemene, 5-Fu + β-elemene, the cell viability was examined by CCK8. (**$p < 0.01$, $n = 3$).

significantly inhibited (**$p < 0.01$), and the effect was higher than β-elemene alone, but HCQ could alleviate this effect (*$p < 0.05$) (**Figures 4A,B**).

DISCUSSION

Autophagy is the process of lysosomal degradation. In the process, the living body can remove intracellular waste and rebuild the structure to promote cell growth and development, maintain the stability of the intracellular environment and the balance of protein metabolism (Ramkumar et al., 2017). The autophagy process is divided into five different phases: the initial phase, the vesicle nucleation phase, the vesicle extension phase, the vesicle fusion phase, and the degradation products within the capsule (Kondo et al., 2005). Autophagy is tightly regulated by many intracellular signaling pathways and molecules. It acts as a regulator of pathogenesis and is a potential therapeutic target in a variety of diseases by regulating apoptosis, inflammation, pathogen clearance, immune response, and other cellular processes (Kondratskyi et al., 2018). The induction of autophagy plays a pro-death or pro-survival role in the treatment of cancer by chemotherapeutic drugs, which is related to the therapeutic effect of anticancer drugs and chemotherapeutic resistance. Autophagy serves as a drug resistance mechanism against chemotherapeutic drug therapy. And autophagy-mediated cell death mechanism is beneficial to the efficacy of anticancer drugs and improve the sensitivity of chemotherapeutic drugs including 5-Fu

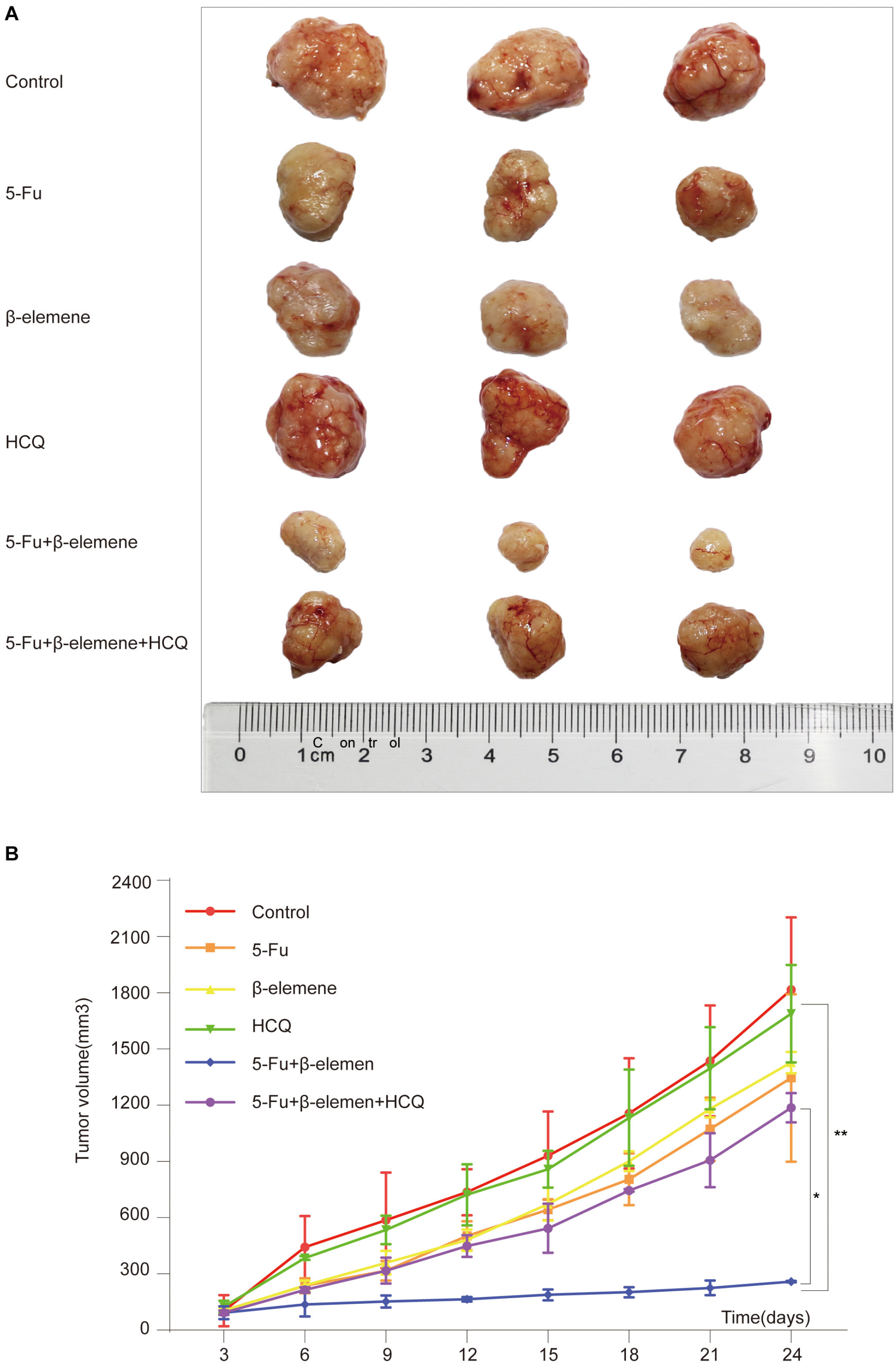

FIGURE 4 | Effect of β-elemene combined with 5-Fu on tumorigenicity of HCT116p53$^{-/-}$ cells in vivo. **(A)** The tumor tissue; **(B)** Tumor volume curve. (*$p < 0.05$, **$p < 0.01$, $n = 3$).

(Sui et al., 2013). In this paper, β-elemene reverses the resistance of p53-deficient colorectal cancer cells to 5-Fu by inducing pro-death autophagy.

So far, based on the delivery of cytosolic substances to lysosomes and substrates, three different main autophagy mechanisms have been distinguished: microautophagy, macroautophagy, and chaperonemediated autophagy. Accompanying protein-mediated autophagy and microautophagy involve direct unfolded soluble proteins into the lysosome as well as nonspecific phagocytosis of the cytoplasm, including organelles. Macroautophagy is a necessary, conservative autophagy process that degrades intracellular components, including soluble proteins, aggregates, organelles, polymer complexes, and foreign bodies (Ravegnini et al., 2017).

Generally, cell autophagy will maintain the stability of the intracellular microenvironment since it is maintained at a lower level. The lower level of autophagy plays a role in protecting cells, mainly degrading some large molecular proteins or organelles damaged by aging. Autophagy can inhibit the formation and growth of tumor cells (Yang and Klionsky, 2010; Sui et al., 2011). However, when the cell is subjected to certain external stimuli, such as starvation, drugs, hypoxia, etc., the level of autophagy that occurs in the cell will greatly increase, related autophagy proteins will be activated, and autophagy-related pathways will be activated. After the formation of autophagosomes, membrane phospholipids and intracellular proteins begin to be degraded by lysosomes. At the same time, autophagy can provide energy for cell survival through the lysosome degradation of organelles (Xin et al., 2017). However, excessive or sustained autophagy can also cause cytotoxicity, promoting cell death rather than survival.

Although the occurrence of autophagy is very common and the detection methods are diverse, the simplest is to detect LC3B, which is an autophagy marker protein (Janku et al., 2011). It can be processed from precursor LC3B into cytosolic soluble LC3B?, while exposing glycine residues are activated by Atg7. It is modified into LC3B?, which can bind to the membrane and is used as a marker of autophagosomes to locate in pre- and autophagosomes. The higher the content, the greater the degree of autophagy. Transient exogenous GFP-RFP-LC3B in this experiment can only prove the autophagosomes of cells, and this method is a benchmark for detecting cell autophagy (Nuta et al., 2019). In this experiment, we observed a large number of autophagosomes in HCT116p53$^{-/-}$ cells treated with β-elemene, which act as an autophagic marker indicating the occurrence of autophagy. There are two types of autophagy induced by chemotherapeutic drugs: one is protective autophagy, as a mechanism to maintain the stability of the intracellular environment, and the other is the cause of drug resistance, which is pro-death autophagy. Autophagy as a death mechanism promotes cell death (Hu et al., 2012; Zou et al., 2012).

β-elemene, as a new plant-derived compound, has a broad anti-cancer spectrum and may be further developed into anti-metastatic drugs. There are many reports on its inhibitory effect on tumors and its role in reversing drug resistance, but its underlying molecular mechanism is still unclear. In our study, the changes in cell autophagy particles were observed after transient transfection GFP-RFP-LC3B plasmid. Autophagy particles were increased in the β-elemene group and 5-Fu + β-elemene group, and Western blot results showed that the expression of LC3B? significantly increased after β-elemene treatment, indicating that β-elemene can increase the apoptosis of p53-deficient colorectal cancer cells by inducing autophagy, thereby increasing the sensitivity of 5-Fu. Besides, by measuring the cell viability after adding the autophagy inhibitor Bafilomycin A1, the cell viability was increased after the inhibition of autophagy, indicating that β-elemene induces pro-death autophagy in HCT116p53$^{-/-}$ cells and reverse the resistance of HCT116p53$^{-/-}$ cells to 5-Fu.

Previous studies have shown that β-elemene can achieve anti-tumor effects by inhibiting the cell cycle (Li et al., 2013a). In this experiment, cell cycle-related proteins were detected, the results showed that the expression of CDK2, CDK4, CDK6, and Cyclin D3 proteins were reduced in β-elemene group and 5-Fu + β-elemene group, indicating that the cell cycle process is blocked by β-elemene and the cell proliferation ability is reduced. Overexpression the Cyclin D3 enhances the activity of HCT116p53$^{-/-}$ cells induced by 5-Fu + β-elemene, indicating that β-elemene can inhibit the expression of cell cycle-related proteins and cause Cyclin D3-dependent cell cycle arrest in HCT116p53$^{-/-}$ cells.

The core part of the cycle mechanism is composed of D-type cyclins Cyclin D1, Cyclin D2, and Cyclin D3. Cyclin-dependent proteins are activated by cyclins and can form complexes, which can regulate the cell cycle from G1 to S change. Tumor cells have stronger proliferation ability than normal cells, so most tumor cells have more cells in the S phase, and Cyclin D protein expression is higher. If Cyclin D-CDK4/CDK6 complex expression is inhibited, it can inhibit the cell cycle process and promote cell aging, which is expected to become a new therapeutic target (Alquézar et al., 2015; Fan et al., 2017; Wang et al., 2017). In this experiment, β-elemene can reduce cell proliferation by inhibiting the cell cycle, and Cyclin D3 may become one of the targets for β-elemene to reverse the resistance to 5-Fu in p53-deficient colorectal cancer.

In summary, β-elemene can inhibit cell proliferation, increase apoptosis, and enhance 5-Fu sensitivity by inducing pro-death autophagy and inhibiting the progression of the Cyclin D3-dependent cell cycle in p53-deficient colorectal cancer. Pro-death autophagy and cell cycle arrest may be new targets for β-elemene to reverse resistance. β-elemene in combination with 5-Fu will hopefully provide a strategy for the treatment of CRC patients with p53 deletion. However, there are still some limitations in the research. Such as, it is unclear whether there is a correlation between β-elemene-induced pro-death autophagy and Cyclin D3-dependent cell cycle arrest, and there are no clinical data to support our conclusions. In the future, we will make further investigations for this limitations.

CONCLUSION

β-elemene can enhance the sensitivity of 5-Fu in p53 wild-type colorectal cancer cells HCT116p53$^{+/+}$. β-elemene can induce pro-death autophagy, affect the expression of cell cycle-related proteins, and cause Cyclin D3-dependent cycle arrest in p53-deficient colorectal cancer cells HCT116p53$^{-/-}$. At the same time, β-elemene can reverse resistance of HCT116p53$^{-/-}$ cells to 5-Fu by inducing pro-death autophagy and Cyclin D3-dependent cycle arrest.

DATA AVAILABILITY STATEMENT

All datasets generated for this study are included in the article/supplementary material.

ETHICS STATEMENT

The animal study was reviewed and approved by Animal Ethical and Welfare Committee of ZCMU Zhejiang Chinese Medical University.

AUTHOR CONTRIBUTIONS

XS, TX, and QW designed the research. RZ, YX, and MZ performed autophagy expriments and cell viability assay. JF, SL, and TD provided technical supports. PC, BZ, WW, RZ, and BC performed animal experiments. XuH, LC, and XC made western blotting analysis. TP, LY, TJ, YL, and GL contributed materials and data analysis. XiH, WZ, YS, QL, QZ, and LZ collected data. RZ wrote manuscript with contributions from the other authors.

FUNDING

This work was was supported by grants from the National Natural Science Foundation of China (Grant Nos. 81672932, 81730108, 81874380, and 81973635), Zhejiang Provincial Natural Science Foundation of China for Distinguished Young Scholars (Grant No. LR18H160001), the Science and Technology Development Fund, Macau SAR (File Nos. 130/2017/A3 and 0099/2018/A3), and Zhejiang Province Science and Technology Project of TCM (Grant No. 2019ZZ016).

REFERENCES

Alquézar, C., Barrio, E., Esteras, N., de la Encarnación, A., Bartolomé, F., Molina, J. A., et al. (2015). Targeting cyclin D3/CDK6 activity for treatment of Parkinson's disease. *J. Neurochem.* 133, 886–897. doi: 10.1111/jnc.13070

Amaravadi, R. K., Kimmelman, A. C., and Debnath, J. (2019). Targeting autophagy in cancer: recent advances and future directions. *Cancer Dis.* 9, 1167–1181. doi: 10.1158/2159-8290.CD-19-0292

Cayrol, C., Knibiehler, M., and Ducommun, B. (1998). p21 binding to PCNA causes G1 and G2 cell cycle arrest in p53-deficient cells. *Oncogene* 16, 311–320. doi: 10.1038/sj.onc.1201543

Chau, I., Fakih, M., García-Alfonso, P., Linke, Z., Ruiz Casado, A., Marques, E. P., et al. (2020). Safety and effectiveness of aflibercept + fluorouracil, leucovorin, and irinotecan (FOLFIRI) for the treatment of patients with metastatic colorectal cancer (mCRC) in current clinical practice: OZONE study. *Cancers* 12:E657. doi: 10.3390/cancers12030657

Chen, J., Wang, T., Xu, S., Zhang, P., Lin, A., Wu, L., et al. (2017). Discovery of novel antitumor nitric oxide-donating β-elemene hybrids through inhibiting the PI3K/Akt pathway. *Eur. J. Med. Chem.* 135, 414–423. doi: 10.1016/j.ejmech.2017.04.045

Chen, W., Zheng, R., Baade, P. D., Zhang, S., Zeng, H., Bray, F., et al. (2016). Cancer statistics in China, 2015. *CA Cancer J. Clin.* 66, 115–132. doi: 10.3322/caac.21338

Chen, X., Deng, L., Jiang, X., and Wu, T. (2016). Chinese herbal medicine for oesophageal cancer. *Cochrane Database Syst. Rev.* 1:CD004520. doi: 10.1002/14651858.CD004520.pub7

Dominijanni, A., and Gmeiner, W. H. (2018). Improved potency of F10 relative to 5-fluorouracil in colorectal cancer cells with p53 mutations. *Cancer Drug Resist.* 1, 48–58. doi: 10.20517/cdr.2018.01

Fan, Y., Mok, C. K., Chan, M. C., Zhang, Y., Nal, B., Kien, F., et al. (2017). Cell cycle-independent role of cyclin D3 in host restriction of influenza virus infection. *J. Biol. Chem.* 292, 5070–5088. doi: 10.1074/jbc.M117.776112

Feng, H. B., Wang, J., Jiang, H. R., Mei, X., Zhao, Y. Y., Chen, F. R., et al. (2017). β-elemene selectively inhibits the proliferation of glioma stem-like cells through the downregulation of notch1. *Stem Cells Transl. Med.* 6, 830–839. doi: 10.5966/sctm.2016-0009

Fidai, S. S., Sharma, A. E., Johnson, D. N., Segal, J. P., and Lastra, R. R. (2018). Dihydropyrimidine dehydrogenase deficiency as a cause of fatal 5-Fluorouracil toxicity. *Autops. Case. Rep.* 8, e2018049. doi: 10.4322/acr.2018.049

Gajjar, K. K., Vora, H. H., Kobawala, T. P., Trivedi, T. I., and Ghosh, N. R. (2018). Deciphering the potential value of 5-fluorouracil metabolic enzymes in predicting prognosis and treatment response of colorectal cancer patients. *Int. J. Biol. Markers* 33, 180–188. doi: 10.1177/1724600817748539

Gao, L., Ge, C., Wang, S., Xu, X., Feng, Y., Li, X., et al. (2020). The role of p53-mediated signaling in the therapeutic response of colorectal cancer to 9F, a spermine-modified naphthalene diimide derivative. *Cancers* 12:E528. doi: 10.3390/cancers12030528

Gokare, P., Finnberg, N. K., Abbosh, P. H., Dai, J., Murphy, M. E., and El-Deiry, W. S. (2017). P53 represses pyrimidine catabolic gene dihydropyrimidine dehydrogenase (DPYD) expression in response to thymidylate synthase (TS) targeting. *Sci. Rep.* 7:9711. doi: 10.1038/s41598-017-09859-x

Guan, C., Liu, W., Yue, Y., Jin, H., Wang, X., and Wang, X. J. (2014). Inhibitory effect of β-elemene on human breast cancer cells. *Int. J. Clin. Exp. Pathol.* 7, 3948–3956. doi: 10.1111/j.2042-7158.2010.01135.x

Hafner, A., Bulyk, M. L., Jambhekar, A., and Lahav, G. (2019). The multiple mechanisms that regulate p53 activity and cell fate. *Nat. Rev. Mol. Cell Biol.* 20, 199–210. doi: 10.1038/s41580-019-0110-x

Hu, Y. L., Jahangiri, A., Delay, M., and Aghi, M. K. (2012). Tumor cell autophagy as an adaptive response mediating resistance to treatments such as antiangiogenic therapy. *Cancer Res.* 72, 4294–4299. doi: 10.1158/0008-5472.Can-12-1076

Imanishi, M., Yamamoto, Y., Wang, X., Sugaya, A., Hirose, M., Endo, S., et al. (2019). Augmented antitumor activity of 5-fluorouracil by double knockdown of MDM4 and MDM2 in colon and gastric cancer cells. *Cancer Sci.* 110, 639–649. doi: 10.1111/cas.13893

Janku, F., McConkey, D. J., Hong, D. S., and Kurzrock, R. (2011). Autophagy as a target for anticancer therapy. *Nat. Rev. Clin. Oncol.* 8, 528–539. doi: 10.1038/nrclinonc.2011.71

Kaizuka, T., Morishita, H., Hama, Y., Tsukamoto, S., Matsui, T., Toyota, Y., et al. (2016). An autophagic flux probe that releases an internal control. *Mol. Cell* 64, 835–849. doi: 10.1016/j.molcel.2016.09.037

Kondo, Y., Kanzawa, T., Sawaya, R., and Kondo, S. (2005). The role of autophagy in cancer development and response to therapy. *Nat. Rev. Cancer* 5, 726–734. doi: 10.1038/nrc1692

Kondratskyi, A., Kondratska, K., Skryma, R., Klionsky, D. J., and Prevarskaya, N. (2018). Ion channels in the regulation of autophagy. *Autophagy* 14, 3–21. doi: 10.1080/15548627.2017.1384887

Lee, R. X., Li, Q. Q., and Reed, E. (2012). β-elemene effectively suppresses the growth and survival of both platinum-sensitive and -resistant ovarian tumor cells. *Anticancer Res.* 32, 3103–3113.

Levy, J. M. M., Towers, C. G., and Thorburn, A. (2017). Targeting autophagy in cancer. *Nat. Rev. Cancer* 17, 528–542. doi: 10.1038/nrc.2017.53

Li, L., Xu, L., Qu, X., Zhao, M., Yu, P., Kang, J., et al. (2011). Cbl-regulated Akt and ERK signals are involved in β-elemene-induced cell apoptosis in lung cancer cells. *Mol. Med. Rep.* 4, 1243–1246. doi: 10.3892/mmr.2011.548

Li, Q. Q., Lee, R. X., Liang, H., Wang, G., Li, J. M., Zhong, Y., et al. (2013a). β-elemene enhances susceptibility to cisplatin in resistant ovarian carcinoma cells via downregulation of ERCC-1 and XIAP and inactivation of JNK. *Int. J. Oncol.* 43, 721–728. doi: 10.3892/ijo.2013.1996

Li, Q. Q., Wang, G., Huang, F., Li, J. M., Cuff, C. F., and Reed, E. (2013b). Sensitization of lung cancer cells to cisplatin by β-elemene is mediated through blockade of cell cycle progression: antitumor efficacies of β-elemene and its synthetic analogs. *Med. Oncol.* 30:488. doi: 10.1007/s12032-013-0488-9

Li, X. P., Wen, F., Yang, W., Deng, Y. B., Li, M., Zhang, P. F., et al. (2014). The role of tiopronin for the prevention of chemotherapy-related liver toxicity in advanced colorectal cancer patients treated with mFOLFOX7: a prospective analysis. *Tumori* 100, 446–451. doi: 10.1700/1636.17908

Mu, L., Wang, T., Chen, Y., Tang, X., Yuan, Y., and Zhao, Y. (2016). β-Elemene enhances the efficacy of gefitinib on glioblastoma multiforme cells through the inhibition of the EGFR signaling pathway. *Int. J. Oncol.* 49, 1427–1436. doi: 10.3892/ijo.2016.3626

Nuta, G. C., Gilad, Y., Gershoni, M., Sznajderman, A., Schlesinger, T., Bialik, S., et al. (2019). A cancer associated somatic mutation in LC3B attenuates its binding to E1-like ATG7 protein and subsequent lipidation. *Autophagy* 15, 438–452. doi: 10.1080/15548627.2018.1525476

Petroni, G., Bagni, G., Iorio, J., Duranti, C., Lottini, T., Stefanini, M., et al. (2020). Clarithromycin inhibits autophagy in colorectal cancer by regulating the hERG1 potassium channel interaction with PI3K. *Cell Death Dis.* 11:161. doi: 10.1038/s41419-020-2349-8

Raimondi, A., Di Maio, M., Peverelli, G., Morano, F., Corallo, S., Bergamo, F., et al. (2019). Health-related quality of life in RAS wild-type metastatic colorectal cancer patients treated with panitumumab plus FOLFOX followed by panitumumab or panitumumab plus 5-FU/LV maintenance: the secondary endpoint of the Valentino study. *Ann. Oncol.* 30:iv115. doi: 10.1093/annonc/mdz156.015

Ramkumar, A., Murthy, D., Raja, D. A., Singh, A., Krishnan, A., Khanna, S., et al. (2017). Classical autophagy proteins LC3B and ATG4B facilitate melanosome movement on cytoskeletal tracks. *Autophagy* 13, 1331–1347. doi: 10.1080/15548627.2017.1327509

Ravegnini, G., Sammarini, G., Nannini, M., Pantaleo, M. A., Biasco, G., Hrelia, P., et al. (2017). Gastrointestinal stromal tumors (GIST): Facing cell death between autophagy and apoptosis. *Autophagy* 13, 452–463. doi: 10.1080/15548627.2016.1256522

Saif, M. W., and Diasio, R. B. (2016). Benefit of uridine triacetate (Vistogard) in rescuing severe 5-fluorouracil toxicity in patients with dihydropyrimidine dehydrogenase (DPYD) deficiency. *Cancer Chemother. Pharmacol.* 78, 151–156. doi: 10.1007/s00280-016-3063-1

Sakamoto, K., Yokogawa, T., Ueno, H., Oguchi, K., Kazuno, H., Ishida, K., et al. (2015). Crucial roles of thymidine kinase 1 and deoxyUTPase in incorporating the antineoplastic nucleosides trifluridine and 2'-deoxy-5-fluorouridine into DNA. *Int. J. Oncol.* 46, 2327–2334. doi: 10.3892/ijo.2015.2974

Satyavarapu, E. M., Das, R., Mandal, C., Mukhopadhyay, A., and Mandal, C. (2018). Autophagy-independent induction of LC3B through oxidative stress reveals its non-canonical role in anoikis of ovarian cancer cells. *Cell Death Dis.* 9:934. doi: 10.1038/s41419-018-0989-8

Shamekhi, S., Abdolalizadeh, J., Ostadrahimi, A., Mohammadi, S. A., Barzegari, A., Lotfi, H., et al. (2019). Apoptotic effect of saccharomyces cerevisiae on human colon cancer SW480 cells by regulation of Akt/NF-?B signaling pathway. *Probiotics Antimicrob. Proteins* 12, 311–319. doi: 10.1007/s12602-019-09528-7

Shi, H., Liu, L., Liu, L. M., Geng, J., and Chen, L. (2015). Inhibition of tumor growth by β-elemene through downregulation of the expression of uPA, uPAR, MMP-2, and MMP-9 in a murine intraocular melanoma model. *Melanoma Res.* 25, 15–21. doi: 10.1097/cmr.0000000000000124

Siegel, R. L., Miller, K. D., and Jemal, A. (2020). Cancer statistics, 2020. *CA Cancer. J. Clin.* 70, 7–30. doi: 10.3322/caac.21590

Sui, X., Chen, R., Wang, Z., Huang, Z., Kong, N., Zhang, M., et al. (2013). Autophagy and chemotherapy resistance: a promising therapeutic target for cancer treatment. *Cell Death Dis.* 4:e838. doi: 10.1038/cddis.2013.350

Sui, X., Jin, L., Huang, X., Geng, S., He, C., and Hu, X. (2011). p53 signaling and autophagy in cancer: a revolutionary strategy could be developed for cancer treatment. *Autophagy* 7, 565–571. doi: 10.4161/auto.7.6.14073

Sui, X., Kong, N., Wang, X., Fang, Y., Hu, X., Xu, Y., et al. (2014). JNK confers 5-fluorouracil resistance in p53-deficient and mutant p53-expressing colon cancer cells by inducing survival autophagy. *Sci. Rep.* 4:4694. doi: 10.1038/srep04694

Sun, M. Y., Zhang, H., Tao, J., Ni, Z. H., Wu, Q. X., and Tang, Q. F. (2019). Expression and biological function of rhotekin in gastric cancer through regulating p53 pathway. *Cancer Manag. Res.* 11, 1069–1080. doi: 10.2147/cmar.S185345

Sun, Y. N., Zhang, Z. Y., Zeng, Y. C., Chi, F., Jin, X. Y., and Wu, R. (2016). Comparative efficacy of whole-brain radiotherapy with and without elemene liposomes in patients with multiple brain metastases from non-small-cell lung carcinoma. *Curr. Oncol.* 23, e377–e382. doi: 10.3747/co.23.3183

Wang, H., Nicolay, B. N., Chick, J. M., Gao, X., Geng, Y., Ren, H., et al. (2017). The metabolic function of cyclin D3-CDK6 kinase in cancer cell survival. *Nature* 546, 426–430. doi: 10.1038/nature22797

Wu, X. S., Xie, T., Lin, J., Fan, H. Z., Huang-Fu, H. J., Ni, L. F., et al. (2009). An investigation of the ability of elemene to pass through the blood-brain barrier and its effect on brain carcinomas. *J. Pharm. Pharmacol.* 61, 1653–1656. doi: 10.1211/jpp/61.12.0010

Xin, Y., Jiang, F., Yang, C., Yan, Q., Guo, W., Huang, Q., et al. (2017). Role of autophagy in regulating the radiosensitivity of tumor cells. *J. Cancer Res. Clin. Oncol.* 143, 2147–2157. doi: 10.1007/s00432-017-2487-2

Yang, Z., and Klionsky, D. J. (2010). Eaten alive: a history of macroautophagy. *Nat. Cell Biol.* 12, 814–822. doi: 10.1038/ncb0910-814

Yao, Y. Q., Ding, X., Jia, Y. C., Huang, C. X., Wang, Y. Z., and Xu, Y. H. (2008). Anti-tumor effect of beta-elemene in glioblastoma cells depends on p38 MAPK activation. *Cancer Lett.* 264, 127–134. doi: 10.1016/j.canlet.2008.01.049

Zhai, B., Zeng, Y., Zeng, Z., Zhang, N., Li, C., Zeng, Y., et al. (2018). Drug delivery systems for elemene, its main active ingredient β-elemene, and its derivatives in cancer therapy. *Int. J. Nanomed.* 13, 6279–6296. doi: 10.2147/ijn.S174527

Zhang, T., Ji, D., Wang, P., Liang, D., Jin, L., Shi, H., et al. (2018). The atypical protein kinase RIOK3 contributes to glioma cell proliferation/survival, migration/invasion and the AKT/mTOR signaling pathway. *Cancer Lett.* 415, 151–163. doi: 10.1016/j.canlet.2017.12.010

Zong, S., Li, J., Yang, L., Huang, Q., Hou, G., Ye, Z., et al. (2019). Mechanism of bioactive polysaccharide from Lachnum sp. acts synergistically with 5-fluorouracil against human hepatocellular carcinoma. *J. Cell. Physiol.* doi: 10.1002/jcp.28202 [Epub ahead of print].

Zou, Z., Yuan, Z., Zhang, Q., Long, Z., Chen, J., Tang, Z., et al. (2012). Aurora kinase A inhibition-induced autophagy triggers drug resistance in breast cancer cells. *Autophagy* 8, 1798–1810. doi: 10.4161/auto.22110

Conflict of Interest: The authors declare that the research was conducted in the absence of any commercial or financial relationships that could be construed as a potential conflict of interest.

frontiers
in Bioengineering and Biotechnology

ORIGINAL RESEARCH
published: 29 May 2020
doi: 10.3389/fbioe.2020.00537

Differently Charged Super-Paramagnetic Iron Oxide Nanoparticles Preferentially Induced M1-Like Phenotype of Macrophages

Wenyue Zhang[1,2]†, Shuwen Cao[1]†, Shunung Liang[3], Chee Hwee Tan[3], Baoming Luo[2], Xiaoding Xu[1]* and Phei Er Saw[1]*

[1] Guangdong Provincial Key Laboratory of Malignant Tumor Epigenetics and Gene Regulation, Medical Research Center, Sun Yat-sen Memorial Hospital, Sun Yat-sen University, Guangzhou, China, [2] Department of Ultrasound, Sun Yat-sen Memorial Hospital, Sun Yat-sen University, Guangzhou, China, [3] The First Clinical Medical School of Guangzhou University of Chinese Medicine, Guangzhou University of Chinese Medicine, Guangzhou, China

OPEN ACCESS

Edited by:
Gianni Ciofani,
Italian Institute of Technology (IIT), Italy

Reviewed by:
Jianxun Ding,
Changchun Institute of Applied Chemistry (CAS), China
Yuling Xiao,
Wuhan University, China

***Correspondence:**
Xiaoding Xu
xuxiaod5@mail.sysu.edu.cn
Phei Er Saw
caipeie@mail.sysu.edu.cn

† These authors have contributed equally to this work

Specialty section:
This article was submitted to Nanobiotechnology, a section of the journal Frontiers in Bioengineering and Biotechnology

Received: 20 March 2020
Accepted: 05 May 2020
Published: 29 May 2020

Citation:
Zhang W, Cao S, Liang S, Tan CH, Luo B, Xu X and Saw PE (2020) Differently Charged Super-Paramagnetic Iron Oxide Nanoparticles Preferentially Induced M1-Like Phenotype of Macrophages. Front. Bioeng. Biotechnol. 8:537. doi: 10.3389/fbioe.2020.00537

Macrophages are mainly divided into two phenotypes: M1-like (anti-tumoral, pro-inflammatory) and M2-like (pro-tumoral, anti-inflammatory). The more abundant M2-like phenotype of tumor associated macrophages (TAMs) has been associated with poor prognosis in various cancers, therefore, many studies have been carried out to modulate TAMs to change from an M2 to M1-like phenotype as an effective way to suppress tumor growth. Previous study indicated that the FDA-approved Ferumoxytol is an iron oxide nanoparticle that has intrinsic tumor inhibiting properties and is accompanied by the increased presence of the pro-inflammatory, anti-tumoral M1-like phenotype. Intrigued by this finding, we hypothesize that differently charged super-paramagnetic iron oxide nanoparticles (SPIONs) would have preferential differences in polarizing macrophages. Herein, we report that differently charged SPIONs have distinct preferences in the modulation of TAM phenotypes. Positively charged SPION (S+) had the highest cellular uptake and highest macrophage polarization effect. Interestingly, although negatively charged SPION (S−) should present charge–charge repulsion with cell membranes, they showed considerably high uptake *in vitro*, nevertheless presenting the highest cellular toxicity. Neutrally charged SPION (SN) showed minimal uptake and cellular toxicity *in vitro*. Both S+ and S− could effectively re-polarize M2-like macrophages toward M1-like macrophages *in vitro*, and significantly increased the Fenton effect and chemotaxis of macrophages. When macrophages pre-treated with these SPIONs were co-injected with tumor cells to obtain a tumor xenograft, S+ and S− treated macrophages significantly induced tumor retardation, indicating the successful repolarization of tumor macrophages by these SPIONs. Taken together, we provide an insight on the importance of SPION charge in immunomodulation of macrophages.

Keywords: TAMs, M2-like phenotype, M1-like phenotype, tumor suppression, SPION

INTRODUCTION

Tumor-associated macrophages (TAMs) are the most abundant immune cells in the tumor microenvironment (TME); in some solid tumors, it counts for up to 50% of the cell population (Komohara et al., 2014; Vitale et al., 2019). Macrophages could be simply classified as M1-like (pro-inflammatory) and M2-like (anti-inflammatory) phenotypes according to the expression of cytokines and chemokines (Mantovani et al., 2002). Preclinical studies have shown macrophages were largely preceding as M2-like phenotype in the TME; they accelerate tumor growth and metastasis by providing nutritional support to tumor cells, inhibiting phagocytosis, reducing activation of T cells and promoting angiogenesis (Barclay and Van den Berg, 2014; Bonapace et al., 2014; Engblom et al., 2016; Vitale et al., 2019). Thus, researchers investigated many ways to modulate TAMs, to change from M2 into M1-like phenotype, and effectively suppress tumor growth (Gunderson et al., 2016; Kaneda et al., 2016a,b; Song et al., 2016; Rodell et al., 2018), including signaling molecules, inhibitors, transcription factors, agonists, and miRNAs.

Iron oxide nanoparticles have been widely used in biomedicine, imaging and drug delivery in preclinical, and clinical settings (Anderson et al., 2019), including photodynamic therapy, anemia, magnetic drug targeting, and modulating macrophage polarization (Ma et al., 2007; Bloemen et al., 2012; Macdougall and Geisser, 2013). Ferumoxytol is an iron oxide nanoparticle that has been approved by Food and Drug Administration (FDA) for nuclear magnetic resonance imaging and iron deficiency (Lu et al., 2010). Super-paramagnetic iron oxide nanoparticles (SPIONs) are the core material in Ferumoxytol. Previous studies have shown that surface modified SPION nanoplatforms can be used for multimodal imaging and tumor therapy, such as photodynamic therapy (Kievit et al., 2012; Sivakumar et al., 2017; Zhang and Song, 2017; Zhuang et al., 2019).

Injection of Ferumoxytol could increase repolarization of TAMs and apoptosis of tumor cells, leading to the inhibition of tumor growth and metastasis (Zanganeh et al., 2016). However, whether differently charged SPIONs could have the same effect, and whether charge would influence the performance of SPIONs on tumor suppression was not clear. To clarify these questions, we synthesized three differently charged SPION (positive S+, neutral SN, and negative S−) and explored their intrinsic effect on TAMs and tumor growth.

MATERIALS AND METHODS

Materials

Ferumoxytol (Feraheme®) was purchased from AMAG Pharmaceuticals Inc., Cambridge, MA, United States. SPIONs of positive, neutral, and negative change were a kind gift from Prof Dr. Morteza Mahmoudi from Harvard Medical School. All SPIONs were characterized for their sizes and charges prior to usage. Other chemicals and cell culture medium were used as purchased. Size, zeta potential and morphology were examined by dynamic light scattering (DLS) and transmission electron microscopy (TEM) respectively.

Cell Culture

HT1080 human fibrosarcoma cells and RAW264.7 macrophages were purchased from the American Type Culture Collection (ATCC). The cells were cultured in Dulbecco's Modified Eagle's Medium (DMEM, Gibco, NY, United States), supplemented with 10% fetal bovine serum (FBS, Gibco) and 1% penicillin/streptomycin (Gibco).

Cell Viability

Cells were seeded at 3000/well in a 96-well plate. After 24 h, cells were treated with respective treatment (SPIONs or Ferumoxytol) for 4 h, before washing out with phosphate buffered saline (PBS). Cells were further incubated for 48 h. Alamar Blue were added at 10 μl/well into the culture medium. After 1 h, the absorbance of the cells was determined using a Tecan UV spectrophotometer at Abs 570 nm.

Cellular Uptake and Prussian Blue Staining

To determine the cellular uptake of all SPIONs (positive, neutral, and negatively charged) and Ferumoxytol, HT1080 cells were first seeded on a glass slide (12×12 mm^3) on 24-well plate. When cells grew to ∼80% confluency, cells were treated with positively charged SPIONs (S+), Neutral-charged SPIONs (SN), negatively charged SPIONs (S−) or Ferumoxytol for 2 h at 37°C. After 2 h, cells were washed thrice with PBS before staining with Prussian Blue Kit (Abcam, Cat# ab150674; MA, United States) according to the manufacturer's protocol.

Transwell Assays

To evaluate the chemotactic effects of SPIONs on macrophages, HT1080 cells and RAW264.7 macrophage cells were co-cultured in dual-chamber transwell systems with 3 μm-sized microporous membranes (Corning, New York, NY, United States), which permits cell translocation between chambers. RAW264.7 cells were pre-labeled with DiD dye (Thermo Fisher Scientific, Cat# V22887; MA, United States). Briefly, 1×10^6 macrophages were incubated with 5 μl of DiD dye/mL whole media SPIONs or Ferumoxytol at a concentration of 2.73 mg/mL at 37°C for 30 min. The cells were then washed thrice with PBS (pH 7.4) and collected through centrifugation (5 min, 400 RCF, 25°C) (Zanganeh et al., 2016). After washing, macrophages were plated onto transwell inserts, HT1080 cells were seeded into the bottom wells of transwell plates (Vallabani and Singh, 2018). All transwell assays were performed with DMEM, supplemented with 10% FBS and 1% penicillin/streptomycin. Cells were incubated for 24 h at 37°C in a humidified atmosphere with 5% CO_2. Subsequently, the bottom chambers were isolated and cells were stained by 4′,6-diamidino-2-phenylindole (DAPI, Invitrogen). DiD positive macrophages that had migrated to the bottom chamber of transwell systems were counted under a Zeiss fluorescence microscope (Zeiss, Oberkochen, Germany), using DAPI and DiD channels and 40× magnification.

The same experiments were carried out to elucidate the Fenton reaction by the macrophages after treatment of various charges of SPIONs with 0.4 μm-sized microporous membranes (Corning, NY, United States). GFP-labeled HT1080 cells were shown as green while cells positive with Caspase-9 were shown as yellow punctate under 40× magnification with an Axio Zeiss microscope (Axio Observer 3.1; Zeiss, Oberkochen, Germany) and the resultant digital images were analyzed using the ImageJ (National Institute of Health, MD, United States).

Reverse Transcription Quantitative Polymerase Chain Reaction (qRT-PCR)

To determine M1- and M2-associated gene expression *in vitro*, macrophages from the upper chamber (transwell system with 0.4 μm-sized microporous membranes and 12 h incubation time) were harvested, followed by RNA extraction with the RNeasy mini/micro kit (Qiagen, Valencia, CA, United States) according to the manufacturer's protocol. Cell culture supernatants were also collected and either used directly or stored in −80°C until analyzed. One microgram of total RNA was reverse-transcribed into complementary DNAs with an iScript complementary cDNA synthesis kit (Bio-Rad, Hercules, CA, United States) containing a mixture of oligo (dT) and random primers. The mRNA level was determined by the comparative Ct method.

Reactive Oxygen Species Assay

To evaluate the production of reactive oxygen species (ROS) by macrophages, RAW264.7 macrophages were co-cultured with HT1080 cells in transwell plates with 0.4 μm pore-size (12-well, Corning), which allowed free diffusion of molecules between the two chambers but not cell translocation. Culture media was retrieved from co-cultures described above and ROS levels were measured using two different ROS indicators: The hydroxyl radical was measured by incubating co-culture media with 3′-(p-hydroxyphenyl) fluorescein (HPF; Thermo Fisher Scientific, Waltham, MA, United States; Cat# H36004) at a concentration of 10 mM for 30 min at 37°C and measuring HPF fluorescence at an emission wavelength of 515 nm (excitation wavelength 490 nm). In addition, hydrogen peroxide in co-culture media was measured by incubating co-culture media with a hydrogen peroxide colorimetric detection kit for 30 min at 25°C (Enzo Life Science, Farmingdale, NY, United States; Cat# ADI907015) and absorbance was measured at 550 nm. All samples were carried out in triplicate, and the average value of ROS for each group was calculated.

Animals

BALB/c normal mice and nude mice (female, 4–5 weeks old) were purchased from the Sun Yat-sen University Experimental Animal Center (Guangzhou, China). All *in vivo* studies were performed in accordance with the Institutional Animal Care and Use Committee at Sun Yat-sen University.

In vivo Tumor Growth Analysis

To determine the effect of macrophage polarization toward tumor growth, 5×10^6 HT1080 cells were mixed with either $1 \times 10^{6+}$ of S+, SN, S− or Ferumoxytol before injecting into the right flank of Balb/c nude mice (*n* = 3). After 14 days, prior to tumor excision, Pacific-Blue Labeled Dextran® (Sigma-Aldrich, Cat# FD10S; Germany) was injected to the tumor site to label TAMs. After 30 min, tumors were excised and analyzed.

Histology

Tumor samples were embedded in Tissue-Tek opti-mum cutting temperature (OCT) compound, snap frozen in liquid nitrogen and cut into 8 μm thick frozen sections using a cryostat. Sections were fixed in ice-cold acetone for 10 min at −20°C followed by two 5 min washes in PBS and 1 h blocking in 1% bovine serum albumin (BSA)-PBS. Antibodies against CD206 (2 μg/mL, PE-conjugated, monoclonal rat anti-mouse IgG2a κ; BioLegend, San Diego, CA, United States), CD80 (4 μg/mL, Alexa Fluor 488-conjugated Armenian Hamster anti-mouse IgG, BioLegend, San Diego, CA, United States), CD11b (4 μg/mL, FITC-conjugated rat anti-mouse IgG2b κ, BD), and the corresponding isotype controls were diluted in 1% BSA-PBS to the indicated concentrations and then applied to the sections followed by overnight incubation at 4°C in the dark. Sections were washed three times with PBS for 5 min and mounted with DAPI and imaged with 40× magnification with an Axio Zeiss microscope (Axio Observer 3.1; Zeiss, Oberkochen, Germany) and the resultant digital images were analyzed using the ImageJ (National Institute of Health).

RESULTS

Synthesis and Characterization of Differently Charged SPIONs

On the basis of the FDA-approved Ferumoxytol, we synthesized three differently charged SPIONs, with zeta potential of +44.72 mV (S+), −2.82e-1 mV (NS), and −27.31 mV (S−) (**Figure 1A**). Each particle, S+, SN, and S−, had a size of about 19.4 ± 0.8 nm, 15.9 ± 0.2 nm, and 21.3 ± 1.6 nm, respectively (**Figure 1A**). The morphology of differently charged SPIONs were characterized by TEM. TEM images showed that S+ aggregated easily, followed by S−, while SN due to the polyethylene glycol (PEG) coating, did not show any aggregations (**Figure 1B**).

In vitro Uptake of SPIONs in RAW 264.7 Macrophage Cells

To see the *in vitro* uptake properties of each SPIONs, we carried out Prussian blue staining and iron assay on RAW 264.7 cells. As seen in **Figure 2A**, S+ has the highest uptake, indicated by blue staining, followed by S−, Ferumoxytol and SN. In **Figures 2B,C**, iron assay was performed to test the iron content with a colorimetric (593 nm) product, and the quantification of iron content is shown in **Figure 2C**. Compared with control, Ferumoxytol and all SPIONs groups showed significantly uptake for iron content ($P < 0.005$). Cells treated by S+ indicated the highest cellular iron content, followed by a similar amount of

A

	SPION (+) (S+)	SPION (neutral) (SN)	SPION (-) (S-)
Size (nm)	19.4	15.9	21.3
S.D. (±)	0.8	0.2	1.6
Zeta potential	+44.72	-2.82e-1	-27.31

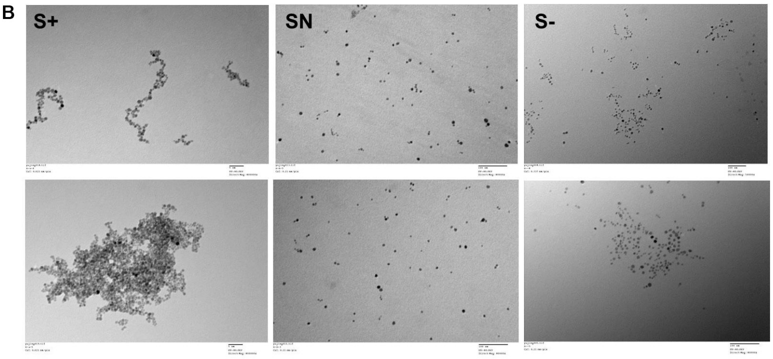

FIGURE 1 | Characterization of differently charged SPIONs. **(A)** Size and zeta potential of differently charged SPIONs. **(B)** TEM images of differently charged SPIONs.

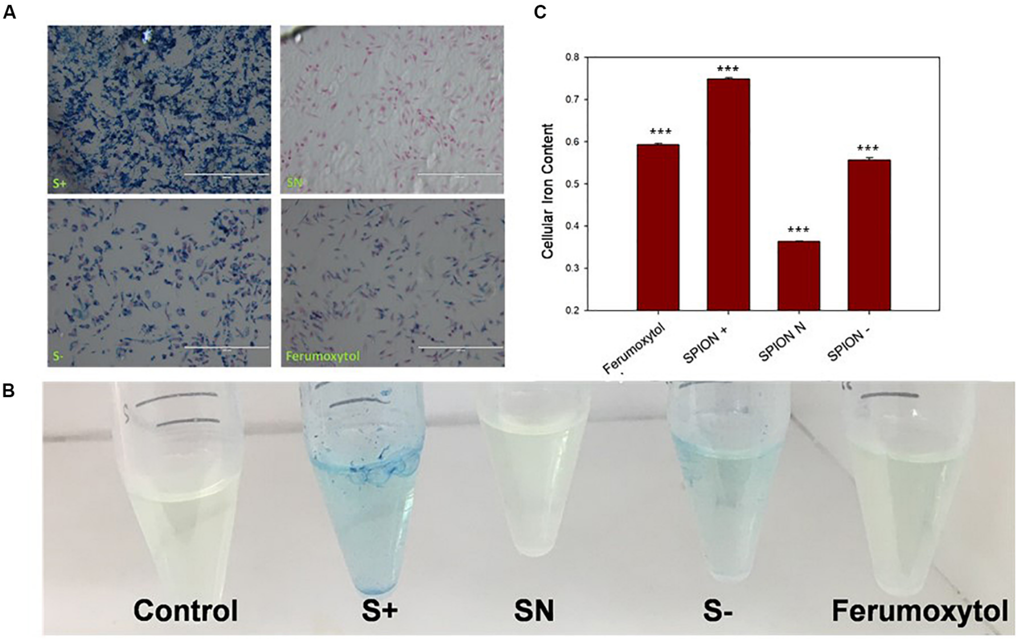

FIGURE 2 | Analysis of cell uptake of Ferumoxytol and SPIONs after Prussian blue staining. Blue, Iron content; red, nucleus. **(A)** *In vitro* quantification of SPIONs after Prussian blue staining and iron assay on RAW 264.7 cells. **(B)** Iron assay of cells after treated with Ferumoxytol and SPIONs. **(C)** Quantification analysis of iron assay in **(B)**. $^{***}P < 0.005$, compared with control.

iron content in S− and Ferumoxytol treated cells, while the SN showed the least cellular uptake.

Effects of Differently Charged SPIONs Toward the Repolarization of Macrophages

The cellular cytotoxicity of differently charged SPIONs toward RAW 264.7 cells is shown in **Figure 3A**. With increasing concentration, cytotoxicity of S+ and S− gradually showed significant toxicity ($P < 0.01$ for S+ group, $P < 0.005$ for S− group). S− the highest cellular toxicity compared to other groups, while SN and Ferumoxytol did not show appreciable cytotoxicity. To explore the repolarization of macrophages, RAW 264.7 cells were incubated with respective formulations for 24 h. Cells were digested and real-time RT-PCR was carried out to determine the expression of representative M1 [tumor necrosis factor-α (TNF-α), inducible nitric oxide synthase (iNOS)] and M2 [interleukin-10 (IL-10), vascular endothelial growth factor (VEGF)] marker. As seen in **Figure 3B**, compared with HT1080

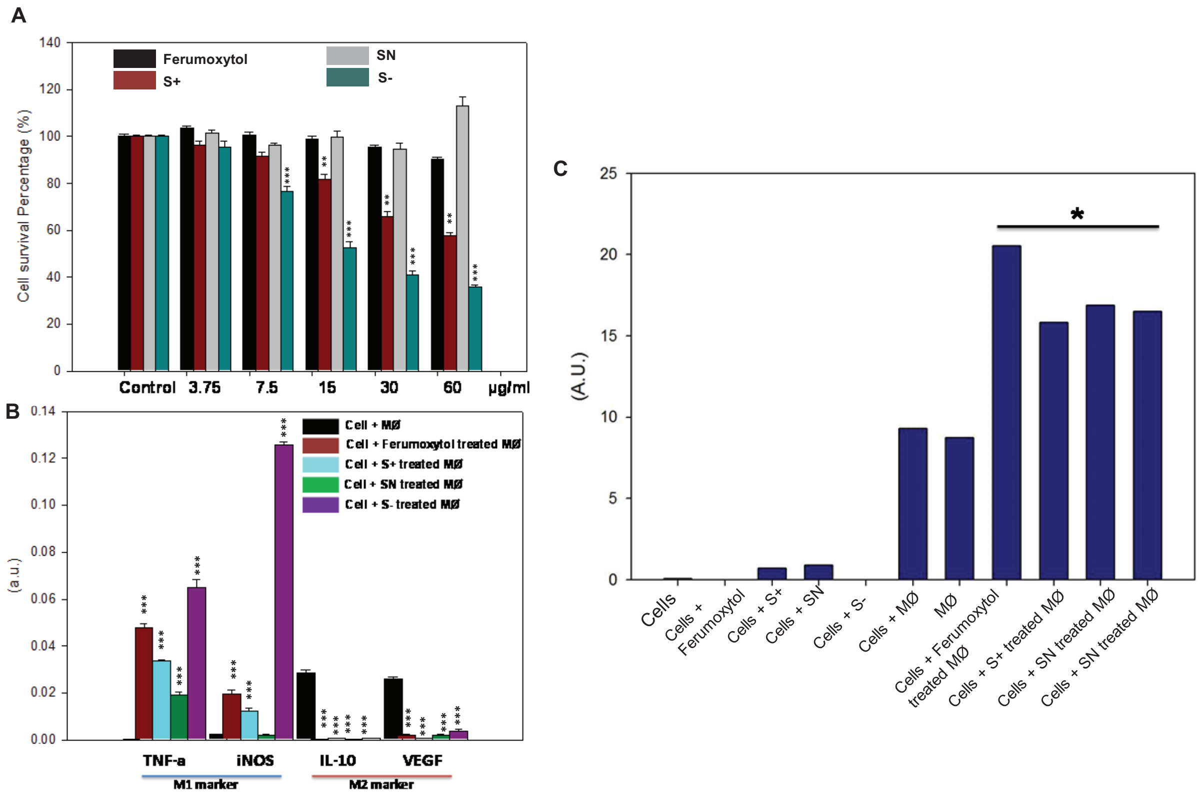

FIGURE 3 | Effect of differently charged SPIONs on macrophages. **(A)** Cellular cytotoxicity of SPIONs toward RAW cells. **$P < 0.01$, ***$P < 0.005$, compared with relative control. **(B)** *In vitro* polarization of RAW cells after being treated with SPIONs. ***$P < 0.005$, compared with relative control (cell + macrophage group, black one). **(C)** Production of ROS after co-treatment of polarized RAW and tumor cells. *$P < 0.05$.

plus macrophage only, Ferumoxytol, S+ and S− groups showed significant repolarization for macrophages ($P < 0.005$). While SN group showed significantly increase expression in TNF-α, and decrease expression in IL-10 and VEGF ($P < 0.005$). In all, S− showed the highest repolarization (from M2-like to M1-like phenotype), followed by S+ and Ferumoxytol, while the SN showed the least polarization effect.

To determine the ROS production after co-culture of polarized macrophage and tumor cells, we incubated HT1080 cells with respective treatments for 6 h, and the media was collected to explore the production of hydrogen peroxide (**Figure 3C**). Co-incubation of HT1080, macrophage and Ferumoxytol or differently charged SPIONs produced significant amounts of hydrogen peroxide, and the production of ROS in the Ferumoxytol treated group was significantly higher than other groups ($P < 0.05$). Treatment of (a) HT1080 + macrophage and (b) macrophage-only groups produced negligible amount of ROS, while treatment of (c) cancer cells only, (d) cancer cells + Ferumoxytol, or (e) differently charged SPIONs did not lead to significant ROS production.

To visualize the polarization of tumor macrophages *in vivo*, we injected RAW 264.7 cells only and treated with Ferumoxytol, S+, SN, and S− intratumorally into HT1080 xenograft tumors. After 7 days, a fraction of the tumor was used for immunohistochemistry (IHC) to detect the expression of CD206 (M2-like marker), CD80, and CD11b (an M1-like marker). As evidenced by the staining in **Figure 4**, compared with tumor cells, Ferumoxytol, S+, and S− pre-treated groups showed higher CD11b and CD80 expression, and less CD206 expression. The SN group did not show significant changes in CD11b and CD80, but had a slight decrease of CD206 expression.

Effect of Macrophages Treated With Differently Charged SPIONs on Tumor Cells

To elucidate the chemotaxis effect of repolarized macrophages, we co-cultured RAW 264.7 cells on the top chamber and HT1080 cancer cells on the lower chamber of the Transwell (**Figure 5A**). The macrophages labeled with DiD were first treated with the respective formulations for 30 min, and then incubated on the top chamber of a 3.0 μm trans well. After 24 h, the number of DiD-positive cells were counted in the lower chamber. The number of DiD-labeled macrophages were calculated in **Figures 5B,C**. Compared with the untreated macrophages, the Ferumoxytol treated group had a significantly higher chemotaxis rate (67%, $P < 0.005$), followed by SN, S+, and S− and groups (53, 44, and 35% respectively, $P < 0.005$). As shown in **Figure 5C**, the fluorescence intensity of macrophages in the Ferumoxytol and all SPION groups was higher than HT1080 + macrophage group.

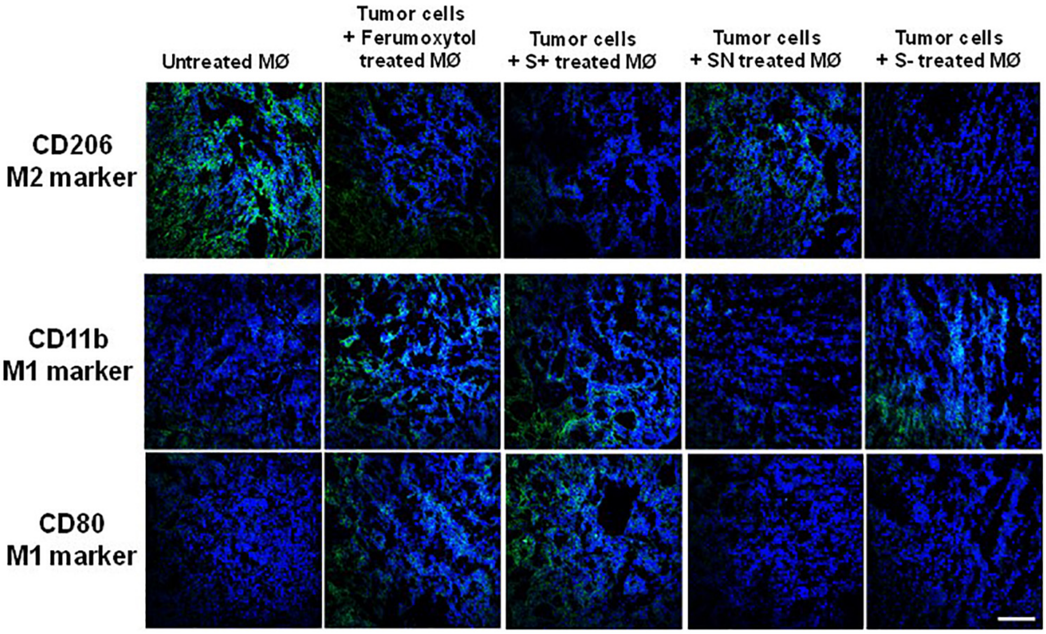

FIGURE 4 | Representative immunohistochemistry staining tumor slices for CD206 (green, M2-associated marker), CD11b (green, M1-associated marker), and CD80 (green, M1-associated marker) after injection of differently treated RAW cells. Scale bar, 100 μm.

We also explored if Fenton reaction occurred when HT1080 cells co-cultured with macrophages treated with differently charged SPIONs. In this experiment, we pre-treated macrophages with Ferumoxytol and various charges of SPIONs, respective macrophages were then incubated at the upper chamber while HT1080 cells were incubated in the lower chamber of a 0.4 μm Transwell (**Figure 5D**). From the fluorescence images and quantitation of Fenton positive cells after 24 h, we can see regardless of SPION charge, all groups including Ferumoxytol induced significant Fenton reactions in the cancer cells, and caused high expression of caspase 9 ($P < 0.005$) (**Figures 5E,F**).

Effect of SPIONs on Macrophage and Tumor Growth *in vivo*

To elucidate the effect of macrophage polarization toward tumor growth, we treated the RAW cells with the respective formulations and co-injected them with HT1080 cells. Images of tumors and tumor sizes are shown in **Figures 6A,B**, 14 days after injection. Results showed that co-injected tumors with prior treatment of Ferumoxytol, S+, and S− macrophages showed significant tumor retardation ($P < 0.01$) as compared to the treatment of tumors with non-polarized macrophages. while the SN pre-treated group exhibited no anti-tumor efficacy.

Prior to tumor excision, we injected Dextran MW10,000 tagged with Cascade blue, specially used to label TAMs. The tumor images and fluorescence intensity are shown in **Figures 6C,D**. As seen in both figures, the intrinsic tumor macrophages of S+ and S− groups were almost deprived compared to SN treated group or cancer cells treated with non-polarized macrophages.

DISCUSSION

In this manuscript, we focused on the ability of differently charged SPIONs to repolarize TAMs and suppress tumor growth. A previous study on Ferumoxytol had shown that it could induce the responses of pro-inflammatory macrophages, increase Caspase-3 expression of tumor cells, and decrease cancer progression (Zanganeh et al., 2016). Other studies on chronic venous leg ulcers, hemolytic diseases and immunotherapy for tumor have also indicated the essential role of iron in polarizing macrophage phenotypes (M1-like phenotype), and further maintaining chronic inflammation and affecting residual fibroblast (Sindrilaru et al., 2011; Vinchi et al., 2016; Costa et al., 2017). Differently charged SPIONs were able to polarize RAW 264.7 cells to an M1-like phenotype, and enhance ROS intensity in tumor cells, which could further create a Fenton reaction and cause tumor suppression. Interestingly, we found that there was efficacy difference among differently charged SPIONs, therefore, it is necessary to determine the most effective "charge-polarization" ratio for potential clinical application.

All SPIONs (S+, SN, and S−)were synthesized with a size range of 15–25 nm, a desirable size range; as they were small enough to escape from the elimination by the reticuloendothelial system; and to be easily penetrate deep into tumor (Popovic et al., 2010; Veiseh et al., 2010). The different surface charges of SPIONs could influence cellular uptake. In Prussian blue staining and iron assay of RAW 264.7 cells, S+ showed the highest uptake ($P < 0.005$), followed by S− ($P < 0.005$), while the PEG coated SN showed the least uptake. As positively charged nanoparticles were preferentially taken up by cells, while negatively charged

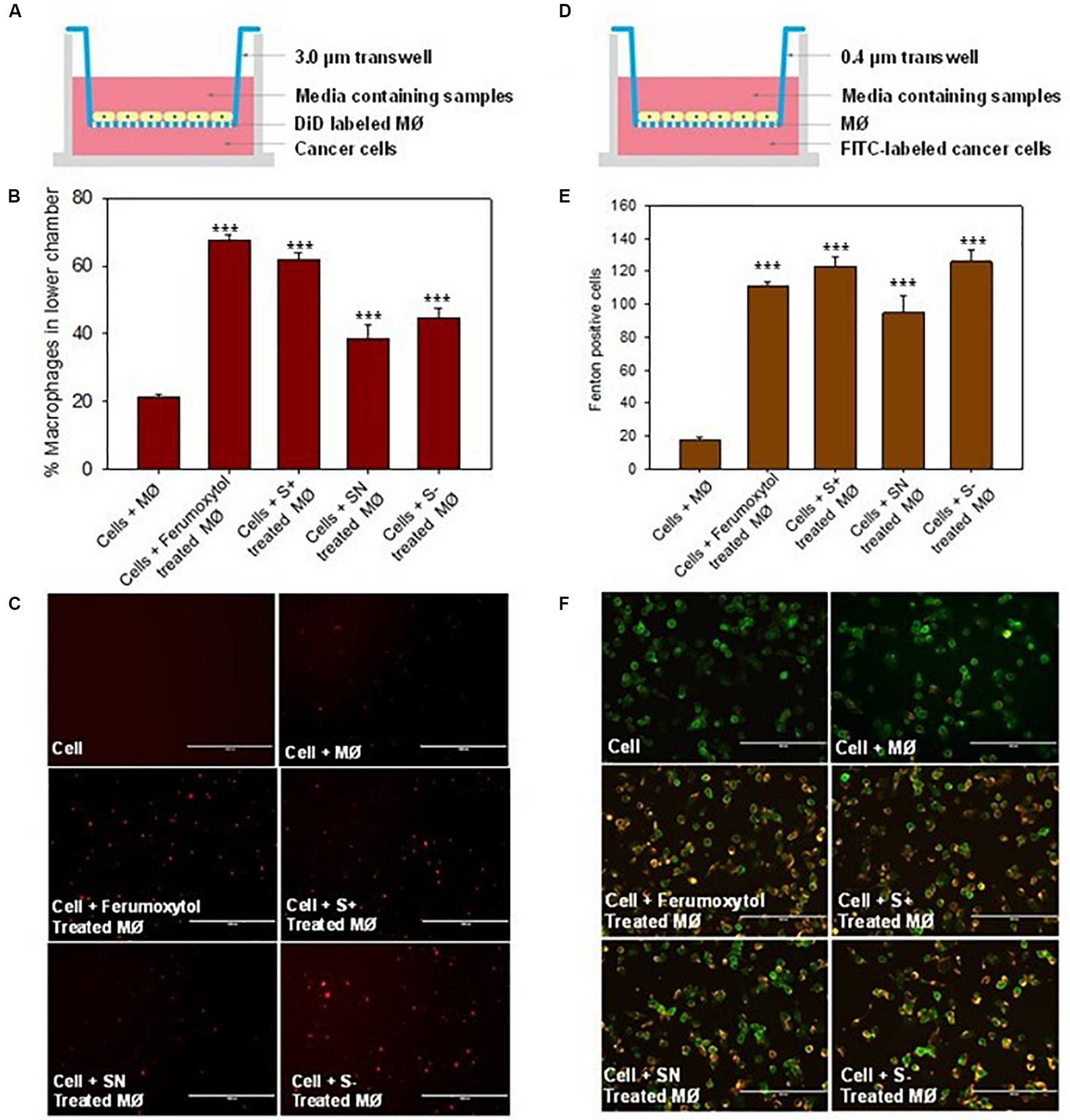

FIGURE 5 | Effect of macrophages treated with differently charged SPIONs on tumor cells. **(A)** Sketches of chemotaxis effect on macrophage incubated with tumor cells. **(B)** Percentage of macrophages on lower chamber in different groups. $^{***}P < 0.005$, compared with control (cell + macrophage). **(C)** The fluorescence images of DID-labeled macrophages (red) in the lower chamber. Scale bar, 1000 µm. **(D)** Co-incubation of macrophage and tumor cells with 0.4 µm trans well. **(E)** Calculation of Fenton positive tumor cells of different groups in lower chamber. $^{***}P < 0.005$, compared with control (cell + macrophage). **(F)** Fluorescence images of Caspase 9 (yellow) expression in tumor cells (green). Scale bar, 200 µm.

nanoparticles could show non-specific electrostatic interactions with proteins on the cell membrane; it is not surprising that both S+ and S− showed significant cellular uptake.

Our data demonstrated both S+ and S− were able to repolarize macrophages, as evidenced by the higher expression of TNF-α, iNOS, CD11b, and CD80, and lower expression of IL10, VEGF and CD206, which were characteristic hallmarks of M1 and M2-like macrophages, respectively. Previous *in vivo* studies on SPIONs confirmed they were ingested by macrophages and would be degraded in lysosomes, causing iron accumulation (Weinstein et al., 2010). The accumulated iron could up-regulate ferritin and cathepsin L levels in macrophages, and alter M2-like macrophages to an M1-like phenotype, with an increased expression of CD86 and TNFα (Laskar et al., 2013).

Macrophage repolarization was also evidenced by the co-culture of tumor cells with pre-treated macrophages (S+,

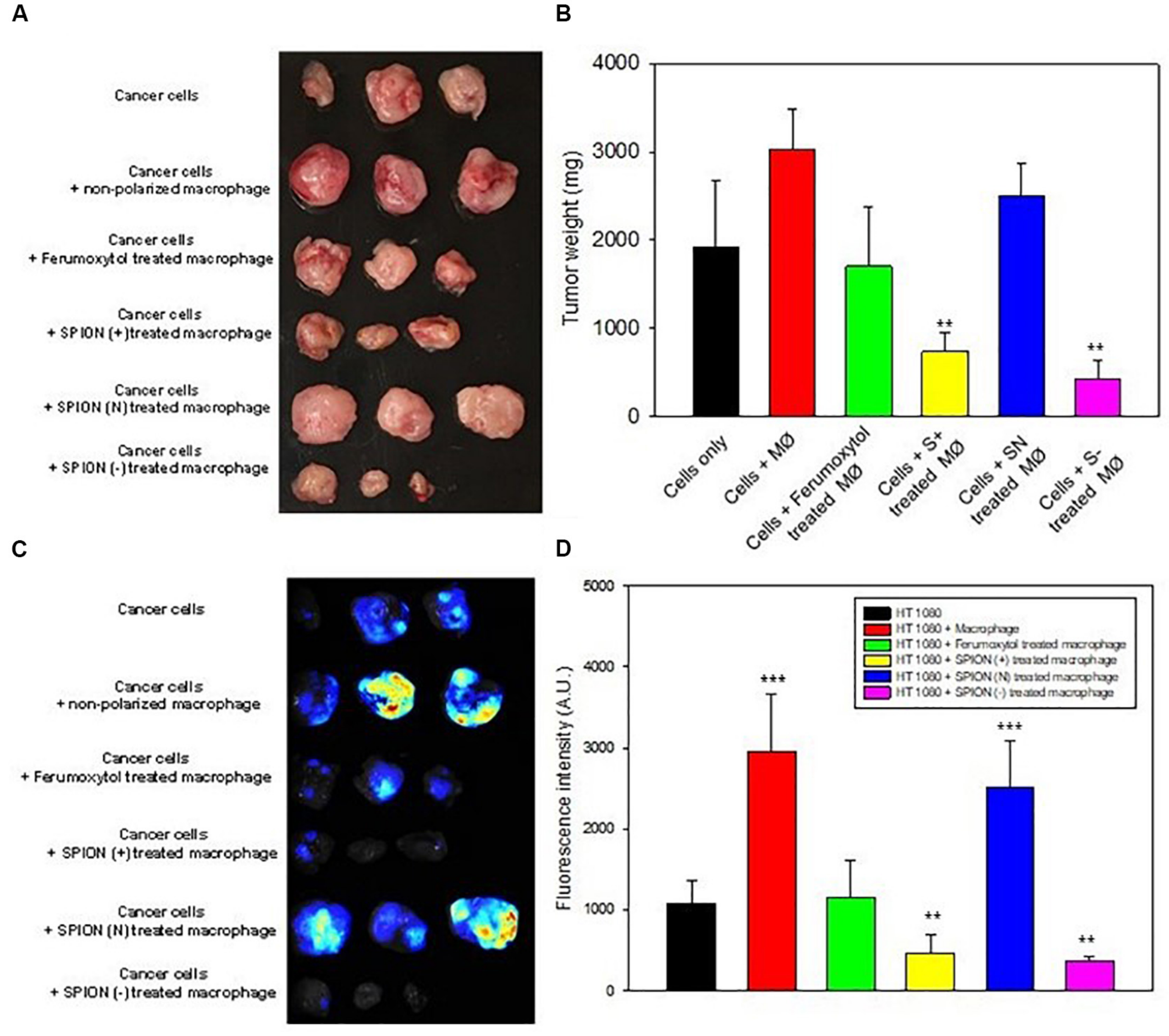

FIGURE 6 | *In vivo* inhibition of tumor growth. **(A)** Images of tumor at day 14 after representative treatment. **(B)** Relative tumor sizes of **(A)**. $^{**}P < 0.01$, compared with control (cancer cells). **(C)** Fluorescence images for TAMs in tumor area after different treatment as labeled by Blue Dextran®. **(D)** Relative fluorescence intensity of **(C)**. $^{**}P < 0.01$ and $^{***}P < 0.001$, compared with control (HT1080).

SN, S−). Co-culture of S+ and S− pre-treated macrophages with HT1080 triggered a high induction of ROS which then triggered an increased expression of Caspase 9, leading to apoptosis. Repolarized macrophages were reported to produce superoxide anions, oxygen radicals and nitrogen radicals (Sindrilaru et al., 2011). As the macrophages were treated with iron oxide nanoparticles, they produced ROS and could further react with iron by Fenton reaction, starting the programmed cell death of tumor cells by Caspase-dependent apoptosis (Zanganeh et al., 2016). Combined with the proinflammatory cytokines released by repolarized macrophages, the killing activities for tumor cells could be effectively enhanced.

S+ and S− pre-treated macrophage proved to have the highest tumor inhibition ability (**Figures 6A,B**). Ferumoxytol-treated macrophage also indicated a significant inhibition, while SN-pretreated macrophage did not show appreciable tumor retardation. And the number of TAMs in the tumor area was consistent with the efficiency of tumor retardation in Ferumoxytol and differently charged SPIONs groups. Our results demonstrate that both positive and negatively charged SPIONs had higher repolarization abilities *in vitro* and *in vivo*. Previous studies on immune cells had proved that repolarized macrophages could enhance the inflammatory reaction by cross regulating some signal pathways such as toll-like receptors (TLR) and tumor necrosis factor (TNF) on STAT3, and finally activating the essential pathway of nuclear factor kappa B (NF-κB) to trigger inflammatory reaction (Stark and Darnell, 2012; Glass and Natoli, 2016; Murray, 2017). In a nutshell, M1-like macrophages could produce proinflammatory cytokines like TNF-α and iNOS, and the newly recruited monocytes might also be triggered to modulate to an M1-like phenotype by iron stored in tumor area, forming the cycle for further enhancement of their antitumor effect.

CONCLUSION

In conclusion, our results confirmed the importance of surface charge for SPIONs in phenotype polarization of macrophage. Compared to SN, S+, and S− could significantly repolarize TAMs and suppress tumor growth. However, considering the toxicity of SPIONs in high concentration, S+ may have greater potential for further clinical anti-tumoral application.

DATA AVAILABILITY STATEMENT

All datasets presented in this study are included in the article/supplementary material.

ETHICS STATEMENT

The animal study was reviewed and approved by the Sun Yat-sen Memorial Hospital.

AUTHOR CONTRIBUTIONS

PS and XX oversaw all the experiments. WZ and SC carried out all the experiments. SL and CT did all the analysis. BL revised the manuscript.

FUNDING

This work was supported by the National Natural Science Foundation of China (81874226 and 81803020), the International Scientific and Technological Cooperation Program from Guangdong Science and Technology Department (2018A050506033 and 2016A030313834), the Thousand Talents Program for Distinguished Young Scholars, the grant from Guangzhou Science and Technology Bureau (201704020131 and 201902020015), the Three Million for Three Years Project of SYSMH, Special Funds for the Cultivation of Guangdong College Students Scientific and Technological Innovation (pdjh2019a0001), the grant from Guangdong Science and Technology Department (2017B030314026), and the Fundamental Research Funds for the Central Universities of China.

REFERENCES

Anderson, S. D., Gwenin, V. V., and Gwenin, C. D. (2019). Magnetic functionalized nanoparticles for biomedical, drug delivery and imaging applications. *Nanoscale Res. Lett.* 14:188. doi: 10.1186/s11671-019-3019-6

Barclay, A. N., and Van den Berg, T. K. (2014). The interaction between signal regulatory protein alpha (SIRPalpha) and CD47: structure, function, and therapeutic target. *Annu. Rev. Immunol.* 32, 25–50. doi: 10.1146/annurev-immunol-032713-120142

Bloemen, M., Brullot, W., Luong, T. T., Geukens, N., Gils, A., and Verbiest, T. (2012). Improved functionalization of oleic acid-coated iron oxide nanoparticles for biomedical applications. *J. Nanopart. Res.* 14:1100. doi: 10.1007/s11051-012-1100-5

Bonapace, L., Coissieux, M. M., Wyckoff, J., Mertz, K. D., Varga, Z., Junt, T., et al. (2014). Cessation of CCL2 inhibition accelerates breast cancer metastasis by promoting angiogenesis. *Nature* 515, 130–133. doi: 10.1038/nature13862

Costa, D. S. M., Breckwoldt, M. O., Vinchi, F., Correia, M. P., Stojanovic, A., Thielmann, C. M., et al. (2017). Iron induces anti-tumor activity in tumor-associated macrophages. *Front. Immunol.* 8:1479. doi: 10.3389/fimmu.2017.01479

Engblom, C., Pfirschke, C., and Pittet, M. J. (2016). The role of myeloid cells in cancer therapies. *Nat. Rev. Cancer* 16, 447–462. doi: 10.1038/nrc.2016.54

Glass, C. K., and Natoli, G. (2016). Molecular control of activation and priming in macrophages. *Nat. Immunol.* 17, 26–33. doi: 10.1038/ni.3306

Gunderson, A. J., Kaneda, M. M., Tsujikawa, T., Nguyen, A. V., Affara, N. I., Ruffell, B., et al. (2016). Bruton Tyrosine kinase-dependent immune cell cross-talk drives pancreas cancer. *Cancer Discov.* 6, 270–285. doi: 10.1158/2159-8290.CD-15-0827

Kaneda, M. M., Cappello, P., Nguyen, A. V., Ralainirina, N., Hardamon, C. R., Foubert, P., et al. (2016a). Macrophage PI3Kgamma drives pancreatic ductal Adenocarcinoma progression. *Cancer Discov.* 6, 870–885. doi: 10.1158/2159-8290.CD-15-1346

Kaneda, M. M., Messer, K. S., Ralainirina, N., Li, H., Leem, C. J., Gorjestani, S., et al. (2016b). PI3Kgamma is a molecular switch that controls immune suppression. *Nature* 539, 437–442. doi: 10.1038/nature19834

Kievit, F. M., Stephen, Z. R., Veiseh, O., Arami, H., Wang, T., Lai, V. P., et al. (2012). Targeting of primary breast cancers and metastases in a transgenic mouse model using rationally designed multifunctional SPIONs. *ACS Nano* 6, 2591–2601. doi: 10.1021/nn205070h

Komohara, Y., Jinushi, M., and Takeya, M. (2014). Clinical significance of macrophage heterogeneity in human malignant tumors. *Cancer Sci.* 105, 1–8. doi: 10.1111/cas.12314

Laskar, A., Eilertsen, J., Li, W., and Yuan, X. M. (2013). SPION primes THP1 derived M2 macrophages towards M1-like macrophages. *Biochem. Biophys. Res. Commun.* 441, 737–742. doi: 10.1016/j.bbrc.2013.10.115

Lu, M., Cohen, M. H., Rieves, D., and Pazdur, R. (2010). FDA report: ferumoxytol for intravenous iron therapy in adult patients with chronic kidney disease. *Am. J. Hematol.* 85, 315–319. doi: 10.1002/ajh.21656

Ma, H. L., Qi, X. R., Maitani, Y., and Nagai, T. (2007). Preparation and characterization of superparamagnetic iron oxide nanoparticles stabilized by alginate. *Int. J. Pharm.* 333, 177–186. doi: 10.1016/j.ijpharm.2006.10.006

Macdougall, I. C., and Geisser, P. (2013). Use of intravenous iron supplementation in chronic kidney disease: an update. *Iran. J. Kidney Dis.* 7, 9–22.

Mantovani, A., Sozzani, S., Locati, M., Allavena, P., and Sica, A. (2002). Macrophage polarization: tumor-associated macrophages as a paradigm for polarized M2 mononuclear phagocytes. *Trends Immunol.* 23, 549–555. doi: 10.1016/s1471-4906(02)02302-5

Murray, P. J. (2017). Macrophage polarization. *Annu. Rev. Physiol.* 79, 541–566. doi: 10.1146/annurev-physiol-022516-034339

Popovic, Z., Liu, W., Chauhan, V. P., Lee, J., Wong, C., Greytak, A. B., et al. (2010). A nanoparticle size series for in vivo fluorescence imaging. *Angew. Chem. Int. Ed. Engl.* 49, 8649–8652. doi: 10.1002/anie.201003142

Rodell, C. B., Arlauckas, S. P., Cuccarese, M. F., Garris, C. S., Li, R., Ahmed, M. S., et al. (2018). TLR7/8-agonist-loaded nanoparticles promote the polarization of tumour-associated macrophages to enhance cancer immunotherapy. *Nat. Biomed. Eng.* 2, 578–588. doi: 10.1038/s41551-018-0236-8

Sindrilaru, A., Peters, T., Wieschalka, S., Baican, C., Baican, A., Peter, H., et al. (2011). An unrestrained proinflammatory M1 macrophage population induced by iron impairs wound healing in humans and mice. *J. Clin. Invest.* 121, 985–997. doi: 10.1172/JCI44490

Sivakumar, B., Aswathy, R. G., Romero-Aburto, R., Mitcham, T., Mitchel, K. A., Nagaoka, Y., et al. (2017). Highly versatile SPION encapsulated PLGA nanoparticles as photothermal ablators of cancer cells and as multimodal imaging agents. *Biomater. Sci.* 5, 432–443. doi: 10.1039/c6bm00621c

Song, M., Liu, T., Shi, C., Zhang, X., and Chen, X. (2016). Bioconjugated manganese Dioxide Nanoparticles enhance chemotherapy response by priming tumor-associated Macrophages toward M1-like phenotype and attenuating Tumor Hypoxia. *ACS Nano* 10, 633–647. doi: 10.1021/acsnano.5b06779

Stark, G. R., and Darnell, J. J. (2012). The JAK-STAT pathway at twenty. *Immunity* 36, 503–514. doi: 10.1016/j.immuni.2012.03.013

Vallabani, N., and Singh, S. (2018). Recent advances and future prospects of iron oxide nanoparticles in biomedicine and diagnostics. *3 Biotech* 8:279. doi: 10.1007/s13205-018-1286-z

Veiseh, O., Gunn, J. W., and Zhang, M. (2010). Design and fabrication of magnetic nanoparticles for targeted drug delivery and imaging. *Adv. Drug Deliv. Rev.* 62, 284–304. doi: 10.1016/j.addr.2009.11.002

Vinchi, F., Costa, D. S. M., Ingoglia, G., Petrillo, S., Brinkman, N., Zuercher, A., et al. (2016). Hemopexin therapy reverts heme-induced proinflammatory phenotypic switching of macrophages in a mouse model of sickle cell disease. *Blood* 127, 473–486. doi: 10.1182/blood-2015-08-663245

Vitale, I., Manic, G., Coussens, L. M., Kroemer, G., and Galluzzi, L. (2019). Macrophages and metabolism in the tumor microenvironment. *Cell Metab.* 30, 36–50. doi: 10.1016/j.cmet.2019.06.001

Weinstein, J. S., Varallyay, C. G., Dosa, E., Gahramanov, S., Hamilton, B., Rooney, W. D., et al. (2010). Superparamagnetic iron oxide nanoparticles: diagnostic magnetic resonance imaging and potential therapeutic applications in neurooncology and central nervous system inflammatory pathologies, a review. *J. Cereb. Blood Flow Metab.* 30, 15–35. doi: 10.1038/jcbfm.2009.192

Zanganeh, S., Hutter, G., Spitler, R., Lenkov, O., Mahmoudi, M., Shaw, A., et al. (2016). Iron oxide nanoparticles inhibit tumour growth by inducing pro-inflammatory macrophage polarization in tumour tissues. *Nat. Nanotechnol.* 11, 986–994. doi: 10.1038/nnano.2016.168

Zhang, Z. Q., and Song, S. C. (2017). Multiple hyperthermia-mediated release of TRAIL/SPION nanocomplex from thermosensitive polymeric hydrogels for combination cancer therapy. *Biomaterials* 132, 16–27. doi: 10.1016/j.biomaterials.2017.03.049

Zhuang, M., Du, D., Pu, L., Song, H., Deng, M., Long, Q., et al. (2019). SPION-decorated exosome delivered BAY55-9837 targeting the pancreas through magnetism to improve the blood GLC response. *Small* 15:e1903135. doi: 10.1002/smll.201903135

Conflict of Interest: The authors declare that the research was conducted in the absence of any commercial or financial relationships that could be construed as a potential conflict of interest.

frontiers
in Bioengineering and Biotechnology

MINI REVIEW
published: 19 June 2020
doi: 10.3389/fbioe.2020.00682

Nanotechnology in Chronic Pain Relief

Jing Chen[1], *Teng Jin*[2]* *and Hua Zhang*[3]*

[1] School of Life Sciences, Shanghai University, Shanghai, China, [2] Department of Radiology, Union Hospital, Tongji Medical College, Huazhong University of Science and Technology, Wuhan, China, [3] Department of Radiology, The Affiliated Hospital of Qingdao University, Qingdao, China

Increasing awareness of chronic pain due to both injury and disease have encouraged drug companies and pharmaceutical researchers alike to design and fabricate better, more specific drugs for pain relief. However, overuse of clinically available pain medication has caused a multitude of negative repercussions, including drug tolerance, addiction, and other severe side effects, which can prolong suffering and reduce pain mediation. Applications of nanotechnology to the field of drug delivery has sought to enhance the treatment efficiency, lower side effects, and mitigate the formation of tolerance. The use of nanomaterials has several advantages for chronic pain relief, such as controlled release, prolonged circulation time, and limited side effects. With the development of nanotechnology, strategies for chronic pain relief have also bourgeoned utilizing a variety of nanomaterials and targeting surface modifications. In addition to using these materials as carriers for drug delivery, nanomaterials can also be designed to have inherent properties that relieve chronic pain. This minireview covers the current status of designed nanomaterials for pain relief and provides a discussion of future considerations for nanotechnology designed for relieving chronic pain.

Keywords: nanotechnology, chronic pain, inflammation, drugs, targeting

OPEN ACCESS

Edited by:
Wei Tao,
Harvard Medical School,
United States

Reviewed by:
Jiang Ouyang,
Central South University, China
Chuang Liu,
Ningbo Institute of Materials
Technology & Engineering (CAS),
China

Correspondence:
Teng Jin
394724768@qq.com
Hua Zhang
wozhanghua@126.com

Specialty section:
This article was submitted to Nanobiotechnology, a section of the journal Frontiers in Bioengineering and Biotechnology

Received: *01 May 2020*
Accepted: *02 June 2020*
Published: *19 June 2020*

Citation:
Chen J, Jin T and Zhang H (2020) Nanotechnology in Chronic Pain Relief.
Front. Bioeng. Biotechnol. 8:682.
doi: 10.3389/fbioe.2020.00682

INTRODUCTION

Chronic pain is characterized by enhanced responses to different external stimuli, also known as hyperalgesia, and is induced by inflammation following injury (Ji et al., 2014). When damage or inflammation occurs, mediators such as prostaglandins, cytokines, chemokines, neuropeptides, and nerve growth factor (NGF), are released (Zhang and An, 2007). These mediators maintain pain signaling that starts in the periphery and results in both peripheral and central sensitization, ultimately contributing to chronic pain. From the tremendous efforts of researchers in the fields of neurology and signaling, we have a deeper understanding of the mechanisms that drive pain. Additionally, chronic pain from a variety of sources, including injuries and disease, has promoted the development of targeted therapies (Mantyh et al., 2002; Binder, 2007; Said, 2007; Francis et al., 2008).

Current methods of pain relief and enhanced quality of life predominantly rely on surgery (Ducic et al., 2008), medication (Volkow et al., 2018), physical therapy (Ambrose and Golightly, 2015), and psychological therapy (De Williams et al., 2012). The use of medications, including opioid drugs (Sullivan and Howe, 2013; Ballantyne and Sullivan, 2015) and non-opioid drugs (Kaye et al., 2018), has increased significantly over the last several decades. Extensive use of medication has been associated with severe side effects, including drug addiction (Pohl and Smith, 2012), tolerance

(Zhuo, 2016), abuse (Vowles et al., 2015; Volkow and McLellan, 2016), and even death. These significant drawbacks of clinically available drugs have shifted the focus of drug development on improving the targeting of drugs, reducing side effects, and prolonging the release of the active compounds (Gao and Ji, 2010). However, due to their rapid metabolism, these current formulations are challenging to manufacture reproducibly, and the required dosing can cause poorly tolerated physical side effects.

The integration of pharmacological sciences with nanotechnology has been a key step toward creating more effective drugs for chronic pain with fewer negative implications (Feynman, 1960). With the advent of nanotechnology, the field of drug delivery has undergone extensive development resulting in several nanomaterials being approved for clinical use (Ventola, 2017). Compared with traditional formulations, nanomaterials can be efficiently loaded with drugs (Farokhzad and Langer, 2009), protect the stability of protein-based drugs (Xu et al., 2019), sustain controlled release with prolonged circulation time (Blanco et al., 2015), and are also designed to be highly biocompatible (Nyström and Fadeel, 2012). In the field of chronic pain relief, nanomaterials have been developed explicitly for the targeted delivery and release of pain medication. Inspired by the first Food and Drug Administration (FDA)-approved nanodrug Doxil (Barenholz, 2012), nanotechnology is being applied to many biomedical applications, but with a limited focus on chronic pain relief. In this minireview, we cover the development of medications for chronic pain relief that employ nanotechnology, including targeted and non-targeted nanomaterials, and provide perspective for future applications of nanotechnology in pain relief (**Figure 1**).

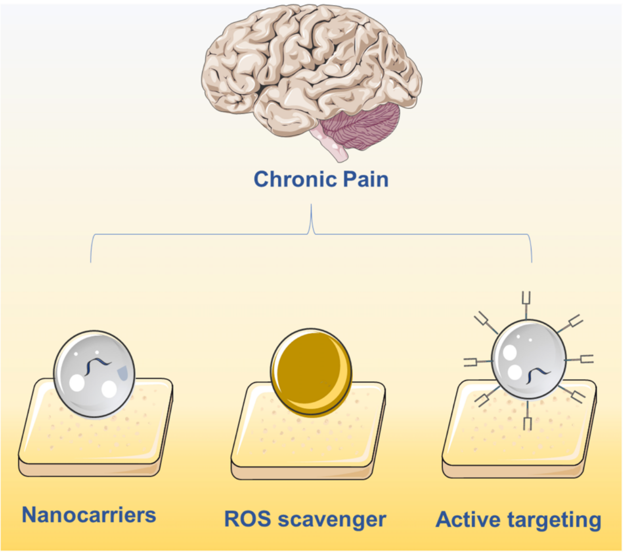

FIGURE 1 | Current main strategies on chronic pain relief using nanotechnology including the delivery of drugs using nanocarriers, active targeting nanocarriers and ROS clearance via nanomaterials.

NON-TARGETED NANOMATERIALS FOR PAIN RELIEF

Nanomaterials can be designated as organic, inorganic, and metal-organic nanomaterials based on their components. All three categories of nanomaterials have been used as controlled release delivery systems to minimize side effects and promote treatment efficacy for pain medication. Nanomaterials can be used to encapsulate both free molecules and protein-based drugs to increase blood circulation time with sustained, controlled release, resulting in long-lasting pain relief with minimal side effects. In this section, we will present the development of organic and inorganic non-targeted nanomaterials, which have been broadly applied to several pain relief drugs.

When introducing nanomaterials into a clinical application, a major preliminary concern is the biocompatibility of the proposed nanomaterial. Consequently, nanomaterials that have already been approved by the FDA are generally the first to be considered by researchers. FDA approved nanomaterials are mainly organic in nature such as liposomes (Koudelka and Turánek, 2012), PLGA (Makadia and Siegel, 2011), and other carbon based polymer nanomaterials (Palazzolo et al., 2018). Several inorganic nanomaterials have also been approved, but remain in the minority (Urie et al., 2018).

Liposomes are especially attractive since they are derived from cellular-like lipids, making them extremely biocompatible, and are relatively well studied. A number of liposome formulations have been the focus of emerging clinical trials. For example, PEGylated-liposomes have been used to encapsulate and enhance the accumulation of zoledronic acid (ZOL), an inhibitor of the ras-dependent Erk-mediated pathway, for the treatment of neuropathic pain (Caraglia et al., 2013). Caraglia et al. proved that this liposomal based delivery system passed across the blood brain barrier (BBB), promoting its ability to release ZOL for efficient pain mitigation. Likewise, Smith et al. (2006) encapsulated the drug hydromorphone using the liposomes and tested its neuropathic pain relief ability in rats. As expected, liposomal delivery enabled prolonged pain relief with only a single injection.

Although liposomes have many advantages and benefit from established synthesis procedures, the next generation of nanomaterials is focused on a myriad of tunable features including size, surface properties, responsiveness, controlled circulation time, high loading efficiency, and the ability to target specific tissues. Durán-Lobato et al. (2015) compared PEG-modified lipid nanomaterials to chitosan-modified lipid nanomaterials and PLGA nanomaterials for their ability to deliver cannabinoids via oral administration. The three biocompatible nanomaterials varied in their performance, providing design criteria for the development of nanomaterials for pain relief drug delivery.

The overproduction of reactive oxygen species (ROS) at sites of inflammation can result in chronic pain; consequently, nanomaterials that consume ROS are a promising avenue for pain relief (Gwak et al., 2013). Along these lines, Liu et al. (2013) employed fullerol nanomaterials, which are known to consume ROS, to protect inflammatory sites and relieve the pain.

Integrating an FDA-approved nanomaterial PLGA with bupivacaine, Garcia et al. (2011) studied its drug release mechanism and ability to relieve pain. Likewise, Shen et al. (2013) synthesized a new combination of nanomaterial, naocurcumin, composed of PLGA and curcumin to attenuate morphine tolerance. Naocurcumin was orally administrated to mice revealing excellent biocompatibility and ability to mitigate tolerance to morphine. Apart from small molecule drug delivery, biomedicine and nanotechnology have also been focused on the delivery of biomolecules such as Ribonucleic Acid (RNA). Based on the ability of p38 small interfering RNA (p38 siRNA) to assuage neuropathic pain, Shin et al. (2018) used PLGA nanomaterials to encapsulate the p38 siRNA enhancing its stability and slow release for pain alleviation.

In addition to organic nanomaterials, inorganic nanomaterials have also been designed and applied to address chronic pain. Compared with their organic counterparts, inorganic nanomaterials are generally more stable, ensuring prolonged circulation, and can be designed to have more physicochemical properties, such as controlled drug release via stimulation by an external field. Recently, Song et al. (2015) published on a graphene oxide (GO) based nano-system for neuropathic pain relief. Specifically, these GO nanomaterials provided a large surface area to load lidocaine and thalidomide, enhancing the capacity of these drugs to relieve neuropathic pain. In a separate study of inorganic nanomaterials, Wu et al. (2017) demonstrated that ultra-small magnetic iron oxide particles exhibited dose-dependent analgesic effects for the treatment of chronic pain. Using hydroxyapatite nanomaterials, which are biocompatible and have been approved for use in bone-related diseases, Gu et al. (2012) encapsulated and efficiently delivered NR2B-siRNA into mice via intrathecal injection. These nanoparticles exhibited statistical levels of pain mitigation that motivate the future development of materials for siRNA delivery.

TARGETED NANOMATERIALS FOR PAIN RELIEF

Despite the advantages of using nanomaterials to encapsulate drugs for the alleviation of chronic pain, their limited treatment efficacy has drawn attention to the critical need to develop more promising solutions. Since the causes of chronic pain are variable, the requirements for drug type and dosing differ depending on the treatment intervention. Enhancing the concentration of the drug at the indented site of action is one way to increase the efficacy of the treatment and minimize off target effects. Modification of nanomaterials using targeting substances such as peptides and antibodies can help achieve this site-specific targeting. Additionally, the route of administration is a critical consideration for the use of these targeted materials in their corresponding chronic pain models. For example, exposed sites of chronic pain on the skin can be topically treated using a smear or spray, whereas an injection through the dorsal root ganglion is more suitable for chronic spinal nerve pain. Internal injury or disease may benefit from oral, intranasal, intramuscular, or intravenous injections, depending on the source and location of the pain. In the following section, we will highlight research focused on targeted strategies to promote efficient chronic pain treatment.

Surface modification of nanomaterials is a simple yet effective way to enhance the location-specific absorption of delivered drugs. For example, Hoekman et al. (2014) synthesized opioid fentanyl-encapsulated liposomes with integrin targeting motifs, revealing increased stability, enhanced analgesic ability, and reduced plasma drug exposure after aerosol administration. Likewise, Tosi et al. (2007) designed polyester-based nanoparticles consisting of PLGA and glycosylated heptapeptides for the delivery of the opioid agonist loperamide. Excitingly, these nanoparticles not only crossed the BBB via peptide targeting but also exhibited sustained release of loperamide. Lalani et al. (2015) modified PLGA nanomaterials with lactoferrin and transferrin as the ligands, ensuring brain targeting for better pain relief. Additionally, Patel et al. (2012) showed enhanced tizanidine HCl delivery to the brain using surface-modified thiolated chitosan nanomaterials when they were administered intranasally.

Pain evoked by cancer, as well as some cancer medications, has drawn substantial attention from researchers studying pain relief. To address cancer-induced bone pain, Gdowski et al. (2017) modified PLGA with the bone microenvironment targeting amino-bisphosphonate, to deliver cabazitaxel for efficient pain relief in a bone metastatic prostate cancer model. To mimic the endogenous response in inflammatory sites, Hua et al. designed opioid loaded liposomes with the capacity to target inflammatory environments and release the corresponding drugs for simultaneous pain relief (Hua and Cabot, 2013). Important research described by Ramírez-García et al. (2019) reveals that their novel pH-responsive nanomaterials with the ability to target neurokinin-1 receptors (NK_1R) in the endosome display excellent capacity for preventing chronic pain. The accumulation of these pH-responsive nanomaterials in NK_1R-containing endosomes resulted in sustained chronic pain relief. To date, targeted nanomaterial design is mostly focused on modification with targeting ligands, but other strategies for active targeting remain largely unexplored, which will be presented in the perspective section.

DISCUSSION AND PERSPECTIVE

The urgent demand for chronic pain relief has highlighted the need for advancements in nanotechnology and pharmaceutical science, attracting attention from scientists in materials science, biomaterials, and chemistry. After decades of progress, the use of nanotechnology for chronic pain relief has been regarded as promising, prompting several clinical trials. However, the development of these smart nanomaterials is still in its infancy, with many unexplored opportunities. This minireview aims to highlight current difficulties in the pharmaceutical field and the advantages of applying nanotechnology to address these shortcomings. Herein, we have detailed some representative examples of organic and inorganic nanomaterials that facilitate controlled release, passive and active targeting, and the utilization of external energy fields. Based on these previous studies, we would like to provide some perspective thoughts on nanomaterial design for chronic pain relief (**Figure 2**):

(1) Oral administration of drugs poses a series of biological barriers requiring enhanced stability in the stomach, followed by the ability to be absorbed and be effective. Therefore, careful consideration of size, surface charge, and whether to modify the targeted ligands are necessary when designing a nanomaterial for this application. Moreover, non-conventional nanomaterials such as exosomes, cell membrane-derived vesicles (Van Dommelen et al., 2012) which have the targeting ability could also be investigated for oral drug delivery.
(2) Since each drug has its own kinetic profile, it is necessary to design appropriate nanomaterials to achieve a balance between drug release rate and drug action time. Additionally, combining interfering RNA with nanotechnology may prove to be an important strategy for pain mitigation.
(3) To improve therapeutic effects while minimizing side effects, a balance between the drug load and the release rate needs to be achieved. Similarly, improving the targeting efficiency of nanocarriers will reduce off-target effects by minimizing exposure to non-targeted organs during circulation.
(4) The phenomenon of protein coronas (Mahmoudi et al., 2016) has been attributed to the low efficacy of targeted nanomaterials, as serum proteins bind to the surface resulting in masking of the targeting epitopes and rapid clearance by phagocytic cells. Avoiding the formation of protein coronas is a critical avenue of research for the advancement of all nanomaterials for drug delivery. One proven method to mitigate corona formation is to modify the surface of nanomaterials with PEG.
(5) In pharmacology, the rapid development of multi-target drugs (Malek et al., 2015) has greatly improved the therapeutic outcome of chronic pain. Integrating nanotechnology with these enhanced formulations could allow for multi-drug co-delivery or their targeted release multiple sites. These methods have the capability to significantly reduce side effects, improve therapeutic outcomes, and reduce drug tolerization.
(6) Although nanomaterials have experienced rapid developmental growth over the past few decades, there is an urgency to ensure the safety of these materials and establish a unified evaluation standard.
(7) Although theranostic is a popular concept in the field of cancer, treatments for chronic pain treatment lack an intuitive imaging modality to monitor treatment progression and directly visualize therapeutic effects. Luminescent nanomaterials (Park et al., 2009) could be introduced into the field to achieve the integration of diagnosis and treatment, similar to their use in cancer therapeutics.
(8) The energy-conversion properties of inorganic nanomaterials can be employed to treat chronic pain, such as generating electrical signals when stimulated by light, (Tang et al., 2018) subsequently activating or inhibiting ion channels from playing an analgesic role. Additionally, magnetic nanomaterials (Zhang et al., 2016)

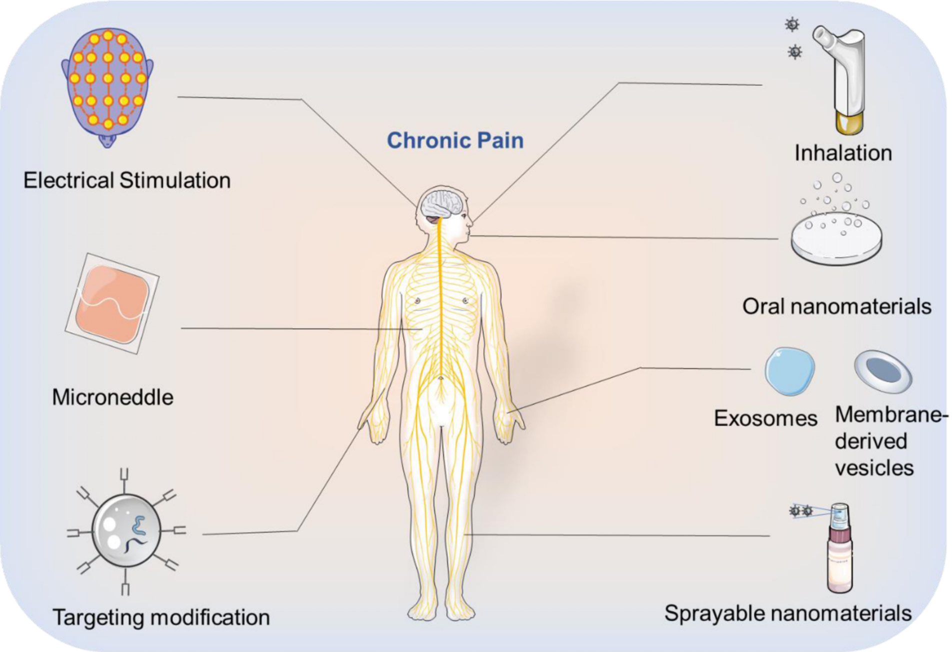

FIGURE 2 | Future outlooks that can be taken up by using nanotechnology for chronic pain relief.

can also use external magnetic fields to achieve targeted magnetic therapy.

(9) Microneedles (Kaushik et al., 2001) can be applied to the field of analgesia, where nanomaterials are integrated into the front end of the device to greatly reduce the pain caused by injecting drugs to patients.

(10) Inhalation of apposite nanomaterials that encapsulate drugs could be leveraged for chronic pain relief, especially lung-related pain.

As a collaboration between many fields of study, we believe that the application of nanotechnology to address chronic pain has a bright future. We hope that this field will develop steadily, with clinical relevance, to improve the quality of life for patients with chronic pain.

AUTHOR CONTRIBUTIONS

All the authors contributed to the writing of the manuscript.

ACKNOWLEDGMENTS

We would like to thank Editage (www.editage.com) for English language editing.

REFERENCES

Ambrose, K. R., and Golightly, Y. M. (2015). Physical exercise as non-pharmacological treatment of chronic pain: why and when. *Best Pract. Res. Clin. Rheumatol.* 29, 120–130. doi: 10.1016/j.berh.2015.04.022

Ballantyne, J. C., and Sullivan, M. D. (2015). Intensity of chronic pain—the wrong metric. *N. Engl. J. Med.* 373, 2098–2099. doi: 10.1056/nejmp1507136

Barenholz, Y. C. (2012). Doxil® —the first FDA-approved nano-drug: lessons learned. *J. Control. Release* 160, 117–134. doi: 10.1016/j.jconrel.2012.03.020

Binder, A. I. (2007). Cervical spondylosis and neck pain. *BMJ* 334, 527–531. doi: 10.1136/bmj.39127.608299.80

Blanco, E., Shen, H., and Ferrari, M. (2015). Principles of nanoparticle design for overcoming biological barriers to drug delivery. *Nat. Biotechnol.* 33:941. doi: 10.1038/nbt.3330

Caraglia, M., Luongo, L., Salzano, G., Zappavigna, S., Marra, M., Guida, F., et al. (2013). Stealth liposomes encapsulating zoledronic acid: a new opportunity to treat neuropathic pain. *Mol. Pharm.* 10, 1111–1118. doi: 10.1021/mp3006215

De Williams, A. C., Eccleston, C., and Morley, S. (2012). Psychological therapies for the management of chronic pain (excluding headache) in adults. *Cochr. Data. Syst. Rev.* 11:CD007407.

Ducic, I., Mesbahi, A. N., Attinger, C. E., and Graw, K. (2008). The role of peripheral nerve surgery in the treatment of chronic pain associated with amputation stumps. *Plastic Reconst. Surgery* 121, 908–914. doi: 10.1097/01.prs.0000299281.57480.77

Durán-Lobato, M., Martín-Banderas, L., Gonçalves, L. M., Fernández-Arévalo, M., and Almeida, A. J. (2015). Comparative study of chitosan-and PEG-coated lipid and PLGA nanoparticles as oral delivery systems for cannabinoids. *J. Nanop. Res.* 17:61.

Farokhzad, O. C., and Langer, R. (2009). Impact of nanotechnology on drug delivery. *ACS Nano* 3, 16–20.

Feynman, R. P. (1960). *There's Plenty of Room at the Bottom*. Pasadena, CA: California Institute of Technology.

Francis, R., Aspray, T., Hide, G., Sutcliffe, A., and Wilkinson, P. (2008). Back pain in osteoporotic vertebral fractures. *Osteopor. Int.* 19, 895–903. doi: 10.1007/s00198-007-0530-x

Gao, Y.-J., and Ji, R.-R. (2010). Targeting astrocyte signaling for chronic pain. *Neurotherapeutics* 7, 482–493. doi: 10.1016/j.nurt.2010.05.016

Garcia, X., Escribano, E., Domenech, J., Queralt, J., and Freixes, J. (2011). In vitro characterization and in vivo analgesic and anti-allodynic activity of PLGA-bupivacaine nanoparticles. *J. Nanopar. Res.* 13, 2213–2223. doi: 10.1007/s11051-010-9979-1

Gdowski, A. S., Ranjan, A., Sarker, M. R., and Vishwanatha, J. K. (2017). Bone-targeted cabazitaxel nanoparticles for metastatic prostate cancer skeletal lesions and pain. *Nanomedicine* 12, 2083–2095. doi: 10.2217/nnm-2017-0190

Gu, Y. H., Yan, X. B., Huang, D., Han, R., and Wu, L. X. (2012). *NR2B-siRNA Mediated by Hydroxyapatite Nanoparticles Relieves for Malin-Induced Pain of Mice*. Pfaffikon: Advanced Materials Research, Trans Tech Publications.

Gwak, Y. S., Hassler, S. E., and Hulsebosch, C. E. (2013). Reactive oxygen species contribute to neuropathic pain and locomotor dysfunction via activation of CamKII in remote segments following spinal cord contusion injury in rats. *PAIN*® 154, 1699–1708. doi: 10.1016/j.pain.2013.05.018

Hoekman, J. D., Srivastava, P., and Ho, R. J. (2014). Aerosol-stable peptide-coated liposome nanoparticles: A proof-of-concept study with opioid fentanyl in enhancing analgesic effects and reducing plasma drug exposure. *J. Pharm. Sci.* 103, 2231–2239. doi: 10.1002/jps.24022

Hua, S., and Cabot, P. J. (2013). Targeted nanoparticles that mimic immune cells in pain control inducing analgesic and anti-inflammatory actions: a potential novel treatment of acute and chronic pain conditions. *Pain Physician* 16, E199–E216.

Ji, R.-R., Xu, Z.-Z., and Gao, Y.-J. (2014). Emerging targets in neuroinflammation-driven chronic pain. *Nat. Rev. Drug Dis.* 13, 533–548. doi: 10.1038/nrd4334

Kaushik, S., Hord, A. H., Denson, D. D., McAllister, D. V., Smitra, S., Allen, M. G., et al. (2001). Lack of pain associated with microfabricated microneedles. *Anesth. Anal.* 92, 502–504. doi: 10.1097/00000539-200102000-00041

Kaye, A. D., Cornett, E. M., Hart, B., Patil, S., Pham, A., Spalitta, M., et al. (2018). Novel pharmacological nonopioid therapies in chronic pain. *Curr. Pain Head. Rep.* 22:31.

Koudelka, Š, and Turánek, J. (2012). Liposomal paclitaxel formulations. *J. Control. Release* 163, 322–334. doi: 10.1016/j.jconrel.2012.09.006

Lalani, J., Patil, S., Kolate, A., Lalani, R., and Misra, A. (2015). Protein-functionalized PLGA nanoparticles of lamotrigine for neuropathic pain management. *AAPS Pharm. Sci.Tech.* 16, 413–427. doi: 10.1208/s12249-014-0235-3

Liu, Q., Jin, L., Mahon, B. H., Chordia, M. D., Shen, F. H., and Li, X. (2013). A novel treatment of neuroinflammation against low back pain by soluble fullerol nanoparticles. *Spine* 38:1443. doi: 10.1097/brs.0b013e31828fc6b7

Mahmoudi, M., Bertrand, N., Zope, H., and Farokhzad, O. C. (2016). Emerging understanding of the protein corona at the nano-bio interfaces. *Nano Today* 11, 817–832. doi: 10.1016/j.nantod.2016.10.005

Makadia, H. K., and Siegel, S. J. (2011). Poly lactic-co-glycolic acid (PLGA) as biodegradable controlled drug delivery carrier. *Polymers* 3, 1377–1397. doi: 10.3390/polym3031377

Malek, N., Mrugala, M., Makuch, W., Kolosowska, N., Przewlocka, B., Binkowski, M., et al. (2015). A multi-target approach for pain treatment: dual inhibition of fatty acid amide hydrolase and TRPV1 in a rat model of osteoarthritis. *Pain* 156, 890–903. doi: 10.1097/j.pain.0000000000000132

Mantyh, P. W., Clohisy, D. R., Koltzenburg, M., and Hunt, S. P. (2002). Molecular mechanisms of cancer pain. *Nat. Rev. Cancer* 2, 201–209.

Nyström, A. M., and Fadeel, B. (2012). Safety assessment of nanomaterials: implications for nanomedicine. *J. Control. Release* 161, 403–408. doi: 10.1016/j.jconrel.2012.01.027

Palazzolo, S., Bayda, S., Hadla, M., Caligiuri, I., Corona, G., Toffoli, G., et al. (2018). The clinical translation of organic nanomaterials for cancer therapy: a focus on polymeric nanoparticles, micelles, liposomes and exosomes. *Curr. Med. Chem.* 25, 4224–4268. doi: 10.2174/0929867324666170830113755

Park, J.-H., Gu, L., Von Maltzahn, G., Ruoslahti, E., Bhatia, S. N., and Sailor, M. J. (2009). Biodegradable luminescent porous silicon nanoparticles for in vivo applications. *Nat. Mater.* 8, 331–336. doi: 10.1038/nmat2398

Patel, D., Naik, S., and Misra, A. (2012). Improved transnasal transport and brain uptake of tizanidine HCl-loaded thiolated chitosan nanoparticles for alleviation of pain. *J. Pharm. Sci.* 101, 690–706. doi: 10.1002/jps.22780

Pohl, M., and Smith, L. (2012). Chronic pain and addiction: challenging co-occurring disorders. *J. Psych. Drugs* 44, 119–124. doi: 10.1080/02791072.2012.684621

Ramírez-García, P. D., Retamal, J. S., Shenoy, P., Imlach, W., Sykes, M., Truong, N., et al. (2019). A pH-responsive nanoparticle targets the neurokinin 1 receptor in endosomes to prevent chronic pain. *Nat. Nanotechnol.* 14, 1150–1159. doi: 10.1038/s41565-019-0568-x

Said, G. (2007). Diabetic neuropathy—a review. *Nat. Clin. Prac. Neurol.* 3, 331–340.

Shen, H., Hu, X., Szymusiak, M., Wang, Z. J., and Liu, Y. (2013). Orally administered nanocurcumin to attenuate morphine tolerance: comparison between negatively charged PLGA and partially and fully PEGylated nanoparticles. *Mol. Pharm.* 10, 4546–4551. doi: 10.1021/mp400358z

Shin, J., Yin, Y., Park, H., Park, S., Triantafillu, U. L., Kim, Y., et al. (2018). p38 siRNA-encapsulated PLGA nanoparticles alleviate neuropathic pain behavior in rats by inhibiting microglia activation. *Nanomedicine* 13, 1607–1621. doi: 10.2217/nnm-2018-0054

Smith, L. J., Valenzuela, J. R., Krugner-Higby, L. A., Brown, C., and Heath, T. D. (2006). A single dose of liposome-encapsulated hydromorphone provides extended analgesia in a rat model of neuropathic pain. *Compar. Med.* 56, 487–492.

Song, T., Gu, K., Wang, W., Wang, H., Yang, Y., Yang, L., et al. (2015). Prolonged suppression of neuropathic pain by sequential delivery of lidocaine and thalidomide drugs using PEGylated graphene oxide. *J. Pharm. Sci.* 104, 3851–3860. doi: 10.1002/jps.24598

Sullivan, M. D., and Howe, C. Q. (2013). Opioid therapy for chronic pain in the United States: promises and perils. *PAIN*® 154, S94–S100.

Tang, Z., Zhao, P., Ni, D., Liu, Y., Zhang, M., Wang, H., et al. (2018). Pyroelectric nanoplatform for NIR-II-triggered photothermal therapy with simultaneous pyroelectric dynamic therapy. *Mat. Horiz.* 5, 946–952. doi: 10.1039/c8mh00627j

Tosi, G., Costantino, L., Rivasi, F., Ruozi, B., Leo, E., Vergoni, A. V., et al. (2007). Targeting the central nervous system: in vivo experiments with peptide-derivatized nanoparticles loaded with Loperamide and Rhodamine-123. *J. Control. Release* 122, 1–9. doi: 10.1016/j.jconrel.2007.05.022

Urie, R., Ghosh, D., Ridha, I., and Rege, K. (2018). Inorganic nanomaterials for soft tissue repair and regeneration. *Ann. Rev. Biomed. Eng.* 20, 353–374. doi: 10.1146/annurev-bioeng-071516-044457

Van Dommelen, S. M., Vader, P., Lakhal, S., Kooijmans, S., van Solinge, W. W., Wood, M. J., et al. (2012). Microvesicles and exosomes: opportunities for cell-derived membrane vesicles in drug delivery. *J. Control. Release* 161, 635–644. doi: 10.1016/j.jconrel.2011.11.021

Ventola, C. L. (2017). Progress in nanomedicine: approved and investigational nanodrugs. *Pharmacy Therapeutics* 42:742.

Volkow, N., Benveniste, H., and McLellan, A. T. (2018). Use and misuse of opioids in chronic pain. *Ann. Rev. Med.* 69, 451–465. doi: 10.1146/annurev-med-011817-044739

Volkow, N. D., and McLellan, A. T. (2016). Opioid abuse in chronic pain—misconceptions and mitigation strategies. *New Eng. J. Med.* 374, 1253–1263. doi: 10.1056/nejmra1507771

Vowles, K. E., McEntee, M. L., Julnes, P. S., Frohe, T., Ney, J. P., and van der Goes, D. N. (2015). Rates of opioid misuse, abuse, and addiction in chronic pain: a systematic review and data synthesis. *Pain* 156, 569–576. doi: 10.1097/01.j.pain.0000460357.01998.f1

Wu, P.-C., Hsiao, H.-T., Lin, Y.-C., Shieh, D.-B., and Liu, Y.-C. (2017). The analgesia efficiency of ultrasmall magnetic iron oxide nanoparticles in mice chronic inflammatory pain model. *Nanomed. Nanotechnol. Biol. Med.* 13, 1975–1981. doi: 10.1016/j.nano.2017.05.005

Xu, C., Lei, C., and Yu, C. (2019). Mesoporous silica nanoparticles for protein protection and delivery. *Front. Chem.* 7:290.

Zhang, C., Bu, W., Ni, D., Zhang, S., Li, Q., Yao, Z., et al. (2016). Synthesis of iron nanometallic glasses and their application in cancer therapy by a localized Fenton reaction. *Angew. Chem. Int. Ed.* 55, 2101–2106. doi: 10.1002/anie.201510031

Zhang, J.-M., and An, J. (2007). Cytokines, inflammation and pain. *Int. Anesthesiol. Clin.* 45:27. doi: 10.1097/aia.0b013e318034194e

Zhuo, M. (2016). Neural mechanisms underlying anxiety–chronic pain interactions. *Trends Neurosci.* 39, 136–145. doi: 10.1016/j.tins.2016.01.006

Conflict of Interest: The authors declare that the research was conducted in the absence of any commercial or financial relationships that could be construed as a potential conflict of interest.

frontiers
in Bioengineering and Biotechnology

REVIEW
published: 10 July 2020
doi: 10.3389/fbioe.2020.00652

Energy Conversion-Based Nanotherapy for Rheumatoid Arthritis Treatment

Pingping Wang[1], *Ao Li*[1*], *Luodan Yu*[2], *Yu Chen*[2*] *and Di Xu*[1*]

[1] Department of Ultrasound, The First Affiliated Hospital of Nanjing Medical University, Nanjing, China, [2] State Key Lab of High Performance Ceramics and Superfine Microstructure, Shanghai Institute of Ceramics, Chinese Academy of Sciences, Shanghai, China

Rheumatoid arthritis (RA) is characterized by synovial hyperplasia and cartilage/bone destruction, which results in a high disability rate on human health and a huge burden on social economy. At present, traditional therapies based on drug therapy still cannot cure RA, in accompany with the potential serious side effects. Based on the development of nanobiotechnology and nanomedicine, energy conversion-based nanotherapy has demonstrated distinctive potential and performance in RA treatment. This strategy employs specific nanoparticles with intrinsic physiochemical properties to target lesions with the following activation by diverse external stimuli, such as light, ultrasound, microwave, and radiation. These nanoagents subsequently produce therapeutic effects or release therapeutic factors to promote necrotic apoptosis of RA inflammatory cells, reduce the concentration of related inflammatory factors, relieve the symptoms of RA, which are expected to ultimately improve the life quality of RA patients. This review highlights and discusses the versatile biomedical applications of energy conversion-based nanotherapy in efficient RA treatment, in together with the deep clarification of the facing challenges and further prospects on the final clinical translations of these energy conversion-based nanotherapies against RA.

Keywords: rheumatoid arthritis, nanomedicine, energy conversion, external stimuli, nanotherapy

Edited by:
Gang Liu,
Xiamen University, China

Reviewed by:
Hanqing Chen,
Institute of High Energy Physics (CAS), China
Qianjun He,
University of Leeds, United Kingdom
Peng Mi,
Sichuan University, China
Bingyang Shi,
Macquarie University, Australia

Correspondence:
Ao Li
liaonj@njmu.edu.cn
Yu Chen
chenyuedu@shu.edu.cn
Di Xu
xudi@njmu.edu.cn

Specialty section:
This article was submitted to Nanobiotechnology, a section of the journal Frontiers in Bioengineering and Biotechnology

Received: *22 April 2020*
Accepted: *27 May 2020*
Published: *10 July 2020*

Citation:
Wang P, Li A, Yu L, Chen Y and Xu D (2020) Energy Conversion-Based Nanotherapy for Rheumatoid Arthritis Treatment. Front. Bioeng. Biotechnol. 8:652. doi: 10.3389/fbioe.2020.00652

INTRODUCTION

Rheumatoid arthritis (RA) is an autoimmune chronic systemic inflammatory disease with a high genetic risk, which affects 0.5–1.0% of adults worldwide and is currently incurable (Rudan et al., 2015; Smolen et al., 2016; Chuang et al., 2018). The prevalence of RA is higher in women than men. It mainly affects the small joints symmetrically, causing joint synovitis, synovial hyperplasia, cartilage and bone destruction, and eventually leading to deprived of labor (Doan and Massarotti, 2005; Sparks, 2019). The etiology of RA is still unclear. To effectively alleviate or control the progress of RA, the treatment is mainly based on medication and supplemented by surgery (Burmester and Pope, 2017). However, due to the serious side effects of traditional RA treatment strategies, and even ineffectiveness for some patients, it is urgent to seek new treatment protocols. Many emerging therapies including gene therapy, immunotherapy, and energy-conversion therapy have been launched in RA treatment (Kumar et al., 2016; Liu and Maeyama, 2016; Chen D. et al., 2019). These treatments have brought more remissions to RA patients with the support of nanobiotechnology and nanomedicine. In recent years, energy conversion-based nanotherapy has represented a promising approach for RA treatment, which is expected to improve the life quality of patients and reduce the social burden. Compared with other therapeutic methods, it can not only convert external energy into pro-apoptotic effect on target cells in RA arthritis, but also make a subclinical diagnosis to control inflammation and reduce side effects with fewer drug doses. In addition, the drug resistance of RA patients can also be avoided in the energy-conversion nanotherapy. This review summarizes and discusses the recent development on energy conversion-based nanotherapy for RA treatment, in accompany with the clarification on the current challenges and future developments regarding the construction of diverse functional nanoparticles with energy-converting performances for efficient RA treatment.

The etiology of RA is unknown, but studies have shown that the cause of RA is related to specific genes, epigenetics, post-translational modifications of proteins, and environmental factors (such as smoking, pathogen infection, and silicon) (Liao et al., 2009; Deane et al., 2017; Song and Lin, 2017; Karami et al., 2019). Under the combined influence of these factors, RA autoantibodies, immune cells and immune organs begin to activate, causing infiltration of cells in the joints. Eventually, it gradually changes from asymptomatic synovitis to symptomatic synovitis, causing stiffness, pain, swelling, and deformity of the joints (Croia et al., 2019) (**Figure 1**). The infiltration of synovium by inflammatory cells, such as B cells, T cells, plasma cells, neutrophils, dendritic cells and macrophages affects the supply of oxygen and nutrients to the joints by the synovium. These factors lead to the characteristics of hypoxia and acidity in RA inflammation joints. At the same time, activated synovial cells release vascular endothelial growth factors (VEGFs), resulting in angiogenesis. This is the so-called "pannus of synovium" (Marrelli et al., 2011; Feng and Chen, 2018). Pannus promotes the transfer of inflammatory cells into the joints to exacerbate arthritis. These inflammatory cells release inflammatory cytokines (such as IL-6, IL-17, IL-1β, TNF-α), chemokines, matrix metalloproteinases (MMPs), and prostaglandins to activate osteoclasts and cause bone destruction (Mateen et al., 2016; Davignon et al., 2018). Meanwhile, inflammatory factors can also enter the systemic circulation to cause systemic inflammation (Falconer et al., 2018).

Chemotherapy is the dominant treatment strategy of RA, supplemented by surgery. Most patients can now get remission after receiving available medications. In general, the agents for RA treatment are divided into non-steroidal anti-inflammatory drugs (NSAIDs), glucocorticoids (GCs), disease-modifying anti-rheumatic drugs (DMARDs), and biological agents (Dolati et al., 2016) (**Figure 2**). NSAIDs, such as aspirin, can reduce inflammation-related symptoms by inhibiting cyclooxygenase-2 (COX-2) activity. However, the long-term use may cause edema at the inflammatory site, gastrointestinal bleeding, or other symptoms, which is also limited to pain relief and cannot prevent the disease from progressing (Crofford, 2013; Thakur et al., 2018). The mechanism of GCs curative effect, such as prednisone, is immunosuppression. Although GCs possesses the strongest anti-inflammatory effect, high doses and frequencies are needed to achieve an ideal anti-arthritis effect (Ruyssen-Witrand and Constantin, 2018). In this case, the risk of side effects from taking GCs is substantially increased, which may cause cardiovascular diseases, muscle atrophy, glaucoma, peptic ulcers, infections and osteoporosis (Luís et al., 2019). The mechanism of DMARDs curative effect, such as methotrexate (MTX), is also immunosuppression. However, the curative effect is slow and the use of DMARDs must combine with other drugs in clinic. Its use can also cause bone marrow suppression, liver and kidney damage, and gastrointestinal dysfunction (Brown et al., 2016; Schett et al., 2016). Studies show that biotechnology drugs, such as anti-tumor necrosis factor and interleukin (IL) 1 are much better than traditional anti-rheumatic drugs, but even standard doses may increase the risk of serious infections in RA patients compared to DMARDs (Aletaha and Smolen, 2018), not to mention the prohibitive cost (Joensuu et al., 2015). When drug treatment is not effective for RA synovitis, synovectomy is the treatment choice, especially in the early stages of RA (Springorum et al., 2016; Burmester and Pope, 2017). However, synovectomy can only remove limited synovial tissue, and it can cause a high recurrence rate, post-operative pain, arthritis, fractures, and stiffness.

Due to the long-term and progressive nature of RA, patients must tolerate pain caused by the continued/repeated medication and suffer the adverse reactions caused by the distribution of the drug system. It has progressive joint destruction and extra-articular systemic manifestations. Studies show that 50–70% of patients lose their ability to work after 10–15 years of the disease development, which not only brings mental and economic burden to patients and their families, but also drags social development (Cross et al., 2014). Despite conventional RA treatment has achieved certain results, treatment tolerance and high-risk organ failure still exist. Therefore, it is still highly urgent to develop new treatment strategies for RA therapy.

GENERAL INTRODUCTION OF ENERGY CONVERSION-BASED NANOTHERAPY FOR RA TREATMENT

With the fast development of nanotechnology, nanomedicine and materdicine have improved the targeting of RA inflammation sites, thereby reducing the dosage and frequency of medication with mitigated side effects. Due to the extravasation through leaky vasculature and subsequent inflammatory cell-mediated sequestration (ELVIS effect) of RA arthritis sites (Yan et al., 2019), and the absence of blood vessels in the cartilage, meniscus, or ligaments of joints, nanomedicines feature better targeting of arthritis sites (Hendrich et al., 1997; Sharma et al., 2017). In order to improve the treatment outcome, the nanomedicines were modified with targeting ligands or antibodies against inflammatory cells of RA to enhance their capability of entering cells for inducing therapeutic effects through receptor-ligand or antigen-antibody interactions (Feng and Chen, 2018; Qamar et al., 2019). Very recently, energy conversion-based nanotherapy has gradually raised the research interests of scientific community in RA treatment. It uses specific

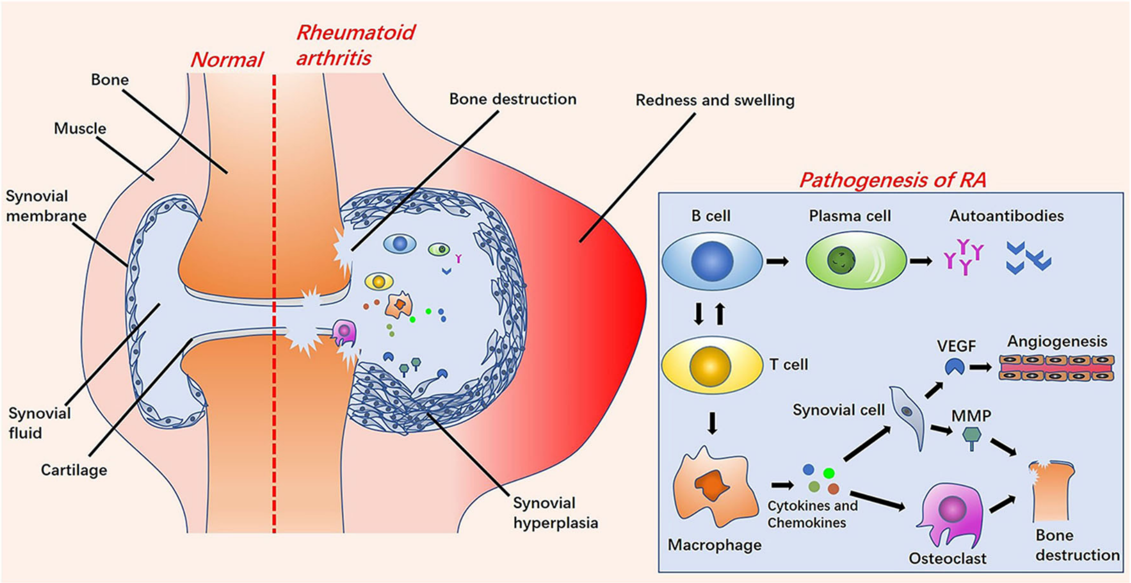

FIGURE 1 | The left side is a comparison diagram of normal joints and rheumatoid arthritis (RA) joints: the symptoms of RA joints are synovial hyperplasia, increased synovial fluid, redness and swelling, and bone destruction. On the right of this figure is a brief overview of the pathological process of RA. Under the influence of various pathogenesis factors, B cells and T cells are activated and interact. After the B cells are activated into plasma cells, they release autoantibodies. The activation of T cells into macrophages releases cytokines and chemokines, further stimulating the activation of synovial cells and osteoclasts. Vascular endothelial growth factors (VEGFs) released by synovial cells stimulate the formation of new blood vessels. Osteoclasts cooperate with matrix metalloproteinases (MMPs) to cause bone destruction.

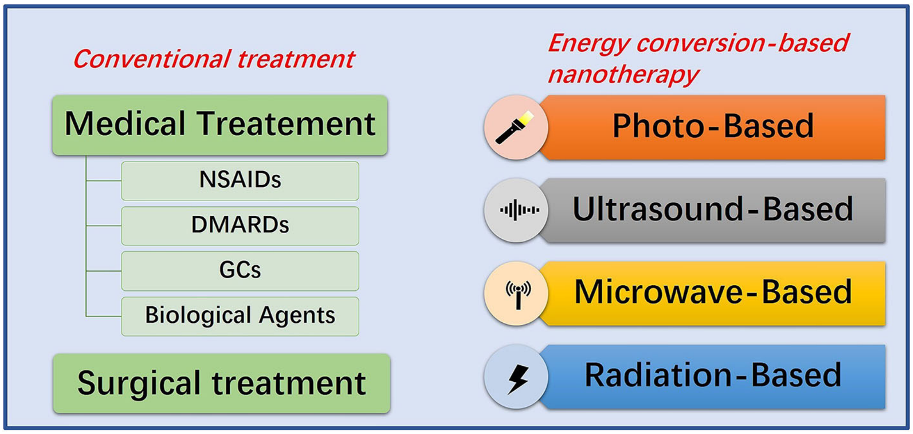

FIGURE 2 | Summative scheme of conventional treatment strategies and energy conversion-based nanotherapies for RA treatment. Conventional treatment strategies include medication and surgery. Energy conversion-based nanotherapies include photo-based, ultrasound-based, microwave-based and radiation-based nanotherapy.

nanomaterials with unique physiochemical properties to target lesions and supplements them with specific external stimuli, such as light, ultrasound, microwave, and radiation. Nanomaterials can convert these external stimuli and corresponding energy input into therapeutic effects or release therapeutic factors through an energy-conversion process (Xiang and Chen, 2019). Light-based, ultrasound-based, microwave-based, and radiation-based energy-conversion nanomedicines have been extensively explored in RA treatment as alternative therapies for RA treatment (**Figure 2**). These emerging technologies promote the necrosis and apoptosis of synovial fibroblasts and inflammatory cells in RA inflammation sites by generating cytotoxic reactive oxygen species (ROS), hyperthermia effects, cavitation effects, mechanical effects, photoelectric effects, and compton effect, and reduce the concentration of related inflammatory factors. After the designed nanoparticles enter the systemic circulation or joint cavity, several effects are produced under the external stimuli. There are two main targets of these effects. The first is inflammatory cells (mainly T cells and macrophages) (Chen X. et al., 2019). By promoting necrosis and apoptosis of inflammatory cells, nanoparticles can reduce the concentration of cytokines and chemokines. This pathway inhibits the activation of synovial cells and osteoclasts to reduce the release of VEGFs and MMPs, facilitating the remission of synovial pannus and bone destruction. The other target is synovial cells (Tang et al., 2017b). By directly targeting synovial cells, nanoparticles can destroy the pannus of synovium, so as to reduce the erosion of normal joint structures (Zhao et al., 2015).

Compared with traditional medicine and surgery, energy-conversion nanotherapy features less trauma and mitigated side effects (Xiang and Chen, 2019). In addition, it exhibits the following distinctive advantages. (1) By controlling the stimulation site directly at the targeted area, there is no relevant damage to the surrounding healthy tissue, which substantially improves the targeting treatment biosafety. (2) Thermal effect-related energy conversion nanotherapy can modulate the drug release by temperature-responsive design, which can also be induced by the cavitation/mechanical effect of ultrasound (Mi, 2020). (3) Nanomedicines with magnetic effect are capable of adopting external static magnetic field to target and gather the nanodrugs into the lesion, therefore it can improve the local drug concentration and maintenance the therapeutic duration and window. (4) Because of the low energy attenuation of ultrasound, microwave and magnetic field during the transmission, their penetration depth is deep, which is highly effective for the treatment of RA arthritis. (5) Some nanosystems that can perform energy conversion can also be developed as the contrast agents for bioimaging, achieving diagnostic imaging-guided/monitored RA nanotherapy.

PHOTO-BASED ENERGY-CONVERSION NANOTHERAPY FOR RA TREATMENT

Photodynamic Therapy (PDT)

Photodynamic therapy (PDT) can induce site-specific cytotoxic effects on many proliferative diseases. It can obtain profound therapeutic effect with a possibility of parallel use with other therapeutic modalities through minimally invasive and even non-invasive treatment, allowing it to be employed in the therapy of diverse diseases (Prazmo et al., 2016; Railkar and Agarwal, 2018; Aniogo et al., 2019; Shi et al., 2019). PDT is the interaction between three components (Kwiatkowski et al., 2018): (1) photosensitizers (PSs); (2) light with the appropriate wavelength; (3) dissolved oxygen molecules. There are two modes of action for PDT treatment (**Figure 3**). In the RA treatment, type II therapy is dominant. The basic principle is that under the light excitation of a specific wavelength, PSs directly transfer energy to the oxygen of the basic energy form ($^3O_2$) and then generate reactive oxygen species (ROS), mainly including $^1O_2$,·OH, and H_2O_2 (Gallardo-Villagrán et al., 2019). ROS can affect all components of the cells, such as proteins and DNA, causing necrosis or apoptosis of RA inflammatory cells (Tørring et al., 2014). Since the 1990s, PDT has been continuously explored for its therapeutic potential on synovium destruction or down-regulation of RA immune activity (Gallardo-Villagrán et al., 2019). Synovium hyperplasia of RA shows local tumor-like changes (infiltration and destruction of articular cartilages, bones, tendons and ligaments) (Senolt et al., 2006). In the past, PDT for RA was mainly employed to complement arthroscopic techniques for achieving more comprehensive synovial destruction. Laing et al. (1995) reported the first human PDT study for RA, in which 6 patients were treated with light activation through arthroscopy. However, one of the limitations of PDT in synovectomy was the poor pharmacokinetics, side effects and poor targeting efficacy of PSs (Trauner and Hasan, 1996). In order to overcome the shortcomings of traditional PSs, nanosized PSs have been broadly studied and applied in PDT treatment of RA very recently. The rational combination of PSs and nanomaterials can enhance drug targeting, reduce side effects and improve PDT efficacy in RA treatment (Liu et al., 2018; Gallardo-Villagrán et al., 2019).

As a common nano-formulation, liposomes feature desirable biocompatibility and biodegradability (Akbarzadeh et al., 2013). The joints of RA are highly vascularized and inflamed, so the penetration and retention in diseased tissue will increase, resulting in passive accumulation of liposome nanoparticles (Quan et al., 2014; Sharma et al., 2017; Chuang et al., 2018). Hansch et al. (2008) found that the use of pegylated liposomes loaded with photosensitizer Temoporfin (m-THPC) significantly elevated the concentration of m-THPC in RA inflammatory joints, which was beneficial to PDT treatment, while the side effects of m-THPC on the skin were reduced. However, the targeting effect achieved by the retention and penetration of vascular endothelial cells at the inflammation site of RA was limited. Schmitt et al. (2010) developed hyaluronic acid (HA)-modified chitosan nanogels and separately encapsulated three anionic PSs: tetra-phenyl-porphyrin-tetra-sulfonate ($TPPS_4$), tetra-phenyl-chlorin-tetra-carboxylate ($TPCC_4$) and chlorin e6 (Ce6) to assess their PDT efficiency. HA is a natural polysaccharide that specifically binds to the CD44 receptor on the surface of activated macrophages, so the constructed nanosized PSs could actively target macrophages in RA inflammatory tissue (Karousou et al., 2017). In addition, HA possesses lubrication and bone protection in the joints (Litwiniuk et al., 2016). *In vitro* PDT experiments of human THP-1 macrophages and mouse RAW 264.7 macrophages, it was found that HA-Ce6-chitosan-nanogel (Ce6-NG) could induce the highest phototoxicity, and the nano-photosensitizers were phagocytosed by macrophages in 4 h, which could retain in the cytoplasm and organelles for 24 h. *In vivo* experiments signified that Ce6-NG presented a high PDT effect on the murine model of RA. After PDT treatment at 25 J/cm^2, the serum amyloid (SAA) level decreased significantly, which was comparable to the standard corticosteroid prednisone as used in clinical treatment of RA. Importantly, this strategy avoided the side effects of corticosteroid (Schmitt et al., 2010).

It has been proved that the toxicity of photosensitizer tetra suplhonatophenyl porphyrin (TSPP) was positively correlated with its concentration, and the combination of titanium dioxide (TiO_2) and TSPP significantly could decrease the toxic effect of TSPP (Rehman et al., 2016). Zhao et al. (2015) studied the therapeutic effect of nanowhisker TiO_2-TSPP (TP) on PDT for

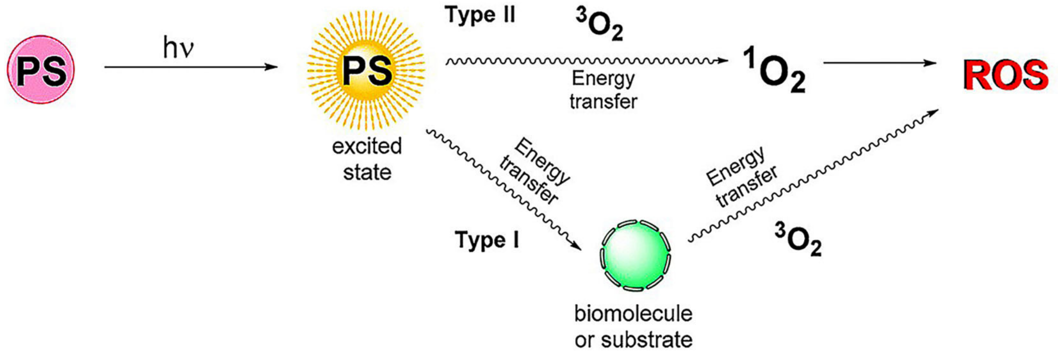

FIGURE 3 | Schematic diagram of PDT mechanism. Type I: PSs transfer energy to substrates or biomolecules. Then, the energy in the substrates and biomolecules is transferred to the oxygen of the basic energy form ($^3O_2$) to generate reactive oxygen species (ROS). Type II: PSs transfer energy directly to $^3O_2$, producing ROS. Reproduced with permission from Gallardo-Villagrán et al. (2019). Copyright 2019, MDPI.

RA treatment by combining TSPP with TiO_2 nanowhiskers (**Figure 4A**). The results demonstrated that after irradiation with 500–550 nm light, the accumulation of TP in the lesion site could produce ROS to kill synovial cells and inflammatory cells, and reduce interleukin (IL) 17 and tumor necrosis factor alpha (TNF-α) concentrations. It was found that PDT not only reduced RA arthritis (**Figure 4B**), but also reduced cachexia by decreasing TNF-α concentrations. This is highly beneficial for RA patients with generally poor life quality. The fluorescence imaging was also used to diagnose damaged joints in subclinical RA (**Figure 4C**), which could potentially assist the early diagnosis and effective treatment of RA clinical symptoms.

In order to solve the critical issue of relatively short plasma half-life of RA drugs and enhance the targeting capability toward inflammatory sites, macromolecular prodrugs have been gradually used in biomedicine. Prodrugs are generally designed where their activity is quenched outside the target tissue. Only after being stimulated at the target site (e.g., enzyme degradation, pH change), they can slowly release the therapeutic drug for elevating the local drug concentration (Wang et al., 2007; Fiehn et al., 2008; Shin et al., 2014). For instance, thrombin, a serine protease of the coagulation cascade, is highly upregulated in synovial tissue of RA (Nakano et al., 1999). Gabriel et al. (2009) developed thrombin-sensitive polymeric photosensitizer prodrugs (T-PS) to control the pharmacokinetics of the drug and targeted release in RA treatment. After the prodrug (>N70 kDa) entered RA hyperplastic synovial tissue through penetration and retention, the site connecting the photosensitizer units could be cleaved by thrombin, thereby slowly releasing the PSs for PDT treatment. The development of this prodrug strengthened the targeting amount into synovial tissue, and the accumulation duration of the drug in the inflammation site could reach more than 12 h.

Photothermal Therapy (PTT)

Another light-based energy-conversion treatment modality is PTT, which employs photothermal agents (PTAs) to convert laser energy into thermal energy, resulting in the local temperature increase (>41°C) to inhibit cell/tissue growth and promote lesion ablation. The damage is irreversible, including protein denaturation and nucleic acid damage (Hussein et al., 2018; Zhang et al., 2019). Since 1860s, the scientific community has conducted PTT research for a long period and achieved considerable progresses (Liu et al., 2019). It was showed that in the PTT of RA, the drug-releasing profile of drug-loaded nanoparticles achieved continuous and controlled pattern, which was dependent on local temperature and pH in comparison with free drug (Lee et al., 2013; Costa Lima and Reis, 2015; Kim et al., 2015; Pandey et al., 2019). Appropriate temperature and acidic environment could accelerate the release of loaded drug (Mi, 2020). Therefore, PTT can not only treat RA through high-temperature ablation, but also accelerate drug release and improve the treatment efficiency of RA. Most of the currently available PTAs are diverse near-infrared (NIR)-responsive nanomaterials, which can absorb NIR light and produce local hyperthermia under the irradiation of NIR laser (Jung et al., 2018). In the PTT for RA treatment, inorganic nanomaterials, such as metallic nanoparticles have been broadly used in RA nanotherapy due to their unique photothermal properties, which can also be developed as the drug nanocarriers or contrast agents for bioimaging (Hu et al., 2018).

Since 1985, gold compounds were admitted to be used as DMARDs because gold could inhibit the formation of vascular pannus by binding VEGFs (Faa et al., 2018; Darweesh et al., 2019). Nowadays, the development of nanotechnology has injected vitality into the application of gold in RA. Gold nanoparticles can absorb or scatter light through local surface plasmon resonance effects. Colloidal gold nanoparticles (Au NPs) are favored by scientific community because they can be easily synthesized with abundant topologies, such as spherical gold nanoparticles, gold nanorods, gold nanoshells, gold nanocages, and gold nanostars (Han et al., 2016; Cao et al., 2018; Fan et al., 2018). Au NPs can be facilely combined with biomarkers for targeted delivery. Especially, their physicochemical properties can be modulated by controlling their size and morphology (Feng and Chen, 2018). For instance, the range of light absorption of gold nanorods was controlled by adjusting their aspect ratio (Hu and Gao, 2011; Vonnemann et al., 2014).

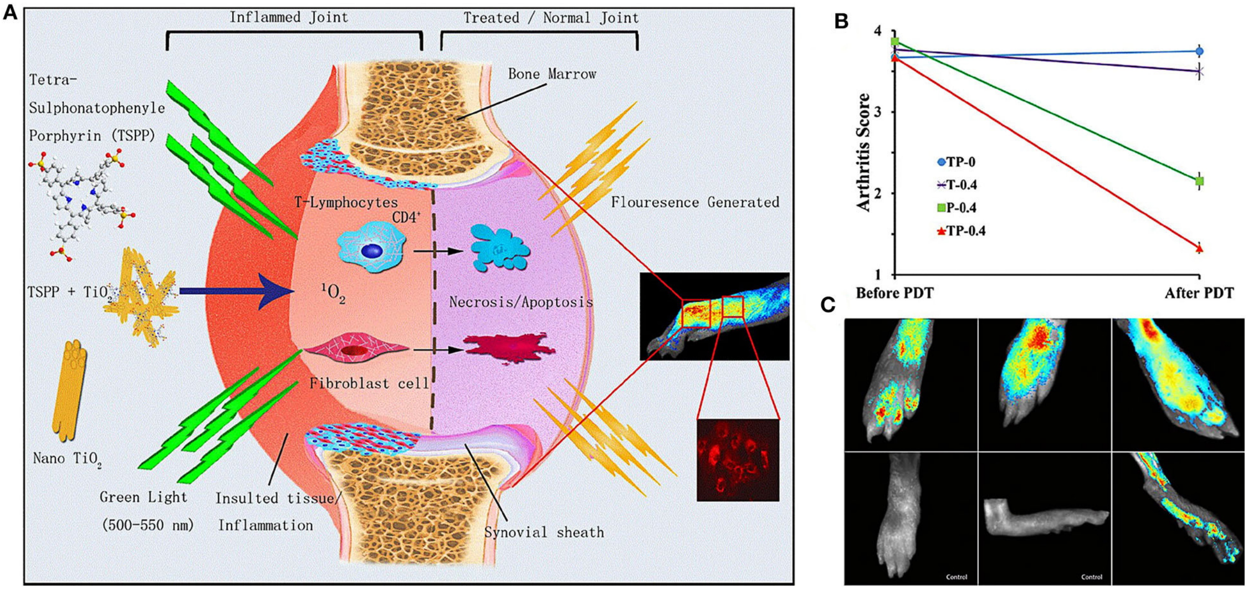

FIGURE 4 | (A) Schematic diagram of the therapeutic mechanism and biological imaging of nanowhisker TiO$_2$-TSPP (TP) in RA arthritis. Under the irradiation of 500–550 nm light, TP produced singlet oxygen ($^1O_2$) to kill synovial cells and T cells to reduce RA joint inflammation. At the same time, TP could also perform fluorescence imaging to monitor joint inflammation. **(B)** Effects of different experimental groups on collagen induced arthritis (CIA) mice arthritis score after PDT treatment. The decrease of TP-0.4 group was the most obvious. **(C)** On the 28th day of collagen-adjuvant injection, the control group showed no fluorescence, but the TP-0.4 group still exhibited fluorescence to monitor subclinical arthritis. Reproduced with permission from Zhao et al. (2015). Copyright 2015, Springer Nature.

Costa Lima and Reis (2015) loaded methotrexate (MTX) and spherical gold nanoparticles into pegylated poly(DL-lactic-co-glycolic acid) (PLGA) nanospheres to achieve chemo-photothermal therapy on targeting RA arthritis. MTX is the first-line drug of choice in curbing the progression of RA (Brown et al., 2016), but it has an non-negligible side effect (Wang W. et al., 2018). PLGA not only has high biocompatibility and excellent film-forming ability, but also is easier to degrade in inflammatory acidic environment and hyperthermia (Costa Lima and Reis, 2015; Ding and Zhu, 2018), so the release of MTX increased in low pH and high temperature. The MTX-PEG-PLGA-Au nanocomposites could significantly reduce the concentration of cytokines (IL-1, IL-6, and TNF-α) secreted by RA inflammatory cells *in vitro*, suggesting a favorable targeted chemo-photothermal platform in future RA treatment.

Compared with spherical gold nanoparticles, gold nanoshells have a larger surface area and higher drug loading capability (Wang Y. et al., 2018). Lee et al. (2013) developed MTX loaded gold half-shell nanoparticles and combined with arginine-glycine-aspartic acid (RGD) peptides for targeted PTT in RA inflammatory joints (**Figure 5**). The RGD peptides could target the RA inflammation sites by binding to $\alpha_v\beta_3$ integrin expressed on endothelial cells of neovascularization (Fu et al., 2019). The results signified that PTT with RGD-MTX-PLGA-Au nanoparticles could effectively reduce synovial hyperplasia and bone erosion in RA inflammatory joints at a dose of only 1/930 of the MTX solution group. This means that in future clinical PTT treatment of RA patients, the side effects of MTX can be greatly reduced and better treatment effect can be achieved.

Pandey et al. (2019) synthesized a nanoGold-core multifunctional dendrimer (Au-DEN) containing MTX to achieve efficient PTT for RA treatment. This gold nanostructure contained dendritic protrusions and a high specific surface area to attain stronger light-to-heat conversion capability and drug-carrying performance than gold nanoparticle with smooth surface (Chandrasekar et al., 2007; Shaunak, 2015). Different from other studies only employing Au NPs as PTAs, another near-infrared active substance IR780 was loaded in the gap of Au-DEN-MTX to improve the efficiency of PTT treatment for RA. *In vitro* experiment results confirmed that Au-DEN-MTX-IR780 nanoparticles upon laser irradiation were more toxic to activated macrophages than non-activated macrophages, meaning the targeting to the inflammatory cells of RA arthritis. Furthermore, MTX was released more due to the rupture of the ester bond in the acidic environment (pH: 5.4) of RA inflammation, which improved the targeting of the drug and mitigated the side effects. It is a pity that there was no *in vivo* RA model experiment in this research. The targeting and therapeutic effect of Au-DEN-MTX-IR780 nanoparticles on RA inflammatory joints needs further verification in the future.

In addition to gold, other metals (such as iron and ruthenium) have been used in the PTT of RA. Iron-based nanoparticles can use an external static magnetic field to magnetically transfer nanoparticles to the targeted site for promoting more concentrated, more effective, and longer-lasting retention of nanoparticles in the targeted tissue and subsequently achieve higher therapeutic efficacy (Xiao et al., 2019). For instance,

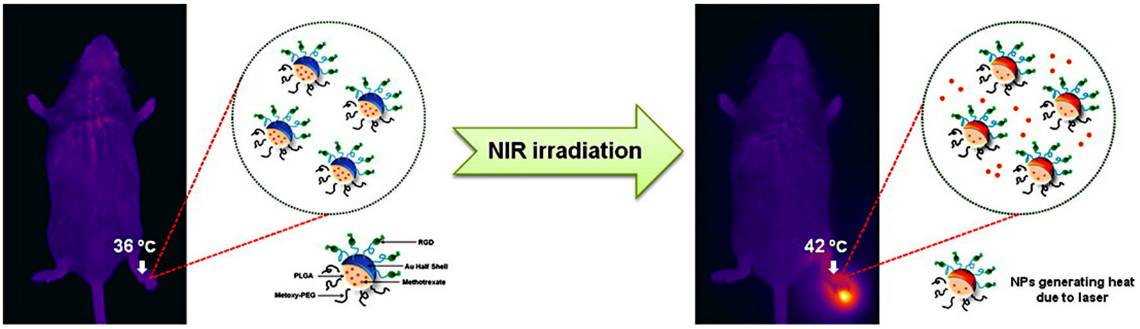

FIGURE 5 | Schematic diagram on the synthesis of RGD-MTX-PLGA-Au nanoparticles and the underlying treatment mechanism. MTX was firstly wrapped in PLGA, then the Au film was deposited on MTX-PLGA nanoparticle monolayer to obtain a half-shell structure (MTX-PLGA-Au). Finally, RGD peptides were conjugated to the Au surface to obtain RGD-MTX-PLGA-Au nanoparticles. In PTT for RA treatment, it could be heated to 42°C. Reproduced with permission from Lee et al. (2013). Copyright 2013, American Chemical Society.

Kim et al. (2015) added an iron half-shell to the original RGD-MTX-PLGA-Au nanoparticles and fabricated gold-iron-gold half-shells MTX-PEG-PLGA nanoparticles (MTX-PEG-PLGA-Au/Fe/Au (half shell) NPs). The iron half-shell layer embedded between the Au half-shell layers was used to retain the drug in the inflammatory joints for more than 1 week. The results demonstrated that compared with conventional treatment, PTT combined with external magnetic field-targeted therapy could achieve higher therapeutic efficacy and mitigated side effects with less doses. In addition, iron-based components supported T_2-weighted magnetic resonance imaging (MRI) *in vivo*, providing the guiding and monitoring functionality for RA treatment.

Magnetic iron oxide nanoparticles (IONPs) feature distinctive light-to-heat conversion performance (Shen et al., 2013; Chen et al., 2016). Due to the high biocompatibility of iron-based composition, iron oxide has been approved by FDA as a contrast agent for MR imaging (Chen et al., 2017). Carneiro et al. (2019) discovered that colloidal gold-coated super-paramagnetic IONPs (abbreviated as AuSPIONs) exhibited a high therapeutic effect on RA murine models accompanied with the decrease of circulation in major organs. For achieving better targeting effect and improved biosafety, Zhang et al. (2018) explored the size of 70–350 nm Fe_3O_4 nanoparticles on the efficacy of PTT for RA treatment. It was found that the smaller size of the nanoparticles made them easier to be engulfed by normal cells, resulting in the decrease of targeting. The nanoparticles with larger particle size caused the difficulty in penetrating the target area. Only the nanoparticles with a diameter of 220 nm featured the best targeting of inflammatory tissue in RA joints. They were difficult to be endocytosed by normal cells in the body but they were easy to penetrate and retain by RA inflammatory tissue. Therefore, the specific advantages of nanoparticles with suitable sizes in the following PTT treatment of RA are obvious, which should be carefully optimized for achieving the desirable RA treatment outcome.

Chen X. et al. (2019) employed quadrilateral ruthenium nanoparticles (QRuNPs) as the core and loaded resveratrol (RES) as an immunomodulator. RES could promote the transformation of M1-type macrophages to M2-type macrophages for inhibiting RA inflammation (**Figure 6**). Activated M1-type macrophages released inflammatory factors to aggravate the inflammation of RA. On the contrary, M2-type macrophages released anti-inflammatory factors to alleviate inflammation (Han et al., 2018). The experiment results exhibited that the QRu-PLGA-RES-DS nanoparticles upon laser irradiation group effectively inhibited arthritis in RA and protected the bone structure of the joints. In this experiment, the advantage of the polarization of RA inflammatory microenvironment macrophages was taken. Combined with the high temperature of PTT, it improved the targeting and therapeutic effect of RES on regulating inflammatory microenvironment of RA.

Combination of PTT and PDT With Synergy

PDT and PTT feature different mechanisms of therapeutic action, but both of them require laser activation to induce the photonic-therapeutic effect on RA. Furthermore, multifunctional photo-responsive biomaterials have been explored to induce both photothermal and photodynamic effects on synergistic RA treatment. For instance, copper sulfide nanoparticles (CuS NPs) and black phosphorus nanosheets (BPNs) have been researched for the combination therapy of PTT and PDT in RA treatment. After NIR irradiation, these photonic nanoagents achieve photothermal-energy conversion to generate hyperthermia effect. Meanwhile, cytotoxic ROS is generated at the inflammation site to promote the apoptosis of target cells (Gulzar et al., 2018; Pan et al., 2020). In addition to excellent photonic-therapeutic effect, CuS NPs and BPNs are conducive to alleviate cartilage and bone erosion caused by RA (Lu et al., 2018a,b; Pan et al., 2020). Nanoparticles with bone protection ability can greatly avoid the deformity and disability of joints in advanced RA patients, which effectively ameliorate their life quality.

CuS nanoparticles are one of the mostly explored metal chalcogenides nanosystems for efficient photonic nanomedicine, featuring high stability, desirable biocompatibility, and distinctive light-to-heat energy-conversion efficiency (Peng et al., 2017; Cao et al., 2018). Lu et al. (2018a) demonstrated that the fabricated $Cu_{7.2}S_4$ nanoparticles used in combination therapy

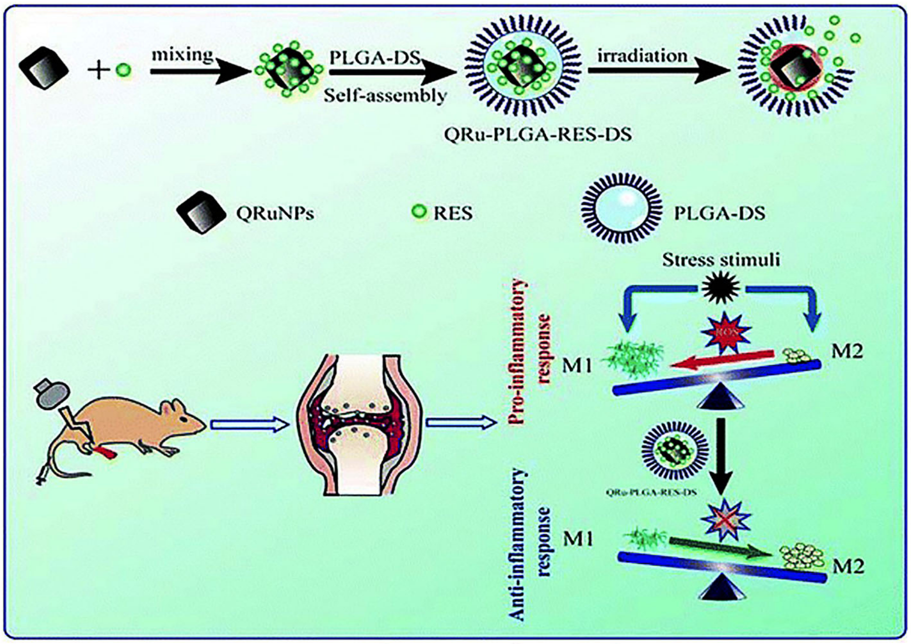

FIGURE 6 | Schematic illustration of the construction of QRu-PLGA-RES-DS nanoparticles for PTT treatment of RA. In detail, QRu-PLGA-RES-DS nanoparticles were synthesized by loading PLGA with conjugated quadrilateral ruthenium nanoparticles (QRuNPs) and resveratrol (RES). Under the irradiation of NIR light, QRuNPs generated heat by converting light to heat, which destroyed the PLGA film to release RES. RES promoted the transformation of M1-type macrophages to M2-type macrophages to inhibit RA inflammation. Reproduced with permission from Chen X. et al. (2019). Copyright 2013, RSC Pub.

of PTT and PDT could relieve symptoms of RA by effectively reducing synovial hyperplasia, inhibiting inflammation, and protecting bones and cartilage. *In vitro* experiments exhibited that $Cu_{7.2}S_4$ nanoparticles raised the temperature of surrounding tissue to 41–55°C under the irradiation of NIR light, and generated a large amount of ROS simultaneously (**Figure 7A**). After 28 days of PTT and PDT treatment, $Cu_{7.2}S_4$ nanoparticles with NIR irradiation mitigated RA in murine models with no destruction of cartilage or bone (**Figure 7B**). What's more, the antibacterial ability of $Cu_{7.2}S_4$ nanoparticles ensured a reduction in the risk of infection in future clinical treatment of RA (Li et al., 2016). This study provided an effective strategy for the development of multiple phototherapies (PTT and PDT in this case) for RA treatments.

Analog to $Cu_{7.2}S_4$ nanoparticles, black phosphorus nanosheets (BPNs) exert profound photo-therapeutic effects in RA treatment based on both PTT and PDT effects. Pan et al. (2020) integrated BPNs with heat-sensitive chitosan nanogels containing platelet-rich plasma (PRP) to construct heat-responsive nanocomposites for intra-articular treatment of RA. Unlike chitosan nanogels for PDT developed by Schmitt et al. (2010), BPNs gave BPNs/Chitosan/PRP thermosensitive hydrogel better photonic-therapeutic effect (a 43.19% photothermal conversion efficiency and excellent ROS generation capacity) to excise RA proliferating synoviocytes. Animal experiment results proved that the treatment effect of NIR irradiated nanogel on RA arthritis is better than that without NIR irradiation. Although the therapeutic effect of the BPNs/chitosan/PRP group on RA arthritis was not significantly better than that of the BPNs group, its hydrogel mechanical properties and PRP biological characteristics were unique to bone remodeling. This was essential to protect the joint structure of RA patients and avoid the loss of labor.

ULTRASOUND-BASED ENERGY-CONVERSION NANOTHERAPY FOR RA TREATMENT

Sonodynamic therapy (SDT) is an ultrasound-based energy-conversion nanotherapy with extensive application prospect (Rengeng et al., 2017). Ultrasound can effectively avoid the loss of energy during tissue penetration, so it features high penetrability and easily affects deep lesions (Yang et al., 2019). Therefore, it can be used for the treatment of RA large inflammatory joints. SDT combines low-frequency and low-intensity ultrasound with sound-sensitive substances to exert targeted therapeutic effects. At present, the specific underlying mechanism of SDT has not been fully revealed, but it may involve ultrasound cavitation, generation of ROS, and ultrasound-induced apoptosis in diseased cells (McHale et al., 2016; Pan et al., 2018). Some photosensitizers stimulated by ultrasound are also capable of killing the targeted cells with the generation of ROS and cavitation effect, such as porphyrin compounds and indocyanine green (ICG) (McHale et al., 2016; Rengeng et al., 2017). Using specific wavelengths of light and specific frequencies of ultrasound to activate

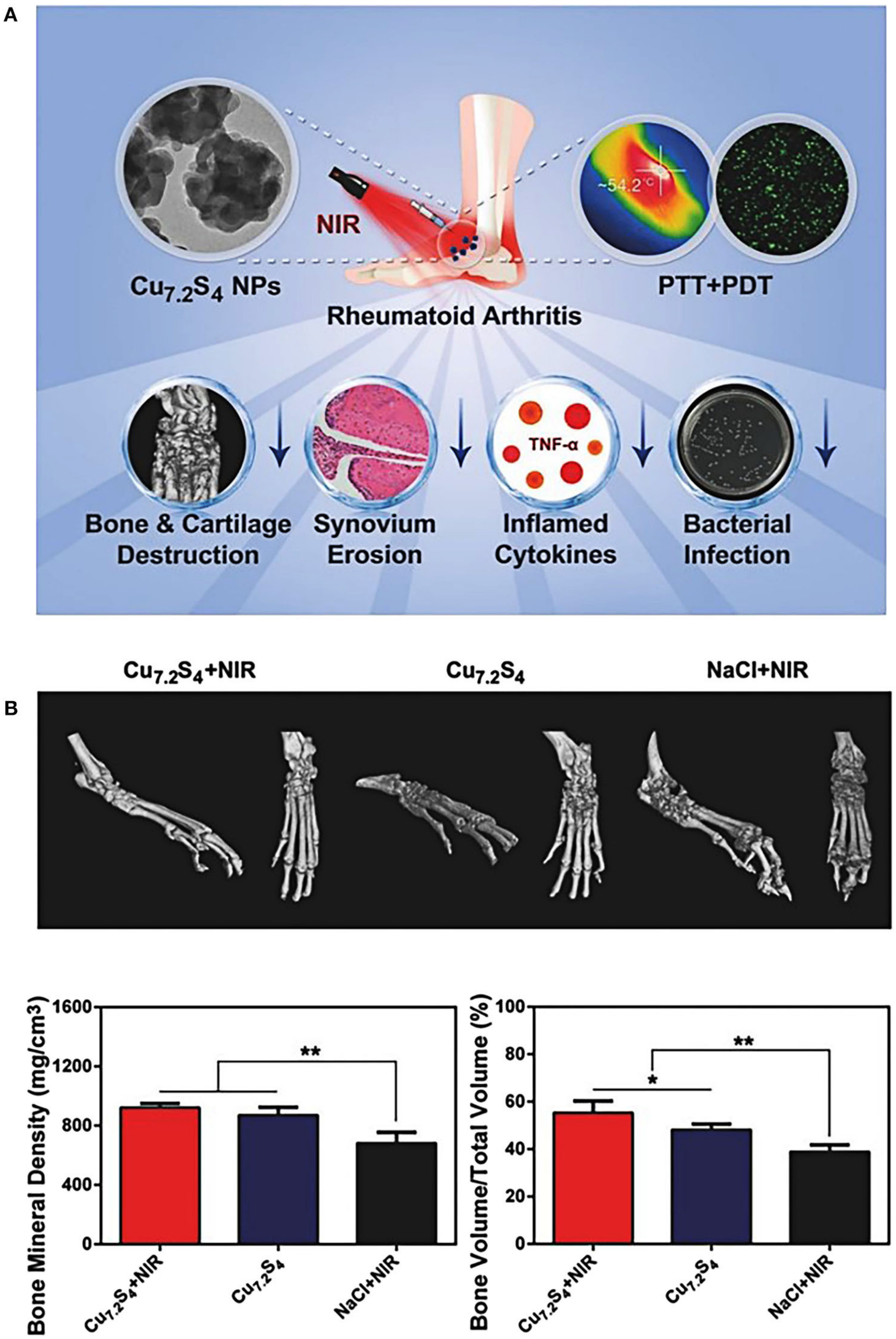

FIGURE 7 | (A) Schematic diagram of the therapeutic effects of $Cu_{7.2}S_4$ nanoparticles. Under the NIR irradiation, these photo-responsive nanoagents could simultaneously exert both therapeutic effects of PDT and PTT. During the *in vivo* experiment of RA murine models, the destruction of hyperplastic synovium and the reduction of bone destruction were clearly observed, and the level of RA inflammatory factor TNF-α was also decreased. In addition, the antibacterial effect of $Cu_{7.2}S_4$ nanoparticles could reduce bacterial infections. **(B)** Three-dimensional reconstructed computed tomography (CT) images, BMD and BV/TV values of arthritis in different groups after treatment of mice. The bone protection effect of $Cu_{7.2}S_4$ nanoparticles + NIR group could be observed (BMD, Bone Mineral Density; BV/TV, Bone Volume over Total Volume). Reproduced with permission from Lu et al. (2018a). Copyright 2018, John Wiley and Sons. $^{*}p < 0.05$, $^{**}p < 0.01$.

these sensitizers that specifically accumulate in tissue can simultaneously produce the therapeutic effects of both SDT and PTT in targeted regions. It has been demonstrated that the combination of PDT with SDT could enhance the therapeutic efficacy (Miyoshi et al., 2016; Binder et al., 2019).

In order to enhance the therapeutic efficacy of indocyanine green (ICG), Tang et al. (2017b) constructed PLGA-encapsulated phase-changeable nanoparticles loaded with oxygen and ICG (OI-NPs) for PSDT (photodynamic therapy followed by sonodynamic therapy) in RA treatment. ICG was used as both photosensitizer and sonosensitizer. To some extent, the oxygen loading addressed the critical issue of hypoxia in RA inflammation sites (McEwan et al., 2015). The experimental results signified that the apoptosis of RA fibroblast-like synoviocytes (RA-FLSs) induced by (OI-NPs)-mediated PSDT was 3-folds as compared to that in the ICG group. It was worth noting that blocking ROS did not completely eliminate the cytotoxic effect of OI-NPs, which indicating additional mechanical damage to RA-FLSs because of phase changes and fractures. This work may provide a paradigm for further improving the destruction effect of SDT on RA joint synovitis.

MICROWAVE-BASED ENERGY-CONVERSION NANOTHERAPY FOR RA TREATMENT

Microwave thermotherapy typically converts microwave energy into thermal energy for killing diseased cells/tissue and subsequently treating various diseases (Peng et al., 2015; Chen et al., 2018). It features the characteristics of facile operation, small trauma, strong controllability, and high therapeutic efficiency. Therefore, it has been extensively used in clinic. Typically, the local deep microwave thermotherapy was often employed for physical therapy of RA. It relieved the pain and stiffness of RA by raising the local temperature of the joint to nearly 41°C (Pentazos et al., 2018; Laskari et al., 2019).

Based on the performance of microwave-activated heat generation, thermally responsive liposomes (TSLs) were combined with microwave hyperthermia to develop thermally responsive drug-release nanoparticles sinomenine hydrochloride (SIN)-TSL to treat RA (Shen et al., 2020). Compared with traditional liposomes, the lipid bilayer structure of TSLs was destroyed at high temperature to promote the release of SIN, which induced the immunosuppressive effect on RA (Kneidl et al., 2014). Unlike the slow release under physiological conditions, SIN-TSL could release 80% of SIN within 6 h at 43°C. Meanwhile, TSL increased the accumulation concentration of nanoparticles, and improved the drug targeting to RA inflammation tissue. In the SIN-TSL with the radiation of microwave group, paw swelling of RA murine models was significantly reduced and so was the arthritic index. The levels of RA inflammatory cytokines of this group were the lowest, especially IL-6. On the basis of the potential of combining targeted therapy with physical therapy in RA treatment, this work provides a feasible solution for the design of thermal-responsive targeting nanocarriers for RA water-soluble drugs like SIN.

RADIATION-BASED ENERGY-CONVERSION NANOTHERAPY FOR RA TREATMENT

Radiation synovectomy (RSV) is a radiotherapy method for synovitis and inflammatory joint effusion, especially in RA arthritis (Cwikla et al., 2014). The appropriate radionuclide is injected into the joint cavity and engulfed by phagocytes at the site of inflammation. Radioactive decay transfers radiant energy to the synovial tissue, which gradually causes fibrosis of the synovial tissue, thereby reducing blood perfusion and effusion of inflammatory joints to reduce the infiltration of inflammatory cells (Ahmad and Nisar, 2018). Given that the nuclides used to treat arthritis are mostly short-range beta radiation (within a distance of 10 mm), the radiation exposure outside the joint is very low (Kamaleshwaran et al., 2015; Shinto et al., 2015). Studies have demonstrated that RSV has a relief effect in 60–80% of RA patients (Karavida and Notopoulos, 2010). However, the heterogeneity of radionuclide distribution in the RA joint cavity and leakage in the synovial cavity will reduce the radiation dose of local RSV and decrease the therapeutic effect on RA (Knut, 2015; Ahmad and Nisar, 2018). The introduction of nanoparticles can enhance the distribution of radionuclides in RA hyperplastic synovial tissue and mitigate their damage to normal joint structures.

Trujillo-Nolasco et al. (2019) coupled ^{177}Lu with MTX-loaded nanoparticles through 1,4,7,10-Tetraazacyclododecane-1,4,7,10-tetraacetic acid (DOTA) to form ^{177}Lu-DOTA-HA-PLGA-MTX for RA treatment. This nanoparticle exhibited obvious cytotoxic effect on RA inflammatory cells *in vitro*. Especially, the combination of targeted drug delivery and radiotherapy not only significantly improved the pharmacokinetics of MTX, but also increased the targeting of radionuclides to macrophages and relieved the radioactive damage to normal tissue in RA joints. However, this nanoparticle still requires to be tested *in vivo* RA models to elucidate the physiological dynamics and dosimetric evaluation of radiolabeled nanoparticles on normal synovial injury.

DISCUSSION

RA usually causes gradual destruction of joints, loss of labor, and a huge burden on society and the economy (Hu et al., 2017; Hyndman, 2017). At present, clinical drug treatment is dominant, but only some patients can achieve remission. Moreover, the clinical use of drugs is hampered by many factors, including severe systemic side effects, frequent dosing, tolerance to long-term administration, and high costs (Yang et al., 2017). In order to solve these problems, the energy-conversion nanotherapy has been extensively used in the treatment of RA

TABLE 1 | The available paradigms on energy-conversion nanotherapy in RA treatments.

Stimulus	Applications	Energy conversion	Nanomaterials	References
Light	PDT	Optical energy—cytotoxic ROS (chemical energy)	PEGylated liposomal m-THPC	Hansch et al., 2008
			Ce6-HA-chitosan nanogel	Schmitt et al., 2010
			TSPP-TiO_2	Zhao et al., 2015
			T-PS	Gabriel et al., 2009
	PTT	Optical energy—thermal effect	MTX-PEG-PLGA-Au	Costa Lima and Reis, 2015
			RGD-MTX-PLGA-Au (half shell)	Lee et al., 2013
			Au-DEN-MTX-IR780	Pandey et al., 2019
			MTX-PEG-PLGA-Au/Fe/Au (half shell)	Kim et al., 2015
			Fe_3O_4	Zhang et al., 2018
			QRu-PLGA-RES-DS	Chen X. et al., 2019
	PDT + PTT	Optical energy—cytotoxic ROS and Optical energy—thermal effect	$Cu_{7.2}S_4$	Lu et al., 2018a
			BPNs/Chitosan/PRP nano hydrogel	Pan et al., 2020
Ultrasound	PSDT	Optical energy—thermal effect and ultrasound energy—cavitation effect, ROS	OI-NP	Tang et al., 2017a
Microwave	MWTT	Microwave energy—thermal effect	SIN-TSL	Shen et al., 2020
Radiation	RSV	Radiant energy—cytotoxic ROS	177Lu-DOTA-HA-PLGA-MTX	Trujillo-Nolasco et al., 2019

and some emerging ideas have been proposed for achieving the desirable RA-therapeutic outcome (**Table 1**).

Despite the therapeutic principles/mechanisms of these treatments are different, they are all based on a variety of nano-formulations with unique physiochemical properties and biological effects. These nanoparticles could obtain "passive targeting" through the penetration and retention effect of the inflammation site. Moreover, some researchers took advantages of the difference of expression levels of the corresponding receptors between the RA site and the normal tissue to modify the nanoparticles to achieve "active targeting". Additionally, some researchers further introduced temperature, magnetic field, and enzyme-sensitive components to construct nanodrug formulations of RA treatment, achieving targeted and controlled drug release and rational combination with imaging technology to realize integrated diagnosis and treatment (Wang et al., 2016; Xu et al., 2018).

The biosafety and biocompatibility of nanomedicine have always received much apprehension. By examining *in vivo* pharmacokinetics, excretion, distribution and toxicity, several reported energy-conversion nanoparticles used for energy conversion exhibited low toxicity and superior biocompatibility both *in vivo* and *in vitro*. For example, Au-DEN NPs, Au-DEN MTX NPs and Au-DEN-MTX-IR780 NPs had no significant effect on hemolysis during intravenous administration ($p > 0.05$) in comparison with the hemolysis of free MTX (Pandey et al., 2019). In another study, by measuring Au concentration, it was manifested that most of the RGD-MTX-PLGA-Au nanoparticles could be excreted from the body after 28 days, and the histological examination of the major organs did not show obvious tissue damage (Lee et al., 2013). The results indicated that RGD-MTX-PLGA-Au nanoparticle with high biocompatibility and biosafety was beneficial for future clinical translation. However, the evaluation of nanoparticle-related biosafety is still preliminary with high complexity, including the standard synthesis of nanoparticles, and the specific interaction with *in vivo* biological systems (e.g., immune system, urinary system, nervous system, reproductive system, etc.) (Lopalco and Denora, 2018; Xiang and Chen, 2019). This fact substantially lengthens the time required for these nanoparticles entering the clinical stage from fundamental research.

Energy-conversion nanotherapy is generally easy to operate and minimally invasive with low side effects of chemotherapy. Especially, it can selectively treat RA inflammatory tissue based on the area covered by external stimulation (Xiang and Chen, 2019). Among the existing energy-conversion nanotherapies, light-based nanotherapy is the mostly developed modality for RA treatment. It can perform the synergy of PDT and PTT, but the attenuation of light in transmission will limit the application in the treatment of articular lesions of RA patients. By contrast, ultrasound- and microwave-based nanotherapies have less attenuation and deep penetration which make them have high potential for large joints treatment, such as knees and hips. However, there are too few related researches on ultrasound- and microwave-based nanotherapies due to the insufficient understanding of their energy-conversion mechanism. Radiation-based nanotherapy has distinctive therapeutic prospects in patients with RA synovitis, but it is not suitable for the early stages of RA. Nevertheless, only by preventing the development of RA in the subclinical stage of RA can it benefit the long-term life quality of RA patients (Burmester and Pope, 2017). Despite the energy-conversion nanotherapy has emerged in the fundamental research for RA treatment, it is still in the infancy and needs further extensive and systematic explorations (**Figure 8**). The ultimate goal is to achieve satisfactory treatment outcomes with low doses, mitigated side effects and less frequencies of administration. We have listed some aspects that need to be valued in future research.

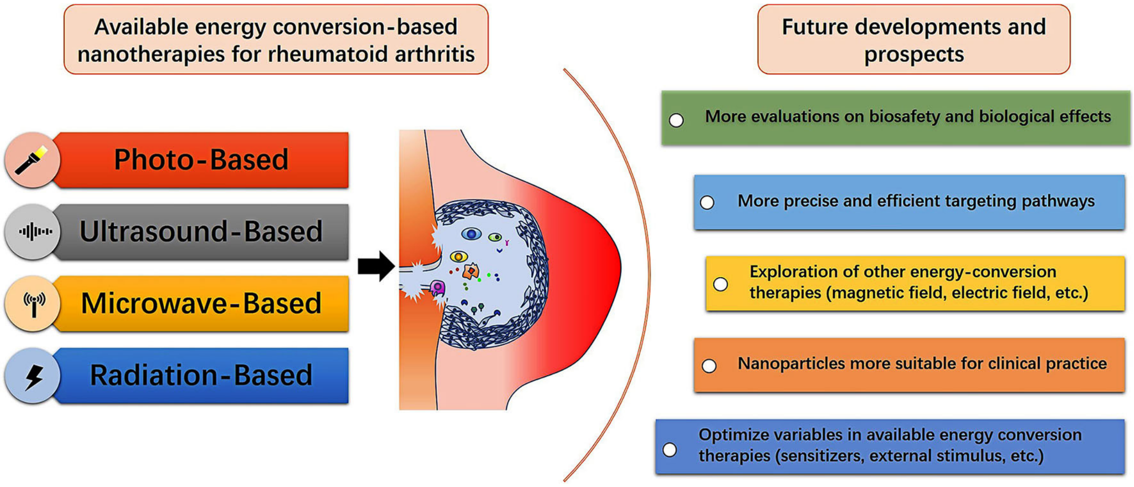

FIGURE 8 | Summative scheme of available energy conversion-based nanotherapies for treating RA, and future developments and prospects for fabricating diverse nanoagents with energy-conversion performances in RA treatment and further clinical translation.

(1) The nanoscale formulations for energy-conversion RA treatment should be rationally designed with some specific features and characteristics for satisfying the requirements of clinical translation, including adequate particle size, high stability, high drug-loading capacity, controlled drug release, targeted action on RA inflammatory sites, biodegradability, *in vivo* environmental friendliness, suitable retention time *in vivo*, easy fabrication, low price, and even the specific functionality of combinatorial/synergistic therapy with diagnostic-imaging guidance and monitoring. The priority among many facing critical issues is the systematic assessment on the biological effect and biosafety. It is highly expected that the long-term action mechanism of nanoparticles in the human body is still the focus of future researches.

(2) In the targeting systems of nanomedicines, a broad variety of RA-targeting markers have distinctive benefits for the treatment of RA, but there are still some inevitable deficiencies. For instance, peptide targets can be easily degraded *in vivo*; antigen-antibody targets can cause targeted toxicity to normal cells (Talotta et al., 2019). In order to obtain better targeting, several strategies, such as more accurate and efficient targets, multi-target combination and biomimetic targeting technology could be used. Simultaneously, the development of RA nano-targeting platform is based on the complex pathological mechanism of RA. In order to develop new RA targets and more stable and safer targeting markers, further research on the pathogenesis of RA is still highly required.

(3) Limited light-penetration depth is one of the attributes that hinders the efficacy of PDT/PTT in treating RA. The excitation light of the mostly available photosensitizers is mainly concentrated in the NIR region (Gallardo-Villagrán et al., 2019). Despite it might penetrate small joints, such as human fingers, it is still highly not sufficient for large joints, such as knees. Therefore, the development of light sources with stronger penetrability and the creation of new photosensitizers are one of the following research directions. In addition, during the PDT treatments, the hypoxic microenvironment of RA inflammation site and the oxygen consumption of PDT may further cause insufficient oxygen supply and decrease the therapeutic efficacy.

(4) High temperature (>48°C, thermal ablation) may cause damage to the surrounding normal tissue if there are thermal effects as induced by either microwave or light. The expected temperature with therapeutic effect is between 42 and 47°C, but the heating temperature is affected by the human body's thermal diffusion and heat conduction, making it difficult to keep the temperature of the lesion (especially deep lesions) constant. There is a need to develop a non-invasive method to monitor the three-dimensional temperature distribution of tissue in real time and to seek the optimal temperature and time of hyperthermia.

(5) Ultrasound-based, microwave-based and radiation-based energy-conversion nanotechnologies are in their infancy in the treatment of RA and require constant breakthroughs. First, there are many newly developed ultrasonic, microwave, and radiation sensitizers, which demand relevant experiments and researches in RA treatment. Second, the mechanism of SDT is still not completely revealed and needs further exploration and improvement to achieve the most effective ultrasound frequency and exposure dose for RA treatment. In addition, despite RSV is dominated by short beta radiation and bone is insensitive to radiation, the synovial tissue distribution of RA inflammation joints is uneven. The radiation of the distributed nanoparticles to the surrounding normal tissue is still unavoidable. Moreover, multiple injections of radioactive material might cause local skin atrophy, necrosis, or infection (Miszczyk et al., 2020). Therefore, the selection of radionuclides and the optimization of treatment are crucial.

(6) Other energy-conversion nanotherapeutics, such as electric field-based, radiofrequency-based, and magnetic heat therapy are also currently available in the treatment of RA, which demand further explorations. What's more, the combinatorial therapeutic modality, such as PDT + SDT and PDT + PTT can achieve improved and synergistic treatment efficiency. In order to obtain a better therapeutic effect on RA, multiple energy-conversion modalities can be combined with immunotherapy and gene therapy. To accurately control synergistic nanotherapy based on energy-conversion procedure, firstly, we need to have a more thorough understanding of the mechanism of energy-conversion technology and the pathological mechanism of RA, and optimize the variables in energy conversion therapy. Secondly, technologies that have the ability to monitor the process and effects of nanotherapy should be developed. Finally, we can employ multifunctional materials to avoid overly complex designs of nanosystems, which is conducive to the control of the treatment process and the future clinical translation.

(7) Last but not the least, the integration of diagnostic bioimaging and therapeutic functionalities into one nanoplatform is also a future development trend. This multifunctional nanoplatform allows subclinical diagnosis and early treatment of RA to improve prognosis, and can evaluate the therapeutic effect of treatments. This efficiently integrated nanoplatform puts forward higher requirements for the development of versatile functional nano-formulations, and requires the persistent efforts of scientific community.

Despite RA features a lower mortality rate in comparison with cancer, it is currently incurable, torturing patients, and putting a huge burden on human health and social economy. Energy conversion-based nanotherapy is a distinctive sprout for the treatment of RA, and its high therapeutic performance prospects the clinical practices for benefiting the RA patients. In the near future, this emerging technology still requires more researches and explorations for implementing the further clinical translations, provided that the facing critical issues and challenges are adequately addressed.

AUTHOR CONTRIBUTIONS

PW and LY prepared the manuscript. YC, AL, and DX proposed the review topic, led the project, and co-wrote/revised the manuscript.

FUNDING

We greatly acknowledge the financial support from the National Key R&D Program of China (Grant No. 2016YFA0203700), National Natural Science Foundation of China (Grant Nos. 81401427, 51672303), Excellent Young Scientist Foundation of NSFC (Grant No. 51722211), and Program of Shanghai Subject Chief Scientist (Grant No. 18XD1404300).

REFERENCES

Ahmad, I., and Nisar, H. (2018). Dosimetry perspectives in radiation synovectomy. *Phys. Med.* 47, 64–72. doi: 10.1016/j.ejmp.2018.02.015

Akbarzadeh, A., Rezaei-Sadabady, R., Davaran, S., Joo, S. W., Zarghami, N., Hanifehpour, Y., et al. (2013). Liposome: classification, preparation, and applications. *Nanoscale Res. Lett.* 8:102. doi: 10.1186/1556-276X-8-102

Aletaha, D., and Smolen, J. S. (2018). Diagnosis and management of rheumatoid arthritis: a review. *JAMA* 320, 1360–1372. doi: 10.1001/jama.2018.13103

Aniogo, E. C., B., Plackal Adimuriyil, G., and Abrahamse, H. (2019). The role of photodynamic therapy on multidrug resistant breast cancer. *Cancer Cell Int.* 19:91. doi: 10.1186/s12935-019-0815-0

Binder, S., Hosikova, B., Mala, Z., Zarska, L., and Kolarova, H. (2019). Effect of ClAlPcS(2) photodynamic and sonodynamic therapy on HeLa cells. *Physiol. Res.* 68, S467–S474. doi: 10.33549/physiolres.934374

Brown, P. M., Pratt, A. G., and Isaacs, J. D. (2016). Mechanism of action of methotrexate in rheumatoid arthritis, and the search for biomarkers. *Nat. Rev. Rheumatol.* 12, 731–742. doi: 10.1038/nrrheum.2016.175

Burmester, G. R., and Pope, J. E. (2017). Novel treatment strategies in rheumatoid arthritis. *Lancet* 389, 2338–2348. doi: 10.1016/S0140-6736(17)31491-5

Cao, Y., Li, S., Chen, C., Wang, D., Wu, T., Dong, H., et al. (2018). Rattle-type Au@Cu(2-x)S hollow mesoporous nanocrystals with enhanced photothermal efficiency for intracellular oncogenic microRNA detection and chemo-photothermal therapy. *Biomaterials* 158, 23–33. doi: 10.1016/j.biomaterials.2017.12.009

Carneiro, M. F. H., Machado, A. R. T., Antunes, L. M. G., Souza, T. E., Freitas, V. A., Oliveira, L. C. A., et al. (2019). Gold-coated superparamagnetic iron oxide nanoparticles attenuate collagen-induced arthritis after magnetic targeting. *Biol. Trace Elem. Res.* 194, 502–513. doi: 10.1007/s12011-019-01799-z

Chandrasekar, D., Sistla, R., Ahmad, F. J., Khar, R. K., and Diwan, P. V. (2007). Folate coupled poly(ethyleneglycol) conjugates of anionic poly(amidoamine) dendrimer for inflammatory tissue specific drug delivery. *J. Biomed Mater. Res. A* 82, 92–103. doi: 10.1002/jbm.a.31122

Chen, C. L., Siow, T. Y., Chou, C. H., Lin, C. H., Lin, M. H., Chen, Y. C., et al. (2017). Targeted superparamagnetic iron oxide nanoparticles for *in vivo* magnetic resonance imaging of T-cells in rheumatoid arthritis. *Mol. Imaging Biol.* 19, 233–244. doi: 10.1007/s11307-016-1001-6

Chen, D., Liu, H., Wang, Y., Chen, S., Liu, J., Li, W., et al. (2019). Study of the adoptive immunotherapy on rheumatoid arthritis with Thymus-derived invariant natural killer T cells. *Int. Immunopharmacol.* 67, 427–440. doi: 10.1016/j.intimp.2018.12.040

Chen, L., Wu, L., Liu, F., Qi, X., Ge, Y., and Shen, S. (2016). Azo-functionalized Fe_3O_4 nanoparticles: a near-infrared light triggered drug delivery system for combined therapy of cancer with low toxicity. *J. Mater. Chem. B* 4, 3660–3669. doi: 10.1039/C5TB02704G

Chen, X., Zhu, X., Ma, L., Lin, A., Gong, Y., Yuan, G., et al. (2019). A core-shell structure QRu-PLGA-RES-DS NP nanocomposite with photothermal response-induced M2 macrophage polarization for rheumatoid arthritis therapy. *Nanoscale* 11, 18209–18223. doi: 10.1039/C9NR05922A

Chen, Z., Niu, M., Chen, G., Wu, Q., Tan, L., Fu, C., et al. (2018). Oxygen production of modified core-shell CuO@ZrO(2) nanocomposites by microwave radiation to alleviate cancer hypoxia for enhanced chemo-microwave thermal therapy. *ACS Nano* 12, 12721–12732. doi: 10.1021/acsnano.8b07749

Chuang, S.-Y., Lin, C. H., Huang, H, T., and Fang, Y. J. (2018). Lipid-based nanoparticles as a potential delivery approach in the treatment of rheumatoid arthritis. *Nanomaterials* 8:42. doi: 10.3390/nano8010042

Costa Lima, S. A., and Reis, S. (2015). Temperature-responsive polymeric nanospheres containing methotrexate and gold nanoparticles: a multi-drug system for theranostic in rheumatoid arthritis. *Colloids Surf B Biointerfaces* 133, 378–387. doi: 10.1016/j.colsurfb.2015.04.048

Crofford, L. J. (2013). Use of NSAIDs in treating patients with arthritis. *Arthritis Res. Ther.* 15:S2. doi: 10.1186/ar4174

Croia, C., Bursi, R., Sutera, D., Petrelli, F., Alunno, A., and Puxeddu, I. (2019). One year in review 2019: pathogenesis of rheumatoid arthritis. *Clin. Exp. Rheumatol.* 37, 347–357.

Cross, M., Smith, E., Hoy, D., Carmona, L., Wolfe, F., Vos, T., et al. (2014). The global burden of rheumatoid arthritis: estimates from the global burden of disease 2010 study. *Ann. Rheum. Dis* 73, 1316–1322. doi: 10.1136/annrheumdis-2013-204627

Cwikla, J. B., Zbikowski, P., Kwiatkowska, B., Buscombe, J. R., and Sudol-Szopinska, I. (2014). Radiosynovectomy in rheumatic diseases. *J. Ultrason.* 14, 241–251. doi: 10.15557/JoU.2014.0024

Darweesh, R. S., Ayoub, N. M., and Nazzal, S. (2019). Gold nanoparticles and angiogenesis: molecular mechanisms and biomedical applications. *Int. J. Nanomed.* 14, 7643–7663. doi: 10.2147/IJN.S223941

Davignon, J.-L., Rauwel, B., Degboé Y., Constantin, A., Boyer, F. J., Kruglov, A., et al. (2018). Modulation of T-cell responses by anti-tumor necrosis factor treatments in rheumatoid arthritis: a review. *Arthritis Res. Ther.* 20, 229–229. doi: 10.1186/s13075-018-1725-6

Deane, K. D., Demoruelle, M. K., Kelmenson, L. B., Kuhn, K. A., Norris, J. M., and Holers, V. M. (2017). Genetic and environmental risk factors for rheumatoid arthritis. *Best Pract. Res. Clin. Rheumatol.* 31, 3–18. doi: 10.1016/j.berh.2017.08.003

Ding, D., and Zhu, Q. (2018). Recent advances of PLGA micro/nanoparticles for the delivery of biomacromolecular therapeutics. *Mater. Sci. Eng. C Mater. Biol. Appl.* 92, 1041–1060. doi: 10.1016/j.msec.2017.12.036

Doan, T., and Massarotti, E. (2005). Rheumatoid arthritis: an overview of new and emerging therapies. *J. Clin. Pharmacol.* 45, 751–762. doi: 10.1177/0091270005277938

Dolati, S., Sadreddini, S., Rostamzadeh, D., Ahmadi, M., Jadidi-Niaragh, F., and Yousefi, M. (2016). Utilization of nanoparticle technology in rheumatoid arthritis treatment. *Biomed. Pharmacother.* 80: 30–41. doi: 10.1016/j.biopha.2016.03.004

Faa, G., Gerosa, C., Fanni, D., Lachowicz, J. I., and Nurchi, V. M. (2018). Gold–old drug with new potentials. *Curr. Med. Chem.* 25, 75–84. doi: 10.2174/0929867324666170330091438

Falconer, J., Murphy, A. N., Young, S. P., Clark, A. R., Tiziani, S., Guma, M., et al. (2018). Review: synovial cell metabolism and chronic inflammation in rheumatoid arthritis. *Arthritis Rheumatol.* 70, 984–999. doi: 10.1002/art.40504

Fan, L., Xu, X., Zhu, C., Han, J., Gao, L., Xi, J., et al. (2018). Tumor catalytic-photothermal therapy with yolk-shell gold@carbon nanozymes. *ACS Appl. Mater. Interfaces* 10, 4502–4511. doi: 10.1021/acsami.7b17916

Feng, X., and Chen, Y. (2018). Drug delivery targets and systems for targeted treatment of rheumatoid arthritis. *J. Drug Target* 26, 845–857. doi: 10.1080/1061186X.2018.1433680

Fiehn, C., Kratz, F., Sass, G., Müller-Ladner, U., and Neumann, E. (2008). Targeted drug delivery by *in vivo* coupling to endogenous albumin: an albumin-binding prodrug of methotrexate (MTX) is better than MTX in the treatment of murine collagen-induced arthritis. *Ann. Rheum. Dis.* 67, 1188–1191. doi: 10.1136/ard.2007.086843

Fu, S., Xu, X., Ma, Y., Zhang, S., and Zhang, S. (2019). RGD peptide-based non-viral gene delivery vectors targeting integrin alphavbeta3 for cancer therapy. *J. Drug Target* 27, 1–11. doi: 10.1080/1061186X.2018.1455841

Gabriel, D., Busso, N., So, A., H., van den Bergh, G.urny R., and Lange, N. (2009). Thrombin-sensitive photodynamic agents: a novel strategy for selective synovectomy in rheumatoid arthritis. *J. Control. Release* 138, 225–234. doi: 10.1016/j.jconrel.2009.05.012

Gallardo-Villagrán, M., Leger, D. Y., Liagre, B., and Therrien, B. (2019). Photosensitizers used in the photodynamic therapy of rheumatoid arthritis. *Int. J. Mol. Sci.* 20:3339. doi: 10.3390/ijms20133339

Gulzar, A., Xu, J., Yang, D., Xu, L., He, F., Gai, S., et al. (2018). Nano-graphene oxide-UCNP-Ce6 covalently constructed nanocomposites for NIR-mediated bioimaging and PTT/PDT combinatorial therapy. *Dalton Trans.* 47, 3931–3939. doi: 10.1039/C7DT04141A

Han, J., Kim, Y. S., Lim, M.-Y., Kim, H. Y., Kong, S., Kang, M., et al. (2018). Dual roles of graphene oxide to attenuate inflammation and elicit timely polarization of macrophage phenotypes for cardiac repair. *ACS Nano* 12, 1959–1977. doi: 10.1021/acsnano.7b09107

Han, J., Zhang, J., Yang, M., Cui, D., and de la Fuente, J. M. (2016). Glucose-functionalized Au nanoprisms for optoacoustic imaging and near-infrared photothermal therapy. *Nanoscale* 8, 492–499. doi: 10.1039/C5NR06261F

Hansch, A., Frey, O., Gajda, M., Susanna, G., Boettcher, J., Bräuer, R., et al. (2008). Photodynamic treatment as a novel approach in the therapy of arthritic joints. *Lasers Surg. Med.* 40, 265–272. doi: 10.1002/lsm.20620

Hendrich, C., Hüttmann, G., Lehnert, C., Diddens, H., and Siebert, W. E. (1997). Photodynamic laser therapy for rheumatoid arthritis. Cell culture studies and animal experiments. *Knee Surg. Sports Traumatol. Arthrosc.* 5, 58–63. doi: 10.1007/s001670050026

Hu, H., Luan, L., Yang K, and Li, C. S. (2017). Psychometric validation of Chinese Health Assessment questionnaire for use in rheumatoid arthritis patients in China. *Int. J. Rheum. Dis.* 20, 1987–1992. doi: 10.1111/1756-185X.12831

Hu, J.-J., Cheng, Y. J., and Zhang, Z. X. (2018). Recent advances in nanomaterials for enhanced photothermal therapy of tumors. *Nanoscale* 10, 22657–22672. doi: 10.1039/C8NR07627H

Hu, X., and Gao, X. (2011). Multilayer coating of gold nanorods for combined stability and biocompatibility. *Phys. Chem. Chem. Phys.* 13, 10028–10035. doi: 10.1039/c0cp02434a

Hussein, E. A., Zagho, M. M., Nasrallah, G. K., and Elzatahry, A. A. (2018). Recent advances in functional nanostructures as cancer photothermal therapy. *Int. J. Nanomed.* 13, 2897–2906. doi: 10.2147/IJN.S161031

Hyndman, I. J. (2017). Rheumatoid arthritis: past, present and future approaches to treating the disease. *Int. J. Rheum. Dis.* 20, 417–419. doi: 10.1111/1756-185X.12823

Joensuu, J. T., Huoponen, S., Aaltonen, K. J., Konttinen, Y. T., Nordström, D., and Blom, M. (2015). The cost-effectiveness of biologics for the treatment of rheumatoid arthritis: a systematic review. *PLoS ONE* 10:e0119683. doi: 10.1371/journal.pone.0119683

Jung, H. S., Verwilst, P., Sharma, A., Shin, J., Sessler, J. L., and Kim, J. S. (2018). Organic molecule-based photothermal agents: an expanding photothermal therapy universe. *Chem. Soc. Rev.* 47, 2280–2297. doi: 10.1039/C7CS00522A

Kamaleshwaran, K. K., Rajamani, V., Krishnan, B., Mallia, M., Kalarikal, R., Mohanan, V., et al. (2015). Radiosynovectomy of proximal interphalangeal joint synovitis in rheumatoid arthritis treated with rhenium-188 labeled tin-colloid and imaging with single-photon emission computerized tomography/computed tomography: a first case report. *World J. Nucl. Med.* 14, 216–218. doi: 10.4103/1450-1147.161730

Karami, J., Aslani, S., Jamshidi, A., Garshasbi, M., and Mahmoudi, M. (2019). Genetic implications in the pathogenesis of rheumatoid arthritis: an updated review. *Gene* 702: 8–16. doi: 10.1016/j.gene.2019.03.033

Karavida, N., and Notopoulos, A. (2010). Radiation Synovectomy: an effective alternative treatment for inflamed small joints. *Hippokratia* 14, 22–27.

Karousou, E., Misra, S., Ghatak, S., Dobra, K., Götte, M., Vigetti, D., et al. (2017). Roles and targeting of the HAS/hyaluronan/CD44 molecular system in cancer. *Matrix Biol.* 59, 3–22. doi: 10.1016/j.matbio.2016.10.001

Kim, H. J., Lee, S. M., Park, H. K., Mun, C. H., Park, Y. B., and Yoo, K. H. (2015). Drug-loaded gold/iron/gold plasmonic nanoparticles for magnetic targeted chemo-photothermal treatment of rheumatoid arthritis. *Biomaterials* 61, 95–102. doi: 10.1016/j.biomaterials.2015.05.018

Kneidl, B., Peller, M., Winter, G., Lindner, L. H., and Hossann, M. (2014). Thermosensitive liposomal drug delivery systems: state of the art review. *Int. J. Nanomed.* 9, 4387–4398. doi: 10.2147/IJN.S49297

Knut, L. (2015). Radiosynovectomy in the therapeutic management of arthritis. *World J. Nucl. Med.* 14, 10–15. doi: 10.4103/1450-1147.150509

Kumar, L. D., Karthik, R., Gayathri, N., and Sivasudha, T. (2016). Advancement in contemporary diagnostic and therapeutic approaches for rheumatoid arthritis. *Biomed. Pharmacother.* 79, 52–61. doi: 10.1016/j.biopha.2016.02.001

Kwiatkowski, S., Knap, B., Przystupski, D., Saczko, J., Kedzierska, E., Knap-Czop, K., et al. (2018). Photodynamic therapy–mechanisms, photosensitizers and combinations. *Biomed. Pharmacother.* 106, 1098–1107. doi: 10.1016/j.biopha.2018.07.049

Laing, T. J., Ike, R. W., Griffiths, C. E., Richardson, B. C., Grober, J. S., Keroack, B. J., et al. (1995). A pilot study of the effect of oral 8-methoxypsoralen and intraarticular ultraviolet light on rheumatoid synovitis. *J. Rheumatol.* 22, 29–33.

Laskari, K., Pentazos, G., Pitsilka, D., Raftakis, J., Konstantonis, G., Toutouzas, K., et al. (2019). Joint microwave radiometry for inflammatory arthritis assessment. *Rheumatology* 59, 839–844. doi: 10.1093/rheumatology/kez373

Lee, S.-M., Kim, H. J., Ha, J. Y, Park, Y. N., Lee, K. S., Park, B. Y., et al. (2013). Targeted chemo-photothermal treatments of rheumatoid arthritis using gold half-shell multifunctional nanoparticles. *ACS Nano* 7, 50–57. doi: 10.1021/nn301215q

Li, M., Ma, Z., Zhu, Y., Xia, H., Yao, M., Chu, X., et al. (2016). Toward a molecular understanding of the antibacterial mechanism of copper-bearing titanium alloys against *Staphylococcus aureus*. *Adv. Healthc. Mater.* 5, 557–566. doi: 10.1002/adhm.201500712

Liao, K. P., Alfredsson, L., and Karlson, E. W. (2009). Environmental influences on risk for rheumatoid arthritis. *Curr. Opin. Rheumatol.* 21, 279–283. doi: 10.1097/BOR.0b013e32832a2e16

Litwiniuk, M., Krejner, A., Speyrer, M. S., Gauto, A. R., and Grzela, T. (2016). Hyaluronic acid in inflammation and tissue regeneration. *Wounds* 28, 78–88.

Liu, S., and Maeyama, K. (2016). Gene therapy for rheumatoid arthritis. *Crit. Rev. Immunol.* 36, 149–161. doi: 10.1615/CritRevImmunol.2016017062

Liu, Y., Bhattarai, P., Dai, Z., and Chen, X. (2019). Photothermal therapy and photoacoustic imaging via nanotheranostics in fighting cancer. *Chem. Soc. Rev.* 48, 2053–2108. doi: 10.1039/C8CS00618K

Liu, Y., Zhen, W., Jin, L., Zhang, S., Sun, G., Zhang, T., et al. (2018). All-in-one theranostic nanoagent with enhanced reactive oxygen species generation and modulating tumor microenvironment ability for effective tumor eradication. *ACS Nano* 12, 4886–4893. doi: 10.1021/acsnano.8b01893

Lopalco, A., and Denora, N. (2018). Nanoformulations for drug delivery: safety, toxicity, and efficacy. *Methods Mol. Biol.* 1800, 347–365. doi: 10.1007/978-1-4939-7899-1_17

Lu, Y., Li, L., Lin, Z., Wang, L., Lin, L., Li, M., et al. (2018a). A new treatment modality for rheumatoid arthritis: combined photothermal and photodynamic therapy using Cu(7.2) S(4) nanoparticles. *Adv. Healthc. Mater.* 7:e1800013. doi: 10.1007/978-1-4939-8802-0

Lu, Y., Li, L., Zhu, Y., Wang, X., Li, M., Lin, Z., et al. (2018b). Multifunctional copper-containing carboxymethyl chitosan/alginate scaffolds for eradicating clinical bacterial infection and promoting bone formation. *ACS Appl. Mater. Interfaces* 10, 127–138. doi: 10.1021/acsami.7b13750

Luís, M., Freitas, J., Costa, F., Buttgereit, F., Boers, M., Jap, D. S., et al. (2019). An updated review of glucocorticoid-related adverse events in patients with rheumatoid arthritis. *Expert. Opin. Drug Saf.* 18, 581–590. doi: 10.1080/14740338.2019.1615052

Marrelli, A., Cipriani, P., Liakouli, V., Carubbi, F., Perricone, C., Perricone, R., et al. (2011). Angiogenesis in rheumatoid arthritis: a disease specific process or a common response to chronic inflammation? *Autoimmun. Rev.* 10, 595–598. doi: 10.1016/j.autrev.2011.04.020

Mateen, S., Zafar, A., Moin, S., Khan, A. Q., and Zubair, S. (2016). Understanding the role of cytokines in the pathogenesis of rheumatoid arthritis. *Clin. Chim. Acta* 455, 161–171. doi: 10.1016/j.cca.2016.02.010

McEwan, C., Owen, J., Stride, E., Fowley, C., Nesbitt, H., Cochrane, D., et al. (2015). Oxygen carrying microbubbles for enhanced sonodynamic therapy of hypoxic tumours. *J. Control. Release* 203, 51–56. doi: 10.1016/j.jconrel.2015.02.004

McHale, A. P., Callan, J. F., Nomikou, N., Fowley, C., and Callan, B. (2016). Sonodynamic therapy: concept, mechanism and application to cancer treatment. *Adv. Exp. Med. Biol.* 880, 429–450. doi: 10.1007/978-3-319-22536-4_22

Mi, P. (2020). Stimuli-responsive nanocarriers for drug delivery, tumor imaging, therapy and theranostics. *Theranostics* 10, 4557–4588. doi: 10.7150/thno.38069

Miszczyk, M., Jochymek, B., Miszczyk, L., Matysiakiewicz, J., Spindel, J., Jabłonska, I., et al. (2020). The results of 394 consecutive cases of knee joint radiation synovectomy (radiosynoviorthesis) using (90)Y. *Ann. Nucl. Med.* 34, 94–101. doi: 10.1007/s12149-019-01418-w

Miyoshi, N., Kundu, S. K., Tuziuti, T., Yasui, K., Shimada, I., and Ito, Y. (2016). Combination of sonodynamic and photodynamic therapy against cancer would be effective through using a regulated size of nanoparticles. *Nanosci Nanoeng.* 4, 1–11. doi: 10.13189/nn.2016.040101

Nakano, S., Ikata, T., Kinoshita, I., Kanematsu, J., and Yasuoka, S. (1999). Characteristics of the protease activity in synovial fluid from patients with rheumatoid arthritis and osteoarthritis. *Clin. Exp. Rheumatol.* 17, 161–170.

Pan, W., Dai, C., Li, Y., Yin, Y., Gong, L., Machuki, J. O., et al. (2020). PRP-chitosan thermoresponsive hydrogel combined with black phosphorus nanosheets as injectable biomaterial for biotherapy and phototherapy treatment of rheumatoid arthritis. *Biomaterials* 239:119851. doi: 10.1016/j.biomaterials.2020.119851

Pan, X., Wang, H., Wang, S., Sun, X., Wang, L., Wang, W., et al. (2018). Sonodynamic therapy (SDT), a novel strategy for cancer nanotheranostics. *Sci. China. Life Sci.* 61, 415–426. doi: 10.1007/s11427-017-9262-x

Pandey, P. K., Maheshwari, R., Raval, N., Gondaliya, P., Kalia, K., and Tekade, R. K. (2019). Nanogold-core multifunctional dendrimer for pulsatile chemo-, photothermal- and photodynamic- therapy of rheumatoid arthritis. *J. Colloid Interface Sci.* 544, 61–77. doi: 10.1016/j.jcis.2019.02.073

Peng, H., Cui, B., Li, G., Wang, Y., Li, N., Chang, Z., et al. (2015). A multifunctional β-CD-modified Fe_3O_4@ZnO:Er(3+),Yb(3+) nanocarrier for antitumor drug delivery and microwave-triggered drug release. *Mater. Biol. Applic.* 46, 253–263. doi: 10.1016/j.msec.2014.10.022

Peng, S., He, Y., Er, M., Sheng, Y., Gu, Y., and Chen, H. (2017). Biocompatible CuS-based nanoplatforms for efficient photothermal therapy and chemotherapy *in vivo*. *Biomater. Sci.* 5, 475–484. doi: 10.1039/C6BM00626D

Pentazos, G., Laskari, K., Prekas, K., Raftakis, J., Sfikakis, P. P., and Siores, E. (2018). Microwave radiometry-derived thermal changes of small joints as additional potential biomarker in rheumatoid arthritis: a prospective pilot study. *J. Clin. Rheumatol.* 24, 259–263. doi: 10.1097/RHU.0000000000000719

Prazmo, E. J., Kwaśny, M., Łapinski, M., and Mielczarek, A. (2016). Photodynamic therapy as a promising method used in the treatment of oral diseases. *Adv. Clin. Exp. Med.* 25, 799–807. doi: 10.17219/acem/32488

Qamar, N., Arif, A., Bhatti, A., and John, P. (2019). Nanomedicine: an emerging era of theranostics and therapeutics for rheumatoid arthritis. *Rheumatology* 58, 1715–1721. doi: 10.1093/rheumatology/kez286

Quan, L., Zhang, Y., Crielaard, B. J., Dusad, A., Lele, S. M., Rijcken, C. J. F., et al. (2014). Nanomedicines for inflammatory arthritis: head-to-head comparison of glucocorticoid-containing polymers, micelles, and liposomes. *ACS Nano* 8, 458–466. doi: 10.1021/nn4048205

Railkar, R., and Agarwal, P. K. (2018). Photodynamic therapy in the treatment of bladder cancer: past challenges and current innovations. *Eur. Urol. Focus* 4, 509–511. doi: 10.1016/j.euf.2018.08.005

Rehman, F. U., Zhao, C., Jiang, H., Selke, M., and Wang, X. (2016). Protective effect of TiO_2 nanowhiskers on tetra sulphonatophenyl porphyrin (TSPP) complexes induced oxidative stress during photodynamic therapy. *Photodiagn. Photodyn. Ther.* 13, 267–275. doi: 10.1016/j.pdpdt.2015.08.005

Rengeng, L., Qianyu, Z., Yuehong, L., Zhongzhong, P., and Libo, L. (2017). Sonodynamic therapy, a treatment developing from photodynamic therapy. *Photodiagn. Photodyn. Ther.* 19, 159–166. doi: 10.1016/j.pdpdt.2017.06.003

Rudan, I., Sidhu, S., Papana, A., Meng, J. S., Xin-Wei, Y., Wang, W., et al. (2015). Prevalence of rheumatoid arthritis in low- and middle-income countries: a systematic review and analysis. *J. Glob. Health* 5:010409. doi: 10.7189/jogh.05.010409

Ruyssen-Witrand, A., and Constantin, A. (2018). Controversies in rheumatoid arthritis glucocorticoid therapy. *Joint Bone Spine* 85, 417–422. doi: 10.1016/j.jbspin.2017.12.002

Schett, G., Emery, P., Tanaka, Y., Burmester, G., Pisetsky, D. S., Naredo, E., et al. (2016). Tapering biologic and conventional DMARD therapy in rheumatoid arthritis: current evidence and future directions. *Ann. Rheum. Dis.* 75, 1428–1437. doi: 10.1136/annrheumdis-2016-209201

Schmitt, F., Lagopoulos, L., Käuper, P., Rossi, N., Busso, N., Barge, J., et al. (2010). Chitosan-based nanogels for selective delivery of photosensitizers to macrophages and improved retention in and therapy of articular joints. *J. Control. Release* 144, 242–250. doi: 10.1016/j.jconrel.2010.02.008

Senolt, L., Grigorian, M., Lukanidin, E., Michel, B. A., Gay, R. E., Gay, S., et al. (2006). S100A4 (Mts1), is there any relation to the pathogenesis of rheumatoid arthritis? *Autoimmun. Rev.* 5, 129–131. doi: 10.1016/j.autrev.2005.09.010

Sharma, G., Saini, M. K., Thakur, K., Kapil, N., Garg, N. K., Raza, K., et al. (2017). Aceclofenac cocrystal nanoliposomes for rheumatoid arthritis with better dermatokinetic attributes: a preclinical study. *Nanomedicine (Lond).* 12, 615–638. doi: 10.2217/nnm-2016-0405

Shaunak, S. (2015). Perspective: Dendrimer drugs for infection and inflammation. *Biochem. Biophys. Res. Commun.* 468, 435–441. doi: 10.1016/j.bbrc.2015.07.033

Shen, Q., Zhang, X., Qi, J., Shu, G., Du, Y., and Ying, X. (2020). Sinomenine hydrochloride loaded thermosensitive liposomes combined with microwave hyperthermia for the treatment of rheumatoid arthritis. *Int. J. Pharm.* 576, 119001–119001. doi: 10.1016/j.ijpharm.2019.119001

Shen, S., Kong, F., Guo, X., Wu, L., Shen, H., Xie, M., et al. (2013). CMCTS stabilized Fe_3O_4 particles with extremely low toxicity as highly efficient near-infrared photothermal agents for *in vivo* tumor ablation. *Nanoscale* 5, 8056–8066. doi: 10.1039/c3nr01447a

Shi, X., Zhang, C. Y., Gao, J., and Wang, Z. (2019). Recent advances in photodynamic therapy for cancer and infectious diseases. *Wiley Interdiscip. Rev. Nanomed. Nanobiotechnol.* 11:e1560. doi: 10.1002/wnan.1560

Shin, J. M., Kim, S.-H., Thambi, T., You, D. G., Jeon, J., Lee, J. O., et al. (2014). A hyaluronic acid-methotrexate conjugate for targeted therapy of rheumatoid arthritis. *Chem. Commun. (Camb).* 50, 7632–7635. doi: 10.1039/c4cc02595d

Shinto, A. S., Kamaleshwaran, K. K., Chakraborty, S., Vyshakh, K., Thirumalaisamy, S. G., Karthik, S., et al. (2015). Radiosynovectomy of painful synovitis of knee joints due to rheumatoid arthritis by intra-articular administration of (177)Lu-labeled hydroxyapatite particulates: first human study and initial indian experience. *World J. Nucl. Med.* 14, 81–88. doi: 10.4103/1450-1147.153908

Smolen, J. S., Aletaha, D., and McInnes, I. B. (2016). Rheumatoid arthritis. *Lancet (London, England)* 388, 2023–2038. doi: 10.1016/S0140-6736(16)30173-8

Song, X., and Lin, Q. (2017). Genomics, transcriptomics and proteomics to elucidate the pathogenesis of rheumatoid arthritis. *Rheumatol. Int.* 37, 1257–1265. doi: 10.1007/s00296-017-3732-3

Sparks, J. A. (2019). Rheumatoid arthritis. *Ann. Intern. Med.* 170, ITC1–ITC16. doi: 10.7326/AITC201901010

Springorum, H. R., Winkler, S., Maderbacher, G., Götz, J., Baier, C., Grifka, J., et al. (2016). Operative therapy for rheumatoid arthritis of the hand. *Z. Rheumatol.* 75, 69–85. doi: 10.1007/s00393-016-0046-x

Talotta, R., Rucci, F., Canti, G., and Scaglione, F. (2019). Pros and cons of the immunogenicity of monoclonal antibodies in cancer treatment: a lesson from autoimmune diseases. *Immunotherapy* 11, 241–254. doi: 10.2217/imt-2018-0081

Tang, Q., Chang, S., Tian, Z., Sun, J., Hao, L., Wang, Z., et al. (2017a). Efficacy of indocyanine green-mediated sonodynamic therapy on rheumatoid arthritis fibroblast-like synoviocytes. *Ultrasound Med. Biol.* 43, 2690–2698. doi: 10.1016/j.ultrasmedbio.2017.06.030

Tang, Q., Cui, J., Tian, Z., Sun, J., Wang, Z., Chang, S., et al. (2017b). Oxygen and indocyanine green loaded phase-transition nanoparticle-mediated photo-sonodynamic cytotoxic effects on rheumatoid arthritis fibroblast-like synoviocytes. *Int. J. Nanomed.* 12, 381–393. doi: 10.2147/IJN.S120902

Thakur, S., Riyaz, B., Patil, A., Kaur, A., Kapoor, B., and Mishra, V. (2018). Novel drug delivery systems for NSAIDs in management of rheumatoid arthritis: an overview. *Biomed. Pharmacother.* 106, 1011–1023. doi: 10.1016/j.biopha.2018.07.027

Tørring, T., Helmig, S., Ogilby, P. R., and Gothelf, K. V. (2014). Singlet oxygen in DNA nanotechnology. *Acc. Chem. Res.* 47, 1799–1806. doi: 10.1021/ar500034y

Trauner, K. B., and Hasan, T. (1996). Photodynamic treatment of rheumatoid and inflammatory arthritis. *Photochem. Photobiol.* 64, 740–750. doi: 10.1111/j.1751-1097.1996.tb01829.x

Trujillo-Nolasco, R. M., Morales-Avila, E., Ocampo-García, B. E., Ferro-Flores, G., Gibbens-Bandala, B. V., Escudero-Castellanos, A., et al. (2019). Preparation and *in vitro* evaluation of radiolabeled HA-PLGA nanoparticles as novel MTX delivery system for local treatment of rheumatoid arthritis. *Mater. Sci. Eng. C Mater. Biol. Appl.* 103, 109766–109766. doi: 10.1016/j.msec.2019.109766

Vonnemann, J., Beziere, N., Böttcher, C., Riese, S. B., Kuehne, C., Dernedde, J., et al. (2014). Polyglycerolsulfate functionalized gold nanorods as optoacoustic signal nanoamplifiers for *in vivo* bioimaging of rheumatoid arthritis. *Theranostics* 4, 629–641. doi: 10.7150/thno.8518

Wang, D., Miller, S. C., Liu, M. X., Anderson, B., Wang, X. S., and Goldring, S. R. (2007). Novel dexamethasone-HPMA copolymer conjugate and its potential application in treatment of rheumatoid arthritis. *Arthritis Res. Ther.* 9:R2. doi: 10.1186/ar2106

Wang, Q., Jiang, J., Chen, W., Jiang, H., Zhang, Z., and Sun, X. (2016). Targeted delivery of low-dose dexamethasone using PCL-PEG micelles for effective treatment of rheumatoid arthritis. *J. Control. Release* 230, 64–72. doi: 10.1016/j.jconrel.2016.03.035

Wang, W., Zhou, H., and Liu, L. (2018). Side effects of methotrexate therapy for rheumatoid arthritis: a systematic review. *Eur. J. Med. Chem.* 158, 502–516. doi: 10.1016/j.ejmech.2018.09.027

Wang, Y., Barhoumi, A., Tong, R., Wang, W., Ji, T., Deng, X., et al. (2018). BaTiO(3)-core Au-shell nanoparticles for photothermal therapy and bimodal imaging. *Acta Biomater.* 72, 287–294. doi: 10.1016/j.actbio.2018.03.029

Xiang, H., and Chen, Y. (2019). Energy-converting nanomedicine. *Small* 15:e1805339. doi: 10.1002/smll.201805339

Xiao, L., Wu, Z., Zhang, J., Wang, G., Ma, Y., Ding, Y., et al. (2019). Synthesis, photothermal effect and cytotoxicity of Fe3O4@Au nanocomposites. *J. Nanosci. Nanotechnol.* 19, 2467–2473. doi: 10.1166/jnn.2019.16031

Xu, X.-L., Li, S. W., Wang, J. X., Du, L. Y., Kang, Q. X., Hu, B. J., et al. (2018). Endogenous sialic acid-engineered micelles: a multifunctional platform for on-demand methotrexate delivery and bone repair of rheumatoid arthritis. *Nanoscale* 10, 2923–2935. doi: 10.1039/C7NR08430G

Yan, F., Li, H., Zhong, Z., Zhou, M., Lin, Y., Tang, C., et al. (2019). Co-delivery of prednisolone and curcumin in human serum albumin nanoparticles for effective treatment of rheumatoid arthritis. *Int. J. Nanomed.* 14, 9113–9125. doi: 10.2147/IJN.S219413

Yang, M., Feng, X., Ding, J., Chang, F., and Chen, X. (2017). Nanotherapeutics relieve rheumatoid arthritis. *J. Control. Release* 252, 108–124. doi: 10.1016/j.jconrel.2017.02.032

Yang, Y., Tu, J., Yang, D., Raymond, J. L., Roy, R. A., and Zhang, D. (2019). Photo- and sono-dynamic therapy: a review of mechanisms and considerations for pharmacological agents used in therapy incorporating light and sound. *Curr. Pharm. Des.* 25, 401–412. doi: 10.2174/1381612825666190123114107

Zhang, S., Wu, L., Cao, J., Wang, K., Ge, Y., Ma, W., et al. (2018). Effect of magnetic nanoparticles size on rheumatoid arthritis targeting and photothermal therapy. *Colloid Surf. B* 170, 224–232. doi: 10.1016/j.colsurfb.2018.06.016

Zhang, X., Xi, Z., Machuki, J. O., L.uo J., Yang, D., Li, J., et al. (2019). Gold cube-in-cube based oxygen nanogenerator: a theranostic nanoplatform for modulating tumor microenvironment for precise chemo-phototherapy and multimodal imaging. *ACS Nano* 13, 5306–5325. doi: 10.1021/acsnano.8b09786

Zhao, C., Ur Rehman, F., Yang, Y., Li, X., Zhang, D., Jiang, H., et al. (2015). Bio-imaging and photodynamic therapy with Tetra Sulphonatophenyl Porphyrin (TSPP)-TiO_2 nanowhiskers: new approaches in rheumatoid arthritis theranostics. *Sci. Rep.* 5:11518. doi: 10.1038/srep11518

Conflict of Interest: The authors declare that the research was conducted in the absence of any commercial or financial relationships that could be construed as a potential conflict of interest.

frontiers
in Bioengineering and Biotechnology

ORIGINAL RESEARCH
published: 28 July 2020
doi: 10.3389/fbioe.2020.00787

Lipidation Approaches Potentiate Adjuvant-Pulsed Immune Surveillance: A Design Rationale for Cancer Nanovaccine

Junqing Wang*[1,2†]*, Harshal Zope*[1†]*, Mohammad Ariful Islam*[1,3†]*, Jamie Rice*[4,5]*,
Sage Dodman*[1]*, Kevin Lipert*[1]*, Yunhan Chen*[1]*, Bruce R. Zetter*[4] *and Jinjun Shi*[1]**

[1] Center for Nanomedicine and Department of Anesthesiology, Brigham and Women's Hospital, Harvard Medical School, Boston, MA, United States, [2] School of Pharmaceutical Sciences (Shenzhen), Sun Yat-sen University, Guangzhou, China, [3] Immuno-Oncology Group, Immunomic Therapeutics, Inc., Rockville, MD, United States, [4] Vascular Biology Program, Boston Children's Hospital, Harvard Medical School, Boston, MA, United States, [5] Silicon Therapeutics, Boston, MA, United States

OPEN ACCESS

Edited by:
Gang Liu,
Xiamen University, China

Reviewed by:
Xiaoyang Xu,
New Jersey Institute of Technology, United States
Changyang Gong,
Sichuan University, China

****Correspondence:***
Jinjun Shi
jshi@bwh.harvard.edu

† These authors have contributed equally to this work

Specialty section:
This article was submitted to Nanobiotechnology, a section of the journal Frontiers in Bioengineering and Biotechnology

Received: *14 May 2020*
Accepted: *22 June 2020*
Published: *28 July 2020*

Citation:
Wang J, Zope H, Islam MA, Rice J, Dodman S, Lipert K, Chen Y, Zetter BR and Shi J (2020) Lipidation Approaches Potentiate Adjuvant-Pulsed Immune Surveillance: A Design Rationale for Cancer Nanovaccine. Front. Bioeng. Biotechnol. 8:787. doi: 10.3389/fbioe.2020.00787

Adjuvant-pulsed peptide vaccines hold great promise for the prevention and treatment of different diseases including cancer. However, it has been difficult to maximize vaccine efficacy due to numerous obstacles including the unfavorable tolerability profile of adjuvants, instability of peptide antigens, limited cellular uptake, and fast diffusion from the injection site, as well as systemic adverse effects. Here we describe a robust lipidation approach for effective nanoparticle co-delivery of low-molecular weight immunomodulators (TLR7/8 agonists) and peptides (SIINFEKL) with a potent *in vivo* prophylactic effect. The lipidation approaches (C_{16}-R848 and C_{16}-SIINFEKL) increased their hydrophobicity that is intended not only to improve drug encapsulation efficiency but also to facilitate the membrane association, intracellular trafficking, and subcellular localization. The polymer–lipid hybrid nanoparticles (PLNs) are designed to sustain antigen/adjuvant levels with less systemic exposure. Our results demonstrated that a lipidated nanovaccine can induce effective immunity by enhancing the expansion and activation of antigen-specific CD8$^+$ T cells. This adaptive immune response led to substantial tumor suppression with improved overall survival in a prophylactic setting. Our new methodology enhances the potential of nanovaccines for anti-tumor therapy.

Keywords: lipidation, nanovaccine, adjuvant, peptide antigen, Toll-like receptors, cancer

INTRODUCTION

The use of peptide epitope-based cancer vaccines to activate tumor-associated antigen (TAA)-specific T cell responses is an attractive option for generating long-term anti-cancer immune protection because of the ease of synthesis, tolerability, and low risk of adverse effects (Nabel, 2013; Skwarczynski and Toth, 2016; Kumai et al., 2017). TAA-based subunit vaccines are known to be poorly immunogenic, however, and require potent adjuvants to augment antigen-presenting cell (APC) activation and TAA presentation (Perrie et al., 2008; Coffman et al., 2010; Reed et al., 2013). Among various cancer vaccine adjuvants, TLR7/8 agonists are of particular interest because of their strong activation of APCs (Napolitani et al., 2005), initiation of cross-priming, promotion of $CD4^{+}/8^{+}$ T and natural killer (NK) cell activation (Kastenmuller et al., 2011), ability to limit the immunosuppressive function of regulatory T (Treg) cells, and association with an inflammatory tumor microenvironment via induction of cytokines and chemokines (Peng et al., 2005; Vasilakos and Tomai, 2013).

The imidazoquinoline compounds imiquimod and resiquimod (R848) are novel TLR7/8 agonists that demonstrate the potential for potent antiviral and antitumor activity when used as adjuvants (Junt and Barchet, 2015; Hu et al., 2017). The physicochemical properties of imidazoquinolines lead to rapid distribution from the site of injection which results in systemic exposure and cytokine-induced immune activation accompanied by adverse influenza-like symptoms (Vasilakos and Tomai, 2013). Nanoparticle (NP)-mediated synchronous delivery of adjuvant and antigen has emerged as a promising strategy, which can accommodate engineering approaches to promote APC uptake and reduce systemic side effects. Different NP platforms such as micelles (Black et al., 2012), liposomes (Gadd et al., 2018), and polymeric NPs (Ilyinskii et al., 2014; Kim et al., 2018) have been established in recent studies for TLR7/8 agonist-based cancer vaccine. These agonists were either physically encapsulated in the NPs or conjugated with poly(lactic acid) (PLA) to enhance the loading efficiency (Kim et al., 2018; Nuhn et al., 2018; Rodell et al., 2018; Thauvin et al., 2019). The physical encapsulation of imidazoquinoline compounds is often restricted to moderate encapsulation efficiency and fast burst release of payloads, whereas the polymer-based conjugation approaches are challenged by low carrying capacity, heterogeneity of polymer molecular weight, and the variable reproducibility (Dane and Irvine, 2015). Although the earlier studies (Ilyinskii et al., 2014; Alexis et al., 2016) demonstrated an effective local immune activation and an excellent safety profile (that attenuates the level of serum inflammatory cytokines for 50- to 200-folds compared with free R848 administration), up until now the prophylactic use of a TLR7/8 agonist-based nanovaccine for cancer prevention in animal models has not been rigorously evaluated. To achieve sustained cancer immune surveillance from a vaccine, the adjuvant strategy needs to consider key factors including the physicochemical properties of imidazoquinolines and peptides, as well as their ability to be formulated with NP encapsulation.

Lipidation is an important modification strategy for bio-active molecules, which has shown exceptional promise in pharmaceutical applications. For example, lipidation can address cytokine storm-like effects from post-subcutaneous injection of TLR agonists (Smirnov et al., 2011). The addition of an alkyl chain lipid moiety to TLR agonist can effectively improve the pharmacokinetic profile via slow dissemination from the site of application (Smirnov et al., 2011). Another key advantage of lipidation is that it enables hitchhiking of molecular vaccines on albumins (through conjugating lipophilic albumin-binding tail on antigen and adjuvant) and transports these molecules to lymph nodes (LNs), leading to dramatic increases in T-cell priming (Liu et al., 2014; Moynihan et al., 2018). Lipidation of the cationic dendrimers with alkyl chains affords lipid-like properties, promoting hydrophobic aggregation with siRNA/mRNA sequences, resulting in formation of more stable nano-formulation by keeping nucleic acids in inner core of NPs (Khan et al., 2014; Whitehead et al., 2014). Such condensed assembly methodology provides a gene delivery *in vivo* with long circulating half-lives and effective accumulation at target site (Kowalski et al., 2019).

In this report, we investigated how lipidation could be exploited to optimize co-formulation and to regulate the pharmacokinetic profiles of peptide antigen and small molecular adjuvant to provide an enhanced vaccine response (**Scheme 1A**). Given the ability of lipid motifs to facilitate condensed particle formation of water-soluble molecules through hydrophobic aggregation, we have developed a novel lipidation approach for delivering a chemical analog of R848 plus the ovalbumin-derived peptide 257-264 (SIINFEKL) (**Scheme 1B**). To address the common formulation challenges including the post-entrapment leakage and rapid release of low molecular weight (LMW) payloads, we capitalized on core-shell polymer–lipid hybrid nanoparticles (PLNs) to incorporate LMW lipophilic molecules. The study here demonstrated a rationale design based on chemical engineering and vaccine formulation science to achieve minimal systemic exposure, consistent APC uptake, and prolonged immune surveillance, leading to an effective prophylactic anti-cancer vaccine.

MATERIALS AND METHODS

Materials

Resiquimod (R848), anhydrous dichloromethane (DCM), anhydrous N,N-dimethylformamide (DMF), palmitic acid, N,N'-dicyclohexylcarbodiimide (DCC), 4-dimethylaminopyridine (DMAP), hydrochloric acid (HCl), magnesium sulfate, N-methylmorpholine (NMM), N,N'-diisopropylcarbodiimide (DIC), trifluoroacetic acid (TFA), triisopropylsilane (TIS), diethyl ether, palmitic acid (C16-COOH), piperidine, hexane, dimethyl sulfoxide (DMSO), ammonium hydroxide (NH4OH), β-mercaptoethanol, methyl-B-cyclodextrin (MBCD), and chlorpromazine were purchased from Sigma-Aldrich. FMOC amino acid conjugates (those of serine, isoleucine, asparagine, phenylalanine, glutamic acid, lysine, and leucine) were from EMD NovaBioChem, a part of EMD Millipore. 1-[Bis(dimethylamino)methylene]-1H-1,2,3-triazolo[4,5-b]pyridinium 3-oxid hexafluorophosphate (HATU) was from Chempep (Wellington, FL, United States). 1-Hydroxy-7-azabenzotriazole (HOAt) was from Advanced Chemtech (Louisville, KY, United States). Acetonitrile (ACN) for HPLC was from VWR (Radnor, PA, United States). FMOC-PEG12-propionic acid was from AAPTec (Louisville, KY, United States). The ester-terminated poly(lactide) (PLA) polymer with viscosity of 0.55–0.75 dL/g was purchased from Lactel Absorbable Polymers (Birmingham, AL, United States). Polyethylene glycol (PEG) polymer, N-palmitoyl-sphingosine-1-succinyl-methoxy(polyethylene glycol)5000 (ceramide-PEG5k), was from Avanti Polar Lipids (Alabaster, AL, United States). EG7-OVA cell line was from ATCC (Manassas, VA, United States).

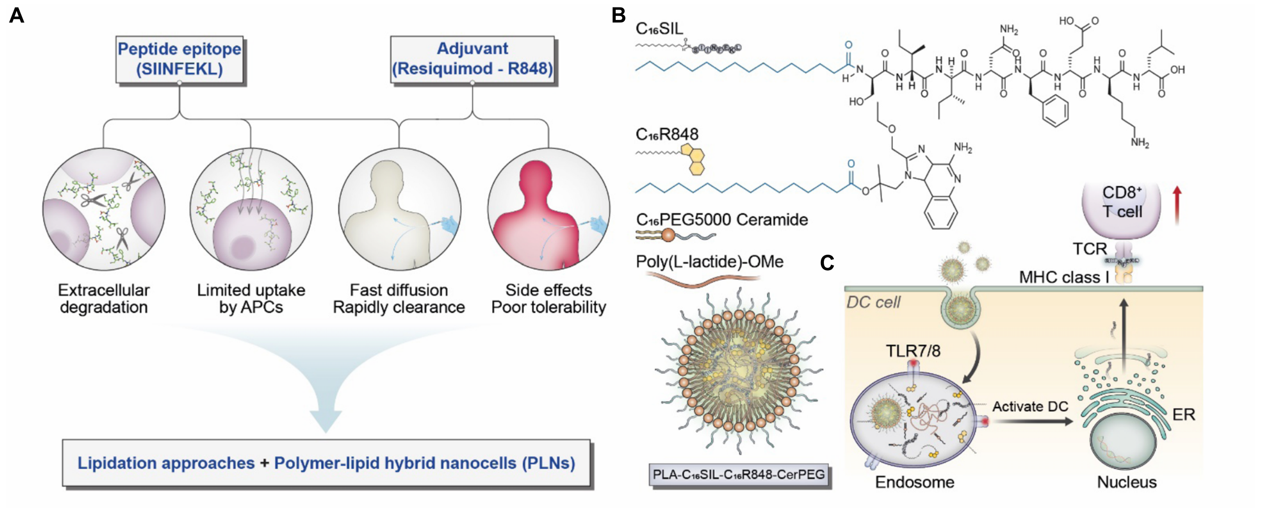

SCHEME 1 | (A) Considerations and proposed formulation design for overcoming biological limitations of TLR7/8 agonists and peptide epitopes. **(B)** Schematic illustration of chemical structures for C_{16}SIL [N-terminal palmitoylation of SIINFEKL (C16:0)] and C_{16}R848 (esterification of palmitic acid with R848 hydroxyl group). The final PLNs (PLA-C_{16}SIL-C_{16}R848-CerPEG) were assembled via PLA assisted co-encapsulation of C_{16}R848 and C_{16}SIL followed by PEGylated ceramide stabilization. **(C)** Desired TLR7 activation and MHC I mediated antigen presentation elicited by PLN vaccine.

C_{16}R848 Synthesis

R848 (50 mg), DCM (3 mL), and DMF (1 mL) were added to a 100 mL round bottomed flask. The solution was stirred at 1600 rpm under nitrogen gas followed by the addition of palmitic acid and DCC, with 100 mg of each. The reaction mixture was stirred for 10 min and 21 mg of DMAP was added. The reaction mixture was then stirred overnight under nitrogen gas. The reaction mixture was vacuum filtered to remove precipitates formed during the reaction. The reaction mixture was then washed six times with water to remove hydrophilic reactants and byproducts. After the final wash, the remaining water was removed by magnesium sulfate. The wax-like crude product was obtained by rotary evaporation. C_{16}R848 was then purified on a Gilson GX-271 HPLC (Gilson, Middleton, WI, United States) using a Vydac 214TP101522 22 × 250 mm C4 column (Grace, Columbia, MD, United States). Identity and purity of the compound was verified using MALDI-TOF (Bruker, Billerica, MA, United States).

C_{16}SIINFEKL Peptide Synthesis

The peptide derivatives were synthesized using a solid phase synthesis method. The scale of the synthesis is 0.1 mmol for C_{16}SIINFEKL. The synthesis was done on a Tribute-UV automatic protein synthesizer (Protein Technologies, Tuscon, AZ, United States), using preloaded Low Load Wang resins with polystyrene support (EMD Millipore NovaBioChem). The resin was housed in a 10 mL batch synthesis fritted reaction vessel. The amino acids were deprotected in a solution of 20% piperidine in DMF, with each deprotection cycle lasting 2:30 min. The cycle was repeated until the UV feedback from the Fmoc cation detector of the synthesizer comes back as 3% or lower of the original UV signal before the first deprotection cycle. The residues were then activated and coupled in a DMF solution with a molar ratio of 1:1:2 for amino acids, HATU, and NMM, respectively. Palmitic acid (C_{16}–COOH) was coupled overnight to amino acid residues in a mixture of DIC and HOAt in DMF solvent. After solid phase-assisted polymerization, the peptide derivatives were cleaved using a mixture of 92.5% TFA, 5% TIS, and 2.5% water (v/v/v) for 2 h. The derivatives were then precipitated in a diethyl ether and hexane mixture in a ratio of 10:1. The precipitation mixture was centrifuged; the ether and hexane supernatant were removed. The precipitate was then reconstituted in an acetic acid or ACN solution. The solution was frozen and then lyophilized. C_{16}SIINFEKL was purified on a Gilson GX-271 HPLC on a TMS-250 10 × 100 mm C1 column (Tosoh, Tokyo, Japan). Identity and purity of the compounds was verified using MALDI-TOF.

PLNs Preparation

All nanoparticles were prepared through nanoprecipitation procedure, where the aqueous to organic phase volume ratio (A/O) did not exceed 1:20. PLA was dissolved in DMSO at 10 mg/mL. Ceramide-PEG5k was dissolved in water at 10 mg/mL. C_{16}R848 was dissolved in DMF at 5 mg/mL. C_{16}SIINFEKL was dissolved in 2 Dr vials at 5 mg/mL in DMSO. The water phase was prepared by adding 10 mL HyClone water to a 20 mL vial containing a stir bar. It was then heated on a hot plate (VWR or Chemglass) to 80°C for 5 min while stirring at 800 rpm; 200 uL of ceramide-PEG solution was added, and the mixture was then heated at 80°C for another 5 min before nanoprecipitation. For the organic phase, 175 uL of PLA was used for drug-loaded PLNs, while 200 uL was used for empty control PLNs. Then, depending on the intended composition, 50 uL of C_{16}R848 solution and/or 50 uL of C_{16}SIINFEKL (for NP-C_{16}SIL-C_{16}R848) were added to organic phase. These stock solutions were sonicated in a water bath sonicator to assist dissolution. Finally, DMSO was added to the organic phase until

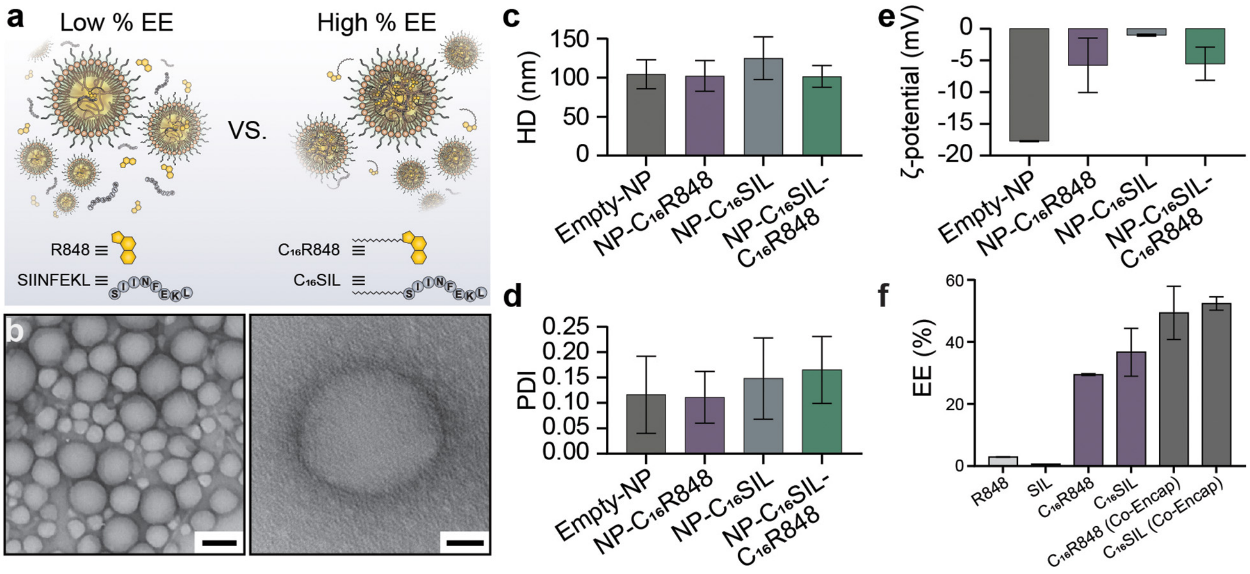

FIGURE 1 | Physicochemical properties of Core-Shell PLNs. **(a)** The comparison of EE between with and without lipidation of R848 and SIL. **(b)** Representative TEM image of lipidated conjugates formulated with PLNs (Scale bar: left, 100 nm; right, 20 nm). **(c)** The mean hydrodynamic diameter (HD), **(d)** polydispersity index (PDI), and **(e)** zeta potential (ζ) of PLNs. **(f)** Optimum mean EE for mono-encapsulation of R848, SIL, C_{16}R848, C_{16}SIL, and co-encapsulation of C_{16}R848 and C_{16}SIL.

final volume was 487.5 uL. The fully prepared organic phase was then sonicated and nanoprecipitation was performed with the organic phase being added to the water phase while the tip was submerged. The solution was stirred for 1.5 min on the hotplate before it was transferred to a stir plate and stirred at 1200 rpm for 1 h. The particle solution was then purified with a 40 μm cell strainer. The organic solvents were removed, and the NPs were concentrated via centrifugation with two water washes using 15 mL Amicon Ultra Filters with 100 K cutoff.

HEK-Blue mTLR7 Assay

HEK293 cells expressing human TLR7 or TLR8 with an NF-κB-inducible responsive SEAP reporter gene were obtained from InvivoGen (San Diego, CA, United States). Cells were cultured in DMEM with 10% FBS and antibiotics. Cells were plated at 96-well plates and stimulated for 24 h. Supernatants were harvested and monitored by NF-κB/SEAP activation using HEK-Blue^{TM} Detection Kit (InvivoGen) according to the manufacturer's instructions.

DC Antigen Presentation Experiment

Day 1 – *Plating Cells*. The media composed of RPMI, 1% penicillin-streptomycin, 10% FBS (HyClone), and 0.05 mM of β-mercaptoethanol. The following directions assume that the dendritic cells (DC2.4) were cultured in a T75 flask. Cells were resuspended in 1 mL of fresh media and counted; 1 mL of this suspension was added to each well in a 24-well plate. The plate was then incubated overnight. Optional Day 2 – *Inhibitor Addition for Endocytosis Experiment*. About 500 uL of media was removed and varying amounts of inhibitors were added. For MBCD, 1.5 mg was added per well, and for chlorpromazine, 3.25 ug was added per well. Day 2/3 – *Treatment Additions*. A 1× PBS solution was made for each nanoparticle suspension and free SIINFEKL so that the concentration was 1 ug of encapsulated or free SIINFEKL per 100 uL. Day 3/4 – *FACS Processing*. FACS buffer was made with 1× PBS and 5% FBS. A solution with 2 uL (1 ug) of CD16/32 antibody per 50 uL of FACS buffer was prepared; 50 uL of the previously prepared CD16/32 solution was added to each Eppendorf tube. They were mixed vigorously with a pipette and then incubated on ice for 10 min; 3 uL of PE/Cy7 anti-mouse H2Kb-SIINFEKL antibody was added to each sample. After centrifugation, 200 uL of 0.2% PFA solution was added to each sample, including cells only, and they were mixed vigorously without creating bubbles; 200 uL of each sample was transferred to a clear, round bottomed 96-well plate. Once completed, the plate was protected with aluminum foil and ran on flow cytometer, using the NIR-B channel for detection.

In vivo Experiments

Vaccination Procedure

Each group of five black (MOUSE TYPE) female mice underwent three rounds of vaccinations. There were three groups—saline, alum control (NPC), and NP-C_{16}SIL-C_{16}R848, and each injection consisted of 100 or 110 uL depending on the group. The suspensions of the experimental particles were rendered into those of PBS 1× by the addition of PBS 10× that is 10% the volume of the particle solutions. Then, each syringe was loaded with 110 uL of this suspension. The alum control, NPC, was created by mixing C_{16}-R848 and C_{16}-SIINFEKL dissolved stock solutions with Imject® Alum reagent and PBS 1×. The stocks were in a solution of 5 mg/mL of DMF and DMSO, respectively, and the amount of drugs per alum injection matched the amount of drugs per injection in the experimental NP-C_{16}SIL-C_{16}R848. A volume equaling six such 100 uL injection stocks was made

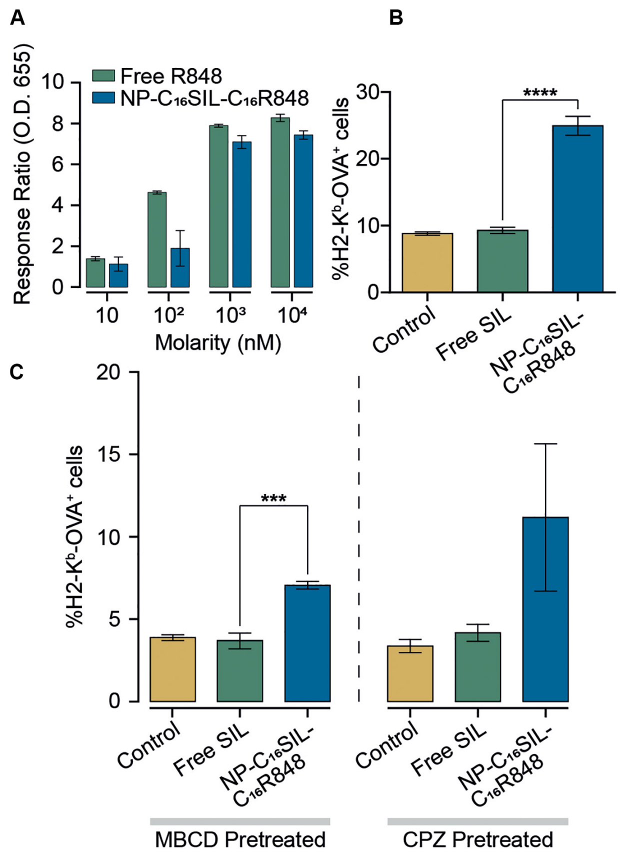

FIGURE 2 | Enhanced immunomodulatory activity of PLNs *in vitro*. **(A)** Detection of TLR7/8 agonist activity when stimulated with increased concentrations of free R848 and co-encapsulated NP (NP-C$_{16}$SIL-C$_{16}$R848). **(B)** The mean percentage of MHC I molecules presenting OVA-derived peptide SIL on DC2.4 surface. **(C)** DC2.4 groups were pretreated with two different cellular uptake inhibitors (MβCD and CPZ) and incubated overnight before treatment with controls and NPs. The mean percentage of SIL display was analyzed by fluorescence-activated cell sorting (FACS).

for injecting five mice per vaccination round. Each mouse in the PBS group was injected with only 100 uL of PBS 1×. Half of the injection went into the footpad while the other half was intraperitoneal. The vaccinations were repeated two times, with the second vaccination given 2 weeks after the first and the third given 1 week after the second. The subsequent tumor inoculation and measurement procedures are demonstrated in **Supplementary Section**.

RESULTS AND DISCUSSION

Lipidation Design Strategy

Palmitic acid (C16:0) is an endogenous fatty acid that plays an important role in posttranslational modification of cytosolic proteins via enzymatic palmitoylation (Linder and Deschenes, 2007; Sobocinska et al., 2017). The hydrophobic attachment of palmitoyl chains to proteins is a key step that facilitates maturational processing, trafficking, and membrane anchoring in cellular compartments (**Scheme 1C**) (Linder and Deschenes, 2007). Recent evidence indicates that both biological palmitoylation and synthetic lipidation can critically influence immune responses (Park et al., 2004; Smirnov et al., 2011; Black et al., 2012; Lochner et al., 2015; Foster et al., 2018). We therefore speculate that covalent attachment of palmitic acid on SIINFEKL and R848 would improve vaccine function by improving their local bioavailability, reducing systemic toxicity and enabling effective co-formulation with PLNs.

Formation and Characterization of PLN Vaccine

The lipidated TLR7/8 agonist (C$_{16}$R848) and epitope (C$_{16}$SIINFEKL) were synthesized via Steglich esterification and solid phase-assisted polymerization, respectively. The final structure of products was confirmed by high performance liquid chromatography/mass spectrometry (HPLC/MS, as illustrated in **Supplementary Figures S1–S6**). PLNs were prepared by the nanoprecipitation method and formulated with C$_{16}$R848 and/or C$_{16}$SIL to result in four different groups: (i) empty-NP, (ii) NP-C$_{16}$R848, (iii) NP-C$_{16}$SIL, and (iv4) NP-C$_{16}$SIL-C$_{16}$R848. The PLN formation was optimized via temperature-assisted nanoprecipitation. We found that the elevated temperature of aqueous phase could effectively reduce viscosity during addition of the organic portion, which resulted in desired encapsulation efficacy (EE) and spherical form under transmission electron microscopy (TEM) (**Supplementary Figure S7**). The final obtained PLNs formulated with both lipidated conjugates exhibited monodispersed colloidal features and a polyethylene glycol (PEG) corona can be observed from high-resolution transmission electron microscopy (HR-TEM) (**Figure 1b**). Interestingly, the encapsulation of lipidated conjugates has little or no impact on the hydrodynamic diameter (HD) but slightly increased the polydispersity indices (PDI) (**Figures 1c,d**). Due to the neutral charge and lipophilicity of C$_{16}$R848 and C$_{16}$SIL, the core-shell structure with the outer layer stabilized by a C$_{16}$-Ceramide-PEG5000 coating gave rise to NP-C$_{16}$SIL-C$_{16}$R848 with a slightly negative surface potential (-5.5 mV) compared with empty-NP (-17.7 mV) (**Figure 1e**). The C$_{16}$R848 and C$_{16}$SIL co-formulated with polylactide (PLA) polymer were intended to promote EE. The PLN co-formulation without lipidation exhibited extremely low, which was attributable to the aqueous solubility of SIINFEKL and small soluble aggregates of R848 (**Figure 1a**). As shown in **Figure 1f**, lipidated conjugates demonstrated 10- and 35-folds improvement in EE (C$_{16}$R848, 29.4% and C$_{16}$SIL, 36.6%) relative to their unmodified counterparts, and additional EE gains were achieved after co-encapsulation of C$_{16}$R848 (49.3%) and C$_{16}$SIL (52.4%). Taken together, these findings suggest that NP-C$_{16}$SIL-C$_{16}$R848 is capable of encapsulating both antigen and adjuvant in a manner that is suited for subsequent *in vitro* study.

In vitro Immunomodulatory Activity of PLN Vaccine

To assess the *in vitro* efficacy of PLNs that co-deliver C$_{16}$R848 and C$_{16}$SIL, TLR7/8 agonist activity was measured in a HEK293T cell-based IRF reporter assay. In a direct comparison of free

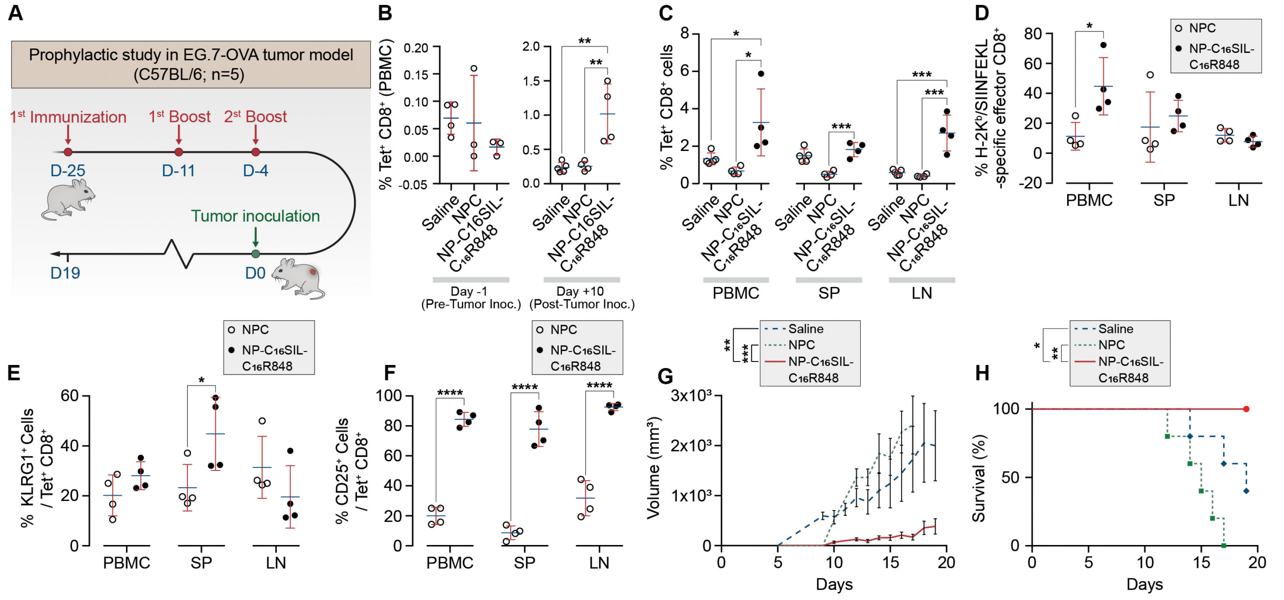

FIGURE 3 | PLN vaccine prevents tumor growth in murine cancer models with a prophylactic setting. **(A)** Regimens of PLN vaccine tested in C57BL/6 mice. **(B)** Longitudinal study of percentages of SIL-positive $CD8^+$ T cells among peripheral blood mononuclear cells (PBMCs) on day -1 before and day 10 after tumor inoculation. **(C)** Percentages of SIL-positive $CD8^+$ T cells among PBMCs, spleens (SP) and lymph node (LN) on day 19. **(D)** Mean percentages of SIL-positive effector $CD8^+$ T cells. **(E)** The frequency of KLRG1-positive subsets from SIL-positive $CD8^+$ T cells. **(F)** Percentages of SIINFEKL-specific $CD25^+$ Tregs on day 19. **(G)** The size of E.G7-OVA tumors was monitored over time. **(H)** Survival curve of immunized mice inoculated with E.G7-OVA tumor cells. Data are representative of two independent experiments. Experimental groups consisted of five mice. $^*P < 0.05$, $^{***}P < 0.001$, and $^{****}P < 0.0001$ analyzed by one-way ANOVA **(B–F)** or two-way ANOVA **(G–H)** with Tukey's multiple comparisons post-test.

R848 and co-formulation form (NP-C_{16}SIL-C_{16}R848) at higher concentration (10^3–10^4 nM) demonstrated a similar *in vitro* potency to free R848 (**Figure 2A**), while a low concentration (10–10^2 nM) of C_{16}R848 (NP-C_{16}SIL-C_{16}R848) had no significant effect on activity, implying that relatively high concentration loading of C_{16}R848 by PLNs could be essential for efficient TLR7/8 activation.

A critical process driving $CD8^+$ primary T cell responses to vaccines *in vivo* is antigen cross-presentation through the formation of exogenously derived peptide with MHC complexes presented on the surface of dendritic cells (DCs). The ability of the PLNs to increase antigen cross-presentation was investigated in murine DC2.4 dendritic cells by fluorescent immunostaining (**Figure 2B**). Notably, groups treated with NP-C_{16}SIL-C_{16}R848 showed higher MHC-I mediated SIL antigen presentation on the cell surface compared to control and free SIL treatment groups. This suggests that DC2.4 cells upregulate peptide-MHC I complex presentation in response to NP-C_{16}SIL-C_{16}R848, consistent with the general concept that dendritic cell activation by TLR7/8 agonists is associated with increased antigen cross-presentation and downstream adaptive responses (Iwasaki and Medzhitov, 2004). Because endocytic pathways can influence nanoparticle-mediated delivery of peptide antigens to dendritic cells, we measured the MHC-I presentation of SIINFEKL while simultaneously blocking the class A scavenger receptor (SR-A), lipid raft or clathrin-dependent endocytosis. The results (**Figure 2C**) indicate that blocking lipid raft-mediated endocytosis with methyl-β-cyclodextrin (MβCD) dramatically inhibited the surface antigen presentation for all groups compared with non-treated controls (**Figure 2C**). However, the epitope expression level mediated by NP-C_{16}SIL-C_{16}R848 remained twofold higher than free SIL without R848. A similar result was observed when chlorpromazine (CPZ) is used to disrupt the SR-A-mediated uptake pathway (**Figure 2C**). Collectively, these results indicate that PLN-mediated co-delivery of C_{16}R848 adjuvant and C_{16}SIL antigen results in dendritic cell activation and a significant increase in antigen presentation at higher loading concentrations.

In vivo Immunomodulatory Activity of PLN Vaccine

Having demonstrated dendritic cell activation *in vitro*, we sought to explore the ability of NP-C_{16}SIL-C_{16}R848 to elicit an antigen-specific immune response *in vivo* (**Figure 3A**). Naïve C57BL/6 mice were immunized with a primary immunization followed by two booster injections with a fixed 100 μL/vaccine dose that included NPC [Alum/C_{16}-SIL (10 μg)/C_{16}-R848 (7 μg)], NP-C_{16}SIL-C_{16}R848 [C_{16}SIL (10 μg)/C_{16}R848 (7 μg)], or vehicle control. On day 3 following the third immunization, we quantified the frequency of SIL-specific $CD8^+$ T cells by the SIL/H-2Kb tetramer (OVA-Tet-PE) staining. We did not detect a significant increase in Tet^+ $CD8^+$ T cells prior to the tumor inoculation in any of the treatment groups (**Figure 3B**, Day 1), indicating any expansion of Tet^+ $CD8^+$ T cells due to vaccination was modest in peripheral blood. To evaluate

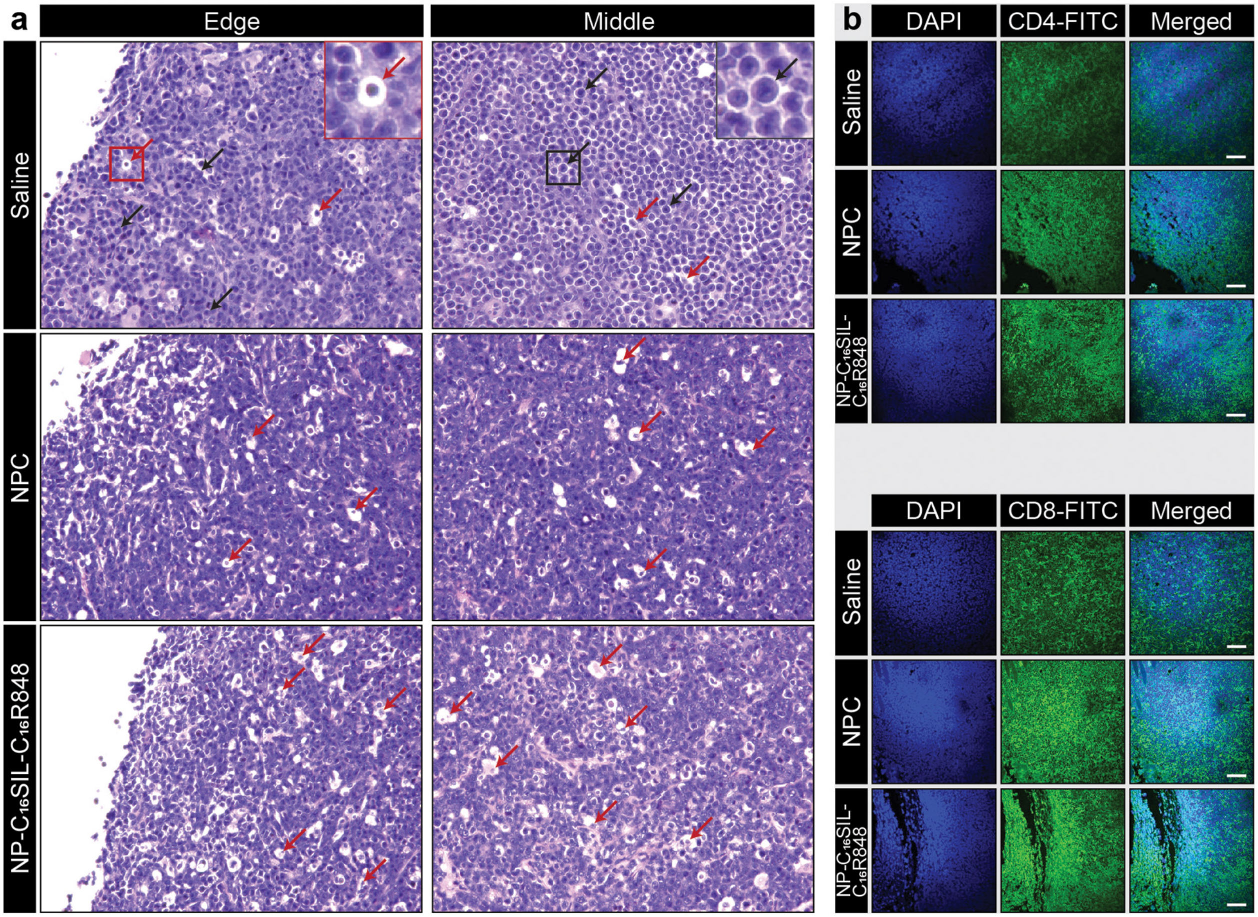

FIGURE 4 | Anti-tumor immunity in the tumor microenvironment (TME). **(a)** Histopathology of representative H&E-stained edge and middle region sections of E.G7-OVA tumors from vaccinated mice. The red arrows indicate apoptotic cells and black arrows indicate normal lymphoma cells. **(b)** Immunofluorescence analysis of $CD4^+$ and $CD8^+$ T cell infiltration in the tumor tissues in each group. Immunofluorescent staining of nucleus (blue), CD4 or CD8 (green) in tumor slices. Scale bar = 100 μm.

the immunogenic effects of the nanovaccine strategy in tumor xenograft model, C57BL/6 mice were then inoculated s.c. with E.G7-OVA thymic lymphoma cells. At 10- and 19-days post tumor inoculation, the NP-C_{16}SIL-C_{16}R848 vaccinated group exhibited a significant increase in the frequency of SIL-specific $CD8^+$ T cells compared with vehicle control ($P = 0.0021$) and NPC groups ($P = 0.0035$) (**Figure 3B**, Day 10). On day 19 post tumor inoculation, there was a higher percentage of Tet^+ $CD8^+$ T cells in the secondary lymphoid tissues including the spleen (SP) and lymph node (LN) (**Figure 3C**); NP-C_{16}SIL-C_{16}R848 vaccination resulted in significantly higher frequencies of SIL-specific $CD8^+$ T cells within the PBMC ($P = 0.0114$), SP ($P = 0.0005$), and LN compartments ($P = 0.0003$) compared to alum-adsorbed OVA R848 vaccine. Besides, effector $CD8^+$ T cells were found to be differentially promoted in both PBMC and SP, but negligible difference was observed as compared with NPC groups (**Figure 3D**).

Effector $CD8^+$ T cells are a key mediator of cell-mediated cytotoxic antitumor immunity (Melief, 2008), and a subset of these T Cells are critical for cancer immune surveillance. The pool of these memory precursor effector cells can be further divided into short-lived effector $CD8^+$ T cells (SLECs) and memory precursors (MPs) (Kaech et al., 2002), and KLRG1 (Killer Cell Lectin Like Receptor G1) is a cell marker expressed by $CD4^+$ and $CD8^+$ T cells that exhibit a memory cell phenotype (Olson et al., 2013; Herndler-Brandstetter et al., 2018). Furthermore, these cells can differentiate into memory cells that are capable of mounting highly effective anti-tumor responses upon tumor rechallenge (Herndler-Brandstetter et al., 2018). To evaluate whether different vaccine strategies could induce this desired T cell phenotype, we assessed KLRG1 expression in antigen-experienced $CD8^+$ T cells in PBMC, SP, and LN compartments. Notably, compared with NPC formulation groups on day 19, NP-C_{16}SIL-C_{16}R848 immunized groups exhibited higher levels of KLRG1 expression in both PBMC and SP ($P < 0.05$) (**Figure 3E**). Importantly, the number of cells expressing the T cell activation marker, IL-2 receptor α chain CD25, was significantly higher in all three compartments following immunization with NP-C_{16}SIL-C_{16}R848 (**Figure 3F**) (Perret et al., 2013; Nishikawa and Sakaguchi, 2014). Together, these results indicate that the co-delivery of adjuvant and peptide antigen augments the development of the antigen-specific CD^{8+} T cell responses, resulting in effector T cells that retain the ability to proliferate and develop into memory $CD8^+$ T cells.

In vivo Anti-tumor Immunity of PLN Vaccine

We next sought to determine whether the lipidation approaches could induce desired anticancer immunity against a solid tumor. Tumor growth was significantly reduced in NP-C_{16}SIL-C_{16}R848 vaccinated groups for more than 2 weeks following inoculation compared with controls (saline, $P = 0.0005$; NPC, $P = 0.0039$) (**Figure 3G**), leading to improved survival of NP-C_{16}SIL-C_{16}R848 vaccinated groups of mice (**Figure 3H**). This prophylactic anticancer efficacy was also observed in the histopathology analysis of the tumor cell morphometry (**Figure 4a**). Compared with saline and soluble formulations, the NP-C_{16}SIL-C_{16}R848 immunized group demonstrated a conspicuous increase in the number of apoptotic bodies (red arrow) within the presence of a "starry sky" pattern in both outer edge and inner middle of the tumor lesions. Additionally, the condensation of the chromatin, shrinking of the lymphoma cells, and fragmentation of the nucleus were also more frequently observed. These phenomena are consistent with antitumor immunity through an activation of SIL-specific $CD8^+$ response. Furthermore, we explored the distribution of the $CD4^+$ and $CD8^+$ T cell populations in the tumor tissues of mice and found that $CD4^+$ and $CD8^+$ T cells labeled by FITC probe are enriched in the tumor nests of both NPC and NP-C_{16}SIL-C_{16}R848 vaccinated mice, while mice immunized with saline showed less infiltration of $CD4^+$ and $CD8^+$ T cells in the E.G7 tumor tissue (**Figure 4b**). These observations demonstrate that our LPN vaccine approach provoked a notable increase of $CD4^+$ and $CD8^+$ T cells at tumor sites.

CONCLUSION

Previously, we showed that co-encapsulation of the model antigen OVA with the TLR7/8 agonist in SVPs improved clinical-grade safety with minimal risk of systemic adverse reactions (Ilyinskii et al., 2014). The present study demonstrates that it is possible to improve anti-tumor immune responses and achieve *in vivo* prophylactic efficacy using a peptide vaccine composed of an SIL epitope with a TLR7/8 agonist, owing to lipidation of adjuvant/peptide epitope and PLN strategy. Our design rationale demonstrated multifaceted benefits, including minimal systemic exposure, enhanced EE, consistent APC uptake, and prolonged immune surveillance. Furthermore, the lipidated PLN formulation approach described here has the potential to be applied beyond TLR-dependent immunostimulatory activity to other adjuvants capable of stimulating innate immune activation. Overall, the combination of medicinal chemistry and formulation science enables the described strategy to address the specific criteria including effective co-encapsulation, *in vivo* stability, prolong release, consistent APC uptake, and safety. Our demonstration could be an important clue to guide the future success of anti-cancer nanovaccines.

DATA AVAILABILITY STATEMENT

The datasets presented in this study can be found in online repositories. The names of the repositories and accession numbers can be found in the article/**Supplementary Material**.

ETHICS STATEMENT

The animal study was reviewed and approved by the Brigham and Women's Hospital Institutional Animal Care and Use Committee.

AUTHOR CONTRIBUTIONS

JS and BZ conceived the idea and directed the project. HZ, MI, JW, JR, SD, KL, and YC performed all the experiments and analyzed the data. JW, HZ, and MI wrote the manuscript and revised it according to the comments of JS, JR, and other co-authors. JR and JS provided the technical support and corrections of the manuscript. All authors contributed to the article and approved the submitted version.

FUNDING

This work was in part supported by the Prostate Cancer Foundation Young Investigator Award. JW was supported by The Hundred Talents Program (75110-18841227) from Sun Yat-sen University, Guangzhou, China, and The Guangdong Basic and Applied Basic Research Foundation (2019A1515110326).

SUPPLEMENTARY MATERIAL

The Supplementary Material for this article can be found online at: https://www.frontiersin.org/articles/10.3389/fbioe.2020.00787/full#supplementary-material

REFERENCES

Alexis, F., Iannacone, M., Shi, J., Basto, P., Moseman, E. A., Von Andrian, U., et al. (2016). *Adjuvant Incorporation in Immunonanotherapeutics*. Patents No. PCT/US2009/060242. Harvard College, Brigham and Womens Hospital Inc., Massachusetts Institute of Technology.

Black, M., Trent, A., Kostenko, Y., Lee, J. S., Olive, C., and Tirrell, M. (2012). Self-assembled peptide amphiphile micelles containing a cytotoxic T-Cell epitope promote a protective immune response in vivo. *Adv. Mater.* 24, 3845–3849. doi: 10.1002/adma.201200209

Coffman, R. L., Sher, A., and Seder, R. A. (2010). Vaccine adjuvants: putting innate immunity to work. *Immunity* 33, 492–503. doi: 10.1016/j.immuni.2010.10.002

Dane, E. L., and Irvine, D. J. (2015). Big thinking for adjuvants. *Nat. Biotechnol.* 33, 1146–1148. doi: 10.1038/nbt.3398

Foster, A. J., Nagata, M., Lu, X., Lynch, A. T., Omahdi, Z., Ishikawa, E., et al. (2018). lipidated brartemicin analogues are potent th1-stimulating vaccine adjuvants. *J. Med. Chem.* 61, 1045–1060. doi: 10.1021/acs.jmedchem.7b01468

Gadd, A. J. R., Castelletto, V., Kabova, E., Shankland, K., Perrie, Y., Hamley, I., et al. (2018). High potency of lipid conjugated TLR7 agonist requires nanoparticulate or liposomal formulation. *Eur. J. Pharm. Sci.* 123, 268–276. doi: 10.1016/j.ejps.2018.07.048

Herndler-Brandstetter, D., Ishigame, H., Shinnakasu, R., Plajer, V., Stecher, C., Zhao, J., et al. (2018). KLRG1+ effector CD8+ T Cells Lose KLRG1, differentiate into all memory T Cell lineages, and convey enhanced protective immunity. *Immunity* 48, 716.e8–729.e8.

Hu, Z., Ott, P. A., and Wu, C. J. (2017). Towards personalized, tumour-specific, therapeutic vaccines for cancer. *Nat. Rev. Immunol.* 18, 168–182. doi: 10.1038/nri.2017.131

Ilyinskii, P. O., Roy, C. J., O'neil, C. P., Browning, E. A., Pittet, L. A., Altreuter, D. H., et al. (2014). Adjuvant-carrying synthetic vaccine particles augment the immune response to encapsulated antigen and exhibit strong local immune activation without inducing systemic cytokine release. *Vaccine* 32, 2882–2895. doi: 10.1016/j.vaccine.2014.02.027

Iwasaki, A., and Medzhitov, R. (2004). Toll-like receptor control of the adaptive immune responses. *Nat. Immunol.* 5, 987–995. doi: 10.1038/ni1112

Junt, T., and Barchet, W. (2015). Translating nucleic acid-sensing pathways into therapies. *Nat. Rev. Immunol.* 15, 529–544. doi: 10.1038/nri3875

Kaech, S. M., Hemby, S., Kersh, E., and Ahmed, R. (2002). Molecular and functional profiling of memory CD8 T cell differentiation. *Cell* 111, 837–851. doi: 10.1016/s0092-8674(02)01139-x

Kastenmuller, K., Wille-Reece, U., Lindsay, R. W., Trager, L. R., Darrah, P. A., Flynn, B. J., et al. (2011). Protective T cell immunity in mice following protein-TLR7/8 agonist-conjugate immunization requires aggregation, type I IFN, and multiple DC subsets. *J. Clin. Invest.* 121, 1782–1796. doi: 10.1172/jci45416

Khan, O. F., Zaia, E. W., Yin, H., Bogorad, R. L., Pelet, J. M., Webber, M. J., et al. (2014). Ionizable amphiphilic dendrimer-based nanomaterials with alkyl-chain-substituted amines for tunable siRNA delivery to the liver endothelium in vivo. *Angew Chem. Int. Ed. Engl.* 53, 14397–14401. doi: 10.1002/anie.201408221

Kim, H., Niu, L., Larson, P., Kucaba, T. A., Murphy, K. A., James, B. R., et al. (2018). Polymeric nanoparticles encapsulating novel TLR7/8 agonists as immunostimulatory adjuvants for enhanced cancer immunotherapy. *Biomaterials* 164, 38–53. doi: 10.1016/j.biomaterials.2018.02.034

Kowalski, P. S., Rudra, A., Miao, L., and Anderson, D. G. (2019). Delivering the messenger: advances in technologies for therapeutic mRNA Delivery. *Mol .Ther.* 27, 710–728. doi: 10.1016/j.ymthe.2019.02.012

Kumai, T., Kobayashi, H., Harabuchi, Y., and Celis, E. (2017). Peptide vaccines in cancer-old concept revisited. *Curr. Opin. Immunol.* 45, 1–7. doi: 10.1016/j.coi.2016.11.001

Linder, M. E., and Deschenes, R. J. (2007). Palmitoylation: policing protein stability and traffic. *Nat. Rev. Mol. Cell Biol.* 8, 74–84. doi: 10.1038/nrm2084

Liu, H., Moynihan, K. D., Zheng, Y., Szeto, G. L., Li, A. V., Huang, B., et al. (2014). Structure-based programming of lymph-node targeting in molecular vaccines. *Nature* 507, 519–522. doi: 10.1038/nature12978

Lochner, M., Berod, L., and Sparwasser, T. (2015). Fatty acid metabolism in the regulation of T cell function. *Trends Immunol.* 36, 81–91. doi: 10.1016/j.it.2014.12.005

Melief, C. J. M. (2008). Cancer immunotherapy by dendritic cells. *Immunity* 29, 372–383.

Moynihan, K. D., Holden, R. L., Mehta, N. K., Wang, C., Karver, M. R., Dinter, J., et al. (2018). Enhancement of peptide vaccine immunogenicity by increasing lymphatic drainage and boosting serum stability. *Cancer Immunol. Res.* 6, 1025–1038. doi: 10.1158/2326-6066.cir-17-0607

Nabel, G. J. (2013). Designing tomorrow's vaccines. *N. Engl. J. Med.* 368, 551–560.

Napolitani, G., Rinaldi, A., Bertoni, F., Sallusto, F., and Lanzavecchia, A. (2005). Selected toll-like receptor agonist combinations synergistically trigger a T helper type 1-polarizing program in dendritic cells. *Nat. Immunol.* 6, 769–776. doi: 10.1038/ni1223

Nishikawa, H., and Sakaguchi, S. (2014). Regulatory T cells in cancer immunotherapy. *Curr. Opin. Immunol.* 27, 1–7.

Nuhn, L., De Koker, S., Van Lint, S., Zhong, Z., Catani, J. P., Combes, F., et al. (2018). Nanoparticle-conjugate TLR7/8 agonist localized immunotherapy provokes safe antitumoral responses. *Adv. Mater.* 30:1803397. doi: 10.1002/adma.201803397

Olson, J. A., Mcdonald-Hyman, C., Jameson, S. C., and Hamilton, S. E. (2013). Effector-like CD8+ T Cells in the memory population mediate potent protective immunity. *Immunity* 38, 1250–1260. doi: 10.1016/j.immuni.2013.05.009

Park, J.-J., Kang, S.-J., De Silva, A. D., Stanic, A. K., Casorati, G., Hachey, D. L., et al. (2004). Lipid–protein interactions: biosynthetic assembly of CD1 with lipids in the endoplasmic reticulum is evolutionarily conserved. *Proc. Natl. Acad. Sci. U.S.A.* 101, 1022–1026. doi: 10.1073/pnas.0307847100

Peng, G., Guo, Z., Kiniwa, Y., Voo, K. S., Peng, W., Fu, T., et al. (2005). Toll-like receptor 8-mediated reversal of CD4+ regulatory T cell function. *Science* 309, 1380–1384. doi: 10.1126/science.1113401

Perret, R., Sierro, S. R., Botelho, N. K., Corgnac, S., Donda, A., and Romero, P. (2013). Adjuvants that improve the ratio of antigen-specific effector to regulatory T cells enhance tumor immunity. *Cancer Res.* 73, 6597–6608. doi: 10.1158/0008-5472.can-13-0875

Perrie, Y., Mohammed, A. R., Kirby, D. J., Mcneil, S. E., and Bramwell, V. W. (2008). Vaccine adjuvant systems: enhancing the efficacy of sub-unit protein antigens. *Int. J. Pharm.* 364, 272–280. doi: 10.1016/j.ijpharm.2008.04.036

Reed, S. G., Orr, M. T., and Fox, C. B. (2013). Key roles of adjuvants in modern vaccines. *Nat. Med.* 19, 1597–1608. doi: 10.1038/nm.3409

Rodell, C. B., Arlauckas, S. P., Cuccarese, M. F., Garris, C. S., Li, R., Ahmed, M. S., et al. (2018). TLR7/8-agonist-loaded nanoparticles promote the polarization of tumour-associated macrophages to enhance cancer immunotherapy. *Nat. Biomed. Eng.* 2, 578–588. doi: 10.1038/s41551-018-0236-8

Skwarczynski, M., and Toth, I. (2016). Peptide-based synthetic vaccines. *Chem. Sci.* 7, 842–854. doi: 10.1039/c5sc03892h

Smirnov, D., Schmidt, J. J., Capecchi, J. T., and Wightman, P. D. (2011). Vaccine adjuvant activity of 3M-052: an imidazoquinoline designed for local activity without systemic cytokine induction. *Vaccine* 29, 5434–5442. doi: 10.1016/j.vaccine.2011.05.061

Sobocinska, J., Roszczenko-Jasinska, P., Ciesielska, A., and Kwiatkowska, K. (2017). Protein palmitoylation and its role in bacterial and viral infections. *Front. Immunol.* 8:2003. doi: 10.3389/fimmu.2017.02003

Thauvin, C., Widmer, J., Mottas, I., Hocevar, S., Allémann, E., Bourquin, C., et al. (2019). Development of resiquimod-loaded modified PLA-based nanoparticles for cancer immunotherapy: a kinetic study. *Eur. J. Pharm. Biopharm.* 139, 253–261. doi: 10.1016/j.ejpb.2019.04.007

Vasilakos, J. P., and Tomai, M. A. (2013). The use of Toll-like receptor 7/8 agonists as vaccine adjuvants. *Expert Rev. Vaccines* 12, 809–819. doi: 10.1586/14760584.2013.811208

Whitehead, K. A., Dorkin, J. R., Vegas, A. J., Chang, P. H., Veiseh, O., Matthews, J., et al. (2014). Degradable lipid nanoparticles with predictable in vivo siRNA delivery activity. *Nat. Commun.* 5:4277.

Conflict of Interest: JR was employed by the company Silicon Therapeutics, Boston, MA, United States. MI was employed by the company Immuno-Oncology Group, Immunomic Therapeutics, Inc., Rockville, MD, United States.

The remaining authors declare that the research was conducted in the absence of any commercial or financial relationships that could be construed as a potential conflict of interest.

frontiers
in Bioengineering and Biotechnology

ORIGINAL RESEARCH
published: 31 August 2020
doi: 10.3389/fbioe.2020.00769

Zinc Ion-Stabilized Aptamer-Targeted Black Phosphorus Nanosheets for Enhanced Photothermal/Chemotherapy Against Prostate Cancer

Li Gao[1]†, Ruobing Teng[2]†, Sen Zhang[1], Yun Zhou[2], Miaomiao Luo[2], Youqiang Fang[3], Lei Lei[4]* and Bo Ge[1,5]*

[1] Department of Urology, Affiliated Hospital of Guilin Medical University, Guilin Medical University, Guilin, China, [2] School of Pharmaceutical Sciences (Shenzhen), Sun Yat-sen University, Shenzhen, China, [3] Department of Urology, The Third Affiliated Hospital of Sun Yat-sen University, Guangzhou, China, [4] State Key Laboratory of Ophthalmology, Zhongshan Ophthalmic Center, Sun Yat-sen University, Guangzhou, China, [5] Department of Urology, The Second Affiliated Hospital of Guilin Medical University, Guilin Medical University, Guilin, China

Edited by:
Wei Tao,
Harvard Medical School,
United States

Reviewed by:
Han Zhang,
Shenzhen University, China
Chuang Liu,
Ningbo Institute of Materials Technology & Engineering (CAS), China

***Correspondence:**
Lei Lei
leilei25@mail.sysu.edu.cn
Bo Ge
ge1123@sina.com

†These authors have contributed equally to this work

Specialty section:
This article was submitted to Nanobiotechnology, a section of the journal Frontiers in Bioengineering and Biotechnology

Received: *21 April 2020*
Accepted: *18 June 2020*
Published: *31 August 2020*

Citation:
Gao L, Teng R, Zhang S, Zhou Y, Luo M, Fang Y, Lei L and Ge B (2020) Zinc Ion-Stabilized Aptamer-Targeted Black Phosphorus Nanosheets for Enhanced Photothermal/Chemotherapy Against Prostate Cancer. Front. Bioeng. Biotechnol. 8:769. doi: 10.3389/fbioe.2020.00769

Prostate cancer is the second most common malignancy among men worldwide. However, conventional chemotherapy, such as taxane therapy, fails to exhibit efficient treatment for almost half of the patients. In this study, a nano-drug delivery system based on black phosphorus nanosheets (BP NSs) was developed, which was then employed as a multifunctional nanoplatform for targeted combinational chemo-photothermal therapy against prostate cancer. Zinc ion (Zn^{2+}), which has been proven to be able to inhibit prostate cancer cell proliferation, was also introduced into this system. Zn^{2+} coordination could not only enhance the therapeutic effect of combined chemo-photothermal therapy, but also improve the intrinsic instability of BP NSs through the stabilization of its lone pair electrons. The *in vivo* study showed the outstanding performance of this system in targeted photothermal/chemotherapy of prostate cancer without side effect to normal organs.

Keywords: black phosphorus, photothermal therapy, chemotherapy, zinc ion, targeted therapy

INTRODUCTION

Prostate cancer is the second most common malignancy among men around the world (Heidenreich et al., 2014). Early stage localized prostate cancer can be treated effectively by hormone and radiation therapy with less difficulty, however, the treatment of advanced-stage prostate cancer remains a significant challenge due to its frequent pathophysiological changes, epithelial-mesenchymal transition and drug resistance (Chen et al., 2018; Mollica et al., 2019; Wang et al., 2019c). Unfortunately, most patients with prostate cancer are already in late-stage at the time of consultation (Wang et al., 2019c; Teo et al., 2019). Chemotherapy is often employed for the treatment of advanced-stage aggressive and metastatic prostate cancer, nonetheless, chemotherapy, such as taxane therapy, fails to exhibit a good response for half of the patients (Li and Mahato, 2014, 2015). Research and development of new drugs is a potential option, however, the long time and significant investment of developing new drug molecules inevitably results in a high cost of therapy. Therefore, it is of great urgency to develop a high effective and relatively affordable method for the treatment of prostate cancer, especially late-stage prostate cancer.

Nowadays, with some novel therapeutic methods such as gene therapy, photodynamic therapy (PDT), and photothermal therapy (PTT) etc., emerging, the combination of two or more treatments has become a promising strategy to improve the therapeutic efficacy of chemotherapy (Cheng et al., 2017a; Guo et al., 2019). Due to the noninvasive, controllable and highly selective characteristics for cancer treatment, PTT has attracted wide attention for the past few decades (Yang et al., 2018; Cheng et al., 2019; Wang et al., 2019a). To date, various types of photothermal agents have been reported, including carbon-based nanomaterials, semiconductor nanoparticles, metal-based nanostructures, organic polymers and metal-organic frameworks (Li et al., 2015; Cheng et al., 2017c; Yin et al., 2017; Zhang et al., 2017; Liang et al., 2019).

As a novel 2D material, black phosphorus nanosheets (BP NSs) possess excellent extinction coefficient and high photothermal conversion efficacy, which enables BP NSs to be promising photothermal agents (Sun et al., 2015; Luo et al., 2019b). In addition, BP NSs completely meet the strict safety requirements in clinical use. The metabolism of BP is phosphate or phosphonate, which would not cause certain immune responses (Liu et al., 2019a; Luo et al., 2019a; Yang et al., 2019). Besides, compare with other 2D nanomaterials, such as Xenes, boron NSs, antimonene and MXene (Liu et al., 2017; Tao et al., 2019; Xue et al., 2019a; Tang et al., 2020), BP NSs possess large specific surface area due to a corrugated plane configuration, and thus can serve as an efficient delivery platform for a variety of different cargos, such as anticancer drugs, mental ions, targeting molecules, and so on, forming synergistic therapeutic systems.

However, although BP is the most stable allotrope of phosphorus, BP is susceptible to degradation upon exposure to ambient conditions (Liu et al., 2019b; Tao et al., 2019). BP is very reactive to water and oxygen, causing compositional and physical changes of BP (Favron et al., 2015; Ryder et al., 2016). The biomedical applications of BP are greatly limited owing to its instability under ambient environment. One P atom of BP is covalently bonded to another three single-layer P atoms, thereby exposing a pair of lone pair electrons (Ziletti et al., 2015). Such lone pair electrons would readily react with oxygen to form P_xO_y, which would be subsequently removed by water, resulting in the destruction of P network of BP NSs (Zhou et al., 2016; Liu et al., 2019a). Thus, it is supposed to be an effective strategy to mitigate oxidation of BP NSs under ambient environment if the lone pair electrons could be stabilized through occupation by other elements (Zhao et al., 2016; Guo et al., 2017). Herein, zinc ion (Zn^{2+}) was employed to interact with BP to form Zn^{2+}-modified BP NSs. The coordination of Zn^{2+} with the lone pair electrons of BP may impede the reaction between P and O_2, thus ultimately improving the stability of BP.

More importantly, the organ with the highest level of Zn in human body is prostate. Zn can inhibit the activity of mitochondrial aconitase, which is of great significance in maintaining health and normal functions of prostate (Kelleher et al., 2011). However, Zn concentration dramatically diminishes during prostate malignancy (Kolenko et al., 2013; Xue et al., 2019b). Zn in prostate epithelial cells is present in the form of Zn^{2+}. Although the specific mechanism remains to be further studied, it has been reported that an increase of Zn^{2+} level in prostate cancer cells can inhibit cell proliferation, invasion and metastasis, and induce its apoptosis as well via inhibiting some cellular signaling pathways (Uzzo et al., 2006; Yan et al., 2010; Chen et al., 2013). Therefore, it is expected that the introduction of Zn^{2+} in our system could not only improve the stability of BP, but also enhance the therapeutic effect of combined photothermal/chemotherapy against prostate cancer.

To improve the efficacy of the combined treatment in prostate cancer therapy, endowing such theraputic system with tumor targeting property is a promising strategy. Aptamers (Apts), a single-stranded RNA or DNA oligonucleotide, have been shown as an excellent targeting agent for efficient penetration into biological compartments with nonimmunogenicity (Li et al., 2017; Liu et al., 2018). Different aptamers can be produced through chemical synthesis at low cost. As one of the DNA Aptamers, AS1411 Apt is able to bind to nucleolin (NCL) with high specificity and affinity (Tao et al., 2016). NCL is a multifunctional protein overexpressed on the plasma membrane in a variety of solid tumors including prostate cancer, which has been widely recognized as an attractive tumor marker (Kim et al., 2012). Here, in order to improve the active tumor targeting ability, our system was further modified with NH_2-PEG-Apt.

In this study, we constructed a multifunctional system based on BP NSs for Zn^{2+} enhanced combined chemo/photothermal treatment against prostate cancer. Apt modification allowed this platform to possess great tumor targeting property, increasing accumulation of the nanoparticles in tumor sites. Additionaly, zinc ion conjugation could also improve the stability of BPs.

MATERIALS AND METHODS

Materials

The bulk BP was purchased from Smart-Elements (Vienna, Austria). MTT, 1-Methyl-2-pyrrolidinone (NMP), dimethyl sulfoxide (DMSO), tris-(2-carboxyethyl)-phosphine hydrochloride (TCEP) and 4′,6-diamidino-2-phenylindole (DAPI) were purchased from Sigma-Aldrich (St. Louis, MO, United States). Zinc acetate was obtained from Aladdin (Los Angeles, CA, United States). Methoxy-PEG_{2k}-amine (NH_2-PEG) and maleimide-PEG_{2k}-amine (NH_2-PEG-MAL) were provided by Shanghai Yare Biotech, Inc. (Shanghai, China). Doxorubicin hydrochloride (DOX) was bought from Dalian Meilun Biology Technology Co., Ltd. (Dalian, China). Dulbecco minimum essential medium (DMEM), streptomycin, penicillin, FBS, were purchased from Thermo Fisher Scientific (Waltham, MA, United States). Human prostate cancer cell (PC3) was obtained from Guilin Medical University (Guilin, Guangxi, China).

Preparation of BP NSs

BP nanosheets (BP NSs) were synthesized via a modified liquid exfoliation method (Zeng et al., 2018). Briefly, 5 mg of bulk BP crystal powder was dispersed in 20 mL NMP solution, and then the mixture was subjected to probe sonication in an ice bath using a power of 700 W for 8 h (On/Off cycle: 2 s/4 s). The resulting brown suspension was centrifuged at 3000 rpm for 15 min to remove the unexfoliated bulk BP. The supernatant was collected gently and centrifuged for another 15 min at 10,000 rpm. The precipitate was collected and resuspended in NMP. The BP NSs were stored under 4°C for further experiments.

Preparation of BP-P-Apt

20 OD of Apt-SH was dissolved in 1 mL tris buffer (pH = 7.4, 10 mM), followed by addition of 2 mg NH_2-PEG-MAL and 40 μg TCEP. The mixture was stirred in the dark for 3 h to obtain NH_2-PEG-Apt. Then, 2 mg BP NSs was added to the above solution. After probe sonication for 10 min and stirring for 5 h, BP-P-Apt was obtained by centrifugation for 15 min at 10,000 rpm and washed with deionized water for two times.

Zinc Ion Conjugation

7.5 mg of zinc acetate was mixed with 5 mL BP-P-Apt nanosheets suspension (0.5 mg mL^{-1} BP) and subjected to probe sonication for 3 min. After stirring for 3 h, the mixture solution was centrifuged at 10,000 rpm for 15 min. The precipitate (Zn-BP-P-Apt) was collected and washed with deionized water.

Drug Loading

Two milligram of Zn-BP-P-Apt was dispersed in 2 mL of DOX aqueous solution (1.5 mg mL^{-1}) and then stirred for 6 h in the dark. After centrifugation (10,000 rpm, 15 min), the final product Zn-BP-P-Apt/D was separated and washed, and then freeze-dried for further use.

Characterization of NSs

Transmission electron microscopy (TEM) images were acquired using FEI Tecnai G2 F30 transmission electron microscope. Atomic force microscopy (AFM) was performed on Bruker Diension Icon microscope. X-ray photoelectron spectroscopy (XPS) was performed using a Kratos Axis Ultra DLD spectrometer with Al Kα radiation (1486.6 eV photons, 150 W). The size and zeta potential of samples were measured on Malvern Mastersizer 2000 (Zetasizer Nano ZS90, Malvern Instruments Ltd., United Kingdom).

pH/NIR Dual-Responsive DOX Release

The drug release experiments of Zn-BP-P-Apt/D were investigated in PBS with different pH values. For each study, 2mL of Zn-BP-P-Apt/D suspension (5 mg mL^{-1}) was sealed in a dialysis bag (MWCO 3500, Shanghai Sangon, China). The dialysis bag was then immersed in 10mL PBS buffer medium (pH = 5.0 or 7.4) and shaken gently at 37°C (120 rpm). At predetermined time points, the Zn-BP-P-Apt/D suspension with pH 5.0 was irradiated by 808nm NIR laser (6min, 1.0W cm^{-2}). At given time intervals, 0.5mL of the outside release medium was collected, and an equal volume of fresh medium was replenished to the old PBS. The cumulative amount of DOX released from NPs was measured using fluorescence spectrophotometry.

In vitro Photothermal Effect

Photothermal performance of prepared NPs was evaluated via measuring temperature changes with an infrared thermal camera (Ti450, Fluke, United States). Zn-BP-P-Apt/D NPs with different concentrations from 50 to 200 μg mL^{-1} were irradiated with an 808 nm laser (Shanxi Kaisite Electronic Technology Co., Ltd., Xi'an, China) at power densities of 0.5, 1.0, and 2.0W cm^{-2} for 10min. To compare the photothermal effect of different NPs, BP, Zn-BP-P-Apt/D, and water were exposed under an 808nm laser for 10min with a power density of 1.0W cm^{-2}.

Stability Evaluation of BP NSs

To evaluate the influence of Zn^{2+} coordination on BP stability, bare BP and Zn-BP-P-Apt/D NSs with the same amount of BP concentration (100 μg mL^{-1}) were dispersed in water and exposed to air for 6 days and then their photothermal properties were tested at predetermined time intervals. Then, bare BP and Zn-BP NSs were dispersed in water and exposed to air for 2 days. The morphology of these two samples were observed by ultra-depth three-dimensional microscope.

Cell Culture and Cellular Uptake

Human prostate cancer cell (PC3) was cultured in high glucose DMEM medium containing 20% FBS, streptomycin (100μg mL^{-1}), and penicillin (100 units mL^{-1}). The cell culture condition at 37°C under 5% CO_2.

PC3 cells (10^6 cells per well) were seeded in a 20 mm glass-bottom Petri dish overnight. Then fresh medium containing DOX or DOX-loaded BP NSs at the concentration of 5 μg mL^{-1} DOX were added and incubated for 2 h. After that, cells were washed with PBS for three times, fixed with 4% (w/v) formaldehyde solution for 20 min, and stained with DAPI for 10 min, successively. Finally, the cells were observed on a confocal laser scanning microscope (CLSM, Olympus Fluoview FV-1000, Tokyo, Japan).

In vitro Cytotoxicity Assay

To evaluate the cytotoxicity of zinc ion, PC3 cells (about 10^5 cells per well) were allowed to culture in 96-well plates overnight. Afterward, the old DMEM was replaced by fresh culture medium containing different concentrations of zinc ion (1, 2.5, 5, 7.5, 10, 20, and 30 μg mL^{-1}) and incubated for another 24, 48, and 72 h, respectively. The cell viability was determined by MTT assay. The percentage of cell viability was measured by comparison with the media alone group (negative control).

The evaluation of cytotoxicity of DOX on PC3 cells was performed using a similar procedure as described above except that the DOX concentration was 0.05, 0.1, 0.5, 1, 2.5, 5, and 10 μg mL^{-1}.

The enhancement of zinc ion on chemotherapy of DOX was assessed using MTT assay. The concentration of zinc ion was 1 μg mL^{-1} and DOX concentration was from 0.05 to 10 μg mL^{-1}. The culture time was 48 h.

To evaluate the combinational photothermal chemotherapy enhanced by zinc ion, PC3 cells at a density of 10^5 cells per well were cultured in 96-well plates. After incubation overnight, fresh culture medium containing various samples with different concentrations (0.1, 0.5, 1, 2.5, and 5 μg DOX mL^{-1}) were added to each well. For the NIR irradiation groups, cells were exposed to NIR laser at 1 W cm^{-2} for 10 min after addition of NPs for 4 h. Then the cells were incubated for another 48 h and the cell viabilities were calculated by MTT assay.

In vitro Photothermal Therapy Study

PC3 cells were first seeded in a 96-well plate for 24 h. After that, the culture medium of each well was refreshed, and cells were incubated with BP, BP-P, and BP-P-Apt at different concentrations for 4 h at 37°C. The cells were subsequently subjected to 808 nm laser irradiation (1 W cm^{-2}) for 10 min. The treated cells were incubated again for an additional 12 h. Finally, the cell viabilities were evaluated by MTT assay.

Tumor Model Establishment

Female sever combined immunodeficient (SCID) mice were purchased from the Sun Yat-sen University Laboratory Animal Center. Animal experiments were performed following protocols approved by the Administrative Committee on Animal Research in Sun Yat-sen University. To develop the tumor model, PC3 cells (1×10^6) in 100 μL PBS were subcutaneously injected into the right flank area of each mouse. Tumor sizes were measured with a digital vernier caliper every the other day. The tumor volume (V) was calculated by the equation: $V = 0.5 \times a \times b^2$, where a and b represented length and width of the tumor, respectively.

In vivo Infrared Thermal Imaging

When the volumes of the PC3 tumors reached about 500 mm^3, the mice were injected with PBS, Zn-BP-P/D, and Zn-BP-P-Apt/D via the tail vein. After 24 h, the mice were anesthetized and the tumor sites were irradiated with a 808 nm NIR laser (1.5 W cm^{-2}, 5 min). During the irradiation, an infrared thermal image camera was used to monitor the temperature changes and infrared thermographic maps.

In vivo Biodistribution

Tumor bearing mice were administered intravenously with 100 μL DOX, Zn-BP-P/D, and Zn-BP-P-Apt/D (100 μL, 5 mg DOX mL^{-1}), respectively. 3 or 24 h later, the mice were sacrificed, and the heart, liver, spleen, lung, kidney and tumor were collected. Subsequently, the distributions of DOX in these tissues were measured using the Maestro^{TM} Automated *In-Vivo* Imaging system (CRi Maestro^{TM}, United States).

In vivo Antitumor Therapy and Histochemistry Analysis

When the tumor volume reached 80mm^3, PC3 tumor-bearing mice were randomly divided into 6 groups ($n \geq 5$) and treated with (1) PBS, (2) DOX, (3) BP-P/D, (4) BP-P-Apt/D, (5) BP-P-Apt/D + NIR, and (6) Zn-BP-P-Apt/D + NIR (fixed DOX concentration at 5 mg kg^{-1}, 100 μL). The injection was conducted every 4 days. The NIR groups were irradiated by 808 nm laser at power density of 1.0 W cm^{-2} for 5min after intravenous injection for 24h. Tumor volumes and body weights of the mice were monitored every 2 days. After 16 days of treatment, All the mice were euthanized. Tumors and main organs including heart, liver, spleen, lung and kidney were dissected, washed and used for histology analysis and TUNEL immunofluorescence staining.

RESULTS AND DISCUSSION

Preparation of Zn-BP-P-Apt/D

The synthetic process of Zn-BP-P-Apt/D nanoplatform was displayed in **Scheme 1**. The BP NSs used in this work were successfully prepared according to a modified liquid exfoliation technique from bulk BP. NH_2-PEG-Apt was firstly modified on the surface of BP NSs via electrostatic adsorption to elevate targeting ability as well as the biocompatibility. Then, zinc ion was conjugated to BP NSs surface and the loading content of Zn^{2+} was about 12.8% (see **Supplementary Figure S1**). The conjugation of Zn^{2+} was expected to enhance the therapeutic effect of the combinational photothermal/chemotherapy. Meanwhile, the introduction of Zn^{2+} also contributed to improve the stability of BP NSs. After that, anticancer drug DOX was loaded for chemotherapy with loading content (LC) of 15.2% (**Supplementary Figure S2**).

Characteristics of BP Based NSs

TEM was utilized to characterize the morphology of BP and BP based nanosheets. As shown in **Figures 1C–F**, the size of bare BP and modified BP NSs were about 200–300nm, which was consisted with that from dynamic light scattering analysis (**Figures 1A,B** and **Supplementary Figure S3**). After introduction of Apt and Zn^{2+}, the morphology of BP did not show any obvious difference (**Figures 1D,E**). In **Figure 1F**, as the drugs loaded on the BP NSs, a rougher surface could be obviously observed in TEM picture, indicating the successful loading of drugs. AFM image (**Supplementary Figure S5**) showed that the height of Zn-BP-P-Apt/D was about 5.1 nm.

As shown in **Figure 2C**, the original zeta potential of bare BP was around −28.3mV, and zeta potential subsequently increased to −24.1mV after introdution of NH_2-PEG-Apt on the surface of BP. With the conjugation of Zn^{2+}, zeta potential of PB-P-Apt-Zn changed to −5.3 mV. Lastly, it increased to 12.7mV after loading DOX.

The chemical composition of various NSs was examined by XPS (**Figures 2A,B** and **Supplementary Figure S4**). **Figure 2A** displays the Zn2p spectra of the four samples. The Zn2p peaks at 1045.3 and 1022.2 eV were observed from Zn-BP-P-Apt and Zn-BP-P-Apt/D, but no Zn2p peaks were detected from the bare BP and BP-P-Apt, proving the successful conjugation of zinc ion. Compared with BP-P-Apt-Zn, the Zn2p peak intensity of Zn-BP-P-Apt/D was weaker, which was due to the loading

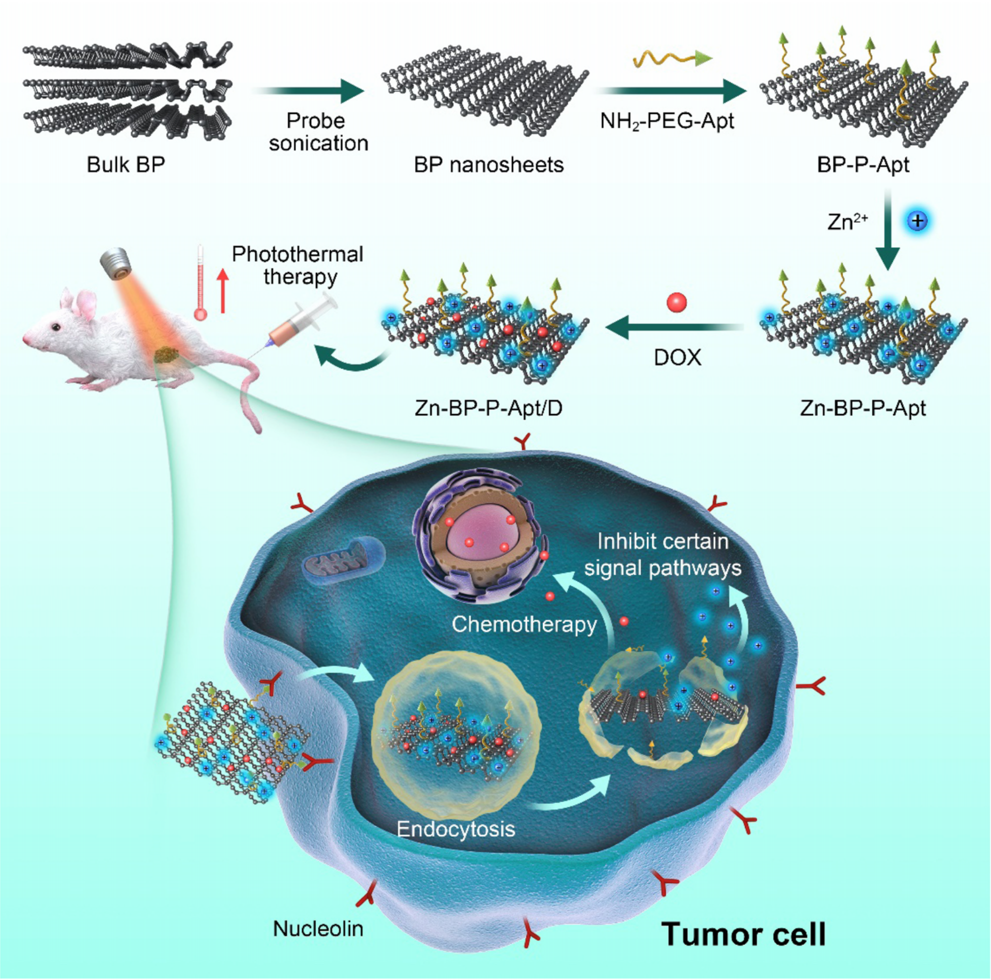

SCHEME 1 | Schematic illustration for the fabrication process, and combined anticancer therapy of Zn-BP-P-Apt/D.

of DOX. Moreover, The P2p peak intensity of bare BP, BP-P-Apt, Zn-BP-P-Apt, and Zn-BP-P-Apt/D gradually decreased (**Supplementary Figure S4A**). This trend was because that there is no P element in PEG, Apt, Zn^{2+} and DOX. Therefore, this result suggested again the successful modification of the corresponding compounds.

pH- and Temperature-Dependent Drug Release

As can be seen from **Figure 2D**, the cumulative amount of DOX released from Zn-BP-P-Apt/D within 24 h was about 43.1%. As a contrast, only 22.4% of DOX was released during the same period at pH 7.4. This exhibited that the acidic environment would accelerate the release of loaded DOX. It might be owing to the fact that acidic environment could increase the water solubility of DOX, thus leading to a faster release of drug. This release behavior was very meaningful. DOX would not be released from Zn-BP-P-Apt/D when the NSs were circulated in the neutral environment of blood (pH = 7.4). Once these NSs entered tumor region, the acidic environment of tumor would accelerate the release of anticancer drugs. Stimulated by 3 cycles of 808nm laser on/off treatment, DOX cumulative rate at pH 5.0 increased to 56.8% after 24 h, proving the photothermal-induced drug release behavior. These results suggested pH- and temperature-responsive drug release of Zn-BP-P-Apt/D, which could not only reduce the side effects of drugs but also improve its utilization rate. Besides, the drug release profiles of Zn-BP-P-Apt/D at pH6.5 and 6.0 were also tested (**Supplementary Figure S6**).

Photothermal Properties of Different NSs

To examine the photothermal properties of different NSs, water, aqueous solutions of BP and Zn-BP-P-Apt/D were exposed to laser irradiation of 808nm. The temperature changes were monitored and quantified by an infrared thermal imaging camera (**Figure 3**). According to the equations in supporting information, the photothermal conversion efficiency of BP NSs, Zn-BP-P-Apt, and Zn-BP-P-Apt/D was calculated to be 29.6, 27.1, and 24.3% separately. As shown in **Figure 3A**, the temperature of BP solution (100μg mL^{-1})

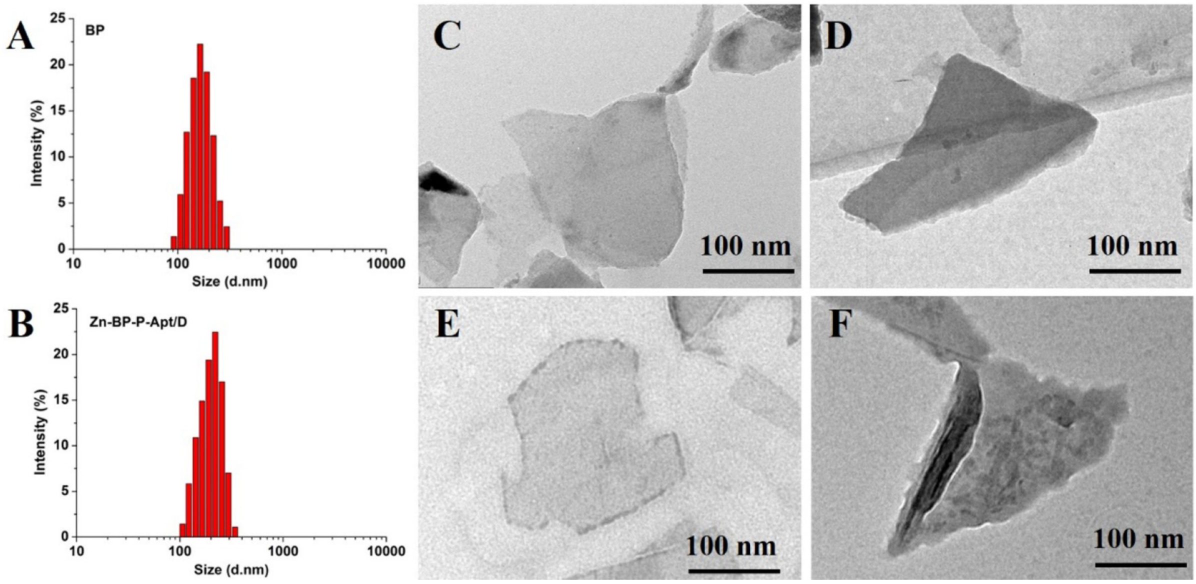

FIGURE 1 | DLS size distribution of **(A)** BP NSs and **(B)** Zn-BP-P-Apt/D. TEM images of **(C)** BP sheets, **(D)** BP-P-Apt, **(E)** Zn-BP-P-Apt, and **(F)** Zn-BP-P-Apt/D.

increased by ~29.6°C after irradiation (1 W cm^{-2}) for 10min, while the pure water was hardly heated by the irradiation, indicating that BP could effectively convert NIR light into thermal energy. The temperature rise of Zn-BP-P-Apt/D was about 3°C lower than BP (ΔT = 26.6°C). However, this temperature change was higher enough to induce irreversible cell apoptosis owing to hyperthermia (Wust et al., 2002). We next investigated the impact of power density of NIR laser on the Zn-BP-P-Apt/D-induced hyperthermia (**Figure 3C**). A dispersion of Zn-BP-P-Apt/D at 100µg BP mL^{-1} was irradiated with 808 nm laser with different laser power density, implying that the temperature change of the dispersion could still reach about 16.1°C even the power density was as low as 0.5 W cm^{-2}. Moreover, Zn-BP-P-Apt/D exhibited a concentration-dependent photothermal property (**Figure 3B**). As presented in **Figure 3D**, after irradiation with NIR laser light for 4 cycles, the process of temperature changes did not show any significant change, suggesting satisfactory photostability of Zn-BP-P-Apt/D.

Stability Evaluation

To study whether coordination with Zn^{2+} could improve the stability of BP, the photothermal performance of bare BP and Zn-BP-P-Apt/D (100µg BP mL^{-1}) in air-exposed water was tested (**Figures 4A,B**). The temperature of bare BP rose by about 29.8°C within 10min, but irradiation elevated the temperature by only 20°C after 6 days, so the photothermal performance of BP was quickly attenuated due to its degradation. By contrast, Zn-BP-P-Apt/D was obviously more photothermally stable. The temperature rise only changed about 3.3°C (from 26.4to 23.1°C) after 6 days. Therefore, coordination with Zn^{2+} could considerably stabilize BP.

Next, we visually observed the stability of BP and Zn-BP-P-Apt/D by using ultra-depth three-dimensional microscope (**Figures 4C–F**). Being kept in air at room temperature with 95% humidity for 48h, the degradation of bare BP could be evidently noted, especially at the edges. On the contrary, the surface of Zn-BP-P-Apt/D NSs hardly changed, proving the robust stability of Zn-BP-P-Apt/D. These results altogether directly demonstrated that the coordination between zinc ion and BP NSs could effectively prohibit the BP oxidation in humid air, thus improving its stability.

Cellular Uptake

It was reported that AS1411 aptamers could bind to a variety of tumor cells (Tao et al., 2016). To confirm this, the cellular uptake of DOX or DOX loaded NSs against PC3 cells was evaluated by CLSM. As shown in **Figure 5A**, compared with Zn-BP-P/D group, Zn-BP-P-Apt/D group exhibited a stronger fluorescent signal, implying that aptamer modified NPs were able to bind to PC3 cells efficiently. To further verify the tumor targeting ability of aptamers, an excessive amount of free AS1411 aptamers was added in Zn-BP-P-Apt/D group. After incubation together for 2 h, the red fluorescence intensity dramatically decreased. The reason for this might be that a large amount of free AS1411 aptamers bound to nucleolin (Apt receptors) on the plasma membrane, thus inhibiting the binding between Zn-BP-P-Apt/D and nucleolin to a large extent.

Interestingly, we found than free DOX group showed the strongest red fluorescent intensity, even better than Zn-BP-P-Apt/D. This might be ascribed to the fact that DOX could penetrate through the plasma membrane and nuclear membrane freely and quickly via passive diffusion effect due to its small molecule size (Cheng et al., 2017b). However, the *in vivo* microenvironment is way more complicated, owing

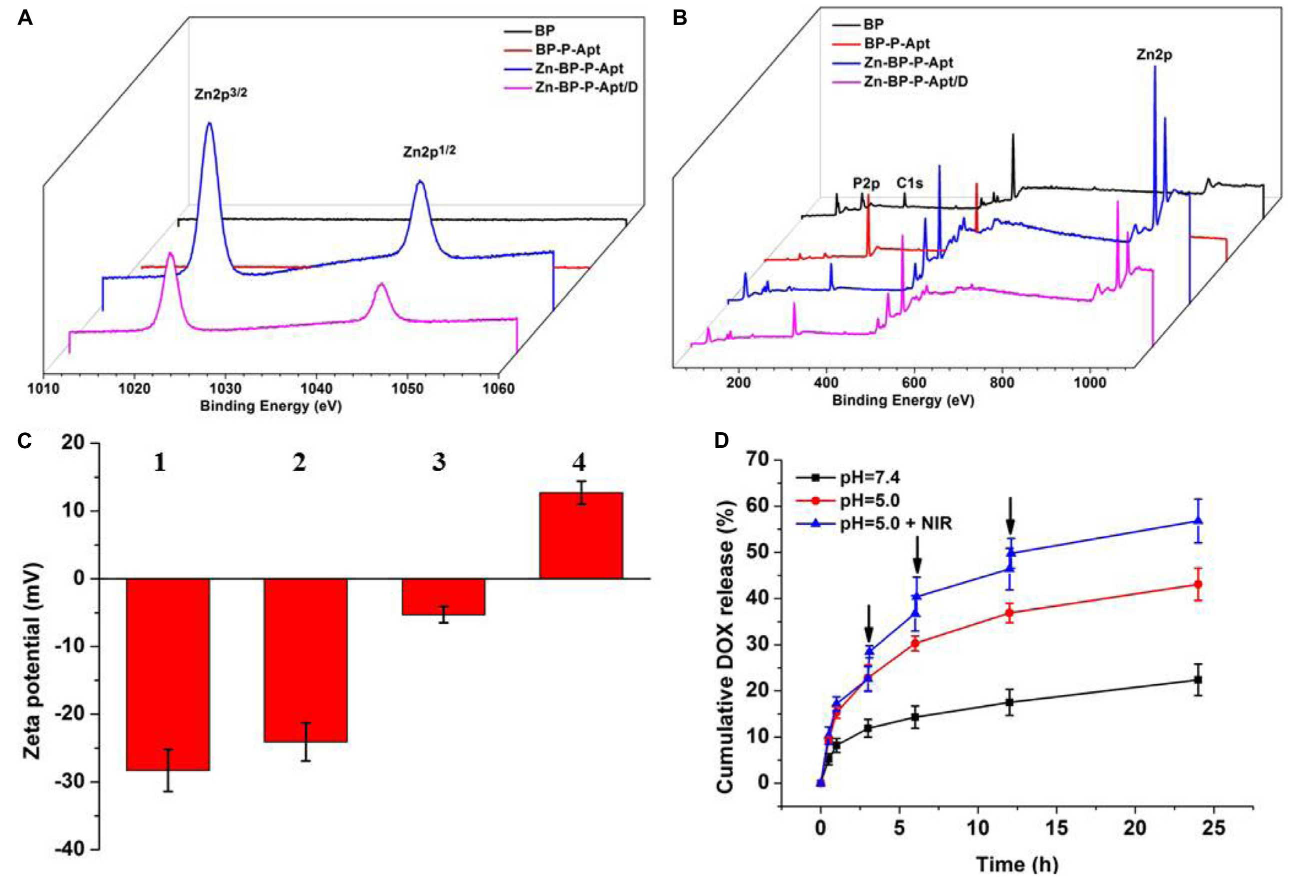

FIGURE 2 | XPS spectra of BP, BP-P-Apt, Zn-BP-P-Apt and Zn-BP-P-Apt/D. **(A)** Narrow scan for Zn2p peaks **(B)** Survey of all tested peaks. Zeta potentials of BP-based NPs. **(C)** Zeta potentials of BP-based NPs. 1, 2, 3, and 4 represent BP, BP-P-Apt, Zn-BP-P-Apt, and Zn-BP-P-Apt/D, respectively. **(D)** Drug release profiles of Zn-BP-P-Apt/D at pH 7.4 and pH 5.0 with or without NIR irradiation, ↓: NIR irradiation for 10min.

to the sustained release and active tumor targeting effect, DOX-loaded NSs can improve the *in vivo* biocompatibility and biodistribution of anticancer drug, thus enhancing its therapeutic effect.

In vitro Photothermal Therapy

To test the photothermal cytotoxicity of different BP NSs based nanomaterials *in vitro*, MTT assay was performed on PC3 cells. As shown in **Figure 5B**, BP, BP-P and BP-P-Apt displayed a concentration-dependent photothermal effect. As expected, due to active tumor targeting ability, Apt modified BP NSs (BP-P-Apt) showed the highest photothermal cytotoxicity and about 87.8% of PC3 cells were killed at the BP-P-Apt concentration of 50 μg mL^{-1}, which was much higher than that of BP (70.8%) and BP-P (72.7%) groups at the same concentration. In contrast, NIR irradiation alone showed negligible cytotoxicity to PC3 cells.

In vitro Cytotoxicity

To access the cytotoxicity of BP based NSs to PC3 cells, MTT assay was employed. As displayed in **Figure 5C**, BP, BP-P and BP-P-Apt NSs exerted negligible cytotoxicity. For example, PC3 cells treated with BP-P-Apt still had about 91.8% cell viability even at a concentration of 100μg mL^{-1} after 48 h, confirming the excellent biocompatibility of the bare NSs. And the toxicity of Zn^{2+} to PC3 cells showed a time and dosage dependent manner. Zn^{2+} began to exhibit obvious cytotoxicity to PC3 cells after 48 or 72 h treatment when its concentration is more than 5 μg mL^{-1} (**Figure 6A**). The cytotoxicity of DOX to PC3 cells was also studied (**Figure 6B**). **Figure 6C** shows the combined cytotoxicity of Zn^{2+} and DOX to PC3 cells (at a fixed Zn^{2+} concentration of 1μg mL^{-1}). It could be observed that zinc ion could enhance the *in vitro* theraputic efficacy of DOX to PC3 cells to a certain extent for all tested DOX concentrations.

Next, we investigated the combined cytotoxicity of zinc ion, DOX and photothermal therapy (**Figure 6D**). BP NSs loaded with DOX but without Apt and Zn^{2+} (denoted as BP-P/D) showed a moderate cytotoxicity, with about 57.1% cell viability at 5μg DOX mL^{-1} after 48 h. In contrast, after introduction of Apt, BP-P-Apt/D exhibited a stronger toxicity to PC3 cells due to active tumor targeting ability of Apt. After irradiation by NIR, BP-P-Apt/D showed a better toxicity for tumor cells killing in comparison with other formulas without NIR irradiation,

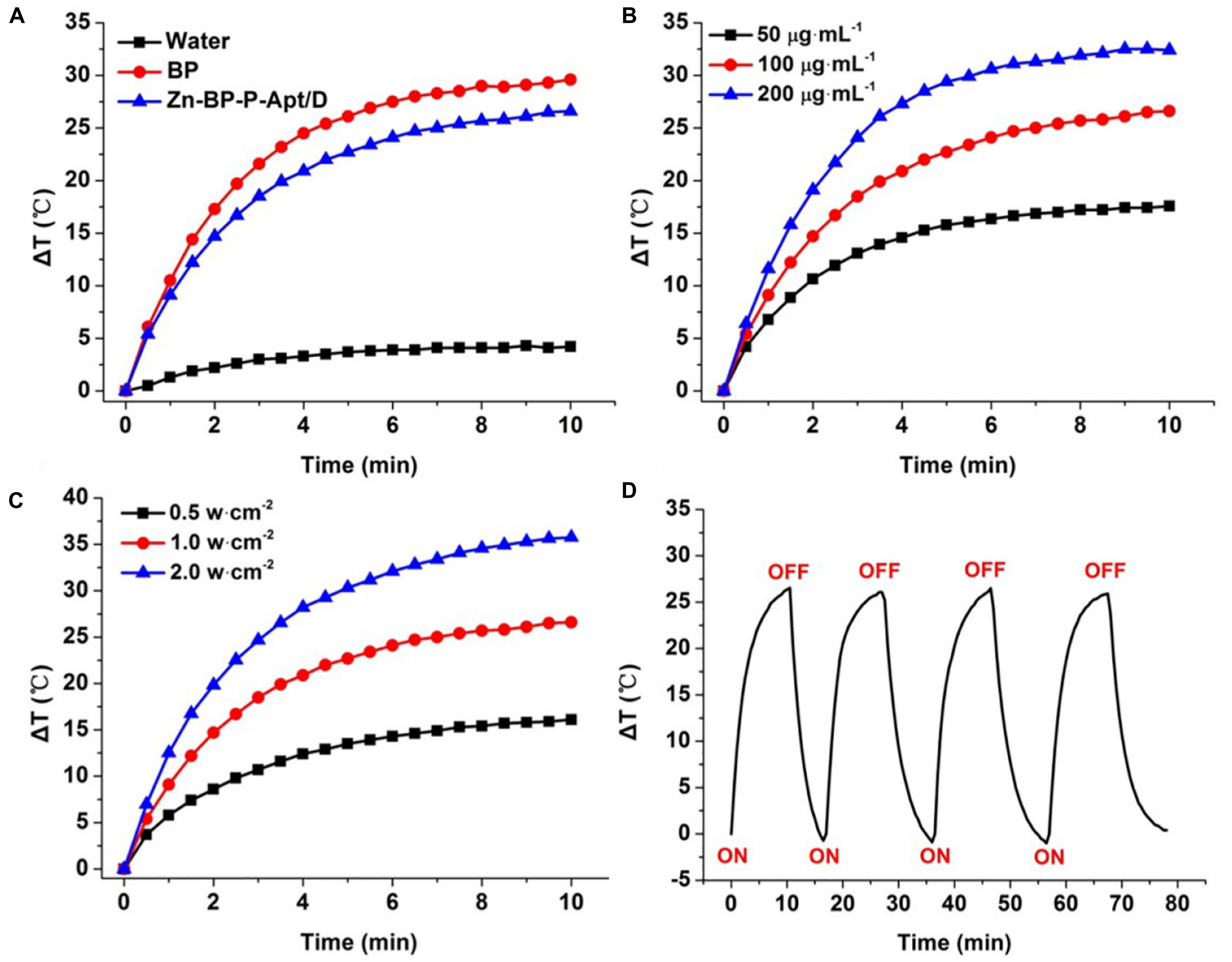

FIGURE 3 | (A) Changes in temperature of pure water, BP NSs and Zn-BP-P-Apt/D. **(B)** Temperature elevation curves of Zn-BP-P-Apt/D suspension with different concentrations at a power density of 1.0 W cm^{-2}. **(C)** Temperature change curves of Zn-BP-P-Apt/D suspension with the concentration of 100μg mL^{-1} at different laser powers. **(D)** Heating of a suspension of the Zn-BP-P-Apt/D in water for four laser on/off cycles with an 808 nm NIR laser at power density of 1.0 W cm^{-2}.

denoting that the combined chemo/photothermal therapy could exert a better therapeutic effect than chemotherapy alone. What's more, after Zn^{2+} conjugation, Zn-BP-P-Apt/D + NIR group showed the best tumor cells killing effect, implying the importance of synergistic actions of zinc ion enhanced combinational chemo/photothermal therapy for prostate cancer.

In vivo Photothermal Imaging

IR thermal imaging of PBS and BP based NSs *in vivo* was investigated under irradiation with 808 nm laser (1.5 W cm^{-2}) for 5 min after 24 h post injection. As presented in **Figure 7A** and **Supplementary Figure S7**, the tumoral temperature of PBS treated group rose slightly after 5 min laser irradiation. Differently, in the group treated with Zn-BP-P/D, hyperthermia was quickly generated in tumor region and reached up to around 47.3°C. Zn-BP-P-Apt/D showed a better performance than Zn-BP-P/D and the temperature rose to about 51.2°C within 5 min, which was high enough to kill tumor cells. These results demonstrated that Zn-BP-P-Apt/D could efficiently accumulate in tumor sites and act as superb photothermal agents to produce hyperthermia *in vivo* to effectively kill tumor cells.

In vivo Biodistribution

The *in vivo* biodistribution of DOX and DOX loaded NSs were investigated in nude mice bearing PC3 tumors after tail vail injection. The fluorescence intensity of DOX was captured at 3 or 24h post injection (**Figure 7B**). After 3 h, DOX in Zn-BP-P/D and Zn-BP-P-Apt/D NSs was mainly distributed to tumor, while a relatively strong fluorescence intensity of DOX could be detected not only in tumor but also in liver for free DOX group. At 24h post injection. DOX intensity became weaker in tumor sites for free DOX group, implying its short retention time in blood and tissues. In contrast, a much stronger fluorescence signals of DOX in tumor were observed in both DOX loaded BP groups after 24 h. As expected, Zn-BP-P-Apt/D exhibited the strongest DOX signal in tumor, indicating an excellent tumor targeting ability. Overall, the DOX signal distribution

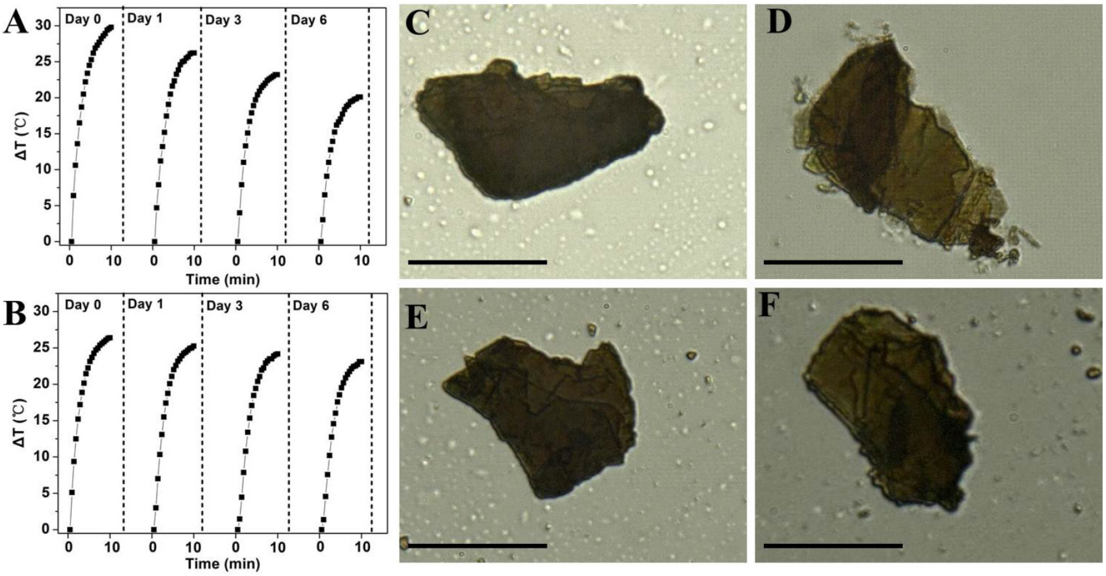

FIGURE 4 | Photothermal heating curves of **(A)** bare BP and **(B)** Zn-BP-P-Apt/D dispersed in air-exposed water for 0, 1, 3, and 6 days. The 808nm laser was used as the irradiation source at the power density of 1 W cm^{-2}. Optical images of bare BP on Si/SiO$_2$ after exposure to the humid air at room temperature for **(C)** 0 and **(D)** 48 h, images of bare Zn-BP after **(E)** 0 and **(F)** 48 h (Scale bar = 10 μm).

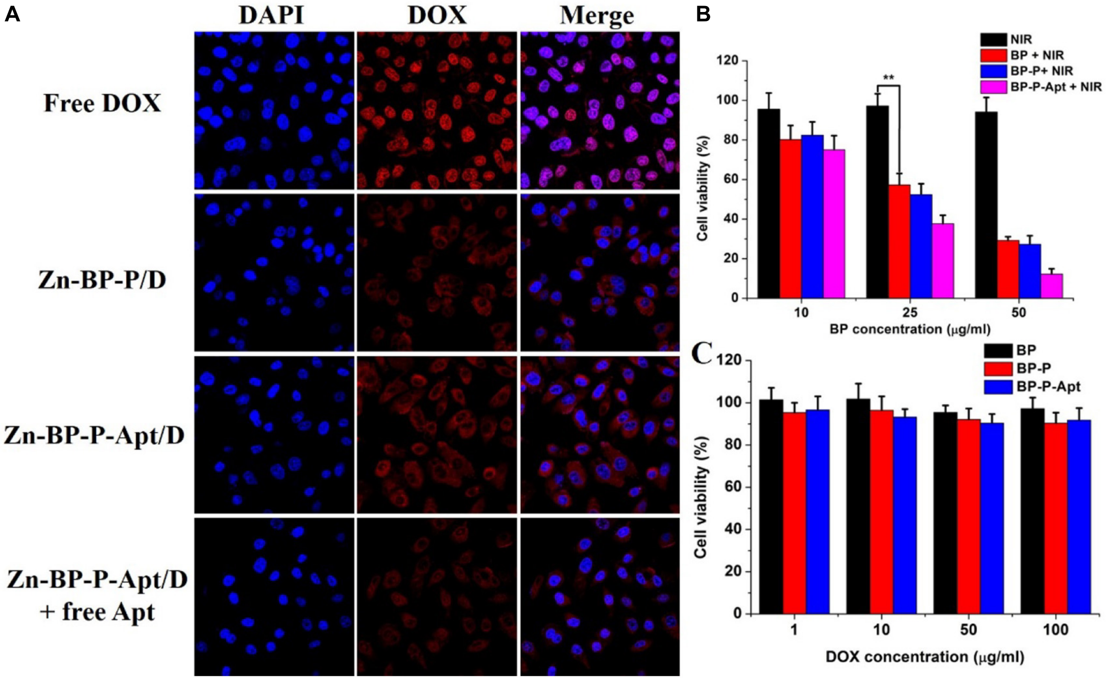

FIGURE 5 | (A) Laser scanning confocal microscopy images of PC3cells treated with DOX, Zn-BP-PEG/D, Zn-BP-P-Apt/D, Zn-BP-P-Apt/D with free Apt added, and the incubation time was 2 h. **(B)** The cell viabilities of PC3 cells incubated with various concentrations of BP, BP-PEG, and BP-P-Apt with NIR laser irradiation. **(C)** *In vitro* cytotoxicity of BP, BP-P, and BP-P-Apt tested by MTT assay (808 nm, 1 W cm^{-2}, 10 min, $^{**}P < 0.01$).

for BP based NSs, especially for Zn-BP-P-Apt/D, revealed a predominant accumulation in tumor, a pattern expected for nanoparticle biodistribution.

In vivo Therapeutic Effect

Motivated by the *in vitro* inspiring results, *in vivo* Zn^{2+} enhanced chemo/photothermal therapy was investigated. As shown in

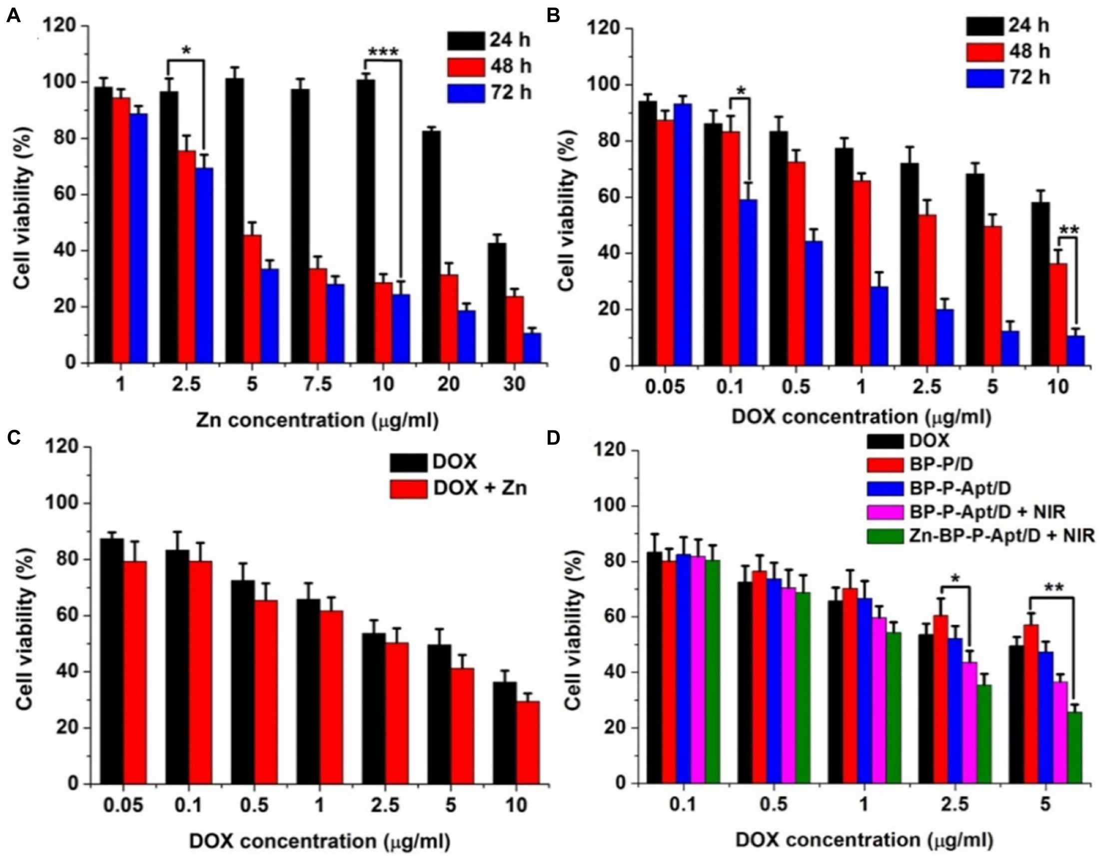

FIGURE 6 | (A) Relative cell viability of PC3 cells after incubation with different concentrations of Zn^{2+} for 24, 48, and 72 h. **(B)** Cell viability of PC3 cells after incubation with DOX at different concentrations for 24, 48, and 72 h. **(C)** Cell viability of PC3 cells treated with DOX or DOX + Zn^{2+} (Zn^{2+} concentration was 1 μg mL^{-1}) at various concentrations of DOX for 48 h. **(D)** Cell viability of PC3 cells treated with different samples with or without NIR laser irradiation at various concentrations of DOX for 48 h. (*p < 0.05, **p < 0.01, ***p < 0.001).

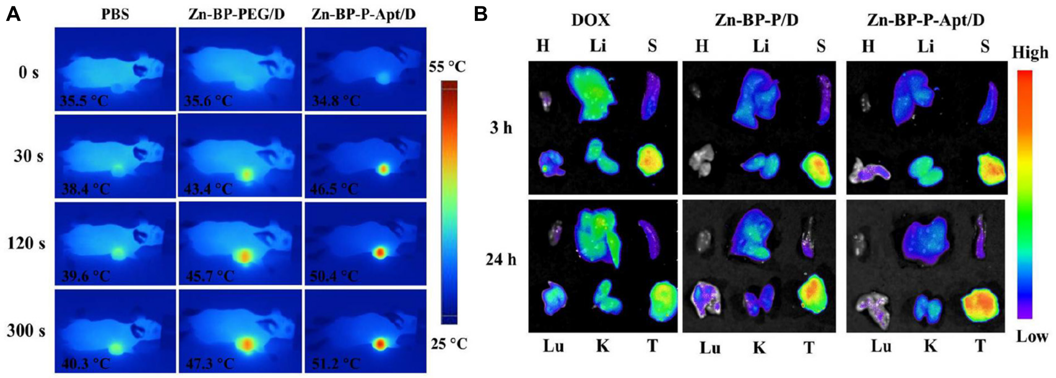

FIGURE 7 | (A) *In vivo* IR thermal images of PC3 tumor-bearing mice treated with 808nm laser for 300 s. **(B)** *Ex vivo* fluorescent images of major organs and tumors after mice were injected with free DOX, Zn-BP-P/D, and Zn-BP-P-Apt/D at 3 and 24 h. H, Li, S, Lu, K, and T represent heart, liver, spleen, lung, kidney, and tumor, respectively.

Figures 8A,B, a rapid growth of tumors was observed in PBS treated group during the 16-day treatment period. The tumor volume of the mice injected with free DOX could be partly but not significantly reduced in comparison with that of the control group, revealing that this dosage of administered DOX was not adequate to effectively kill tumor cells. By contrast, efficient anti-tumor effects were noticed in BP-P/D and BP-P-Apt/D groups compared with free DOX. This is attributed to more

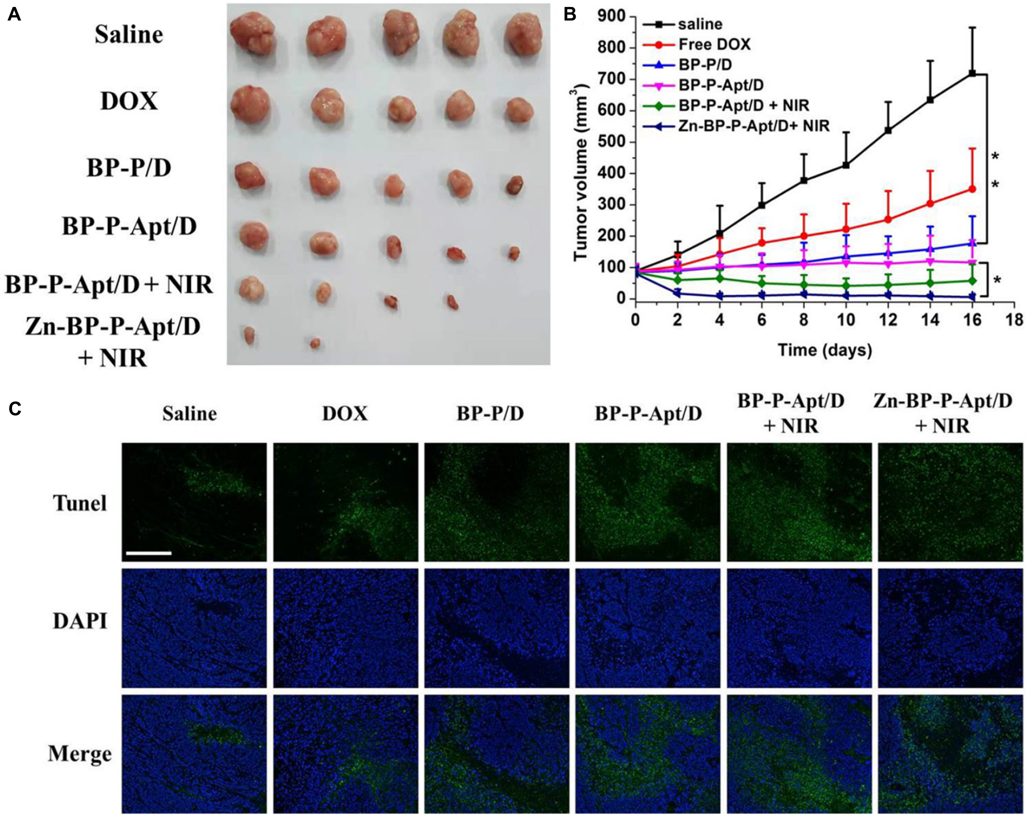

FIGURE 8 | (A) Pictures of the tumors extracted from mice at day 16. **(B)** Curves of tumor growth after different treatments. **(C)** TUNEL fluorescence staining of tumor sections at the end of the *in vivo* antitumor experiment $^*p < 0.05$, $^{**}P < 0.01$). (Scale bar = 200 μm).

accumulation of DOX in tumor sites due to EPR effects (Cheng et al., 2017d; Wang et al., 2019b). Besides, BP-P-Apt/D showed a more effective tumor ablation effect than BP-P/D, implying a good tumor targeting ability of Apt. PC3 tumors were further inhibited in BP-P-Apt/D group after photothermal treatment. Inspiringly, the tumor growth curve in Zn-BP-P-Apt/D + NIR group revealed the lowest growth rate, and three mice in this group were completely cured after 16 days. This result proved the most excellent tumor inhibition effect of Zn-BP-P-Apt/D + NIR, which was ascribed to the Zn^{2+} enhanced combinational chemo/photothermal therapy.

The anticancer efficiency of Zn-BP-P-Apt/D is further analyzed by a terminal deoxynucleotidyl transferase-mediated deoxyuridine triphosphate nick end-labeling (TUNEL) assay, which is generally employed to examine the intratumoral levels of apoptosis. As displayed in **Figure 8C**, few TUNEL-positive cells (green color) were observed from the PBS, and pure DOX groups, while significant TUNEL-positive apoptotic cells could be observed from the Zn-BP-P-Apt/D NSs group.

The potential toxicity of different BP based NSs was studied. During the treatment time, there was no significant decrease in body weight of mice (**Supplementary Figure S8**), suggesting little side effects of the NSs. Moreover, as shown in **Supplementary Figure S10**, histological evaluation of major organs stained with hematoxylin and eosin (H&E) displayed no obvious inflammatory lesion or organ damage in all major organs after the treatment. This again demonstrated the good biocompatibility of NSs. Therefore, the as-prepared Zn-BP-P-Apt/D NSs showed a great potential for Zn^{2+} enhanced dual-modal cancer therapy.

CONCLUSION

In summary, a tumor-targeting nano-drug system (Zn-BP-P-Apt/D NSs) was successfully developed for combined chemo-photothermal therapy against prostate cancer. The drug release experiment showed a pH- and NIR irradiation-responsive drug release behavior. Cytotoxicity assay indicated that Zn^{2+} itself could inhibit the proliferation of prostate cancer cells to some extent. Meanwhile, the photothermal/chemotherapy efficiency was further enhanced through introduction of Zn^{2+} into this multifunctional nanoplatform. Besides, Zn^{2+} coordination improved the stability of BP NSs, which is of great significance to slow down the degradation of its photothermal performance. Moreover, modification of PEG-Apt enabled extended blood circulation time and targeted accumulation at tumor sites. Both *in vitro* and *in vivo* anti-tumor assays demonstrated the excellent therapeutic efficacy of this nanodrug system for prostate cancer therapy.

DATA AVAILABILITY STATEMENT

All datasets generated for this study are included in the article/**Supplementary Material**, further inquiries can be directed to the corresponding authors.

ETHICS STATEMENT

The animal study was reviewed and approved by the Administrative Committee on Animal Research in Sun Yat-sen University.

AUTHOR CONTRIBUTIONS

All authors listed have made a substantial, direct and intellectual contribution to the work, and approved it for publication.

FUNDING

This work was financially supported by the National Natural Science Foundation of China (81660425), Scientific Research and Technology Development of Guilin City (20170226), Guangxi Natural Science Fund (2018GXNSFAA281270, 2019GXNSFAA 185034), and Science, Technology & Innovation Commission of Shenzhen Municipality (JCYJ20180307153300735, JCYJ2018 0507181654186, JCYJ20170818162637217, and JCYJ20160531 195129079).

SUPPLEMENTARY MATERIAL

The Supplementary Material for this article can be found online at: https://www.frontiersin.org/articles/10.3389/fbioe.2020.00769/full#supplementary-material

REFERENCES

Chen, W., Yang, W., Chen, P. Y., Huang, Y. Z., and Li, F. (2018). Disulfiram copper nanoparticles prepared with a stabilized metal ion ligand complex method for treating drug-resistant prostate cancers. *ACS Appl. Mater. Inter.* 10, 41118–41128. doi: 10.1021/acsami.8b14940

Chen, X. C., Che, X. Y., Wang, J. B., Chen, F., Wang, X. J., Zhang, Z. W., et al. (2013). Zinc sensitizes prostate cancer cells to sorafenib and regulates the expression of livin. *Acta Biochimica Et Biophysica Sinica* 45, 353–358. doi: 10.1093/abbs/gmt017

Cheng, W., Liang, C. Y., Wang, X. S., Tsai, H. I., Liu, G., Peng, Y. M., et al. (2017a). A drug-self-gated and tumor microenvironment-responsive mesoporous silica vehicle: "four-in-one" versatile nanomedicine for targeted multidrug-resistant cancer therapy. *Nanoscale* 9, 17063–17073. doi: 10.1039/c7nr05450e

Cheng, W., Liang, C. Y., Xu, L., Liu, G., Gao, N. S., Tao, W., et al. (2017b). TPGS-functionalized polydopamine-modified mesoporous silica as drug nanocarriers for enhanced lung cancer chemotherapy against multidrug resistance. *Small* 13:1700623. doi: 10.1002/smll.201700623

Cheng, W., Nie, J. P., Gao, N. S., Liu, G., Tao, W., Xiao, X. J., et al. (2017c). A multifunctional nanoplatform against multidrug resistant cancer: merging the best of targeted chemo/gene/photothermal therapy. *Adv. Funct. Mater.* 27:1704135

Cheng, W., Nie, J. P., Xu, L., Liang, C. Y., Peng, Y., Liu, G., et al. (2017d). pH-Sensitive delivery vehicle based on folic acid-conjugated polydopamine-modified mesoporous silica nanoparticles for targeted cancer therapy. *ACS Appl. Mater. Inter.* 9, 18462–18473. doi: 10.1021/acsami.7b02457

Cheng, W., Zeng, X. W., Chen, H. Z., Li, Z. M., Zeng, W. F., Mei, L., et al. (2019). Versatile polydopamine platforms: synthesis and promising applications for surface modification and advanced nanomedicine. *Acs Nano* 13, 8537–8565. doi: 10.1021/acsnano.9b04436

Favron, A., Gaufres, E., Fossard, F., Phaneuf-L'Heureux, A. L., Tang, N. Y. W., Levesque, P. L., et al. (2015). Photooxidation and quantum confinement effects in exfoliated black phosphorus. *Nat. Mater.* 14, 826–832. doi: 10.1038/nmat4299

Guo, D. X., Yang, H. L., Zhang, Y., and Chen, L. (2019). Constructing mesoporous silica-grown reduced graphene oxide nanoparticles for photothermal-chemotherapy. *Micropor. Mesopor. Mat.* 288, 109608. doi: 10.1016/j.micromeso.2019.109608

Guo, Z. N., Chen, S., Wang, Z. Z., Yang, Z. Y., Liu, F., Xu, Y. H., et al. (2017). Metal-Ion-modified black phosphorus with enhanced stability and transistor performance. *Adv. Mater.* 29, 1703811. doi: 10.1002/adma.201703811

Heidenreich, A., Bastian, P. J., Bellmunt, J., Bolla, M., Joniau, S., van der Kwast, T., et al. (2014). EAU guidelines on prostate Cancer. Part II: treatment of advanced, relapsing, and castration-resistant prostate Cancer. *Eur. Urol.* 65, 467–479. doi: 10.1016/j.eururo.2013.11.002

Kelleher, S. L., McCormick, N. H., Velasquez, V., and Lopez, V. (2011). Zinc in specialized secretory tissues: roles in the pancreas, prostate, and mammary gland. *Adv. Nutr.* 2, 101–111. doi: 10.3945/an.110.000232

Kim, J. K., Choi, K. J., Lee, M., Jo, M. H., and Kim, S. (2012). Molecular imaging of a cancer-targeting theragnostics probe using a nucleolin aptamer- and microRNA-221 molecular beacon-conjugated nanoparticle. *Biomaterials* 33, 207–217. doi: 10.1016/j.biomaterials.2011.09.023

Kolenko, V., Teper, E., Kutikov, A., and Uzzo, R. (2013). Zinc and zinc transporters in prostate carcinogenesis. *Nat. Rev. Urol.* 10, 219–226. doi: 10.1038/nrurol.2013.43

Li, B., Ye, K. C., Zhang, Y. X., Qin, J. B., Zou, R. J., Xu, K. B., et al. (2015). Photothermal theragnosis synergistic therapy based on bimetal sulphide nanocrystals rather than nanocomposites. *Adv. Mater.* 27, 1339–1345. doi: 10.1002/adma.201404257

Li, F., and Mahato, R. I. (2014). MicroRNAs and drug resistance in prostate cancers. *Mol. Pharmaceut.* 11, 2539–2552. doi: 10.1021/mp500099g

Li, F., and Mahato, R. I. (2015). miRNAs as targets for cancer treatment: therapeutics design and delivery. *Preface. Adv. Drug Deliver Rev.* 81, v–vi. doi: 10.1016/j.addr.2014.11.005

Li, F. Q., Mei, H., Gao, Y., Xie, X. D., Nie, H. F., Li, T., et al. (2017). Co-delivery of oxygen and erlotinib by aptamer-modified liposomal complexes to reverse hypoxia-induced drug resistance in lung cancer. *Biomaterials* 145, 56–71. doi: 10.1016/j.biomaterials.2017.08.030

Liang, X., Ye, X. Y., Wang, C., Xing, C. Y., Miao, Q. W., Xie, Z. J., et al. (2019). Photothermal cancer immunotherapy by erythrocyte membrane-coated black phosphorus formulation. *J. Control. Release* 296, 150–161. doi: 10.1016/j.jconrel.2019.01.027

Liu, G., Tsai, H. I., Zeng, X. W., Qi, J. Y., Luo, M. M., Wang, X. S., et al. (2019a).). Black phosphorus nanosheets-based stable drug delivery system via drug-self-stabilization for combined photothermal and chemo cancer therapy. *Chem. Eng. J.* 375:121917. doi: 10.1016/j.cej.2019.121917

Liu, X., Bai, Y. F., Xu, J., Xu, Q. C., Xiao, L. P., Sun, L. P., et al. (2019b). Robust amphiphobic few-layer black phosphorus nanosheet with improved stability. *Adv. Sci.* 6:1901991. doi: 10.1002/advs.201901991

Liu, G. Y., Zou, J. H., Tang, Q. Y., Yang, X. Y., Zhang, Y. W., Zhang, Q., et al. (2017). Surface modified Ti3C2 MXene nanosheets for tumor targeting photothermal/photodynamic/chemo synergistic therapy. *ACS Appl. Mater. Inter.* 9, 40077–40086. doi: 10.1021/acsami.7b13421

Liu, H. R., Mai, J. H., Shen, J. L., Wolfram, J., Li, Z. Q., Zhang, G. D., et al. (2018). A novel DNA aptamer for dual targeting of polymorphonuclear myeloid-derived suppressor cells and Tumor Cells. *Theranostics* 8, 31–44. doi: 10.7150/thno.21342

Luo, M. M., Cheng, W., Zeng, X. W., Mei, L., Liu, G., and Deng, W. B. (2019a). Folic acid-functionalized black phosphorus quantum dots for targeted chemo-photothermal combination Cancer therapy. *Pharmaceutics* 11:242. doi: 10.3390/pharmaceutics11050242

Luo, M. M., Fan, T. J., Zhou, Y., Zhang, H., and Mei, L. (2019b). 2D Black phosphorus-based biomedical applications. *Adv. Funct. Mater.* 29:1808306. doi: 10.1002/adfm.201808306

Mollica, V., Di Nunno, V., Cimadamore, A., Lopez-Beltran, A., Cheng, L., Santoni, M., et al. (2019). Molecular mechanisms related to hormone inhibition resistance in prostate Cancer. *Cells* 8:43. doi: 10.3390/cells8010043

Ryder, C. R., Wood, J. D., Wells, S. A., Yang, Y., Jariwala, D., Marks, T. J., et al. (2016). Covalent functionalization and passivation of exfoliated black phosphorus via aryl diazonium chemistry. *Nat. Chem.* 8, 597–602. doi: 10.1038/nchem.2505

Sun, Z. B., Xie, H. H., Tang, S. Y., Yu, X. F., Guo, Z. N., Shao, J. D., et al. (2015). Ultrasmall black phosphorus quantum dots: synthesis and use as photothermal agents. *Angewandte Chemie-Int. Ed.* 54, 11526–11530. doi: 10.1002/anie.201506154

Tang, Z. M., Kong, N., Ouyang, J., Feng, C., Kim, N. Y., Ji, X. Y., et al. (2020). Phosphorus science-oriented design and synthesis of multifunctional nanomaterials for biomedical applications. *Matter* 2, 297–322. doi: 10.1016/j.matt.2019.12.007

Tao, W., Kong, N., Ji, X. Y., Zhang, Y. P., Sharma, A., Ouyang, J., et al. (2019). Emerging two-dimensional monoelemental materials (Xenes) for biomedical applications. *Chem. Soc. Rev.* 48, 2891–2912. doi: 10.1039/c8cs00823j

Tao, W., Zeng, X. W., Wu, J., Zhu, X., Yu, X. H., Zhang, X. D., et al. (2016). Polydopamine-based surface modification of novel nanoparticle-aptamer bioconjugates for in vivo breast Cancer targeting and enhanced therapeutic effects. *Theranostics* 6, 470–484. doi: 10.7150/thno.14184

Teo, M. Y., Rathkopf, D. E., and Kantoff, P. (2019). Treatment of advanced prostate cancer. *Annu. Rev. Med.* 70, 479–499.

Uzzo, R. G., Crispen, P. L., Golovine, K., Makhov, P., Horwitz, E. M., and Kolenko, V. M. (2006). Diverse effects of zinc on NF-kappa B and AP-1 transcription factors: implications for prostate cancer progression. *Carcinogenesis* 27, 1980–1990. doi: 10.1093/carcin/bgl034

Wang, Q., Zhang, X. Y., Sun, Y., Wang, L. T., Ding, L., Zhu, W. H., et al. (2019a). Gold-caged copolymer nanoparticles as multimodal synergistic photodynamic/photothermal/chemotherapy platform against lethality androgen-resistant prostate cancer. *Biomaterials* 212, 73–86. doi: 10.1016/j.biomaterials.2019.05.009

Wang, M. Q., Liang, Y., Zhang, Z. C., Ren, G. H., Liu, Y. J., Wu, S. S., et al. (2019b). Ag@Fe3O4@C nanoparticles for multi-modal imaging-guided chemo-photothermal synergistic targeting for cancer therapy. *Anal. Chim. Acta* 1086, 122–132. doi: 10.1016/j.aca.2019.08.035

Wang, X. S., Chen, H. Y., Zeng, X. W., Guo, W. P., Jin, Y., Wang, S., et al. (2019c). Efficient lung cancer-targeted drug delivery via a nanoparticle/MSC system. *Acta Pharmaceutica Sinica B* 9, 167–176. doi: 10.1016/j.apsb.2018.08.006

Wust, P., Hildebrandt, B., Sreenivasa, G., Rau, B., Gellermann, J., Riess, H., et al. (2002). Hyperthermia in combined treatment of cancer. *Lancet Oncol.* 3, 487–497.

Xue, T. Y., Liang, W. Y., Li, Y. W., Sun, Y. H., Xiang, Y. J., Zhang, Y. P., et al. (2019a). Ultrasensitive detection of miRNA with an antimonene-based surface plasmon resonance sensor. *Nat. Commun.* 10:28.

Xue, Y. N., Yu, B. B., Liu, Y. N., Guo, R., Li, J. L., Zhang, L. C., et al. (2019b). Zinc promotes prostate cancer cell chemosensitivity to paclitaxel by inhibiting epithelial-mesenchymal transition and inducing apoptosis. *Prostate* 79, 647–656. doi: 10.1002/pros.23772

Yan, M., Hardin, K., and Ho, E. (2010). Differential response to zinc-induced apoptosis in benign prostate hyperplasia and prostate cancer cells. *J. Nut. Biochem.* 21, 687–694. doi: 10.1016/j.jnutbio.2009.04.002

Yang, G. B., Zhang, R., Liang, C., Zhao, H., Yi, X., Shen, S. D., et al. (2018). Manganese Dioxide coated WS2@Fe3O4/sSiO(2) nanocomposites for ph-responsive mr imaging and oxygen-elevated synergetic therapy. *Small* 14:1702664. doi: 10.1002/smll.201702664

Yang, X. Y., Wang, D. Y., Zhu, J. W., Xue, L., Ou, C. J., Wang, W. J., et al. (2019). Functional black phosphorus nanosheets for mitochondria-targeting photothermal/photodynamic synergistic cancer therapy. *Chem. Sci.* 10, 3779–3785. doi: 10.1039/c8sc04844d

Yin, D. Y., Li, X. L., Ma, Y. Y., and Liu, Z. (2017). Targeted cancer imaging and photothermal therapy via monosaccharide-imprinted gold nanorods. *Chem. Commun.* 53, 6716–6719. doi: 10.1039/c7cc02247f

Zeng, X. W., Luo, M. M., Liu, G., Wang, X. S., Tao, W., Lin, Y. X., et al. (2018). Polydopamine-Modified black phosphorous nanocapsule with enhanced stability and photothermal performance for Tumor multimodal treatments. *Adv. Sci.* 5:1800510. doi: 10.1002/advs.201800510

Zhang, Q., Zhang, L. Y., Li, S. N., Chen, X. J., Zhang, M. J., Wang, T. T., et al. (2017). Designed synthesis of Au/Fe3O4@C janus nanoparticles for dual-modal imaging and actively targeted chemo-photothermal synergistic therapy of Cancer Cells. *Chemistry-a Eur. J.* 23, 17242–17248. doi: 10.1002/chem.201703498

Zhao, Y. T., Wang, H. Y., Huang, H., Xiao, Q. L., Xu, Y. H., Guo, Z. N., et al. (2016). Surface coordination of black phosphorus for robust air and water stability. *Angewandte Chemie-Int. Ed.* 55, 5003–5007. doi: 10.1002/anie.201512038

Zhou, Q. H., Chen, Q., Tong, Y. L., and Wang, J. L. (2016). Light-Induced ambient degradation of few-layer black phosphorus: mechanism and protection. *Angewandte Chemie-Int. Ed.* 55, 11437–11441. doi: 10.1002/anie.201605168

Ziletti, A., Carvalho, A., Campbell, D. K., Coker, D. F., and Neto, A. C. (2015). Oxygen defects in phosphorene. *Phys. Rev. Lett.* 114:046801.

Conflict of Interest: The authors declare that the research was conducted in the absence of any commercial or financial relationships that could be construed as a potential conflict of interest.

frontiers
in Bioengineering and Biotechnology

REVIEW
published: 08 September 2020
doi: 10.3389/fbioe.2020.00883

A Spellbinding Interplay Between Biological Barcoding and Nanotechnology

Shehla Munir[1], *Sarfraz Ahmed*[2], *Muhammad Ibrahim*[1], *Muhammad Khalid*[3] *and* *Suvash Chandra Ojha*[4]*

[1] Department of Biochemistry, Bahauddin Zakariya University, Multan, Pakistan, [2] Department of Basic Sciences, University of Veterinary and Animal Sciences, Lahore, Pakistan, [3] Department of Chemistry, Khwaja Fareed University of Engineering & Information Technology, Rahim Yar Khan, Pakistan, [4] Department of Infectious Diseases, The Affiliated Hospital of Southwest Medical University, Luzhou, China

Great scientific research with improved potential in probing biological locales has remained a giant stride. The use of bio-barcodes with the potential use of nanotechnology is a hallmark being developed among recent advanced techniques. Biobarcoding is a novel method used for screening biomolecules to identify and divulge ragbag biodiversity. It establishes successful barcoding projects in the field of nanomedical technology for massively testing disease diagnosis and treatment. Biobarcoding and nanotechnology are recently developed technologies that provide unique opportunities and challenges for multiplex detection such as DNAs, proteins and nucleic acids of animals, plants, viruses, and various other species. These technologies also clump drug delivery, gene delivery, and DNA sequencing. Bio-barcode amplification assay (BCA) is used at large for the detection and identification of proteins and DNAs. DNA barcoding combined with nanotechnology has been proven highly sensitive rendering fast uniplex and multiplex detection of pathogens in food, blood, and other specimens. This review takes a panoramic view of current advances in nano bio-barcodes which have been summarized to explore additional applications such as detection of cytokines, neurotransmitters, cancer markers, prostate-specific antigens, and allergens. In the future, it will also be possible to detect some fungi, algae, protozoa, and other pollutants in food, agriculture, and clinical samples. Using these technologies, specific and efficient sensors would possibly be developed that can perform swift detections of antigens, allergens, and other specimens.

Keywords: nano-barcoding, nano-biosensors, biobarcoding, barcoded nanoparticles, nanotechnology, cytokines, proteins, nucleic acids

Edited by:
Lin Mei,
Sun Yat-sen University, China

Reviewed by:
Luciana Dini,
Sapienza University of Rome, Italy
Hemant Kumar Daima,
Amity University Jaipur, India

***Correspondence:**
Suvash Chandra Ojha
suvash_ojha@swmu.edu.cn

Specialty section:
This article was submitted to Nanobiotechnology, a section of the journal Frontiers in Bioengineering and Biotechnology

Received: *27 April 2020*
Accepted: *09 July 2020*
Published: *08 September 2020*

Citation:
Munir S, Ahmed S, Ibrahim M, Khalid M and Ojha SC (2020) A Spellbinding Interplay Between Biological Barcoding and Nanotechnology. Front. Bioeng. Biotechnol. 8:883. doi: 10.3389/fbioe.2020.00883

INTRODUCTION

Many scientific and industrial sectors can be significantly improved and revolutionized by the new science of nanotechnology (Lyle et al., 2015). Two main factors have proved nanotechnology as a powerful engine of innovations: (1) industrial interest in nano-engineered materials. It leads to the development of many innovations like chemically active or inert additives (that impart beneficial qualities to consumer products such as increased surface area or hardness), coloring, ultraviolet protection, and antimicrobial agents; (2) interest to improve human-environmental interaction, especially concerns about the harmful effects on environment and humans (Stark et al., 2015). With time, nanotechnology emerged as an integral field due to its extensive applications in information technology and telecommunication, physics, chemistry, and life sciences (Ochs et al., 2006). It is also used in effective drug delivery and gene delivery to make liposomes in cardiac therapy and dental care (Ochs et al., 2006). Its vast applications are in molecular fields like structural DNA nanotechnology for assembling barcodes like nucleic acid barcodes (Wang P. et al., 2014). DNA sequencing performed through nanopores can also help in the diagnosis of infectious and cancerous diseases (Wanunu, 2012; Grodzinski et al., 2014). In recent years, several research studies have been conducted for developing nanotechnology-based DNA barcoding and biobarcoding (Wanunu, 2012; Grodzinski et al., 2014). Currently, recent challenges in research studies are to explore marvelous applications of nanotechnology with the potential use of DNA barcoding and biobarcoding.

Bio-barcode is a bioinformatics platform to be utilized as a coding system using nanotechnology. Biologists built a DNA barcode server and database using a biobarcoding system. It facilitates the compilation, depository, analysis, and publication of high-quality barcoded DNA records (Goluch et al., 2009). Bio-barcode provides the tools that launch successful barcoding projects in biodiversity research (Lim et al., 2009). For clinical purposes, Bio-barcode Assay (BCA) is used for the detection and specification of proteins and target DNA, which may have been proved to be pathogenic (Goluch et al., 2009). At an elaboration level, BCA also provides Polymerase Chain Reaction (PCR)-like amplification for nucleic acid and protein without the use of enzymatic amplification (Goluch et al., 2009). In BCA (bio-barcoded amplification) based assays, barcoded DNA and nanoparticles are used that can detect trace proteins, cytokines, and some neurotransmitters (Thaxton et al., 2005, 2009). Barcoded nanotechnology is used for the detection and diagnosis of cancer markers, and other vast range of infectious antigens in blood, food, and clinical samples. It can also detect prostate-specific antigens (Bao et al., 2006) by barcode lateral flow immunoassay. A barcode lateral flow immunoassay is used to optimize antibody affinity for a specific antigen (Liu et al., 2015).

DNA is a central part of genetic material which is also used in nanoscale engineering (Peng et al., 2012). DNA has many unique properties like biocompatibility, nanoscale controllability (Roh et al., 2011), and the capacity to recognize subcellular molecules. Therefore, nanotechnology in combination with DNA barcodes is an innovative technique to diagnose infectious pathogens in food, blood, and clinical samples. DNA is an extraordinary multifaceted material for developing nanoarchitecture motifs. Its vast applications have evolved between physics, chemistry, biology, computer science, and material science, etc. DNA based nanotubes and nanogrids have been constructed (Lund et al., 2006). Similarly, DNA scaffolds have been used for developing nanoelectronics. Even, DNA based nanomechanical devices have been designed (Lund et al., 2006). To identify the species, standard regions of the DNAs are sequenced in the form of a barcode. Since its origin back in 2003, DNA barcoding has been emerged as a novel tool and helped scientists to identify millions of species. Taxonomic classification consumes a lot of time to identify the species based on morphology (Coissac et al., 2016).

Approximately, 950 years are required to identify species worldwide using taxonomic methods (Rajpoot et al., 2016; Zinger and Philippe, 2016). DNA barcoding replaces the traditional taxonomic method to identify species as an innovative tool (Smith et al., 2008). In DNA barcoding, short genetic sequences in a DNA sample of animal, plant or any other species are used as markers for their identification and authentication (Hebert and Gregory, 2005). The universal barcode marker in animals is cytochrome c oxidase (CO1) that has been sliced from the mitochondrial genome, while in plants matK, ITS, rbcL, trnL-F, trnH-psbA, 5S-rRNA, and 18S-rRNA are specific barcode markers (Cowan and Fay, 2012). DNA barcoding is also applicable in the assessment of conservation impact, monitoring of biodiversity and illegal trades, and forensic analyses (Ferri et al., 2008; Ghosh et al., 2011; Nithaniyal et al., 2014). DNA barcoding has also been helpful to probe the *Mycobacterium tuberculosis,* and single–point mutation in exon21 of the epidermal growth factor receptor which implies lung cancer (Lebonah et al., 2014). It can also be used as a universal tool for food traceability to identify and quantify biological specimens. Thus, DNA barcoding using nanotechnology is being adopted as a novel tool to be used widely (Lebonah et al., 2014).

Use of nano-based detection has incremented the sensitivity up to ten folds as compared to the conventional methods of detection like radio-immunoassay, microarrays, enzyme-linked immunosorbent assay (ELISA), PCR, micro electrochemical biosensors, mass sensitive biosensors, and others (Tallury et al., 2010). However, there is a dire urge for diagnosing some fungi, algae, protozoa, and pollutants in food and agriculture using nano barcoding system (Tallury et al., 2010). In this study, we have summarized some applications developed by nanotechnology, biobarcoding, and with a major focus on DNA barcoding into the unified application so that all the features of these three technologies may view as a solo platform. This review would provide a panoramic overview of some recently developed applications of nanotechnology combined with DNA barcodes and a minor coverage of related bio-barcodes.

Classification of Nanoparticles

Nanoparticles can be classified into various types according to the size, morphology, physical, and chemical properties. They have gained prominence in technological advancements due to their astounding physicochemical and biological properties including melting point, electrical and thermal conductivity, catalytic activity, light absorption, and scattering resulting in enhanced performance over their bulk counterparts. Based on physicochemical properties, they can be organized into: carbon-based nanoparticles, ceramic nanoparticles, metal nanoparticles, semiconductor nanoparticles, polymeric nanoparticles, and lipid-based nanoparticles (Khan et al., 2019). For detailed description on nanoparticles classification, readers are directed to these references (Jeevanandam et al., 2018; Khan et al., 2019). In recent years, nanoparticles have been used effectively in research areas, photocatalysis, photodegradation of dyes, diagnostics, detection and imaging of biomolecules, drug delivery to targeted sites, and in environmental and bio-analytical applications (**Table 1**). Some of the important ones used in biobarcoding include:

Nanobots/Nanorobots

Nanorobotics exhibits wide applications in the field of medicine. It is used for the early diagnosis and monitoring of various diseases and targeted drug delivery (Shetty et al., 2013). Nanobots on denitrification can be consumed as toothpaste and or mouthwash for covering all the subgingival surface areas. These are also used for trapping toxic organic materials into colorless and harmless vapors. They can perform functions at the cellular level when injected into patients. The examples of nanobots may include ultra-sensitive bio-chips. Because of their splendid technological characteristics, they can be utilized as biobarcoding.

Nanotubes

Nanotubes are generally made up of carbon molecules. These have a cylindrical shape, and are used in electronics, material sciences, and nanotechnology. These exhibits astounding unique strength and electrical properties. When bound with gold nanoparticles, they are used to develop special type of biosensors that can sense various types of cancer (Mishra, 2019). A wide variety of materials such as semiconductors, metals, and polymers have been developed using nanotubes technology (Escrig et al., 2008). Literature shows that magnetic nanotubes have been industriously investigated. However, barcode-types of nanostructures were less able to get attention, in spite of customizing their multisegmented nanotube structure utilizing their functionalization with various molecules such as DNA and proteins. Furthermore, it is hypothesized that these can be useful in the development of barcode-type magnetic nanostructures, molecules separation, and magnetic and biological sensors (Stoermer et al., 2006).

Quantum Dots/Nanocrystals

Quantum dots (QDs)/nanocrystals can be defined as fluorescent crystalline inorganic nanomaterials. These novel dots emit fluorescent light whose color or wavelength depends upon the size of dots (Shah et al., 2015). These are usually less than 1 μm in size. It has been reported that 10 nm nanocrystals seem sound as semi-conductors exhibiting nanopores situated between the crystals. Surface of these nanopores could adsorb proteins through the addition of silica molecules. These hydroxyapatite nanoparticles can also be utilized for the detection of bone defects (Jackson et al., 2017). These dots specifically produce a spectrum of colors when embedded into specific microbeads in excitation state. This makes QDs very handy for image-guided surgery, molecular diagnostics, and genotype determination. These dots can be operated as diagnostics as well as therapeutics in conjugation with different diagnostic techniques. For instance, when QDs get conjugated with fluorescence microscopy, help to observe living cells and labeling of various cancer markers (Jackson et al., 2017). Other applications of the quantum dot may include multiplexed detection and viral diagnostics (Maralla and Bharathi, 2019). It has been reported that QDs have several expedient features when compared to fluorescent dyes, for instance, (i) the dots can be excited by the same narrow band sources; (ii) these are less prone to photobleaching; (iii) these have symmetric and narrow emission spectra; (iv) higher encodings capacity; and (v) better signal to noise (Rauf et al., 2010). Researchers have developed and characterized a new modern type of barcoded magnetic bead using conjugated QDs through a layer-by-layer assembly approach. These magnetic based barcodes can be spotted on the basis of various spectral responses from different QDs which are assembled on the bead surface via biological self-assembly of quantum dot–biotin and quantum dot–streptavidin conjugates. These can be exploited to use the free biotin binding site on the biologically assembled code for the utilization of these quantum barcodes in the designing of a multiplex model qualitative immunoassay (Rauf et al., 2010).

Nanowires

Nanowires are deemed as tiny channels derived from metal oxides, silicon, and or carbon nanotubes. Nanowires may exhibit very low amplitude electrical current and have been proved to be sensitive to minute changes in electrical currents (Reimhult and Höök, 2015). These are used as probes when antibodies get attached to their surfaces. The interaction of these antibodies with the target biomolecules results in conformational changes in provision of electrical signals from these nanowires for interpretations. The attachment of nanowires with antibodies can be used to form sensitive devices that can detect various types of diseases (Reimhult and Höök, 2015). It has been reported that silicon nanowires can be extensively used to detect biomarkers of prostate cancer. Another research has shown that zinc and silicon nanowires can detect DNA as the binding of these p-type nanowires to negatively charged poly-anionic macromolecule enhanced electrical conductance. Furthermore, these DNA biosensors can be able to probe all types of mutations in cancer like diseases (Lyberopoulou et al., 2015). Barcode arrangements of nanowires are considered as a special case because of their specific arraying, and multiple functionality with enhanced properties when compared to their single-component counterparts. For example, Co–Cu barcoded nanowires have been developed with high magnetoresistance for the detection, separation, and transport of cells (Lee et al., 2007).

Barcoded nanowires are a promising alternative to fluorescent tags in some applications. These particles can be used as coded substrates for biosensing, analog to DNA microarray chips, alternative to tags for detection and identification, and substitute to nanocrystals or fluorescent molecules (Nicewarner-Peña et al., 2003). Barcoded nanowires may be used as tags for the detection and identification of DNA hybridizations. A glass slide spotted with multiple capture sequences of DNA selective to the 3′ or 5′ region of the target sequences is utilized in this approach. Labeled double prime (″) and target sequences are supposed to bind to the surface through hybridization to these specific capture strands. These can then be detected by hybridization-driven assembly of bio-barcoded nanowires which generally carry a third strand of DNA that is complementary to the 5′ or 3′ (or) region of the specific targeted sequences (Nicewarner-Peña et al., 2003). The wires bound to each of the spots on the surface can be counted and identified by optical

TABLE 1 | General data on nanoparticle-based bio-barcode sensing.

Types of nanoparticles	Role of nanoparticles	Barcoding molecules	Specific targets	Detection techniques	Applications	References
Magnetic nano- particles and Quantum dot	Label	Barcoded oligonucleotide sequences	Bacterial DNA	Electrophoresis	Multiplex detection of *S. aureus*, MRSA, and *K. pneumoniae*	Nam et al., 2005
Gold nano- particles and Magnetic nano- particles	Capture probes	Barcoded oligonucleotide sequences	DNA	Fluorescence	Detection of Exotoxin A gene in *P. aeruginosa*	Amini et al., 2016
Gold nano- particles	Label and probe capture	Barcoded oligonucleotide sequences	HIV Capsid protein p24 antigen	Electrophoresis	Diagnosis of hepatitis	Dong et al., 2012
Magnetic nano- particles	Immunocomplex	–	PVX	Light scattering	Diagnosis of plant diseases	Panferov et al., 2016
Silver nano- particles	Label	Tumor penetrating peptide RPARPAR	PPC1 Prostate cancer cells	MS	Diagnosis of Prostate cancer	Fogal et al., 2008; Teesalu et al., 2009; Agemy et al., 2011
Silver nano- particles	Label	Tumor homing peptide GKPK	M21 melanoma cells	MS	Diagnosis of skin cancer	Fogal et al., 2008; Teesalu et al., 2009; Agemy et al., 2011
Gold nano- particles	Label	Single stranded thiol capped oligonucleotide sequences	Small molecules	Fluorescence	Development of optical biosensor for detection of very small molecules	Rees et al., 2016
Silver nano- particles	Transducer modifier	Barcoded dsDNA	DNA	Fluorescence	Detection of known piece of DNA	Zhou et al., 2014
Polystyrene nanoparticles	Immunocomplex	Bio-barcoded DNA	Target protein	Fluorescence	Detection of CRP in plasma	Broto et al., 2017
Silicon nano- particles	Label	Barcoded ssDNA	IL-2	Light absorption	Detection of IL-2	Nam et al., 2005
Gold nano-particles	Label	Bio-barcoded dsDNA	TAP	Fluorescence	Detection of small molecules e.g., TAP	Zhang et al., 2018
Gold nano- particles	Capture probe	Barcoded ssDNA	PSA	Light scattering	Detection of PSA	Bao et al., 2006
Silver enhancement gold nanoparticles	Scatter light	Thiol capped ssDNA	TAP	Light scattering	Detection of TAP	Zhang et al., 2018
Gold nanoparticles	Capture probe	Thiol capped dsDNA	Target protein	qPCR	Detection of PCBs in hair	Yang et al., 2015
Gold nano- particles	Capture probe	Thiol capped dsDNA	Target protein	qPCR	Detection of 3,4,3,′,4′-tetrachloro biphenyl protein	Yang et al., 2014
Magnetic microparticles	Capture probe	Barcoded aptamers	Cytochrome c	SPR	Detection of cytochrome c	Loo et al., 2017
Gold nano- particles	Capture probe	Oligonucleotide sequences	miRNA	Fluorescence	Determination of different levels of miRNA levels from cancer cells	Lund et al., 2006
Nanowires	Label	Oligonucleotide sequences	Target DNA	Optical reflectance microscopy	Identification of specific DNA hybridization events	Lyberopoulou et al., 2015
Nanowires	Capture probe	Oligonucleotide sequences	Target DNA	Fluorescence	Detection and quantification of DNA	Lee et al., 2007

Abbreviations*: PVX, potato virus X; dsDNA, double stranded DNA; ssDNA, single stranded DNA; CRP, C-reactive protein; IL, interleukin; PSA, prostate specific antigen; TAP, triazophous; qPCR, real-time PCR; MS, mass spectrometry; SRP, surface plasmon resonance; miRNA, micro ribonucleic acid; and PCB, polychlorinated biphenyls.*

reflectance microscopy which ultimately presents the amount and identification of targeted molecules or specimens present in the samples. This method is substantially simple with no requirement of fluorescence tags. A use of selective nanoparticles attachment will deliver a multiplexed analysis at broader scale (**Figure 1A**; Nicewarner-Peña et al., 2003).

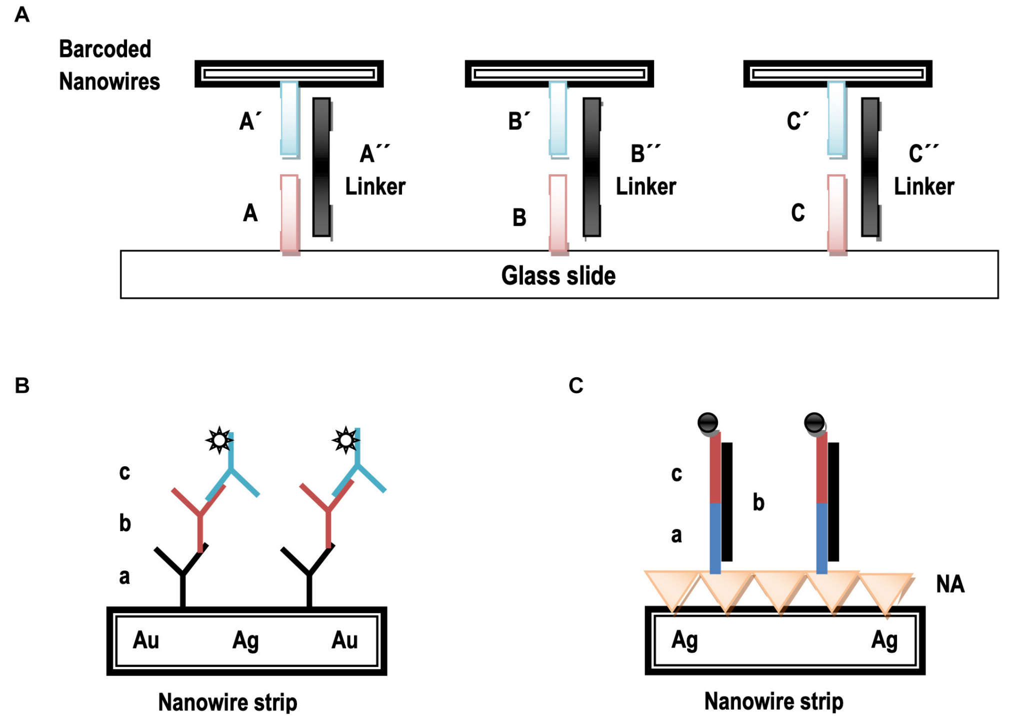

FIGURE 1 | An illustration of nonfluorescent bioassay using bio-barcoded nanowires. **(A)** DNA strands labeled A–C are likely to be not complementary to the respective primed counterparts **(A′–C′)**. The strands double prime (″) labeled are likely to link the respective sequences to their primed counterparts through complementary DNA hybridization. **(B)** The striped particles are derivatized using capture antibody **(a)**, analyte **(b)**, and the fluorescent labeled detection antibody addition **(c)**. **(C)** The striped particles are derivatized through NeutrAvidin (NA), a biotinylated capture sequence's reaction **(a)**, a special phase analyte **(b)**, and fluorescent labeled oligonucleotides for detection **(c)**.

It has been investigated that nanowires serve as identifying markers as well as detectable substrates for binding (Wang, 2008). **Figure 1B** shows the usage of barcoded nanowires as substrates for DNA and antigen detection. It demonstrates that a standard sandwich immunoassay using nanowires surface for the detection of antigens or proteins. An analogous detection of DNA detection using nanowires has been shown in **Figure 1C**, where nanowires serve as the substrates for probes attachment.

Bio-Chips and Microarrays

Chip-based nanotechnology has emerged as a new epitome for total chemical analysis systems. Chips can be silicon or a glass-based simple device that may have many processes for DNA analysis. A chip usually consists of channels in which biomolecules flow to biosensors. It consists of heat-based sensors for temperature, fluorescence detectors, fluidic channels, and electrophoretic chambers which are designed with microfabricates for nano-sized DNA analysis. Nanotechnology-based chips may measure biomolecules such as DNA digestion, DNA isolation, and DNA analysis (Jain, 2003). These novel innovations make biological and chemical information easier for healthcare and molecular diagnostics. Proteins based nanochips and nanofluidic arrays are examples of these devices. It may be postulated that detection of microorganisms, development of medicines, systems biology, and personalized medicines can be the unique possibilities of these techniques (Bahadorimehr et al., 2010).

Magnetic Nanoparticles

Magnetic nanoparticles (MNPs) are a type of iron nanoparticles. Their size may range in 15–20 nm. These particles can be constructed from glycidyl methacrylate with embodiment in copolymer beads (Jackson et al., 2017). Super MNPs have been described for calcium-sensing and tracking of cells. MNPs conjugated with magnetic resonance imaging (MRI) disclose small and undetectable metastasis of lymph nodes. Conjugation of super paramagnetic iron oxide enhances MRI for cerebral ischemic lesions. It has been documented that dextran coated MNPs may enhance MRI for intracranial visualization of tumors (Jackson et al., 2017). It has been reported that DNA bio-barcoded assays use oligonucleotide-modified magnetic gold nanoparticles for amplification and for separation of a targeted protein from the samples (Jackson et al., 2017). The theory of the bio-barcoded assay is special and presents a potential alternative source to the PCR technique.

Gold Nanoparticles

Gold nanoparticles manifest small pieces of DNA and gold particles within range of 13 nm in diameter. These can be particularly used as labels for the development of various types of sensors (Mieszawska et al., 2013). It has been observed that oligonucleotide-functionalized gold nanoparticles (AuNPs) have advantages in terms of performance, selectivity, and sensitivity over conventional probes in a wide variety of bio-detection protocols. The bio-barcode assays are generally based on AuNPs functionalization with a number of strands of oligonucleotides strands (assumed as barcodes) and a corresponding recognition agent which can be antibody in terms of protein detection, and a small segment of the barcoded strand in case of nucleic acids detection (Stoeva et al., 2006). Nanoprobes of magnetic gold nanoparticles when functionalized with locked nucleic acid and bio-barcode DNA, are used for the sensitive detection of miRNA.

Nanoshells

Literature reports show that nanoshells are mainly used in the delivery of chemotherapeutic agents to treat tumors. In its mechanism, drugs and polymer complexes are embedded in nanoshells and then injected into the body where they get accumulated near to tumors for their action. Nanoshells may melt by absorbing a certain infrared frequency from infrared rays resulting in site-specific drug release from polymer complex (Loo et al., 2004). The use of metal nanoshell-coated microbeads instead of uncoated microbeads reported a potential increase in analytical sensitivity for the detection of genetic targets. The assay process has been assumed to be very reliable, simple, and fast (Chapin and Doyle, 2011). It makes it advantageous as an ideal approach for ultra-sensitivity and high throughput multiplexed biosensing applications in clinical diagnosis (Chen et al., 2013), and for the detection of various organic targets including biological targets (Chan et al., 2019), such as peptides, pathogens, genomic and proteomic targets, nucleic acid sequences, amino acid sequences, carbohydrates, and lipids.

Nanopores

Data shows that nanopores can be implemented to sequence a complete codon in the DNA strand. It is ultimately an ultra-fast DNA sequencing. Detection and characterization of simple molecules by nanopores show a novel method for the interpretation of information directly from linear polymers (Soni and Meller, 2007). Specific individual DNA and proteins can be detected using solid-state nanopores through engineering of programmed binding sites at the centre of double-stranded long DNA. The DNA is likely to act as a "carrier" which selectively drives out proteins through the nanopores (Li et al., 2015; Bell and Keyser, 2016).

Nanobiosensors

Nanobiosensors are presumed as the nanosensors used for diagnosis of diseases through detection of specific biological and chemical entities (Escrig et al., 2008). These sensors can detect specific cells and peculiar body areas. Nanobiosensors are usually constructed of two entities; (1) biological entity which is used as sampling and (2) physical entity for sampling toward result production and transduction. These may differentiate between normal cells and cancerous cells by detecting specific biomolecules released by such cells. Genetic defects or mutations can be probed earlier by recognizing peculiar DNA using these sensors. These sensors can be of many types such as electrochemical nano biosensors, optical biosensor, carbon nanotube biosensors, nanowire biosensors, viral nanosensors, ion channel switch biosensors, and quartz nanobalance DNA sensors (Escrig et al., 2008). Current research is trying to amplify weak peptides biomarkers coated on nanomaterials which can be released into the bloodstream by specific proteases. These proteases are produced by cancerous cells and released into the urine where these can be ultimately detected (Escrig et al., 2008). Researchers have developed a very highly sensitive and selective biosensor for the detection of microRNAs (miRNAs) utilizing bio-barcode DNA assay with catalytic hairpin assembly via multiple probes (Dong et al., 2015). A new development of bio-barcoded biosensors for the detection of DNA in poor biological samples has been proclaimed using nanomagnetic beads (Trévisan et al., 2010).

DNA BARCODING AND NANOTECHNOLOGY

DNA Barcoding of Bacteria

In current scenario, PCR methods are going to be replaced by nanotechnology usage for nucleic acid detection. Scientific literature shows that fluorescence probes such as fluorescent metal ions (Zhang et al., 2013), nanoparticles (Zanoli et al., 2012), metal complexes, and bio-barcoded DNA are likely to be sole bio-detection methods which represent PCR-like sensitivity for both nucleic acid and proteins exempting the need of enzymatic amplification. Thus, the use of nanomaterials has opened a new eon in bio-analytical technology by introducing "Fluorescence bio-barcode DNA assay." This assay involves the use of nanoparticles of metals and semiconductors exhibiting exclusive electronic, optical, catalytic and magnetic properties (Saha et al., 2012; Li and Antonietti, 2013).

It has been reported that fluorescent, super magnetic and metallic nanostructures are of critical importance for bioimaging and detection of infectious microorganisms, viruses, and bacteria in biological samples. Literature shows that "fluorescent bio-barcode DNA assay" has been used to probe the *Salmonella enteritidis* genes (Yin et al., 2012). This assay was based on two types of nanoparticles: (1) Gold nanoparticles, and (2) MNPs. *S. enteritidis* has been recognized as an infectious bacterium that causes diarrhea, fever, and abdominal cramps after transmitted in body. This technique can detect even trace amounts of pathogens with high sensitivity and proficiency to save human lives. Similarly, gold, silver, and nickel barcoded nanowires have been reported to be used for the detection of bacterial antigens that have been supposed to be life-threatening.

Conjugated polymer nanoparticles (CPNs) are used in molecular imaging or cell imaging. These are very critical in drug discovery, gene profiling, and clinical diagnosis. Their potential use is based on the self-assembly of CPNs and bacteria which lead to multicolor emissions. Various color-barcoded micro particles are prepared by mixing of *Escherichia coli* and CPNs together. These multicolored particles exhibit low toxicity toward cells and can be widely applicable for optical barcoding and cell imaging (Khan et al., 2019). Nowadays, barcoded nanoparticles (BNPs) are used to detect specific gene sequences in bacteria. In this method, target DNA is sandwiched between nanoparticle and microparticle probes containing barcode DNA. Thus, barcode DNA can be detected by using a universal probe (Amini et al., 2016).

Amini along with colleagues in 2016 detected exotoxin-A by fluorescence bio-barcode DNA assay based on magnetic and gold nanoparticles as shown in **Figure 2**. *Pseudomonas aeruginosa* is a gram-negative aerobic bacterium. It produces exotoxin-A (ETA) which presumes to be a very toxic substance (Tok et al., 2006). If this bacterium enters the human body, then it releases exotoxin-A which may lead to stomach disturbance, vomiting, and even mortality (Feng et al., 2012). For this purpose, thiol-capped alternative oligonucleotide sequences are taken as probe-1 and probe-2. DNA barcode is made as thiol-capped. Probe-2 forms complex on the surface of MNPs, while probe-1 and barcode DNA form a complex with gold nanoparticles (GNPs). After this, the target DNA of *P. aeruginosa* is allowed to co-hybridize with both probes to form a sandwich structure. The target DNA of *P. aeruginosa* is then separated by applying a magnetic field, and free barcode DNA is detected by fluorescence spectrophotometer. From target DNA, the gene for exotoxin-A is amplified by PCR, and resultant bands are observed by gel electrophoresis. However, this technique requires less time with unfortunate less sensitivity when compared to conventional and classical methods of detection (Amini et al., 2016).

Traditional detection methods of bacterial infections are time-consuming, complex with lack of detection of pooled samples of pathogens. To counter these mentioned challenges, "Barcoded quantum dot assay" can be demonstrated as effective alternative tool. This essay utilizes magnetic and non-magnetic micro- and nanoparticles providing a most suitable platform for barcoded assay (Zhao et al., 2015). The nanoparticles act as carriers for molecules for the detection of a targeted component. The capturing molecules spotted on nanoparticles and the targeted component of the bacteria must have affinity of specific binding. The capturing molecules are nucleic acids and antibodies in the form of genes or oligonucleotides. Barcode assay for the detection of bacteria is generally based on labeled oligonucleotides because antibodies may pose a cross reactivity and difficult availability. For the detection of microorganisms in a multiplex analysis, and identification of individual or exclusive species, QDs are considered to be highly preferable (Zahavy et al., 2010).

Researchers used "barcode-quantum dot (Fluorescent nanoparticles) assay" for the detection of three bacterial pathogens: *Methicillin-resistant Staphylococcus aureus* (MRSA), *Staphylococcus aureus,* and *Klebsiella pneumonia* (Nam et al., 2005; **Figure 3**). They took a mixture of these bacteria and added this mixture to magnetic particles, which non-specifically capture these bacteria. After this, these bacteria were lysed, and resulting bacterial lysates were also amplified by multiplex PCR. Gold magnetic particles (oligonucleotides barcode labeled) were then added, which magnetically purify the individual bacteria by complementary binding to their oligonucleotide barcodes. In the end, QDs (oligonucleotides barcode labeled) were allowed to bind with their complementary binding sites on Au-MPs. Final products were magnetically purified which represented the separate genes for three specific bacterial species. This method has been proven very sensitive which can detect even minute concentrations of bacteria (Nam et al., 2005).

DNA Barcoding and Detection of Cytokines

Cytokines are small proteins that aid cell signaling in immune responses. Interleukin-2 (IL-2) is a cytokine protein, secreted during inflammation, and immune responses in humans. It shows local interactions between white blood cells (Zhao et al., 2015). Advanced method for the detection of these biological targets such as protein (IL-2), and nucleic acid is known as "bio-barcode amplification assay." This assay is based on porous particles of silica and gold nano particles-based on calorimetric DNA detection schemes (**Figure 2**). The porous particles enable the loading of millions of barcodes of DNA through amplification principle (Zahavy et al., 2010). Previously, some researchers detected cytokines proteins using this method. This method encompasses three steps (Nam et al., 2005); (1) The barcode probe is prepared by immobilizing monoclonal antibodies (IL-2) to amino-functionalized porous silica microparticles. Then amino-functionalized barcode DNA complements are added to modify silica particles; (2) magnetic probe preparation is carried out when the monoclonal antibody for IL-2 is immobilized to Amino-functionalized magnetic particles; (3) barcode DNA quantification is carried out when this magnetic probe is allowed to form a complex with a barcode probe in the presence of IL-2. In abutting step, using magnetic separations, many barcode DNAs are released. These released barcode DNAs are then captured on gold nanoparticles. By spotting particles on the TLC plate and detection of barcode DNA is carried out using colorimeter. In interpretation, nanoparticles without barcode DNA appear more reddish as compared to the nanoparticles with barcode DNA (Nam et al., 2005; **Figure 4**).

It has been observed that classical methods for the detection need many tedious experimental steps such as microarray-based immobilization of oligonucleotide on a glass chip, silver enhancement of immobilized gold nanoparticles on a chip, light scattering measurement, and a quantification step. Experimental requirements can be minimized by using the colorimetric bio-barcode method with the potential use of nanotechnology (Nam et al., 2005).

DNA Barcoding and Analysis of Neurotransmitters

Data shows that "nanoparticle based bio-barcode DNA assay" presents a highly sensitive detection of nucleic acids and proteins (Cao et al., 2010). This assay includes two types of particles: magnetizable spheres having modified a functional group with an affinity for the target, and nanoparticles with a second modified group that possesses an affinity for the same target, and as well as for an oligonucleotide barcode DNA that is likely to be a reporter for the target. The nanoparticle-based bio-barcode DNA assay proclaims the use of gold nanoparticles as a key feature. This warrants a simultaneous loading of detection probes/antibodies, a huge

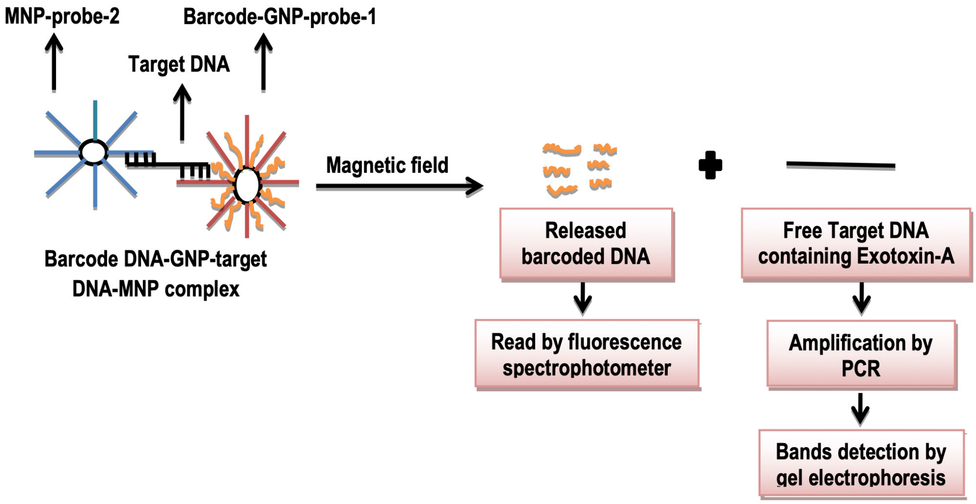

FIGURE 2 | Schematic illustration of DNA barcoding assay.

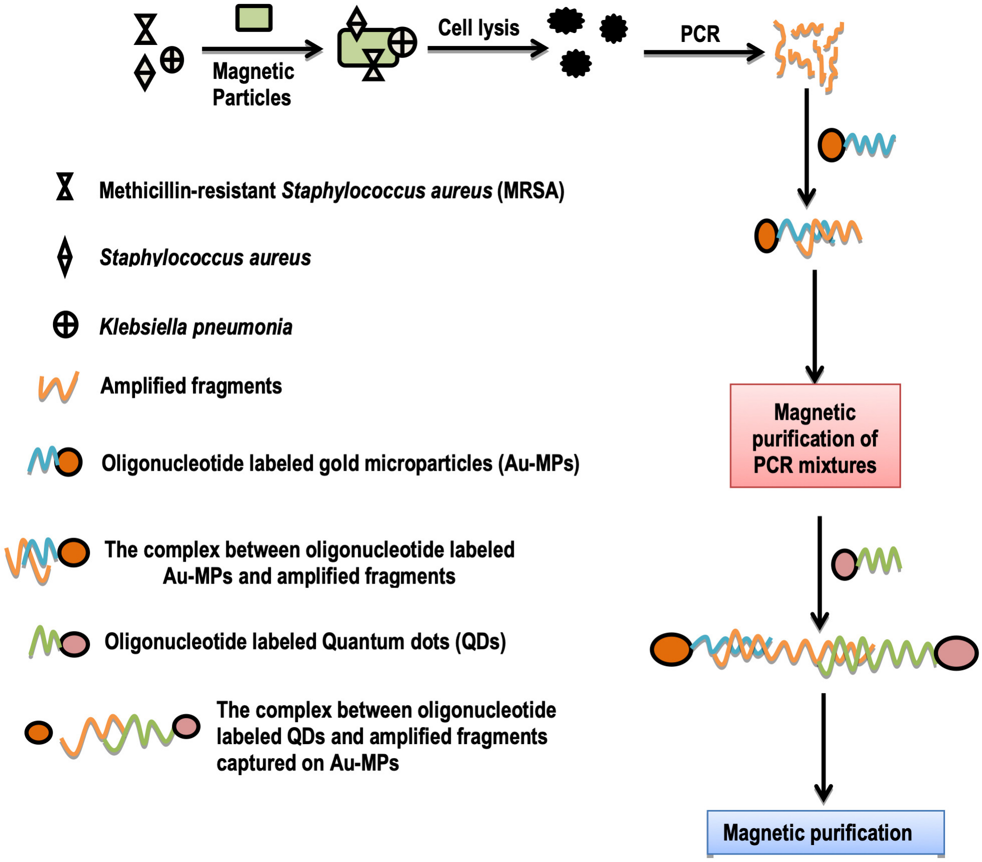

FIGURE 3 | Schematic illustration of detection of three bacterial species by barcode-quantum dot assay.

quantity of barcoded DNA per single gold nanoparticle, and high sensitivity by avoiding the complicated preparation of antibody – DNA conjugate as required in immuno-PCR (Duan et al., 2010).

Neurotransmitters are sort of chemical messengers that carry signals from neurons. Norepinephrine is a neurotransmitter that belongs to a class of catecholamines. It controls motivation, alertness, heartbeat, gastrointestinal activity, and blood pressure

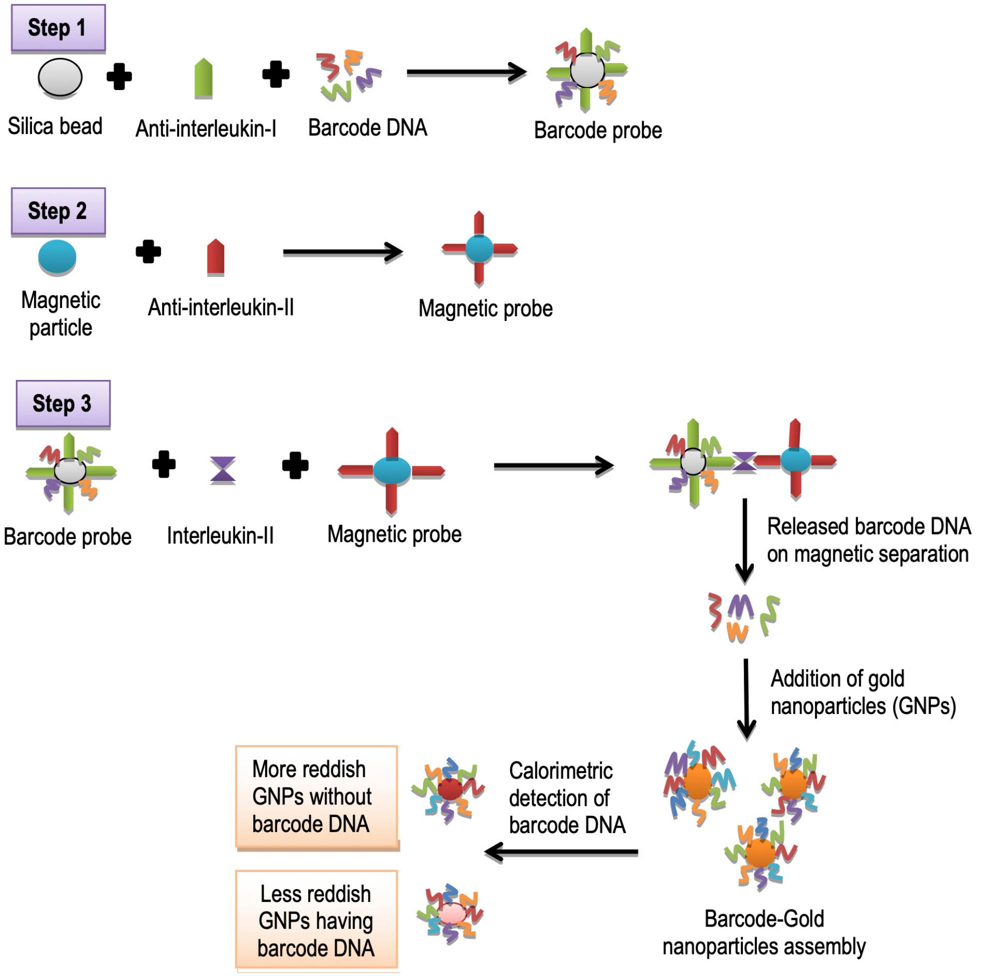

FIGURE 4 | Schematic illustration of detection of interleukin-II using DNA barcoding and nanotechnology.

(Shankaran and Miura, 2007). "Nanoparticles based bio-barcode assay" is a very advanced technique. It is used to analyze nucleic acids and proteins. The number of neurotransmitters can also be determined by using a nanoparticles-based bio-barcode technique. Rabbit's norepinephrine polyclonal antibodies were mixed with magnetizable polystyrene beads in a PCR tube and incubated at 37°C for 24 h. Gold nanoparticles were treated with antibodies and oligonucleotides as bio-barcodes. The norepinephrine made a sandwich structure between the rabbit polyclonal antibodies, and the antibodies of gold nanoparticles. This sandwich structure was separated magnetically. Resultant norepinephrine (NE) barcodes DNA was analyzed by surface-enhanced Raman spectroscopy (Hee et al., 2016; **Figure 5**). This tool is rapid, and has high throughput screening for analyzing neurotransmitters as compared to conventional methods. In recent years, diagnosis and treatment of neurological disorders are the most challenging issues. In nifty words, using DNA barcoding and nanotechnology, it will be possible to diagnose all neurological disorders by detecting neurotransmitters which are presumed to be involved in these disorders (Hee et al., 2016).

DNA Barcoding and Assessment of Sensitivity of Anticancer Drugs

Anticancer drugs perform their function only if being sensitive to cancer disease. Assessment of the sensitivity of anticancer drugs is recognized very critical prior their recommendation to the patients (Yaari et al., 2016). BNPs are also used to probe the sensitivity of tumors toward anticancer drugs. For this purpose, researchers showed loading of nanoparticles with anticancer drugs (Yaari et al., 2016). Each nanoparticle was loaded with at least 15 barcodes. These BNPs were then injected intravenously to the cancer patients. BNPs were found to move toward target cancer tissue inside the body of the patients pursuing therapeutic activity. Approximately 48 h later, a biopsy was taken from the tumor tissues. Biopsied tissues were dissociated enzymatically generating multiple cells, and each cell was sorted by FACS (fluorescence-activated cell sorting) according to their viability. Live and dead cells were washed, lysed, and DNA barcodes from them were extracted. These barcodes were amplified by real-time PCR. In presumption determination, barcodes found in the dead cells belong to active

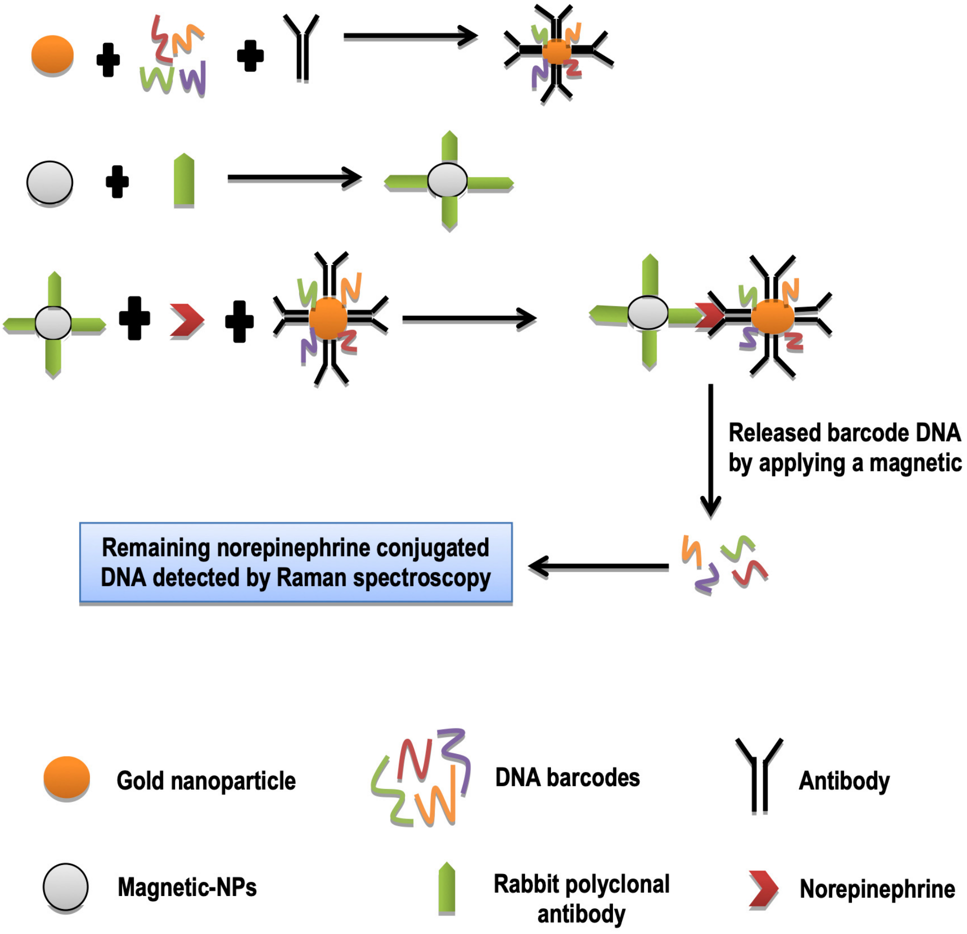

FIGURE 5 | Quantification of norepinephrine.

drugs, while those of living cells belong to inactive drugs. On the basis of the sensitivity of anticancer drugs, thus barcodes could be suggested for treatment and to enhance treatment target's sensitivity (Yaari et al., 2016; **Figure 6**). Silica nanoparticles bound to proteins surfaces can be used as nano bio-chips. This provides a lot of potential for detecting cancerous cells. Protein enzymes or antibodies are immobilized on a glass slide. This chip is probed with a sample that binds to a relevant protein on the chip, and is analyzed for detection. Proteins on chips can be used to differentiate normal cells from cancerous cells (Stoermer et al., 2006).

Conventional methods for the assessment of drugs sensitivity may include quantitative scoring approach, analytical methods, and analytical instrumentation which desire many experimental steps to assess the sensitivity of anticancer drugs. However, nano-based DNA barcoded chips are very sensitive technique to predict the therapeutic efficacy of anticancer drugs. In the future, work should be done to check the sensitivity of all anticancer drugs by using DNA barcoding and nanotechnology. Specific sensors using nanotechnology will measure the sensitivity of anticancer drugs by detecting tumor-specific DNA barcodes (Stoermer et al., 2006).

BIOBARCODING AND NANOTECHNOLOGY

Aptamers and Nanoparticles Integration for Barcoding

Aptamers are defined as receptor molecules made up of single- and/or double-stranded oligonucleotides. These are obtained from large libraries by an *in vitro* sequential process of systematic evolution of ligands by exponential enrichment (SELEX; Li et al., 2010). Aptamers have clinched an attention to be important molecular tools in diagnostics because of their affinity, inherent selectivity, flexibility, and stability (Li et al., 2010). Aptamer-based biosensors (aptasensors) possess unprecedented advantages compared with biosensors using natural receptors such as antibodies and enzymes (Li et al., 2010). Li et al. (2010), introduced an electrochemical sensing strategy for a quick and simultaneous detection of thrombin and adenosine-based aptamers as switching structures. A gold electrode was used as a sensor which was modified with two types of thiolated capture probes complementary to the linker DNA. The linker DNA holds either a thrombin aptamer or an adenosine aptamer. The capture

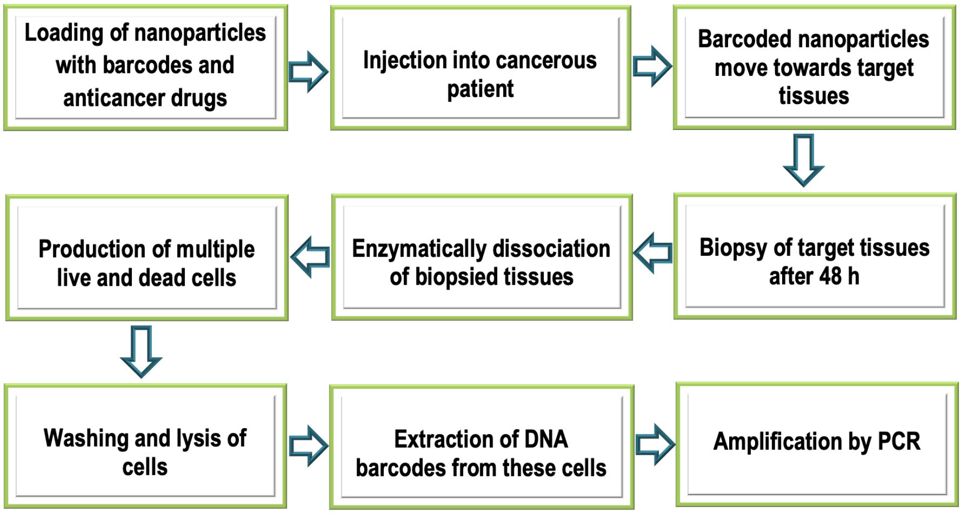

FIGURE 6 | Schematic illustration of analysis of tumor sensitivity of anticancer drugs.

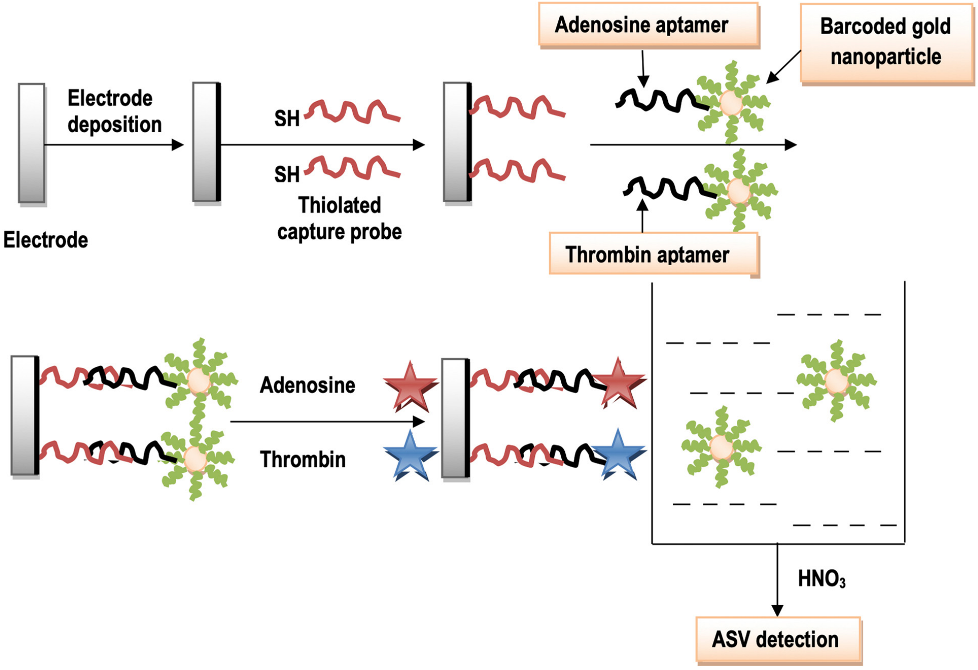

FIGURE 7 | Schematic illustration of the formation of sensing interface using aptamers with AuNPs.

probes have the ability to hybridize with the corresponding linker DNA. The AuNPs possess two types of bio-barcode DNA; (a) one is complementary to the linker DNA (as reporter), while the other is not (signal), but is tagged with a different type of metal sulfide nanoparticles. Thus, a "sandwich-type" sensing surface has been developed fabricated with adenosine and thrombin. The aptamer parts (adenosine and thrombin) bind with their targets to form the quite complex structures. This results in the release of bio-barcoded AuNPs into solution. The concentration of adenosine and thrombin is supposed to be proportional to the signal of either metal ion, while the measurement of metal sulfide nanoparticles comes up by anodic stripping voltammetry (ASV; **Figure 7**; Li et al., 2010).

Barcoding and Detection of Allergens

Allergy is caused by plant pollens or some foodstuff which contain allergenic proteins that cause allergic reactions (Hochwallner et al., 2014). "Mass barcode-based mass spectrometry (MS) signal amplification" has been introduced as a very advanced technique used in tissue imaging (Yan et al., 2013),

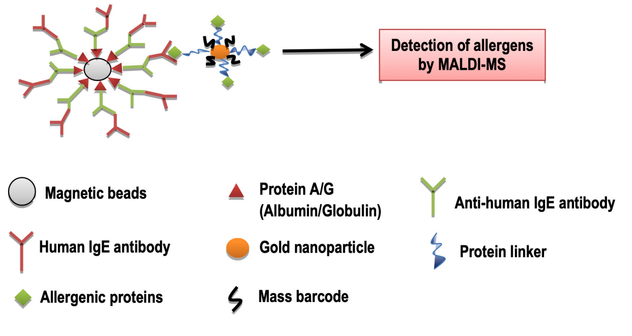

FIGURE 8 | Detection of allergens by MALDI-MS. Legends: MALDI, Matrix-assisted laser desorption/ionization; MS, Mass spectrometry.

immunoassay (Lee et al., 2008), and DNA assays (Qiu et al., 2008). In this technique, small tagged molecules (mass barcodes) are attached to micro or nanoparticles, and are targeted to large biomolecules. After this, they can easily be detected by MS that results in an amplified signal of the targets. The combination of mass barcodes and magnetic beads has been proved to be a very effective for MS detection of large biomolecules, e.g., allergens (Nam et al., 2015).

In mass barcode signal amplification, mass barcode amplification is used with the combination of commercial protein-coated magnetic beads, which diagnose multiplex allergy components with MS detection. The molecules of polyethylene glycol are chosen as a mass barcode that have different chain lengths. These mass barcodes are placed on biological chips and or plates which act as surface. Then these barcodes are made to join with gold nanoparticles, which further get attachment with commercially available magnetic beads linked A/G allergenic proteins to design gold nanoparticles probes. These probes are attached to anti-human IgE antibodies that make a sandwich structure. On detection by MS, it indicates the presence of specific IgE antibodies (Zhong et al., 2016; **Figure 8**). Traditional immunoassay methods for the detection of allergens are time-consuming and they are not very highly sensitive, but recent mass barcodes amplification in combination with magnetic beads proves to be highly sensitive in detecting allergens. In the future, this technology would be helpful for the treatment of different allergies (Zhong et al., 2016).

Barcoding and Detection of Viruses

Barcoded-nanotechnology is used to detect viruses using “barcode lateral flow immune-assay.” A barcode lateral flow immunoassay based on magnetic nanoparticle is used to optimize antibody affinity for a specific antigen. To increase sensitivity and broaden the applications of lateral flow immunoassay, modifications have been made by controlling the cut-off level and insertion of MNPs (Zvereva et al., 2015; Orlov et al., 2016). In this way, this assay can be used to diagnose hormones, cardiac and cancer biomarkers, and to detect plant diseases (Wang L. et al., 2014). Research has shown that the cut-off level of sensitive barcode lateral flow assay with magnetic nanoparticle for the detection of potato viruses. In the initial stage, monoclonal (3G4 and 1A5), and polyclonal mouse antibodies (pAb) specific to PVX (potato virus X) are developed. Then, immune complexes are formed between monoclonal and polyclonal antibodies, potato virus and secondary anti-mouse antibodies (IgG) on the chip surface. Consequently, MNPs make conjugates with immune complexes. Transmission electron microscopy is brought in use to visualize the immune complexes with MNPs (magnetic nanoparticles) followed by barcode lateral flow assay for the detection of potato viruses. The lateral flow test strips are dipped in a solution containing immune complexes with and without MNPs (Panferov et al., 2016). Nanowire field-effect transistors are also used to detect viral pathogens. Viral antibodies modify binding and unbinding characteristics of nanowire arrays. It helps in the real-time detection of selective viruses (Shah et al., 2015).

Human immunodeficiency virus (HIV) p24 is a major disease-causing antigen of the human immunodeficiency virus (HIV-1; Fiebig et al., 2003). In the past, this antigen was detected by the ELISA technique, but the ELISA process is time consuming with low sensitivity. Currently, BCA assay based on gold nanoparticles and magnetic microparticles has been introduced to detect this antigen in less time and high sensitivity. Researchers have shown that this assay can be used to detect HIV p24 antigen. In that process, microplates or magnetic microplates are coated with a 1G12 monoclonal antibody (Tang et al., 2007). Then, HIV p24 antigens are made to be treated to form a complex with these monoclonal antibodies. Gold nanoparticles are modified by the attachment of barcoded oligonucleotides (DNA). Then these gold nanoparticles are allowed to form a sandwich complex with these antigens. This complex is heated to release bio-barcode DNA and followed to get amplified by PCR. The resulting bands are separated through gel electrophoresis (**Figure 9**). In biomedical research, work has been started to diagnose viral diseases using this potential technology (Dong et al., 2012).

Barcoding and Evaluation of Ligand-Receptor Affinity

Nanoparticles are delivered to cells and tissues on the basis of the affinity of ligand bounded nanoparticles to their specific receptors on cells or tissues. Willmore and colleagues demonstrated that barcoded silver nanoparticles (AgNPs) can be used to determine the binding affinity of the ligand with tumor cell receptors (Agemy et al., 2013; Chaudhary et al., 2014). They made AgNPs isotopically, i.e., by mixing silver and palladium isotopes and coated these nanoparticles with Neutravidins (NA). Two types of barcoded ligands were used; the first one is RPARPAR (tumor penetrating peptide) and the second is SGKRK (tumor homing peptide). In their demonstration, these barcoded ligands were bounded to biotin by amino hexanoic acid as intermediate. Then this biotin part of barcoded peptide ligands attached to the NeutrAvidin part of AgNPs. They made three types of barcoded nanoparticles, (I) RPARPAR biotin AgNPs, (II) SGKRK biotin AgNPs, and (III) Control biotin AgNPs (with no peptide ligand linkage). Two types of cancer cells were used, PPC-1 prostate cancer cell and M21 melanoma cells. These cells were incubated with these two barcoded nanoparticles and control

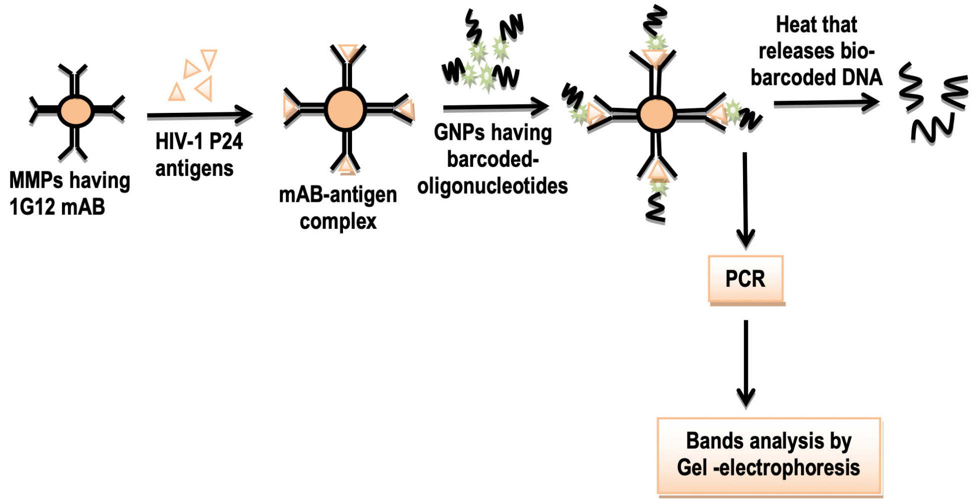

FIGURE 9 | Schematic illustration of detection of HIV p24 antigen using barcoding and nanotechnology. Legends: MMPs, *Matrix metalloproteinases*; 1G12 mAB, 1G12 monocolonal antibody. GNPs, Gold nanoparticles; and PCR, polymerase chain reaction.

biotin nanoparticles (Agemy et al., 2013; Chaudhary et al., 2014). Binding affinity between tumor cell receptors and barcoded nanoparticles was assessed by plasma mass spectrometry. The SGKRK barcoded nanoparticles demonstrated an affinity to bind with p32 receptors on M21 melanoma cells. The RPARPAR barcoded nanoparticles showed an affinity to bind with NRP-1 receptors on PPC-1 (prostate cancer cells; Fogal et al., 2008; Teesalu et al., 2009; Agemy et al., 2011; **Figure 10** and **Table 2**). P32 protein is a mitochondrial chaperone, while NRP-1 is the neutrophilic-1 receptor. Both are overexpressed on the surface of tumor cells. It is presumed that barcoding and nanotechnology will be used to check the affinity of anticancer drugs to tumor cell receptors so that scientists would be able to treat cancer at best (Agemy et al., 2013; Chaudhary et al., 2014).

Generation of Multicolored Bio-Barcodes

The effect of changing colored barcodes and errors in barcodes with different nanoparticles can be determined *in vitro*. The purpose of this technology is to ensure the possible number of colored barcodes using sequential loading protocol (Agemy et al., 2013). For this purpose, varied numbers of nanoparticle loaded vesicles as a colored barcode are produced using a protocol named "Sequential loading protocol." This protocol involves a cell population that is sequentially loaded with nanoparticles carrying different emission wavelengths. Every cell in the population generates its own barcode. Then the effect of changing colors of barcode and misreading in cellular code on encoding the cells is observed (Agemy et al., 2013).

At present, this is a recent technology that has been set forth to use nanoparticle colored barcode for tracking and identification of cells. Nano based generation of multicolored barcodes has been raised as a rapid, and highly sensitive technique as compared to the other conventional methods. It is anticipated that multicolored barcodes will be used for multiplex detection in coming years (Agemy et al., 2013).

Generation of Optical Bio-Barcodes

It has been reported that various optical barcodes can be generated using nanotechnology. These barcodes manifest their use in multiplex detection (Wang G. et al., 2014). These optical barcodes can be manipulated by mixing (polystyrene-co-maleic anhydride; PSMA) microsphere near-infrared emitting QDs, and Fe_3O_4 containing super-paramagnetic nanoparticles by membrane emulsification technique. As a result, various bifunctional optical barcodes are produced. In emulsification technique, optical barcodes can be encoded by the "single-wavelength" encoding model that can be used to detect tumor or other biomarkers (Rees et al., 2016). This is deduced as a very sensitive method of detection compared to traditional ELISA, magnetic microspheres technology, and fluorescence-encoded microsphere technology (Wang G. et al., 2014). It is speculated that special sensors can be designed that can quickly encode these optical barcodes.

Generation of Digital Bio-Barcodes

Literature proclaims that digital bio-barcodes simultaneously detect multiple biomolecular analytes with more precision. Currently, it is possible to generate digital barcodes by "Laser-induced breakdown spectroscopy" (LIBS) in which nanomaterials are well used (Leng et al., 2016). In principle, this technique generates digital barcodes with high sensitivity as compared to other conventional digital methods. LIBS is a method that converts analog barcodes into a digital form (He et al., 2016). By LIBS technology, analysis of industrial products, drugs or medicines, and monitoring of environment can be carried out efficiently. LIBS based polystyrene microspheres are prepared by using layer-by-layer self-assembly method, carrying some surface modifications. These microspheres are encoded with nanoparticles. Subsequently, some binding groups are coated on the surface of these microspheres that help in the binding of these microspheres to target analytes (e.g., ssDNA;

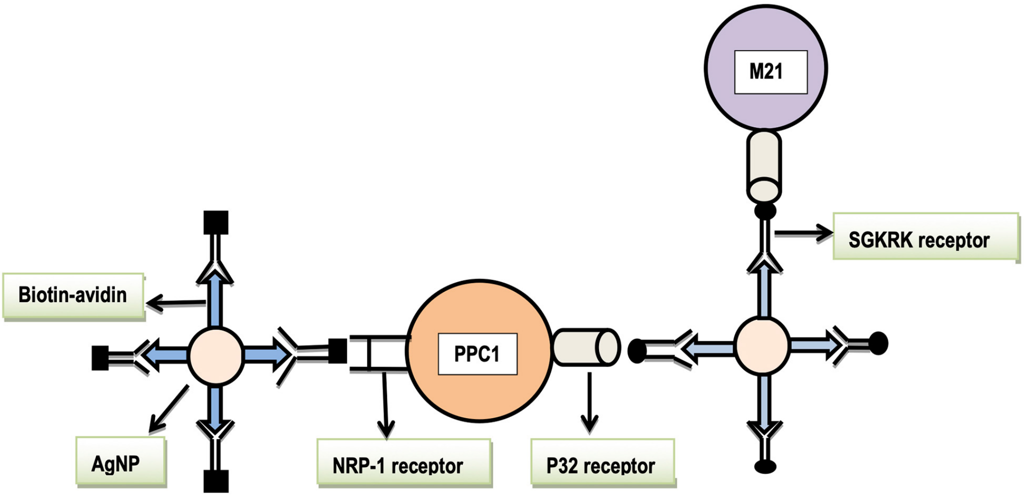

FIGURE 10 | The affinity of barcoded AgNPs to their respective tumor cell receptors. Legends: NRP-1, neuropilin-1, SGKRK, a peptide name, AgNPs, silver nanoparticles, PPC1, cancer cell line type, and M21, melanoma cancer cell line type.

Lin et al., 2013). The analytes are labeled with QDs as fluorescent tags. Fluorescent tags and nanoparticles are stimulated by a pulse laser, which shows colored emissions to detect target analytes. On the basis of colored coding emissions, a map of digital barcodes is generated. These digital barcodes can be further used in multiplex detection. In the future, work will be conducted to develop such biosensors which can quickly encode these digital barcodes with high sensitivity and precision (Lin et al., 2013).

Diagnosis of Different Pathogenic Organisms

The predominant conventional methods to identify the pathogens rely upon clinical monitoring approaches. These methods are based upon culturing the microorganisms which are contemplated as laborious, expensive, and time-consuming (Khiyami et al., 2014; Sautter et al., 2015). Another drawback of the conventional methods is that these do not support to manage a large number of clinical samples. In contrast, the "nano-barcode diagnostic systems" are more accurate and reliable tools for the detection of pathogenic microorganisms. Nano-barcode diagnostic system is a system used to analyze DNA, RNA, proteins, mycotoxins, bacteria, and viruses. In this assay, oligonucleotide associated magnetic gold nanoparticles (AuMNPs) are used. This assay is very effective and more proficient than PCR technology as it has high sensitivity to diagnose the pathogens in a short span of time. However, the nanobarcode diagnosis of fungi, algae, protozoa, and some pollutants in food and agriculture is an under-phase area, and it requires more work for further exploration (Khiyami et al., 2014; Sautter et al., 2015).

Diagnosis of Diseases by Quantum Dot Barcode Technology

Quantum dots are synthesized by semi-conductor materials. Their size is about 10 nm, and more than one antigen can be detected through QD barcode technology (Giri et al., 2011). QDs emit various colors by absorbing a specific wavelength. Like metallic nanoparticles, QDs are utilized in nano-enhanced imaging for environmental monitoring, molecular diagnostics, and related treatment (Giri et al., 2011). "Bio-barcode quantum dot technology" has been introduced to diagnose diseases by detecting disease-causing antigens (Gao et al., 2011; Rai and Ingle, 2012). This technology involves QD barcodes which can be synthesized by using porous silica beads, swelling process, polymerization, and by fluidic-flow focusing approach. In this process, antigens form complex with QD barcodes and give an inferring signal (Giri et al., 2011). For the detection of one antigen, a specific buffer solution is prepared and antigen detecting probes are dispersed in this solution. These probes are fluorescent/radioactive labeled. QD based bio-barcodes are added in it and antigen will form a complex with barcodes, and show fluorescence which can be read out by the optical device. This type of assay in which only one antigen or anyone molecule is detected is called single-plexed QD barcode assay (Jennings et al., 2008). While in multiplexed QD barcode assay, multiple analytes are detected by forming many QD barcodes. These QD barcode assays can be used to diagnose multiple range of diseases. It can be predicted for the future that this tool will be utilized for clinical validation of important diseases (Kim et al., 2016).

TABLE 2 | The affinity of barcoded AgNPs to their respective tumor cell receptor.

Barcoded AgNPs	Specific receptors	Targeted tumor cells
RPARPAR-AgNPs	NRP-1 and p32	PPC-1 prostate cancer cell
SGKRK-AgNPs	Only P32	M21 melanoma cells
Control biotin AgNPs (with no barcode)	Have no affinity with any receptors	–

CONCLUSION

The progressive development of diagnostic methods for the analysis of pathogens, allergens, diseases, and their treatment is a hallmark task in the modern era. The avalanche approaches in nanoscience reveal how biological data can be acquired quickly, easily, and inexpensively, then interpreted, thus enormously increase the possibilities of wonderful achievements. These may also lead to a move in diagnosis, and therapy with new outcomes. DNA barcoding and biobarcoding combined with potential nanotechnology fulfill technological advancement. Contribution of nanobarcoding toward multiplex detection, diagnosis, and treatment of diseases, is highly promising and rapidly growing.

FUTURE PERSPECTIVES

In the future, this innovative approach will be nifty and/or worthwhile for the detection of fungi, algae, protozoa, and various range of pollutants. It will also be agile for the development of advanced nano-biosensors in life sciences. Furthermore, nanotechnology interplay with bio-barcodes will lead for nanoscale products which can then be used with entailed biological systems. The new dimension of nanotechnology research may focus on recognizing cells and their constituents, and individual genes of impaired functions and their self-repair. It can easily be predicted that this field would witness a same exponential growth as the other two technological field such as information technology in the year of 1960s and biotechnology in 1980s witnessed earlier.

AUTHOR CONTRIBUTIONS

SM and SA drafted the DNA and nanotechnology part, while MI and MK wrote the biobarcoding part of the manuscript. SCO and SA conceived the idea, reviewed, and edited the manuscript. All authors read and approved the final version of manuscript.

REFERENCES

Agemy, L., Friedmann-Morvinski, D., Kotamraju, V. R., Roth, L., Sugahara, K. N., Girard, O. M., et al. (2011). Targeted nanoparticle enhanced proapoptotic peptide as potential therapy for glioblastoma. *Proc. Natl. Acad. Sci. U.S.A.* 108, 17450–17455. doi: 10.1073/pnas.1114518108

Agemy, L., Kotamraju, V. R., Friedmann-Morvinski, D., Sharma, S., Sugahara, K. N., and Ruoslahti, E. (2013). Proapoptotic peptide-mediated cancer therapy targeted to cell surface p32. *Mol. Ther.* 21, 2195–2204. doi: 10.1038/mt.2013.191

Amini, B., Kamali, M., Salouti, M., and Yaghmaei, P. (2016). Fluorescence bio-barcode DNA assay based on gold and magnetic nanoparticles for detection of Exotoxin A gene sequence. *Biosens. Bioelectron.* 92, 679–686. doi: 10.1016/j.bios.2016.10.030

Bahadorimehr, A., Yunas, J., and Majlis, B. Y. (2010). "Low cost fabrication of microfluidic microchannels for Lab-On-a-Chip applications," in *Proceedings of the 2010 International Conference on Electronic Devices, Systems and Applications*, (Kuala Lumpur: IEEE), 242–244.

Bao, Y. P., Wei, T.-F., Lefebvre, P. A., An, H., He, L., Kunkel, G. T., et al. (2006). Detection of protein analytes via nanoparticle-based bio bar code technology. *Anal. Chem.* 78, 2055–2059. doi: 10.1021/ac051798d

Bao, Y. P., Wei, T. F., Lefebvre, P. A., An, H., He, L., Kunkel, G. T., et al. (2006). Detection of protein analytes via nanoparticle-based bio bar code technology. *Anal. Chem.* 78, 2055–2059. doi: 10.1021/ac051798d

Bell, N. A., and Keyser, U. F. (2016). Digitally encoded DNA nanostructures for multiplexed, single-molecule protein sensing with nanopores. *Nat. Nanotechnol.* 11:645. doi: 10.1038/nnano.2016.50

Broto, M., Galve, R., and Marco, M. P. (2017). Sandwich NP-based biobarcode assay for quantification C-reactive protein in plasma samples. *Anal. Chim. Acta* 992, 112–118. doi: 10.1016/j.aca.2017.09.007

Cao, C., Dhumpa, R., Bang, D. D., Ghavifekr, Z., Høgberg, J., and Wolff, A. (2010). Detection of avian influenza virus by fluorescent DNA barcode-based immunoassay with sensitivity comparable to PCR. *Analyst* 135, 337–342. doi: 10.1039/b916821b

Chan, W., Leo, Y. T., and Chen, K. (2019). *U.S. Patent Application No. 14/768,051.*

Chapin, S. C., and Doyle, P. S. (2011). Ultrasensitive multiplexed microRNA quantification on encoded gel microparticles using rolling circle amplification. *Anal. Chem.* 83, 7179–7185. doi: 10.1021/ac201618k

Chaudhary, B., Khaled, Y. S., Ammori, B. J., and Elkord, E. (2014). Neuropilin 1: function and therapeutic potential in cancer. *Cancer Immunol. Immunother.* 63, 81–99. doi: 10.1007/s00262-013-1500-0

Chen, K., Chou, L. Y., Song, F., and Chan, W. C. (2013). Fabrication of metal nanoshell quantum-dot barcodes for biomolecular detection. *Nano Today* 8, 228–234. doi: 10.1016/j.nantod.2013.04.009

Coissac, E., Hollingsworth, P. M., Lavergne, S., and Taberlet, P. (2016). From barcodes to genomes: extending the concept of DNA barcoding. *Mol. Ecol.* 25, 1423–1428. doi: 10.1111/mec.13549

Cowan, R. S., and Fay, M. F. (2012). Challenges in the DNA barcoding of plant material. *Methods Mol. Biol.* 862, 23–33. doi: 10.1007/978-1-61779-609-8_3

Dong, H., Liu, J., Zhu, H., Ou, C.-Y., Xing, W., Qiu, M., et al. (2012). Two types of nanoparticle-based bio-barcode amplification assays to detect HIV-1 p24 antigen. *Virol. J.* 9:180. doi: 10.1186/1743-422x-9-180

Dong, H., Meng, X., Dai, W., Cao, Y., Lu, H., Zhou, S., et al. (2015). Highly sensitive and selective microRNA detection based on DNA-bio-bar-code and enzyme-assisted strand cycle exponential signal amplification. *Anal. Chem.* 87, 4334–4340. doi: 10.1021/acs.analchem.5b00029

Duan, R., Zhou, X., and Xing, D. (2010). Electrochemiluminescence biobarcode method based on cysteamine- gold nanoparticle conjugates. *Anal. Chem.* 82, 3099–3103. doi: 10.1021/ac100018z

Escrig, J., Bachmann, J., Jing, J., Daub, M., Altbir, D., and Nielsch, K. (2008). Crossover between two different magnetization reversal modes in arrays of iron oxide nanotubes. *Phys. Rev. B* 77, 214421.

Feng, X., Yang, G., Liu, L., Lv, F., Yang, Q., Wang, S., et al. (2012). A convenient preparation of multi-spectral microparticles by bacteria-mediated assemblies of conjugated polymer nanoparticles for cell imaging and barcoding. *Adv. Mater.* 24, 637–641. doi: 10.1002/adma.201102026

Ferri, G., Alù, M., Corradini, B., Angot, A., and Beduschi, G. (2008). Land plants identification in forensic botany: multigene barcoding approach. *Foren. Sci. Int. Genet. Suppl. Ser.* 1, 593–595. doi: 10.1016/j.fsigss.2007.10.023

Fiebig, E. W., Wright, D. J., Rawal, B. D., Garrett, P. E., Schumacher, R. T., Peddada, L., et al. (2003). Dynamics of HIV viremia and antibody seroconversion in plasma donors: implications for diagnosis and staging of primary HIV infection. *Aids* 17, 1871–1879. doi: 10.1097/00002030-200309050-00005

Fogal, V., Zhang, L., Krajewski, S., and Ruoslahti, E. (2008). Mitochondrial/cell-surface protein p32/gC1qR as a molecular target in tumor cells and tumor stroma. *Cancer Res.* 68, 7210–7218. doi: 10.1158/0008-5472.can-07-6752

Gao, Y., Stanford, W. L., and Chan, W. C. (2011). Quantum-dot-encoded microbeads for multiplexed genetic detection of non-amplified DNA samples. *Small* 7, 137–146. doi: 10.1002/smll.201000909

Ghosh, S., Majumder, P., and Mandi, S. S. (2011). Species-specific AFLP markers for identification of *Zingiber officinale*, *Z. montanumand Z. zerumbet* (Zingiberaceae). *Genet. Mol. Res.* 10, 218–229. doi: 10.4238/vol10-1gmr1154

Giri, S., Sykes, E. A., Jennings, T. L., and Chan, W. C. (2011). Rapid screening of genetic biomarkers of infectious agents using quantum dot barcodes. *ACS Nano* 5, 1580–1587. doi: 10.1021/nn102873w

Goluch, E. D., Stoeva, S. I., Lee, J.-S., Shaikh, K. A., Mirkin, C. A., and Liu, C. (2009). A microfluidic detection system based upon a surface immobilized biobarcode assay. *Biosens. Bioelectron.* 24, 2397–2403. doi: 10.1016/j.bios.2008.12.017

Grodzinski, P., Silver, M., and Molnar, L. K. (2014). Nanotechnology for cancer diagnostics: promises and challenges. *Exp. Rev. Mol. Diagn.* 6, 307–318. doi: 10.1586/14737159.6.3.307

He, Q., Liu, Y., He, Y., Zhu, L., Zhang, Y., and Shen, Z. (2016). Digital barcodes of suspension array using laser induced breakdown spectroscopy. *Sci. Rep.* 6:36511.

Hebert, P. D., and Gregory, T. R. (2005). The promise of DNA barcoding for taxonomy. *Syst. Biol.* 54, 852–859. doi: 10.1080/10635150500354886

Hee, J., An, K.-J., Lee, and Choi, J.-W. (2016). Gold nanoparticles-based barcode analysis for detection of Norepinephrine. *J. Biomed. Nanotechnol.* 12, 357–365. doi: 10.1166/jbn.2016.2185

Hochwallner, H., Schulmeister, U., Swoboda, I., Spitzauer, S., and Valenta, R. (2014). Cow's milk allergy: from allergens to new forms of diagnosis, therapy and prevention. *Methods* 66, 22–33. doi: 10.1016/j.ymeth.2013.08.005

Jackson, T. C., Patani, B. O., and Ekpa, D. E. (2017). Nanotechnology in diagnosis: a review. *Adv. Nanopart.* 6:93. doi: 10.4236/anp.2017.63008

Jain, K. K. (2003). Nanodiagnostics: application of nanotechnology in molecular diagnostics. *Exp. Rev. Mol. Diagn.* 3, 153–161. doi: 10.1586/14737159.3.2.153

Jeevanandam, J., Barhoum, A., Chan, Y. S., Dufresne, A., and Danquah, M. K. (2018). Review on nanoparticles and nanostructured materials: history, sources, toxicity and regulations. *Beilstein J. Nanotechnol.* 9, 1050–1074. doi: 10.3762/bjnano.9.98

Jennings, T., Rahman, K., Fournier-Bidoz, S., and Chan, W. (2008). Effects of microbead surface chemistry on DNA loading and hybridization efficiency. *Anal. Chem.* 80, 2849–2856. doi: 10.1021/ac7026035

Khan, I., Saeed, K., and Khan, I. (2019). Nanoparticles: properties, applications and toxicities. *Arab. J. Chem.* 12, 908–931. doi: 10.1016/j.arabjc.2017.05.011

Khiyami, M. A., Almoammar, H., Awad, Y. M., Alghuthaymi, M. A., and Abd-Elsalam, K. A. (2014). Plant pathogen nanodiagnostic techniques: forthcoming changes? *Biotechnol. Biotechnol. Equip.* 28, 775–785. doi: 10.1080/13102818.2014.960739

Kim, J., Biondi, M. J., Feld, J. J., and Chan, W. C. (2016). Clinical validation of quantum dot barcode diagnostic technology. *ACS Nano* 10, 4742–4753. doi: 10.1021/acsnano.6b01254

Lebonah, D., Dileep, A., Chandrasekhar, K., Sreevani, S., Sreedevi, B., and Pramoda Kumari, J. (2014). DNA barcoding on bacteria: a review. *Adv. Biol.* 2014, 1–9.

Lee, J. H., Wu, J. H., Liu, H. L., Cho, J. U., Cho, M. K., An, B. H., et al. (2007). Iron–gold barcode nanowires. *Angew. Chem. Int. Ed.* 46, 3663–3667. doi: 10.1002/anie.200605136

Lee, J. R., Lee, J., Kim, S. K., Kim, K. P., Park, H. S., and Yeo, W. S. (2008). Mass spectrometry signal amplification method for attomolar detection of antigens using small-molecule-tagged gold microparticles. *Angew. Chem. Int. Ed.* 47, 9518–9521. doi: 10.1002/anie.200803893

Leng, Y., Wu, W., Li, L., Lin, K., Sun, K., Chen, X., et al. (2016). Magnetic/fluorescent barcodes based on cadmium-free near-infrared-emitting quantum dots for multiplexed detection. *Adv. Funct. Mater.* 26, 7581–7589. doi: 10.1002/adfm.201602900

Li, T., Liu, L., Li, Y., Xie, J., and Wu, H. C. (2015). A universal strategy for aptamer-based nanopore sensing through host–guest interactions inside α-hemolysin. *Angew. Chem. Int. Ed.* 54, 7568–7571. doi: 10.1002/anie.201502047

Li, X., Xia, J., Li, W., and Zhang, S. (2010). Multianalyte electrochemical biosensor based on aptamer-and nanoparticle-integrated bio-barcode amplification. *Chem.Asian J.* 5, 294–300. doi: 10.1002/asia.200900217

Li, X. H., and Antonietti, M. (2013). Metal nanoparticles at mesoporous N-doped carbons and carbon nitrides: functional Mott–Schottky heterojunctions for catalysis. *Chem. Soc. Rev.* 42, 6593–6604. doi: 10.1039/c3cs60067j

Lim, J., Kim, S.-Y., Kim, S., Eo, H.-S., Kim, C.-B., Paek, W. K., et al. (2009). BioBarcode: a general DNA barcoding database and server platform for Asian biodiversity resources. *BMC Genomics* 10:S8. doi: 10.1186/1471-2164-10-S3-S8

Lin, Q., Niu, G., Wang, Q., Yu, Q., and Duan, Y. (2013). Combined laser-induced breakdown with Raman spectroscopy: historical technology development and recent applications. *Appl. Spectro. Rev.* 48, 487–508. doi: 10.1080/05704928.2012.751028

Liu, D., Huang, Y., Wang, S., Liu, K., Chen, M., Xiong, Y., et al. (2015). A modified lateral flow immunoassay for the detection of trace aflatoxin M1 based on immunomagnetic nanobeads with different antibody concentrations. *Food Control* 51, 218–224. doi: 10.1016/j.foodcont.2014.11.036

Loo, C., Lin, A., Hirsch, L., Lee, M.-H., Barton, J., Halas, N., et al. (2004). Nanoshell-enabled photonics-based imaging and therapy of cancer. *Technol. Cancer Res. Treat.* 3, 33–40. doi: 10.1177/153303460400300104

Loo, J. F. C., Yang, C., Tsang, H. L., Lau, P. M., Yong, K. T., Ho, H. P., et al. (2017). An Aptamer Bio-barCode (ABC) assay using SPR, RNase H, and probes with RNA and gold-nanorods for anti-cancer drug screening. *Analyst* 142, 3579–3587. doi: 10.1039/c7an01026e

Lund, K., Williams, B., Ke, Y., Liu, Y., and Yan, H. (2006). DNA nanotechnology: a rapidly evolving field. *Curr. Nanosci.* 2, 113–122. doi: 10.2174/157341306776875811

Lyberopoulou, A., Efstathopoulos, E., and Gazouli, M. (2015). Nanodiagnostic and nanotherapeutic molecular platforms for cancer management. *J. Cancer Res. Updates* 4, 153–162. doi: 10.6000/1929-2279.2015.04.04.3

Lyle, S. N., Lourtioz, J.-M., Lahmani, M., Dupas-Haeberlin, C., and Hesto, P. (2015). *Nanosciences and Nanotechnology: Evolution or Revolution?*. Berlin: Springer.

Maralla, S., and Bharathi, D. (2017). New modalities for drug delivery in the treatment of chronic diseases through Nanosize drug delivery systems. *International Journal of Pharmacy and Life Sciences* 8, 5407–5411.

Mieszawska, A. J., Mulder, W. J., Fayad, Z. A., and Cormode, D. P. (2013). Multifunctional gold nanoparticles for diagnosis and therapy of disease. *Mol. Pharmaceut.* 10, 831–847. doi: 10.1021/mp3005885

Mishra, A. K. (2019). *Application of Nanotechnology in Diagnosis, Drug Dissolution, Drug Discovery, and Drug Carrier, Nanobiotechnology in Bioformulations*. Berlin: Springer, 449–475.

Nam, J., Yoo, M., and Yeo, W.-S. (2015). Measurement of prostate-specific antigen level as a biomarker for breast cancer by using mass signal amplification. *BioChip J.* 9, 124–129. doi: 10.1007/s13206-015-9205-4

Nam, J.-M., Wise, A. R., and Groves, J. T. (2005). Colorimetric bio-barcode amplification assay for cytokines. *Anal. Chem.* 77, 6985–6988. doi: 10.1021/ac0513764

Nicewarner-Peña, S. R., Carado, A. J., Shale, K. E., and Keating, C. D. (2003). Barcoded metal nanowires: optical reflectivity and patterned fluorescence. *J. Phys. Chem. B* 107, 7360–7367. doi: 10.1021/jp034139i

Nithaniyal, S., Newmaster, S. G., Ragupathy, S., Krishnamoorthy, D., Vassou, S. L., and Parani, M. (2014). DNA barcode authentication of wood samples of threatened and commercial timber trees within the tropical dry evergreen forest of India. *PLoS One* 9:e107669. doi: 10.1371/journal.pone.0107669

Ochs, H. D., Smith, C. E., and Puck, J. M. (2006). *Primary Immunodeficiency Diseases: a Molecular & Cellular Approach*. Oxford: Oxford University Press.

Orlov, A. V., Bragina, V. A., Nikitin, M. P., and Nikitin, P. I. (2016). Rapid dry-reagent immunomagnetic biosensing platform based on volumetric detection of nanoparticles on 3D structures. *Biosens. Bioelectron.* 79, 423–429. doi: 10.1016/j.bios.2015.12.049

Panferov, V. G., Safenkova, I. V., Zherdev, A. V., and Dzantiev, B. B. (2016). Setting up the cut-off level of a sensitive barcode lateral flow assay with magnetic nanoparticles. *Talanta* 164, 69–76. doi: 10.1016/j.talanta.2016.11.025

Peng, S., Derrien, T. L., Cui, J., Xu, C., and Luo, D. (2012). From cells to DNA materials. *Mater. Today* 15, 190–194. doi: 10.1016/s1369-7021(12)70089-5

Qiu, F., Jiang, D., Ding, Y., Zhu, J., et al. (2008). Monolayer-barcoded nanoparticles for on-chip DNA hybridization assay. *Angew. Chem.* 120, 5087–5090. doi: 10.1002/ange.200800435

Rai, M., and Ingle, A. (2012). Role of nanotechnology in agriculture with special reference to management of insect pests. *Appl. Microbiol. Biotechnol.* 94, 287–293. doi: 10.1007/s00253-012-3969-4

Rajpoot, A., Kumar, V. P., Bahuguna, A., and Kumar, D. (2016). DNA barcoding and traditional taxonomy: an integrative approach. *Int. J. Curr. Res.* 8, 42025–42031.

Rauf, S., Glidle, A., and Cooper, J. M. (2010). Application of quantum dot barcodes prepared using biological self-assembly to multiplexed immunoassays. *Chem. Commun.* 46, 2814–2816. doi: 10.1039/b927149j

Rees, P., Rowan, M., Brown, J. W., Wills, and Summers, H. (2016). An analysis of the practicalities of multi-color nanoparticle cellular bar-coding. *Combinat. Chem. High Throughput Screen.* 19, 362–369. doi: 10.2174/1386207319666160408150649

Reimhult, E., and Höök, F. (2015). Design of surface modifications for nanoscale sensor applications. *Sensors* 15, 1635–1675. doi: 10.3390/s150101635

Roh, S., Chung, T., and Lee, B. (2011). Overview of the characteristics of micro-and nano-structured surface plasmon resonance sensors. *Sensors* 11, 1565–1588. doi: 10.3390/s110201565

Saha, K., Agasti, S. S., Kim, C., Li, X., and Rotello, V. M. (2012). Gold nanoparticles in chemical and biological sensing. *Chem. Rev.* 112, 2739–2779. doi: 10.1021/cr2001178

Sautter, V., Toplis, M., Wiens, R., Cousin, A., Fabre, C., Gasnault, O., et al. (2015). In situ evidence for continental crust on early Mars. *Nat. Geosci.* 8, 605–609.

Shah, A., Jani, M., Venkatesh, C., Thukral, N., and Patel, S. (2015). Nanotechnology in dentistry: a review. *J. Adv. Med. Dent. Sci. Res.* 3:60.

Shankaran, D. R., and Miura, N. (2007). Recent progress and challenges in nanotechnology for biomedical applications: an insight into the analysis of neurotransmitters. *Recent Patents Nanotechnol.* 1, 210–223. doi: 10.2174/187221007782360484

Shetty, N. J., Swati, P., and David, K. (2013). Nanorobots: future in dentistry. *Saudi Dent. J.* 25, 49–52. doi: 10.1016/j.sdentj.2012.12.002

Smith, M. A., Rodriguez, J. J., Whitfield, J. B., Deans, A. R., Janzen, D. H., Hallwachs, W., et al. (2008). Extreme diversity of tropical parasitoid wasps exposed by iterative integration of natural history, DNA barcoding, morphology, and collections. *Proc. Natl. Acad. Sci. U.S.A.* 105, 12359–12364. doi: 10.1073/pnas.0805319105

Soni, G. V., and Meller, A. (2007). Progress toward ultrafast DNA sequencing using solid-state nanopores. *Clin. Chem.* 53, 1996–2001. doi: 10.1373/clinchem.2007.091231

Stark, W. J., Stoessel, P. R., Wohlleben, W., and Hafner, A. (2015). Industrial applications of nanoparticles. *Chem. Soc. Rev.* 44, 5793–5805.

Stoermer, R. L., Cederquist, K. B., McFarland, S. K., Sha, M. Y., Penn, S. G., and Keating, C. D. (2006). Coupling molecular beacons to barcoded metal nanowires for multiplexed, sealed chamber DNA bioassays. *J. Am. Chem. Soc.* 128, 16892–16903. doi: 10.1021/ja0658261

Stoeva, S. I., Lee, J. S., Thaxton, C. S., and Mirkin, C. A. (2006). Multiplexed DNA detection with biobarcoded nanoparticle probes. *Angew. Chem. Int. Ed.* 45, 3303–3306. doi: 10.1002/anie.200600124

Tallury, P., Malhotra, A., Byrne, L. M., and Santra, S. (2010). Nanobioimaging and sensing of infectious diseases. *Adv. Drug Deliv. Rev.* 62, 424–437. doi: 10.1016/j.addr.2009.11.014

Tang, S., Zhao, J., Storhoff, J. J., Norris, P. J., Little, R. F., Yarchoan, R., et al. (2007). Nanoparticle-based biobarcode amplification assay (BCA) for sensitive and early detection of human immunodeficiency type 1 capsid (p24) antigen. *JAIDS J. Acq. Immune Defic. Syndrom.* 46, 231–237. doi: 10.1097/qai.0b013e31814a554b

Teesalu, T., Sugahara, K. N., Kotamraju, V. R., and Ruoslahti, E. (2009). C-end rule peptides mediate neuropilin-1-dependent cell, vascular, and tissue penetration. *Proc. Natl. Acad. Sci. U.S.A.* 106, 16157–16162. doi: 10.1073/pnas.0908201106

Thaxton, C. S., Elghanian, R., Thomas, A. D., Stoeva, S. I., Lee, J.-S., Smith, N. D., et al. (2009). Nanoparticle-based bio-barcode assay redefines "undetectable" PSA and biochemical recurrence after radical prostatectomy. *Proc. Natl. Acad. Sci. U.S.A.* 106, 18437–18442. doi: 10.1073/pnas.0904719106

Thaxton, C. S., Hill, H. D., Georganopoulou, D. G., Stoeva, S. I., et al. (2005). A bio-bar-code assay based upon dithiothreitol-induced oligonucleotide release. *Anal. Chem.* 77, 8174–8178. doi: 10.1021/ac0514265

Tok, J. B. H., Chuang, F., Kao, M. C., Rose, K. A., Pannu, S. S., Sha, M. Y., et al. (2006). Metallic striped nanowires as multiplexed immunoassay platforms for pathogen detection. *Angew. Chem. Int. Ed.* 45, 6900–6904. doi: 10.1002/anie.200601104

Trévisan, M., Schawaller, M., Quapil, G., Souteyrand, E., Mérieux, Y., and Cloarec, J. P. (2010). Evanescent wave fluorescence biosensor combined with DNA bio-barcode assay for platelet genotyping. *Biosens. Bioelectron.* 26, 1631–1637. doi: 10.1016/j.bios.2010.08.038

Wang, G., Leng, Y., Guo, H., Song, S., Jiang, Z., Yuan, X., et al. (2014). Efficient preparation of magnetic quantum dot barcodes. *J. Mater. Chem. B* 2, 8310–8313. doi: 10.1039/c4tb01672f

Wang, J. (2008). Barcoded metal nanowires. *J. Mater. Chem.* 18, 4017–4020. doi: 10.1039/b803807d

Wang, L., Cai, J., Wang, Y., Fang, Q., Wang, S., Cheng, Q., et al. (2014). A bare-eye-based lateral flow immunoassay based on the use of gold nanoparticles for simultaneous detection of three pesticides. *Microchim. Acta* 181, 1565–1572. doi: 10.1007/s00604-014-1247-0

Wang, P., Tian, C., Li, X., and Mao, C. (2014). Assembly of barcode-like nucleic acid nanostructures. *Small* 10, 3923–3926. doi:10.1002/smll.201400942

Wanunu, M. (2012). Nanopores: a journey towards DNA sequencing. *Phys. Life Rev.* 9, 125–158. doi: 10.1016/j.plrev.2012.05.010

Yaari, Z., da Silva, D., Zinger, A., Goldman, E., Kajal, A., Tshuva, R., et al. (2016). Theranostic barcoded nanoparticles for personalized cancer medicine. *Nat. Commun.* 7:13325.

Yan, B., Kim, S. T., Kim, C. S., Saha, K., Moyano, D. F., Xing, Y., et al. (2013). Multiplexed imaging of nanoparticles in tissues using laser desorption/ionization mass spectrometry. *J. Am. Chem. Soc.* 135, 12564–12567.

Yang, G., Zhuang, H., Chen, H., Ping, X., and Bu, D. (2015). A gold nanoparticle based immunosorbent bio-barcode assay combined with real-time immuno-PCR for the detection of polychlorinated biphenyls. *Sens. Actuat. B Chem.* 214, 152–158. doi: 10.1016/j.snb.2015.02.128

Yang, G. X., Zhuang, H. S., Chen, H. Y., Ping, X. Y., and Bu, D. (2014). A sensitive immunosorbent bio-barcode assay based on real-time immuno-PCR for detecting 3, 4, 3′, 4′-tetrachlorobiphenyl. *Anal. Bioanal. Chem.* 406, 1693–1700. doi: 10.1007/s00216-013-7583-9

Yin, H. Q., Jia, M. X., Yang, S., Wang, S. Q., and Zhang, J. G. (2012). A nanoparticle-based bio-barcode assay for ultrasensitive detection of ricin toxin. *Toxicon* 59, 12–16. doi: 10.1016/j.toxicon.2011.10.003

Zahavy, E., Heleg-Shabtai, V., Zafrani, Y., Marciano, D., and Yitzhaki, S. (2010). 1; Application of fluorescent nanocrystals (q-dots) for the detection of pathogenic bacteria by flow-cytometry. *J. Fluoresc.* 20, 389–399.

Zanoli, L. M., D'Agata, R., and Spoto, G. (2012). Functionalized gold nanoparticles for ultrasensitive DNA detection. *Anal. Bioanal. Chem.* 402, 1759–1771. doi: 10.1007/s00216-011-5318-3

Zhang, C., Du, P., Jiang, Z., Jin, M., Chen, G., Cao, X., et al. (2018). A simple and sensitive competitive bio-barcode immunoassay for triazophos based on multi-modified gold nanoparticles and fluorescent signal amplification. *Anal. Chim. Acta* 999, 123–131. doi: 10.1016/j.aca.2017.10.032

Zhang, Y., Zhao, H., Wu, Z., Xue, Y., Zhang, X., He, Y., et al. (2013). A novel graphene-DNA biosensor for selective detection of mercury ions. *Biosens. Bioelectron.* 48, 180–187. doi: 10.1016/j.bios.2013.04.013

Zhao, Y., Cheng, Y., Shang, L., Wang, J., Xie, Z., and Gu, Z. (2015). Microfluidic synthesis of barcode particles for multiplex assays. *Small* 11, 151–174. doi: 10.1002/smll.201401600

Zhong, X., Qiao, L., Gasilova, N., Liu, B., et al. (2016). Mass barcode signal amplification for multiplex allergy diagnosis by MALDI-MS. *Anal. Chem.* 88, 6184–6189. doi: 10.1021/acs.analchem.6b01142

Zhou, Z., Li, T., Huang, H., Chen, Y., Liu, F., Huang, C., et al. (2014). A dual amplification strategy for DNA detection combining bio-barcode assay and metal-enhanced fluorescence modality. *Chem. Commun.* 50, 13373–13376. doi: 10.1039/c4cc05554c

Zinger, L., and Philippe, H. (2016). Coalescing molecular evolution and DNA barcoding. *Mol. Ecol.* 25, 1908–1910. doi: 10.1111/mec.13639

Zvereva, E. A., Byzova, N. A., Sveshnikov, P. G., Zherdev, A. V., et al. (2015). Cut-off on demand: adjustment of the threshold level of an immunochromatographic assay for chloramphenicol. *Anal. Methods* 7, 6378–6384. doi: 10.1039/c5ay00835b

Conflict of Interest: The authors declare that the research was conducted in the absence of any commercial or financial relationships that could be construed as a potential conflict of interest.

frontiers
in Bioengineering and Biotechnology

ORIGINAL RESEARCH
published: 15 September 2020
doi: 10.3389/fbioe.2020.01027

Drug-Loaded Lipid-Coated Hybrid Organic-Inorganic "Stealth" Nanoparticles for Cancer Therapy

*Xue Li[1], Giuseppina Salzano[1], Jingwen Qiu[1], Mathilde Menard[2], Kristian Berg[2], Theodossis Theodossiou[2], Catherine Ladavière[3] and Ruxandra Gref[1]**

[1] Université Paris-Saclay, CNRS UMR 8214, Institut des Sciences Moléculaires d'Orsay, Orsay, France, [2] Department of Radiation Biology, Institute for Cancer Research, Oslo University Hospital, Oslo, Norway, [3] University of Lyon, CNRS, UMR 5223, IMP, Villeurbanne, France

Hybrid porous nanoscale metal organic frameworks (nanoMOFs) made of iron trimesate are attracting increasing interest as drug carriers, due to their high drug loading capacity, biodegradability, and biocompatibility. NanoMOF surface modification to prevent clearance by the innate immune system remains still challenging in reason of their high porosity and biodegradable character. Herein, FDA-approved lipids and poly(ethylene glycol) (PEG)-lipid conjugates were used to engineer the surface of nanoMOFs by a rapid and convenient solvent-exchange deposition method. The resulting lipid-coated nanoMOFs were extensively characterized. For the first time, we show that nanoMOF surface modification with lipids affords a better control over drug release and their degradation in biological media. Moreover, when loaded with the anticancer drug Gem-MP (Gemcitabine-monophosphate), iron trimesate nanoMOFs acted as "Trojan horses" carrying the drug inside cancer cells to eradicate them. Most interestingly, the PEG-coated nanoMOFs escaped the capture by macrophages. In a nutshell, versatile PEG-based lipid shells control cell interactions and open perspectives for drug targeting.

Keywords: metal organic frameworks, nanoparticles, lipids, poly(ethylene glycol), stealth, sustained drug release

Edited by:
Gang Liu,
Xiamen University, China

Reviewed by:
Paolo Bigini,
Mario Negri Institute
for Pharmacological Research
(IRCCS), Italy
Clara Mattu,
Politecnico di Torino, Italy

Correspondence:
Ruxandra Gref
ruxandra.gref@universite-paris-saclay.fr;
ruxandra.gref@u-psud.fr

Specialty section:
This article was submitted to
Nanobiotechnology,
a section of the journal
Frontiers in Bioengineering and
Biotechnology

Received: *28 May 2020*
Accepted: *06 August 2020*
Published: *15 September 2020*

Citation:
Li X, Salzano G, Qiu J, Menard M, Berg K, Theodossiou T, Ladavière C and Gref R (2020) Drug-Loaded Lipid-Coated Hybrid Organic-Inorganic "Stealth" Nanoparticles for Cancer Therapy. Front. Bioeng. Biotechnol. 8:1027. doi: 10.3389/fbioe.2020.01027

INTRODUCTION

Despite progresses in drug development and cancer biology, cancer mortality rate remains over 30%, and the morbidity much higher. Nanomedicine has shown great promise through drug delivery by achieving drug transcytosis, drug targeting and theranostics (Rosenblum et al., 2018; Senapati et al., 2018). Nanoscale metal organic frameworks (nanoMOFs) recently emerged as an attracting class of hybrid nanomaterials for biomedical applications due to their biodegradability, biocompatibility, elevated drug loading capacity and high versatility in terms of architecture and physico-chemical properties (Horcajada et al., 2010, 2012; He et al., 2015; Rojas et al., 2019). NanoMOFs are formed by the self-assembly of metal centers and organic ligands, leading to the formation of open crystalline structures with regular and high porosities.

Iron (III) trimesate nanoMOFs (**Figure 1** upper panel) are among the most widely studied MOFs for drug delivery (Horcajada et al., 2010; Agostoni et al., 2013; Baati et al., 2013; Simon-Yarza et al., 2016; Li et al., 2019a). Recently, they were shown to display several intrinsic properties of main interest in the nanomedicine field: radio-enhancement properties when submitted to γ-irradiation (Li et al., 2019a); they behaved as T_2-weighted MRI imaging contrast agents (Horcajada et al., 2010) and they had intrinsic antibacterial effects killing intracellular bacteria (Li et al., 2019b).

In addition, iron trimesate nanoMOFs MIL-100 (Fe) (MIL stands for Material from Institut Lavoisier) exhibited high drug loading capacity soaking a variety of drugs from their aqueous solutions with yields close to 100%. In the case of Gemcitabine-monophosphate (Gem-MP), the drug payload reached ∼30 wt% with >98% drug loading efficiency (Rodriguez-Ruiz et al., 2015). Gem-MP, the active intermediate of Gem, is widely used in various carcinomas, including pancreatic cancer, bladder cancer, and non-small cell lung cancer. The administration of Gem-MP is of high interest for resistant cancer treatment since the phosphorylation of Gem can be a rate-limiting step especially difficult for resistant cancer cells. However, Gem-MP administration is hampered by its poor stability in biological media and low cellular uptake (Bouffard et al., 1993). In this challenging context, some of us showed that Gem-MP could be protected against degradation with increased cellular uptake by encapsulation in nanoMOFs (Rodriguez-Ruiz et al., 2015).

Surface modifications are essential to control drug release and modulate the *in vivo* fate of nanoMOFs in the living body. Silica coatings were employed in an attempt to control the release of loaded molecules from nanoMOFs MIL-101 (Taylor-Pashow et al., 2009). NanoMOFs were coated with lipid bilayers to improve their uptake by cancer cells (Wuttke et al., 2015) or with chitosan to increase their intestinal permeability (Hidalgo et al., 2017). Heparin coatings endowed the nanoMOFs with longer-blood circulation time (Bellido et al., 2015).

Poly(ethylene glycol) (PEG) based materials remain the most employed ones to engineer coatings able to prevent nanoparticles (NPs) clearance by the innate immune system, which is a prerequisite for biomedical applications (Gref et al., 1994, 1995). However, as compared to dense polymeric NPs, the porous nanoMOFs are more challenging to be coated with PEG, because these linear chains readily penetrate within their porosity, inducing an uncontrolled "burst" drug release (Agostoni et al., 2015). There are still scarce examples of successful PEGylated nanoMOF formulations. PEG was crosslinked onto the nanoMOF's surface to avoid its penetration inside the porous cores (Giménez-marqués et al., 2018) but resulted in a non-biodegradable coating. Alternatively, nanoMOFs were coated with inclusion complexes consisting of functionalized

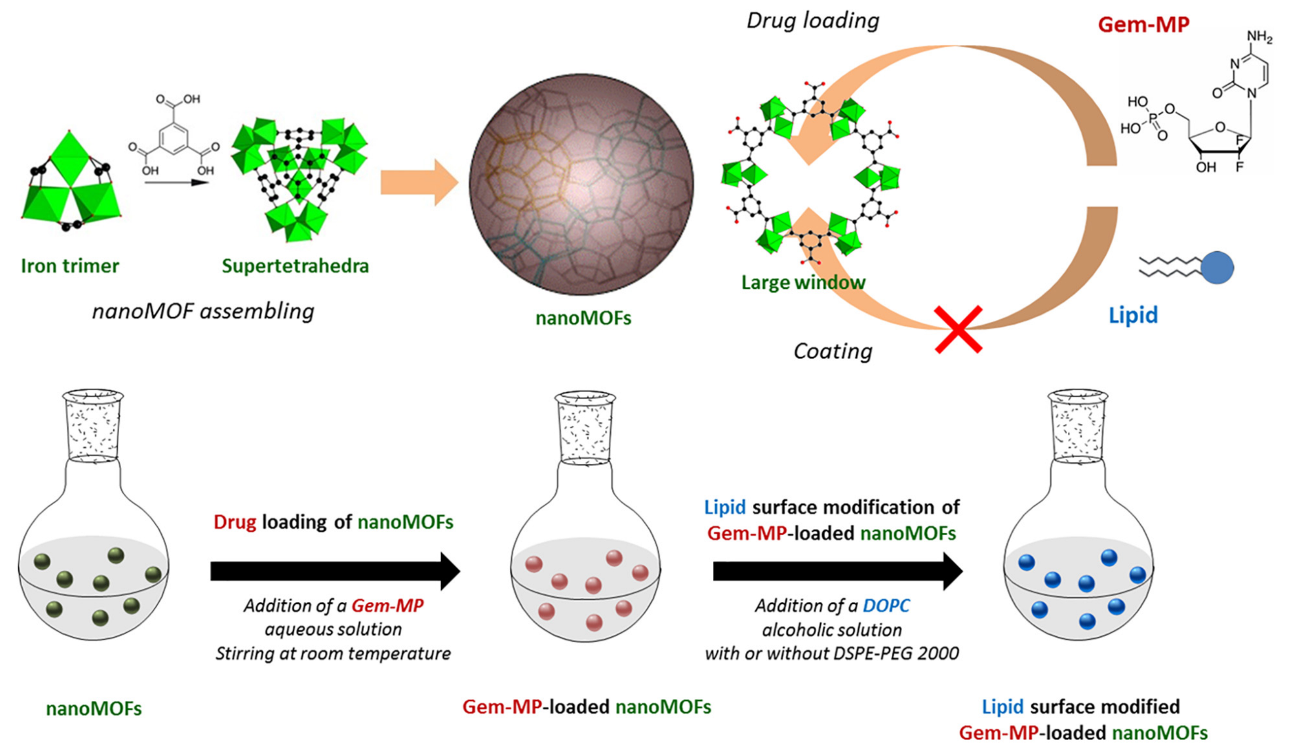

FIGURE 1 | Upper panel: Schematic representation of the MIL-100(Fe) nanoMOF assembly from iron trimers and trimesic acid. Gem-MP was loaded by impregnation from aqueous solutions, penetrating inside the nanoMOFs through their largest windows (approx. 9 Å in size). Lipid molecules (DOPC and DSPE-PEG 2000) with larger molecular dimensions than the large windows were used to coat the nanoMOFs. **Lower panel**: Preparation steps of lipid-coated nanoMOFs. First, Gem-MP was loaded, into the nanoMOFs followed by their coating with lipid shells and PEG-lipid conjugates.

cyclodextrins (CDs) and PEG chains coupled to adamantine (Agostoni et al., 2015; Aykac et al., 2017; Cutrone et al., 2019a). Finally, comb-like copolymers consisting of polysaccharides grafted with moieties able to coordinate to the nanoMOFs and PEG chains were synthesized and anchored onto the nanoMOFs (Cutrone et al., 2019b). However, all these coatings imply sophisticated chemistry strategies and/or several preparation steps, which might restrict their further applications. Moreover, all the PEGylated (macro) molecules used in the previous studies are not approved by Food and Drug Administration (FDA).

In this context, we propose to engineer for the first time PEGylated coatings on nanoMOFs by using only FDA-approved materials using a convenient one-step method. To date, Doxil R and Onivyde R represent the only FDA-approved PEGylated NPs (Barenholz, 2012), where DSPE-PEG 2000 (1,2-distearoyl-*sn*-glycero-3-phosphoethanolamine-N-[amino (polyethylene glycol)-2000] sodium salt) were used in both cases. Herein, DSPE-PEG 2000 was used in combination with DOPC (1,2-dioleoyl-*sn*-glycero-3-phosphocholine) to functionalize the surface of iron trimesate MOFs (**Figure 1** lower panel). Moreover, we show that the PEG-based coating have an impact on both drug release and nanoMOFs degradation, which was not the case with the coatings used so far. Finally, the coatings were able not only to reduce macrophage uptake *in vitro* but also to kill cancer cells.

MATERIALS AND METHODS

Materials

Iron (III) chloride hexahydrate (98%) was purchased from Alfa Aesar (Schiltigheim, France). 1,3,5-benzenetricarboxylic acid (BTC, 95%) and absolute ethanol (99%) were from Sigma-Aldrich (Saint-Quentin-Fallavier, France). These materials were used for the synthesis of nanoMOFs. Amoxicillin (Amox) from Sigma-Aldrich (Saint-Quentin-Fallavier, France) and 2′,2′-difluorodeoxycytidine monophosphate (Gem-MP) from Toronto Research Chemicals (North York, Canada) were the drugs used in this study. 1,2-dioleoyl-sn-glycero-3-phosphocholine (DOPC) and (1,2-distearoyl-*sn*-glycero-3-phosphoethanolamine-N-[amino(polyethylene glycol)-2000] sodium salt (DSPE-PEG 2000) were ordered from Avanti Polar Lipids (Alabama, United States) as coating materials. 3-(4,5-Dimethyl-2-thiazolyl)-2,5-diphenyl-2H-tetrazolium bromide (MTT, Sigma-Aldrich, Oslo, Norway) was used for toxicity evaluation of nanoMOFs. All the chemicals were used without further purification.

Cell Culture

Murine macrophage cell line J774A.1, *CelluloNet biobank BB-0033-00072*, were grown in RPMI-1640 medium (Thermo Fisher Scientific, Villebon-sur-Yvette, France) supplemented with 10% v/v decomplemented fetal bovine serum (FBS, Thermo Fisher Scientific, Villebon-sur-Yvette, France), 1% L-Gluthamine (Sigma-Aldrich, Oslo, Norway), and 1% (P/S, Sigma-Aldrich, Oslo, Norway) at 37°C in humidified air containing 5% CO_2. SKOV3 ovarian cancer cell were cultivated in a RPMI-1640 media without phenol red supplemented with 10% FBS, 5% L-Gluthamine and 5% penicillin/streptomycin (P/S) at 37°C in a 5% CO_2 humidified atmosphere.

Synthesis and Characterization of MIL-100(Fe) NanoMOFs

Iron trimesate nanoMOFs was synthesized by microwave assisted hydrothermal reaction as previously described [6]. Briefly, 20 mL of aqueous mixture containing 6.0 mM of iron chloride hexahydrate and 4.02 mM of trimesic acid (TA, 1,3,5-benzenetricarboxylic acid) was heated at 130°C for 6 min under stirring. The reaction was carried out with the power of 1600 W (Mars-5, CEM, United States). The as-synthesized nanoMOFs were harvested by centrifugation (10,000 *g*, 15 min) and washed with absolute ethanol to remove the excessive TA until the supernatant became colorless. NanoMOFs were stored in ethanol at room temperature for further usage at the concentration of 18.2 mg/mL.

SEM images were acquired on a Zeiss SUPRA 55 VP field emission gun scanning electron microscope fitted with an EDAX EDS analytical system. It was set to a low voltage (1 kV) and low current (a few pA) in order not to damage the samples and to avoid any conductive coating that could bother direct observation of the samples. Secondary electron type detector was used to record the images.

Dynamic light scattering (DLS) measurements were performed at 25°C on a Malvern Zetasizer Nano-ZS instrument at 90° angle. The mean hydrodynamic diameter of the particles was determined in a diluted aqueous suspension at 50 μg/mL.

Nanoparticle tracking analysis (NTA) was performed on Malvern NanoSight (LM10 Instrument, Malvern Instruments Ltd., Orsay, France), which combines a conventional optical microscope with a laser to illuminate the NPs in Brownian motion. It is used to individually follow nanoMOFs to gain insight into their size distribution and concentration.

Zeta potential (ZP) of nanoMOFs were measured at 25°C using a Zetasizer Nano-ZS instrument at different pH ranging from 3 to 10. NanoMOFs was diluted to 100 μg/mL with 1 mM KCl. Measured electrophoretic mobilities were converted to zeta potential values according to the Smoluchowski equation. Nitrogen sorption measurements were performed on a Micromeritics Instruments ASAP 2020 at 77 K. Samples were degassed at 100°C for 15 h. BET surface area was calculated in the partial pressure range of 0.05 – 0.20 P/P_0.

Drug Encapsulation in NanoMOFs

Drugs (Gem-MP and Amox) were loaded within nanoMOFs simply by impregnation of drug(s) aqueous solutions and nanoMOFs. Practically, nanoMOFs suspension (1.0 mg) were centrifuged for 10 min at 10,000 *g* and re-suspended in 1 mL of aqueous drug solutions (0.125 ∼ 1 mg/mL for Amox and 0.08 ∼ 0.2 mg/mL for Gem-MP) or water as a control. Different drug concentrations were used to optimize the drug encapsulation. After incubation at room temperature under gentle stirring for several hours (12 h for Amox and 4 h for Gem-MP), the nanoMOFs were recovered by centrifugation at 10,000 *g* for 10 min. The non-encapsulated drug in the supernatant was quantified by adapting previously described High Performance Liquid Chromatography (HPLC) methods (Li et al., 2019a,b). Specifically, HPLC analysis was performed on an Agilent system using a tunable UV absorbance detector. The injection volume of AMOX was 10 μL followed by eluant flow at a rate of 0.5 mL/min through a C18 Silica column (4.6 × 250 mm, 5 μm; Phenomenex) maintained at 30°C. The mobile phase consisted of 30% (v/v) methanol containing 5.2 mg/mL of sodium dihydrogene phosphate monohydrate. The pH was adjusted to 5 using phosphoric acid solution. AMOX were detected at 247 nm and retention times were 4.6 min. Similarly, Gem-MP was detected using the same Agilent system and column. The mobile phase was composed of 84% buffer [0.2 M (TEAA)]: 16% methanol. It was detected at 254 nm with an injection volume of 10 μl. The drug payload was calculated as Equation (1):

$$Payload\ \ (\%) = \frac{Encapsulated\ \ Drug(mg)}{nanoMOFs(mg)} \times 100 \qquad (1)$$

Surface Modification of NanoMOFs With DOPC Lipids and PEG-Lipid Conjugates

Surface modification was performed using a "green" method. To prepare DOPC coated nanoMOFs, 60 μl of nanoMOFs were mixed with 40 μl of DOPC alcoholic solution containing 100 μg of DOPC. Subsequently, 900 μl of water were rapidly added using an electronic pipette. The weight ratio between DOPC and nanoMOF was in the range of 1:20 ∼ 1:1. In the case of PEG-lipid conjugates coated nanoMOFs, 20 wt% of DOPC was replaced by DSPE-PEG 2000.

Characterization of Lipid Coated NanoMOFs

Lipid Quantification

DOPC quantification was performed by a colorimetric, enzymatic method (BIOLABO, Maizy, France) which is commonly used to determine the phospholipid amount in serum. This titration is based on the assay of the choline moiety of phospholipids. To do this, 10 μL of specimens or a standard solution were mixed with the reagents in the BIOLABO titration kit. The mixtures were stirred 10 min. at 37°C. Then, the absorbance at 500 nm of all samples was measured. The DOPC concentration was finally calculated as Eq. (2):

$$\begin{aligned} &DOPC\,concentration = \\ &Standard\,concentration \times \frac{Abs(specimen)}{Abs(standard)} \times 100 \qquad (2)\end{aligned}$$

NPs Concentration Measurements by NP Tracking Analysis (NTA)

The concentration of nanoMOFs modified with DOPC or PEG-lipid conjugates at different weight ratios was investigated by Nanosight (LM10 Instrument, Malvern Instruments Ltd., Orsay, France), which combines a conventional optical microscope with a laser to illuminate the NPs in Brownian motion. Of main interest here, the size distribution and concentration could be determined simultaneously. Results are expressed as means of five independent measurements.

Colloid Stability Characterization by DLS

The colloid stability of the nanoMOFs before and after lipid surface modification was monitored in water every day during 3 weeks' storage at 4°C. The stability in biological medium, including cell culture medium and phosphate buffer saline (PBS) used in this study, was also measured at 0, 0.5, 1, 2, 4, 6, and 8 h after incubation at 37°C.

Drug Release and Degradation of nanoMOFs

Drug release was performed in PBS of different concentrations at 37°C. Briefly, drug loaded nanoMOFs were centrifuged at 10,000 *g* for 10 min and the pellet was re-dispersed in 1 mL water by vortex. Aliquots of 100 μL were taken and mixed with 900 μl of the media used for release. The final concentration of PBS was 1, 3, and 6 mM and nanoMOFs of 2.0 mg/mL. After different incubation times (30 min, 1 h, 2 h, 4 h, 6 h and 24 h), the suspensions were centrifuged and the supernatants were assessed by HPLC as previously described to determine the amount of released drug. Moreover, the trimesate release was also evaluated by HPLC. Briefly, trimesate was analyzed with a mobile phase consisting of 90% buffer (5.75 g/L of $NH_4H_2PO_4$): 10% Acetonitrile containing 5 mM TBAP. The injection volume was 5 μl and the detection wavelength was set at 220 nm.

Human Plasma Protein Adhesion Tests

Human serum albumin (HSA) was used in this study. NanoMOFs modified or not (300 μg/mL) were incubated with HSA at 100 μg/mL in 10 mM phosphate buffer at 37°C. The samples were centrifuged at 10,000 *g* for 5 min to remove the nanoMOFs after 1, 2, 4, 6, 8 and 12 h incubation. The excessive amounts of HSA in the supernatant were quantified using a bicinchoninic acid (BCA) assay.

NanoMOF Internalization in Macrophage

NanoMOF internalization was quantified by Inductively Coupled Plasma Mass Spectrometry (ICP-MS). Macrophage cells (J774A.1) were seeded at a density of 2.0×10^5 cells per well in 24-well plates. Cells were cultured at 37°C in 5% CO_2 overnight for attachment. Cells were then incubated with 1 mL cell culture media containing nanoMOFs coated or not with lipids (nanoMOF concentration = 50 μg/mL). At the end of the 4 h incubation, the cells were washed with PBS for three times to eliminate the excess of MOFs. Cells were finally dried and digested using aqua regia (15 min under ultrasonic bath), Fe quantification was performed using an ICP-MS equipped with a triple quadrupole (Agilent 8800, Agilent Technologies, Japan). Fe and Co were added as internal standard on samples and calibration standards solution at a concentration of 10 μg/L. Isotopes were detected using "on-mass mode" ($^{54}Fe^+$, $^{56}Fe^+$, $^{59}Co^+$). Helium was introduced into the collision/reaction cell at a flow rate of 3 mL/min. Dwell time for each of the targeted isotopes was 1 s. Fe was quantified using external calibration prepared using certified 1000 mg/L Fe standard solution (Merck, Germany). Operation conditions were daily optimized using a tuning solution.

Cytotoxicity Assessment

MTT assays were carried out on SKOV3 ovarian cancer cell line to investigate the cytotoxicity of NPs. The cells were plated in 96 well plates at a concentration of 10,000 cells per well. The media was removed after 24 h incubation and replaced by fresh media containing the MOFs nanoparticles at different concentrations. The cytotoxicity was assessed by MTT assay at 24, 48 and 72 h following the incubation of the cells with the MOFs. In brief, 100 μL of complete media containing 0.5 mg/mL of MTT were added to cells and incubated for 2 h at 37°C in a 5% CO_2 humidified atmosphere. Subsequently, the MTT media were removed and replaced by 100 μL of DMSO per well to dissolve the MTT-formazan crystals. The plates were shaken for 10 min at 350 rpm in a Heidolph Titramax 101 orbital shaker, and the absorbance at 595 nm was measured with the Tecan spark M10 plate reader. Each MTT experiment was reproduced three times.

RESULTS AND DISCUSSION

MIL-100 (Fe) nanoMOF Surface Modification and Characterization of Functionalized NanoMOFs

Iron trimesate nanoMOFs with mean diameters of 232 ± 14 nm and Brunauer–Emmett–Teller (BET) surface areas of 1519 ± 50 $m^2.g^{-1}$ were successfully synthesized by a "green" organic solvent-free hydrothermal method exempt of toxic additives such as hydrofluoric acid (Agostoni et al., 2013). They were crystalline and exhibited a facetted morphology (**Figure 2A**) in agreement with previously reported data (Cutrone et al., 2019a,b).

In an attempt to achieve "stealth" NPs, the as-synthesized nanoMOF were surface functionalized with PEG-lipid conjugates in a one-step procedure using a mixture of DSPE-PEG 2000 and DOPC. Lipids were associated within less than 2 min at room temperature by dispersing the nanoMOFs in an ethanolic aqueous solution containing both DSPE-PEG 2000 and DOPC, followed by a quick addition of water to favor lipid deposition onto the nanoMOF surface. Indeed, lipids were freely soluble in ethanol/water mixtures, but they readily precipitated upon progressive addition of water which drastically reduced their solubility, leading to precipitation onto the nanoMOF surfaces (Wuttke et al., 2015). DOPC-coated nanoMOFs were prepared as controls using the same method. The bare and coated nanoMOFs were characterized by a set of complementary methods.

Firstly, SEM images show that the lipid-coated nanoMOFs displayed similar shapes but with more rounded edges (**Figure 2B**) as compared to the uncoated ones (**Figure 2A**), possibly because surface modification. No significant differences were observed for the coated nanoMOFs with or without PEG-lipid conjugates (**Figure 2C**). Secondly, EDX experiments were performed to detect the presence of elements specific to the MOF cores (C, O, Fe) and to the shells (C, O, N) in the top layers of the NPs (around 10 nm depth). The presence of the DOPC coating was evidenced by the detection of an N peak characteristic of DOPC which was not found with bare nanoMOFs (**Supplementary Figure S1**). Interestingly, in the PEG shells obtained with the lipid mixtures, the relative O content was increased by a factor of 4 as compared to DOPC coatings (**Supplementary Figure S1**) possibly due to the presence of PEG chains in the nanoMOFs' top layers, as PEG has the highest O content from all the nanoMOF components. These data offer a straightforward proof for both the presence of DOPC and PEG-lipid conjugates in the nanoMOF top layers.

The amount of DOPC in the nanoMOFs was quantified by using a colorimetric enzymatic method. For this, the DOPC:nanoMOF weight ratio in the preparation procedure was varied from 1:20 to 1:1. As shown in **Figure 3A**, the amount of lipids associated to the nanoMOFs increased with the amount of lipids used in the coating procedure. A plateau was reached at a DOPC: nanoMOF weight ratio of 1:3, corresponding to 25 ± 4 wt% lipids associated to the nanoMOFs. These quantities of coating material are among the highest reported so far (Horcajada et al., 2010; Agostoni et al., 2015; Bellido et al., 2015; Hidalgo et al., 2017; Giménez-marqués et al., 2018; Cutrone et al., 2019a,b). As comparison, phosphorylated cyclodextrin (CD-P) coatings on same iron trimesate nanoMOFs reached ∼ 17 wt% (Agostoni et al., 2015). The important lipid association could be possibly due to: i) the fast precipitation of lipids at the hydrophobic surface of nanoMOFs, and ii) the strong affinity of the phosphate groups in the lipids for the iron sites at the nanoMOFs' surface.

The nanoMOFs, coated or not, were characterized by a set of complementary methods. First, X-ray powder diffraction

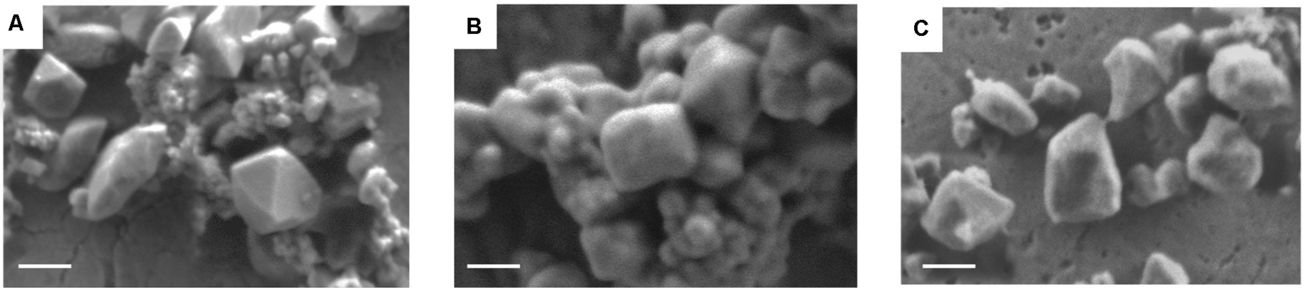

FIGURE 2 | Representative scanning electron microscope (SEM) images of nanoMOFs before and after lipid modification. **(A)** nanoMOFs; **(B)** nanoMOFs after modification with DOPC; **(C)** nanoMOFs after modification with DOPC and DSPE-PEG 2000. Scale bar: 100 μm.

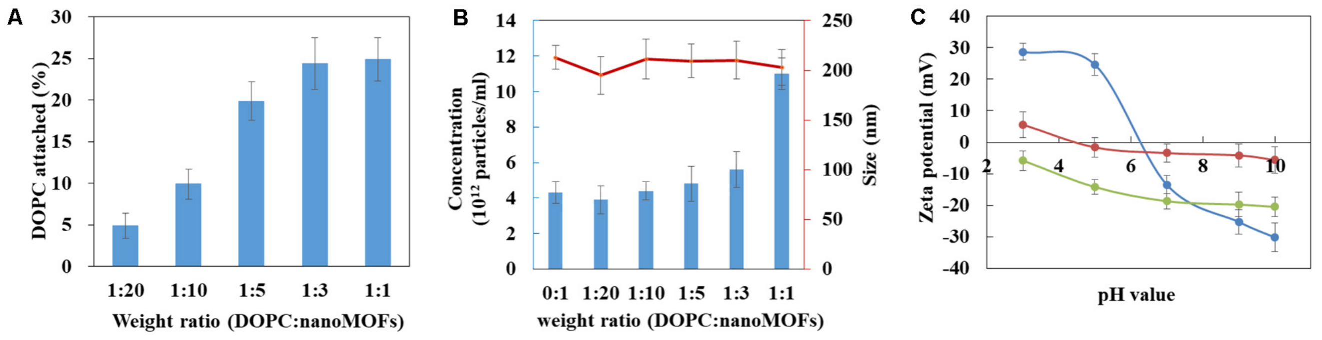

FIGURE 3 | Characterization of lipid-coated nanoMOFs. **(A)** Quantification of the amount of DOPC in the nanoMOFs; **(B)** Mean hydrodynamic diameter (red) and concentration (blue) of DOPC-coated nanoMOFs determined by NTA. **(C)** Zeta potential of nanoMOFs as a function of pH before (blue) and after lipid coating with (red) or without (green) the addition of DSPE-PEG 2000.

(XRPD) showed that the crystalline structure of the nanoMOFs was preserved after surface modification (**Supplementary Figure S2**). Dynamic light scattering (DLS) proved that there were no significant differences between the mean hydrodynamic diameters of nanoMOFs before and after surface functionalization (232 ± 14 nm, 241 ± 17 nm and 238 ± 11 nm for uncoated nanoMOFs, lipid coated nanoMOFs at a DOPC: nanoMOF weight ratio of 1:3, with and without DSPE-PEG 2000, respectively). Moreover, the BET surface areas were not affected by surface modification with lipids (1519 ± 50 $m^2.g^{-1}$, 1486 ± 70 $m^2.g^{-1}$, and 1547 ± 80 $m^2.g^{-1}$ for uncoated nanoMOFs, lipid coated nanoMOFs with and without DSPE-PEG 2000, respectively), suggesting that the bulky lipids were located onto the nanoMOF's external surfaces rather than into their porosity.

Before surface modification, the nanoMOF concentration was around (4 ± 0.8) × 10^{12} particles/mL, as determined by Nanoparticle Tracking Analysis (NTA). Interestingly, the nanoMOF particle concentration did not change upon modification with lipids (**Figure 3B**, blue histograms), suggesting that the lipids adhered at their surface and did not remain into the suspension medium. Indeed, at DOPC:nanoMOFs weight ratios from 0:1 up to 1:3, both particle concentrations and mean hydrodynamic diameters were unaffected [(5.6 ± 0.8) × 10^{12} particles/mL, and 210 ± 23 nm, respectively]. To support this hypothesis, DLS analysis of supernatants (**Supplementary Table S1**) after particle centrifugation revealed that they were devoid of any lipid vesicles (<1% particles free).

However, addition of excess lipids (weight DOPC:nanoMOF ratio of 1:1) resulted in a dramatic increase of total particle concentration [from (4 ± 0.8) × 10^{12} to (1.1 ± 0.4) × 10^{13} particles/mL], presumably because the nanoMOF surfaces were saturated with lipids. Of note, the mean hydrodynamic diameter of the nanoMOFs was unaffected, only the polydispersity index (PdI) increased from 0.15 to 0.25, possibly because of the presence of lipid vesicles in excess. Note that the association of DSPE-PEG 2000 didn't significantly influence the mean hydrodynamic diameter, nor the nanoMOF's concentration (less than 10% variations) suggesting that the PEGylated lipids also attached onto the nanoMOFs. In conclusion, lipids were associated up to 25 ± 4 wt% without inducing any changes in nanoMOF porosities, size distribution, and crystallinity.

Interestingly, the presence of the coatings affected the nanoMOFs electrophoretic mobility, as shown by Zeta potential (ZP) investigations in **Figure 3C**. Indeed, the ZP of the uncoated nanoMOFs was strongly dependent upon the pH of the suspension medium, shifting from positive values (+ 23 ± 3 mV) at pH lower than 5 to negative values (−15 ± 3 mV) at basic pH. This could be probably due to the presence of both uncoordinated iron sites and terminal carboxyl groups of the trimesate ligands at the external nanoMOFs surface (Cutrone et al., 2019b). The ZP values were dramatically altered after surface modification (**Figure 3C**). DOPC-coated nanoMOFs displayed negative ZP values (−6 to −20 mV) whatever the pH in the range of 3 to 10, in line with data reported for DOPC liposomes (Chibowski and Szcześ, 2016). These results support the presence of DOPC lipid layers onto the nanoMOFs which shield their charged surface moieties. Interestingly, when the nanoMOFs were surface-functionalized with PEG chains, their ZP values were shifted to neutral (–1.6 ± 3.4 mV). This is in good agreement with other studies on PEG-coated NPs (Gref et al., 1995; Thevenot et al., 2007; Troutier and Ladavière, 2007; Troutier-Thuilliez et al., 2009; Bugnicourt et al., 2019).

Effect of the Coatings on the Colloidal Stability of NanoMOFs in Biological Media

As the majority of uncoated NPs, nanoMOFs suffer from poor stability in biological media, which hampers their biomedical applications. **Figure 4** clearly shows that uncoated nanoMOFs undergo a fast aggregation in both phosphate buffer saline (PBS, pH = 7.4, 10 mM) and cell culture medium DMEM (Dulbecco's Modified Eagle Medium) without fetal bovine serum (FBS), with the mean hydrodynamic diameters rapidly increasing to more than 1 μm within only 6 h at 37°C (**Figure 4**). No significant variation was observed for the mean hydrodynamic diameter of uncoated nanoMOFs in water in the first 1 h, however, they tended to aggregate upon storage (**Supplementary Figure S3**). They were stable only in DMEM supplemented with 10% (v/v)

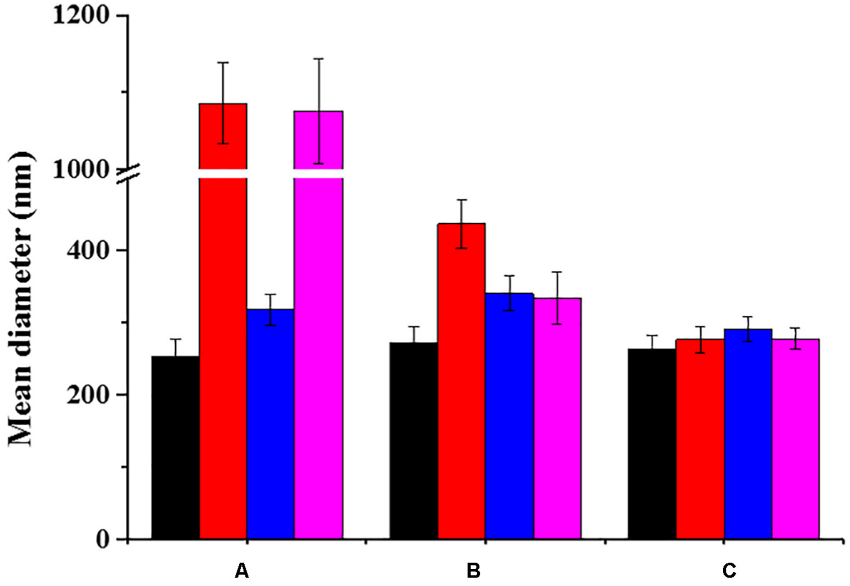

FIGURE 4 | Colloidal stability of nanoMOFs in different media, before **(A)** and after surface functionalization with DOPC **(B)** or PEG-lipid conjugates **(C)**. Mean hydrodynamic diameters of nanoMOF suspensions at 100 μg/mL were determined by DLS after 6 h incubation at 37°C. (Black: water; red: PBS; blue: DMEM supplemented with 10v/v% FBS; pink: DMEM without FBS).

FBS, possibly due to the formation of a protein corona at their surface preventing their aggregation (see section "Effect of surface functionalization of nanoMOFs on protein adsorption and macrophage uptake").

In contrast, DOPC coated nanoMOFs were stable both in water and DMEM. No aggregation was observed even after 3 weeks storage. However, they still underwent aggregation in PBS (**Figure 4**). Remarkably, PEGylation allowed circumventing stability issues, whatever the suspension media (less than 10% diameter variation in PBS).

As all the coated and uncoated nanoMOFs were stable in DMEM supplemented with 10% (v/v) FBS, it was possible to explore further their cytotoxicity and interactions with cancer cell lines and macrophages. The PEGylated nanoMOFs exhibited excellent colloidal stability in all the tested biological media and thus appeared as optimal candidates for biological applications.

Control of Degradation and Drug Release by Lipid Coating

There is a general agreement on the fact that once the nanomaterials release their drug cargo, they should degrade to avoid accumulation inside the body (Horcajada et al., 2012). However, Fe-based nanoMOFs are reported to degrade rapidly in the biological media, because of coordination of various ions (phosphates, sulfates, etc.) to their iron sites, sometimes leading to uncontrolled "burst" drug release (Agostoni et al., 2013; Li et al., 2017, 2019b). It was therefore interesting to investigate if the hydrophobic lipid coatings could interfere with the rapid penetration of the aqueous degrading media inside the pores, thus allowing gaining better control upon the release and degradation mechanisms.

Degradation of nanoMOFs is generally monitored by the release of the constituting ligand trimesate (Agostoni et al., 2013; Rodriguez-Ruiz et al., 2015; Li et al., 2017). The degradation of the lipid-coated or bare nanoMOFs was studied by assaying ligand trimesate by HPLC in PBS (**Figure 5A**). In PBS 1 mM, uncoated nanoMOFs (blue curve, **Figure 5A**) underwent a fast degradation in the first 1 h at 37°C with around 15.5 ± 1.1% trimesate released, in agreement with previous reports (Li et al., 2017). It was discovered that in the same conditions, the lipid-coated nanoMOFs, with (red curve, **Figure 5A**) or without PEG-lipids conjugates (green curve, **Figure 5A**), exhibited much slower degradation profiles than the uncoated nanoMOFs, with only 10 ± 0.2% trimesate release in the first 1 h. This suggests a more progressive diffusion of the phosphate ions into the coated nanoMOFs, slowing down their degradation. However, the same plateau was reached after 24 h incubation, corresponding to a total complexation of the phosphates in the medium (Li et al., 2017). In conclusion, the shell efficiently delayed the degradation process.

Then, the effect of lipid coatings on drug release was studied. Selected drug of interest was Gem-MP, a hydrophilic drug with low cell permeability. NanoMOFs acted as efficient "nanosponges", soaking Gem-MP from their aqueous solution with almost perfect efficiency (>98%). Maximal loadings reached 25 wt% reflecting the strong interaction between the drug and the iron trimesate matrices. Advantageously, the lipid coating process didn't induce any significant drug release (less than 3% variations before and after coating).

Gem-MP release is governed by a competition of coordination between the phosphate moieties in Gem-MP and free phosphates in PBS for the iron(III) Lewis acids

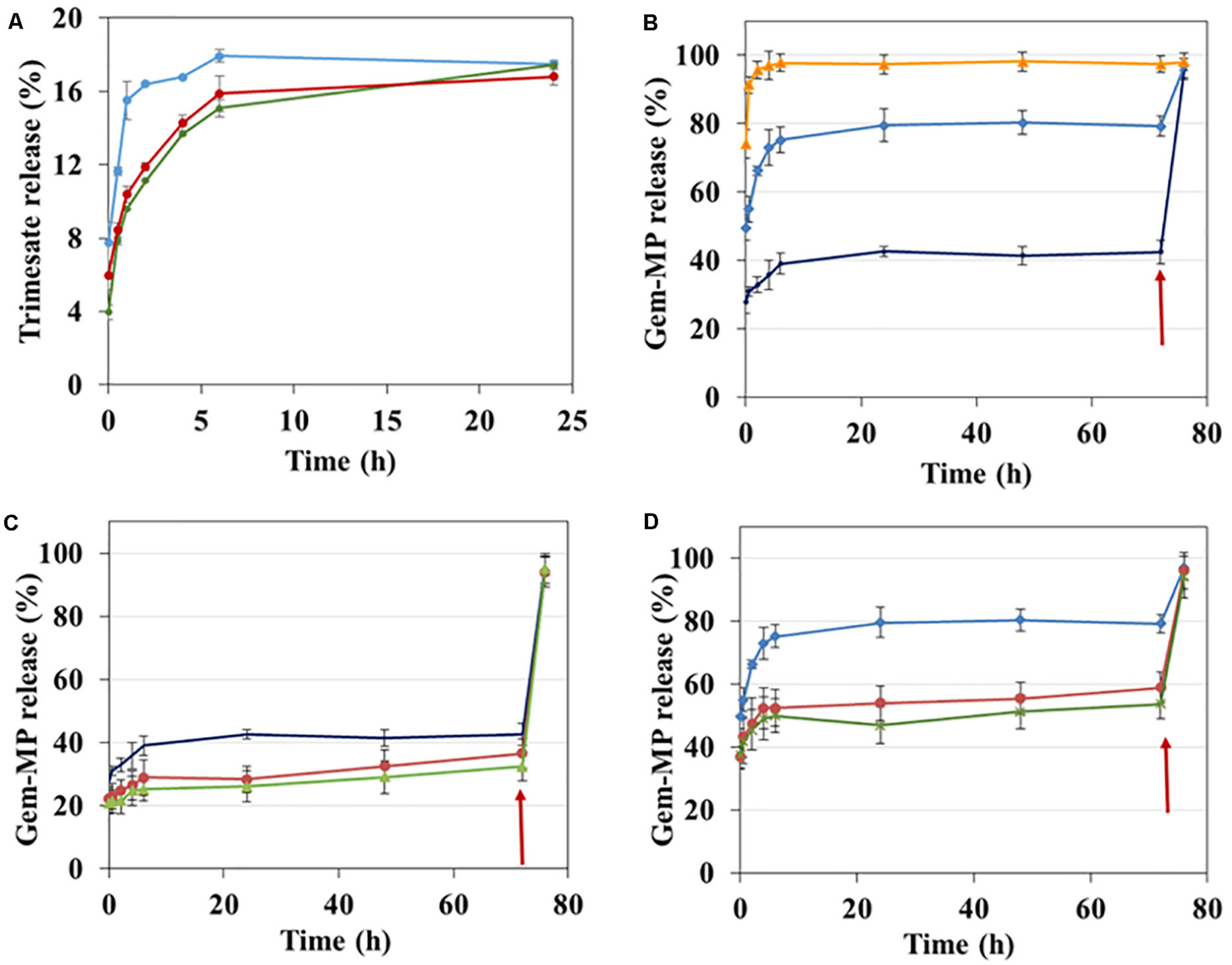

FIGURE 5 | Effect of surface modification on Gem-MP and trimesate release analyzed by HPLC. **(A)** Trimesate release in 1 mM PBS from nanoMOFs before (blue) and after lipid coating with (red) or without (green) coating with PEG-lipid conjugates after incubation at 37°C. **(B)** Gem-MP release from uncoated nanoMOFs in PBS with different molarities (orange: 6 mM, blue: 3 mM; dark blue: 1 mM). Gem-MP release in 1 mM **(C)** or 3 mM **(D)** PBS from nanoMOFs before (blue/dark blue) and after lipid coating with (red) or without (green) coating with PEG-lipid conjugates. In all cases **(B–D)**, phosphate concentration was adjusted to 10 mM after 72 h incubation at 37°C (red arrows), followed by further incubation for 4 h at 37°C.

of nanoMOFs (Agostoni et al., 2013, 2015; Rodriguez-Ruiz et al., 2015). As expected, it was found that the higher the amount of phosphates, the higher the amount of drug released (**Figure 5B**). At low phosphate concentrations (PBS 1 mM or 3 mM), a plateau (around 40% or 80% Gem-MP release) was reached in 24 h, when all the phosphate molecules present in the release medium were complexed to the iron sites, as previously reported (Agostoni et al., 2013, 2015; Rodriguez-Ruiz et al., 2015). When additional phosphates were added in the release medium, all the drug still remaining in the nanoMOFs was immediately released (**Figure 5B**, arrow). Gem-MP release was well correlated with particle degradation, resulting in trimesate release (**Supplementary Figure S4**).

The presence of the lipid coating reduced the drug release from the nanoMOFs (**Figure 5C**). For instance, after 6 h incubation in PBS 1 mM, around 30% Gm-MP was released from the coated nanoMOFs, in comparison to 40% with the uncoated ones. This is possibly due to the restricted diffusion of phosphates into the nanoMOFs because of the lipid coating. Similarly, after 6 h incubation in PBS 3 mM, around 50% Gem-MP was released from the coated nanoMOFs, in comparison to 78% with the uncoated ones (**Figure 5D**). The Gem-MP release from coated nanoMOFs gradually increased in a sustained manner in the following days (**Figures 5C,D**). All the remained drugs could be released out after 4 h incubation in concentrated phosphate buffer (10 mM PBS).

Similar results were found with another drug, amoxicillin (Amox). The amount of Amox released in the first hour of incubation release was reduced by a factor of two in the case of lipid-coated nanoMOFs as compared to the naked ones (**Figure 6A**), confirmed by different dilution factors at 10, 20, and 40 (**Figure 6B**). However, in the presence of strongly

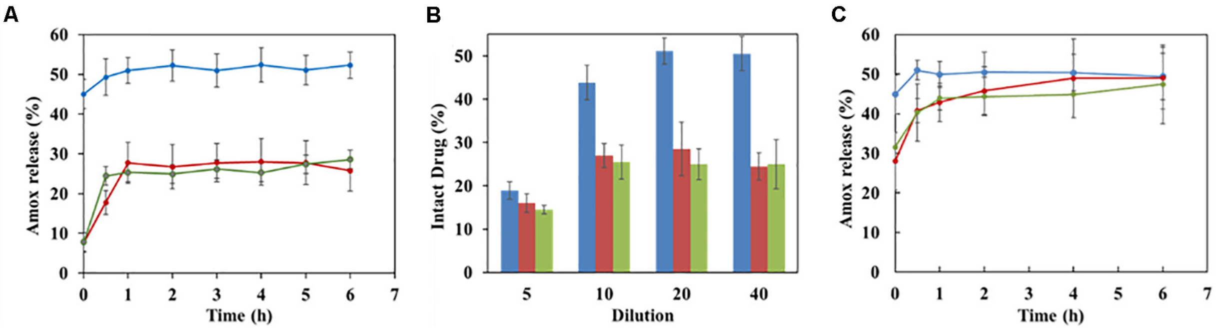

FIGURE 6 | Effect of coating on Amox release in water **(A,B)** and in PBS **(C)**. **(A)** Release kinetics of Amox in water from nanoMOFs (1 mg/mL) before or after coating, with a dilution factor of 20; **(B)** Effect of dilution factor on Amox release after 4 h incubation at 37°C in water (Blue: uncoated nanoMOFs; red: DOPC coated nanoMOFs; Green: DOPC and PEG-lipid conjugate coated nanoMOFs).

complexing phosphates, the degradation was only delayed, but not avoided (**Figure 6C**).

Cytotoxicity Assays of nanoMOFs on Ovarian Cancer Cells

All the studied nanoMOFs were non-toxic for the SKOV3 ovarian cancer cells up to 100 μg/mL (**Figure 7A**, blue histograms), with more than 98% cell viability in 24 h, which is in agreement with the previously reported lack of toxicity of these materials (Horcajada et al., 2010; Baati et al., 2013; Bellido et al., 2015; Giménez-marqués et al., 2018; Li et al., 2019b). In contrast, as expected, the anticancer drug Gem-MP (20 μg/mL, **Figure 7A**, brown histograms) exerted a cytotoxic effect with 45% cell viability after 48 h incubation, which further diminished to 29% in 72 h. Remarkably, Gem-MP loaded nanoMOFs showed a strong *in vitro* activity on SKOV3 ovarian cancer cells, higher than the free drug (**Figure 7**). At equivalent Gem-MP concentrations, whatever the drug loading (8 or 20 wt%) and the amount of nanoMOF in contact with the cells (10 to 100 μg/mL), the drug-loaded nanoMOFs outperformed the free drug in terms of toxicity on cancer cells (**Figure 7** and **Supplementary Figure S5**).

This is in line with previous studies showing the efficient internalization of nanoMOFs bearing or not a lipid coating in pancreatic, breast, or bladder cancer cell lines (Rodriguez-Ruiz et al., 2015; Wuttke et al., 2015; Li et al., 2019a). It was recently shown that nanoMOFs acted as "Trojan horses" internalized by cancer cells, carrying their Gem-MP cargo to interfere with DNA (Li et al., 2019a). In this study it was shown that interestingly, the presence of a lipid coating (PEGylated or not) did not reduce the nanoMOF anticancer efficacy on SKOV3 ovarian cancer cells.

Effect of Surface Functionalization of NanoMOFs on Protein Adsorption and Macrophage Uptake

It is well known that intravenously administered NPs are readily covered by plasma proteins, creating the so-called "protein corona", which plays a crucial role on the NPs' biodistribution and *in vivo* fate (Gref et al., 2000). To gain insight on the influence of lipid coating of nanoMOFs on protein adsorption, HSA (human serum albumin), the most abundant protein in human blood plasma, was selected for this study.

NanoMOFs coated or not with DOPC lipids and PEG-lipid conjugates were incubated for 4 h at 37°C with HSA. After separation of the supernatants by centrifugation, the amount of non-adsorbed HSA was quantified using a BCA titration in order to determine the adsorbed HSA amounts onto nanoMOFs, lipid-modified or not. These amounts, expressed as μg/mg of nanoMOFs, are reported in **Figure 8A**. In the case of uncoated nanoMOFs (**Figure 8A**, blue curve), the amount of adsorbed HSA reached a plateau within 6 h, with around 50 μg HSA/mg nanoMOFs. Interestingly, lipid coating dramatically reduced HSA adsorption, to only ∼5 μg HSA/mg nanoMOFs (**Figure 8A**, green curve), regardless of the addition of DSPE-PEG 2000 (**Figure 8A**, red curve). To the best of our knowledge, these adsorbed HSA amounts are among the lowest reported with MIL-100 (Fe) nanoMOFs (Gref et al., 2000; Cutrone et al., 2019b), suggesting that lipid-based coating on nanoMOFs is efficient to avoid albumin adsorption.

The potential "stealth" effect of the lipid-coated nanoMOFs, PEGylated or not, was evaluated on the murine macrophage cell line J774. Quantitative data on the amounts of nanoMOFs internalized by cells were obtained by ICP-MS, after extensive washing to remove the non-associated particles. An incubation time of 4 h was chosen as it corresponds to the typical blood circulation time of PEG-coated NPs (Cutrone et al., 2019b). Interestingly, the DOPC coating of nanoMOFs reduced their macrophage uptake by a factor of 2.4, from 75 ± 6% to 31 ± 3% (**Figure 8B**). The nanoMOF functionalization with PEG chains was even more effective, reducing their interactions with macrophage to 21 ± 2%. Despite these great *in-vitro* results, it is widely known that numerous complex interactions can occur after NP administration in multicellular organisms. Therefore, *in vivo* studies need to be carried on to demonstrate the efficacy of the PEG coating to reduce reticuloendothelial system (RES) uptake.

Nevertheless, it has to be noted that, in similar experimental conditions, other coating materials showed higher interactions with macrophages, for instance, 41 ± 3% for CD-P coating, and

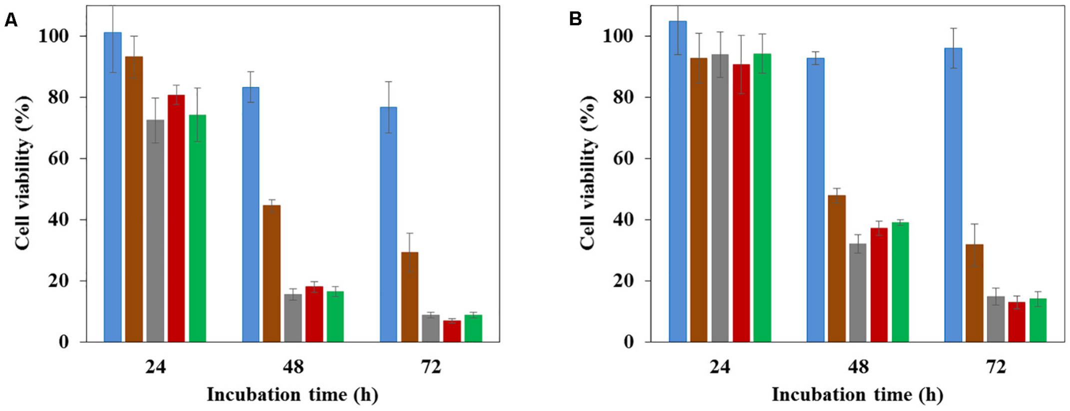

FIGURE 7 | Cytotoxcity measured by MTT assays of nanoMOFs (blue), anticancer efficacy of Gem-MP (brown), Gem-MP loaded nanoMOFs before (gray) and after coating with DOPC (red) or PEG-lipid conjugates (green). The experiments were performed on SKOV3 ovarian cancer cells, at different incubation times, with different concentrations nanoMOFs. **(A)** 100 µg/mL; **(B)** 30 µg/mL. Gem-MP loading was 20 wt%.

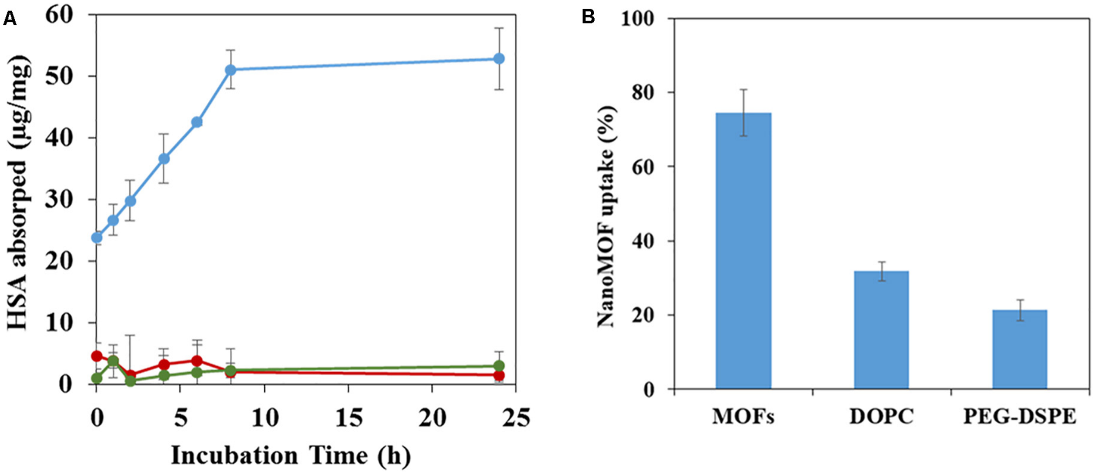

FIGURE 8 | HSA adsorption assayed by BCA assay **(A)** and J774 murine macrophage uptake **(B)** of nanoMOFs before and after lipid surface functionalization. **(A)** HSA adsorption by nanoMOFs before (blue) and after lipid coating with (red) or without (green) the addition of DSPE-PEG 2000. **(B)** NanoMOFs (before and after lipid coating, with or without addition of DSPE-PEG 2000) internalization inside murine macrophage J774 cells. 50 µg/mL nanoMOFs were incubated with 3 × 10^5 J774 cells for 4 h, and the amount of internalized nanoMOFs was determined by ICP-MS and expressed as a% of the initial nanoMOF amount in contact with the cells. Significant difference was observed for nanoMOFs before and after surface modification ($p < 0.01$).

39 ∼ 24% for comb-like copolymers (Cutrone et al., 2019a,b). The advantage of lipid coating, demonstrated in this work, is a straightforward method, leading to efficient and stable coatings based on already FDA-approved materials. Lipid coatings on NPs are considered to be a promising strategy for the treatment of severe pathologies such as cancer (Luchini and Vitiello, 2019). In this study, the lipid coating not only afforded a control upon cell interaction but also provided a biocompatible protective barrier, modulating drug release and nanoMOF degradation. Of note, the nanoMOFs used in this study were shown to be biocompatible after intravenous administration in rats (Baati et al., 2013). However, the biocompatibility of the supermolecules assembled resulting from nanoMOFs coating with lipids has to be demonstrated *in vivo*.

CONCLUSION

The surface of iron trimesate nanoMOFs was successfully modified with FDA approved DSPE-PEG 2000 in combination with DOPC by a fast solvent-exchange deposition method. We described herein the preparation and comprehensive characterization of the lipid modified NPs. We showed, for the first time, that the lipid surface modification of porous nanoMOFs reduced their tendency to degrade rapidly in PBS. Moreover, the coating of nanoMOFs with PEG-lipid conjugates successfully decreased their uptake by macrophages *in vitro* by a factor of 3.6. Finally, nanoMOFs acted as “Trojan horses” internalizing inside the cancer cells, and carrying their Gem-MP cargo to interfere with DNA.

DATA AVAILABILITY STATEMENT

The datasets generated for this study are available on request to the corresponding author.

AUTHOR CONTRIBUTIONS

RG conceived the study. RG, XL, and GS designed the experiments. XL, GS, and JQ preformed the experiments. CL contributed to the lipid investigations. XL and RG wrote the manuscript. MM, KB, and TT contributed to the biological evaluations. All authors approved the submitted version.

FUNDING

Financial support for this work was provided the French National Research Agency (ANR-14-CE08-0017 and ANR-16-CE18-0018) and Euronanomed III (project PCInano). This work was also supported by a public grant overseen by the French National Research Agency as part of the "Investissements d'Avenir" program (Labex NanoSaclay, ANR-10-LABX-0035).

ACKNOWLEDGMENTS

We acknowledge Dr. B. Moreira-Alvarez and Dr. J. R. Encinar for their kind help with ICP-MS analysis. We also thank Dr. D. Constantin for help with XRPD experiments.

SUPPLEMENTARY MATERIAL

The Supplementary Material for this article can be found online at: https://www.frontiersin.org/articles/10.3389/fbioe.2020.01027/full#supplementary-material

REFERENCES

Agostoni, V., Chalati, T., Horcajada, P., Willaime, H., Anand, R., Semiramoth, N., et al. (2013). Towards an improved anti-HIV activity of NRTI via Metal-Organic Frameworks nanoparticles. *Adv. Healthc. Mater.* 2, 1630–1637. doi: 10.1002/adhm.201200454

Agostoni, V., Horcajada, P., Noiray, M., Malanga, M., Aykaç, A., Jicsinszky, L., et al. (2015). A "green" strategy to construct non-covalent, stable and bioactive coatings on porous MOF nanoparticles. *Sci. Rep.* 5:7925. doi: 10.1038/srep07925

Aykac, A., Noiray, M., Malanga, M., Agostoni, V., Casas-Solvas, J. M., Fenyvesi, E., et al. (2017). A non-covalent "click chemistry" strategy to efficiently coat highly porous MOF nanoparticles with a stable polymeric shell. *BBA Gen. Subj.* 1861, 1606–1616. doi: 10.1016/j.bbagen.2017.01.016

Baati, T., Njim, L., Neffati, F., Kerkeni, A., Bouttemi, M., Gref, R., et al. (2013). In depth analysis of the in vivo toxicity of nanoparticles of porous iron(iii) metal-organic frameworks. *Chem. Sci.* 4, 1597–1607. doi: 10.1039/c3sc22116d

Barenholz, Y. (2012). Doxil® - The first FDA-approved nano-drug: lessons learned. *J. Control. Release* 160, 117–134. doi: 10.1016/j.jconrel.2012.03.020

Bellido, E., Hidalgo, T., Lozano, M. V., Guillevic, M., Simón-Vázquez, R., Santander-Ortega, M. J., et al. (2015). Heparin-engineered mesoporous iron Metal-Organic Framework nanoparticles: toward stealth drug nanocarriers. *Adv. Healthc. Mater.* 4, 1246–1257. doi: 10.1002/adhm.201400755

Bouffard, D. Y., Laliberté, J., and Momparler, R. L. (1993). Kinetic studies on 2',2'-difluorodeoxycytidine (gemcitabine) with purified human deoxycytidine kinase and cytidine deaminase. *Biochem. Pharmacol.* 45, 1857–1861. doi: 10.1016/0006-2952(93)90444-2

Bugnicourt, L., Peers, S., Dalverny, C., and Ladavière, C. (2019). Tunable morphology of lipid/chitosan particle assemblies. *J. Colloid Interface Sci.* 534, 105–109. doi: 10.1016/j.jcis.2018.08.098

Chibowski, E., and Szcześ, A. (2016). Zeta potential and surface charge of DPPC and DOPC liposomes in the presence of PLC enzyme. *Adsorption* 22, 755–765. doi: 10.1007/s10450-016-9767-z

Cutrone, G., Li, X., Casas-Solvas, J. M., Menendez-Miranda, M., Qiu, J., Benkovics, G., et al. (2019a). Design of engineered cyclodextrin derivatives for spontaneous coating of highly porous Metal-Organic Framework nanoparticles in aqueous media. *Nanomaterials* 9, 1–26. doi: 10.3390/nano9081103

Cutrone, G., Qiu, J., Menendez-Miranda, M., Casas-Solvas, J. M., Aykaç, A., Li, X., et al. (2019b). Comb-like dextran copolymers: a versatile strategy to coat highly porous MOF nanoparticles with a PEG shell. *Carbohydr. Polym.* 223:115085. doi: 10.1016/j.carbpol.2019.115085

Giménez-marqués, M., Bellido, E., Berthelot, T., Simón-yarza, T., Hidalgo, T., Simón-vázquez, R., et al. (2018). GraftFast surface engineering to improve MOF nanoparticles furtiveness. *Small* 14, 1–11. doi: 10.1002/smll.201801900

Gref, R., Domb, A., Quellec, P., Blunk, T., Müller, R. H., Verbavatz, J. M., et al. (1995). The controlled intravenous delivery of drugs using PEG-coated sterically stabilized nanospheres. *Adv. Drug Deliv. Rev.* 16, 215–233. doi: 10.1016/0169-409x(95)00026-4

Gref, R., Lück, M., Quellec, P., Marchand, M., Dellacherie, E., Harnisch, S., et al. (2000). "Stealth" corona-core nanoparticles surface modified by polyethylene glycol (PEG): Influences of the corona (PEG chain length and surface density) and of the core composition on phagocytic uptake and plasma protein adsorption. *Colloids Surfaces B Biointerfaces* 18, 301–313. doi: 10.1016/s0927-7765(99)00156-3

Gref, R., Minamitake, Y., Peracchia, M. T., Trubetskoy, V., Torchilin, V., and Langer, R. (1994). Biodegradable long-circulating polymeric nanospheres. *Science* 263, 1600–1603. doi: 10.1126/science.8128245

He, C., Liu, D., and Lin, W. (2015). Nanomedicine applications of hybrid nanomaterials built from Metal-Ligand Coordination bonds: Nanoscale Metal-Organic Frameworks and Nanoscale Coordination Polymers. *Chem. Rev.* 115, 11079–11108. doi: 10.1021/acs.chemrev.5b00125

Hidalgo, T., Bellido, E., Avila, J., Asensio, M. C., and Salles, F. (2017). Chitosan-coated mesoporous MIL-100 (Fe) nanoparticles as improved bio-compatible oral nanocarriers. *Sci. Rep.* 100, 1–14. doi: 10.1038/srep43099

Horcajada, P., Chalati, T., Serre, C., Gillet, B., Sebrie, C., Baati, T., et al. (2010). Porous Metal-Organic-Framework nanoscale carriers as a potential platform for drug delivery and imaging. *Nat. Mater.* 9, 172–178. doi: 10.1038/nmat2608

Horcajada, P., Gref, R., Baati, T., Allan, P. K., Maurin, G., and Couvreur, P. (2012). Metal-Organic Frameworks in biomedicine. *Chem. Rev.* 112, 1232–1268. doi: 10.1021/cr200256v

Li, X., Lachmanski, L., Safi, S., Sene, S., Serre, C., Grenèche, J. M., et al. (2017). New insights into the degradation mechanism of Metal-Organic Frameworks drug carriers. *Sci. Rep.* 7, 1–17. doi: 10.1038/s41598-017-13323-1

Li, X., Porcel, E., Menendez-Miranda, M., Qiu, J., Yang, X., Pastor, A., et al. (2019a). Highly porous hybrid metal-organic nanoparticles loaded with gemcitabine-monophosphate: a multimodal approach to improve chemo and radiotherapy. *ChemMedChem* 15, 274–283. doi: 10.1002/cmdc.201900596

Li, X., Semiramoth, N., Hall, S., Tafani, V., Josse, J., Laurent, F., et al. (2019b). Compartmentalized encapsulation of two antibiotics in porous nanoparticles: an efficient strategy to treat intracellular infections. *Part. Part. Syst. Charact.* 36, 1–9. doi: 10.1002/ppsc.201970009

Luchini, A., and Vitiello, G. (2019). Understanding the nano-bio interfaces: lipid-coatings for inorganic nanoparticles as promising strategy for biomedical applications. *Front. Chem.* 7:343. doi: 10.3389/fchem.2019.00343

Rodriguez-Ruiz, V., Maksimenko, A., Anand, R., Monti, S., Agostoni, V., Couvreur, P., et al. (2015). Efficient "green" encapsulation of a highly hydrophilic anticancer drug in Metal-Organic Framework nanoparticles. *J. Drug Target.* 23, 759–767. doi: 10.3109/1061186x.2015.1073294

Rojas, S., Arenas-Vivo, A., and Horcajada, P. (2019). Metal-Organic Frameworks: a novel platform for combined advanced therapies. *Coord. Chem. Rev.* 388, 202–226. doi: 10.1016/j.ccr.2019.02.032

Rosenblum, D., Joshi, N., Tao, W., Karp, J. M., and Peer, D. (2018). Progress and challenges towards targeted delivery of cancer therapeutics. *Nat. Commun.* 9, 1–12. doi: 10.1038/s41467-018-03705-y

Senapati, S., Mahanta, A. K., Kumar, S., and Maiti, P. (2018). Controlled drug delivery vehicles for cancer treatment and their performance. *Signal Transduct. Target. Ther.* 3, 1–19. doi: 10.1038/s41392-017-0004-3

Simon-Yarza, M. T., Baati, T., Paci, A., Lesueur, L. L., Seck, A., Chiper, M., et al. (2016). Antineoplastic busulfan encapsulated in Metal Organic Framework nanocarrier: first in vivo results. *J. Mater. Chem. B* 4, 585–588. doi: 10.1039/c5tb02084k

Taylor-Pashow, K. M. L., Della Rocca, J., Xie, Z., Tran, S., and Lin, W. (2009). Postsynthetic modifications of iron-carboxylate nanoscale Metal-Organic Frameworks for imaging and drug delivery. *J. Am. Chem. Soc.* 131, 14261–14263. doi: 10.1021/ja906198y

Thevenot, J., Troutier, A., David, L., Delair, T., and Ladavière, C. (2007). Steric stabilization of lipid/polymer particle assemblies by poly (ethylene glycol)-lipids. *Biomacromolecules* 8, 3651–3660. doi: 10.1021/bm700753q

Troutier, A., and Ladavière, C. (2007). An overview of lipid membrane supported by colloidal particles. *Adv. Colloid Interface Sci.* 133, 1–21. doi: 10.1016/j.cis.2007.02.003

Troutier-Thuilliez, A. L., Thevenot, J., Delair, T., and Ladavière, C. (2009). Adsorption of plasmid DNA onto lipid/polymer particle assemblies. *Soft. Matter.* 5, 4739–4747. doi: 10.1039/b911260j

Wuttke, S., Braig, S., Preiß, T., Zimpel, A., Sicklinger, J., Bellomo, C., et al. (2015). MOF nanoparticles coated by lipid bilayers and their uptake by cancer cells. *Chem. Commun.* 51, 15752–15755. doi: 10.1039/c5cc06767g

Conflict of Interest: The authors declare that the research was conducted in the absence of any commercial or financial relationships that could be construed as a potential conflict of interest.

frontiers
in Bioengineering and Biotechnology

MINI REVIEW
published: 20 October 2020
doi: 10.3389/fbioe.2020.594491

Recent Advances in Self-Exciting Photodynamic Therapy

Nicholas Thomas Blum[1,2], Yifan Zhang[1], Junle Qu[2], Jing Lin[1] and Peng Huang[1]**

[1] Marshall Laboratory of Biomedical Engineering, Laboratory of Evolutionary Theranostics (LET), International Cancer Center, School of Biomedical Engineering, Shenzhen University Health Science Center, Shenzhen, China, [2] Key Laboratory of Optoelectronic Devices and Systems of Ministry of Education and Guangdong Province, College of Optoelectronic Engineering, Shenzhen University, Shenzhen, China

Photodynamic therapy (PDT) is already (Food and Drug Administration) FDA approved and used in the clinic for oncological treatment of pancreatic, lung, esophagus, bile duct, and of course several cancers of skin. It is an important tool in the oncological array of treatments, but for it exist several shortcomings, the most prominent of which is the shallow depth penetration of light within tissues. One-way researchers have attempted to circumvent this is through the creation of self-exciting "auto-PDT" nanoplatforms, which do not require the presence of an external light source to drive the PDT process. Instead, these platforms are driven either through oxidative chemical excitation in the form of chemiluminescence or radiological excitation from beta-emitting isotopes in the form of Cherenkov luminescence. In both, electronic excitations are generated and then transferred to the photosensitizer (PS) *via* Resonance Energy Transfer (RET) or Cherenkov Radiation Energy Transfer (CRET). Self-driven PDT has many components, so in this review, using contemporary examples from literature, we will breakdown the important concepts, strategies, and rationale behind the design of these self-propagating PDT nanoplatforms and critically review the aspects which make them successful and different from conventional PDT. Particular focus is given to the mechanisms of excitation and the different methods of transfer of excited electronic energy to the photosensitizer as well as the resulting therapeutic effect. The papers reviewed herein will be critiqued for their apparent therapeutic efficiency, and a basic rationale will be developed for what qualities are necessary to constitute an "effective" auto-PDT platform. This review will take a biomaterial engineering approach to the review of the auto-PDT platforms and the intended audience includes researchers in the field looking for a new perspective on PDT nanoplatforms as well as other material scientists and engineers looking to understand the mechanisms and relations between different parts of the complex "auto-PDT" system.

Keywords: nanoplatform, photodynamic therapy, ROS, chemiluminescence, bioluminescence, Cerenkov, cancer

Edited by:
Wei Tao,
Harvard Medical School,
United States

Reviewed by:
Chao Wang,
Soochow University, China
Dalong Ni,
Shanghai Jiao Tong University, China

Correspondence:
Jing Lin
jingl@szu.edu.cn
Peng Huang
peng.huang@szu.edu.cn

Specialty section:
This article was submitted to
Nanobiotechnology,
a section of the journal
Frontiers in Bioengineering and
Biotechnology

Received: *13 August 2020*
Accepted: *07 September 2020*
Published: *20 October 2020*

Citation:
Blum NT, Zhang Y, Qu J, Lin J and Huang P (2020) Recent Advances in Self-Exciting Photodynamic Therapy.
Front. Bioeng. Biotechnol. 8:594491.
doi: 10.3389/fbioe.2020.594491

INTRODUCTION

Photodynamic therapy (PDT) has been approved by the Food Drug Administration (FDA) to treat a variety of tumors and malignancies in the clinic (Dąbrowski and Arnaut, 2015; van Straten et al., 2017). While effective, the primary limitation is the penetration of light within human tissue (Bashkatov et al., 2005, 2011) restricting applications essentially to areas where light can be directly applied like skin, lungs, and partially resected tumors (Bargo and Jacques, 2001; Huang, 2005; Cohen and Lee, 2016; Naidoo et al., 2018). PDT works by illuminating a molecule belonging to a class of compounds known as photosensitizers (PSs). Electrons excited by the incoming radiation will jump to the higher energy orbital in the PS, after which two things may happen. One is the electron immediately relaxes back to the ground state (time scale $\sim 10^{-10}$ s) (Laor et al., 1973; DeRosa, 2002; Zhao et al., 2013b); this is the unproductive pathway for PDT. The other pathway is to undergo intersystem crossing, a spin forbidden electronic orbital transition ($\sim 10^{-8}$ s), and then react with, most typically, an oxygen molecule generating singlet oxygen (Menzel and Thiel, 1998; DeRosa, 2002; Zhao et al., 2013b). Singlet oxygen is a highly reactive oxygen species (ROS) which oxidizes biological compounds, causing cell damage and stress (Dougherty, 1987; Clennan, 2000). This is the productive pathway where PDT is concerned; PSs are different from typical fluorescent compounds because their fluorescent quantum efficiency is quite low; they are designed or chosen to have high rates of intersystem crossing, making ROS generation the preferred pathway (Zhou et al., 2016). ROS induced cell damage can be localized with *via* specific light illumination, as this generation of ROS's does not occur outside of light illumination, sparing non-illuminated, healthy cells. In this way, PDT can effectively target cancerous cells and has led to effective treatments where light can easily be applied.

Of course, this entire process begins with excitation from an externally applied light source, however, one of the main disadvantages is the limited penetration depth of light in animal tissue (Bashkatov et al., 2005, 2011). Particularly as in the case for inoperable cancers, or those sitting deep within organs or other tissues, which are generally unable to be treated by conventional PDT. Besides the limited penetration depth of light, there is also the issue of limited cellular uptake of PS (Windahl et al., 1993; Miller et al., 1994; Costanzo et al., 2016), which may reduce therapeutic efficacy. There are several recent examples of clinically relevant efficacy for PDT treatment of cancers (Kawczyk-Krupka et al., 2015; Hauge et al., 2016; Almerie et al., 2017; Rizzo et al., 2018; DeWitt et al., 2019; Fisher et al., 2019; Mahmoudi et al., 2019), so it would be beneficial to bring these same therapeutic effects to deep-seated tumors. These therapeutic effects are numerous and there are a few aspects which elevate PDT as compared to other competing treatments (e.g., chemotherapy, radiation therapy). For example, PDT mediated therapies do not generally suffer from whole body toxicity for therapeutic effect, because the applied light is site-specific and the PSs are only activated in the illuminated area. Moreover, healthy cells have been reported to be able to tolerate increased ROS stress better than cancer cells (Trachootham et al., 2006, 2009; Cairns et al., 2011). PDT has also been shown to elicit very strong immune responses which has been shown to decrease resultant tumor size or in some cases shrink the tumor mass below the initial size for robust anti-tumor immunity when combined with checkpoint inhibitors (Duan et al., 2016; Xu et al., 2017; Yang G. et al., 2018; Liu et al., 2019).

Thus, biomedical and materials scientists began looking for ways to excite PSs using chemical or radiological methods. Many of these methods can be grouped into a class of therapies known as "Auto-PDT" (APDT), where the PDT is initiated from compounds co-administered or co-loaded with the PSs. The advantage of this type of excitation lies in that the excitation of the PS is then independent of the applied light source, eliminating the major shortcoming of PDT-based treatment (Kotagiri et al., 2015; Fan et al., 2016). APDT is defined in this review as the self-driven excitation of the PS from other compounds or materials injected into the body. The electronic excitation, either chemical or radiological in origin, is transferred to the PS which can then generate ROSs in the absence of any externally (i.e., from outside of the body) applied radiation or trigger. A scheme showing the important components and possible pathways within an APDT system is depicted in **Scheme 1**.

This review uses a materials standpoint to focus on the excitation schemes and compositions for the construction of a self-exciting PDT system, with emphasis given to the corresponding mechanisms of PDT. First, the mechanisms of excitation of the PS are discussed and separated into four sections: intermolecular chemically induced electron exchange excitation (CIEEL-like), Resonance Energy Transfer (RET), Two-Stage RET, and Cherenkov Radiation Energy Transfer (CRET). CRET in this review will always refer to CRET and never Chemiluminescent RET. Then, the types of nanoparticle platforms are categorized by their essential function and coupling of functional components. This review provides a critical view on the terminology, claims, and proposed mechanisms in the included papers; in turn, a basic design strategy is prescribed for the development of auto-PDT nanoparticle systems, while identifying challenges and themes in their synthesis and application. These analyses are necessary for accurate portrayal of the materials science in an emerging field.

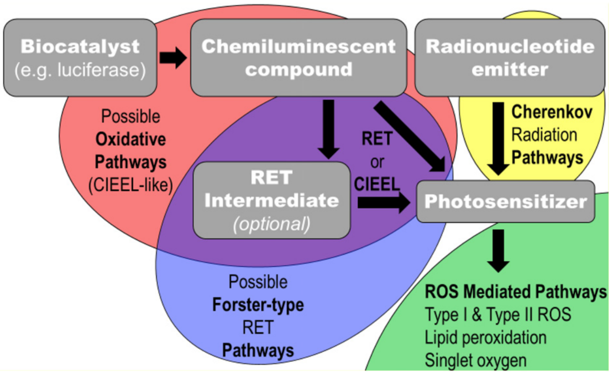

SCHEME 1 | An abstracted flow chart for self-exciting PDT pathways and significant components. In this this scheme, gray boxes indicate important physical components to self-exciting PDT nanoplatforms and the semi-transparent ellipses indicate possible pathways of possible energy transfers; the black arrows indicate transfer of energy to or excitation of the compound being pointed to.

METHOD OF ELECTRONIC EXCITATION

In most cases, APDT therapies are restricted in the use of an excitation donor far more so than PSs, as the library of known chemiluminescent compounds, and materials that emit beta radiation, are comparatively small. As a result, self-exciting PDT materials and strategies usually concern themselves primarily with methods to incorporate one of the few available excitation methods, then choose a suitable PS. Thus, in this review, the focus will be on the method of excitation, and the choice of PS will be largely ignored except where directly relevant. Method of excitation, PS choice, and composition of the of key papers referenced herein can be found in **Table 1**.

Intermolecular Chemically Induced Electronic Excitation

The most fundamental, but perhaps the least commonly applied, method to excite the PS is direct excitation of the PS *via* molecular chemically initiated electron excitation. Chemically initiated electron exchange luminescence (CIEEL) was first posited by Schuster (Koo and Schuster, 1978; Schuster, 1979), but many mechanistic studies have since shown the basis of his theory flawed, particularly in the way of unexplained low quantum efficiencies for certain CL reactions (Catalani and Wilson, 1989; Isobe et al., 2005; Almeida de Oliveira et al., 2012; Yue et al., 2012). Many revised and a few alternative mechanisms (e.g., ICIC) (Pinto da Silva and Esteves da Silva, 2013a,b) now exist but no one theory is currently accepted to explain all facets of the chemiexcitation (Augusto et al., 2013). In this paper, we will use the term CIEEL to refer to the collection of revised mechanisms as a whole (CIEEL-like) and the apparent direct chemical excitation reported in some papers for certain CL and PS compounds. Due to the complexity of CIEEL-like excitation chemistry as compared to other methods, i.e., RET and CRET, relatively few papers have used this method for excitation of PS compounds. CIEEL-like excitation requires delicate tuning of oxidation potentials *via* organic syntheses (Shim et al., 1997; Zhen et al., 2016), whereas RET and, to a lesser extent, CRET merely require information about the emission and excitation spectra of the molecule undergoing chemical excitation and the PS, respectively, in order to be properly applied.

Since the CIEEL mechanism is covered in detail by many papers, an expanded discussion will not take place here (Schuster, 1979; Stevani et al., 2000; Orlova et al., 2003; Matsumoto, 2004; Ciscato et al., 2009). The key points of the above mechanisms, by which nearly all bioluminescent compounds as well as many chemiluminescent compounds produce light, are the formation of a 1,2-dioxetanone ring (**Figure 1A**), the presence of an electron donator, and the creation of an excited electronic state within the electron donating compound or within the dioxane containing compound itself, corresponding to intermolecular or intramolecular CIEEL-like CL, respectively, after the dioxetane ring decomposes. The excited electronic state can then relax to the ground state emitting an electron or transfer the excited energy *via*

TABLE 1 | A summary of the key papers for nanoplatforms for self-exciting photodynamic therapy with associated key aspects.

Author	Nanoparticle type	Excitation type	Transfer method	Exciting component	Photosensitizer	Components	Year
Lin et al.	MOF	Bioluminescence	RET	D-fluorescein	TCPP	CL, PS	2019
Yang et al.	PLGA	Bioluminescence	RET	Luciferin	RB	Bio. Cat., PS	2018
Hsu et al.	QDs	Bioluminescence	RET w/Int.	Coelenterazine	m-THPC	RET Int., Bio. Cat.	2013
Kim et al.	QDs	Bioluminescence	RET w/Int.	Coelenterazine	Ce6	RET Int., Bio. Cat.	2015
Yang et al.	CDs	Bioluminescence	RET w/Int.	Luciferin	PPIX	RET Int., PS	2018
Zhao et al.	Microcapsules	Bioluminescence	RET	Luciferin	RB + Hypocrellin B	CL, Bio. Cat., PS	2013
Yu et al.	HMSN	Chemiluminescence	CIEEL + RET	CPPO	Ce6	CL, PS	2018
Xu et al.	Self-assembled NP	Chemiluminescence	RET	Luminol	Ce6	CL, PS	2019
Fang et al.	MOF	Chemiluminescence	RET	Luminol	TCPP	CL, PS	2019
An et al.	Self-assembled NP	Chemiluminescence	RET	Luminol	Ce6	CL, PS	2020
Al-Ani et al.	Protein NP	Chemiluminescence	RET	Coelenterazine	ZnPP	Bio. Cat., PS	2019
Jiang et al.	Protein/polymer NP	Chemiluminescence	RET	Luminol	MEH-PPV	PS	2019
Berwin Singh et al.	Polymer Micelle	Chemiluminescence	CIEEL	Peroxalate Polymer	PPIX	CL, PS	2017
Yang et al.	Functionalized CDs	Chemiluminescence	RET w/Int.	Luminol	Ce6	RET Int., PS	2019
Wu et al.	Polymer NPs	Chemiluminescence	CIEEL	CPPO	TPP	CL, PS, RET Int.	2019
Zhang et al.	Polymer NPs	Chemiluminescence	RET	Luminol	m-THPC	RET Int., PS	2014
Kotagiri et al.	TiO2 NP	Cherenkov Radiation	CRET	FDG	TiO2	BNE, PS	2015
Kamkaew et al.	HMSN	Cherenkov Radiation	CRET	^{89}Zr	Ce6	BNE, PS	2016
Ni et al.	MNP	Cherenkov Radiation	CRET	^{89}Zr	TCPP	BNE, PS	2018

Metal organic framework, MOF; poly(D,L-lactide-co-glycolide), PLGA; quantum dots, QD; carbon dots, CD; hollow mesoporous silica nanoparticle, HMSN; nanoparticle, NP; magnetic nanoparticle, MNP; resonance energy transfer, RET; RET with Intermediates, RET w/Int.; chemically induced electron exchange luminescence type mechanism, CIEEL; bis(2,3,5-trichloro-6-((pentyloxy)carbonyl)phenyl) oxalate, CPPO; 2′-deoxy-2′-(^{18}F)fluoro-D-glucose, FDG; tetra (4-carboxyphenyl) porphyrin, TCPP; Rose Bengal, RB; meta-tetra(hydroxyphenyl)chlorin, m-THPC; Chlorin e6, Ce6; Zinc (II)-protoporphyrin IX, ZnPP; protoporphyrin IX, PPIX; poly[2-methoxy-5-(2-ethylhexyloxy)-1,4-phenylenevinylene], MEH-PPV; tetraphenylporphyrin, TPP; Chemiluminescent compound, CL; Bioluminescence catalyst, Bio. Cat.; photosensitizer, PS; Beta nucleotide emitter, BNE.

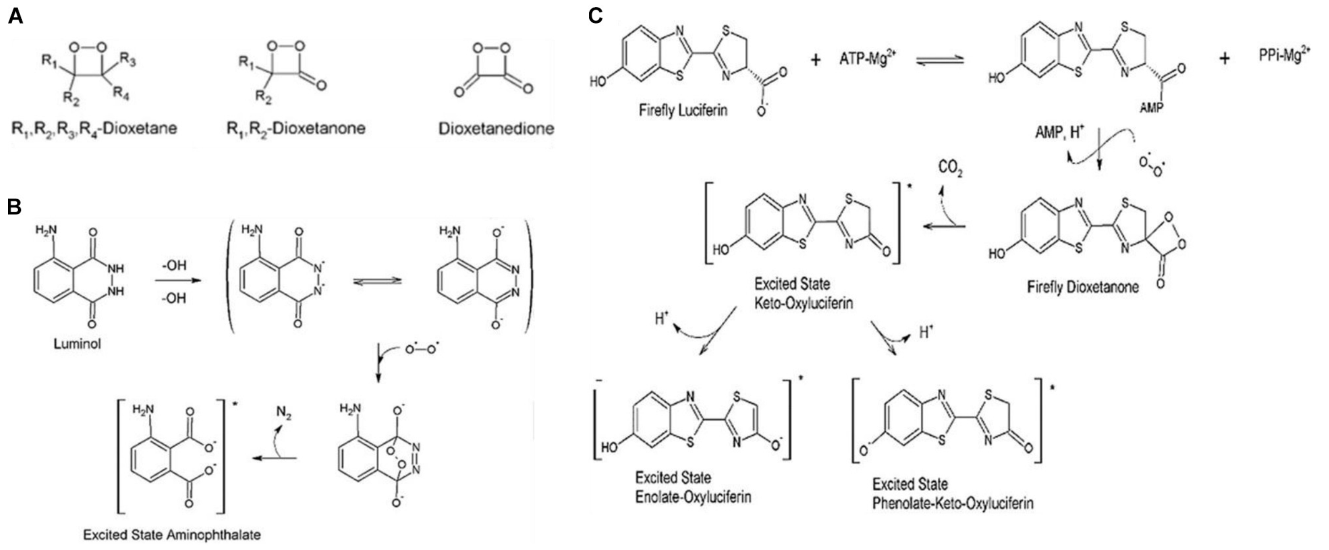

FIGURE 1 | Mechanisms chemical and biochemical luminescence. **(A)** Generalized chemical formulae for possible dioxetanedione structure. **(B)** Luminescence mechanism for luminol. **(C)** Mechanistic pathways for firefly luciferin, catalyzed by firefly luciferase in the second reaction step, toward bioluminescence (Magalhães et al., 2016).

RET as will be seen later in this review. Mechanisms for the chemiluminescence of two of the most commonly utilized chemiluminescent compounds luminol and firefly luciferin can be seen in **Figures 1B,C**, respectively.

In a paper published by Mao et al. (2017), it can be seen how a chemiluminescent compound such as Bis[2,4,5-trichloro-6-(pentyloxycarbonyl)phenyl] oxalate (CPPO) can be used to directly excite a custom-made PS compound, named TBD, for APDT of a 4T1 xenograft cell cancer cell line in BALB/c mice.

The nanoparticle was formed by co-precipitation of the TBD and CPPO in soybean oil droplets, stabilized by F127 polymer (**Figure 2A**). **Figure 2B** shows the theorized CIEEL mechanism for the excitation of the PS TBD where it acts as the electron donor, and, as the dioxetane ring decomposes, becomes excited. It can either then fluoresce or undergo intersystem crossing and generate singlet oxygen. **Figure 2C** shows an intraperitoneal cancer model with administration of C-TBD NPs where fluorescence imaging and chemiluminescent imaging show different biodistributions of the nanotheranostic agent. It is important to note that chemiluminescence generally occurs independently of PS excitation. For direct intermolecular CIEEL-like excitation of PSs, the chemiluminescence is the same as fluorescence in terms of the wavelength emitted, because there is only one compound capable of undergoing electronic excitation. The difference in chemiluminescence and fluorescence is whether or not an external light needs to be applied to observe fluorescence. In this case, and this terminology will be held consistent within this review, fluorescence shows the biodistribution of TBD (or another PS) when exposed to an external light source, and chemiluminescence is imaging in the dark (no external excitation). Thus, TBD is required to be present for both but only in the presence of CPPO and ROSs does it undergo luminescence in the dark.

Other images within the report show colocalization of the fluorescence and chemiluminescence in the tumor, and **Figure 2C** shows how the distribution of can appear significantly different. Preferential accumulation of the PS appears in the liver, but there is an obvious absence of chemiluminescence. It is also plausible that the nanotheranostic agent is not retaining its original structure; partial or complete breakdown of the theranostic could result in such images. The authors support their proposed mechanism of ROS induced therapy by adding a therapeutic adjuvant β-phenylethyl isothiocyanate (FEITC) which enhances H_2O_2 levels in cells (**Figure 2D**). The addition of FEITC increased the intensity and persistence of detectable chemiluminescent signal from the tumor. Moreover, lysates of various organs show that only tumor tissue generates significant H_2O_2 as determined by chemiluminescent imaging (**Figure 2E**), but this is subject to the caveat from part C where it is clear there is an unexplained absence of CPPO in the liver despite TBD presence; this should not occur if the nanoparticle formulation is intact. Further, the authors showed supportive results in terms of the proposed therapeutic mechanisms; they ran gels on the tumor cell cytosol which showed lowered levels of Caspase3 and Bax, with increased levels of cytosolic C (**Figure 2D**). The way these results are presented indicate several indicators of apoptotic activity, but the authors fail to propose any concerted mechanism correlating the observed phenomena.

There are scant other reports that claim to use CIEEL directly to excite the PS (Berwin Singh et al., 2017; Wu et al., 2019), and this is likely because adequate excitation of the PS involves careful tuning of the oxidation potentials of the chemiexcited donor and the recipient PS. However, this

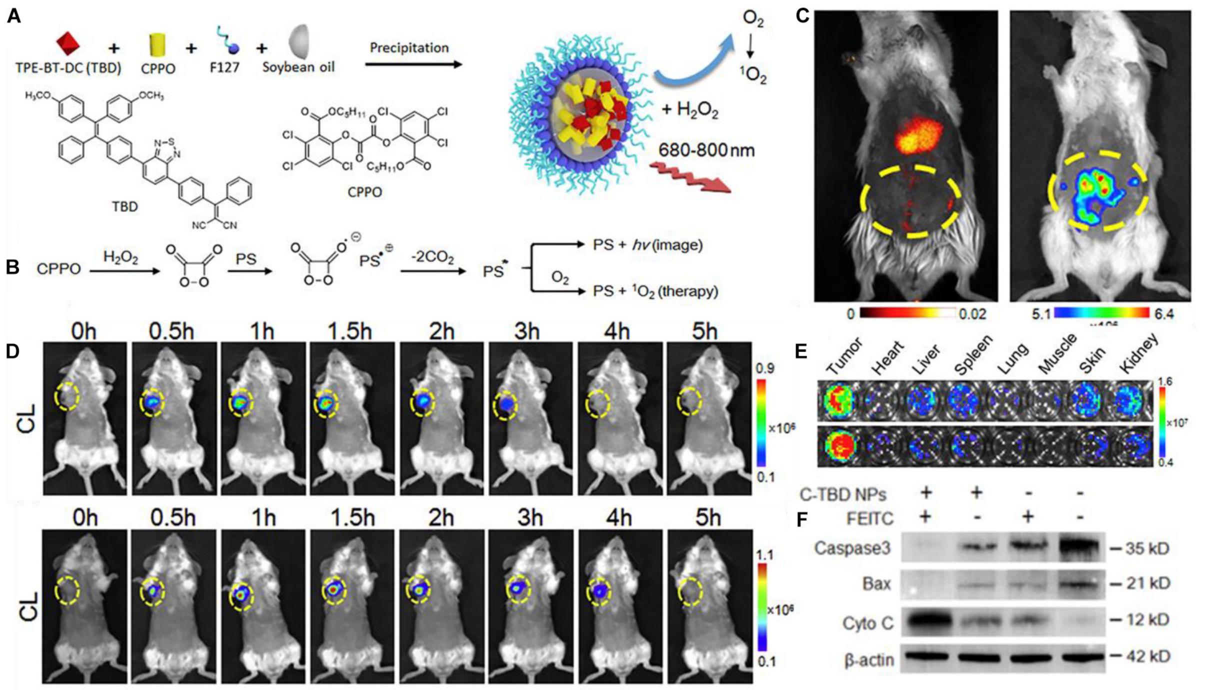

FIGURE 2 | (A) A schematic showing the chemical structure of TBD and CPPO and their co-precipitation into a soybean oil droplet stabilized by F127 amphiphilic polymer. **(B)** The proposed mechanism by which CPPO can undergo CIEEL with the PS TBD for direct excitation of the PS for chemiluminescence or singlet oxygen generation. **(C)** Fluorescence imaging (left) vs. chemiluminescence imaging (right) of the TBD group imaging of intraperitoneal metastatic tumor bear mice after administration of C-TBD NPs; chemiluminescence occurs only in the intraperitoneal area, whereas fluorescence mainly occurs in the liver. **(D)** Chemiluminescence of mice with C-TBD NPs intravenously administered at 100 μL (1 mg/mL TBD) (upper) and after co-administration of anti-oxidant inhibiting agent, FEITC (5 μmol) (lower); persistence of chemiluminescent signals is extended for an additional hour. Also note the change in the chemiluminescent scale. **(E)** Chemiluminescent signals from lysates of major organs after adding C-TBD NPs directly to the well. **(F)** Western blot assay showing decreased Caspase3 and Bax, and increased cytochrome C, with C-TBD NPs and FEITC addition (Mao et al., 2017).

does not preclude the possibility that some reports have not correctly identified the precise pathway by which PSs are excited in an APDT system.

Resonance Energy Transfer (RET) Excitation

In terms of popularity, the most common excitation methods for self-propagating PDT therapies in the absence of light are those supplied by chemiluminescence which is subsequently transferred to the PS *via* RET. RET will be used in the broadest sense of RET, including the subtype Forster resonance energy transfer. FRET cannot be used to described generally the excitation of PS by CL because many of the assumptions made by Forster break down in biological and nanoscale systems, both of which are relevant in the reviewed works. Bioluminescence resonance energy transfer (BRET) and chemiluminescent resonance energy transfer will both be referred to as resonance energy transfer (RET) since the mechanism of energy transfer is identical. Attempts will be made to keep in line with the terminology of the referenced papers and figures where appropriate, so BRET will sometimes be used interchangeably with RET.

An ideal chemiluminescent compound will emit light in the blue wavelengths, as the energy potential should sufficiently large to excite, *via* RET, most photosensitizing compounds, given that energy is always lost during a RET transfer (Jares-Erijman and Jovin, 2003). However, a blue light emission spectrum in the RET donor is not required, since the efficiency of RET is related to the overlap of the donor emission and acceptor absorption spectra (Haugland et al., 1969; Scholes, 2003). Regardless, many chemifluorescent compounds do emit in the blue or green wavelengths, which generally have high attenuation in biological tissues (Bashkatov et al., 2005), effectively ensuring that virtually all excitation of the PS ought not to come from the actual emission of the photon from the donor, but rather the RET process itself. This is distinct from CIEEL-like mechanisms, because CIEEL is a chemical oxidative mechanism by which a molecule can enter an excited state. RET PS excitation occurs when the chemiluminescent molecule is already in an excited state (such a state can arise through a CIEEL-like mechanism) but then transfers the energy to a PS *via* FRET.

Perhaps the most studied chemiluminescent compound is luminol, which was discovered in 1928 to react with blood to fluoresce more brightly as a result of the iron (and likely other substances) in blood which catalyzes the oxidation of luminol (Albreacht, 1928). Luminol was first used as a source

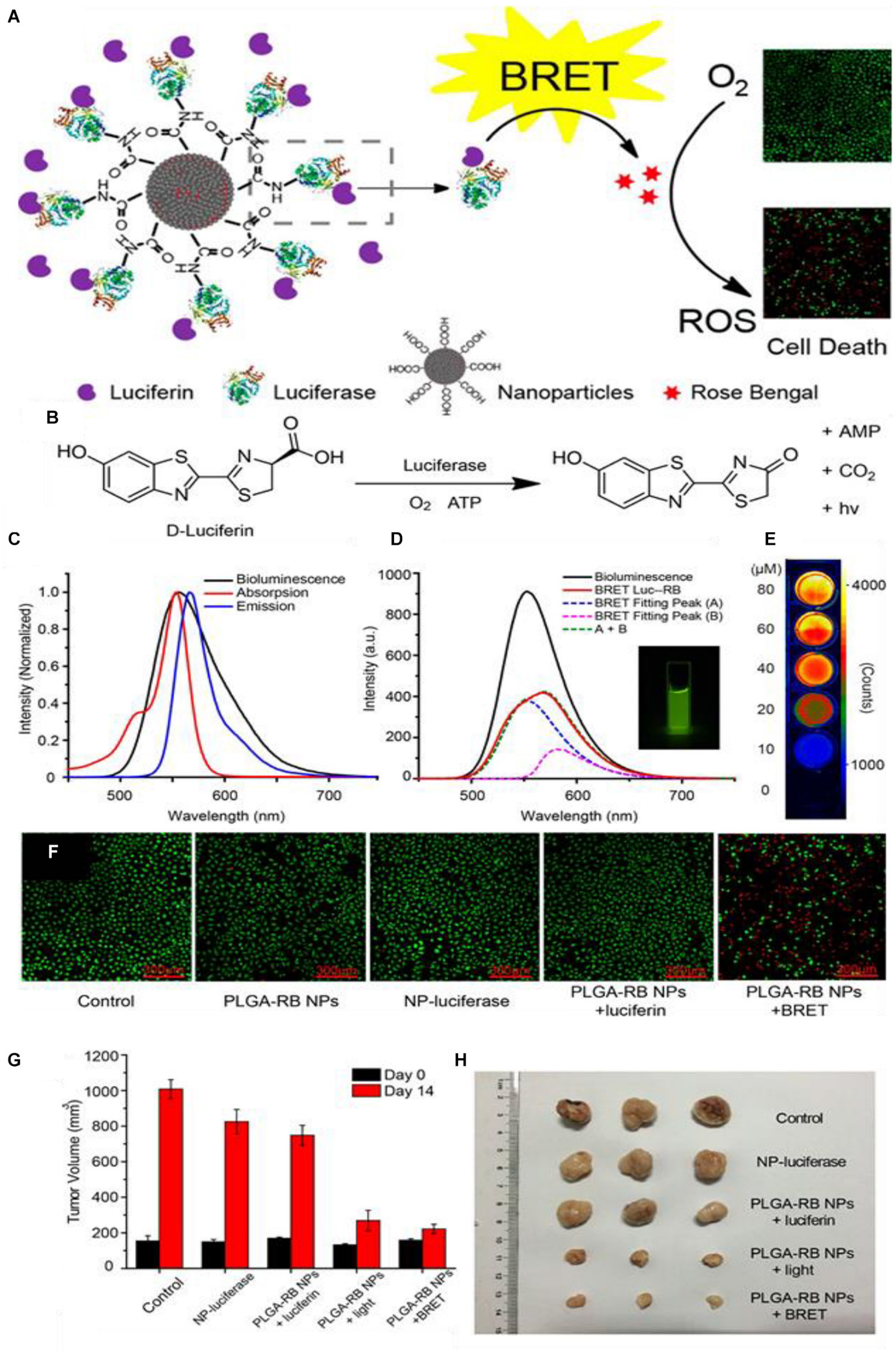

FIGURE 3 | (A) Generalized scheme of the synthesis of the PLGA-RB nanoparticles: RB is first conjugated to PLGA then precipitated to form the nanoparticles, after which the luciferase is conjugated to the PLGA-RB surface. The luciferase can catalyze the oxidative luciferin electronic excitation which then transfers the energy *via* BRET to the RB. The RB reacts with oxygen generate ROSs for PDT. **(B)** The reaction scheme for the luciferin light emission which requires the luciferase, oxygen, and ATP. **(C)** Bioluminescent spectra of the luciferase-luciferin system, absorption, and emission of the PLGA-RB NPs. **(D)** Bioluminescent emission spectra of luciferase luciferin system, the emission spectra of the BRET Luc-RB system which is composed of fLuc mediated emission (Fitting peak A) plus fluorescent emission from RB (Fitting peak B); inset: emission of Luc-RB system. **(E)** Dose dependent emission based on varying luciferin concentrations. **(F)** Cell viability for different treatments measured by fluorescence 40 μg/mL PLGA-RB NPs with calcein-AM and propidium iodide stains; red fluorescence indicates dead cells. **(G)** End-point tumor size comparison of treatments and **(H)** photographs (citealpBR93).

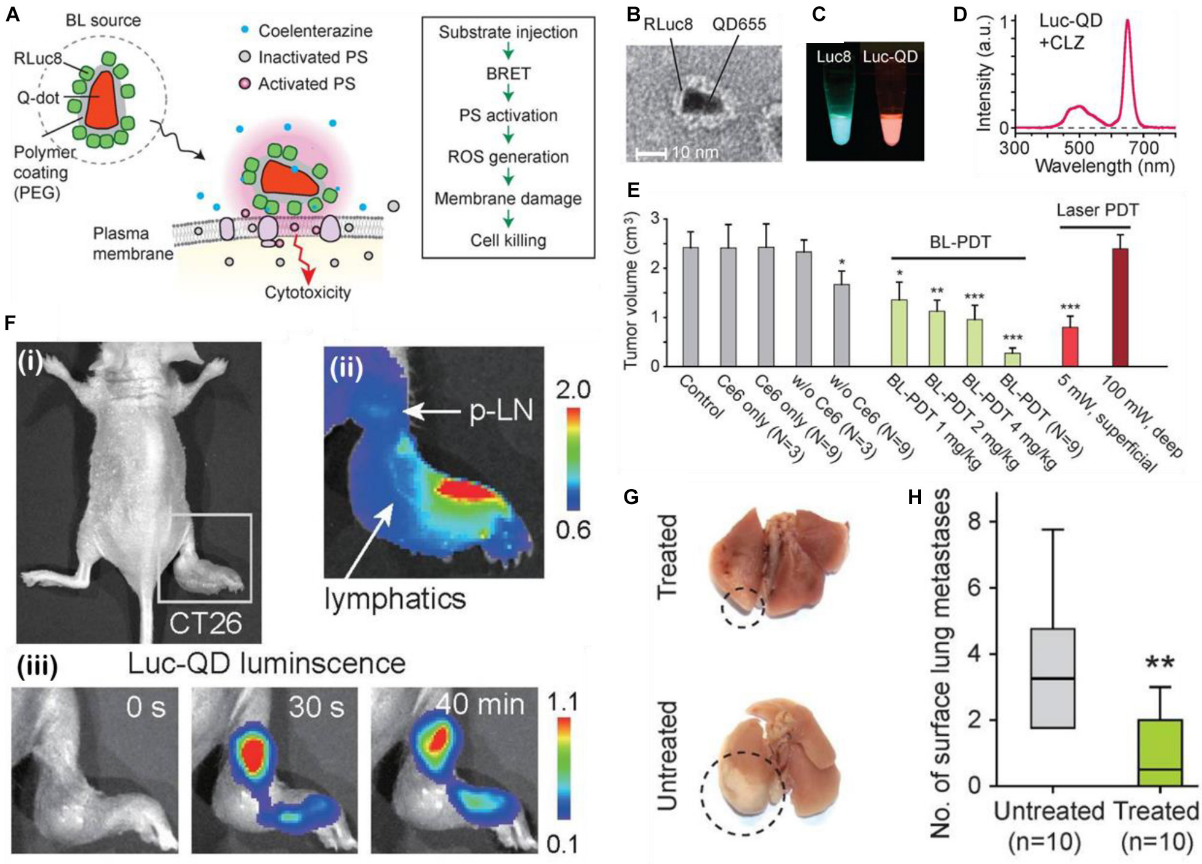

FIGURE 4 | (A) Schematic of the design and cell killing action of Luc-QDs. **(B)** TEM image of Luc-QDs. **(C)** Chemiluminescent spectra of the Luc8 coelenterazine complex (left) and the post-FRET, redshifted Luc-QD (right) solutions and **(D)** associated red-shifted emission spectrum. **(E)** End point tumor volumes for controls, BL-PDT, and laser PDT. **(F)** (i) Footpad CT26 tumor model of a mouse before injection; (ii) Luminescence images immediately after injection at of the Luc-QD complex as the distal part of the footpad tumor. Arrows showing the travel *via* lymphatic system to the proximal lymph node; (iii) Luc-QD fluorescence traveling to and remaining in the lymph node up to 40 min. **(G)** Images of Luc-QD treated and untreated LN LCC-GFP tumor bearing mouse lungs, with **(H)** associated quantification of lung metastases (Kim et al., 2015). **p* < 0.05, ***p* < 0.01, ****p* < 0.001.

for *in situ* PDT in Chen et al. (2012) where it was shown that by adding luminol to a cellular solution with $FeSO_4$ and 5-aminolevulinic acid. Cancer cell viability dropped to 18% in flow cytometry experiments. $FeSO_4$ served as the oxidative catalyst acting on luminol, with 5-aminolevulinic acid converted *via* cell metabolism into the photosensitizer protoporphyrin IX, which generated the ROSs necessary to induce cell toxicity (Chen et al., 2012). This work was closely followed by publication from Yuan et al. (2012) where luminol stimulated PDT was used an anti-cancer and anti-fungal agent for *in vitro* and *in vivo* experiments. Similar drops in cancer cell viabilities were observed in addition to a ~60% decrease in tumor growth of a xenograft model.

Despite luminol being the most well-studied and well-known chemiluminescent compound, perhaps the most popular method for FRET induced excitation of PS is *via* the use of luciferases and luciferins, particularly that of firefly luciferase (fLuc) and its luciferin. It is important to note that by looking at the CIEEL-like mechanism for firefly luciferin excitation (**Figure 1C**), one may notice that the excited electronic energy does indeed come from the luciferin, and the luciferase merely catalyzes the oxidation. Nevertheless, many researchers and reports refer to luciferase as emitting the photon. In any case, the excited electronic state before photon emission exists on the order of nanoseconds, and the reaction absolutely does not proceed without the luciferase, so it is not functionally incorrect in terms of effect. We will use the term luciferase similarly in this review.

In a report by Yang Y. et al. (2018), they show how Rose-Bengal (RB) can be functionalized to poly(lactic acid) (PLA), then condensed into a poly(lactic-coglycolide acid) (PLGA) nanoparticle (**Figure 3A**). The resulting nanocomplex is then functionalized with fLuc on the surface *via* N-ethyl-N-(3-(dimethylamino)propyl)carbodiimide (EDC) mediated conjugation; the luciferin is applied independently as a free molecule. In the presence of fLuc, chemi-excitation occurs of the luciferin (**Figure 3B**), and this is transferred *via* FRET to the RB PS. In the presence of luciferin but without RB, the fLuc spectrum as seen in the "bioluminescence" emission curve and inset in **Figure 3C**. With the addition of RB, and the associated occurrence of FRET, the intensity of the emissions is reduced overall. Bioluminescence of the fLuc complex still occurs (Fitting Peak A) but much of the energy is transferred via RET to the RB PS, which undergoes fluorescence in its PDT non-productive pathway (Fitting Peak B); both curves combine to make a new, lower intensity fluorescence (A + B, BRET Luc-RB) (**Figure 3D**). Additional electronic energy which would otherwise be emitted is lost during RET and when RB undergoes intersystem crossing to produce singlet oxygen. **Figure 3E** shows a light emission heatmap of wells with varying concentrations of luciferin. As expected, increasing luciferin concentration increases light emission, however, the paper does not explicitly specify the wavelengths used, an omission which is serious when considering RET systems. **Figure 3F** shows fluorescence images of stained live-dead cells; notably, there is a decrease in cell density in addition to generation of dead cells in the NP BRET treatment group.

When Wu and coworkers applied their PLGA-RD BRET formulation to an *in vivo* model, they found tumor growth suppression curves like those found when the PLGA-RD nanoparticles were irradiated with light and corresponding endpoint tumor volumes (**Figures 3G,H**). These results are promising as far as RET-driven PDT therapy is concerned; as they imply that while the intensity of catalyzed luminescence by fLuc and other luciferases are considerably lower in intensity than that of applied external light source, they can still be effective for PDT. There have been several studies which have attempted to quantify and compare the true PDT efficiencies of an external as compared to an internal tumor light source. Some authors have published conflicting results, notably with Dr. Gambhir and coworkers claiming that the bioluminescence produced by luciferins is too weak in luminescent intensity as compared to traditional PDT to initiate any significant toxicity (Theodossiou et al., 2003; Schipper et al., 2006; Magalhães et al., 2016; Shramova et al., 2018). Such uncertainty has not stopped the continued application of such systems in APDT; given the now numerous nanoparticle APDT papers showing efficacious treatment of cancer cells and tumors, it may be very tentatively said that RET in these formulations is sufficiently efficient to activate PS in an *in vivo* model. This may be due to inconsistencies in the ways these comparisons are made, or indeed, inclusion of APDT systems in a nanoparticle formulation allows for enhanced toxicity over free APDT systems.

Two-Stage Photosensitizer Excitation/Excitation by RET Intermediary

One of the ways the PDT efficacy with RET can be improved is *via* addition of an intermediary. This intermediary usually has an excitation band gap that is between that of the CL compound and that of the PS acceptor. If the choice of a PS and CL compound do not have overlapping absorption and emission spectra, respectively, or whose spectra overlap poorly, then researchers may utilize an intermediary fluorescent compound; this intermediary's absorption spectrum should overlap with the CL compound emission and its emission spectra better overlaps the PS absorption, thereby enacting a second RET step (Watrob et al., 2003b). While additional energy is lost as a result of a second RET step, it is possible that the kinetics from the increased overlap in absorption/emission spectra between the CL compound/intermediate and intermediate/PS as compared to the CL compound/PS overlap contribute to enhanced CL and as a result enhanced PS activation (Watrob et al., 2003b). Such couplings have also been shown to have greater sensitivity and efficiencies in biological systems (Hu et al., 2015). Moreover, the presence of an intermediate does not exclude direct CL/PS RET, but merely supplements for increased efficiency (Watrob et al., 2003b; Galperin et al., 2004; Chen et al., 2009; Hu et al., 2015).

As might be expected, quantum dots are a very appropriate choice for playing the part of a FRET intermediate. Their small size, customizable absorption/emission bands allow for a broader utilization of photosensitizers which may be activated. In this work done by Kim et al. (2015) a chemiluminator RLuc8 is conjugated to a quantum dot with a maximum absorption at 655 nm (**Figures 4A,B**), which shifted the effective emission peak from blue light (peak around 500 nm) to around 670 nm, permitting the Luc-QD complex to excite the Ce6 PS; since the redshifting of the chemifluorescence signal can be observed in the Luc8-QD combination (**Figures 4C,D**). The nanotherapeutic agent was then applied to a tumor mouse model; the *in vivo* tests show that by increasing the RLuc-QD dosage, and by increasing the number of subsequent treatments *via* RET PDT ($N = 9$), the resulting tumor suppression is more significant than three treatment ($N = 3$) of superficially illuminated PDT (**Figure 4E**); the single dose equivalent to the conventional PDT for single treatment is 4 mg/kg, an uncommonly high dose. These results seem to suggest that it requires at least three times the dosage of the Luc-QD as compared to a conventional PDT treatment. However, in this paper, the authors stress that this application is designed for deep-seated tumors, and in this treatment scenario, they used a sham of tissue 5 mm thick to stress that even a small addition of simulated depth renders conventional PDT ineffective. What is most interesting about this report is the alternative application of the Luc8-QD PDT system wherein the authors noticed, from chemiluminescent imaging, that the Luc8-QD nanoparticle system drained into the nearby lymph node after injection into a footpad tumor (**Figure 4F**) which contributed to lower mortality. This resulted in the reduction of lung metastases when the Luc-QD PDT system was applied (**Figures 4G,H**). This result is interesting in that it provides a plausible mechanism by which an overall mouse survival curve can be influenced by factors other than main tumor growth suppression. In this case, the researchers diligently observed a characteristic of the nanoparticle auto-PDT system and was able to induce a reasonable conclusion about the broad mechanism of increasing mouse survival.

While there is an increase in complexity with the inclusion of a secondary electronic excitation step, there are undeniable increases in chemiexcited PDT effect, but these gains would likely depend heavily on the type of system being considered (Sadhu et al., 2010; Hu et al., 2015). For example, if a donor and acceptor were chosen based on some other criterion other than emission-absorption overlap (e.g., biocompatibility or possessing some desired functional group) the inclusion of a FRET intermediary would allow for effective excitation of the acceptor from the donor. Two stage PS excitation has some advantages, but it is possible that smart choice of donor and PS, or their rational coupling considering orientation/distance with respect to each other would lead to higher efficiencies. Certainly, the maximum achievable theoretical efficiency ought to be higher with fewer energy transfers *via* a FRET-based mechanism.

Cherenkov Radiation Energy Transfer (CRET)

Cherenkov radiation is a phenomenon associated with beta emission from radioactive particles that was first described and characterized by Cherenkov experimentally (Čerenkov, 1937). Cherenkov radiation arises when an emitted charged particle (usually an electron) moves through a dielectric medium (like water) at a speed faster than the speed of light in that medium (Spinelli and Boschi, 2015; Tanha et al., 2015). An electromagnetic field is always generated as a charged particle moves through a medium, and this can induce an associated polarization in the electrons of nearby atoms. This is not an excitation nor an ionization but the generation of spherical wavelets composed of *en masse* fluctuations of surrounding electrons from every point along the path of the original traveling charged particle (Jelley, 1955; Klein et al., 2019). When this particle exceeds the speed of light in the medium, these wavelets constructively interfere, not unlike a sonic boom, to produce electromagnetic waves in the visible wavelengths. The reason Cherenkov radiation is observed to be blue is because the intensity of this radiation is proportional to the frequency (Jelley, 1955). When this radiation is observed, it is of sufficient intensity to excite fluorophores, quantum dots, PSs, or any other molecule/material with an excitable bandgap in the blue light region (Bernhard et al., 2017; Shaffer et al., 2017).

Thus, Cherenkov radiation is also capable of acting as a donor in CRET. By utilizing radioactive isotopes with high beta-emissions (e.g., ^{18}F, ^{64}Cu, or ^{68}Ga, ^{90}Y, etc.), several research groups have been able to induce electronic excitation of fluorophores and photosensitizers. Much like FRET, CRET efficiencies are usually dependent on the concentration of the emitting isotope (the donor), the concentration of the fluorophore (acceptor), and the overlap between Cherenkov luminescence emission peak and the acceptor absorbance peak (Bernhard et al., 2017). However, the mechanism of Cherenkov radiation donating electronic energy to fluorophores is certainly not the same as chemiluminescent molecules donating to fluorophores given that the difference in the source excited electronic energy; one arises from an excited electronic state generated *via* chemical reaction, the other arising from the constructive interference of induced electromagnetic waves. Further, it is known that RET is a radiationless transfer of energy, and that Cherenkov arises from the propagation of radiation itself. Unfortunately, the exact mechanism of neither RET nor CRET are fully understood.

An example of using CRET to initiate PDT can be seen in the work by Kamkaew et al. (2016) wherein a mesoporous silica framework was loaded with beta radiation emitting ^{89}Zr and the photosensitizer chlorin e6 (Ce6) for an auto-PDT nanosystem ([^{89}Zr]HMSN-Ce6) as seen in **Figure 5A**. The loading of the radioisotope was achieved by surface chelation of the deprotonated silanol groups on the MSNs to the ^{89}Zr. The [^{89}Zr] loading was sufficiently high to excite the Ce6 PS (**Figure 5B**). Both Ce6 and [^{89}Zr] loadings were directly were directly related to the cancer cell toxicity (**Figures 5C,D**) with increasing concentration of both lowering observed viabilities. However, the doubling concentration of ^{89}Zr appeared to have a more dramatic effect between 10 and 20 μC, but little to no effect when doubling again; this contrasts with Ce6 loading which appears to show a monotonic decrease with each doubling up to 40 μM. The nanoparticle shell itself apparently imparting no toxicity on the cells (**Figure 5E**). When applied *in vivo*, significant PS fluorescence from both the tumor and liver can be observed, which shows that active CRET is occurring in these areas (**Figure 5F**); tumor growth was totally inhibited in the [^{89}Zr]HMSN-Ce6 treatment group over a span of 14 days with tumors retaining their starting diameter. The disadvantages of this approach become evident from **Figure 5F** where active PDT is occurring both in the tumor and in the tumor tissue unlike CL based APDT.

What perhaps is most interesting about CRET-based APDT, is that despite the extremely low light fluence rate of Cherenkov luminescence related to β-radiation as compared to conventional PDT, significant cancer cell toxicity and tumor growth inhibition can still be observed (Gonzales et al., 2014; Glaser et al., 2015). It is not clear how markedly lower (several orders of magnitude) light intensities can still produce significant toxicities, but some authors are generally quick to point out that CRET based PDT is long lasting with isotope half-times commonly on the order of several days.

External Radiation Applications

After examining the main processes, whereby the auto-excitation of the PS can occur *via* CRET or RET, it is worth mentioning a few modalities which are decidedly not APDT, as they require an external trigger to become activated and generate a therapeutic effect.

Afterglow PDT is generally described as set of compounds or nanomaterials which, after irradiation with an external light source, possess long-lived excited triplet states and can create singlet oxygen or other ROSs after irradiation has stopped. The types of materials used to form these afterglow PS generally consist of noble metalloorganic complexes, porphyrins, or carbon NPs, or most recently organic crystals (Fan et al., 2017; Liu et al., 2018; Wang et al., 2018; Xu et al., 2020; Yang J. et al., 2020). Zinc-Gallium-chromium nanoparticles are a popular modality, and have been shown to have phosphorescence half-lives of approximately 1 min (Fan et al., 2017). However, these materials still cannot be classified as APDT systems since they still require an initial excitation *via* an external lights source, eliminating the advantages offered by true APDT systems. In theory, if afterglow materials with long enough half-life are created, then these materials can be irradiated before injection into the body, effecting treating the irradiation step as a part of the preparatory synthetic procedure, and these materials could be considered

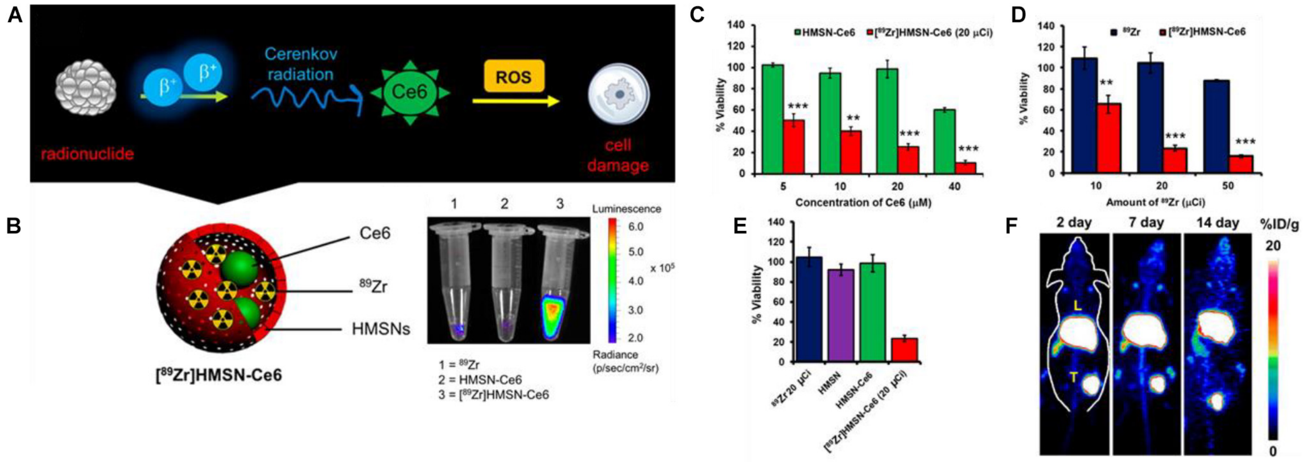

FIGURE 5 | (A) Scheme showing the mechanism by which radionuclides in $[^{89}Zr]$HMSN-Ce6 can induce ROS cell damage mediated by Cerenkov radiation excitement of PS Ce6. **(B)** Luminescence of $[^{89}Zr]$HMSN-Ce6 vs. free $[^{89}Zr]$ and HMSN-Ce6 controls. **(C)** Cell viability after incubation with varying concentrations of [89Zr]HMSN-Ce6 and HMSN-Ce6 as controlled by Ce6 concentrations. **(D)** The same but controlling $[^{89}Zr]$ and $[^{89}Zr]$HMSN-Ce6 concentrations. **(E)** Tumor growth suppression of $[^{89}Zr]$HMSN-Ce6 and control treated mice. **(F)** Cerenkov radiation imaging of mice over a 14-day span post-injection (Kamkaew et al., 2016). $^{**}p < 0.01$ and $^{***}p < 0.001$.

APDT, however, the exponential decay of chemical excitation states of PSs ensures that they will always be most toxic upon administration into the blood stream (Ware et al., 1973), and will exhibit lesser toxicity as they accumulate in the desired, and sometimes undesired, regions.

X-ray is another technique which also requires external radiation in order to generate reactive oxygen species; this technique typically utilizes either a direct X-Ray to ROS generation (e.g., Cu-Cy metalloganic) or a scintillator intermediate which transfers the X-Ray radiation into infrared light which can be used with certain photosensitizers (SAO nanoparticles LaF materials, etc.) (Ma et al., 2014; Chen et al., 2015; Wang et al., 2016; Song et al., 2018; Sun et al., 2020). X-Ray based PDT also break the depth dependence, due to the low attenuation in tissue, but are still a form of externally applied radiation so these are not discussed further in this review.

FORMULATION SCHEME

The formulations are categorized by the quantity of steps within the APDT system of which there are three main parts: (1) the chemi- or radio-luminescent compound, (2) the optional inclusion of an intermediary RET compound, and (3) the photosensitizer itself. Many formulations choose to incorporate other catalysts or targeting functionalities which are not counted as directly relevant to APDT. Even the bioluminescent catalysts for luminol are not counted as a "component" of the APDT since luciferin itself undergoes the excitation.

Single Component

In most papers, few utilize NPs for a singular purpose; these will be referred to as single component schemes. Single component nanoparticles systems for APDT, wherein only a single component of the APDT system is incorporated in the nanoparticle, can still exhibit high levels of apparent complexity. Take for example work done by Jiang et al. (2019) where they formulated a conjugated polymer poly[2-methoxy-5-(2ethylhexyloxy)-1,4-phenylenevinylene] (MEH-PPV) and co-precipitated it with poly(styrene-co-maleic anhydride) (PSMA) to produce nanoparticles. The nanoparticles were then modified with hemoglobin (Hb) using NHS/EDC coupling to create Hb-NPs. The Hb-NPs were then encapsulated in liposomes for administration. Luminol, the CL compound, was administered separately. In this scheme, while Hb is reported to catalyze the oxidation of luminol for APDT therapy, it is not a necessary component. Thus, a complex multi-component nanoparticle system actually possesses only one component of the APDT system, which is the photosensitizing polymer MEH-PPV in this case. Other components either merely improve cellular uptake or improve the reactive oxygen species conversion efficiency.

This paper and another by Kotagiri et al. (2015) show how the nanoparticle structure itself can also serve as a component of the APDT system. In this paper they utilize TiO_2-Transferrin-Titanocene (TiO_2-Tf-Tb) NPs for APDT excited by Cerenkov radiation originating from ^{18}F or ^{64}Cu atoms, with ^{64}Cu giving enhanced PDT outcomes as compared to ^{18}F. While the transferrin provided targeting capabilities, the titanocene, a failed clinical chemotherapeutic which was shown to create peroxyl radicals when excited by light radiation, provided a secondary route of ROS generation, with the primary originating from TiO_2's intrinsic ability to generate singlet oxygen when exposed to radiation; the TiO_2-Tf-Tb NPs were able to generate impressive anti-cancer and anti-tumor effects.

Single component systems need not merely include the PS itself of course, and many choose to conjugate a bioluminescent catalyst to the nanoparticle. These systems can still be considered single-component APDT systems since the catalyst, while enabling chemical oxidation of the substrate toward chemical excitation, is not technically involved in the transfer or generation of ROS. Such are the cases for Yang Y. et al. (2018) and Al-Ani et al. (2019) where the biocatalyst is attached to a photosensitizing polymer nanoparticle and a protoporphyrin functionalized protein nanoparticle, respectively.

In the above examples for single component systems, the photosensitization often serves as the single component function of the nanoparticle. There are several examples of nanoparticle-based systems where the RET intermediate serves as the single-component nanoparticle, most obviously for the case of QD type nanoparticles. Such examples have been published in papers like those by Hsu et al. (2013) and Kim et al. (2015) as already discussed where the QDs are conjugated to luciferases to catalyze the luciferin excitation and thus transfer to the QD RET intermediate.

Bi-Component

In terms of nanoparticle formulations, most seek to combine at least two aspects of the APDT system; these can be collectively referred to as coupled schemes, or bi-component schemes.

PS and Chemi-Exciting Compound

The most direct way of potentially increasing the FRET efficiency is by directly coupling the donator and the photosensitizer. In an exemplary paper written by Xu et al. (2019), they synthetically combined a luminol molecule with a Ce6 PS and a PEG tail. This allowed the Ce6-Luminol-PEG conjugate (CLP) to self-assemble into micelles which could enact auto-PDT. The CLP conjugate showed increasing chemiluminescence in the presence of H_2O_2, myeloperoxidase (MPO) and a chlorine salt (**Figure 6A**). MPO is a common peroxidase found in primarily neutrophils and monocytes which catalyzes the formation of ROSs including HOCl for microbial killing (Aratani, 2018). Inhibition of chemifluorescence *via* addition of either Tempol, an ROS scavenger, or 4-aminobenzoic hydrazide (4-ABAH), and MPO inhibitor, confirms the importance of this enzyme in generating ROS for luminol chemifluorescence (**Figures 6B,C**). Cellular uptake was improved significantly when luminol was included in the CLP nanoparticle (**Figure 6D**). When this group utilized CLP-NPs for PDT tumor treatment, they found a modest tumor growth suppression effect (**Figure 6E**), but what made the paper exemplary in this case was the following elucidation of the tumor suppression mechanism. Xu and coworkers found that there was significant co-localization of the CLP to the mitochondria (**Figure 6F**); increasing CLP dosage and incubation dose showed a related decrease in mitochondrial membrane potential as measured by a tetramethylrhodamine ethyl ester (TMRE) fluorescent probe suggesting a disruption of mitochondrial function (**Figures 6G,H**). Western blot analysis of the lysed cells showed that there was a concomitant increase in the amount of cleaved caspase-3 with increases in administered CLP concentration (**Figures 6I,J**), and that this increase in cleaved caspase could be correlated to the increase in percentage of apoptotic cells (**Figure 6K**). The authors proposed that the apoptosis in A549 cancer cells was induced by incubation with CLP NPs; the NPs are endocytosed within the cell then undergo chemiluminescence initiated by intracellular ROSs already present. Then, RET/BRET occurs and the PS Ce6 generates singlet oxygen which destabilizes the potential of the nearby mitochondria. The decreased potential finally causes caspase activation and cleavage which is a major pathway cell signaling apoptosis. This group published a follow up paper showing equally impressive results (An et al., 2020).

PS and donor coupling Cherenkov platforms are some of the simplest auto-PDT platforms since no substrate or chemical is required for initiation of luminescence. As of yet, no Cherenkov radiation platforms have been published using a RET intermediate for PDT, but this can be done (Bernhard et al., 2017). Thus, all that is required is the radioactive isotope and the PS to be contained in the same platform. Ni et al. (2018) took the design a step further and created magnetic Zn-Mn-Fe_2O_4 nanoparticles with surface labeled [^{89}Zr] as the beta radiation emitter and TCPP functionalized to the surface *via* a DSPE-PEG moiety (^{89}Zr-MNP/TCPP) (**Figure 7A**). The ^{89}Zr-MNP/TCPP retained significant magnetism in solution and the complex showed detectable RET *in vitro* (**Figure 7B**) as measured by the fluorescence of the TCPP PS in the absence of externally applied light. *In vitro* results confirmed that toxicity was related to the beta radiation intensity (**Figure 7C**). *In vivo* results of the magnetic induced targeting were impressive with a clear increase of the measured RET in a bilateral tumor model wherein the tumor to which a magnet was applied showed significant increase in the amount of RET and thus tumor growth suppression (**Figures 7D,E**). It is interesting that in the tumor growth suppression curves (**Figure 7F**), the tumors to which magnetism was not applied showed little suppression; this is in stark contrast to results published in other papers where targeting is not necessary for tumor growth suppression. This is probably due to insufficient CRET based PDT occurring in the tumor, but whether this is due to insufficient ^{89}Zr-MNP/TCPP accumulation or insufficient PDT initiated events per ^{89}Zr-MNP/TCPP complex is still debatable. Perhaps significant accumulation is required for Cherenkov radiation driven PDT outside what can be achieved without targeting or otherwise enhanced uptake.

Yu et al. (2018) have also utilized hollow mesoporous silica nanoparticles for the loading of the CPPO in perfluorocarbon along with the Ce6 PS concomitantly with glucose oxidase which generates hydrogen peroxide from the conversion of glucose to gluconic acid. Lin et al. (2019) claim to use fluorescein as a bioluminescent molecule for the excitation of a PCN-224 type metal organic framework NP, but as is commonly known, fluorescein does not luminesce without the application of external light. They nevertheless published results which show significant generation of cancer cell cytotoxicity and generation of ROS *in vitro* without light application. It is unclear whether this paper suffers from improper terminology usage, improper handling procedures which expose fluorescein to light, or is subject to other phenomena which generate ROS and cancer cell death. Berwin Singh et al. (2017) also published a formulation which encases peroxalate polymer and protoporphyrin in a F-127 amphiphilic polymer shell. The peroxalate polymer generates the dioxetanedione intermediary

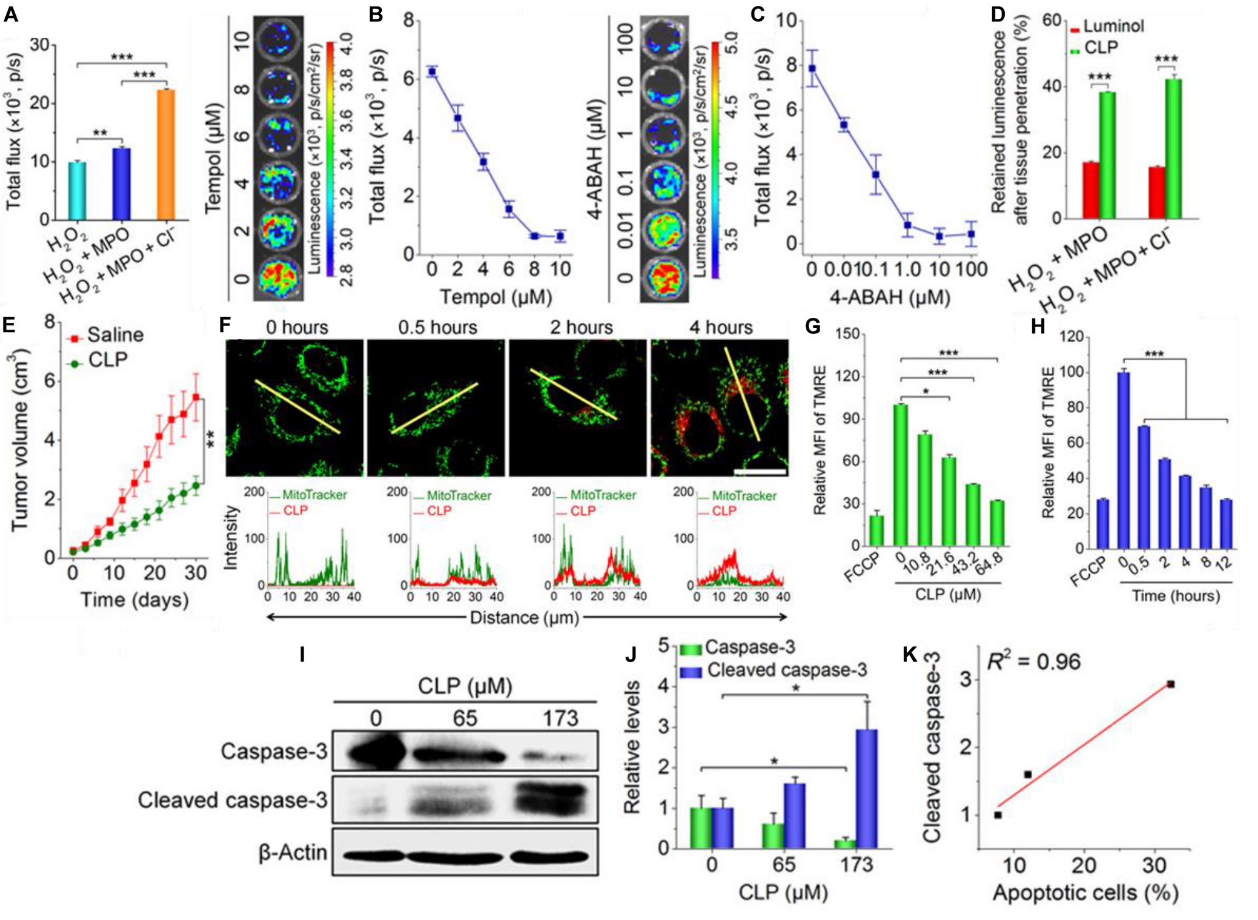

FIGURE 6 | (A) The PEG-Ce6-Luminol conjugate and its self-assembly into a CLP nanoparticle for PDT. **(B)** The chemiluminescence of the CLP NP in the presence of hydrogen peroxide, H_2O_2 plus MPO, and H_2O_2 plus MPO + Cl^- and the measured chemiluminescent flux of light. **(C)** The inhibition of CLP chemiluminescence via 4-ABAH, an MPO inhibitor. **(D)** The inhibition of CLP chemiluminescence via Tempol, a ROS scavenger. **(E)** Tumor growth suppression of a A549 lung cancer xenograft tumor treated by CLP NPs vs. a saline control. **(F)** Confocal microscopy images (upper) of cells stained with MitroTracker Green after 0–4 h of incubation with CLP NPs with fluorescent quantification (lower) along the yellow line; CLP NPs show apparent colocalization with the tumor cell mitochondria. **(F)** The mean fluorescence intensity (MFI) of tetramethylrhodamine ethyl ester (TMRE), a mitochondrial membrane fluorescent probe, as a function of CLP NP concentration; carbonyl cyanide *p*-trifluoromethoxy phenylhydrazone (FCCP) serves as a positive control as it is a known mitochondrial membrane depolarizer. **(H)** The same as **(G)** but with increasing incubation time. **(G)** Florescenc intensity as measured by flow cytometry of a indicator of mitochondrial membrane potential (TMRE). **(I)** Gel picture and **(J)** quantification of Western blot bands showing the relative amounts of caspsase-3 and cleaved caspsase-3 in A549 cells with increasing CLP NP concentration after ***$P < 0.001$; ns, no significance. *$P < 0.05$, treatment for 24 h. **(K)** The correlation between the amount of cleaved caspsase-3 and percent of total cell population that became apoptotic (Xu et al., 2019).

which directly excites the protoporphyrin that generates ROSs resulting in *in vitro* cancer cell death.

Another apparent rational coupling can be made between a CL compound with a PS in the presence of a bioluminescent catalyst; interestingly, there has only been one published example using this type of co-functionalization as done by Zhao et al. (2013a) In their work, by loading the luciferin, luciferase, photosensitizer all in a polymer microcapsule, they show a reduction in measured cancer cell toxicity as compared to administrating *via* a free luciferin solution. This is an interesting result; the free luciferin solution alone generated more toxicity than the microcapsule containing luciferin in equal concentration. This raises question about studies using externally administered luciferin in combination with a nanoparticle; cell toxicity experiments in other papers utilizing a luciferin-luciferase BRET excitation of PS may well have their results confounded by the toxicity of free luciferase. Control experiments where luciferin is omitted are common in these papers, but none show free luciferin by itself. Given the observed highly toxic effect it can have on cells, papers in this line of research ought to include luciferin control experiments.

RET Intermediate and PS

Lastly, the FRET intermediate and the photosensitizer can be coupled, as was done in work by Yang K. et al. (2019), wherein the photosensitizer PpIX was coupled to upconverting carbon nanodots (CDs). The emission of the fLuc, normally centered at 560 nm under basic conditions yielded significantly redshifted

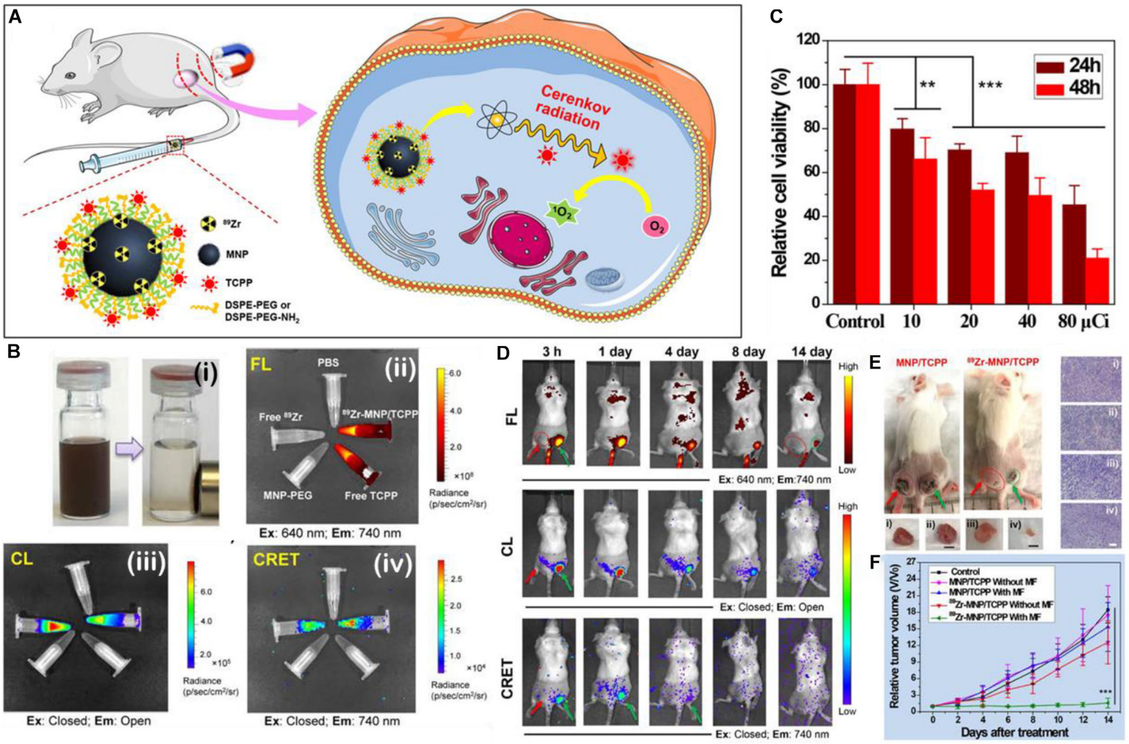

FIGURE 7 | (A) A schematic illustration of the make-up, delivery, and the generation of singlet oxygen by ^{89}Zr-MNP/TCPP. **(B)** Figure showing (i) a solution of ^{89}Zr-MNP/TCPP with and without a magnet applied; (ii) the fluorescence of various solutions, clockwise: PBS control, ^{89}Zr-MNP/TCPP, free TCPP control, MNP-PEG (no PS) control, and free ^{89}Zr with TCPP as control; (iii) the Cherenkov luminescence (all wavelengths) of the same; (iv) CRET (740 nm emission only) of the same. **(C)** Cell viability after 24 and 48 h incubation with ^{89}Zr-MNP/TCPP dose controlled by effective radiation dose. **(D)** Luminescent imaging of bilateral tumor bearing mice at various time points after injection with the ^{89}Zr-MNP/TCPP as measured by fluorescent imaging (top), chemiluminescent imaging (middle), and CRET imaging (bottom). **(E)** Scheme showing a bilateral 4T1 tumor model of a BALB/c mouse: one tumor with applied external magnetic field (right, green arrow), and one without (left, red arrow). **(F)** associated tumor growth profiles (Ni et al., 2018). **$p < 0.01$ and ***$p < 0.001$.

emission spectra (620 nm), and thus the wavelength was too low to excite the PpIX PS (abs. ~380 nm). Thus, the upconverting CDs were functionalized to the PS *via* NHS/EDC coupling reaction. FRET transfer from the fLuc-luciferin to the CD is then upconverted to a wavelength of approx. 440 nm before a second RET transfer to the PpIX PS. The generation of ROS *via* PDT was measured with DPBF and showed significant generation of ROS during confocal microscopy. In a following paper by the same researcher, Yang K. et al. (2020) similarly used a CD-PS conjugation but with the PS being Ce6 instead, and also showed extensive emission and absorption characterization. The group again showed extensive cellular experiments, achieving 92% toxicity of SMMC-7721 cancer cells, but with no elucidation of the mechanism of cell death, assuming the mechanism was similar to that of H_2O_2 induced cell death. Here, the group expanded their work to include *in vivo* models showing that their PDT system decreased proliferating cell nuclear antigen and degree of vascularization which limited tumor growth to a size increase of approximately 40% as compared to 300–400% in control tumors. No explanation is given as to why these markers decrease with APDT treatment.

In a report by Zhang et al. (2014), they coprecipitated meta-tetra(hydroxyphenyl)-chlorin (m-THPC), a PS, an amphiphilic dendrimer, and semi-conducting polymer poly[2-methoxy-5-((2-ethylhexyl)oxy)-p-phenylenevinylene] (MEH-PPV) in order to create hydroxyl terminated photosensitizer doped polymer dots (HO-Pdots), which were then covalently linked to folic acid and horseradish peroxidase (FH-Pdots). The importance of this study lies in the specificity exhibited by preferential uptake and ROS generation of FH-Pdots in MCF-7 and C6 cancer cells as opposed to none in healthy normal NIH 3T3 cells; this is an important analysis omitted by many papers. While showing overall cancer cell toxicity is an acceptable step in showing therapeutic efficacy, many studies also only use cancer cells as measures for non-toxicity of controls. The real value in any therapeutic system, if it is to outcompete traditional chemotherapy, is showing minimal toxicity to healthy cells. This is suggested to become standard practice in future works. There is a conflict shown in this paper when compared to a similar work; Jiang et al. (2019) utilize MEH-PPV as the only method by which PDT can occur in their system, but using the same polymer. Zhang et al. (2014) show that this same polymer is not sufficient to sustain significant ROS generation. In fact, Zhang et al. (2014) claim that MEH-PPV is primarily responsible for the observable fluorescence signature emitted by their FH-Pdots, and in this system can function as a FRET intermediate, and is not responsible for the PDT effect. While it is true that any polymer or molecule with a band gap can undergo either fluorescence or intersystem crossing, many dedicated PDT systems nearly always utilize a PS that prefers the singlet oxygen generation route. Nevertheless, Jiang et al. (2019) still shows impressive cell toxicities toward HeLa cancer cells. Due to the differences in cell choice and ROS generation characterization techniques, direct comparisons cannot be made.

Tri-Component

Some authors choose to combine more than two aspects of the PDT scheme in tri-component schemes. Multicomponent schemes are relatively rare in the literature, likely due to their synthetic complexity and the sometimes unneeded inclusion of a RET intermediate; this increased complexity does necessarily create increased anti-cancer effect.

A notable example was published by Wu et al. (2019), where CPPO was used to directly excite poly[(9,9'-dioctyl-2,7-divinylene-fluorenylene)-alt-2-methoxy-5-(2-ethyl-hexyloxy)-1,4-phenylene] (PFPV) *via* a CIEEL-like mechanism. PFPV then transfers the electronic energy *via* RET to the PS TPP, which, in the PDT productive pathway, undergoes intersystem crossing and electron transfer to generate singlet oxygen for cellular damage and death. As the amount of TPP is increased, the chemiluminescence of PFPV decreases as more energy is transferred *via* FRET to the PS (**Figure 8A**). The increased PDT efficiency can be clearly seen in **Figure 8B** where the absence of PFPV show similar cell toxicities as formulations without CPPO or TPP, with viabilities near 100%. This is because CPPO cannot chemically excite TPP. However, when PFPV is included to make the nanoparticle formulation (POCL), and even more so with folic acid (FA) attached, cell viabilities plummet as can be seen in live/dead assay microscopy (**Figure 8C**). Results here suggest that efficient cytotoxicity via PDT occurs primarily when the formulation is uptaken by the cell. *In vivo* results showed good tumor growth suppression as compared to relevant controls (**Figure 8D**). Better controls might include administration of a mixture of CPPO/PFPV/TPP without encapsulation in a nanoparticle capsule, but the authors were constrained by solubility limitations. In any case, the fluorescence signal of the PS TPP can be seen distributed throughout the body (**Figure 8E**), there is apparent targeting as far as the chemiluminescence of the APDT nanocomplex is concerned, again likely due to the oxidative conditions of the intratumor region (**Figure 8F**). This apparently sidesteps the issue brought up by Magalhães et al. (2016) wherein they claim that the use of APDT systems cannot be specific and thus do not have the advantages of conventional PDT.

DISCUSSION

The therapeutic efficacy and design of these APDT platforms are interesting, and have potential for further development in certain cases. APDT, or perhaps one might say nanoparticle theranostics in general, have recently been met with suspicion in terms of ability to translate successfully to clinic. In this respect, we feel that the potential of these APDT system lies in their ability to enhance diagnostic or therapy in a way beyond mere cancer treatment and tumor growth suppression. This potential can only manifest if researchers are diligent about understanding the underlying mechanism(s) by which APDT provides a therapeutic effect. The example set by Xu et al. (2019) where, despite seeing relatively modest tumor growth suppression when compared to other articles, they provide a plausible caspase cleavage mechanism by which tumor growth suppression is observed. The advantage of this is that now it is understood how the nanoplatform drives toxicity in this cancer models, allow for the derivation of formulation-therapy effects. This mechanism may be similar to toxicity induced by other types of nanoparticle formulations, or it may be different. Unfortunately, because many researchers choose to end their investigation with simply observing the differences in survival or tumor growth, comparison via nanoparticle formulation and cancer cell therapy is difficult; some of these measures concerning murine survival or tumor growth have been found to not correlate well with actual observed clinical success. Mechanistic characterization will allow researchers to derive structure-function-therapy relationships between nanoparticles and effects on the cellular environment.

In some cases of CL based excitation of PS, the unwillingness of some authors to verify the mechanism of excitation for their APDT system is problematic. While a full proof is not necessary, supporting evidence for the method of excitation of the CL and the following transfer to the PS should be included in all papers. Besides this, it is frequently difficult to discern what plays the role of the substrate, luminescence source, the transfer agent, if present, and the acceptor/ROS generator in some papers. While some papers clearly include a proposed mechanism or scheme of the proposed method of therapy, some do not and some are quite ambiguous about which aspect of their own, often quite complex, nanoparticle system fulfills which requirements for effective APDT. On a related note, the authors did not find in their search any current reports directly coupling CL compounds and a RET intermediate in a nanoparticle formulation, so this section is omitted in this report. This is curious given the apparent functional relation between these two components.

What is clear, broadly, at least, is that simple hydroxyl radical, singlet oxygen, and ROSs in general can cause cell toxicity in a number of ways (Huang, 2005; Dąbrowski and Arnaut, 2015; van Straten et al., 2017). Does the structure, functionality, or method of excitation change the mechanism of cancer cell toxicity? Many of these questions are unclear, however, there has been at least one function that appears consistent: cellular uptake of APDT platforms is a critical component of their toxicity to cell *in vitro* and *in vivo*. As shown clearly in work by Wu et al. (2019), the FA moiety promotes cellular uptake and is used commonly as a functional group for the nanoparticle APDT system in many other papers. This is most probably because the generation of singlet oxygen, a short-lived molecular specie, or any other ROS is most effective when generated from within the cell, as it can more directly disrupt cellular processes from within.

One area where the literature is lacking greatly is a plausible explanation, or set of plausible explanations which account

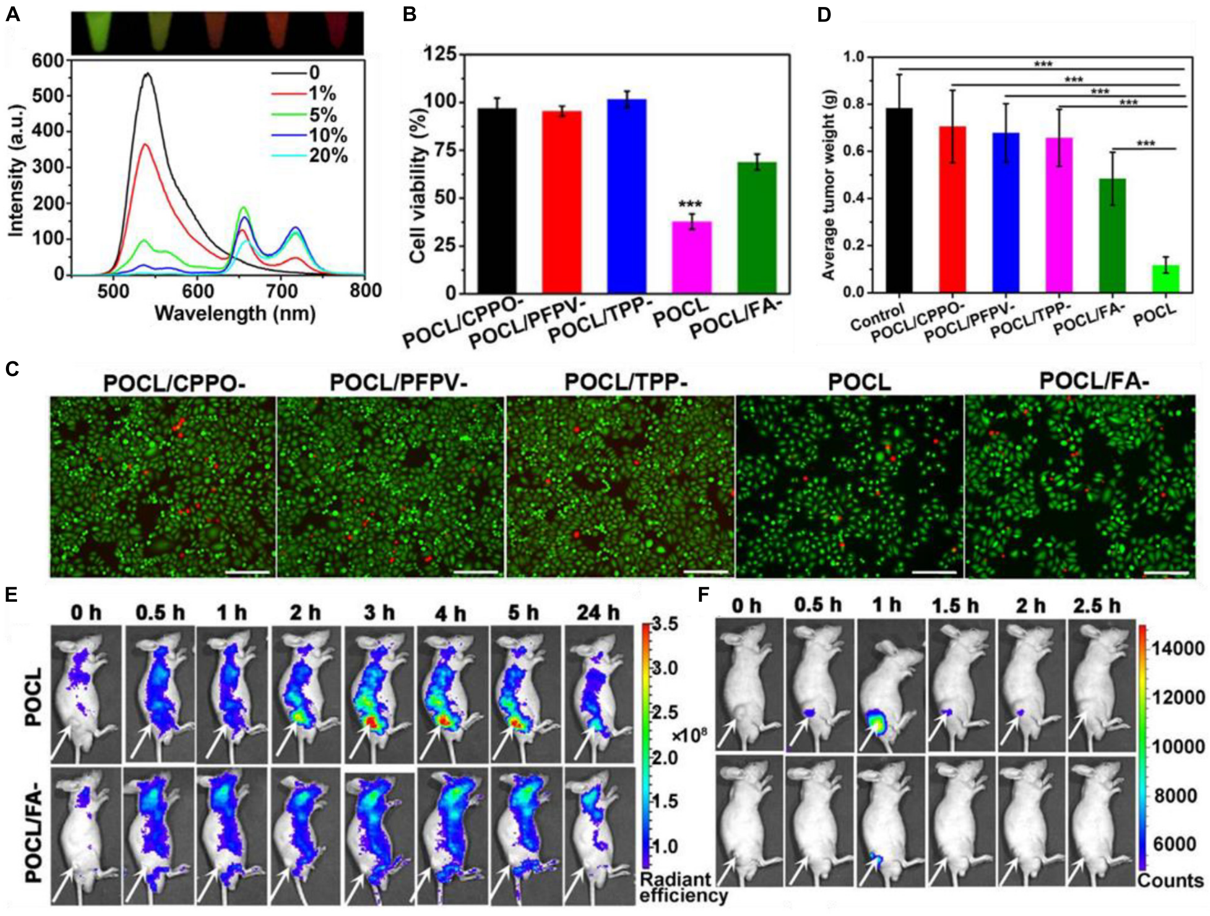

FIGURE 8 | (A) The change in fluorescence emission spectrum of a POCL solution containing different TPP:PFPV ratios. **(B)** HeLa cancer cell toxicity of the POCL *sans* varying components as controls. **(C)** live/dead stain of HeLa cells. **(D)** End-point tumor size values for different treatments. **(E)** Fluorescence imaging of POCL or POCL/FA$^-$ over time as compared to **(F)** chemiluminescent images (Wu et al., 2019). $^{***}P < 0.001$.

for the large discrepancy between expected light fluence in a tissue and the resulting PDT therapeutic effects. Both RET and CRET based treatments exhibit much lower (at least 100–1000x weaker) light fluence rates, below what is considered actionable for effective PDT (Schipper et al., 2006), yet nanoparticle based papers are still observing significant anti-cancer effects with supporting mechanistic proof of PDT-type disruption. It is entirely possible that the presence of the nanoparticle itself contributes to this toxicity or else modifies the excitation of the PS beyond what is considered typical in a theoretical model. Of course, biological and nanoscale systems are areas where the assumptions put forward by Forster for RET breakdown considerably (Scholes, 2003; Watrob et al., 2003a), which of course would alter the efficiency of PDT. Also, Cerenkov radiation is not generally subject to absorption in the same way as traditional light since the medium itself is what gives rise to the observed radiation. Future fundamental research ought to elucidate the precise mechanism by which these low fluence rates can give rise to such efficacious PDT, since hitherto the literature consensus is that the total energy transferred to the PS is almost certainly less than competing illuminated PDT. However, little seems to be known what the true "effective" dose appears to be and certainly even less is known how formulation within a nanoparticle system may affect this "minimum" excitation dosage. Given the repeated success in this field for anti-cancer therapy, it appears that pure illuminating power may not be the most critical factor in determining a PS's ability to induce cytotoxicity. However, the ultimate goal of APDT is to remove the depth penetration issue of external illumination, so some researchers consider this point moot and so many of the proposed uses covered in this review are with regard to deep-seated or metastatic tumor models.

The advantages to using CRET for PDT and imaging lie in that no stimulus needs to be provided whatsoever to the luminescent compound, the beta-radiation emitting isotope, which functions totally independently of the microenvironment. Further, the RET-driven PDT is long-lasting for as long as the PS remain active and the particles remain in the body. The disadvantage is lack of specificity. As just mentioned, RET driven PDT occurs regardless of the environment. Since most CLs are able to generate excited electronic states in oxidative, or ROS-rich, environments, like those found in the tumor cell, a specific

PDT treatment can still be accomplished, which is one of the main advantages of utilizing PDT in the first place. This can counter a main detraction of APDT in RET systems which says that APDT driven systems lose specificity (Magalhães et al., 2016). However, because the conditions inside tumor cells are considerably more oxidative than the rest of the body, perhaps this is not a limitation as far as some instances of RET-based APDT is concerned. For example, CPPO and luminol both generate excited electronic states from oxidation by ROSs, which are naturally elevated in some tumor tissues. Thus, oxidative intratumoral environments generate more excited electronic states which transfer *via* RET to the PS generating singlet oxygen for therapy. Wu et al. (2019) in the paper by Bin Liu and coworkers, there is a clear preference for the chemiexcitation of CPPO to occur only in the tumor microenvironment. This specificity is still retained as far as chemiluminescence generation of ROS.

Additionally, it is sometimes unclear how functionalizing PSs into nanoparticle system affects their ability to generate ROSs. While papers show generally an increase in intracellular ROS when using nanoparticle systems, this could result from increased intracellular uptake (phagocytosis) of nanoparticle complexes as compared with free PS; some papers omit these comparisons altogether, which is unacceptable as a formulation obviously needs to improve upon existing therapy in some concrete way. Further experiments should always use appropriate comparative controls showing how nanoparticles can induce a specific increase in efficacy of APDT. Further, the stability of the auto-PDT nanoparticle platforms is also problematic. While inorganic or inorganic components of NPs are unlikely to undergo significant degradation in the presence of ROSs or singlet oxygen, organic NP components are likely to do so. Little work has been done in this vein, and whether or not NPs are capable of resisting or undergoing breakdown in the biological environment is a major concern for translating nanomedicine to the clinic. Some CL and RET based systems show specific activity or therapy in tumor regions, but such action could also occur after partial or complete breakdown of the nanoparticle system *in vivo*.

As a final point of consideration, many papers seek to validate their methods of therapeutic efficacy by showing increased toxicity to cancer cells *in vitro* or *in vivo*. However, there is a second aspect to cancer nanotheranostics, which appears to be downplayed in favor of greater toxicity: PDT or any other therapy can induce toxicity in healthy cells as well, so a formulation that does not immediately generate greater *in vitro* toxicity should not necessarily be looked upon as a failure, as Zhao et al. showed that by modifying the amount and type of PS and the microcapsule environment, lower cell toxicity can be observed (Zhao et al., 2013a). Further, lowered toxicity may have resulted from the relatively poor uptake of the microcapsules into the cells, but the results are interestingly at odds with the rest of the literature. The other multi-component systems relevant to this review have already been discussed in previous sections.

Concluding, there is much research in the area of using Cherenkov radiation and chemiluminescent compounds for driving PDT in order to solve the depth penetration issue suffered by more conventional PDT methods. Nanoparticles can be beneficial for increasing the effectiveness of APDT by increasing the cellular uptake of PSs, increasing the tumor intracellular toxicity, and bringing together, *via* co-functionalization, the various components of a sometimes quite complex APDT platform. Success has been shown in several papers for the suppression of tumor growth in murine models despite the presence of conflicting results in an emerging field. Perhaps the root of these contradictions will be made apparent by characterizing the methods by which ROS generation by NP functionalized PSs can lead to cancer cell toxicity, as some groups have already started doing. Real promise in this area largely remains in the characterization of cancer cell specific toxicity, as compared directly to toxicity induced in normal healthy cells, and derivation of relationships between how nanoparticle formulation can influence the mechanism of induced toxicity in cells.

AUTHOR CONTRIBUTIONS

NB reviewed most of the literatures and wrote the majority of the main text. YZ provided several ideas about organization and topics, and contributed to parts of the text. JL and JQ discussed and edited the text. JL and PH provided the review direction, contributed original ideas for content, reviewed areas of the literature, and contributed to parts of the text. All authors contributed to the article and approved the submitted version.

FUNDING

This work was financially supported by the National Key Research and Development Program of China (2018YFA0704000), Basic Research Program of Shenzhen (JCYJ20170412111100742 and JCYJ20180507182413022), Ying-Tong Education Foundation for Young Teachers in the Higher Education Institutions of China (161032), Shenzhen Science and Technology Program (KQTD20190929172538530), and Guangdong Province Natural Science Foundation of Major Basic Research and Cultivation Project (2018B030308003).

ACKNOWLEDGMENTS

We thank the support of Shenzhen University.

REFERENCES

Al-Ani, A. W., Zhang, L., Ferreira, L., Turyanska, L., Bradshaw, T. D., and Thomas, N. R. (2019). Listeria innocua Dps as a nanoplatform for bioluminescence based photodynamic therapy utilizing *Gaussia princeps* luciferase and zinc protoporphyrin IX. *Nanomed. Nanotechnol. Biol. Med.* 20:102005. doi: 10.1016/j.nano.2019.04.008

Albreacht, H. O. (1928). Concerning the chemo luminescence of aminophthalic acid hydrazides. *Z Für. Phys. Chem. Stochiomet. Verwandtschaftslehre* 136, 321–330.

Almeida de Oliveira, M., Bartoloni, F. H., Augusto, F. A., Ciscato, L. F. M. L., Bastos, E. L., and Baader, W. J. (2012). Revision of singlet quantum yields in the catalyzed decomposition of cyclic peroxides. *J. Org. Chem.* 77, 10537–10544. doi: 10.1021/jo301309v

Almerie, M. Q., Gossedge, G., Wright, K. E., and Jayne, D. G. (2017). Treatment of peritoneal carcinomatosis with photodynamic therapy: systematic review of current evidence. *Photodiagn. Photodyn. Ther.* 20, 276–286. doi: 10.1016/j.pdpdt.2017.10.021

An, H., Guo, C., Li, D., Liu, R., Xu, X., Guo, J., et al. (2020). Hydrogen peroxide-activatable nanoparticles for luminescence imaging and in situ triggerable photodynamic therapy of cancer. *ACS Appl. Mater. Interf.* 12, 17230–17243. doi: 10.1021/acsami.0c01413

Aratani, Y. (2018). Myeloperoxidase: its role for host defense, inflammation, and neutrophil function. *Arch. Biochem. Biophys.* 640, 47–52. doi: 10.1016/j.abb.2018.01.004

Augusto, F. A., de Souza, G. A., de Souza Júnior, S. P., Khalid, M., and Baader, W. J. (2013). Efficiency of electron transfer initiated chemiluminescence. *Photochem. Photobiol.* 89, 1299–1317. doi: 10.1111/php.12102

Bargo, P. R., and Jacques, S. L. (2001). "Clinical study assessing the photosensitizer accumulation and light penetration for esophageal cancer prior to treatment by PDT," in *Proceedings of SPIE - The International Society for Optical Engineering*, San Jose, CA.

Bashkatov, A. N., Genina, E. A., Kochubey, V. I., and Tuchin, V. V. (2005). Optical properties of human skin, subcutaneous and mucous tissues in the wavelength range from 400 to 2000 nm. *J. Phys. Appl. Phys.* 38, 2543–2555. doi: 10.1088/0022-3727/38/15/004

Bashkatov, A. N., Genina, E. A., and Tuchin, V. V. (2011). Optical properties of skin, subcutaneous, and muscle tissues: a review. *J. Innov. Opt. Health Sci.* 04, 9–38. doi: 10.1142/S1793545811001319

Bernhard, Y., Collin, B., and Decréau, R. A. (2017). Redshifted Cherenkov radiation for in vivo imaging: coupling Cherenkov radiation energy transfer to multiple Förster resonance energy transfers. *Sci. Rep.* 7:45063. doi: 10.1038/srep45063

Berwin Singh, S. V., Kim, J., Park, H., Khang, G., and Lee, D. (2017). Novel chemi-dynamic nanoparticles as a light-free photodynamic therapeutic system for cancer treatment. *Macromol. Res.* 25, 749–755. doi: 10.1007/s13233-017-5078-5079

Cairns, R. A., Harris, I. S., and Mak, T. W. (2011). Regulation of cancer cell metabolism. *Nat. Rev. Cancer* 11, 85–95. doi: 10.1038/nrc2981

Catalani, L. H., and Wilson, T. (1989). Electron transfer and chemiluminescence. Two inefficient systems: 1,4-dimethoxy-9,10-diphenylanthracene peroxide and diphenoyl peroxide. *J. Am. Chem. Soc.* 111, 2633–2639. doi: 10.1021/ja00189a043

Čerenkov, P. A. (1937). Visible radiation produced by electrons moving in a medium with velocities exceeding that of light. *Phys. Rev.* 52, 378–379. doi: 10.1103/PhysRev.52.378

Chen, H., Wang, G. D., Chuang, Y.-J., Zhen, Z., Chen, X., Biddinger, P., et al. (2015). Nanoscintillator-mediated X-ray inducible photodynamic therapy for in vivo cancer treatment. *Nano Lett.* 15, 2249–2256. doi: 10.1021/nl504044p

Chen, H. H., Ho, Y.-P., Jiang, X., Mao, H.-Q., Wang, T.-H., and Leong, K. W. (2009). Simultaneous non-invasive analysis of DNA condensation and stability by two-step QD-FRET. *Nano Today* 4, 125–134. doi: 10.1016/j.nantod.2009.02.008

Chen, T.-C., Huang, L., Liu, C.-C., Chao, P.-J., and Lin, F.-H. (2012). Luminol as the light source for in situ photodynamic therapy. *Process Biochem.* 47, 1903–1908. doi: 10.1016/j.procbio.2012.06.025

Ciscato, L. F. M. L., Bartoloni, F. H., Bastos, E. L., and Baader, W. J. (2009). Direct kinetic observation of the chemiexcitation step in peroxyoxalate chemiluminescence. *J. Org. Chem.* 74, 8974–8979. doi: 10.1021/jo901402k

Clennan, E. L. (2000). New mechanistic and synthetic aspects of singlet oxygen chemistry. *Tetrahedron* 56, 9151–9179. doi: 10.1016/S0040-4020(00)00794-798

Cohen, D., and Lee, P. (2016). Photodynamic therapy for non-melanoma skin cancers. *Cancers* 8, 1–9. doi: 10.3390/cancers8100090

Costanzo, M., Scolaro, L., Berlier, G., Marengo, A., Grecchi, S., Zancanaro, C., et al. (2016). Cell uptake and intracellular fate of phospholipidic manganese-based nanoparticles. *Int. J. Pharm.* 508, 83–91. doi: 10.1016/j.ijpharm.2016.05.019

Dąbrowski, J. M., and Arnaut, L. G. (2015). Photodynamic therapy (PDT) of cancer: from local to systemic treatment. *Photochem. Photobiol. Sci.* 14, 1765–1780. doi: 10.1039/C5PP00132C

DeRosa, M. (2002). Photosensitized singlet oxygen and its applications. *Coord. Chem. Rev.* 233–234, 351–371. doi: 10.1016/S0010-8545(02)00034-36

DeWitt, J. M., Sandrasegaran, K., O'Neil, B., House, M. G., Zyromski, N. J., Sehdev, A., et al. (2019). Phase 1 study of EUS-guided photodynamic therapy for locally advanced pancreatic cancer. *Gastrointest. Endosc.* 89, 390–398. doi: 10.1016/j.gie.2018.09.007

Dougherty, T. J. (1987). Photosensitizers: therapy and detection of malignant tumors. *Photochem. Photobiol.* 45, 879–889. doi: 10.1111/j.1751-1097.1987.tb07898.x

Duan, X., Chan, C., Guo, N., Han, W., Weichselbaum, R. R., and Lin, W. (2016). Photodynamic therapy mediated by nontoxic core-shell nanoparticles synergizes with immune checkpoint blockade to elicit antitumor immunity and antimetastatic. *J. Am. Chem. Soc.* 138, 16686–16695. doi: 10.1021/jacs.6b09538

Fan, W., Huang, P., and Chen, X. (2016). Overcoming the Achilles' heel of photodynamic therapy. *Chem. Soc. Rev.* 45, 6488–6519. doi: 10.1039/C6CS00616G

Fan, W., Lu, N., Xu, C., Liu, Y., Lin, J., Wang, S., et al. (2017). Enhanced afterglow performance of persistent luminescence implants for efficient repeatable photodynamic therapy. *ACS Nano* 11, 5864–5872. doi: 10.1021/acsnano.7b01505

Fisher, C., Ali, Z., Detsky, J., Sahgal, A., David, E., Kunz, M., et al. (2019). Photodynamic therapy for the treatment of vertebral metastases: a Phase I clinical trial. *Clin. Cancer Res.* 25, 5766–5776. doi: 10.1158/1078-0432.CCR-19-0673

Galperin, E., Verkhusha, V. V., and Sorkin, A. (2004). Three-chromophore FRET microscopy to analyze multiprotein interactions in living cells. *Nat. Methods* 1, 209–217. doi: 10.1038/nmeth720

Glaser, A. K., Zhang, R., Andreozzi, J. M., Gladstone, D. J., and Pogue, B. W. (2015). Cherenkov radiation fluence estimates in tissue for molecular imaging and therapy applications. *Phys. Med. Biol.* 60, 6701–6718. doi: 10.1088/0031-9155/60/17/6701

Gonzales, J., Wang, F., Zamora, G., Trinidad, A., Marcu, L., Cherry, S., et al. (2014). "Ultra low fluence rate photodynamic therapy: simulation of light emitted by the Cerenkov effect," in *Proceedings of the Volume 8928, Optical Techniques in Neurosurgery, Neurophotonics, and Optogenetics*, San Francisco, CA.

Hauge, T., Hauge, P. W., Warloe, T., Drolsum, A., Johansen, C., Viktil, E., et al. (2016). Randomised controlled trial of temoporfin photodynamic therapy plus chemotherapy in nonresectable biliary carcinoma—PCS Nordic study. *Photodiagnosis Photodyn. Ther.* 13, 330–333. doi: 10.1016/j.pdpdt.2015.09.004

Haugland, R. P., Yguerabide, J., and Stryer, L. (1969). Dependence of the kinetics of singlet-singlet energy transfer on spectral overlap. *Proc. Natl. Acad. Sci. U.S.A.* 63, 23–30. doi: 10.1073/pnas.63.1.23

Hsu, C.-Y., Chen, C.-W., Yu, H.-P., Lin, Y.-F., and Lai, P.-S. (2013). Bioluminescence resonance energy transfer using luciferase-immobilized quantum dots for self-illuminated photodynamic therapy. *Biomaterials* 34, 1204–1212. doi: 10.1016/j.biomaterials.2012.08.044

Hu, X., Li, Y., Liu, T., Zhang, G., and Liu, S. (2015). Intracellular cascade FRET for temperature imaging of living cells with polymeric ratiometric fluorescent thermometers. *ACS Appl. Mater. Interf.* 7, 15551–15560. doi: 10.1021/acsami.5b04025

Huang, Z. (2005). A review of progress in clinical photodynamic therapy. *Technol. Cancer Res. Treat.* 4, 283–293. doi: 10.1177/153303460500400308

Isobe, H., Takano, Y., Okumura, M., Kuramitsu, S., and Yamaguchi, K. (2005). Mechanistic insights in charge-transfer-induced luminescence of 1,2-dioxetanones with a substituent of low oxidation potential. *J. Am. Chem. Soc.* 127, 8667–8679. doi: 10.1021/ja043295f

Jares-Erijman, E. A., and Jovin, T. M. (2003). FRET imaging. *Nat. Biotechnol.* 21, 1387–1395. doi: 10.1038/nbt896

Jelley, J. V. (1955). Cerenkov radiation and its applications. *Br. J. Appl. Phys.* 6, 227–232. doi: 10.1088/0508-3443/6/7/301

Jiang, L., Bai, H., Liu, L., Lv, F., Ren, X., and Wang, S. (2019). Luminescent, oxygen-supplying, hemoglobin-linked conjugated polymer nanoparticles for photodynamic therapy. *Angew. Chem. Int. Ed.* 58, 10660–10665. doi: 10.1002/anie.201905884

Kamkaew, A., Cheng, L., Goel, S., Valdovinos, H. F., Barnhart, T. E., Liu, Z., et al. (2016). Cerenkov radiation induced photodynamic therapy using chlorin e6-loaded hollow mesoporous silica nanoparticles. *ACS Appl. Mater. Interf.* 8, 26630–26637. doi: 10.1021/acsami.6b10255

Kawczyk-Krupka, A., Bugaj, A. M., Latos, W., Zaremba, K., Wawrzyniec, K., and Sieroń, A. (2015). Photodynamic therapy in colorectal cancer treatment: the state of the art in clinical trials. *Photodiagn. Photodyn. Ther.* 12, 545–553. doi: 10.1016/j.pdpdt.2015.04.004

Kim, Y. R., Kim, S., Choi, J. W., Choi, S. Y., Lee, S.-H., Kim, H., et al. (2015). Bioluminescence-activated deep-tissue photodynamic therapy of cancer. *Theranostics* 5, 805–817. doi: 10.7150/thno.11520

Klein, J. S., Sun, C., and Pratx, G. (2019). Radioluminescence in biomedicine: physics, applications, and models. *Phys. Med. Biol.* 64:04TR01. doi: 10.1088/1361-6560/aaf4de

Koo, J.-Y., and Schuster, G. B. (1978). Chemiluminescence of diphenoyl peroxide. Chemically initiated electron exchange luminescence. A new general mechanism for chemical production of electronically excited states. *J. Am. Chem. Soc.* 100, 4496–4503. doi: 10.1021/ja00482a030

Kotagiri, N., Sudlow, G. P., Akers, W. J., and Achilefu, S. (2015). Breaking the depth dependency of phototherapy with Cerenkov radiation and low-radiance-responsive nanophotosensitizers. *Nat. Nanotechnol.* 10, 370–379. doi: 10.1038/nnano.2015.17

Laor, U., Hsieh, J. C., and Ludwig, P. K. (1973). Intersystem crossing to higher triplet states in isolated molecules. *Chem. Phys. Lett.* 22, 150–153.

Lin, W., Gong, J., Fang, L., and Jiang, K. (2019). A photodynamic system based on endogenous bioluminescence for in vitro anticancer studies. *Z. Für. Anorg. Allg. Chem.* 645, 1161–1164. doi: 10.1002/zaac.201900144

Liu, D., Chen, B., Mo, Y., Wang, Z., Qi, T., Zhang, Q., et al. (2019). Redox-activated porphyrin-based liposome remote-loaded with indoleamine 2,3-dioxygenase (IDO) inhibitor for synergistic photoimmunotherapy through induction of immunogenic cell death and blockage of IDO pathway. *Nano Lett.* 19, 6964–6976. doi: 10.1021/acs.nanolett.9b02306

Liu, G., Zhang, S., Shi, Y., Huang, X., Tang, Y., Chen, P., et al. (2018). "Wax-sealed" theranostic nanoplatform for enhanced afterglow imaging-guided photothermally triggered photodynamic therapy. *Adv. Funct. Mater.* 28:1804317. doi: 10.1002/adfm.201804317

Ma, L., Zou, X., and Chen, W. (2014). A new X-ray activated nanoparticle photosensitizer for cancer treatment. *J. Biomed. Nanotechnol.* 10, 1501–1508. doi: 10.1166/jbn.2014.1954

Magalhães, C. M., Esteves da Silva, J. C. G., and Pinto da Silva, L. (2016). Chemiluminescence and bioluminescence as an excitation source in the photodynamic therapy of cancer: a critical review. *Chemphyschem* 17, 2286–2294. doi: 10.1002/cphc.201600270

Mahmoudi, K., Garvey, K. L., Bouras, A., Cramer, G., Stepp, H., Jesu Raj, J. G., et al. (2019). 5-aminolevulinic acid photodynamic therapy for the treatment of high-grade gliomas. *J. Neurooncol.* 141, 595–607. doi: 10.1007/s11060-019-03103-3104

Mao, D., Wu, W., Ji, S., Chen, C., Hu, F., Kong, D., et al. (2017). Chemiluminescence-guided cancer therapy using a chemiexcited photosensitizer. *Chemistry* 3, 991–1007. doi: 10.1016/j.chempr.2017.10.002

Matsumoto, M. (2004). Advanced chemistry of dioxetane-based chemiluminescent substrates originating from bioluminescence. *J. Photochem. Photobiol. C Photochem. Rev.* 5, 27–53. doi: 10.1016/j.jphotochemrev.2004.02.001

Menzel, R., and Thiel, E. (1998). Intersystem crossing rate constants of rhodamine dyes: influence of the amino-group substitution. *Chem. Phys. Lett.* 291, 237–243. doi: 10.1016/S0009-2614(98)00566-561

Miller, G. G., Brown, K., Moore, R. B., Diwu, Z., Liu, J., Huang, L., et al. (1994). "Intracellular uptake kinetics of hypocrellin photosensitizers for photodynamic therapy," in *Proceedings of the Volume 2371, 5th International Photodynamic Association Biennial Meeting*, Amelia Island, FL.

Naidoo, C., Kruger, C. A., and Abrahamse, H. (2018). Photodynamic therapy for metastatic melanoma treatment: a review. *Technol. Cancer Res. Treat.* 17:153303381879179. doi: 10.1177/1533033818791795

Ni, D., Ferreira, C. A., Barnhart, T. E., Quach, V., Yu, B., Jiang, D., et al. (2018). Magnetic targeting of nanotheranostics enhances cerenkov radiation-induced photodynamic therapy. *J. Am. Chem. Soc.* 140, 14971–14979. doi: 10.1021/jacs.8b09374

Orlova, G., Goddard, J. D., and Brovko, L. Y. (2003). Theoretical study of the amazing firefly bioluminescence: the formation and structures of the light emitters. *J. Am. Chem. Soc.* 125, 6962–6971. doi: 10.1021/ja021255a

Pinto da Silva, L., and Esteves da Silva, J. C. G. (2013a). Interstate crossing-induced chemiexcitation as the reason for the chemiluminescence of dioxetanones. *Chemphyschem* 14, 1071–1079. doi: 10.1002/cphc.201200872

Pinto da Silva, L., and Esteves da Silva, J. C. G. (2013b). Mechanistic study of the unimolecular decomposition of 1,2-dioxetanedione. *J. Phys. Org. Chem.* 26, 659–663. doi: 10.1002/poc.3149

Rizzo, J. M., Segal, R. J., and Zeitouni, N. C. (2018). Combination vismodegib and photodynamic therapy for multiple basal cell carcinomas. *Photodiagn. Photodyn. Ther.* 21, 58–62. doi: 10.1016/j.pdpdt.2017.10.028

Sadhu, K. K., Chatterjee, S., Sen, S., and Bharadwaj, P. K. (2010). Role of spacer in single- or two-step FRET: studies in the presence of two connected cryptands with properly chosen fluorophores. *Dalton Trans.* 39, 4146–4154. doi: 10.1039/c000681e

Schipper, M. L., Patel, M. R., and Gambhir, S. S. (2006). Evaluation of firefly luciferase bioluminescence mediated photodynamic toxicity in cancer cells. *Mol. Imaging Biol.* 8, 218–225. doi: 10.1007/s11307-006-0048-41

Scholes, G. D. (2003). Long-range resonance energy transfer in molecular systems. *Annu. Rev. Phys. Chem.* 54, 57–87. doi: 10.1146/annurev.physchem.54.011002.103746

Schuster, G. B. (1979). Chemiluminescence of organic peroxides. Conversion of ground-state reactants to excited-state products by the chemically initiated electron-exchange luminescence mechanism. *Acc. Chem. Res.* 12, 366–373. doi: 10.1021/ar50142a003

Shaffer, T. M., Pratt, E. C., and Grimm, J. (2017). Utilizing the power of Cerenkov light with nanotechnology. *Nat. Nanotechnol.* 12, 106–117. doi: 10.1038/nnano.2016.301

Shim, H. K., Lee, J. I., Kang, I. N., Jeoung, S. C., Kim, D., and Zyung, T. (1997). Light emitting properties of poly(2-fluoro-1,4-phenylene vinylene) as compared with poly(1,4-phenylenevinylene). *Mol. Cryst. Liq. Cryst. Sci. Technol. Sect. Mol. Cryst. Liq. Cryst.* 294, 117–122. doi: 10.1080/10587259708032262

Shramova, E. I., Deyev, S. M., and Proshkina, G. M. (2018). Efficiency of bioluminescence resonance energy transfer in the NanoLuc-miniSOG-Furimazine system. *Russ. J. Bioorgan. Chem.* 44, 755–758. doi: 10.1134/S1068162018060080

Song, L., Li, P.-P., Yang, W., Lin, X.-H., Liang, H., Chen, X.-F., et al. (2018). Low-dose X-ray activation of W(VI)-doped persistent luminescence nanoparticles for deep-tissue photodynamic therapy. *Adv. Funct. Mater.* 28:1707496. doi: 10.1002/adfm.201707496

Spinelli, A. E., and Boschi, F. (2015). Novel biomedical applications of Cerenkov radiation and radioluminescence imaging. *Phys. Med.* 31, 120–129. doi: 10.1016/j.ejmp.2014.12.003

Stevani, C. V., Silva, S. M., and Baader, W. J. (2000). Studies on the mechanism of the excitation step in peroxyoxalate chemiluminescence. *Eur. J. Org. Chem.* 2000, 4037–4046.

Sun, W., Zhou, Z., Pratx, G., Chen, X., and Chen, H. (2020). Nanoscintillator-mediated X-ray induced photodynamic therapy for deep-seated tumors: from concept to biomedical applications. *Theranostics* 10, 1296–1318. doi: 10.7150/thno.41578

Tanha, K., Pashazadeh, A. M., and Pogue, B. W. (2015). Review of biomedical Èerenkov luminescence imaging applications. *Biomed. Opt. Express* 6, 3053–3065. doi: 10.1364/BOE.6.003053

Theodossiou, T., Hothersall, J. S., Woods, E. A., Okkenhaug, K., Jacobson, J., and MacRobert, A. J. (2003). Firefly luciferin-activated rose bengal: in vitro photodynamic therapy by intracellular chemiluminescence in transgenic NIH 3T3 cells. *Cancer Res.* 63, 1818–1821.

Trachootham, D., Alexandre, J., and Huang, P. (2009). Targeting cancer cells by ROS-mediated mechanisms: a radical therapeutic approach? *Nat. Rev. Drug Discov.* 8, 579–591. doi: 10.1038/nrd2803

Trachootham, D., Zhou, Y., Zhang, H., Demizu, Y., Chen, Z., Pelicano, H., et al. (2006). Selective killing of oncogenically transformed cells through a ROS-mediated mechanism by β-phenylethyl isothiocyanate. *Cancer Cell* 10, 241–252. doi: 10.1016/j.ccr.2006.08.009

van Straten, D., Mashayekhi, V., de Bruijn, H., Oliveira, S., and Robinson, D. (2017). Oncologic photodynamic therapy: basic principles, current clinical status and future directions. *Cancers* 9:19. doi: 10.3390/cancers9020019

Wang, G. D., Nguyen, H. T., Chen, H., Cox, P. B., Wang, L., Nagata, K., et al. (2016). X-ray induced photodynamic therapy: a combination of radiotherapy and photodynamic therapy. *Theranostics* 6, 2295–2305. doi: 10.7150/thno.16141

Wang, J., Li, J., Yu, J., Zhang, H., and Zhang, B. (2018). Large hollow cavity luminous nanoparticles with near-infrared persistent luminescence and tunable sizes for tumor afterglow imaging and chemo-/photodynamic therapies. *ACS Nano* 12, 4246–4258. doi: 10.1021/acsnano.7b07606

Ware, W. R., Doemeny, L. J., and Nemzek, T. L. (1973). Deconvolution of fluorescence and phosphorescence decay curves. Least-squares method. *J. Phys. Chem.* 77, 2038–2048. doi: 10.1021/j100636a003

Watrob, H. M., Pan, C. P., and Barkley, M. D. (2003a). Beyond Förster resonance energy transfer in biological and nanoscale systems. *J. Am. Chem. Soc.* 125, 7336–7343. doi: 10.1021/ja034564p

Watrob, H. M., Pan, C. P., and Barkley, M. D. (2003b). Two-step FRET as a structural tool. *J. Am. Chem. Soc.* 125, 7336–7343.

Windahl, T., Peng, Q., Moan, J., Hellsten, S., Axelsson, B., and Löfgren, L. (1993). Uptake and distribution of intravenously or intravesically administered photosensitizers in the rat. *Cancer Lett.* 75, 65–70. doi: 10.1016/0304-3835(93)90209-R

Wu, M., Wu, L., Li, J., Zhang, D., Lan, S., Zhang, X., et al. (2019). Self-luminescing theranostic nanoreactors with intraparticle relayed energy transfer for tumor microenvironment activated imaging and photodynamic therapy. *Theranostics* 9, 20–33. doi: 10.7150/thno.28857

Xu, J., Xu, L., Wang, C., Yang, R., Zhuang, Q., Han, X., et al. (2017). Near-infrared-triggered photodynamic therapy with multitasking upconversion nanoparticles in combination with checkpoint blockade for immunotherapy of colorectal cancer. *ACS Nano* 11, 4463–4474. doi: 10.1021/acsnano.7b00715

Xu, L., Zhou, K., Ma, H., Lv, A., Pei, D., Li, G., et al. (2020). Ultralong organic phosphorescent nanocrystals with long-lived triplet excited states for afterglow imaging and photodynamic therapy. *ACS Appl. Mater. Interf.* 12, 18385–18394. doi: 10.1021/acsami.0c04005

Xu, X., An, H., Zhang, D., Tao, H., Dou, Y., Li, X., et al. (2019). A self-illuminating nanoparticle for inflammation imaging and cancer therapy. *Sci. Adv.* 5:sciadv.aat2953. doi: 10.1126/sciadv.aat2953

Yang, G., Xu, L., Xu, J., Zhang, R., Song, G., Chao, Y., et al. (2018). Smart nanoreactors for pH-responsive tumor homing, mitochondria-targeting, and enhanced photodynamic-immunotherapy of cancer. *Nano Lett.* 18, 2475–2484. doi: 10.1021/acs.nanolett.8b00040

Yang, Y., Hou, W., Liu, S., Sun, K., Li, M., and Wu, C. (2018). Biodegradable polymer nanoparticles for photodynamic therapy by bioluminescence resonance energy transfer. *Biomacromolecules* 19, 201–208. doi: 10.1021/acs.biomac.7b01469

Yang, J., Zhao, Y., Meng, Y., Zhu, H., Yan, D., Liu, C., et al. (2020). Irradiation-free photodynamic therapy in vivo induced by enhanced deep red afterglow within NIR-I bio-window. *Chem. Eng. J.* 387:124067. doi: 10.1016/j.cej.2020.124067

Yang, K., Wang, C., Wei, X., Ding, S., Liu, C., Tian, F., et al. (2020). Self-illuminating photodynamic therapy with enhanced therapeutic effect by optimization of the chemiluminescence resonance energy transfer step to the photosensitizer. *Bioconjug. Chem.* 31, 595–604. doi: 10.1021/acs.bioconjchem.9b00740

Yang, K., Wang, C., Liu, C., Ding, S., Tian, F., and Li, F. (2019). Bioluminescence-initiated photodynamic therapy bridged on high-luminescent carbon dots-conjugated protoporphyrin IX. *J. Mater. Sci.* 54, 3383–3391. doi: 10.1007/s10853-018-3038-3031

Yu, Z., Zhou, P., Pan, W., Li, N., and Tang, B. (2018). A biomimetic nanoreactor for synergistic chemiexcited photodynamic therapy and starvation therapy against tumor metastasis. *Nat. Commun.* 9:5044. doi: 10.1038/s41467-018-07197-7198

Yuan, H., Chong, H., Wang, B., Zhu, C., Liu, L., Yang, Q., et al. (2012). Chemical molecule-induced light-activated system for anticancer and antifungal activities. *J. Am. Chem. Soc.* 134, 13184–13187. doi: 10.1021/ja304986t

Yue, L., Liu, Y.-J., and Fang, W.-H. (2012). Mechanistic insight into the chemiluminescent decomposition of firefly dioxetanone. *J. Am. Chem. Soc.* 134, 11632–11639. doi: 10.1021/ja302979t

Zhang, Y., Pang, L., Ma, C., Tu, Q., Zhang, R., Saeed, E., et al. (2014). Small molecule-initiated light-activated semiconducting polymer dots: an integrated nanoplatform for targeted photodynamic therapy and imaging of cancer cells. *Anal. Chem.* 86, 3092–3099. doi: 10.1021/ac404201s

Zhao, J., Fei, J., Gao, L., Cui, W., Yang, Y., Wang, A., et al. (2013a). Bioluminescent microcapsules: Applications in activating a photosensitizer. *Chem. Eur. J.* 19, 4548–4555. doi: 10.1002/chem.201203922

Zhao, J., Wu, W., Sun, J., and Guo, S. (2013b). Triplet photosensitizers: from molecular design to applications. *Chem. Soc. Rev.* 42, 5323–5351. doi: 10.1039/c3cs35531d

Zhen, X., Zhang, C., Xie, C., Miao, Q., Lim, K. L., and Pu, K. (2016). Intraparticle energy level alignment of semiconducting polymer nanoparticles to amplify chemiluminescence for ultrasensitive in vivo imaging of reactive oxygen species. *ACS Nano* 10, 6400–6409. doi: 10.1021/acsnano.6b02908

Zhou, Z., Song, J., Nie, L., and Chen, X. (2016). Reactive oxygen species generating systems meeting challenges of photodynamic cancer therapy. *Chem. Soc. Rev.* 45, 6597–6626. doi: 10.1039/C6CS00271D

Conflict of Interest: The authors declare that the research was conducted in the absence of any commercial or financial relationships that could be construed as a potential conflict of interest.

frontiers in Bioengineering and Biotechnology

REVIEW
published: 23 October 2020
doi: 10.3389/fbioe.2020.594247

Exosomes as a Novel Approach to Reverse Osteoporosis: A Review of the Literature

Xudong Xie[1], Yuan Xiong[1], Adriana C. Panayi[2], Liangcong Hu[1], Wu Zhou[1], Hang Xue[1], Ze Lin[1], Lang Chen[1], Chenchen Yan[1], Bobin Mi[1]* and Guohui Liu[1]*

[1] Department of Orthopedics, Union Hospital, Tongji Medical College, Huazhong University of Science and Technology, Wuhan, China, [2] Division of Plastic Surgery, Brigham and Women's Hospital, Harvard Medical School, Boston, MA, United States

Edited by:
Gang Liu,
Xiamen University, China

Reviewed by:
Junqing Wang,
Sun Yat-sen University, China
Luciana Dini,
Sapienza University of Rome, Italy

***Correspondence:**
Guohui Liu
liuguohui@hust.edu.cn
Bobin Mi
mibobin@hust.edu.cn

Specialty section:
This article was submitted to Nanobiotechnology, a section of the journal Frontiers in Bioengineering and Biotechnology

Received: 12 August 2020
Accepted: 06 October 2020
Published: 23 October 2020

Citation:
Xie X, Xiong Y, Panayi AC, Hu L, Zhou W, Xue H, Lin Z, Chen L, Yan C, Mi B and Liu G (2020) Exosomes as a Novel Approach to Reverse Osteoporosis: A Review of the Literature. Front. Bioeng. Biotechnol. 8:594247. doi: 10.3389/fbioe.2020.594247

Osteoporosis is a chronic disease requiring long-term, sometimes lifelong, management. With the aging population, the prevalence of osteoporosis is increasing, and with it so is the risk of hip fracture and subsequent poor quality of life and higher mortality. Current therapies for osteoporosis have various significant side effects limiting patient compliance and use. Recent evidence has demonstrated the significant role of exosomes in osteoporosis both *in vivo* and *in vitro*. In this review, we summarize the pathogenesis of senile osteoporosis, highlight the properties and advantages of exosomes, and explore the recent literature on the use of exosomes in osteogenesis regulation. This is a very helpful review as several exosomes-based therapeutics have recently entered clinical trials for non-skeletal applications, such as pancreatic cancer, renal transplantation, and therefore it is urgent for bone researchers to explore whether exosomes can become the next class of orthobiologics for the treatment of osteoporosis.

Keywords: osteoporosis, exosomes, mesenchymal stem cells (MSCs), osteoblasts, osteoclasts

INTRODUCTION

Osteoporosis is a systemic skeletal disease characterized by low bone mass and decreased bone quality, both of which contribute to an increase in bone fragility (van den Bergh et al., 2012). Fractures are more likely to occur when traumatic forces are exerted on osteoporotic bone, and, hence, osteoporosis is a significant risk factor for fracture. Furthermore, fractures due to osteoporosis are becoming increasingly more common, especially in women over the age of 55 and men over the age of 65, resulting in adverse physical and psychosocial consequences and increased mortality and health-care costs.

Currently available drugs for osteoporosis can be divided into antiresorptive modulators, which include estrogen, estrogen receptor modulators, calcitonin and bisphosphonates, and anabolic therapies, which includes teriparatide. These drugs usually cause adverse effects, and consequently result in decreased adherence. In the case of teriparatide, research has shown that 77% of participants taking 20 μg and 78% of participants taking 40 μg experienced an adverse side effect, including joint pain, muscle cramp, and fatigue (Tsai et al., 2019). Estrogen therapy has known side effects on the breasts and uterus particularly with long-term use. Long-term calcitonin therapy can result in tolerance due to production of circulating antibodies to calcitonin (Wada et al., 1996). Bisphosphonates, the most common current therapy for osteoporosis, result in general side effects including gastrointestinal irritation, bone and joint pain and jaw osteonecrosis (Marx, 2003; Ruggiero et al., 2004). Thus, development of therapies with high bone targeting ability and low toxicity is imperative. Exosomes may be a promising approach to reverse osteoporosis due to their fewer safety considerations as well as powerful pro-osteogenesis abilities.

This review aims to cover the knowledge advances that have been made on the pathogenesis of osteoporosis, the properties of exosomes, and is primarily focused on postmenopausal or senile osteoporosis. We review target cells for the action of exosomes on reversing osteoporosis, and the future for new treatment paradigms for osteoporosis.

THE PATHOGENESIS OF OSTEOPOROSIS

Normal Bone Homeostasis

Bone is a dynamic tissue that maintains homeostasis through a balance of bone resorption by osteoclasts and bone formation by osteoblasts, through which old bone is replaced with new bone. During this process, osteoclasts are recruited to initiate the resorption of mineralized bone, followed by a reversal phase during which osteoclasts undergo apoptosis. Recruitment of osteoblasts is followed by the formation and mineralization of new bone within the resorption cavity. The sequence of the events is always bone resorption followed by bone formation, and the two processes are tightly coupled, both spatially and temporally. The OPG/RANK/RANKL pathway (**Figure 1**) has been shown to be associated with osteoclast formation whereas the Wnt/β-catenin (**Figure 2**) has been shown to play a significant role in osteoblast formation (Lacey et al., 1998). Osteoclasts derived from cells of the myeloid lineage differentiate into pre-osteoclasts which express RANK in the presence of M-CSF and RANKL on the cell membrane of stromal and osteoblast lineage cells. They proliferate and fuse to form bone-resorbing osteoclasts. However, OPG, is a naturally circulating inhibitor/decoy receptor for RANKL, and can bind to RANKL to inhibit osteoclastogenesis and prevent bone resorption (**Figure 1**) (Simonet et al., 1997; Khosla, 2001). Wnt is the key initiating factor of the Wnt/β-catenin signal pathway. WNT ligands bind to a receptor formed by low-density lipoprotein (LDL)-related receptor (LRP)5/6 and Frizzled (FZD) to activate the signal pathway, and β-catenin is translocated to the nucleus to promote osteoblast formation.

Pathophysiology of Age-Related Osteoporosis

Briefly, osteoporosis is due to an imbalance between the activities of osteoblasts and osteoclasts. Aging in women is associated with a decline in serum estrogen that has the potential to promote bone formation through inhibition of receptor activator of nuclear factor-κB ligand (RANKL) (Eghbali-Fatourechi et al., 2003), resulting in bone loss and disruption of bone microarchitecture. Trabecular thinning and loss of trabeculae in cancellous bone, cortical thickness and increased cortical porosity in cortical bone have been noted in older women (Parfitt et al., 1983; Compston et al., 1987; Zebaze et al., 2010). In men, aging plays a predominant role in osteoporosis, resulting in decreased bone formation through reduced proliferation and differentiation of multipotent stem cells (MSCs) and decreased bone matrix production depended on decreased osteoblast function and increased apoptosis of mature osteoblasts (Manolagas and Parfitt, 2010). Cell-to-cell communication is becoming increasingly accepted as a mechanism impacting the development of osteoporosis. A therapy that affects the activities of MSCs, osteoblasts and osteoclasts by influencing intercellular communication would, therefore, be a potential future treatment. Given that exosomes, which are extracellular vesicles, have this ability, we set out to investigate these vesicles in depth.

THE PROPERTIES OF EXOSOMES

Exosomes, nanoscale vesicles ranging from 30–120 nm in diameter (**Table 1**) (EL Andaloussi et al., 2013b), are extracellular vesicles widely distributed in almost all biological fluids, including plasma, urine, saliva, ascites, amniotic fluid, lactic acid and cerebrospinal fluid (Simons and Raposo, 2009; Gross et al., 2012). Almost all cells, including B cells (Raposo et al., 1996), T cells (Blanchard et al., 2002), dendritic cells (Thery et al., 1999), mast cells (Raposo et al., 1997), and endothelial cells (Song et al., 2019), can secrete exosomes. Exosomes, as intraluminal endosomal vesicles, are released by exocytosis when multivesicular bodies (MVBs) fuse with the plasma membrane (**Figure 3**) (Heijnen et al., 1999). The exosome membrane is mainly composed of lipids and proteins, and the exosomal lumen is enriched with bioactive molecules, including proteins, lipids, metabolites, mRNA, microRNA (miRNA), and other non-coding RNA (ncRNA) (Gross et al., 2012; Sato-Kuwabara et al., 2015). Exosomes directly activate cell surface receptors through protein and bioactive lipid ligands, and initiate fusion of their membrane contents with the recipient cell plasma membrane, playing a significant role in regulating the bioactivity of recipient cells by conveying lipids, proteins and nucleic acids. In this way, exosomes are not only involved in the maintenance of normal physiology, such as stem cell maintenance (Mehta et al., 2015), tissue repair (Li et al., 2013), organ development, hematopoietic function, but also participate in diseases processes, such as cancer metastasis and angiogenesis (Al-Nedawi et al., 2008).

Among their cargoes, miRNAs in the exosomal lumen have garnered increasing attention. MiRNAs, a class of 17–24 nt non-coding RNAs, play a regulatory role in recipient cells through targeting mRNAs for cleavage or translational repression (Bartel, 2004). In addition, some miRNAs, such as tumor-secreted miRNA-21 and miRNA-29a, have the capacity to act as

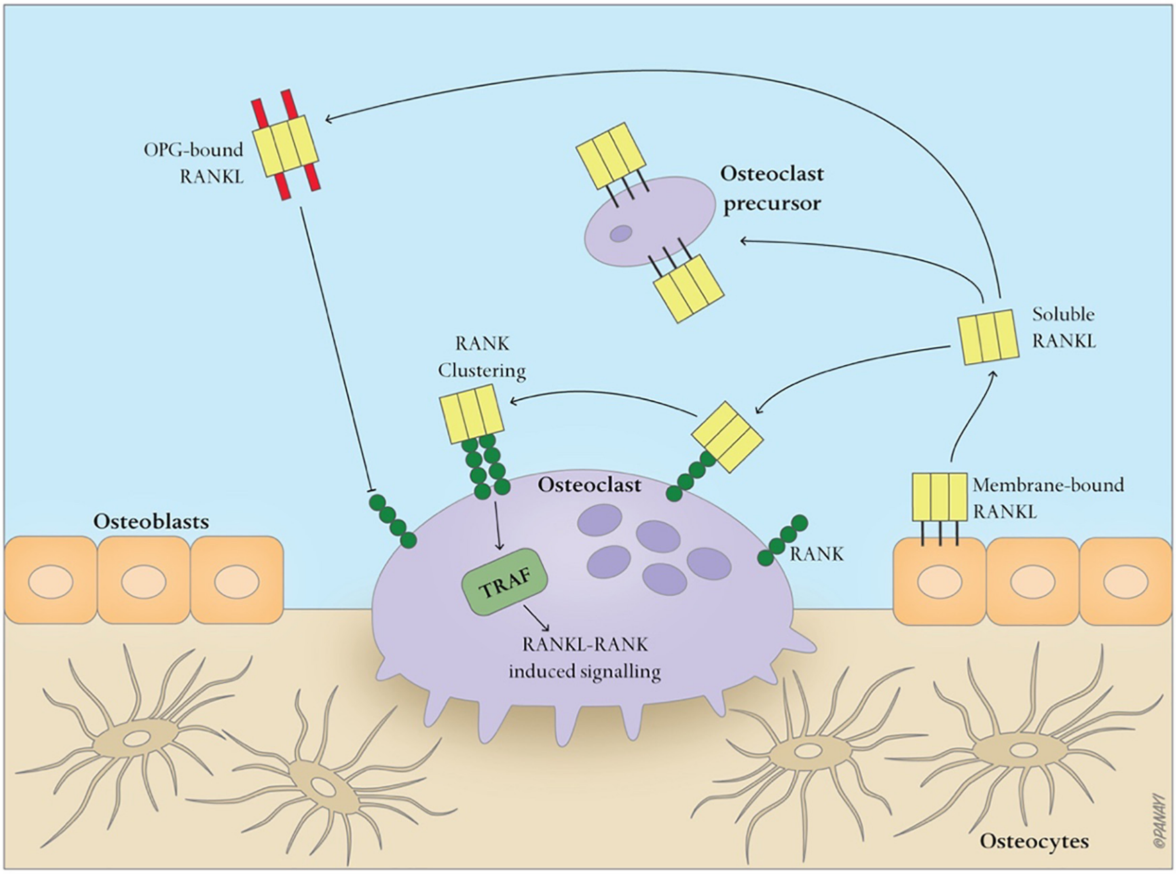

FIGURE 1 | Simplified OPG-RANK-RANKL pathway in bone. RANKL, a homotrimer, is mainly expressed either on the cell membrane of osteoblasts or as a soluble ligand. After RANK binds to RANKL, RANK cluster, recruiting TNFR-associated factors (TRAFs), especially TRAF6, which activate RANK within the cells, and regulate osteoclasts-related gene expression. OPG, a secreted decoy receptor of RANKL, serves as a physiological inhibitor of RANKL-driven osteoclast activities.

ligands that bind to toll-like receptors (TLRs) and then activate immune cells (Fabbri et al., 2012). Additionally, lncRNAs, non-coding RNAs with a length of more than 200 nucleotides (Ulitsky and Bartel, 2013), are known to be involved in various biological processes, and have important roles in bone formation and regeneration (Wang et al., 2015). Currently, it is recognized that lncRNAs act mainly through regulation of RNA and protein through interactions between RNA and RNA or RNA and DNA (Li Y. et al., 2016).

In addition to naturally secreted exosomes, however, genetically engineered or chemically modified exosomes which enable cell-specific delivery of cargoes have been studied in recent years (Armstrong et al., 2017). For example, chondrocyte-specific dendritic cell-derived exosomes modified through genetic engineering successfully achieved targeted delivery of miRNA-140 to chondrocytes in deep regions of the cartilage. This was shown to improve the osteoarthritic cartilage (Liang et al., 2020). Treatment with iExosomes (engineered exosomes) in mice with pancreatic cancer significantly increased overall survival through targeting oncogenic KRAS (Kamerkar et al., 2017). Hence, conventional drug delivery vehicles have disadvantages that are largely absent when exosomes are used as drugs carriers, including potential toxicity, immunogenicity and inability to penetrate target specific organs.

EXOSOMES REGULATE MESENCHYMAL STEM CELL OSTEOGENIC DIFFERENTIATION

Mesenchymal stem cells (MSCs), non-hematopoietic multipotent stem cells, have multilineage differentiation potential including differentiation into osteoblasts, chondrocytes and adipocytes (Caplan, 1991). MSCs play a significant role in maintaining the homeostasis between bone resorption and bone formation.

Exosome-Mediated Differentiation of MSCs

Exosomes are important vesicles in intercellular communication for modulating or mediating cellular processes. Therefore, exosomes can direct MSCs differentiation toward osteoblastic lineage. For instance, exosomes secreted by MSCs derived from human induced pluripotent stem cells (hiPSCs,

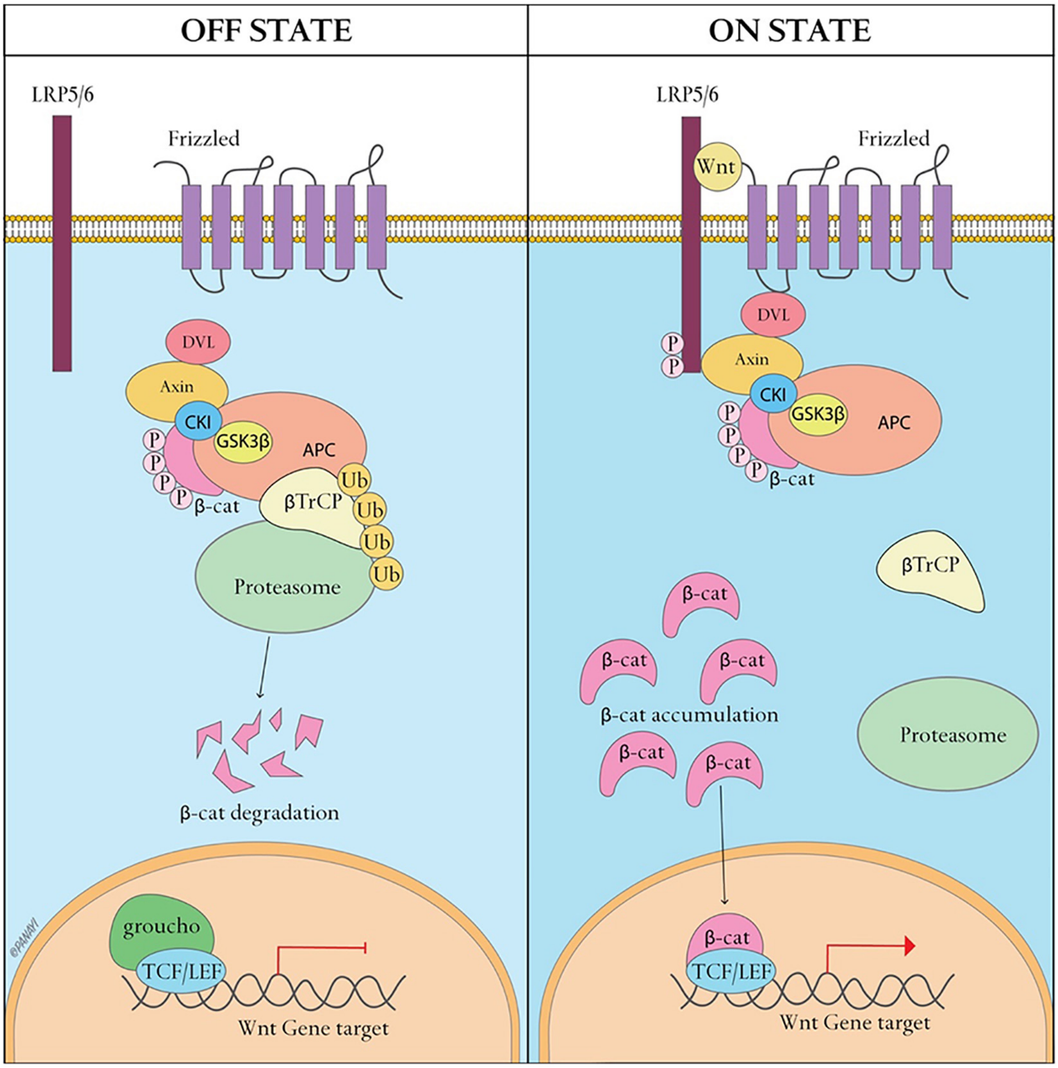

FIGURE 2 | Canonical WNT signaling. A WNT ligand can activate the canonical signaling pathway through binding to a receptor complex formed by low-density lipoprotein (LDL)-related receptor (LRP)5/6 and Frizzled. This results in the translocation of hypophosphorylated β-catenin to the nucleus. In the inactive state, β-catenin is degraded by the proteasome after it becomes phosphorylated by the glycogen synthase kinase 3β(GSK3β)-Axin-casein kinase 1 (CK1)–adenomatous polyposis coli (APC) complex and subsequently ubiquitinated.

TABLE 1 | Exosome, microvesicle, apoptotic body: major differences.

	Vesicle types		
Characteristics	**Exosomes**	**Microvesicles**	**Apoptotic bodies**
Size	30–120 nm	50–1,000 nm	500–2,000 nm
Morphology	Cup-shaped	Heterogeneous	Heterogeneous
Origin	Endolysosomal pathway; multivesicular bodies	Plasma membrane	Apoptotic cell membrane
Marker	Tetraspanins, ESCRT Components,TSG101, ALIX	Integrins, selectins, CD40	Phosphatidylserine
Mechanism of discharge	Exocytosis of multivesicular bodies	Outward budding of plasma membrane	Outward blebbing of apoptotic cell membrane
Contents	Protein, miRNA, mRNA, non-coding RNAs	Protein, miRNA, mRNA, non-coding RNAs	Nuclear fractions, cell organelles

ESCRT, endosomal sorting complex required for transport; TSG101, tumor susceptibility gene 101 protein; ALIX, programmed cell death 6 interacting protein (also known as PDCD6IP).

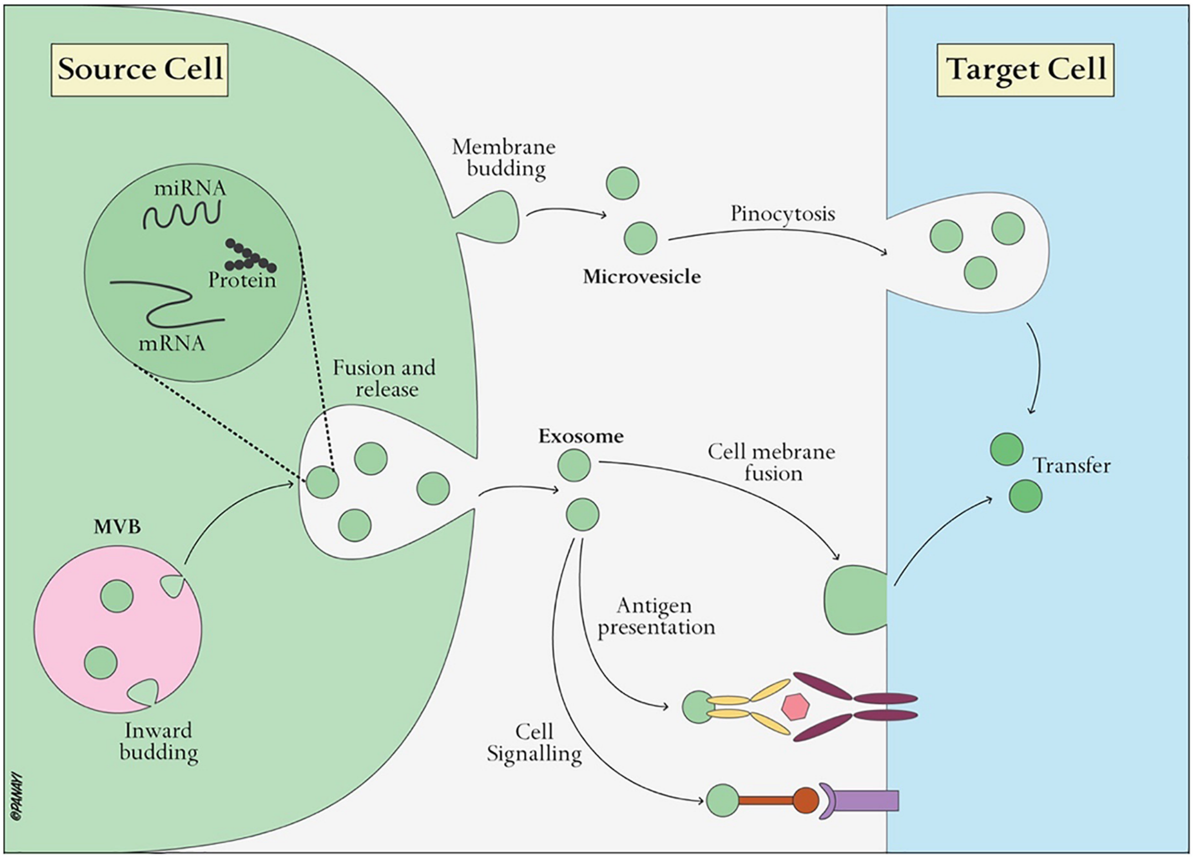

FIGURE 3 | Exosome biogenesis and interaction with target cells. Exosomes are vesicles of endocytic origin formed by the inward budding of the multivesicular body (MVB) membrane. Exosomes can then directly activate cell surface receptors via protein and bioactive lipid ligands, transfer cell surface receptors or deliver effectors including transcription factors, oncogenes and infectious particles into target cells. In addition, various RNA species including mRNAs and small regulatory RNAs such as microRNAs (miRNAs) and non-coding RNAs are contained in extracellular vesicles and delivered to target cells.

hiPSC-MSC-Exos) effectively promote the proliferation and osteogenic differentiation of BMSC *in vitro*. There was a dose-response relationship between the effect and exosomes concentration (Qi et al., 2016). Similarly, one study suggested that exosomes derived from osteogenic MSCs can direct undifferentiated MSCs toward osteogenic differentiation both *in vivo* and *in vitro* (Narayanan et al., 2016). Furthermore, osteoblast-derived exosomes can increase osteogenic differentiation by enhancing osteogenic gene expression in MSCs (Narayanan et al., 2018), establishing a positive feedback of bone formation or growth. In addition, exosomes derived from monocytes have been proven to be stimulatory on MSCs osteogenic differentiation *in vitro* (Gebraad et al., 2018). Among them, miRNA in exosomes has been shown to be a critical component in stem cell differentiation (Shim and Nam, 2016). Nine exosome-derived miRNAs (including let-7a, miRNA-199b, miRNA-218, miRNA-148a, miRNA-135b, miRNA-203, miRNA-219, miRNA-299-5p, and miRNA-302b) have been shown to be significantly up-regulated and three exosome-derived miRNAs (miRNA-885-5p, miRNA-181a, and miRNA-320c) showed significant down-regulation (Xu et al., 2014). Additionally, some studies have shown that miRNA-138a, miRNA-141 and miRNA-200a can inhibit MSCs differentiation into osteoblasts (Itoh et al., 2009; Eskildsen et al., 2011). In addition to miRNA, lncRNA might be involved in the process of osteogenic differentiation of MSCs, such as lncRNA H19 (Wang et al., 2017). Although MSCs osteogenic differentiation is regulated by exosomes, it cannot be concluded which cell type-derived exosome was dominant.

Possible Regulatory Mechanism

Exosomes are more likely to play an important role in regulating MSCs differentiation through their non-coding RNA (miRNA and lncRNA), and thus affect expression of some transcription factors. Differentiation of MSCs toward osteocytes is regulated by various transcription factors, such as Runt-related transcription factor 2 (Runx2), osterix, β-catenin, and bone morphogenetic proteins (BMPs), whose expression is regulated by many signaling pathways, such as essential Wnt, BMP. The Runx2 transcription factor is an essential regulator for the osteogenic differentiation of MSCs, which can induce differentiation of MSCs into pre-osteoblasts and inhibits adipogenic and chondrogenic differentiation (Komori, 2006). For example, miRNA-133 can inhibit differentiation of

MSCs into osteoblasts by down-regulation of the expression of Runx2 (Li et al., 2008). Osterix, a specificity protein 1 family (Sp1) of transcription factors, is downstream of Runx2, and is essential for bone formation (Nakashima et al., 2002). For example, lncRNA MALAT1 stimulates osterix expression and osteogenesis of MSCs by sponging miRNA-143 (Gao et al., 2018), and the lncRNA-miRNA pathway is the most classic mechanism of action. In addition, some miRNAs regulate MSCs differentiation through indirect interaction with transcription factors, and lncRNA regulates differentiation of MSCs through others pathways, including Wnt/β-catenin pathway, p38 MAPK pathway, and BMP4 signaling (Ju et al., 2019).

Exosomes Acting on MSCs Reverse Osteoporosis

Stem cell therapies have shown great potential in the treatment of various diseases, and as exosomes carry a cargo of functional signals in the form of RNA, miRNA, or protein, they can act as pivotal messengers of intercellular communication. Therefore, exosomes treatment may offer similar potential as stem cell transplantation. For example, exosomes originating from exogenous MSCs can promote osteogenic differentiation of endogenous MSCs and improve osteoporosis (Liu et al., 2015). Exosomes from endogenous BMSCs can target endogenous MSCs to enhance osteogenic differentiation and reduce adipogenic differentiation, while miRNA-151-5p administered alone also achieves the same effect (Chen et al., 2017). Additionally, a study demonstrated that normal MSCs-derived extracellular vesicles (containing rich exosomes) can promote proliferation and reduce DNA damages of MSCs after radiation exposure (Wen et al., 2016). Thus, intravenous injection of MSCs-derived exosomes to patients with osteoporosis is a promising therapy.

EXOSOMES REGULATE OSTEOBLAST PROLIFERATION AND ACTIVITY

Approximately 4–6% of the total resident cells in bone are osteoblasts, which are essential for the growth and maintenance of the skeleton. Additionally, osteoblasts are responsible for synthesis and mineralization of bone matrix, which increase the bone mineral density and prevent fragility fractures.

Exosomes Participate in Osteoblast Proliferation and Activity

Exosomes can affect osteoporosis by directly regulating osteoblast proliferation and activity. Exosomes derived from different cells or cells with different functional status might have significantly different effects on osteoblasts. MSCs-derived exosomes can promote bone formation *in vivo* through stimulation of osteoblast differentiation, activity and proliferation mainly through miRNA-196a (Qin et al., 2016). Osteoclast-derived exosomes were shown to decrease bone formation through inhibition of osteoblast activity through miRNA-214-3p (Li D. et al., 2016). One study, which found elevated miRNA-214 levels in aged postmenopausal women and aged men, showed that miRNA-214 directly targets ATF4 to inhibit osteoblast activity and antagomirna-214 can promote osteoblast activity and matrix mineralization *in vitro* (Wang et al., 2013). Interestingly, although patients with tumors usually exhibit osteoporosis, exosomes originating from tumors can stimulate osteoblast proliferation and activity. Osteoblasts treated with exosomes derived from breast cancer cells, decreased in number, metabolic activity, and alkaline phosphatase (ALP) activity (Loftus et al., 2020). Similarly, prostate cancer cell-derived exosomes increases osteoblast proliferation by 1.5-fold (Inder et al., 2014).

Possible Regulatory Mechanism

Although the specific mechanism has yet to be defined, some recognized pathways might be involved. Firstly, proteins on the exosomal membranes, such as cell recognition molecules, can facilitate selective targeting and uptake by target cells. Exosomes entering the osteoblasts through endocytosis, transpor luminal components into the cytosol of the target cell. Finally, some RNAs, such as miRNA, lncRNA, translocate into the nucleus and regulate expression of osteoblast-related genes. For example, the miRNA-214 in osteoclast-derived exosomes could be transferred into osteoblasts through EphrinA2/EphA2 recognition (Sun et al., 2016). MiRNA-214 directly targets activating transcription factor 4 (ATF4) by binding to its 3′untranslated region (UTR) (Wang et al., 2013). Thus, the exosomes inhibit osteoblast proliferation and activity by significantly decreasing bone formation marker gene expression, including expression of osteocalcin (BGLAP) and alkaline phosphatase (ALP).

Exosomes Undergoing Modification or Material Loading Can Reverse Osteoporosis

Exosomes undergoing modification or material loading have shown great promise for the treatment of osteoporosis. Prior research has shown that exosome-integrated titanium oxide nanotubes can stimulate bone regeneration by promoting osteogenic differentiation (Wei et al., 2019). Similarly, self-assembly of biotinylated MSCs-EVs onto the surface of biotin-doped polypyrrole titanium (Bio-Ppy-Ti) exhibits enhanced osteoinductive ability *in vivo* and *in vitro* through stimulation of osteogenic differentiation, proliferation and activity (Chen et al., 2019). Remarkably, some materials *in vivo* might serve as a bioreactor, which can affect exosome or growth factor production. For example, a recent animal study suggested that magnetic hydroxyapatite (MHA) scaffolds are capable of altering osteoclast-derived exosomal cargoes and decreasing the efficiency of exosome uptake by osteoblasts, further promoting osteoblast proliferation and reversing osteoporosis (Zhu et al., 2020). This evidence suggests that osteoporotic patients with fractures may be treated with materials integrated in exosomes which promote bone formation and reverse osteoporosis. However, more evidence is needed given the scarcity of knowledge on this subject.

EXOSOMES REGULATE OSTEOCLAST MATURATION AND ACTIVITY

Osteoclasts, multinucleated giant cells formed by the fusion of mononuclear progenitors of the monocyte/macrophage family, are the exclusive cells of bone resorption in the human body, originating from haematopoietic progenitors (Xing et al., 2005). In the process of osteoclastogenesis, pre-osteoclasts (preOCs) are formed first.

Exosomes Affect Osteoclast Differentiation and Activity

Research has shown that osteoclast activity can determine the development of osteoporosis (Teitelbaum, 2000). Exosomes, as an important intercellular messenger, play a significant role in regulating osteoclast maturation and activity. First, the bone system itself is the most significant regulator of osteoclast differentiation. For example, exosomes from pre-osteoclasts can promote osteoclast formation, whereas exosomes from osteoclasts are pro-inhibitory (Huynh et al., 2016). Exosomes from osteoblasts can facilitate the differentiation of pre-osteoclasts to osteoclasts through bioactive molecular content (RANKL) (Deng et al., 2015). However, osteoclast-derived exosomes inhibit osteoclast formation (Xie et al., 2017). Such evidence suggests that exosomes might participate in intercellular communication among the different types of bone cells. In addition, a recent study has demonstrated that compared to exosomes derived from osteoblasts and BMSCs, endothelial cell-derived exosomes show more efficient bone targeting that suppresses osteoclast differentiation and activity through miRNA-155 (Song et al., 2019). In addition, tumor cells have been shown to increase the number and activity of other cells. Breast cancer cell-derived exosomes can promote the proliferation and differentiation of osteoclasts through miRNA-20a-5p (Guo et al., 2019), and prostate cancer cell-derived exosomes exhibit strong promotion of osteoclastogenesis *in vitro* (Inder et al., 2014). This may contribute to the inherent mechanism through which patients with tumors exhibit osteoporosis. Multiple myeloma-derived exosomes can also stimulate osteoclastogenesis via abundant EGFR ligand amphiregulin (AREG) (Raimondo et al., 2019). Additionally, other tumors, such as non-small cell lung cancer (NSCLC), colon cancer, are rich sources of AREG (Taverna et al., 2017).

Possible Regulatory Mechanism

According to prior research, the most important signaling pathway regulating osteoclast differentiation and maturation is the RANK/RANKL signaling pathway. The mitogen-associated protein kinase (MAPK) signaling pathways, including p38, extracellular signal-regulated kinase (Erk), Jun N-terminal kinase (JNK), c-Fos and AP-1, also participate in osteoclast formation (Matsumoto et al., 2000; Keshet and Seger, 2010). Thus, these may be possible mechanisms through which exosomes regulate osteoclast differentiation and activity. Notably, exosomes cargoes components, including protein, miRNA, lncRNA, may all play a regulatory role in osteoclast differentiation and activity. AREG, a tumor-derived exosome, can activate the epidermal growth factor receptor (EGFR) pathway in pre-osteoclasts to increase RANKL expression. LncRNA-MALAT 1 from endothelial progenitor cells (EPCs) promote osteoclastogenesis through directly binding to miRNA-124 (Cui et al., 2019). Expression of NFATc1, a downstream signal of RANK, is suppressed by miRNA-124 (Lee et al., 2013). MiRNA-155 in endothelial cell-derived exosomes disrupts osteoclast differentiation and activation through targeting several essential transcription factors, including Spi1, microphthalmia-associated transcription factor (Mitf), and suppressor of cytokine signaling 1 (Socs1) (Song et al., 2019).

Exosomes Inhibiting Osteoclast Differentiation and Activity Are Predicted to Treat Osteoporosis

Clinical treatment of osteoporosis typically focuses on inhibiting the excessive activation of osteoclasts and exosomes might be a promising candidate for this in the future. Accumulating evidence has shown that exosomes strongly inhibit osteoclast differentiation and activity, effectively reversing osteoporosis *in vitro* and in animal studies (Song et al., 2019). In comparison with other exosomes, endothelial cell-derived exosomes show superiority in targeting bone. Remarkably, exosomal miRNA is thought to be an important component in gene expression regulation participating in the differentiation and activity of osteoclasts, such as endothelial cell-derived exosomal miRNA-155 (Song et al., 2019), miRNA-503 (Chen et al., 2014), miRNA-133a (Wang et al., 2012), and miRNA-422a (Cao et al., 2014), which may offer potential for developing future drugs against osteoporosis. Clinic trials are, however, required to assess the effect of these exosomes on the human body.

ADVANTAGES OF EXOSOMAL TREATMENT

Compared to conventional therapy, exosomal therapy has several advantages. First, exosomes have low immunogenicity. Human marrow-derived MSCs express MHC I molecules on their cell surface, resulting in immunological rejection. Animal studies, however, have shown that MSCs-exosomes can promote bone formation without any adverse events (Zhang et al., 2016). Further, exosomes have low toxicity. In recent years, pharmaceutical carriers, especially nanoscale pharmaceutical carriers, have received extensive attention, but their use is limited due to their synthetic lipid membranes resulting in unavoidable toxic reactions. Exosomes, as natural endogenous nano-microvesicles, have not been shown to induce toxicity neither *in vivo* nor *in vitro* trials (Narayanan et al., 2016; Qin et al., 2016). In addition, exosomes offer excellent targeting. For example, osteoclast-exosomes can target osteoblasts through their EphrinA2 (Sun et al., 2016). Exosomes also display great permeability, with studies showing that exosomes can penetrate cytomembranes and biological barriers (El Andaloussi et al., 2013a; Janas et al., 2015). Furthermore, studies have highlighted their excellent stability; PTX (Paclitaxel) incorporated into exosomes by mild sonication can maintain stability at various conditions for over a month (Kim et al., 2016). Finally, their function can be enhanced through modification or material loading. Given the aforementioned advantages, exosomes have strong potential to treat osteoporosis through bone tissue engineering and as targeted delivery vehicles. In bone tissue engineering, exosomes loaded with materials offer unique advantages in patients with osteoporosis following a fracture. Exosomes, as targeted delivery vehicles, can also effectively load compounds such as miRNA, and siRNA.

CLINICAL PERSPECTIVE: STILL A WAY TO GO

Although some clinical trials have been completed, there are currently no clinically approved therapies utilizing exosomes. This is largely due to lack of knowledge on the fundamentals of exosome biology and methodology. It should be noted, for example, that the specimen from which exosomes are to be harvested determines their potential as regulators. A decision must also be made whether to choose autografts or allografts. Another challenge is the limited ability of current isolation methods resulting in only low yield and low-purity exosomes. For example, 5×10^6 myeloma cells provide only 5–6 μg of exosomes (Peinado et al., 2012). In addition, current isolation methods of exosomes include mainly repeated ultracentrifugation and ultrafiltration (Lobb et al., 2015), techniques which are too time-consuming and remain somewhat controversial. Another major challenge is that the exact function of the cargoes in exosomes has yet to be established. For example, cargoes from the same cells derived from different tissues or organs are likely to differ. Research has shown that exosomes derived from bone marrow and adipose tissue differ vastly in tRNAs, especially for Sox2, POU5F1A/B, and Nanog (Baglio et al., 2015). Furthermore, some contents in the exosomes, such as tumor-supportive miRNA found in MSCs-exosomes, might play a role in disease promotion (Vallabhaneni et al., 2015). Therefore, thorough understanding of how to best utilize the function of exosomes in treating osteoporosis still has a way to go.

CONCLUSION

Overall, exosomes are natural membrane vesicles involved in intercellular communication by conveying their cargoes, which include proteins, as well as coding and non-coding RNA. Studies have shown that exosomes participate in bone homeostasis through regulation of the differentiation and activity of bone cells including MSCs, osteoblasts and osteoclasts. Thus far their regulatory mechanisms have not been fully elucidated. Given their several intrinsic advantages, such as their low immunogenicity and toxicity, exosomes offer promising therapeutic potential and are expected to become a reliable new approach to treating osteoporosis. Finally, further efforts must be made to improve the isolation and purity methods, as well as gain a better understanding on the roles that exosomes play in the regulation of osteoporosis.

AUTHOR CONTRIBUTIONS

XX, YX, and LH proposed the research questions, developed the protocol, and drafted the manuscript. XX guarantor. XX, WZ, and HX refined the search strategy. XX, ZL, LC, and CY searched and collected the studies. AP created the illustrations in Adobe Illustrator 2020. YX, BM, and GL critically reviewed the manuscript for relevant intellectual content. All authors have read and approved the final version of the manuscript.

FUNDING

This work was supported by funding from the National Science Foundation of China (Grant No. 81772345) and National Key Research & Development Program of China (Grant Nos. 2018YF2001502 and 2018YFB1105705).

REFERENCES

Al-Nedawi, K., Meehan, B., Micallef, J., Lhotak, V., May, L., Guha, A., et al. (2008). Intercellular transfer of the oncogenic receptor EGFRvIII by microvesicles derived from tumour cells. *Nat. Cell Biol.* 10, 619–624. doi: 10.1038/ncb1725

Armstrong, J. P., Holme, M. N., and Stevens, M. M. (2017). Re-engineering extracellular vesicles as smart nanoscale therapeutics. *Acs Nano* 11, 69–83. doi: 10.1021/acsnano.6b07607

Baglio, S. R., Rooijers, K., Koppers-Lalic, D., Verweij, F. J., Perez, L. M., Zini, N., et al. (2015). Human bone marrow- and adipose-mesenchymal stem cells secrete exosomes enriched in distinctive miRNA and tRNA species. *Stem Cell Res. Ther.* 6:127.

Bartel, D. P. (2004). MicroRNAs: genomics, biogenesis, mechanism, and function. *Cell* 116, 281–297. doi: 10.1016/s0092-8674(04)00045-5

Blanchard, N., Lankar, D., Faure, F., Regnault, A., Dumont, C., Raposo, G., et al. (2002). TCR activation of human T cells induces the production of exosomes bearing the TCR/CD3/zeta complex. *J. Immunol.* 168, 3235–3241. doi: 10.4049/jimmunol.168.7.3235

Cao, Z., Moore, B. T., Wang, Y., Peng, X. H., Lappe, J. M., Recker, R. R., et al. (2014). MiR-422a as a potential cellular microRNA biomarker for postmenopausal osteoporosis. *PLoS One* 9:e97098. doi: 10.1371/journal.pone.0097098

Caplan, A. I. (1991). Mesenchymal stem cells. *J. Orthop. Res.* 9, 641–650. doi: 10.1002/jor.1100090504

Chen, C., Cheng, P., Xie, H., Zhou, H. D., Wu, X. P., Liao, E. Y., et al. (2014). MiR-503 regulates osteoclastogenesis via targeting RANK. *J. Bone. Miner. Res* 29, 338–347. doi: 10.1002/jbmr.2032

Chen, C., Wang, D., Moshaverinia, A., Liu, D., Kou, X., Yu, W., et al. (2017). Mesenchymal stem cell transplantation in tight-skin mice identifies miR-151-5p as a therapeutic target for systemic sclerosis. *Cell Res.* 27, 559–577. doi: 10.1038/cr.2017.11

Chen, L., Mou, S., Li, F., Zeng, Y., Sun, Y., Horch, R. E., et al. (2019). Self-assembled human adipose-derived stem cell-derived extracellular vesicle-functionalized biotin-doped polypyrrole titanium with long-term stability and potential osteoinductive ability. *ACS Appl. Mater. Interfaces* 11, 46183–46196. doi: 10.1021/acsami.9b17015

Compston, J. E., Mellish, R. W., and Garrahan, N. J. (1987). Age-related changes in iliac crest trabecular microanatomic bone structure in man. *Bone* 8, 289–292. doi: 10.1016/8756-3282(87)90004-4

Cui, Y., Fu, S., Sun, D., Xing, J., Hou, T., and Wu, X. (2019). EPC-derived exosomes promote osteoclastogenesis through LncRNA-MALAT1. *J. Cell Mol. Med.* 23, 3843–3854. doi: 10.1111/jcmm.14228

Deng, L., Wang, Y., Peng, Y., Wu, Y., Ding, Y., Jiang, Y., et al. (2015). Osteoblast-derived microvesicles: a novel mechanism for communication between osteoblasts and osteoclasts. *Bone* 79, 37–42. doi: 10.1016/j.bone.2015.05.022

Eghbali-Fatourechi, G., Khosla, S., Sanyal, A., Boyle, W. J., Lacey, D. L., and Riggs, B. L. (2003). Role of RANK ligand in mediating increased bone resorption in early postmenopausal women. *J. Clin. Invest.* 111, 1221–1230. doi: 10.1172/JCI17215

El Andaloussi, S., Lakhal, S., Mager, I., and Wood, M. J. (2013a). Exosomes for targeted siRNA delivery across biological barriers. *Adv. Drug Deliv. Rev.* 65, 391–397. doi: 10.1016/j.addr.2012.08.008

EL Andaloussi, S., Mager, I., Breakefield, X. O., and Wood, M. J. (2013b). Extracellular vesicles: biology and emerging therapeutic opportunities. *Nat. Rev. Drug Discov.* 12, 347–357. doi: 10.1038/nrd3978

Eskildsen, T., Taipaleenmaki, H., Stenvang, J., Abdallah, B. M., Ditzel, N., Nossent, A. Y., et al. (2011). MicroRNA-138 regulates osteogenic differentiation of human stromal (mesenchymal) stem cells in vivo. *Proc. Natl. Acad. Sci. U.S.A.* 108, 6139–6144. doi: 10.1073/pnas.1016758108

Fabbri, M., Paone, A., Calore, F., Galli, R., Gaudio, E., Santhanam, R., et al. (2012). MicroRNAs bind to Toll-like receptors to induce prometastatic inflammatory response. *Proc. Natl. Acad. Sci. U.S.A.* 109, E2110–E2116. doi: 10.1073/pnas.1209414109

Gao, Y., Xiao, F., Wang, C., Wang, C., Cui, P., Zhang, X., et al. (2018). Long noncoding RNA MALAT1 promotes osterix expression to regulate osteogenic differentiation by targeting miRNA-143 in human bone marrow-derived mesenchymal stem cells. *J. Cell. Biochem.* 119, 6986–6996. doi: 10.1002/jcb.26907

Gebraad, A., Kornilov, R., Kaur, S., Miettinen, S., Haimi, S., Peltoniemi, H., et al. (2018). Monocyte-derived extracellular vesicles stimulate cytokine secretion and gene expression of matrix metalloproteinases by mesenchymal stem/stromal cells. *FEBS J.* 285, 2337–2359. doi: 10.1111/febs.14485

Gross, J. C., Chaudhary, V., Bartscherer, K., and Boutros, M. (2012). Active Wnt proteins are secreted on exosomes. *Nat. Cell Biol.* 14, 1036–1045. doi: 10.1016/j.ceb.2009.03.007

Guo, L., Zhu, Y., Li, L., Zhou, S., Yin, G., Yu, G., et al. (2019). Breast cancer cell-derived exosomal miR-20a-5p promotes the proliferation and differentiation of osteoclasts by targeting SRCIN1. *Cancer Med.* 8, 5687–5701. doi: 10.1002/cam4.2454

Heijnen, H. F., Schiel, A. E., Fijnheer, R., Geuze, H. J., and Sixma, J. J. (1999). Activated platelets release two types of membrane vesicles: microvesicles by surface shedding and exosomes derived from exocytosis of multivesicular bodies and alpha-granules. *Blood* 94, 3791–3799.

Huynh, N., VonMoss, L., Smith, D., Rahman, I., Felemban, M. F., Zuo, J., et al. (2016). Characterization of regulatory extracellular vesicles from osteoclasts. *J. Dent. Res.* 95, 673–679. doi: 10.1177/0022034516633189

Inder, K. L., Ruelcke, J. E., Petelin, L., Moon, H., Choi, E., Rae, J., et al. (2014). Cavin-1/PTRF alters prostate cancer cell-derived extracellular vesicle content and internalization to attenuate extracellular vesicle-mediated osteoclastogenesis and osteoblast proliferation. *J. Extracell Vesicles* 3:23784. doi: 10.3402/jev.v3.23784

Itoh, T., Nozawa, Y., and Akao, Y. (2009). MicroRNA-141 and -200a are involved in bone morphogenetic protein-2-induced mouse pre-osteoblast differentiation by targeting distal-less homeobox 5. *J. Biol. Chem.* 284, 19272–19279. doi: 10.1074/jbc.M109.014001

Janas, T., Janas, M. M., Sapon, K., and Janas, T. (2015). Mechanisms of RNA loading into exosomes. *FEBS Lett.* 589, 1391–1398. doi: 10.1016/j.febslet.2015.04.036

Ju, C., Liu, R., Zhang, Y. W., Zhang, Y., Zhou, R., Sun, J., et al. (2019). Mesenchymal stem cell-associated lncRNA in osteogenic differentiation. *Biomed. Pharmacother.* 115:108912. doi: 10.1016/j.biopha.2019.108912

Kamerkar, S., LeBleu, V. S., Sugimoto, H., Yang, S., Ruivo, C. F., Melo, S. A., et al. (2017). Exosomes facilitate therapeutic targeting of oncogenic KRAS in pancreatic cancer. *Nature* 546, 498–503. doi: 10.1038/nature22341

Keshet, Y., and Seger, R. (2010). The MAP kinase signaling cascades: a system of hundreds of components regulates a diverse array of physiological functions. *Methods Mol. Biol.* 661, 3–38. doi: 10.1007/978-1-60761-795-2_1

Khosla, S. (2001). Minireview: the OPG/RANKL/RANK system. *Endocrinology* 142, 5050–5055. doi: 10.1210/endo.142.12.8536

Kim, M. S., Haney, M. J., Zhao, Y., Mahajan, V., Deygen, I., Klyachko, N. L., et al. (2016). Development of exosome-encapsulated paclitaxel to overcome MDR in cancer cells. *Nanomed. U. K.* 12, 655–664. doi: 10.1016/j.nano.2015.10.012

Komori, T. (2006). Regulation of osteoblast differentiation by transcription factors. *J. Cell. Biochem.* 99, 1233–1239. doi: 10.3390/ijms20071694

Lacey, D. L., Timms, E., Tan, H. L., Kelley, M. J., Dunstan, C. R., Burgess, T., et al. (1998). Osteoprotegerin ligand is a cytokine that regulates osteoclast differentiation and activation. *Cell* 93, 165–176. doi: 10.1016/s0092-8674(00)81569-x

Lee, Y., Kim, H. J., Park, C. K., Kim, Y. G., Lee, H. J., Kim, J. Y., et al. (2013). MicroRNA-124 regulates osteoclast differentiation. *Bone* 56, 383–389. doi: 10.1016/j.bone.2013.07.007

Li, D., Liu, J., Guo, B., Liang, C., Dang, L., Lu, C., et al. (2016). Osteoclast-derived exosomal miR-214-3p inhibits osteoblastic bone formation. *Nat. Commun.* 7:10872. doi: 10.1038/ncomms10872

Li, Y., Fan, L., Liu, S., Liu, W., Zhang, H., Zhou, T., et al. (2013). The promotion of bone regeneration through positive regulation of angiogenic-osteogenic coupling using microRNA-26a. *Biomaterials* 34, 5048–5058. doi: 10.1016/j.biomaterials.2013.03.052

Li, Y., Syed, J., and Sugiyama, H. (2016). RNA-DNA triplex formation by long noncoding RNAs. *Cell Chem. Biol.* 23, 1325–1333. doi: 10.1016/j.chembiol.2016.09.011

Li, Z., Hassan, M. Q., Volinia, S., van Wijnen, A. J., Stein, J. L., Croce, C. M., et al. (2008). A microRNA signature for a BMP2-induced osteoblast lineage commitment program. *Proc. Natl. Acad. Sci. U.S.A.* 105, 13906–13911. doi: 10.1073/pnas.0804438105

Liang, Y., Xu, X., Li, X., Xiong, J., Li, B., Duan, L., et al. (2020). Chondrocyte-targeted MicroRNA delivery by engineered exosomes toward a cell-free osteoarthritis therapy. *ACS Appl. Mater. Interfaces* 12, 36938–36947. doi: 10.1021/acsami.0c10458

Liu, S., Liu, D., Chen, C., Hamamura, K., Moshaverinia, A., Yang, R., et al. (2015). MSC transplantation improves osteopenia via epigenetic regulation of notch signaling in lupus. *Cell Metab.* 22, 606–618. doi: 10.1016/j.cmet.2015.08.018

Lobb, R. J., Becker, M., Wen, S. W., Wong, C. S., Wiegmans, A. P., Leimgruber, A., et al. (2015). Optimized exosome isolation protocol for cell culture supernatant and human plasma. *J. Extracell Vesicles* 4:27031.

Loftus, A., Cappariello, A., George, C., Ucci, A., Shefferd, K., Green, A., et al. (2020). Extracellular vesicles from osteotropic breast cancer cells affect bone resident cells. *J. Bone. Miner. Res.* 35, 396–412. doi: 10.1002/jbmr.3891

Manolagas, S. C., and Parfitt, A. M. (2010). What old means to bone. *Trends Endocrinol. Metab.* 21, 369–374. doi: 10.1016/j.tem.2010.01.010

Marx, R. E. (2003). Pamidronate (Aredia) and zoledronate (Zometa) induced avascular necrosis of the jaws: a growing epidemic. *J. Oral Maxillofac. Surg.* 61, 1115–1117. doi: 10.1016/s0278-2391(03)00720-1

Matsumoto, M., Sudo, T., Saito, T., Osada, H., and Tsujimoto, M. (2000). Involvement of p38 mitogen-activated protein kinase signaling pathway in osteoclastogenesis mediated by receptor activator of NF-kappa B ligand (RANKL). *J. Biol. Chem.* 275, 31155–31161. doi: 10.1074/jbc.M001229200

Mehta, A., Zhao, J. L., Sinha, N., Marinov, G. K., Mann, M., Kowalczyk, M. S., et al. (2015). The MicroRNA-132 and MicroRNA-212 cluster regulates hematopoietic stem cell maintenance and survival with age by buffering FOXO3 expression. *Immunity* 42, 1021–1032. doi: 10.1016/j.immuni.2015.05.017

Nakashima, K., Zhou, X., Kunkel, G., Zhang, Z., Deng, J. M., Behringer, R. R., et al. (2002). The novel zinc finger-containing transcription factor osterix is required for osteoblast differentiation and bone formation. *Cell* 108, 17–29. doi: 10.1016/s0092-8674(01)00622-5

Narayanan, K., Kumar, S., Padmanabhan, P., Gulyas, B., Wan, A., and Rajendran, V. M. (2018). Lineage-specific exosomes could override extracellular matrix mediated human mesenchymal stem cell differentiation. *Biomaterials* 182, 312–322. doi: 10.1016/j.biomaterials.2018.08.027

Narayanan, R., Huang, C. C., and Ravindran, S. (2016). Hijacking the cellular mail: exosome mediated differentiation of mesenchymal stem cells. *Stem Cells Int.* 2016:3808674. doi: 10.1155/2016/3808674

Parfitt, A. M., Mathews, C. H., Villanueva, A. R., Kleerekoper, M., Frame, B., and Rao, D. S. (1983). Relationships between surface, volume, and thickness of iliac trabecular bone in aging and in osteoporosis. Implications for the microanatomic and cellular mechanisms of bone loss. *J. Clin. Invest.* 72, 1396–1409. doi: 10.1172/JCI111096

Peinado, H., Aleckovic, M., Lavotshkin, S., Matei, I., Costa-Silva, B., Moreno-Bueno, G., et al. (2012). Melanoma exosomes educate bone marrow progenitor cells toward a pro-metastatic phenotype through met. *Nat. Med.* 18, 883–891.

Qi, X., Zhang, J., Yuan, H., Xu, Z., Li, Q., Niu, X., et al. (2016). Exosomes secreted by human-induced pluripotent stem cell-derived mesenchymal stem cells repair critical-sized bone defects through enhanced angiogenesis and osteogenesis in osteoporotic rats. *Int. J. Biol. Sci.* 12, 836–849. doi: 10.7150/ijbs.14809

Qin, Y., Wang, L., Gao, Z., Chen, G., and Zhang, C. (2016). Bone marrow stromal/stem cell-derived extracellular vesicles regulate osteoblast activity and differentiation in vitro and promote bone regeneration in vivo. *Sci. Rep.* 6:21961. doi: 10.1038/srep21961

Raimondo, S., Saieva, L., Vicario, E., Pucci, M., Toscani, D., Manno, M., et al. (2019). Multiple myeloma-derived exosomes are enriched of amphiregulin (AREG) and activate the epidermal growth factor pathway in the bone microenvironment leading to osteoclastogenesis. *J. Hematol. Oncol.* 12:2. doi: 10.1186/s13045-018-0689-y

Raposo, G., Nijman, H. W., Stoorvogel, W., Liejendekker, R., Harding, C. V., Melief, C. J., et al. (1996). B lymphocytes secrete antigen-presenting vesicles. *J. Exp. Med.* 183, 1161–1172. doi: 10.1084/jem.183.3.1161

Raposo, G., Tenza, D., Mecheri, S., Peronet, R., Bonnerot, C., and Desaymard, C. (1997). Accumulation of major histocompatibility complex class II molecules in mast cell secretory granules and their release upon degranulation. *Mol. Biol. Cell* 8, 2631–2645. doi: 10.1091/mbc.8.12.2631

Ruggiero, S. L., Mehrotra, B., Rosenberg, T. J., and Engroff, S. L. (2004). Osteonecrosis of the jaws associated with the use of bisphosphonates: a review of 63 cases. *J. Oral Maxillofac. Surg.* 62, 527–534. doi: 10.1016/j.joms.2004.02.004

Sato-Kuwabara, Y., Melo, S. A., Soares, F. A., and Calin, G. A. (2015). The fusion of two worlds: non-coding RNAs and extracellular vesicles–diagnostic and therapeutic implications (Review). *Int. J. Oncol.* 46, 17–27. doi: 10.3892/ijo.2014.2712

Shim, J., and Nam, J. W. (2016). The expression and functional roles of microRNAs in stem cell differentiation. *Bmb Rep.* 49, 3–10. doi: 10.5483/BMBRep.2016.49.1.217

Simonet, W. S., Lacey, D. L., Dunstan, C. R., Kelley, M., Chang, M. S., Luthy, R., et al. (1997). Osteoprotegerin: a novel secreted protein involved in the regulation of bone density. *Cell* 89, 309–319. doi: 10.1016/s0092-8674(00)80209-3

Simons, M., and Raposo, G. (2009). Exosomes–vesicular carriers for intercellular communication. *Curr. Opin. Cell Biol.* 21, 575–581.

Song, H., Li, X., Zhao, Z., Qian, J., Wang, Y., Cui, J., et al. (2019). Reversal of osteoporotic activity by endothelial cell-secreted bone targeting and biocompatible exosomes. *Nano Lett.* 19, 3040–3048. doi: 10.1021/acs.nanolett.9b00287

Sun, W., Zhao, C., Li, Y., Wang, L., Nie, G., Peng, J., et al. (2016). Osteoclast-derived microRNA-containing exosomes selectively inhibit osteoblast activity. *Cell Discov.* 2:16015. doi: 10.1038/celldisc.2016.15

Taverna, S., Pucci, M., Giallombardo, M., Di Bella, M. A., Santarpia, M., Reclusa, P., et al. (2017). Amphiregulin contained in NSCLC-exosomes induces osteoclast differentiation through the activation of EGFR pathway. *Sci. Rep.* 7:3170. doi: 10.1038/s41598-017-03460-y

Teitelbaum, S. L. (2000). Bone resorption by osteoclasts. *Science* 289, 1504–1508. doi: 10.1126/science.289.5484.1504

Thery, C., Regnault, A., Garin, J., Wolfers, J., Zitvogel, L., Ricciardi-Castagnoli, P., et al. (1999). Molecular characterization of dendritic cell-derived exosomes. Selective accumulation of the heat shock protein hsc73. *J. Cell Biol.* 147, 599–610. doi: 10.1083/jcb.147.3.599

Tsai, J. N., Lee, H., David, N. L., Eastell, R., and Leder, B. Z. (2019). Combination denosumab and high dose teriparatide for postmenopausal osteoporosis (DATA-HD): a randomised, controlled phase 4 trial. *Lancet Diabetes Endocrinol.* 7, 767–775. doi: 10.1016/S2213-8587(19)30255-4

Ulitsky, I., and Bartel, D. P. (2013). lincRNAs: genomics, evolution, and mechanisms. *Cell* 154, 26–46. doi: 10.1016/j.cell.2013.06.020

Vallabhaneni, K. C., Penfornis, P., Dhule, S., Guillonneau, F., Adams, K. V., Mo, Y. Y., et al. (2015). Extracellular vesicles from bone marrow mesenchymal stem/stromal cells transport tumor regulatory microRNA, proteins, and metabolites. *Oncotarget* 6, 4953–4967.

van den Bergh, J. P., van Geel, T. A., and Geusens, P. P. (2012). Osteoporosis, frailty and fracture: implications for case finding and therapy. *Nat. Rev. Rheumatol.* 8, 163–172. doi: 10.1038/nrrheum.2011.217

Wada, S., Udagawa, N., Nagata, N., Martin, T. J., and Findlay, D. M. (1996). Physiological levels of calcitonin regulate the mouse osteoclast calcitonin receptor by a protein kinase Alpha-mediated mechanism. *Endocrinolog* 137, 312–320. doi: 10.1210/endo.137.1.8536630

Wang, L., Wang, Y., Li, Z., Li, Z., and Yu, B. (2015). Differential expression of long noncoding ribonucleic acids during osteogenic differentiation of human bone marrow mesenchymal stem cells. *Int. Orthop.* 39, 1013–1019. doi: 10.1007/s00264-015-2683-0

Wang, Q., Li, Y., Zhang, Y., Ma, L., Lin, L., Meng, J., et al. (2017). LncRNA MEG3 inhibited osteogenic differentiation of bone marrow mesenchymal stem cells from postmenopausal osteoporosis by targeting miR-133a-3p. *Biomed. Pharmacother.* 89, 1178–1186. doi: 10.1016/j.biopha.2017.02.090

Wang, X., Guo, B., Li, Q., Peng, J., Yang, Z., Wang, A., et al. (2013). miR-214 targets ATF4 to inhibit bone formation. *Nat. Med.* 19, 93–100. doi: 10.1038/nm.3026

Wang, Y., Li, L., Moore, B. T., Peng, X. H., Fang, X., Lappe, J. M., et al. (2012). MiR-133a in human circulating monocytes: a potential biomarker associated with postmenopausal osteoporosis. *PLoS One* 7:e34641. doi: 10.1371/journal.pone.0034641

Wei, F., Li, M., Crawford, R., Zhou, Y., and Xiao, Y. (2019). Exosome-integrated titanium oxide nanotubes for targeted bone regeneration. *Acta Biomater.* 86, 480–492. doi: 10.1016/j.actbio.2019.01.006

Wen, S., Dooner, M., Cheng, Y., Papa, E., Del, T. M., Pereira, M., et al. (2016). Mesenchymal stromal cell-derived extracellular vesicles rescue radiation damage to murine marrow hematopoietic cells. *Leukemia* 30, 2221–2231. doi: 10.1038/leu.2016.107

Xie, Y., Chen, Y., Zhang, L., Ge, W., and Tang, P. (2017). The roles of bone-derived exosomes and exosomal microRNAs in regulating bone remodelling. *J. Cell Mol. Med.* 21, 1033–1041. doi: 10.1111/jcmm.13039

Xing, L., Schwarz, E. M., and Boyce, B. F. (2005). Osteoclast precursors, RANKL/RANK, and immunology. *Immunol. Rev.* 208, 19–29. doi: 10.1111/j.0105-2896.2005.00336.x

Xu, J. F., Yang, G. H., Pan, X. H., Zhang, S. J., Zhao, C., Qiu, B. S., et al. (2014). Altered microRNA expression profile in exosomes during osteogenic differentiation of human bone marrow-derived mesenchymal stem cells. *PLoS One* 9:e114627. doi: 10.1371/journal.pone.0114627

Zebaze, R. M., Ghasem-Zadeh, A., Bohte, A., Iuliano-Burns, S., Mirams, M., Price, R. I., et al. (2010). Intracortical remodelling and porosity in the distal radius and post-mortem femurs of women: a cross-sectional study. *Lancet* 375, 1729–1736. doi: 10.1016/S0140-6736(10)60320-0

Zhang, J., Liu, X., Li, H., Chen, C., Hu, B., Niu, X., et al. (2016). Exosomes/tricalcium phosphate combination scaffolds can enhance bone regeneration by activating the PI3K/Akt signaling pathway. *Stem Cell Res. Ther.* 7:136. doi: 10.1186/s13287-016-0391-3

Zhu, Y., Li, Z., Zhang, Y., Lan, F., He, J., and Wu, Y. (2020). The essential role of osteoclast-derived exosomes in magnetic nanoparticle-infiltrated hydroxyapatite scaffold modulated osteoblast proliferation in an osteoporosis model. *Nanoscale* 12, 8720–8726. doi: 10.1039/d0nr00867b

Conflict of Interest: The authors declare that the research was conducted in the absence of any commercial or financial relationships that could be construed as a potential conflict of interest.

frontiers in Molecular Biosciences

ORIGINAL RESEARCH
published: 23 October 2020
doi: 10.3389/fmolb.2020.603817

Injecting Immunosuppressive M2 Macrophages Alleviates the Symptoms of Periodontitis in Mice

Yibin Miao[1†], Liuting He[2†], Xiaoyu Qi[3†] and Xiaoping Lin[1]*

[1] Department of Stomatology, Shengjing Hospital of China Medical University, Liaoning, China, [2] Department of Stomatology, The First Affiliated Hospital of Shenzhen University, Shenzhen Second People's Hospital, Shenzhen, China, [3] Shenyang Medical College, Liaoning, China

Periodontitis is the second most common oral disease affecting tooth-supporting structures. The tissue damage is mainly initiated by the excessive secretion of proinflammatory cytokines by immune cells. Macrophages are a type of antigen-presenting cells that influence the adaptive immunity function. We used a unique set of cytokines, i.e., a combination of IL-4, IL-13, and IL-10, to stimulate macrophages into a subset of M2 polarization cells that express much higher levels of ARG-1, CD206, and PDL-2 genes. The cells' anti-inflammatory potential was tested with mixed-lymphocyte reaction assay, which showed that this subset of macrophages could increase IL-2 secretion and suppress IL-17, IL-6, and TNF-α secretion by splenocytes. The gram-negative bacterial species *P*orphyromonas *gingivalis* was used to initiate an inflammatory process in murine periodontal tissues. In the meantime, cell injection therapy was used to dampen the excessive immune reaction and suppress osteoclast differentiation during periodontitis. Maxilla was collected and analyzed for osteoclast formation. The results indicated that mice in the cell injection group exhibited less osteoclast activity within the periodontal ligament region than in the periodontitis group. Moreover, the injection of M2 macrophages sustained the regulatory population ratio. Therefore, the M2 macrophages induced under the stimulation of IL-4, IL-13, and IL-10 combined had tremendous immune modulation ability. Injecting these cells into local periodontal tissue could effectively alleviate the symptom of periodontitis.

Keywords: M2 macrophages, IL-10, inflammation, periodontitis, regulatory T cells

Edited by:
Wei Tao,
Harvard Medical School,
United States

Reviewed by:
Xiaowei Zeng,
Sun Yat-sen University, China
Zhengguo Cao,
Wuhan University, China

***Correspondence:**
Xiaoping Lin
xiaoping_ba@126.com

†These authors have contributed equally to this work

Specialty section:
This article was submitted to Nanobiotechnology, a section of the journal Frontiers in Molecular Biosciences

Received: *08 September 2020*
Accepted: *05 October 2020*
Published: *23 October 2020*

Citation:
Miao Y, He L, Qi X and Lin X (2020) Injecting Immunosuppressive M2 Macrophages Alleviates the Symptoms of Periodontitis in Mice. Front. Mol. Biosci. 7:603817. doi: 10.3389/fmolb.2020.603817

INTRODUCTION

Periodontitis is the second most prevalent oral disease, mainly caused by a bacterial infection. Lymphocytes heavily involved in chronic inflammation play a significant role in the disintegration of tooth-supporting structures and contribute to bone resorption, which is the hallmark of periodontitis, followed by tooth loosening. However, the real damage is inflicted not by the bacteria directly, but by the excessive secretion of inflammatory mediators by the local immune cells (Bonner et al., 2018). Periodontitis is an autoimmune disease similar to rheumatoid arthritis. However, the treatment is limited to drugs and the physical removal of dental plaque. Previous research has shown that the effector T cell in the tissue contributes to osteoclast differentiation in the periodontal ligament (Kanzaki et al., 2016). The research about autoimmune diseases have come up with many theories in term of pathogenesis (Cronin et al., 2019), many treatment methods revolve around suppressing the function of infiltrating T cells or enhancing the function of a specific cell type (Chambers and Matosevic, 2019).

Macrophages found in most tissues constitute an essential part of the first defense line against foreign pathogens. There are two major subclasses of macrophages, the proinflammatory M1 subset and anti-inflammatory M2 subtype. In the event of bacterial infection, the macrophages in the tissue quickly polarize into M1 state under the influence of gram-negative bacteria and secrete large amounts of nitric oxide and inflammatory cytokines. On the contrary, when the pathogen is cleared, and the wound begins to heal, the paradigm in the tissue shifts to M2 macrophages, featuring high levels of ARG-1, to promote tissue regeneration and PDL-2 to suppress T cell proliferation (Yu et al., 2016). Regulatory T cells featuring a high expression of Foxp3 play a pivotal role in suppressing the immune system and maintaining tolerance to specific antigens, with its depletion leading to enhanced immunity against pathogens (Sakaguchi, 2003). A deficiency in regulatory T cells also leads to a tendency to develop an allergic reaction. It has been reported that the ratio of regulatory T cells in the progressive state of periodontitis tissue is lower than the healthy tissue (Hays et al., 2019). Macrophages play an essential role in shaping adaptive immunity by presenting antigens and secreting cytokines. The phenotype of macrophages heavily depends on the surrounding microenvironment.

Injecting viable cells into the tissue to induce a medicinal effect has extensively been used to treat many diseases, such as cancer and neurological disorders. The transfer of tumor cell reactive lymphocytes has shown a positive result in the clinical trial (Tran et al., 2008). Stem cells have also been used in the cell transfer therapy to either enhance immunity or promote tolerance (Gattinoni et al., 2012). In the event of chronic inflammation, the immune system regulation became abnormal. In order to regain the control, many immune-suppressive drugs are used to restrain the function of pro-inflammatory cells. The adoptive transfer of anti-inflammatory cells such as the regulatory T cells offers many advantages compared to using drugs (Riley et al., 2009). Previous study has demonstrated that an antigen presentation cell transfer therapy treating pre-induced inflammation. The intra-peritoneal injection of immuno-suppressive macrophages induced higher Foxp3$^+$ regulatory T cells ratio in the spleen (Bonnamain et al., 2012). This study transplanted differentiated immune cells instead of undifferentiated progenitor cells. Traditional drug treatment for periodontitis aims to suppress the function of T cells. We hypothesized that the expansion of immune-suppressive cells locally could positively impact the development of inflammatory diseases. The effect of macrophages on T cells has not sufficiently been explored compared to that of T cells on macrophages. This study aimed to investigate the effect of mature immune-suppressive macrophages on T cells *in vitro* and determine how the transplantation of this specific cell subset affects the development of periodontitis *in vivo*.

MATERIALS AND METHODS

Generation of M2 Macrophages

Bone marrow cells were flushed out and passed through a 70-mm nylon mesh into a centrifuge tube. After red blood cells were lyzed, the remaining cells were resuspended and cultured in DMEM medium (Biological Industries, United States) supplement with 10% heat-inactivated fetal bovine serum (Serana, Germany) and 10 ng/mL of M-CSF (Cell Signaling Technology, United States) for several days until all the cells were differentiated into macrophages. The macrophages were equally divided into four groups, including a control group. The second group was stimulated with 10 ng/mL of IL-4 and 10 ng/mL of IL-13 (Sino, China) for 24 h; the third group was treated with 10 ng/mL of IL-10 (Peprotech, United States) for 24 h; the forth group was treated with IL-4, IL-13, and IL-10 for 24 h.

Real-Time Quantitative Polymerase Chain Reaction (RT-PCR)

After the cells were collected from each group, the total RNA was extracted using Trizol reagent (Invitrogen, United States), and cDNA was synthesized with HiScript II QRT SuperMix with gDNA wiper (Vazyme Biotech, China). SYBR Green-based qPCR was run on a LightCycler 480 (Rouche, United States) using ChamQ Universal SYBR® qPCR Master Mix (Vazyme Biotech, China). The amplification process data were analyzed using Ct ($2-\Delta\Delta$Ct) method.

Lymphocyte Mixed Culture Method

The lymphocyte mixed culture method was used to explore the immune-suppressive properties of each group of macrophages. Briefly, the splenocytes were extracted from the same donor mice and cultured in the DMEM medium for 12 h to eliminate the remaining macrophages. The splenocytes were then cultured with each macrophage group under a ratio of 10:1 for 5 days. The culture medium was supplemented with 1 mg/mL of CD3 monoclonal antibody (Invitrogen, United States).

Cell Counting (CCK8) and Cytometric Beads Array (CBA)

The lymphocyte proliferation was determined every day from the first to the fifth day using a CCK8 kit (Vazyme Biotech, China). The optical absorbance was measured at 450 nm by a microplate reader. The cytokines in the culture medium were analyzed using a CBA kit (BD Bioscience, United States); the assay was carried out according to the manufacturer's instructions. Data were acquired with a BD FACS Calibur flow cytometer and analyzed with the FCAP array software. IL-2, IL-4, IL-6, IFN-g, TNF-a, IL-17, and IL-10 were recorded and compared.

Animals

Balb/c mice (8–10 weeks old), procured from the China Medical University Laboratory Animal Center, were housed in the laboratory's standard breeding facility with food and water available *ad libitum*. The mice were divided into three groups: healthy (H), periodontitis (P), and cell injection (CI) groups.

Mice in the periodontitis group received *P. gingivalis* injection in the gingival sulcus around the maxillary third molar once every 2 days for three times; mice in the cell injection group received injection of cells suspension once every week. All the procedures were approved by the Animal Etheric Committee of China Medical University.

P. gingivalis Culture and Induction of Periodontitis

P. gingivalis was cultured on tryptic soy broth agar in an anaerobic environment. After 7 days, the bacteria colony was collected and suspended in PBS solution, the concentration was adjusted in accordance with the McFarland standards to 10^9CFU/mL approximately. Equal volume of bacteria suspension and sodium carboxymethyl cellulose were mixed together, a 10 μL mixture was injected into the gingival sulcus of the third molar every 2 days for three times.

Cell Suspension Injection

The M2 macrophages induced by IL-4, IL-13, and IL-10 were detached using StemPro Accutase (Gibco, United States). The concentration of the cell suspension was adjusted to 10^9 cells/mL; 10 μL of cell suspension was injected into the gingival sulcus of the third molar through a 33-G needle every week after the last time of *P. gingivalis* injection.

Flow Cytometry Analysis

The gingival tissue was harvested and analyzed for the cell population. Briefly, the gingival tissue was processed and digested using collagenase at 37°C for 30 min. The cells collected through a nylon mesh were fixed and permeabilized using a Foxp3 staining kit (BD Bioscience, United States). The Foxp3 T cells were marked with perCP-CY5.5 conjugated anti-CD4 antibody (BD Bioscience, United States) and PE-conjugated anti-Foxp3 antibody (Elabscience, China). The M2 macrophage population was marked with PE-conjugated anti-F4/80 antibodies (BD Bioscience, United States) and FITC conjugated anti-CD206 antibody (BD Bioscience, United States). Data were acquired with a BD FACS Calibur flow cytometer.

Tartrate-Resistant Acid Phosphatase (TRAP) Staining

The c was harvested and fixed in a neutral formalin solution for 48 h to evaluate bone resorption. After fixation, the tissue was subjected to a 7-day decalcification process in a neutral EDTA solution in a warm incubator. The tissues were embedded in the OTC compound and snap-frozen to −80°C; 5-μm cross-sections were obtained and subjected to TRAP staining.

Statistical Analysis

The results were reported as means ± SDs from three repeated experiments. Statistical analyses were performed with the two-tailed Student's *t*-test. The regulatory T cell and M2 macrophage population ratios were subjected to the linear regression analysis. $P < 0.05$ was set as the standard for statistical significance.

RESULTS

IL-10 Combined With IL-4/IL-13-Activated M2 Macrophages

Bone marrow cells were collected and stimulated with M-CSF for five consecutive days to obtain and evaluate the mRNA expression of M2 macrophages. The immunofluorescent assay was used to stain the F4/80 membrane protein for its identification (**Figure 1A**). The results indicated that the bone marrow cells successfully differentiated into macrophages. 5 ng/mL of IL-4 and IL-13 were added to the culture medium to achieve M2 subset differentiation. After 24 h, CD206 expression, the signature protein of M2 macrophages, was analyzed using flow cytometry, as shown in **Figure 1B**. RT-PCR was used to quantify ARG-1, CD206, and PDL-2 mRNA expression of the macrophages in different groups. The results showed that IL-10 combined with IL-4 and IL-13 results in a much higher ARG-1, CD206, and PDL-2 mRNA levels than IL-4 and IL-13. However, in the third group, macrophages stimulated solely with IL-10 did not exhibit any significant changes. Taken together, using a combination of IL-10, IL-4, and IL-13 to stimulate macrophages could induce a much higher level of M2 anti-inflammatory protein expression (**Figure 1C**).

M2 Macrophages Enhance IL-2 Secretion While Reduce IL-6 and IL-7 Secretion in the Mixed Lymphocytes Reaction

A mixed cell culture was set up to assess the difference between the three groups of macrophages in terms of immunostimulatory activity. Three groups of macrophages were cultured with splenocytes with the ratio of one macrophage to ten splenocytes (**Figure 2A**) for 5 days. Daily cell proliferation was analyzed using a CCK8 kit. The results indicated that the macrophages treated with IL-10, IL-4, and IL-13 exhibited a higher ability to suppress lymphocyte proliferation (**Figure 2B**). Furthermore, the concentration of the cytokines in the culture supernatant was analyzed using a CBA, which showed that the IL-12 level was much higher, and IL-6, IL-17, and TNF-α levels were much lower compared to the macrophages treated by only IL-4 and IL-13 (**Figures 2C,D**).

The Injection of M2 Macrophages Increased the Ratio of Regulatory T Cells and Reduced Osteoclast Differentiation

In the mouse periodontitis model, the ratios of M2 macrophages and regulatory T cells in the gingival tissue were lower than the healthy group, while in the cell injection group, the ratio was higher than the periodontitis group (**Figures 3A,B**). This finding indicated that the injection of M2 macrophages positively affected the regulatory T cell population. Besides, the ARG-1 protein and proinflammatory cytokine IL-6 levels were determined in the gingiva using western blot. The periodontitis group exhibited an elevated level of IL-6 and a lower level of ARG-1 compared to the healthy group, while in the cell injection group, the

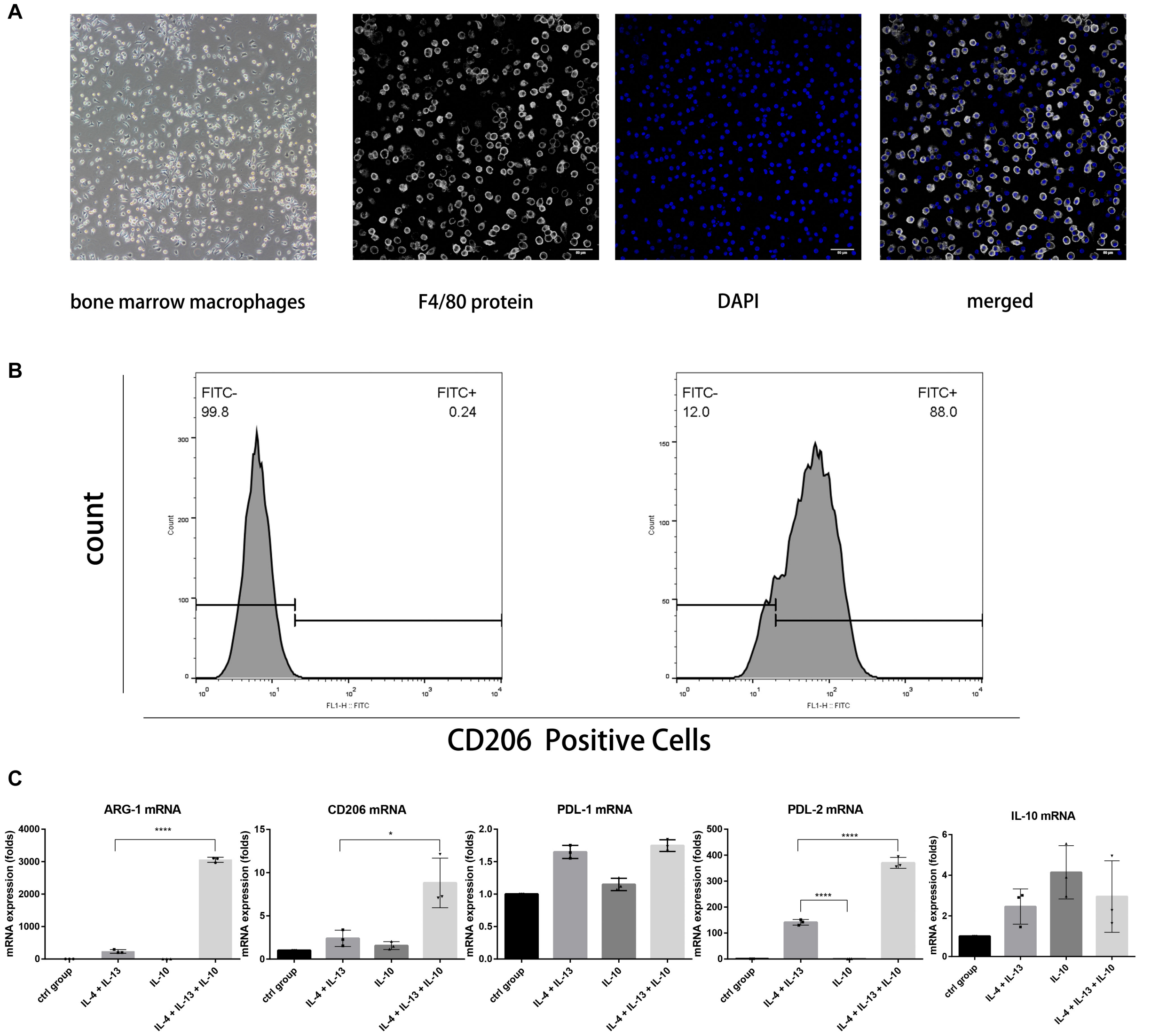

FIGURE 1 | The use of IL-4 and IL-13 with IL-10 in combination to stimulate macrophages resulted in much higher mRNA levels of ARG-1, CD206, and PDL-2 than without them. **(A)** The morphology of bone marrow macrophages and the F4/80 protein immunostaining. The bone marrow cells attached to the bottom and shown macrophage morphology after 5 days culture; the three fluorescent photos are showing F4/80 protein staining with fluorescent antibody, nucleus staining with DAPI and two staining merged together, respectively. **(B)** The flow cytometric analysis of CD206 intracellular staining of macrophages stimulated with IL-4 and IL-13. **(C)** The ARG-1, CD206, PDL-1, PDL-2, and IL-10 mRNA levels of macrophages in each group. The macrophages in the fourth group expressed higher levels of ARG-1, CD206, and PDL-2 mRNA. Data are shown as means ± SD.

IL-6 level was significantly suppressed. TRAP staining showed significant osteoclast differentiation in the periodontal ligament region; however, in the cell injection group, osteoclast activity was significantly low (**Figure 4**).

DISCUSSION

The present study compared the immune properties of macrophages activated under various conditions. Stimulating with IL-13 and IL-4 could induce macrophages into an immune-suppressing M2 subtype. Although IL-10 alone could not alter the phenotype of macrophages, when combined with IL-4 and IL-13, the macrophages exhibited a much higher level of M2-related gene expression, capable of promoting IL-2 expression while suppressing IL-6, TNF-α, and IL-17 expression when cultured with splenocytes.

A periodontitis model was induced in mice to monitor the M2 macrophages' ratios and regulatory T cells in the local gingival tissue using flow cytometry during inflammation. Besides, the mechanism through which the injection of immuno-suppressive macrophages affected the local site of periodontitis was evaluated. The results showed that the ratio of M2 macrophages and regulatory T cells significantly decreased in the periodontitis

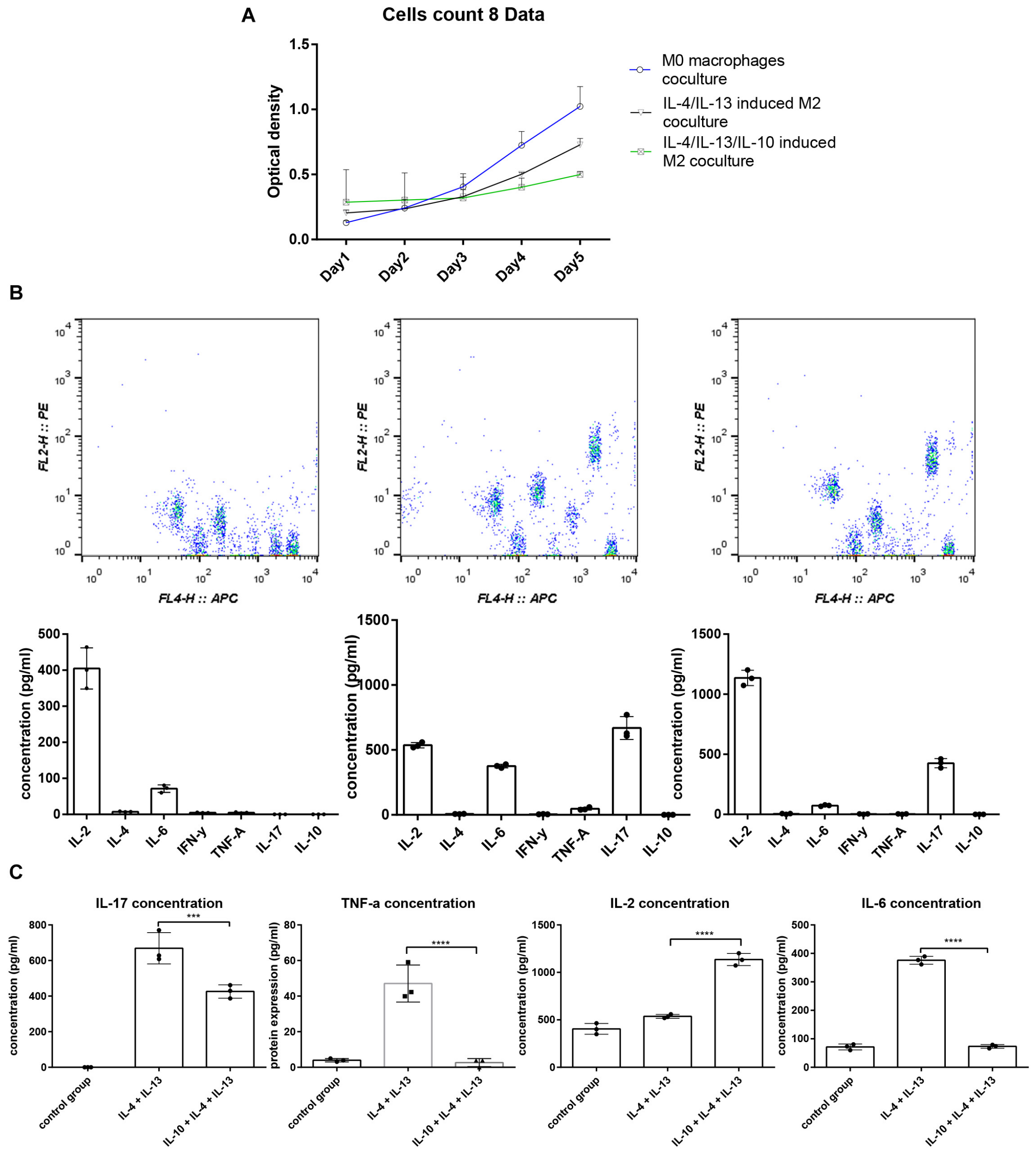

FIGURE 2 | The splenocyte proliferation analysis and cytokine profile difference cocultured with macrophages. **(A)** Five days of splenocyte proliferation in the mixed culture using CCK-8 kit. The relative cell count is represented by optical density (OD) value. **(B)** CBA analysis of cytokine profiles in the supernatant of mixed culture; the IL-4, IL-13, and IL-10 groups exhibited higher IL-2, IL-6, TNF-α, and lower IL-17 concentration compared to the IL-4, IL-13 group.

group's gingiva compared to the healthy group. This outcome led to the assumption that expanding the M2 macrophage population might positively affect periodontitis treatment. The model in the present study was created with *P. gingivalis* to induce periodontitis in the local region. The infected mice exhibited a decrease in the ratio of M2 macrophages and regulatory T cells compared to the healthy group in the inflamed gingival tissue. Periodontitis is induced mainly by the infection with gram-negative organisms, but the host's immune response, such as leukocyte activation and osteoclast differentiation, largely contributes to bone resorption (Ernst et al., 2007). Regulatory T cells tend to migrate to the inflammatory tissue as one of the leukocyte populations and balance proinflammatory reactions. However, they are likely to lose their suppressive properties due to a high concentration of cytokines, such as IL-6 and TNF-a, in the bone resorption lesion (Alvarez et al., 2018). In the CI group, the gingival tissue contained a higher level of ARG-1 and a lower level of IL-6 protein concentration. The results indicated that the injection of the immunosuppressive M2 macrophages could expand the M2

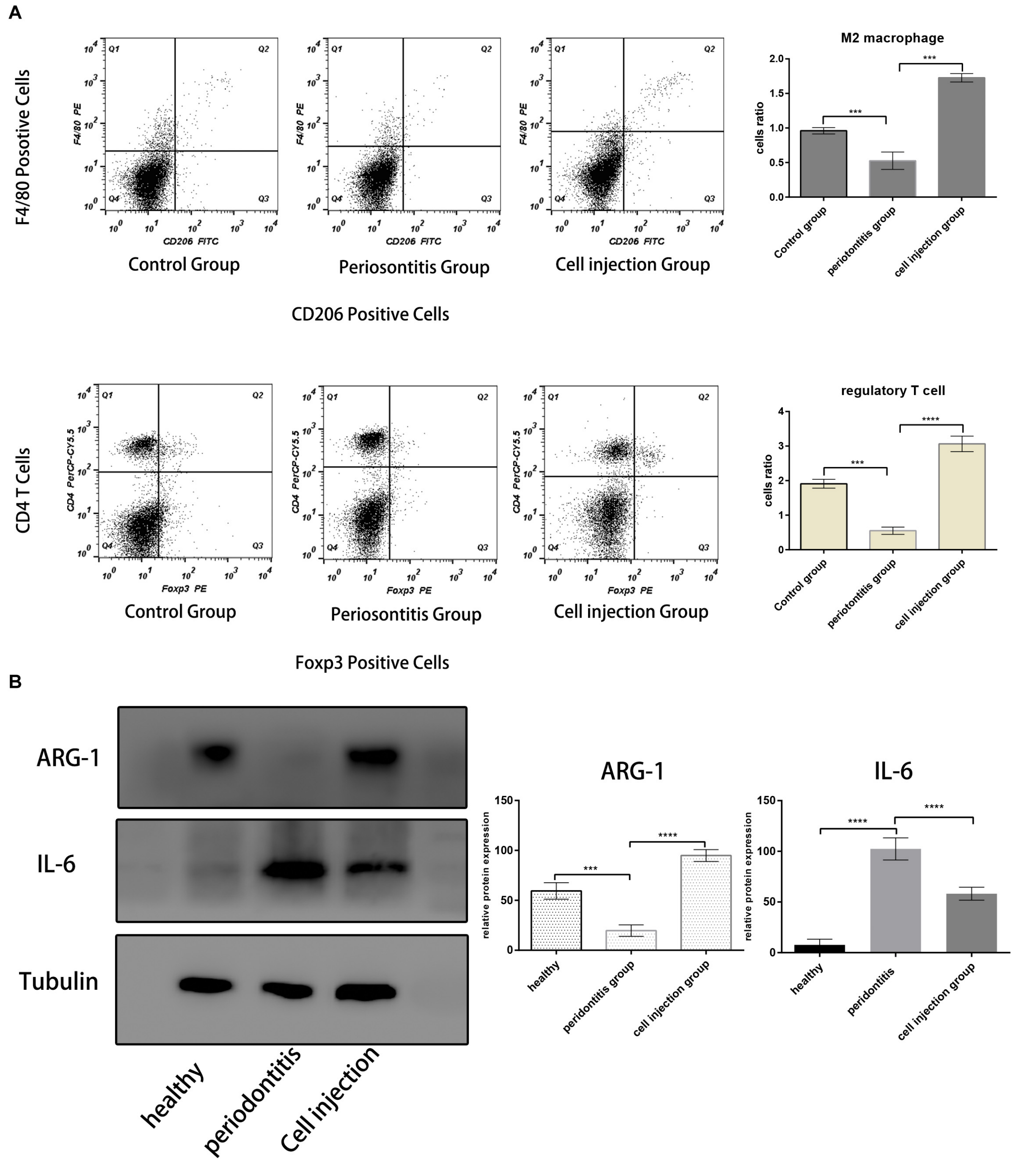

FIGURE 3 | M2 macrophages and regulatory T cell population analysis. **(A,B)** Flow cytometric analysis of cells in the mice periodontal tissue in each group. The M2 macrophages were gated with F4/80$^+$ and CD206$^+$; the Treg cells were gated with CD4$^+$ and Foxp3$^+$. Both the ratios of F4/80$^+$ and CD206$^+$ cells and CD4$^+$ and Foxp3$^+$ cells are lower in the periodontitis group and higher in the healthy group and cell injection group. **(C)** Western blot analysis of IL-6 and ARG-1 protein in the gingival tissue. The statistical significance was determined by *P*-value (***$P < 0.001$, ****$P < 0.0001$).

macrophage ratio and suppress the cytokine expression of proinflammatory M1 macrophages.

In the present study, the F4/80$^+$, CD206$^+$, and CD4$^+$/Foxp3$^+$ cells were monitored in the mice gingival tissue from the healthy (H), periodontitis (P), and cell injection (CI) groups. The M2 macrophages are specialized in wound healing and inflammation resolution (Ferrante and Leibovich, 2012); they express B7 PDL-2 protein as a mechanism to inhibit the expansion of effector T cells while sustaining the regulatory T cell population (DiDomenico et al., 2018). iNOS is the signature

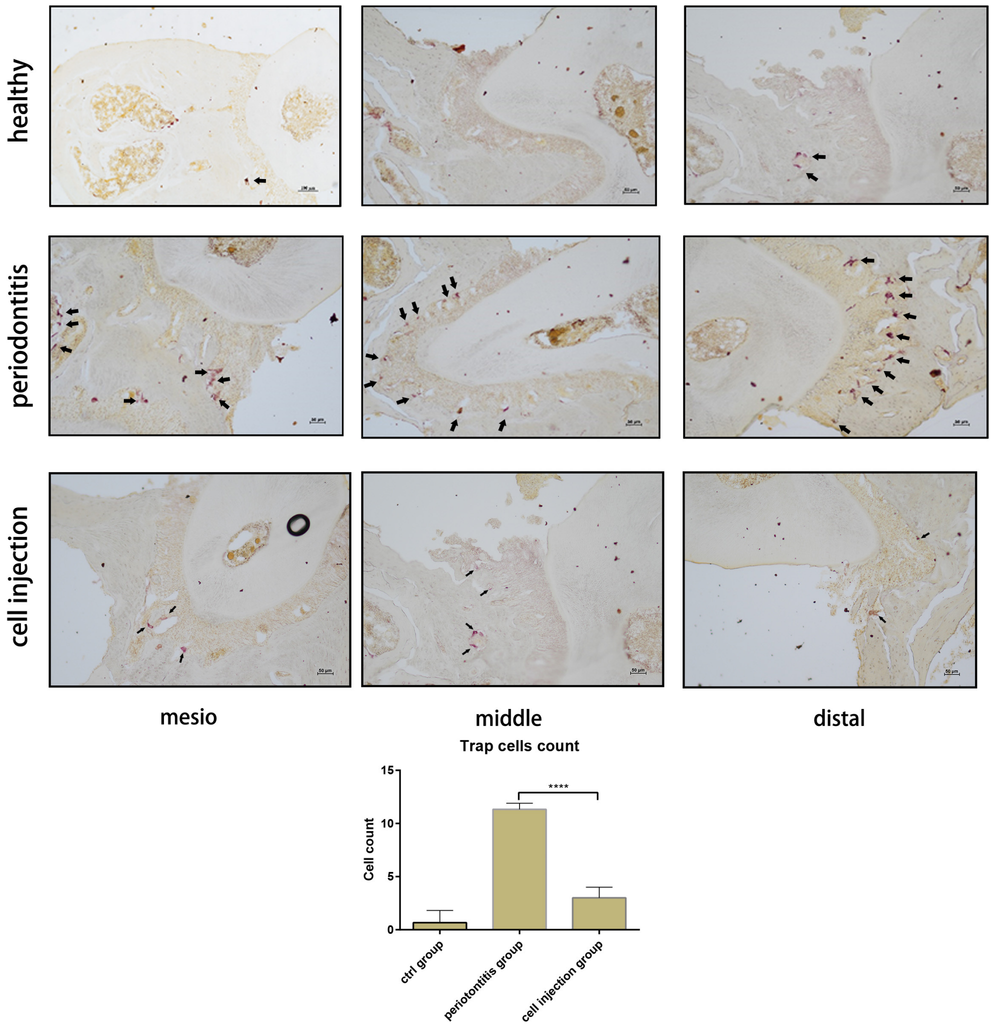

FIGURE 4 | Tartrate-resistant acid phosphatase (TRAP) staining of osteoclast in the periodontal ligament of the distal, middle, and mesial sites of the second molar. The cell counts of TRAP-positive cells are shown as means ± SD; the statistical significance was determined by *P*-value ($^{***}P < 0.001$).

of M1 macrophages that can help destroy pathogens; on the contrary, ARG-1 is an M2 macrophage signature that promotes tissue repair (Yang and Ming, 2014). It has been reported that during the progressive state of periodontitis, the M1/M2 ratio is higher than that in the steady-state or healthy tissues (Yang et al., 2018). Compared to the M1 macrophages, the M2 macrophages secrete ornithine from L-arginine via ARG-1 (Mills et al., 2000). Nitric oxide and ornithine exert a different effect; nitric oxide facilities the clearance of pathogens and inhibits cell proliferation, while ornithine promotes tissue repair (Morris, 2007). ARG-1 and iNOS production have been considered as M2 and M1 activities, respectively.

M2 macrophages, induced by a combination of IL-10, IL-4, and IL-13, express much higher levels of ARG-1, PDL-2, and mannose receptor CD206 than regular M2 macrophages induced by IL-4 and IL-13. Although the mannose receptor has little to do with the antigen-presenting process or priming of the immune reaction, the function of CD206 is still to be elucidated (Gazi and Martinez-Pomares, 2009). Macrophages are one of the antigen-presenting cells, and among the first defense cells to encounter pathogens and activate the adaptive immune reaction. The macrophage and splenocyte mixed cultures were used to investigate the effect of different macrophages on the lymphocytes. The quantitative results of cytokine concentrations in the culture supernatant showed that in the normal state, T cells secrete low levels of IL-2 continuously, as shown in the control group, where the splenocytes were cultured with inactivated macrophages. Maintaining a certain level of IL-2 is essential to maintaining immune homeostasis (Arenas-Ramirez et al., 2015).

The splenocytes were also cultured with two groups of M2 macrophages; the cytokine profiles in the culture supernatant showed that the novel M2 macrophages, stimulated by IL-4, IL-13, and IL-10, resulted in a much higher IL-2 production and a lower IL-17, IL-6, and TNF-a production during the culture period compared to traditional M2 macrophages activated by

IL-4 and IL-13. The primary source of IL-2 is not regulatory T cells, but the effector T cells; however, the regulatory T cells and their Foxp3 expression mainly depend on IL-2 stimulation (Hill et al., 2007). T cells' survival and expansion closely relate to level of IL-2 (Polhill et al., 2012). An increase in IL-2 concentration could lead to an increase in the regulatory T cell population, suppressing the effector T cell activation (Amado et al., 2013). The fact that M2 macrophages promote IL-2 while suppressing IL-6, TNF-a, and IL-17 expression indicates great potential in suppressing inflammation.

It is well established that programmed death-ligand protein plays a role in enhancing and sustaining the master transcription factor Foxp3 (Francisco et al., 2009). PD-1 ligand PDL-1 is expressed by many cell types, such as dendritic cells, macrophages, T cells, and B cells. However, the PDL-2 is mainly expressed by dendritic cells and macrophages (Keir et al., 2008). The PD-1 and PDL interaction suppresses effector T cell function and expansion while sustaining the regulatory T cell population by affecting mTOR signaling pathways (Strauss et al., 2007). The cell count in the mixed cell culture indicated that the M2 macrophages induced by IL-10, IL-4, and IL-13 possess a higher suppressive effect on the lymphocyte proliferation than the traditional M2 macrophages.

Macrophages stimulated by a combination of IL-4, IL-13, and IL-10 express significantly higher levels of ARG-1, with possibly more significant potential of immune suppression ability. Immunomodulatory therapy has been employed to treat many autoimmune diseases (Pannell et al., 2016; Kang et al., 2019). However, the problem with regulatory T cells' adoptive transfer therapy is that T cells are target-specific (Tonkin et al., 2008). The macrophages could influence the function of adaptive immune cells. We developed an immune-suppressive type of M2 macrophages to not only delay the onset of inflammation but also protect tissues from destruction. A change in the M1/M2 ratio is related to the severity of many autoimmune diseases (Fukui et al., 2017). Immunotherapy, such as immunosuppressive drugs, is utilized to suppress the system reaction and increase the Foxp3$^+$ cell population (Liu et al., 2015). A study demonstrated that the peritoneal-injected M2 macrophages migrated to the local region and suppressed the activation of infiltrated proinflammatory immune cells (Parsa et al., 2012). This outcome could also relate to the expansion of the regulatory T cell population. In contrast to the study above, our method is to directly deliver macrophages into the local periodontal tissue.

The RANKL protein secreted by effector T cells promotes osteoclast differentiation (Monasterio et al., 2018) and promotes the expression of many osteoclast precursor genes, including TRAP, leading to bone resorption. Previous research has shown that the regulatory T cells suppress osteoclast genesis during periodontitis (Zaiss et al., 2010). We analyzed the M2 macrophage and Foxp3 T cell populations during periodontitis. The results showed that the regulatory T cell ratio in the inflammatory tissue was lower compared to the healthy group. The data from the cell injection group showed that incorporating the M2 macrophage population not only expanded the regulatory T cell population but also effectively reduced the TRAP-positive cell counts. In conclusion, the M2 macrophages induced by IL-10, IL-4, and IL-13 exhibited higher immune-modulating potential than regular M2 macrophages. They were better at suppressing effector T cell proliferation and sustaining the regulatory T cell population. The adoptive transfer of M2 macrophages successfully alleviated the severity of periodontitis.

Moreover, the macrophages could also be used for nano-drug delivery (Xuan et al., 2019). Recently, macrophage-based nanosystems have been employed for periodontitis treatment. Due to their versatile and unique properties, macrophages and macrophage membranes are quite suitable for coating nanoparticles to build biomimetic systems for biomedical applications. Macrophages are emptied through a hypotonic lysis process for obtaining their outer membranes. The drug (artesunate, antibiotics, etc.) loading macrophage membrane surfaces with nanoparticles can be carried out by extrusion or in an ultrasonic bath. Macrophage membrane coatings have been critical in prolonging the circulation time of nano-drug delivery systems *in vivo*, further enhancing the efficiency of drug delivery and therapeutic efficacy (Tong et al., 2016; Zhang et al., 2018; Xia et al., 2020). Therefore, the macrophage-based nanosystems exhibit great potential for controlled drug delivery in periodontitis treatment.

DATA AVAILABILITY STATEMENT

The raw data supporting the conclusions of this article will be made available by the authors, without undue reservation.

ETHICS STATEMENT

The animal study was reviewed and approved by Animal Etheric Committee of China Medical University.

AUTHOR CONTRIBUTIONS

YM conceived and designed the experiments, analyzed the data, and wrote the manuscript. LH and XQ performed the experiments. All authors contributed equally to the article and approved the submitted version.

FUNDING

This work was supported by the National Natural Science Foundation of China (Grant number 81570988).

SUPPLEMENTARY MATERIAL

The Supplementary Material for this article can be found online at: https://www.frontiersin.org/articles/10.3389/fmolb.2020.603817/full#supplementary-material

REFERENCES

Alvarez, C., Rojas, C., Rojas, L., Cafferata, E. A., Monasterio, G., and Vernal, R. (2018). Regulatory T lymphocytes in periodontitis: a translational view. *Mediat. Inflamm* 2018:7806912. doi: 10.1155/2018/7806912

Amado, I. F., Berges, J., Luther, R. J., Mailhé, M. P., Garcia, S., Bandeira, A., et al. (2013). IL-2 coordinates IL-2-producing and regulatory T cell interplay. *J. Exp. Med.* 210, 2707–2720. doi: 10.1084/jem.20122759

Arenas-Ramirez, N., Woytschak, J., and Boyman, O. (2015). Interleukin-2: biology, design and application. *Trends Immunol.* 36, 763–777. doi: 10.1016/j.it.2015.10.003

Bonnamain, V., Neveu, I., and Naveilhan, P. (2012). Neural stem/progenitor cells as a promising candidate for regenerative therapy of the central nervous system. *Front. Cell Neurosci.* 6:17. doi: 10.3389/fncel.2012.00017

Bonner, M., Fresno, M., Girones, N., Guillen, N., and Santi-Rocca, J. (2018). Reassessing the role of entamoeba gingivalis in periodontitis. *Front. Cell Infect. Microbiol.* 8:379. doi: 10.3389/fcimb.2018.00379

Chambers, A. M., and Matosevic, S. (2019). Immunometabolic dysfunction of natural killer cells mediated by the hypoxia-CD73 axis in solid tumors. *Front. Mol. Biosci.* 6:60. doi: 10.3389/fmolb.2019.00060

Cronin, S. J. F., Woolf, C. J., Weiss, G., and Penninger, J. M. (2019). The role of iron regulation in immunometabolism and immune-related disease. *Front. Mol. Biosci.* 6:116. doi: 10.3389/fmolb.2019.00116

DiDomenico, J., Lamano, J. B., Oyon, D., Li, Y., Veliceasa, D., Kaur, G., et al. (2018). The immune checkpoint protein PD-L1 induces and maintains regulatory T cells in glioblastoma. *Oncoimmunology* 7:e1448329. doi: 10.1080/2162402x.2018.1448329

Ernst, C. W., Lee, J. E., Nakanishi, T., Karimbux, N. Y., Rezende, T. M., Stashenko, P., et al. (2007). Diminished forkhead box P3/CD25 double-positive T regulatory cells are associated with the increased nuclear factor-kappaB ligand (RANKL+) T cells in bone resorption lesion of periodontal disease. *Clin. Exp. Immunol.* 148, 271–280. doi: 10.1111/j.1365-2249.2006.03318.x

Ferrante, C. J., and Leibovich, S. J. (2012). Regulation of macrophage polarization and wound healing. *Adv. Wound Care (New Rochelle)* 1, 10–16. doi: 10.1089/wound.2011.0307

Francisco, L. M., Salinas, V. H., Brown, K. E., Vanguri, V. K., Freeman, G. J., Kuchroo, V. K., et al. (2009). PD-L1 regulates the development, maintenance, and function of induced regulatory T cells. *J. Exp. Med.* 206, 3015–3029. doi: 10.1084/jem.20090847

Fukui, S., Iwamoto, N., Takatani, A., Igawa, T., Shimizu, T., Umeda, M., et al. (2017). M1 and M2 monocytes in rheumatoid arthritis: a contribution of imbalance of M1/M2 monocytes to osteoclastogenesis. *Front. Immunol.* 8:1958. doi: 10.3389/fimmu.2017.01958

Gattinoni, L., Klebanoff, C. A., and Restifo, N. P. (2012). Paths to stemness: building the ultimate antitumour T cell. *Nat. Rev. Cancer* 12, 671–684. doi: 10.1038/nrc3322

Gazi, U., and Martinez-Pomares, L. (2009). Influence of the mannose receptor in host immune responses. *Immunobiology* 214, 554–561. doi: \url{https://org/10.1016/j.imbio.2008.11.004}

Hays, A., Duan, X., Zhu, J., Zhou, W., Upadhyayula, S., Shivde, J., et al. (2019). Down-regulated Treg cells in exacerbated periodontal disease during pregnancy. *Int. Immunopharmacol.* 69, 299–306. doi: 10.1016/j.intimp.2019.01.031

Hill, J. A., Feuerer, M., Tash, K., Haxhinasto, S., Perez, J., Melamed, R., et al. (2007). Foxp3 transcription-factor-dependent and -independent regulation of the regulatory T cell transcriptional signature. *Immunity* 27, 786–800. doi: 10.1016/j.immuni.2007.09.010

Kang, S. A., Park, M. K., Park, S. K., Choi, J. H., Lee, D. I., Song, S. M., et al. (2019). Adoptive transfer of Trichinella spiralis-activated macrophages can ameliorate both Th1- and Th2-activated inflammation in murine models. *Sci. Rep.* 9:6547. doi: 10.1038/s41598-019-43057-1

Kanzaki, H., Makihira, S., Suzuki, M., Ishii, T., Movila, A., Hirschfeld, J., et al. (2016). Soluble RANKL cleaved from activated lymphocytes by TNF-α-converting enzyme contributes to osteoclastogenesis in periodontitis. *J. Immunol.* 197, 3871–3883. doi: 10.4049/jimmunol.1601114

Keir, M. E., Butte, M. J., Freeman, G. J., and Sharpe, A. H. (2008). PD-1 and its ligands in tolerance and immunity. *Annu. Rev. Immunol.* 26, 677–704. doi: 10.1146/annurev.immunol.26.021607.090331

Liu, Z. M., Wang, K. P., Ma, J., and Guo Zheng, S. (2015). The role of all-trans retinoic acid in the biology of Foxp3+ regulatory T cells. *Cell Mol. Immunol.* 12, 553–557. doi: 10.1038/cmi.2014.133

Mills, C. D., Kincaid, K., Alt, J. M., Heilman, M. J., and Hill, A. M. (2000). M-1/M-2 macrophages and the Th1/Th2 paradigm. *J. Immunol.* 164, 6166–6173. doi: 10.4049/jimmunol.164.12.6166

Monasterio, G., Castillo, F., Ibarra, J. P., Guevara, J., Rojas, L., Alvarez, C., et al. (2018). Alveolar bone resorption and Th1/Th17-associated immune response triggered during Aggregatibacter actinomycetemcomitans-induced experimental periodontitis are serotype-dependent. *J. Periodontol.* 89, 1249–1261. doi: 10.1002/jper.17-0563

Morris, S. M. Jr. (2007). Arginine metabolism: boundaries of our knowledge. *J. Nutr.* 137(6 Suppl. 2), 1602s–1609s. doi: 10.1093/jn/137.6.1602S

Pannell, M., Labuz, D., Celik, M., Keye, J., Batra, A., Siegmund, B., et al. (2016). Adoptive transfer of M2 macrophages reduces neuropathic pain via opioid peptides. *J. Neuroinflammation* 13:262. doi: 10.1186/s12974-016-0735-z

Parsa, R., Andresen, P., Gillett, A., Mia, S., Zhang, X. M., Mayans, S., et al. (2012). Adoptive transfer of immunomodulatory M2 macrophages prevents type 1 diabetes in NOD mice. *Diabetes* 61, 2881–2892. doi: 10.2337/db11-1635

Polhill, T., Zhang, G. Y., Hu, M., Sawyer, A., Zhou, J. J., Saito, M., et al. (2012). IL-2/IL-2Ab complexes induce regulatory T cell expansion and protect against proteinuric CKD. *J. Am. Soc. Nephrol.* 23, 1303–1308. doi: 10.1681/asn.2011111130

Riley, J. L., June, C. H., and Blazar, B. R. (2009). Human T regulatory cell therapy: take a billion or so and call me in the morning. *Immunity* 30, 656–665. doi: 10.1016/j.immuni.2009.04.006

Sakaguchi, S. (2003). Control of immune responses by naturally arising CD4+ regulatory T cells that express toll-like receptors. *J. Exp. Med.* 197, 397–401. doi: 10.1084/jem.20030012

Strauss, L., Whiteside, T. L., Knights, A., Bergmann, C., Knuth, A., and Zippelius, A. (2007). Selective survival of naturally occurring human CD4+CD25+Foxp3+ regulatory T cells cultured with rapamycin. *J. Immunol.* 178, 320–329. doi: 10.4049/jimmunol.178.1.320

Tong, H. I., Kang, W., Shi, Y., Zhou, G., and Lu, Y. (2016). Physiological function and inflamed-brain migration of mouse monocyte-derived macrophages following cellular uptake of superparamagnetic iron oxide nanoparticles-Implication of macrophage-based drug delivery into the central nervous system. *Int. J. Pharm.* 505, 271–282. doi: 10.1016/j.ijpharm.2016.03.028

Tonkin, D. R., He, J., Barbour, G., and Haskins, K. (2008). Regulatory T cells prevent transfer of type 1 diabetes in NOD mice only when their antigen is present in vivo. *J. Immunol.* 181, 4516–4522. doi: 10.4049/jimmunol.181.7.4516

Tran, K. Q., Zhou, J., Durflinger, K. H., Langhan, M. M., Shelton, T. E., Wunderlich, J. R., et al. (2008). Minimally cultured tumor-infiltrating lymphocytes display optimal characteristics for adoptive cell therapy. *J. Immunother.* 31, 742–751. doi: 10.1097/CJI.0b013e31818403d5

Xia, Y., Rao, L., Yao, H., Wang, Z., Ning, P., and Chen, X. (2020). Engineering macrophages for cancer immunotherapy and drug delivery. *Adv. Mater.* 20:2002054. doi: 10.1002/adma.202002054

Xuan, M., Shao, J., and Li, J. (2019). Cell membrane-covered nanoparticles as biomaterials. *Nat. Sci. Rev.* 6, 551–561. doi: 10.1093/nsr/nwz037

Yang, J., Zhu, Y., Duan, D., Wang, P., Xin, Y., Bai, L., et al. (2018). Enhanced activity of macrophage M1/M2 phenotypes in periodontitis. *Arch. Oral. Biol.* 96, 234–242. doi: 10.1016/j.archoralbio.2017.03.006

Yang, Z., and Ming, X. F. (2014). Functions of arginase isoforms in macrophage inflammatory responses: impact on cardiovascular diseases and metabolic disorders. *Front. Immunol.* 5:533. doi: 10.3389/fimmu.2014.00533

Yu, T., Zhao, L., Huang, X., Ma, C., Wang, Y., Zhang, J., et al. (2016). Enhanced activity of the macrophage M1/M2 phenotypes and phenotypic switch to M1 in periodontal infection. *J. Periodontol.* 87, 1092–1102. doi: 10.1902/jop.2016.160081

Zaiss, M. M., Frey, B., Hess, A., Zwerina, J., Luther, J., Nimmerjahn, F., et al. (2010). Regulatory T cells protect from local and systemic bone destruction in arthritis. *J. Immunol.* 184, 7238–7246. doi: 10.4049/jimmunol.0903841

Zhang, Y., Cai, K., Li, C., Guo, Q., Chen, Q., He, X., et al. (2018). Macrophage-membrane-coated nanoparticles for tumor-targeted chemotherapy. *Nano. Lett.* 18, 1908–1915. doi: 10.1021/acs.nanolett.7b05263

Conflict of Interest: The authors declare that the research was conducted in the absence of any commercial or financial relationships that could be construed as a potential conflict of interest.

frontiers
in Bioengineering and Biotechnology

ORIGINAL RESEARCH
published: 19 November 2020
doi: 10.3389/fbioe.2020.599058

Mesenchymal-Stem-Cell–Derived Extracellular Vesicles Mitigate Trained Immunity in the Brain

Yiwei Feng[1†], *Min Guo*[1†], *Hongchen Zhao*[1], *Sida Han*[1], *Qiang Dong*[2*] *and Mei Cui*[1*]

[1] *Department of Neurology, Huashan Hospital, Fudan University, Shanghai, China,* [2] *State Key Laboratory of Medical Neurobiology, MOE Frontiers Center for Brain Science, Department of Neurology, Huashan Hospital, Fudan University, Shanghai, China*

Trained immunity was recently discovered in innate immune cells and shown to facilitate the clearance of pathogens at the time of occurrence of the second insult. However, it exacerbates several aspects of neuropathologies, and proper therapy is needed to rectify this abnormal immune reaction. Mesenchymal-stem cells (MSCs) exhibit a distinct capability for brain repair but are associated with safety concerns. Extracellular vesicles derived from MSCs are a promising alternative therapy. In this study, we used lipopolysaccharides to activate trained immunity in the brain and examined the therapeutic potential of MSC-derived extracellular vesicles in mitigating the trained-immunity-induced exacerbated neuropathology. We found that MSC-derived extracellular vesicles showed comparable effects to those of MSCs in the mitigation of trained immunity in the brain. Moreover, the administration of MCS-derived extracellular vesicles mitigated the aggregated inflammatory responses in the acute stage of stroke and alleviated the trained-immunity-induced increased load of amyloid-β in APP/PS1 mice. We further investigated the molecular machinery of MSC-derived extracellular vesicles and found that IL-10 is important for the mediation of the therapeutic potential of MSC-derived extracellular vesicles toward the alleviation of trained immunity. Our study indicates that extracellular-vesicle-based regenerative strategies might be useful to mitigate trained immunity in the brain.

Keywords: trained immunity, stroke, Alzheimer's disease, MSC (1991) 49N10, MSC-derived EVs

Edited by:
Wei Tao,
Harvard Medical School,
United States

Reviewed by:
Francesca Taraballi,
Houston Methodist Research Institute, United States
Junqing Wang,
Sun Yat-sen University, China

****Correspondence:***
Mei Cui
cuimei@fudan.edu.cn
Qiang Dong
dong_qiang@fudan.edu.cn;
qiangdonghs@163.com

† These authors have contributed equally to this work

Specialty section:
This article was submitted to Nanobiotechnology, a section of the journal Frontiers in Bioengineering and Biotechnology

Received: *26 August 2020*
Accepted: *26 October 2020*
Published: *19 November 2020*

Citation:
Feng Y, Guo M, Zhao H, Han S, Dong Q and Cui M (2020) Mesenchymal-Stem-Cell–Derived Extracellular Vesicles Mitigate Trained Immunity in the Brain. Front. Bioeng. Biotechnol. 8:599058. doi: 10.3389/fbioe.2020.599058

INTRODUCTION

Immune memory has long been believed to exist only in the adaptive immune system. However, recent evidence indicates that innate immune cells also display memory effects, namely trained immunity (Netea et al., 2015, 2016; Wendeln et al., 2018). For example, certain inflammatory stimuli, such as lipopolysaccharides (LPS), prime peripheral monocytes, leading them to respond more efficiently when the second inflammatory insult occurs (Biswas and Lopez-Collazo, 2009; Saeed et al., 2014). Trained immunity triggers the more efficient clearance of pathogens by myeloid cells. However, in the central nervous system (CNS), microglia, which are the brain-resident macrophages, exhibit a different aspect of trained immunity. It has been demonstrated that mice subjected to initial inflammatory stimuli, such as LPS, exhibit activation of the innate immune memory in the brain, which exacerbated stroke prognosis and deteriorated the pathology of

Alzheimer's disease in the long term (Wendeln et al., 2018). The loss of dopaminergic neurons and aggregated α-synuclein are also prominent in an MPTP-induced model of Parkinson's disease (PD) after a single LPS injection (Qin et al., 2007). Once activated, trained immunity appears as a long-lasting effect that modulates the progression of many brain diseases. Therefore, adequate therapies are urgently needed to rectify this abnormal immune status in the CNS.

Advances in regenerative medicine have revealed the great potential of mesenchymal-stem cells (MSCs) in brain repair based on their remarkable anti-inflammatory and immunomodulatory properties (Galindo et al., 2011; Sherman et al., 2019). Our previous study found that MSCs triggered the remission of trained immunity through the inhibition of H3K4 methylation (Feng et al., 2020). However, concerns regarding their safety as well as their tumor- or microinfarction-inducing potential limit the translational capacity of MSCs (Kunter et al., 2007).

Mesenchymal-stem cells are potent producers of extracellular vesicles (EVs). These vesicles (50–1000 nm in size) contain substantial components that can promote tissue repair and mediate MSC paracrine function (El Andaloussi et al., 2013; Ha et al., 2016). As MSCs cannot cross the blood—brain barrier (BBB) and most MSCs injected show a lung-predominant distribution, MSC-derived EVs may represent an alternative option as they could reach the brain parenchyma and, to a large extent, mimic the regenerative and immunosuppressive effects of MSCs (Wood et al., 2011; Wang et al., 2019).

The vast research efforts dedicated to the elucidation of the anti-inflammatory mechanism of MSCs identified IL-10 as an important mediator of the switch of the macrophage phenotype from the M1 (proinflammatory) to the M2 (anti-inflammatory) types and as a trigger of the MSC-induced reparative process (Eirin et al., 2017; Park et al., 2019). However, whether the protective effect of MSCs or MSC-derived EVs via the remission of trained immunity is dependent on an IL-10-mediated mechanism remains elusive.

In this study, we tested the therapeutic effect of MSC-derived EVs on trained immunity in the brain and further examined this process in the context of two neurological diseases in which the relative pathology is substantially exacerbated by trained immunity. Moreover, we studied whether this protective effect was dependent on an IL-10-mediated mechanism.

RESULTS

Characteristics of MSC-Derived EVs

Ultracentrifugation was used to isolate MSC-derived EVs in our study. The isolated exosomes were observed to exhibit spherical structures via transmission electron microscopy (**Figure 1A**), and were mainly distributed among diameters of 100—150 nm, as assessed by nanoparticle tracking analysis (**Figure 1B**). Moreover, we validated the expression of key proteins in our isolated EVs by identifying the expression of characteristic EV and MSC markers, such as CD9, CD29, and CD63 (**Figures 1D,E**). In addition, IL-10 knockdown significantly inhibited IL-10 expression in MSC-derived EVs, as shown in **Figure 1D**. Next, we labeled EVs with a red fluorescent dye and injected the labeled EVs into the tail vein of mice. Thirty minutes after the injection, mice were sacrificed and EVs were tracked in frozen sections of the brain. We detected the distribution of EVs across the brain parenchyma and the internalization of MSC-derived EVs by microglia (**Figure 1C**). These results suggest that peripherally administered MSC-derived EVs were able to cross the BBB and were engulfed by microglia in the CNS.

MSC-Derived EVs Attenuate the Innate Immune Memory in the Brain

It has been established that inflammation in the periphery can prompt immune responses in the brain, and that peripheral low-dose lipopolysaccharide (LPS) stimulation can induce microglial immune memory (Wendeln et al., 2018). As MSC-derived EVs were able to cross the brain parenchyma and affect microglia, we wondered whether MSC-derived EVs could alleviate the innate immune memory and whether this alleviation was dependent on an IL-10 mediated mechanism.

First, we established a mouse model in which the innate immune memory was activated by low-dose LPS administration. And these mice were re-stimulated using PBS or LPS (1× or 2× LPS) 30 days after the initial LPS stimulation, to examine the inflammatory responses in the brain or peripheral blood serum (**Figure 2A**). We found that the secondary LPS stimulation (both 1× and 2× LPS) exacerbated brain cytokine production, as evidenced by the significantly increased levels of pro-inflammatory and anti-inflammatory cytokine IL-1β, TNF-α, and IL-10 (**Figures 2B,C**) and 2× LPS mice showed a significant elevation of pro-inflammatory cytokines IL-1β, TNF-α compared with 1× LPS mice. These results indicate the successful establishment of innate immune memory in the brain.

We further tested the therapeutic potential of MSC-derived EVs regarding the remittance of these arrogated inflammatory responses. MSC-derived EVs (2×10^9 NVs) were intravenously injected at day 14 after the first LPS stimulation. MSCs (1×10^7/ml, 0.5 ml per mouse) were injected at the same time point in a separate group, to compare the therapeutic effect of MSC-derived EVs with that of MSCs regarding immune training. At day 30, the exacerbated inflammatory responses that were observed in mice re-stimulated with LPS (2× LPS) were diminished in mice subjected to MSC-derived EV and MSC administration; however, the alleviation afforded by MSC-derived EVs was abolished by IL-10 knockdown in these EVs (**Figures 2B–D**). Interestingly, neither MSCs nor MSC-derived EVs affected the levels of inflammatory cytokines in the serum of mice stimulated with both 1× and 2× LPS (**Figures 2E–G**).

Together, these results indicate that MSC-derived EVs can penetrate into the CNS and alleviate the innate immune memory in the brain to an extent comparable to MSC administration.

MSC-Derived EVs Rescued the Deteriorated Neuropathology Caused by Immune Training

The results reported above indicated the therapeutic potential of MSC-derived EVs in remitting the innate immune memory in the

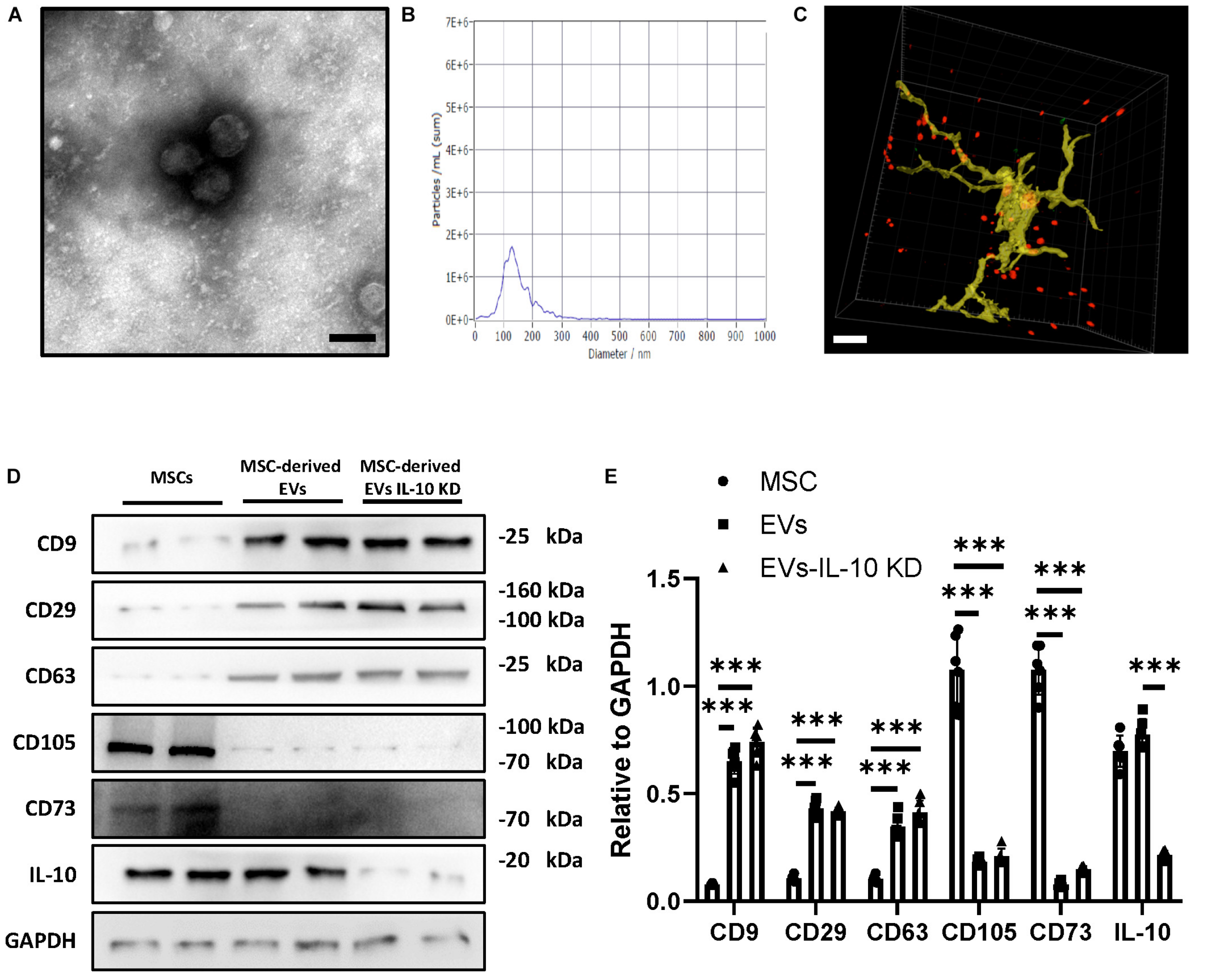

FIGURE 1 | Characteristic of MSC-derived EVs. **(A)** Representative TEM images of MSC-derived EVs. Scale bar, 100 nm. **(B)** NTA analysis of MSC-derived EVs. **(C)** Representative 3-dimensional confocal images showing microglia (Iba1, green) engulfing MSC-derived EVs (red). Scale bar, 10 μm. **(D)** Immunoblot **(D)** and quantitative analysis **(E)** of CD9, CD29, CD63, CD105, CD73, IL-10, GAPDH in MSCs, MSC-derived EVs, and MSC-derived EVs with IL-10 knockdown. Data are presented as the mean ± standard deviation (***$p < 0.001$).

brain. Next, we examined this therapeutic effect of MSC-derived EVs on various disease pathologies in the CNS that are greatly affected by the innate immune memory.

It has been previously demonstrated that low-dose LPS stimulation exacerbated stroke prognosis 1 month after exposure to this agent, and that this effect was dependent on the innate immune memory (Wendeln et al., 2018). Wild-type mice were injected with single LPS, and focal ischemia was induced 1 month later. At 1-day post-ischemia, neuronal damage and microglial density were undistinguishable among the various treatment groups (**Figures 3A–C**). However, an aggregated inflammatory response was observed in mice that were pre-injected with LPS, showing as elevated IL-1β, IL-6, and TNF-α and decreased IL-10 (**Figures 3D–G**). Both MSCs and MSC-derived EVs abolished this increased production of proinflammatory cytokines and rescued the production of IL-10. However, knockdown of IL-10 in MSC-derived EVs abolished this alleviation (**Figures 3D–G**). At 7-day post-ischemia, we observed that although LPS treatment did not increase the infarct size, MSCs and MSC-derived EVs significantly alleviated the infarct volume when compared with LPS + PBS group; however, knockdown of IL-10 in MSC-derived EVs failed to abolish this therapeutic effect (**Figures 3H–J**).

Next, we tested the therapeutic potential of MSC-derived EVs in a second disease model. It has been established that the innate immune memory promotes the pathological progression of Alzheimer's disease (AD) (Wendeln et al., 2018). The model consists in a single injection of low-dose LPS (1× LPS) into 3-month-old APP23 mice, which exacerbates the formation of plaques of insoluble amyloid-β (Aβ) at the age of 9 months (**Figure 4A**). Based on this model, trained immunity was induced by low-dose LPS administration to 3-month-old APP23 mice, and MSC/MSC-derived EVs were injected intravenously 1 month later. A pathological analysis was performed in 9-month-old APP23 mice (**Figure 4B**). Although neither 1× LPS administration nor MSCs/MSC-derived EVs/MSC-derived EVs with IL-10 knockdown affected the number of cortical

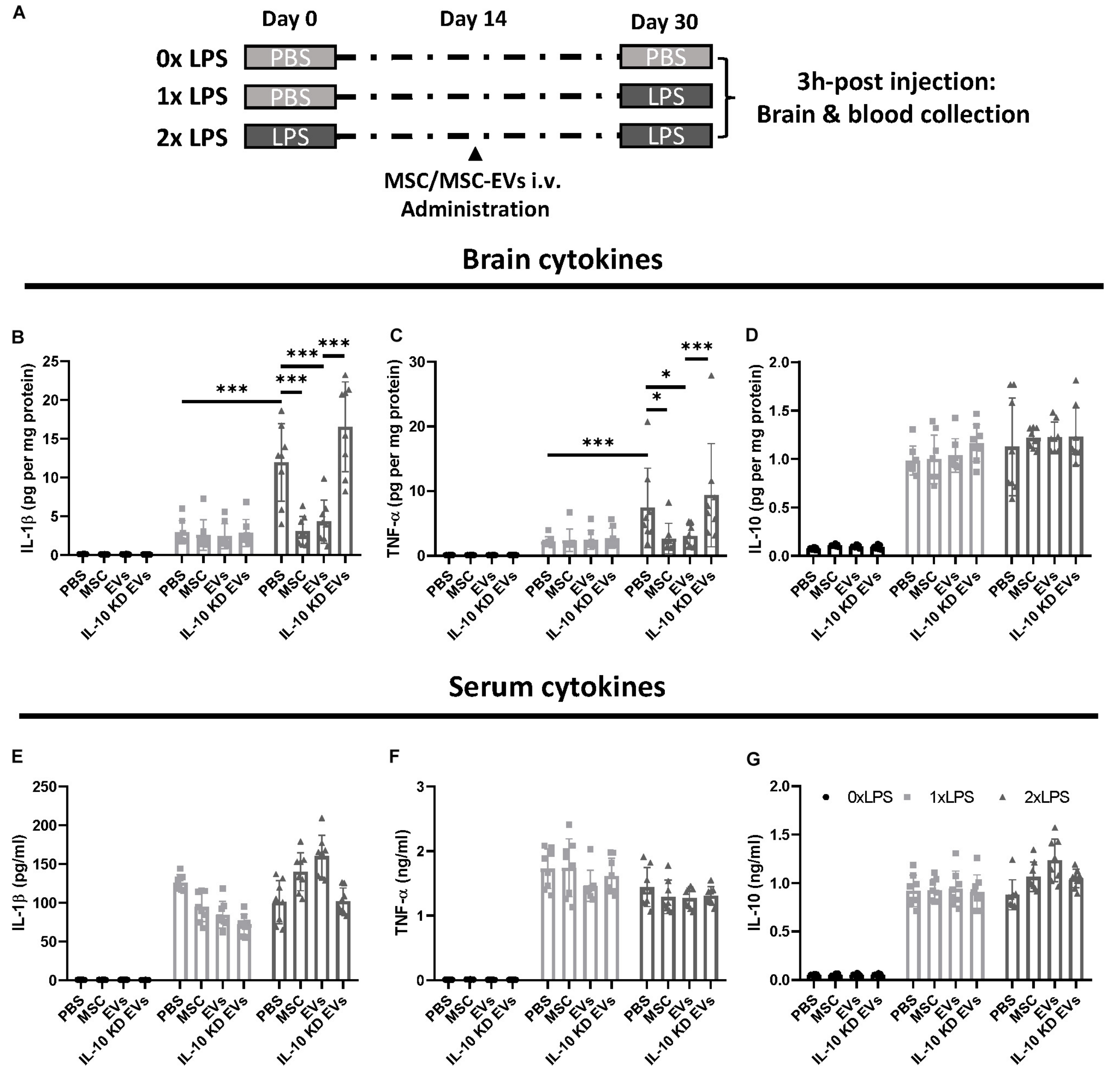

FIGURE 2 | MSC-derived EVs mitigated LPS-induced trained immunity. **(A)** Schematic diagram of the experimental design. **(B–D)** Quantitative ELISA analysis of cytokine profiles in brain parenchyma following LPS administration (*n* = 8 mice per group). **(E–G)** Quantitative ELISA analysis of cytokine profiles in peripheral blood following LPS administration (*n* = 8 mice per group) Data are presented as the mean ± standard deviation ($^{*}p < 0.05$; $^{***}p < 0.001$).

microglia or plaque-associated microglia (**Figures 4C,D**), 1× LPS significantly increased the plaque load and total Aβ levels compared with control animals (**Figures 4E,F**). MSCs and MSC-derived EVs yielded a similar alleviation of the plaque load and total Aβ levels, whereas MSC-derived EVs with IL-10 knockdown abolished the therapeutic effect of MSC-derived EVs on AD pathology (**Figures 4E,F**). Moreover, MSCs and MSC-derived EVs mitigated the upregulation of the proinflammatory TNF-α and IL-1β in 1× LPS-stimulated 9-month-old APP23 mice (**Figures 4G–J**). Finally, MSCs and MSC-derived EVs rescued the inhibited IL-10 production in 1× LPS-stimulated 9-month-old APP23 mice and MSC-derived EVs with IL-10 knockdown abolished this therapeutic effect (**Figures 4G–J**). Therefore, it could be observed that the exacerbated AD pathology caused by trained immunity was mitigated by MSC-derived EVs via an IL-10 dependent mechanism.

DISCUSSION

In this study, we uncovered the therapeutic potential of MSC-derived EVs in mitigating trained immunity in the CNS. The initial LPS training exacerbated the inflammatory responses caused by the secondary LPS challenge administered 1 month later, and MSC-derived EVs remitted this aggregated response via an IL-10-dependent mechanism. We further examined this

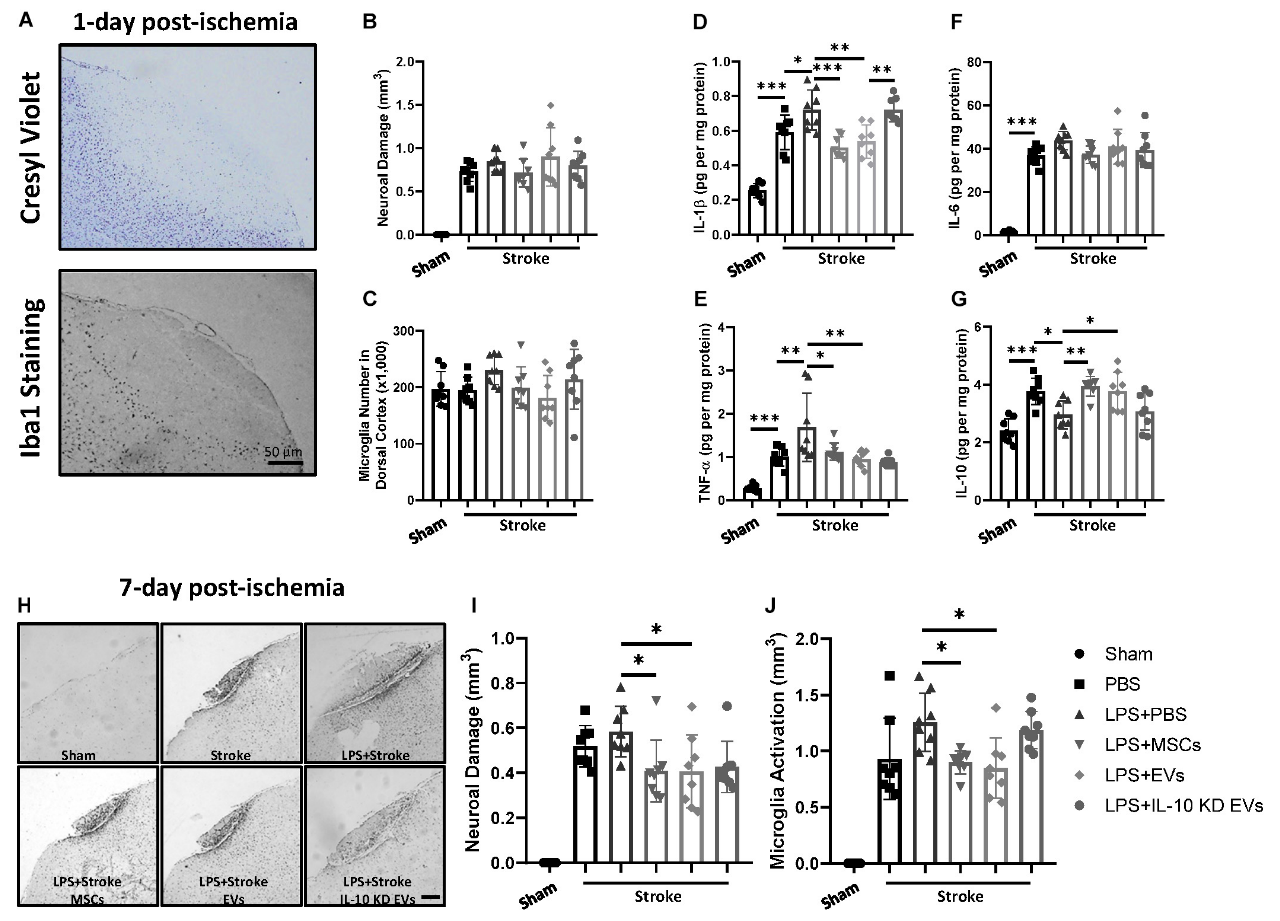

FIGURE 3 | The exacerbated stroke pathology caused by trained immunity was mitigated by MSC-derive EVs. **(A)** Representative cresyl violet staining and Iba1 IHC staining of the ischemic brain cortex at 1 day post-ischemia. Scale bar: 50 μm. **(B,C)** Quantitative analysis of neuronal damage **(B)** (cresyl violet, *n* = 8 mice per group) and number of microglia in the dorsal cortex **(C)** (Iba1 IHC staining, *n* = 8 mice per group) at 1 day post-ischemia. **(D–G)** Quantitative ELISA analysis of cytokine profiles in the ischemic cortex at 1 day post-ischemia (*n* = 8 mice per group). **(H)** Representative IHC staining of Iba1-positive microglia in the ischemic cortex at 7 days post-ischemia. Scale bar: 50 μm. **(I,J)** Quantitative analysis of infarct volume **(I)** and microglial activation **(J)** at 7 days post-ischemia (*n* = 8 mice per group). Data are presented as the mean ± standard deviation ($^*p < 0.05$; $^{**}p < 0.01$; $^{***}p < 0.001$).

therapeutic potential of MSC-derived EVs in two neurological models in which the pathological changes were caused by trained immunity. We found that the exacerbated inflammatory responses resulting from LPS training in the acute phase of stroke were remitted by MSCs or MSC-derived EVs. In addition, MSCs or MSC-derived EVs decreased the infarct volume at 7 days after ischemic stroke. Moreover, the exacerbated deposition of amyloid-β plaques triggered by LPS training was also remitted by MSCs or MSC-derived EVs.

The participation of trained immunity in the development of neurological pathologies has been discovered recently (Wendeln et al., 2018). Once activated by a proinflammatory stimulus, such as LPS, oxLDL, DAMPs, or TNF-α, microglia undergo an epigenetic reprogramming that increases the H3K4 methylation or H3K27 acetylation levels in inflammation-related genes, resulting in a stronger response to secondary stimuli upon re-challenge (Crişan et al., 2016). In contrast with the function of trained immunity in the periphery, where it clears pathogens more efficiently, trained immunity has detrimental effects in the CNS (Netea et al., 2016). This may be attributed to the longevity of microglia and the vicious cycle in which the presence of insoluble aggregated proteins, such as Aβ and α-synuclein, activates microglia, with trained microglia further exacerbating these pathologies through enhanced inflammatory responses (Qin et al., 2007; Wendeln et al., 2018). As a result, the activation of trained immunity deteriorates stroke prognosis, exacerbates the pathologies of AD, and promotes the aggregation of α-synuclein in PD in the long term (Sacino et al., 2013; Rutherford et al., 2015; Wendeln et al., 2018).

Regarding this long-term effect of trained immunity, we should pay attention to the factors that can initiate it in the brain. It could be noted that trained immunity can be activated not only by LPS, but also by many high-risk factors that deteriorate the microenvironment of the brain parenchyma. For example, the western diet can induce epigenetic reprogramming of the innate immune system in a NLRP3-dependent manner

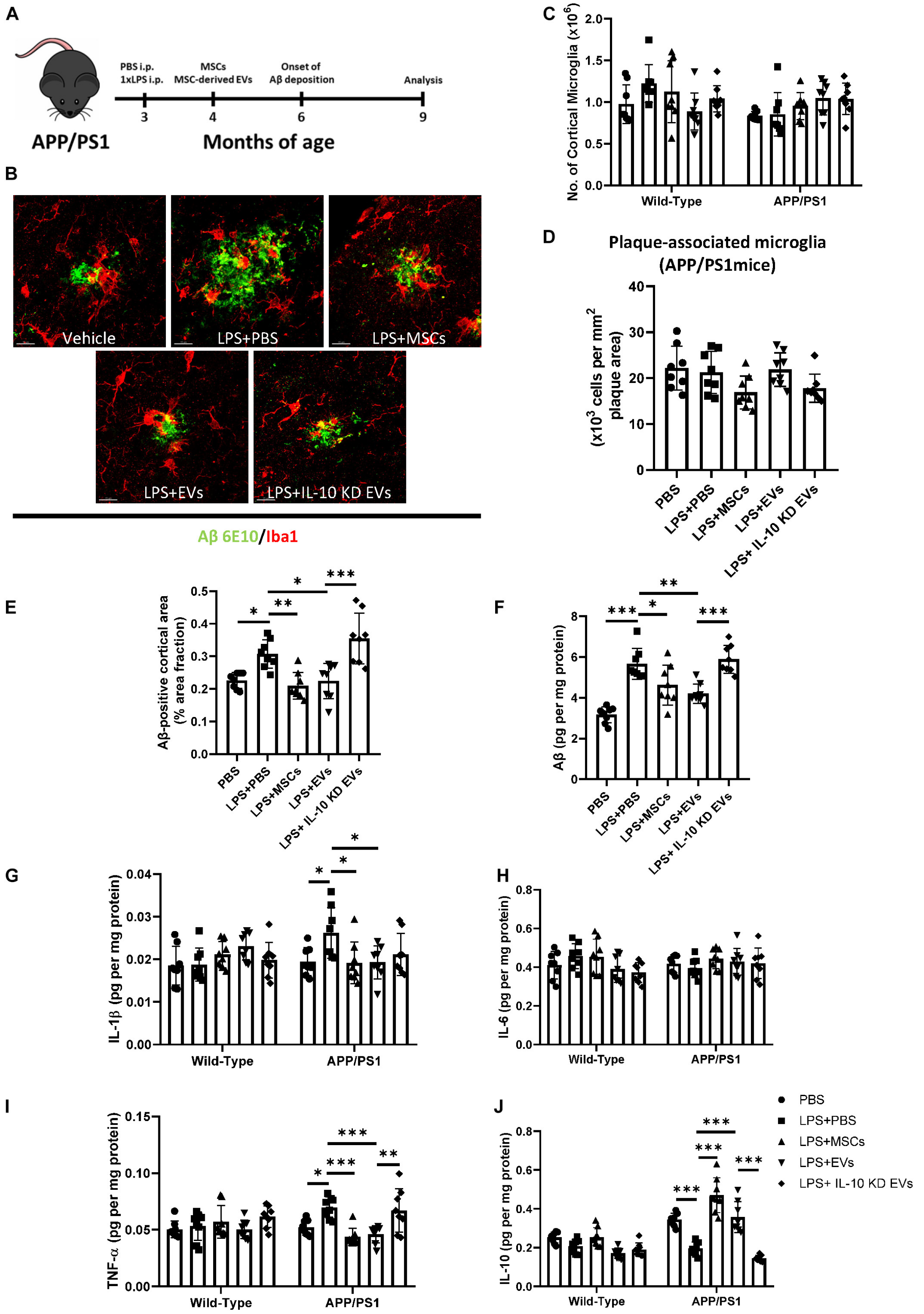

FIGURE 4 | The exacerbated β-amyloidosis caused by trained immunity was mitigated by MCS-derived EVs. **(A)** Schematic diagram of the experimental design. **(B)** Representative immunofluorescence images showing Aβ deposition (green) and surrounding Iba1 (red). Scale bar: 5 μm. **(C,D)** Quantitative analysis of total cortical **(C)** and plaque-associated **(D)** microglia (*n* = 8 mice per group). **(E,F)** Quantitative analysis of cortical Aβ plaque load **(E)** (*n* = 8 mice per group) and Aβ protein levels by ELISA **(F)** (*n* = 8 mice per group). **(G–J)** Quantitative ELISA analysis of cytokine profiles in wild-type and APP/PS1 mice at 9 months (*n* = 8 mice per group). Data are presented as the mean ± standard deviation. (*$p < 0.05$; **$p < 0.01$; ***$p < 0.001$).

(Christ et al., 2018). Moreover, hypertension exacerbates the pathologies of amyloid-β and worsens stroke prognosis, which is related to the priming of microglia (Perry and Holmes, 2014; Shen et al., 2015). It is expected that other risk factors, such as atherosclerosis and diabetes, also exacerbate neuropathologies through the activation of trained immunity (Perry and Holmes, 2014). Finally, proper therapeutics aim to rectify this fatal effect of trained immunity in the CNS.

Our previous study found that MSCs could alleviate trained immunity through the inhibition of H3K4 methylation (Feng et al., 2020). Although MSC therapy shows potential regarding the mitigation of neuropathologies, the main distribution of MSCs after their intravenous injection is mostly restricted to the lungs, indicating that the therapeutic effect of MSCs occurs mainly via a paracrine-mediated mechanism (Gnecchi et al., 2016; Sherman et al., 2019). Therefore, MSC-derived EVs can be an alternative method to execute the therapeutic potential of MSCs, as MSC-derived EVs share a comparable therapeutic component with the parental MSCs and can easily cross the blood brain barrier (Zagrean et al., 2018). Moreover, MSC-derived EVs, as a cell-free therapy, can overcome the limitations of MSC therapy, such as safety and tumor induction.

The therapeutic effects of MSC-derived EVs on many pathological processes have been demonstrated and are mediated by vesicular membrane proteins, cytosolic proteins, mRNAs, and miRNAs (Phinney and Pittenger, 2017; Yin et al., 2019). In particular, EV-associated proteins are critical in the mediation of the therapeutic potential of MSC-derived EVs. The anti-inflammatory component of MSC-derived EVs has been shown to promote brain repair in mice with ischemic stroke and other neurological diseases (Yang et al., 2017; Chen and Chopp, 2018; Hong et al., 2018; Mendt et al., 2019). Here, we found that MSC-derived EVs alleviated trained immunity and remitted the associated exacerbation of neuropathologies. In a model of focal ischemia, the proinflammatory cytokines that were released in the acute stage of stroke were upregulated by LPS training, and this effect was abolished by MSC-derived EVs. We also evaluated the therapeutic potential of MSC-derived EVs in a model of AD. Notably, LPS training significantly increased the plaque load of insoluble amyloid-β, whereas MSC-derived EVs significantly remitted this exacerbation.

In addition to the direct therapeutic effect of MSC-derived EVs, we investigated the plausible mediator of their effects. The production of the anti-inflammatory cytokine IL-10 is one of the most important mechanisms evolved by many immune cells to counteract the damage driven by excessive inflammation (Strle et al., 2001; Couper et al., 2008; Lobo-Silva et al., 2016). Binding of IL-10 to its receptor activates a series of signaling cascades that are mediated by the JAK and STAT pathway and regulate several steps of the immune response, such as decreasing the expression of genes encoding inflammatory cytokines and preventing apoptosis (Riley et al., 1999). IL-10 in MSC-derived EVs has been shown to polarize macrophages from the proinflammatory M1 to the anti-inflammatory M2 type and to attenuate kidney inflammation and bacteria-induced sepsis (Eirin et al., 2017). Here, we found that MSC-derived EVs expressed IL-10 at a level that was comparable to that of their parent MSCs, and that the administration of MSC-derived EVs also upregulated IL-10 in the infarct region and brain parenchyma in APP/PS1 mice. Upon knockdown of IL-10 in MSC-derived EVs, they failed to exert their protective effect of remitting trained immunity and mitigating the associated exacerbation of the neuropathology caused by trained immunity, thus underscoring the role of this anti-inflammatory cytokine in the mediation of the alleviation of trained immunity by EV administration.

Although we found that MSC-derived EVs mitigated trained immunity, further research is needed to clarify the molecular machinery underlying this phenomenon. Moreover, the current knowledge about trained immunity in the CNS focuses mainly on its mechanism and its relationship with brain diseases. There is an urgent need to find a proper strategy to detect this malfunction in the CNS. We believe that the development of such a detection method will allow MSC-derived EVs to rectify this abnormal activation of trained immunity in the CNS, thus promoting the development of an EV-based cell-free therapy.

MATERIALS AND METHODS

Animals

C57BL/6J male mice (3 months of age) were purchased from Charles River, and APPswe/PS1dE9 (APP/PS1) mice (3 months of age) were purchased from Guangdong Medical Experimental Animal Center. Animals were housed in the Experimental Animal Center of Fudan University in a temperature- and humidity-controlled specific-pathogen-free laboratory with a 12 h/12 h light/dark cycle. All procedures were performed in accordance with the Guide of the National Science Council of the People's Republic of China, and the study was approved by the Ethics Committee of Fudan University, Shanghai, China (IRB approval number 20190972A259). This manuscript was written in accordance with the Animal Research: Reporting of *In Vivo* Experiments (ARRIVE) guidelines.

Peripheral Immune Stimulation

Three-month-old mice were randomly assigned to treatment groups and were injected intraperitoneally (i.p.) with bacterial lipopolysaccharides (LPS from *Salmonella enterica* serotype typhimurium; Sigma) at a dose of 500 μg/kg of bodyweight or with vehicle (PBS). In the 2× LPS group, mice were re-stimulated with the same dose of LPS 1 month after the initial injection.

At the specified time points, animals were deeply anesthetized using sedaxylan and ketamine (64 and 472 mg/kg, respectively), blood was collected from the right ventricle of the heart, and animals were transcardially perfused with ice-cold PBS through the left ventricle. The brain was removed and sagitally separated into the two hemispheres, which were either fixed in 4% paraformaldehyde (PFA) or fresh frozen on dry ice. Fresh-frozen hemispheres were homogenized using a Cell Lysis Buffer (Invitrogen) containing phosphatase and protease inhibitors (Thermo Fisher Scientific). Fixed hemispheres were kept in 4% PFA for 24 h, dehydrated in 30% sucrose in PBS, frozen in 2-methylbutane, and coronally sectioned at 25 μm using a freezing-sliding microtome (Leica).

Isolation of MSCs and MSC-Derived EVs

Umbilical cords were sampled from healthy women who underwent delivery via cesarean section. Each donor had been confirmed not to have infectious diseases, pregnancy complications, HBV, HIV, or syphilis. Approval was granted by the donors, and all procedures were in accordance with the guideline of the Medical Ethics Committee of the Health Bureau.

The isolation of hUCMSCs was performed as described previously. Briefly, the umbilical cord was placed in ice-cold PBS, and the arteries and veins of the umbilical cord were separated and discarded. Umbilical cords were carefully minced into small fragments, and the pieces were digested at 37°C for 3 h with 10 ml of 0.62 Wünsch units/mL of collagenase I. The same volume of DMEM as that of the digested fluid was added to stop the digestion, and the digested fluid was passed through a 70 μm strainer and centrifuged to collect the cells. hUCMSCs were cultured in DMDM/F12 with 10% FBS and incubated at 37°C in a humidified atmosphere with 5% CO_2.

MSC-derived EVs were obtained from the supernatants of 10^7 MSCs. Briefly, the supernatants were centrifugated at 2000 × *g* for 10 min, to remove cell debris. Subsequently, the supernatants were ultracentrifuged at 10,000 × *g* for 30 min, to discard microparticles, and underwent a second ultracentrifugation at 100,000 × *g* for 70 min. The pellets were suspended and stored at − 80°C.

TEM

The morphology of isolated EVs was assessed by TEM. Briefly, EVs were blotted for 5 min onto glow-discharged 200-mesh formvar carbon-coated copper grids (Electron Microscopy Sciences, Hatfield, PA, United States). Subsequently, EVs were washed with water, followed by fixation with 2.5% glutaraldehyde in PBS. After further washing with water, the samples were stained using 2% uranyl acetate for 1 min. Negative-stained NVs were observed on an electron microscope (G2 spititi, FEI).

Nanoparticle Tracking Analysis

The concentration and size distribution of the isolated EVs were assessed by nanoparticle tracking analysis. Briefly, NVs (10 μg/mL by BCA) were dispersed in PBS, and the particle concentration of NVs was assessed using a ZetaView Particle Metrix instrument (ZetaView PMX 110, Particle Metrix GmbH, Meerbusch, Germany). The measurements were performed in triplicate, and each individual datum was acquired from two stationary layers with five measurements from each layer. The sensitivity of the camera was configured at 70 in all measurements.

EVs Labeling and Tissue Distribution

MSC-derived EVs were labeled with PKH26 according to the manufacturer's instructions (Sigma). Labeled EVs (10^7) were intravenously injected into mice. Mice were sacrificed 30 min after the injection. The distribution of EVs was evaluated in 5 μm brain sections by immunofluorescence staining with an anti-Iba1 antibody.

Knockdown of IL-10 in MSCs

A lentiviral vector containing the IL-10 shRNA and puromycin cloning were constructed by GeneChem. MSC medium containing 8 μg ml^{-1} polybrene and the virus at an MOI of 10 were added to the cells. Half of the medium was changed every 24 h. Infected MSCs were selected by continuous incubation in MSC medium containing 10 μg ml^{-1} puromycin (Sigma), starting 1 day after transduction.

Focal Brain Ischemia

The induction of focal cortical stroke was performed as described previously (Wendeln et al., 2018). Briefly, mice were anesthetized with 4% isoflurane in 30% O_2 and 70% N_2 and maintained on 2% isoflurane in 30% O_2 and 70% N_2 using a mask. Three-month-old mice were fixed in a stereotactic frame and a circular piece of skull was removed (5 mm in diameter, centered on Bregma). The dura mater was carefully removed with the help of a microhook (Fine Science Tools) and 5 μl of ET-1 (Bachem; 64 μM) in Hanks buffered salt solution (Invitrogen) or vehicle solution was topically applied to the cortex and incubated for 10 min. The craniotomy was then covered with a 5 mm glass coverslip, which was fixed in place with dental cement (Hybond). The skin was sutured and the mice received adrenergic receptor antagonists (flumazenil and atipamezole: 0.5 and 2.5 mg/kg of body weight, respectively) and their health was monitored. Control mice underwent the same surgical procedure with application of vehicle solution to the cortex.

Western Blot Analysis

Samples were lysed in RIPA buffer (50 mM Tris–HCl, pH 7.5, 150 mM NaCl, 1% Triton X-100, 0.1% SDS, 0.5% deoxycholate) with phosphatase and protease inhibitors (Thermo Fisher Scientific). EVs (25 μg) and whole-cell lysates (25 μg) were subjected to SDS—PAGE and transfected to a polyvinylidene difluoride membrane. The membrane was blocked with non-fat milk for 1 h and then incubated with primary antibodies overnight at 4°C. After washing with TBST, the membranes were incubated with the secondary antibodies for 1 h and then subjected to chemiluminescence analysis.

The following primary antibodies were used: rabbit anti-CD9 (1:1000; 13403, Cell Signaling Technology, United States), rabbit anti-CD29 (1:1000; 4706, Cell Signaling Technology, United States), rabbit anti-CD63 (1:1000; 55051, Cell Signaling Technology, United States), mouse anti-CD105 (1:1000; 14606, Cell Signaling Technology, United States), rabbit anti-CD73 (1:1000; 13160, Cell Signaling Technology, United States), rabbit anti-GAPDH (1:1000; 5174, Cell Signaling Technology, United States).

The following secondary antibodies were used: goat-anti-rabbit HRP-conjugated antibody (1:1000; Cell Signaling Technology, United States) and goat-anti-mouse HRP-conjugated antibody (1:1000; Cell Signaling Technology, United States).

Immunostaining

Immunohistochemical staining was performed on free-floating sections using either the Mouse or Rabbit Specific HRP/DAB IHC Detection Kit (ab236466, Abcam, United States) or fluorescent secondary antibodies (Abcam, United States). Unless otherwise noted, brain sections were blocked for 1 h with 5% normal serum of the species in which the secondary antibody was developed, followed by incubation with the primary antibody overnight at 4°C. Sections were then washed and incubated with secondary antibodies. Cresyl violet staining was performed according to the manufacturer's instructions.

The following primary antibodies were used: rabbit anti-Iba1 (1:500; ab5076, Abcam, United States) and mouse anti-Aβ (1:1,000; SIG-39320, BioLegend, United States).

Stereological Quantification

Stereological quantification of neuronal damage and microglia was performed by a blinded observer on random sets of every 200 μm systematically sections throughout the neocortex. Analysis was conducted using the Image J (NIH, United States).

ELISA

The quantification of Aβ by ELISA (Meso Scale Discovery) in brain homogenates was performed according to the manufacturer's instructions. Briefly, samples were pre-treated with 70% of formic acid (Sigma-Aldrich), sonicated for 35 s on ice, and centrifuged at 25,000 × *g* for 1 h at 4°C. Neutralization buffer [1 M Tris base, 0.5 M Na_2HPO_4, and 0.05% NaN_3 (wt/vol)] was then added at a 1:20 ratio. Aβ was measured by an observer blinded to the treatment groups using the human (6E10) Aβ triplex assay (Meso Scale Discovery, MSD).

For cytokine measurements, brain homogenates were centrifuged at 12,000 × *g* for 15 min at 4°C. The supernatants were analyzed according to the manufacturer's instructions. To determine blood cytokine levels, the serum was obtained by coagulation of whole blood in Vacuettes (363080, BD, United States) for 10 min at room temperature and centrifugation for 10 min at 2,000 × *g*. Serum samples were diluted 1:2 before measurements. The investigator was blinded to the treatment groups.

Statistical Analysis

Data were analyzed using SPSS Statistics 22 and GraphPad Prism 8.0 and are presented as the mean ± standard deviation. The number of experiments performed with independent mice (n) is indicated in the figure legends. Different treatment groups were evaluated using one-way analysis of variance with Tukey's test for multiple comparisons among individual groups. A probability of $P < 0.05$ was considered indicative of a significant difference between groups. Regardless of the method used, the results are equivalent in magnitude and statistically significant. Sample size was calculated based on a power value of 0.95 and an α value of 0.05.

DATA AVAILABILITY STATEMENT

The raw data supporting the conclusions of this article will be made available by the authors, without undue reservation.

ETHICS STATEMENT

The animal study was reviewed and approved by Ethics Committee of Fudan University, Shanghai, China.

AUTHOR CONTRIBUTIONS

YF and MG drafted the manuscript. YF, SH and HZ accomplished the experiment. QD and MC designed the experiment and provided financial support. All authors contributed to the article and approved the submitted version.

FUNDING

This study was supported by the National Natural Science Foundation of China (81971013 to MC, 81870915 and 81571109 to QD). Grant from the Science and Technology Commission of Shanghai Municipality (16411970200).

REFERENCES

Biswas, S. K., and Lopez-Collazo, E. (2009). Endotoxin tolerance: new mechanisms, molecules and clinical significance. *Trends Immunol.* 30, 475–487. doi: 10.1016/j.it.2009.07.009

Chen, J., and Chopp, M. (2018). Exosome therapy for stroke. *Stroke* 49, 1083–1090. doi: 10.1161/strokeaha.117.018292

Christ, A., Günther, P., Lauterbach, M. A. R., Duewell, P., Biswas, D., Pelka, K., et al. (2018). Western diet triggers NLRP3-dependent innate immune reprogramming. *Cell* 172, 162.e14–175.e14.

Couper, K. N., Blount, D. G., and Riley, E. M. (2008). IL-10: the master regulator of immunity to infection. *J. Immunol.* 180:5771. doi: 10.4049/jimmunol.180.9.5771

Crişan, T. O., Netea, M. G., and Joosten, L. A. B. (2016). Innate immune memory: implications for host responses to damage-associated molecular patterns. *Eur. J. Immunol.* 46, 817–828. doi: 10.1002/eji.201545497

Eirin, A., Zhu, X.-Y., Puranik, A. S., Tang, H., McGurren, K. A., Wijnen, A. J. V., et al. (2017). Mesenchymal stem cell–derived extracellular vesicles attenuate kidney inflammation. *Kidney Int.* 92, 114–124. doi: 10.1016/j.kint.2016.12.023

El Andaloussi, S., Lakhal, S., Mäger, I., and Wood, M. J. A. (2013). Exosomes for targeted siRNA delivery across biological barriers. *Adv. Drug Deliv. Rev.* 65, 391–397. doi: 10.1016/j.addr.2012.08.008

Feng, Y. W., Wu, C., Liang, F. Y., Lin, T., Li, W. Q., Jing, Y. H., et al. (2020). hUCMSCs Mitigate LPS-induced trained immunity in ischemic stroke. *Front. Immunol.* 11:1746. doi: 10.3389/fimmu.2020.01746

Galindo, L. T., Filippo, T. R. M., Semedo, P., Ariza, C. B., Moreira, C. M., Camara, N. O. S., et al. (2011). Mesenchymal stem cell therapy modulates the inflammatory response in experimental traumatic brain injury. *Neurol. Res. Int.* 2011:564089.

Gnecchi, M., Danieli, P., Malpasso, G., and Ciuffreda, M. C. (2016). Paracrine mechanisms of mesenchymal stem cells in tissue repair. *Methods Mol. Biol.* 1416, 123–146. doi: 10.1007/978-1-4939-3584-0_7

Ha, D., Yang, N., and Nadithe, V. (2016). Exosomes as therapeutic drug carriers and delivery vehicles across biological membranes: current perspectives and future challenges. *Acta Pharm. Sin. B* 6, 287–296. doi: 10.1016/j.apsb.2016.02.001

Hong, S.-B., Yang, H., Manaenko, A., Lu, J., Mei, Q., and Hu, Q. (2018). Potential of exosomes for the treatment of stroke. *Cell Transplant.* 28, 662–670. doi: 10.1177/0963689718816990

Kunter, U., Rong, S., Boor, P., Eitner, F., Müller-Newen, G., Djuric, Z., et al. (2007). Mesenchymal stem cells prevent progressive experimental renal failure but maldifferentiate into glomerular adipocytes. *J. Am. Soc. Nephrol.* 18, 1754–1764. doi: 10.1681/asn.2007010044

Lobo-Silva, D., Carriche, G. M., Castro, A. G., Roque, S., and Saraiva, M. (2016). Balancing the immune response in the brain: IL-10 and its regulation. *J. Neuroinflammation* 13:297.

Mendt, M., Rezvani, K., and Shpall, E. (2019). Mesenchymal stem cell-derived exosomes for clinical use. *Bone Marrow Transplant.* 54, 789–792.

Netea, M. G., Joosten, L. A. B., Latz, E., Mills, K. H. G., Natoli, G., Stunnenberg, H. G., et al. (2016). Trained immunity: a program of innate immune memory in health and disease. *Science* 352:aaf1098. doi: 10.1126/science.aaf1098

Netea, M. G., Latz, E., Mills, K. H. G., and O'Neill, L. A. J. (2015). Innate immune memory: a paradigm shift in understanding host defense. *Nat. Immunol.* 16, 675–679. doi: 10.1038/ni.3178

Park, K.-S., Svennerholm, K., Shelke, G. V., Bandeira, E., Lässer, C., Jang, S. C., et al. (2019). Mesenchymal stromal cell-derived nanovesicles ameliorate bacterial outer membrane vesicle-induced sepsis via IL-10. *Stem Cell Res. Ther.* 10;231.

Perry, V. H., and Holmes, C. (2014). Microglial priming in neurodegenerative disease. *Nat. Rev. Neurol.* 10, 217–224. doi: 10.1038/nrneurol.2014.38

Phinney, D. G., and Pittenger, M. F. (2017). Concise review: MSC-derived exosomes for cell-free therapy. *Stem Cells* 35, 851–858. doi: 10.1002/stem.2575

Qin, L., Wu, X., Block, M. L., Liu, Y., Breese, G. R., Hong, J.-S., et al. (2007). Systemic LPS causes chronic neuroinflammation and progressive neurodegeneration. *Glia* 55, 453–462. doi: 10.1002/glia.20467

Riley, J. K., Takeda, K., Akira, S., and Schreiber, R. D. (1999). Interleukin-10 receptor signaling through the JAK-STAT pathway. Requirement for two distinct receptor-derived signals for anti-inflammatory action. *J. Biol. Chem.* 274, 16513–16521. doi: 10.1074/jbc.274.23.16513

Rutherford, N. J., Sacino, A. N., Brooks, M., Ceballos-Diaz, C., Ladd, T. B., Howard, J. K., et al. (2015). Studies of lipopolysaccharide effects on the induction of α-synuclein pathology by exogenous fibrils in transgenic mice. *Mol. Neurodegen.* 10:32.

Sacino, A. N., Brooks, M., McGarvey, N. H., McKinney, A. B., Thomas, M. A., Levites, Y., et al. (2013). Induction of CNS α-synuclein pathology by fibrillar and non-amyloidogenic recombinant α-synuclein. *Acta Neuropathol. Commun.* 1:38. doi: 10.1186/2051-5960-1-38

Saeed, S., Quintin, J., Kerstens, H. H. D., Rao, N. A., Aghajanirefah, A., Matarese, F., et al. (2014). Epigenetic programming of monocyte-to-macrophage differentiation and trained innate immunity. *Science* 345;1251086. doi: 10.1126/science.1251086

Shen, X. Z., Li, Y., Li, L., Shah, K. H., Bernstein, K. E., Lyden, P., et al. (2015). Microglia participate in neurogenic regulation of hypertension. *Hypertension* 66, 309–316. doi: 10.1161/hypertensionaha.115.05333

Sherman, L. S., Romagano, M. P., Williams, S. F., and Rameshwar, P. (2019). Mesenchymal stem cell therapies in brain disease. *Semin. Cell Dev. Biol.* 95, 111–119. doi: 10.1016/j.semcdb.2019.03.003

Strle, K., Zhou, J. H., Shen, W. H., Broussard, S. R., Johnson, R. W., Freund, G. G., et al. (2001). Interleukin-10 in the brain. *Crit. Rev. Immunol.* 21, 427–449.

Wang, X., Chen, H., Zeng, X., Guo, W., Jin, Y., Wang, S., et al. (2019). Efficient lung cancer-targeted drug delivery via a nanoparticle/MSC system. *Acta Pharm. Sin. B* 9, 167–176. doi: 10.1016/j.apsb.2018.08.006

Wendeln, A.-C., Degenhardt, K., Kaurani, L., Gertig, M., Ulas, T., Jain, G., et al. (2018). Innate immune memory in the brain shapes neurological disease hallmarks. *Nature* 556, 332–338. doi: 10.1038/s41586-018-0023-4

Wood, M. J. A., O'Loughlin, A. J., and Lakhal, S. (2011). Exosomes and the blood–brain barrier: implications for neurological diseases. *Ther. Deliv.* 2, 1095–1099. doi: 10.4155/tde.11.83

Yang, Y., Ye, Y., Su, X., He, J., Bai, W., and He, X. (2017). MSCs-derived exosomes and neuroinflammation, neurogenesis and therapy of traumatic brain injury. *Front. Cell Neurosci.* 11:55. doi: 10.3389/fncel.2017.00055

Yin, K., Wang, S., and Zhao, R. C. (2019). Exosomes from mesenchymal stem/stromal cells: a new therapeutic paradigm. *Biomarker Res.* 7:8.

Zagrean, A.-M., Hermann, D. M., Opris, I., Zagrean, L., and Popa-Wagner, A. (2018). Multicellular crosstalk between exosomes and the neurovascular unit after cerebral ischemia. therapeutic implications. *Front. Neurosci.* 12:811. doi: 10.3389/fnins.2018.00811

Conflict of Interest: The authors declare that the research was conducted in the absence of any commercial or financial relationships that could be construed as a potential conflict of interest.

frontiers
in Bioengineering and Biotechnology

ORIGINAL RESEARCH
published: 25 November 2020
doi: 10.3389/fbioe.2020.598977

Rutin-Loaded Silver Nanoparticles With Antithrombotic Function

Haitao Wu, Manlin Su, Hui Jin, Xinyu Li, Puyu Wang, Jingxiao Chen* and Jinghua Chen*

Key Laboratory of Carbohydrate Chemistry and Biotechnology, Ministry of Education, School of Pharmaceutical Sciences, Jiangnan University, Wuxi, China

Edited by:
Wei Tao,
Harvard Medical School,
United States

Reviewed by:
Abbas Amini,
Australian College of Kuwait, Kuwait
Junqing Wang,
Sun Yat-sen University, China

***Correspondence:**
Jingxiao Chen
tomchenjx@jiangnan.edu.cn
Jinghua Chen
chenjinghua@jiangnan.edu.cn

Specialty section:
This article was submitted to Nanobiotechnology, a section of the journal Frontiers in Bioengineering and Biotechnology

Received: *26 August 2020*
Accepted: *04 November 2020*
Published: *25 November 2020*

Citation:
Wu H, Su M, Jin H, Li X, Wang P, Chen J and Chen J (2020) Rutin-Loaded Silver Nanoparticles With Antithrombotic Function. Front. Bioeng. Biotechnol. 8:598977. doi: 10.3389/fbioe.2020.598977

In this paper, we fabricated rutin-loaded silver nanoparticles (Rutin@AgNPs) as the nano-anticoagulant with antithrombotic function. The serum stability, anticoagulation activity, and bleeding risk of Rutin@AgNPs were evaluated. The results showed Rutin@AgNPs had good serum stability, hemocompatibility, and cytocompatibility. The anticoagulation activity of rutin was maintained, and its stability and aqueous solubility were improved. The Rutin@AgNPs could provide a sustained release to prolong the half-life of rutin. The results of the coagulation parameter assay and thrombus formation test in mice model showed that the activated partial thromboplastin time and prothrombin time were prolonged, and Rutin@AgNPs inhibited the thrombosis in the 48 h period. Moreover, the limited bleeding time indicated that the Rutin@AgNPs significantly minimized the hemorrhage risk of rutin. This Rutin@AgNPs is a potential anticoagulant for antithrombotic therapy.

Keywords: rutin, silver nanoparticles, antithrombosis, anticoagulant, sustained release

INTRODUCTION

Thromboembolism is one of the leading causes of cardiovascular diseases (Lippi et al., 2011; Gorog et al., 2017; Dakin, 2019). It leads to circulatory disorders, such as ischemic stroke, myocardial infarction, and pulmonary embolism, which are the major cause of morbidity and mortality (Kyrle et al., 2004). Previous researchers have found irregular coagulation and thrombus formation are the leading causes of thromboembolism (Mackman, 2008). To inhibit abnormal coagulation and thrombus formation, many researchers devote to anticoagulants development which can target blood clots related coagulation factors. Heparin and warfarin (vitamin K antagonist) are two mainstream anticoagulants that are used clinically. Heparin can activate antithrombin III and inhibit factor Xa. However, its half-life is short, and cannot be administered orally (Hirsh et al., 2001a). Moreover, this anticoagulant has a high risk of massive hemorrhage complications (Chen C. et al., 2016). To optimize the safety of heparin treatment, low molecular weight heparin (LMWH), which has a similar mechanism of action, has been developed. LMWH shows a better benefit-to-risk ratio but still cannot make up the complications (such as frequent thrombocytopenia and osteoporosis events) of heparin (Hirsh et al., 2001a,b). Warfarin is an anticoagulant that works on factors II, VII, IX, and X. It can effectively reduce the amount of prothrombin. However, apart from the hemorrhage complications, warfarin can cause a hypercoagulable state which results in thrombosis of the venules and capillaries, and leads to skin necrosis in the further stage (Ansell et al., 2008). The causes of these complications are anticoagulants over inhibit the coagulation. Therefore, researchers keenly aware an effective and safe antithrombotic target is needed. Recent studies have found the protein disulfide isomerase (PDI), which is expressed on the surface of platelets and endothelial cells, plays a critical role in thrombus formation (Jasuja et al., 2011, 2012; Furie and Flaumenhaft, 2014). Inhibition of PDI can affect both platelet aggregation and fibrin generation. Moreover, it is a safe target for the inhibition of thrombus formation (Flaumenhaft, 2013; Kennedy et al., 2013). Quercetin-3-rutinoside (rutin) is a kind of flavonoid glycoside, which is abundant in buckwheat, tea, fruits, and berries (Gullon et al., 2017). Studies have found that rutin is a potential thromboprophylaxis agent, and can be used as an effective inhibitor of PDI both *in vitro* and *in vivo* (Jasuja et al., 2012; Flaumenhaft, 2013; Choi et al., 2015; Lin et al., 2015). As a prescribed traditional medicine and an antioxidant, rutin has been proved to be toxicologically safe and well-tolerated (Sharma et al., 2013). However, the poor bioavailability of rutin, which associates with stability and aqueous solubility, limited its clinical applications (Gullon et al., 2017). Thence, the key, which to develop rutin as an effective anticoagulant, is to improve the bioavailability of the rutin in blood.

Nanomedicine is a popular research topic recently. Engineering nanoparticles (NPs) have been used as nanocarriers to load and to deliver anticoagulant toward the target directly (Tian et al., 2014; Su et al., 2020). They reduce the dose of the anticoagulant while improving the antithrombotic efficacy, and can decrease the hemorrhage complications (Ilinskaya and Dobrovolskaia, 2013a,b). The nanocarrier also can be used to improve the stability and aqueous solubility of the therapeutic agents (Kargl and Kleinschek, 2020). Silver nanoparticles (AgNPs) is widely used as potent antibacterial agents, as it has good biocompatibility. The size, shape, and architecture of AgNPs can be regulated, and surface modification of AgNPs can be used for drug loading in simple and convenient methods. Therefore, this study combined AgNPs and rutin to improve the stability and aqueous solubility of rutin. Here, the phenylboronic acid (PBA) group was chemically introduced onto the surface of AgNPs at first. Then, rutin was loaded on AgNPs to form the Rutin@AgNPs through a dynamic boronate ester bond (Chen J.X. et al., 2016), as shown in **Figure 1**. We expected the Rutin@AgNPs could increase the solubility and stability of rutin, and prolong the half-life of rutin through a sustained release strategy.

MATERIALS AND METHODS

Materials

Rutin and 4-mercaptophenylboronic acid (MPBA) were obtained from Aladdin Reagent Co. (China). Silver nitrate, sodium borohydride ($NaBH_4$), NH_4HCO_3, and dimethyl sulfoxide (DMSO) were purchased from Sinopharm Chemical Reagent Co., Ltd. (China). Heparin sodium was provided by Sangon Biotech (Shanghai) Co., Ltd. Polyvinylpyrrolidone (PVP, Mw: 10 kDa), carrageenan, and urethane were obtained from Sigma-Aldrich Co. (United States). Endothelial cell basal medium (ECM), fetal bovine serum (FBS), and 3-(4,5-Dimethylthiazol-2-yl)-2,5-diphenyltetrazoliumbromide (MTT) were purchased from Thermo Fisher Scientific Co. (United States).

Preparation of Rutin@AgNPs

AgNPs were prepared through a reduction method under the stabilization of PVP (Tejamaya et al., 2012). Briefly, 10 mL of $AgNO_3$ solution (1.02 mg/mL) was added into 60 mL of PVP solution (1.5 mg/mL) under stirring. Then, 10 mL of $NaBH_4$ solution (0.6 mg/mL) was added dropwise into the solution. A light-brown AgNPs solution was obtained after vigorous stirring for 15 min. After that, 0.4 mL of MPBA (2 mg/mL) in DMSO was added into the AgNPs solution. The solution turned brown, and PBA modified AgNPs (PBA@AgNPs) was obtained after stirring for 2 h. Subsequently, the pH of the solution was adjusted to about 8. Then, 2 mL of rutin (10 mg/mL) in DMSO was added to this solution. After stirring for 4 h, the solution was put into a dialysis tube (molecular weight cut-off, MWCO: 14 kDa) and subjected to dialysis against NH_4HCO_3 solution (pH 8.0) for 2 days to remove the organic solvent and other impurities, followed by lyophilization to collect Rutin@AgNPs.

Characterizations of Rutin@AgNPs

The composition of Rutin@AgNPs was identified by the Fourier transform infrared spectroscopy (FTIR) via a TENSOR II spectrometer (Bruker, Germany). The loading amount of rutin on AgNPs was measured by using thermogravimetric analysis (TGA) on a TGA/1100SF instrument (Mettler-Toledo, Switzerland). The flow rate of N_2 was 50 mL/min, the heating rate was 10^oC/min. The freeze-dried AgNPs, PBA@AgNPs, and Rutin@AgNPs were resolved in phosphate buffer saline (PBS, pH 7.4) at the concentration of 1 mg/mL. The ultraviolet-visible light (UV-vis) absorption of rutin and these NPs was measured on a UV 2550 UV-vis spectrophotometer (Shimadzu, Japan) at the wavelength ranges from 200 to 700 nm.

The size distributions of three types of NPs were measured by using a dynamic light scattering technique on a Zetasizer Nano ZS apparatus (Malvern, United Kingdom). The morphology of three types of NPs was observed by using transmission electron microscopy (TEM) on a JEM-2100 instrument (JEOL, Japan) with an accelerating voltage of 80 kV. The particle size in the TEM images was gained by using Image J software.

In vitro Drug Release Assay

Briefly, 10 mL Rutin@AgNPs solution (1 mg/mL) was put into different dialysis tubes (MWCO: 3,500 Da). Next, the dialysis tubes were immersed into 20 mL of PBS (pH 7.4), which excluded/included glucose (5.5 mmol/L, 20 mmol/L). Then, the dialysis tubes were placed in the 37°C shaking bath to allow the release of rutin. At the assigned time interval, the samples were withdrawn, and the PBS was refreshed. The amount of released rutin in the medium was determined by UV-vis spectrophotometer at 262 nm. The cumulative release ratio of rutin was calculated according to the equation below. Three independent trials were carried out, and their average results were used.

$$Cumulative\ release\ (\%) = \frac{20}{2.83} \times \sum_{i=1}^{n} C_i \times 100\%$$

where C_i represents the rutin concentration of sample i, n is the total number of samples.

Stability and Hemolysis Test

The serum stability of the Rutin@AgNPs was determined through the UV-vis spectrum and particle size distribution, where the Rutin@AgNPs solutions contain 10% FBS (v/v) were placed in the dark environment for 3 days before the test.

The hemocompatibility of the Rutin@AgNPs was evaluated through the hemolytic rate. The fresh blood sample (10 mL) was placed in K_2-EDTA-coated Vacutainer tubes firstly. Next, the red blood cells (RBCs) were gained through centrifugation (2,500 × g for 10 min) and washed with PBS (pH 7.4) three times. Then, the RBCs were suspended into 7×10^9 cells/mL with PBS and were distributed into six sample groups (2 mL each). Four groups of the samples were added Rutin@AgNPs in different concentrations (10, 50, 100, and 1,000 mg/L). The PBS and the PBS containing 20% Triton X-100 were added into the negative control group and positive control group, respectively. All the sample groups were incubated in a water bath (37^{o}C) on a shaker for 1 h. After centrifugation (2,500 × g for 10 min), the supernatant's UV-vis absorption of the test sample group (A), the negative control group (A_0), and the positive control group (A_{100}) were measured at 545 nm. These three measurement results were used to calculate the hemolytic rate, as shown in the equation below. Note here, three independent trials were carried out, and their average results were used.

$$\text{Hemolytic rate (\%)} = \frac{A - A_0}{A_{100} - A_0} \times 100\%$$

In vitro Cytotoxicity Assay

The human umbilical vein endothelial cells (HUVECs) were cultured in ECM (containing 10% FBS) at 37^{o}C in a humidified condition containing 5% CO_2. The cytotoxicity of rutin, AgNPs, and Rutin@AgNPs were tested by MTT assay using HUVECs as the model cell. Briefly, the HUVECs were seeded on a 96 well-plate (5,000 cell/well) and cultured overnight. Then, rutin solution with different concentrations (1.25, 6.25, 12.5, 25, 75, and 125 mg/L, containing 5% DMSO), AgNPs and Rutin@AgNPs (10, 50, 100, 200, 600, and 1,000 mg/L) were added, respectively. After 48 h, the cultural mediums were replaced by 100 μL MTT solution (0.5 mg/mL), and add in 100 μL DMSO after another 4 h. The optical density (OD) at 570 nm was measured by using a Multiskan MK3 microplate reader (Thermo Fisher Scientific United States). The cell viability rate was calculated by using the

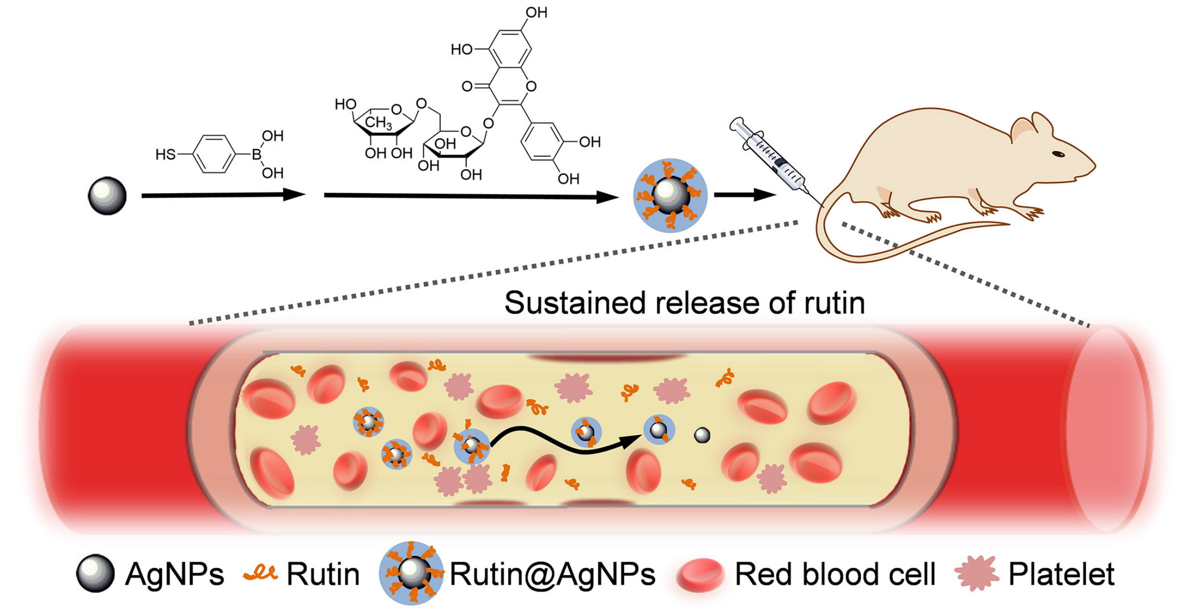

FIGURE 1 | Construction of Rutin@AgNPs for long-term rutin release and antithrombotic therapy.

equation below. The data was obtained from the average value of three independent trials.

$$\text{Cell viability (\%)} = \left(\frac{OD_{sample}}{OD_{control}} \times 100\%\right)$$

where the OD_{sample} is the OD value of the presence of samples, the $OD_{control}$ is the OD value of control well with absence samples.

Animals

ICR mice (5-weeks old, 28–32 g) were obtained from SLAC Laboratory Animal Co., Ltd., Shanghai, China). All animal care and experiments were conducted following the guidelines of the Institutional Animal Care and Use Committee of Jiangnan University.

In vivo Coagulation Parameter Assay

Briefly, 36 ICR mice were randomly divided into six groups (*n* = 6). Group 1–6 were intravenously injected through mice tail with saline (control group), AgNPs (600 µg/kg), Rutin@AgNPs (300 µg/kg), Rutin@AgNPs (600 µg/kg), rutin (200 µg/kg), and heparin (500 µg/kg), respectively. Administration for 1 h, the blood was drawn from the mice and added a 3.8% citrate solution (1:9 citrate/blood, v/v) to avoid coagulation. Finally, the activated partial thromboplastin time (aPTT) and prothrombin time (PT) were measured by a coagulometer (Sysmex CA-8,000, Japan) (Tian et al., 2014).

Carrageenan-Induced Tail Thrombosis Assay

Thirty mice were randomly divided into five groups (*n* = 6). Group 1–5 were intravenously injected through mice tail with saline, AgNPs (600 µg/kg), Rutin@AgNPs (600 µg/kg), rutin (200 µg/kg), and heparin (500 µg/kg), respectively. After 1 h of the intravenous administration, 1% carrageenan (50 mg/kg) was intraperitoneally injected into mice to induce the tail thrombosis model (Hagimori et al., 2009). The length of the tail thrombus was measured twice, after 24 and after 48 h.

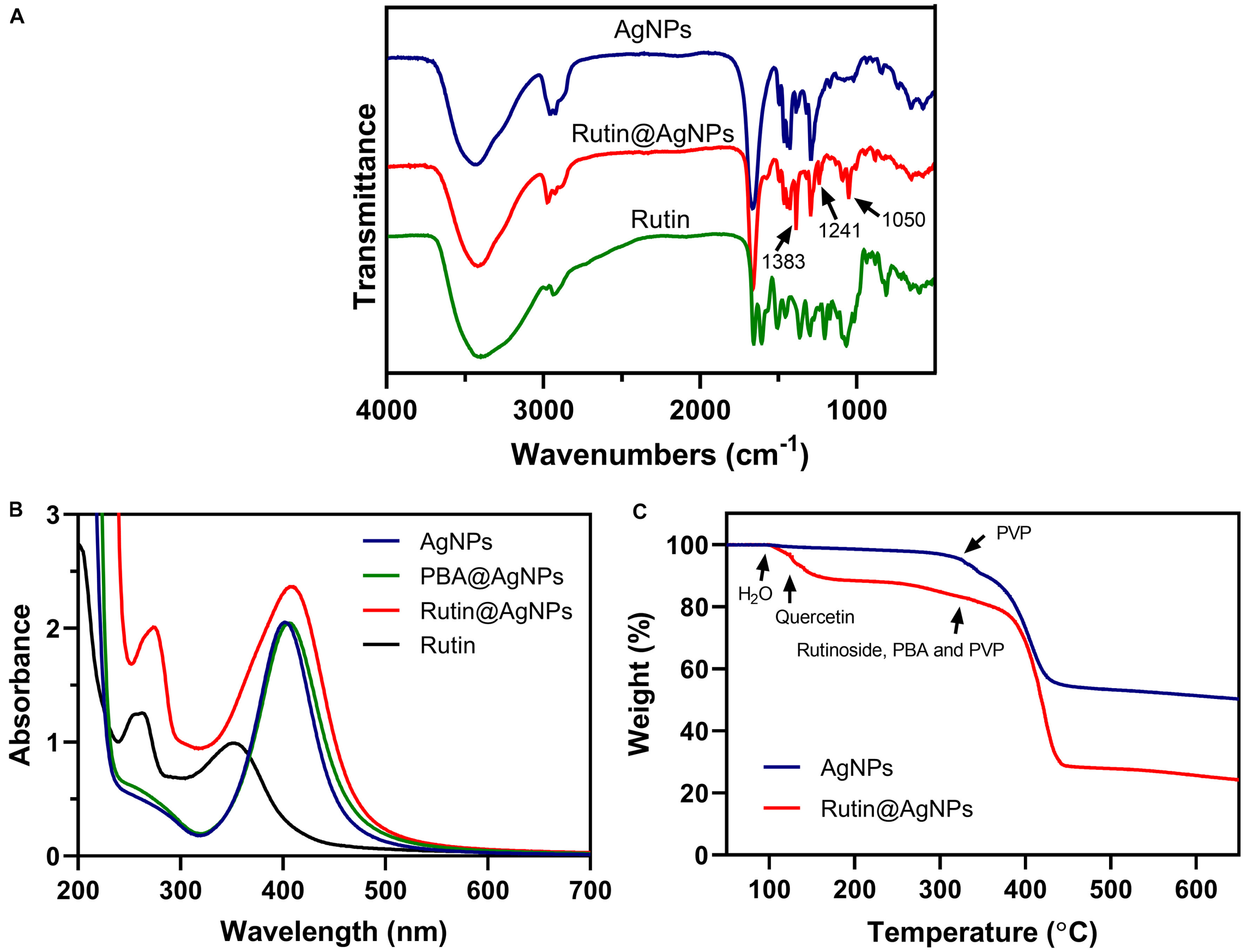

FIGURE 2 | (A) FTIR spectra of AgNPs, Rutin@AgNPs, and rutin; **(B)** UV-vis spectra of AgNPs, PBA@AgNPs, Rutin@AgNPs, and rutin; **(C)** TGA curves of AgNPs and Rutin@AgNPs.

Mouse Tail Bleeding Test

The mouse tail bleeding test was used to evaluate the thrombus formation (Dejana et al., 1982). Thirty mice were randomly divided into 5 groups ($n = 6$). Group 1 was set as a control group, which was injected with saline. Groups 2, 3, 4, and 5 were intravenously injected through mice tail with AgNPs (600 μg/kg), Rutin@AgNPs (600 μg/kg), rutin (200 μg/kg), and heparin (500 μg/kg), respectively. After administration for 1 h, urethane (20%, w/v, 0.1 mL/10 g) was intraperitoneally injected into each mouse for anesthesia. The mouse tail was cut 1 cm from the rare, then we started the timing. The bleed out blood was removed every 20 s until coagulation. The timing stopped and recorded it as the bleeding time.

Statistical Analysis

All data were presented with mean ± SD. One-way ANOVA *post hoc* tests were performed by using SPSS 23.0 software, and the significance level was set at 0.05. One (*) and two (**) represent $p < 0.05$ and $p < 0.01$, respectively.

RESULTS AND DISCUSSION

Composition of Rutin@AgNPs

Chemical modification is an important strategy to functionalize NPs. It varies the composition and physicochemical properties of NPs and enriches their applications. Due to the poor thermostability of the rutin, we tried to find a gentle manner to load rutin on the AgNPs. We noticed that rutin is composed of quercetin (including catechol structure) and glycoside, which possess 1,2-diol functional group. This inspired us to choose boronate ester (a dynamic covalent bond) to load rutin on the AgNPs. Boronate ester bond can form between phenylboronic acid and 1,2-diol in a weak alkaline environment (pH 8.0)

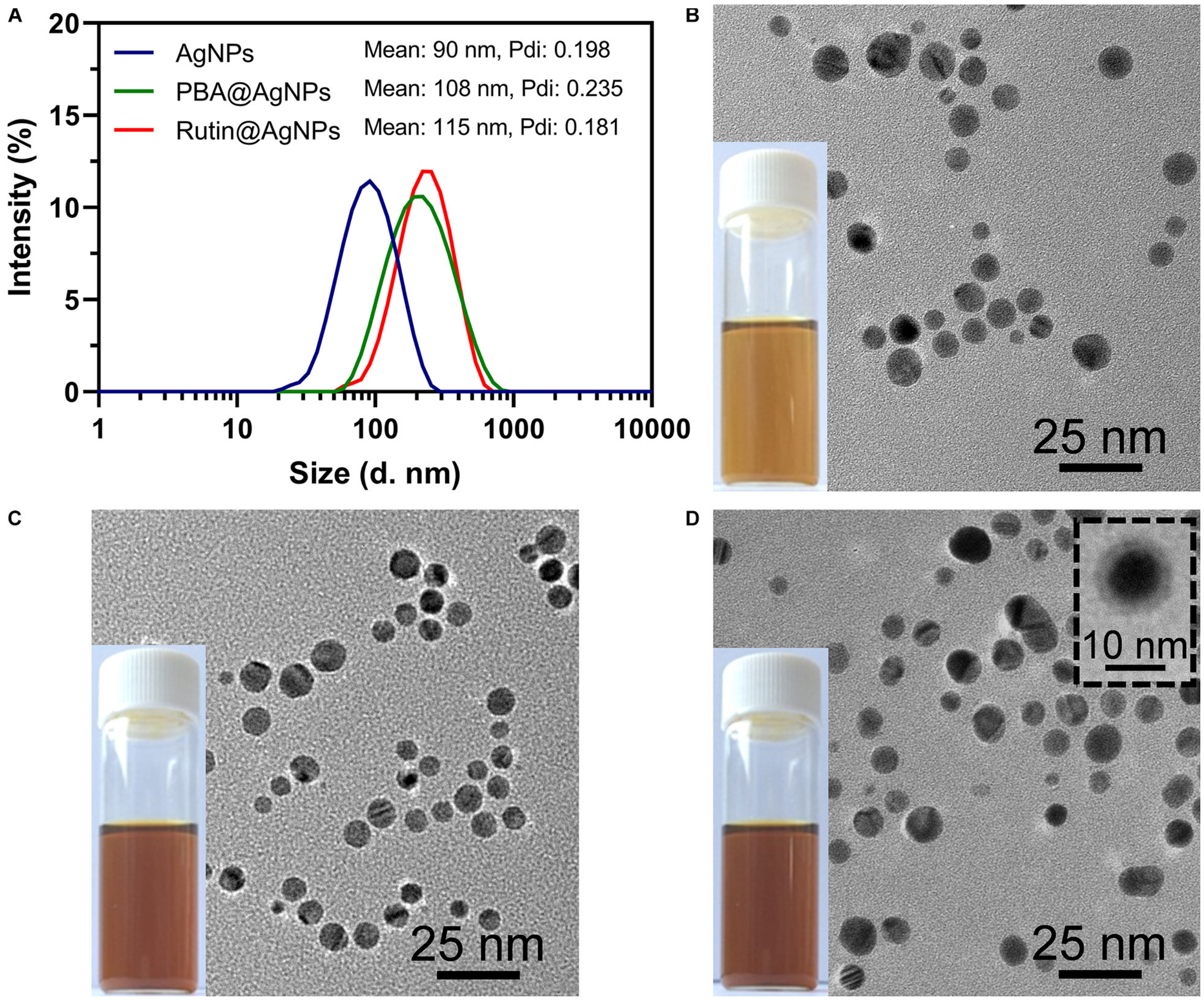

FIGURE 3 | (A) Size distributions of three types of NPs; TEM images and photographs of **(B)** AgNPs, **(C)** PBA@AgNPs, and **(D)** Rutin@AgNPs. The insert image showed Rutin@AgNPs were negatively stained with phosphotungstic acid.

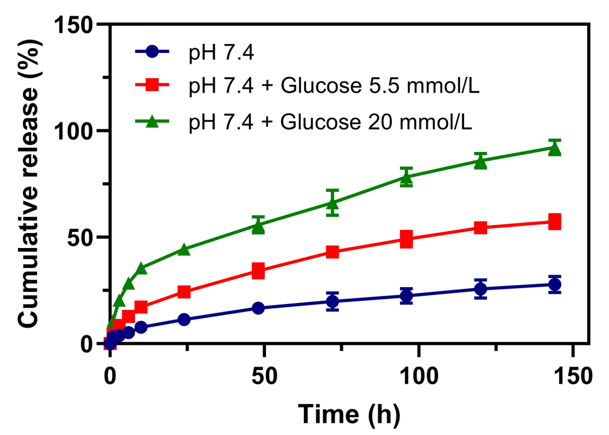

FIGURE 4 | Rutin release profiles of Rutin@AgNPs in PBS (pH 7.4) excluded or included glucose (5.5 and 20 mmol/L).

at room temperature (25^{o}C). Since the thermal decomposition temperature of rutin is higher than 70^{o}C (Chaaban et al., 2017), this reaction is gentle and straightforward for rutin loading. The composition of Rutin@AgNPs was first confirmed by FTIR and UV-vis spectra. As shown in **Figure 2A**, the peaks appeared at 3,400, 2,935, and 1,650 cm^{-1} in the FTIR spectrum of rutin belonged to $-$OH, CH$_2$, and C = O stretching vibrations, respectively. These peaks also appeared in the FTIR spectrum of AgNPs, but they belonged to the PVP that coated on the outer layer of AgNPs (Zhang et al., 2011). The characteristic peak at 1,450 cm^{-1} exhibited in spectra of both AgNPs and Rutin@AgNPs belonged to the C-N stretching vibration of PVP, indicated that the PVP was also coating on the outer surface of Rutin@AgNPs. For the FTIR spectra of Rutin@AgNPs and Rutin, the peaks appeared at 1,383 and 1,050 cm^{-1} belonged to the C-OH stretching vibrations of quercetin structure and glycoside structure, respectively (Zahoor et al., 2018). This result not only suggested rutin was successfully loaded on the AgNPs, but showed the rutin structure remained complete as well. What's more, a newly generated peak at 1,241 cm^{-1} only appeared in the FTIR spectrum of Rutin@AgNPs. This peak was ascribed to the C-O stretching vibration and served as a solid proof of the boronate ester formation between PBA and catechol in rutin (Thompson et al., 2017). As shown in **Figure 2B**, the maximum absorption of rutin in the UV-vis spectrum was at 262 nm. Comparing with the spectra of three NPs, this absorption appeared in the spectrum of Rutin@AgNPs and red-shifted to 273 nm. This was due to the loaded rutin gather on the surface of the AgNPs that would be influenced by the plasmonic resonance of AgNPs. These results also proved that rutin was loaded successfully.

The rutin loading amount was evaluated through the percentage of weight loss, as shown in **Figure 2C**. Comparing the thermal decomposition process of the AgNPs and Rutin@AgNPs, the Rutin@AgNPs showed a stepwise thermal decomposition, but AgNPs only contained one stage. In the AgNPs curve, the stage began at about 320^{o}C was attributed to the thermal decomposition of coated PVP. In the Rutin@AgNPs curve, the decomposition stages belonged to water, quercetin, and rutinoside of the rutin, the PBA, and the PVP (da Costa et al., 2002; Wang et al., 2015). The first stage appeared at 100–123^{o}C belonged to the absorbed water (about 3.4% in weight). The second stage exhibited at 123–320^{o}C ascribed to the decomposition of quercetin (about 13.2% in weight). The stage that appeared beyond 320^{o}C belonged to the decomposition of rutinoside, the PBA, and the PVP. As the weight loss of rutinoside was mixed with that of the PBA and the PVP, the loading amount of the rutin was determined through the weight loss of quercetin only. Therefore, the loading amount of rutin on Rutin@AgNPs was calculated as 28.3%, by analyzing the quercetin content in rutin through the molecular weight.

Morphology of Rutin@AgNPs

The morphology of Rutin@AgNPs was investigated by using DLS and TEM (**Figure 3**). The size distributions and the average hydrodynamic diameters of AgNPs, PBA@AgNPs, and

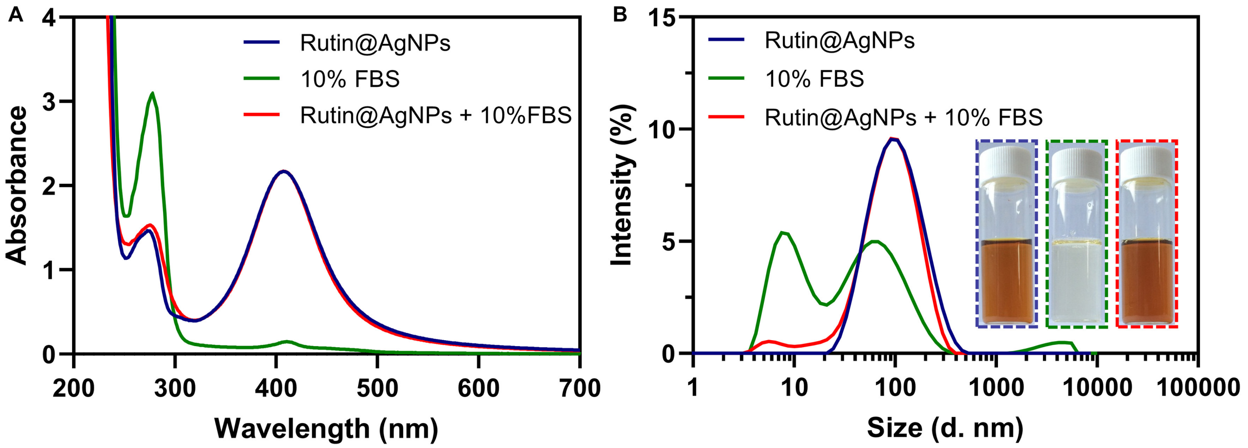

FIGURE 5 | (A) UV-vis spectra, **(B)** size distributions, and photographs of Rutin@AgNPs cultivated in the solution containing 10% FBS for 3 days.

TABLE 1 | Hemolysis of human erythrocytes at various concentrations of Rutin@AgNPs.

C (mg/L)	10	50	100	1,000
Hemolysis (%)	0 ± 0	0.1 ± 0.01	0.4 ± 0.05	4.8 ± 0.12

Rutin@AgNPs were shown in **Figure 3A**. Comparing the size distributions of three types of NPs, the average diameters of PBA@AgNPs and Rutin@AgNPs were larger than that of AgNPs, but their distribution ranges remained visually constant. The mean hydrodynamic diameters of AgNPs, PBA@AgNPs, and Rutin@AgNPs were 90, 108, and 115 nm, respectively. Their polydispersity index values were at 0.198, 0.235, and 0.181, respectively. These values were all below 0.3, which indicated that three NPs were homogenous, and Rutin@AgNPs was acceptable for rutin delivery (Danaei et al., 2018). Also, the values inferred that the enlargement of AgNPs was along with the PBA and rutin successively decoration. The morphological properties of these NPs were further investigated by TEM. All three NPs appeared to have a homogenously spherical shape and a well-dispersed feature, as shown in **Figures 3B–D**. The average size of AgNPs and Rutin@AgNPs, which evaluated by Image J, were 12.2 ± 1.3 nm and 14.5 ± 1.8 nm, respectively. They exhibited a similar rising trend of average diameter in the results of DLS. Note here, the size in TEM was relatively smaller than the one in DLS. This was attributed to the PVP outer layer of NPs, which were spread in the aqueous medium but shrunken in a dry state. The Rutin@AgNPs was further negatively stained with phosphotungstic acid. A magnified image of it is inserted in **Figure 3D**. In this image, the coated PVP and loaded rutin at the outer hydrophilic layer can be identified visually. The results above proved the prepared NPs achieved successfully.

In vitro Rutin Release of Rutin@AgNPs

The release of rutin in the physiological environment is the precondition of Rutin@AgNPs to be an anticoagulant. The rutin release was investigated in different simulated physiological environments, which were the PBS and the PBS containing glucose (5.5 and 20 mmol/L). In **Figure 4**, the cumulative release rate of rutin in 6 days was 27.9 and 57.3%, for Rutin@AgNPs in the PBS and the PBS containing glucose (5.5 mmol/L), respectively. The release rate of rutin accelerated in the PBS containing glucose. As the boronate ester bond was glucose sensitive (Roy and Sumerlin, 2012; Zhao et al., 2017), it would dynamically occur glucose exchange in a hyperglycemia environment. To verify this speculation, the rutin release was further carried out in a PBS containing glucose (20 mmol/L). The release rate of rutin obviously increased, and the cumulative release amount of rutin reached 92.1% in 6 days. Since venous thromboembolism is one of the common complications of diabetes (Piazza et al., 2012; Bell et al., 2016), the Rutin@AgNPs, which had a glucose-sensitive rutin release feature, was potentially applied in diabetes-related venous thromboembolism therapy. More importantly, the rutin release curves in the simulated physiological environments were smooth and continuous, close to the zero-order sustained release behavior. This finding indicated that the Rutin@AgNPs provided a steady-state of rutin concentration in blood circulation, which might overcome the short half-life barrier of rutin.

Serum Stability and Biocompatibility of Rutin@AgNPs

The stability of NPs in blood circulation is one of the fundamental conditions for an antithrombotic trial. The serum stability of Rutin@AgNPs was investigated through UV-vis spectra and size distributions. In **Figure 5A**, two UV-vis spectra, which related to the Rutin@AgNPs, were overlapped at above 320 nm, but showed different absorption peaks below 320 nm. These two absorption peaks were at 273 and 277 nm, for Rutin@AgNPs and Rutin@AgNPs cultivated with FBS (Rutin@AgNPs + FBS), respectively. The FBS curve showed a characteristic absorption peak at 277 nm, which appeared at the same wavelength of the Rutin@AgNPs + FBS curve. This implied that the peak of the Rutin@AgNPs + FBS curve at 277 nm appeared as the addition of the FBS solution. Since the curves related to the Rutin@AgNPs overlapped above 320 nm, the results inferred that the size

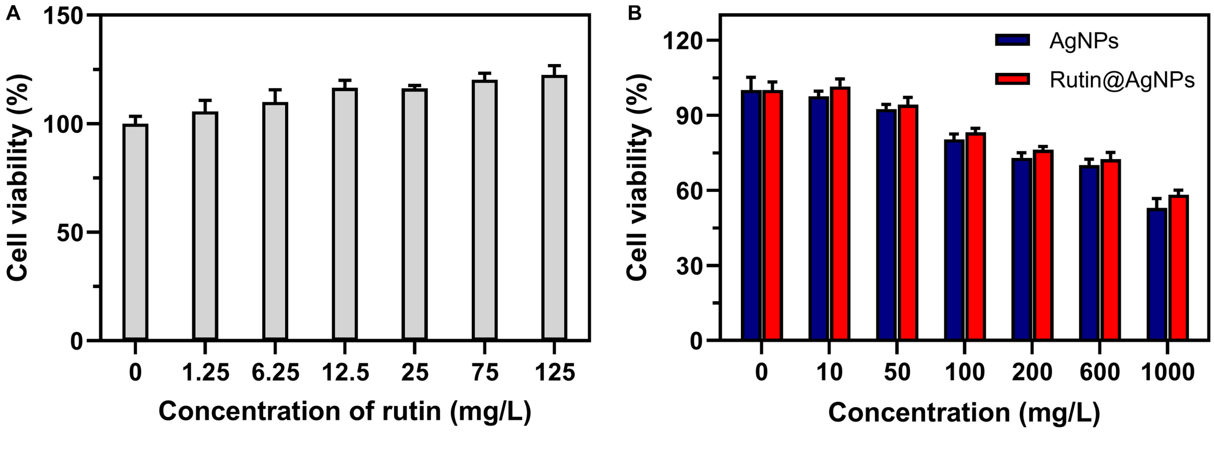

FIGURE 6 | Cell viability of HUVECs cultured with **(A)** rutin, **(B)** AgNPs, and Rutin@AgNPs at different concentrations.

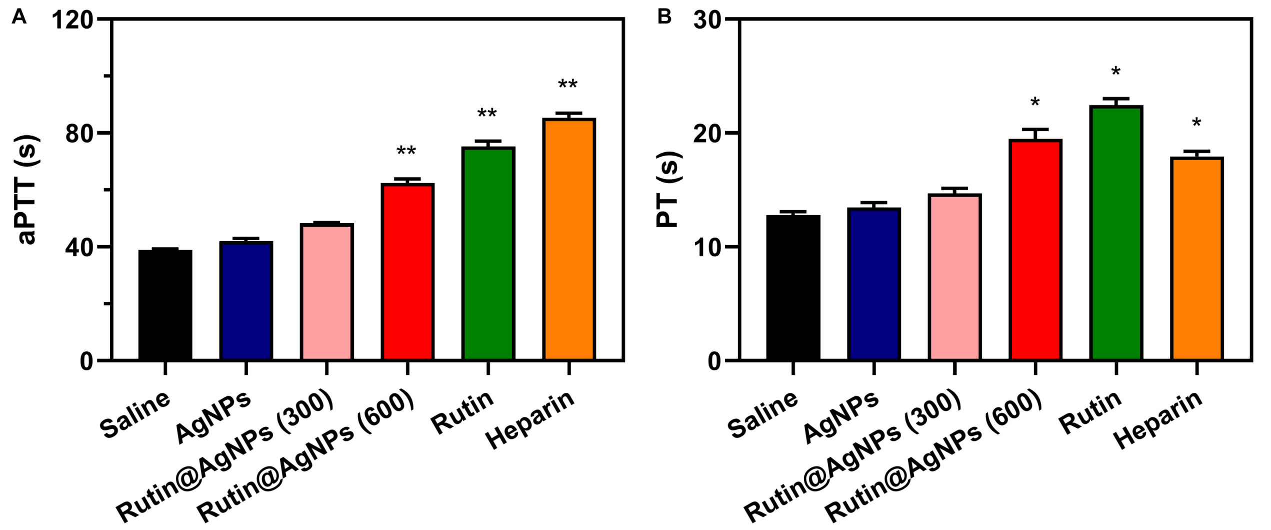

FIGURE 7 | Effect of Rutin@AgNPs on **(A)** aPTT and **(B)** PT *in vivo*. Each value represents the mean ± SD (n = 6 for each test). $^*p < 0.05$, $^{**}p < 0.01$ as compared to values in the saline control group by one-way ANOVA *post hoc* tests.

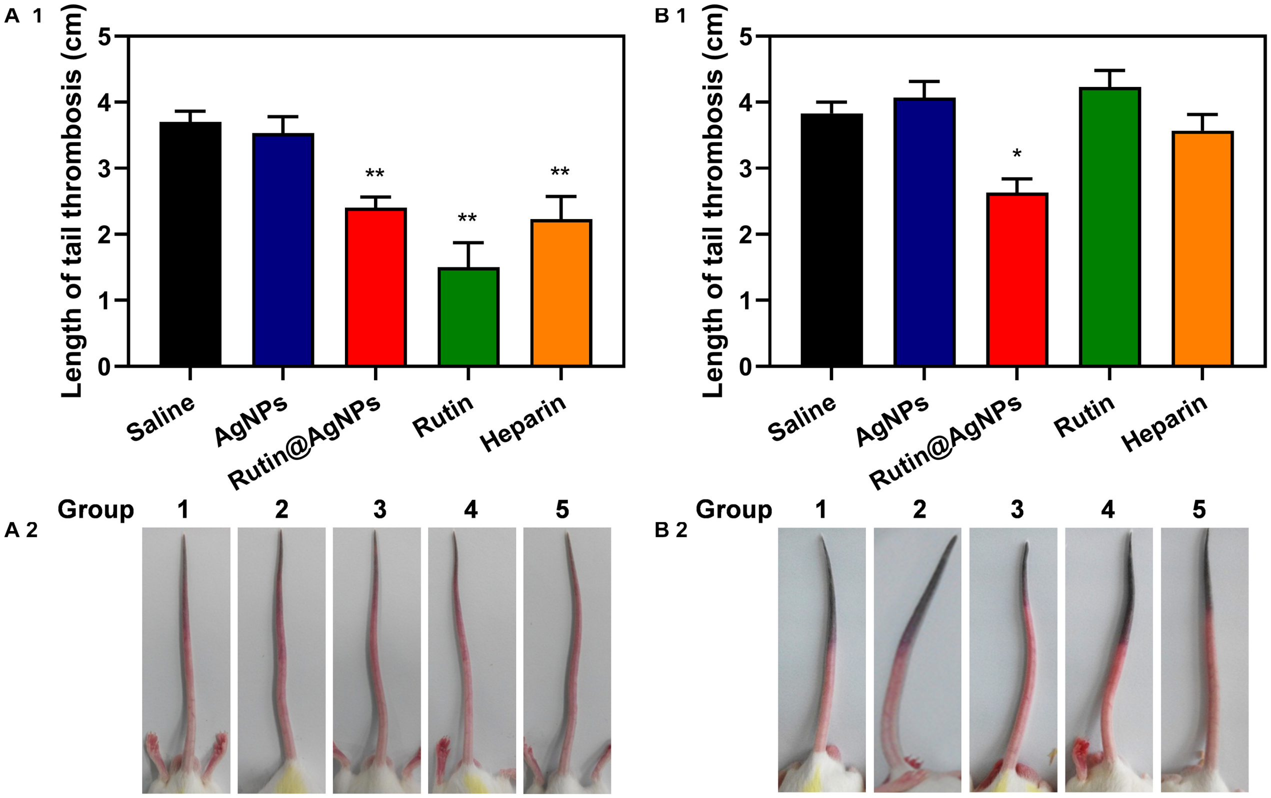

FIGURE 8 | Effect of Rutin@AgNPs on carrageenan-induced tail thrombosis in mice for **(A1,A2)** 24 and **(B1,B2)** 48 h. Each value is shown as the mean ± SD (n = 6). $^*p < 0.05$, $^{**}p < 0.01$ as compared to values in the saline control by one-way ANOVA *post hoc* tests.

change of the NP was limited. Comparing the size distributions of Rutin@AgNPs and Rutin@AgNPs + FBS, two curves illustrated a good match between 30 and 200 nm, as shown in **Figure 5B**. The peak appeared at about 2–10 nm of Rutin@AgNPs + FBS could attribute to the particles in the FBS. These findings indicated that Rutin@AgNPs was stable and could resist serum binding and serum-induced aggregation in the solution containing FBS, which revealed good serum stability of Rutin@AgNPs.

Hemolysis and cytocompatibility are two important indices for the NP to use in the blood circulation. So, experiments were carried out *in vitro* to evaluate the hemocompatibility and cytocompatibility of Rutin@AgNPs. The hemolytic rates, as listed in **Table 1**, showed that the hemolysis raised along with the increasing Rutin@AgNPs concentration. Even though the hemolysis showed a rising trend, the hemolytic rate only exceeded 5%, when the Rutin@AgNPs concentration above 1,000 mg/L. This implied that the Rutin@AgNPs had a satisfactory concentration range to meet the requirement of hemocompatibility (International Organization for Standardization, 2017). The cytocompatibility was evaluated by the MTT assay. In **Figure 6A**, the growth of HUVECs increased with the increasing concentration of rutin. This revealed that rutin is a kind of flavonoid with good cytocompatibility (Gullon et al., 2017). The cell viability rate of HUVECs gradually reduced while the increasing concentration of AgNPs and Rutin@AgNPs, as shown in **Figure 6B**. But the cell viability rates were above 80% when the NPs concentration reached 100 mg/L. Therefore, both NPs satisfied the safety requirement of biomedical applications (International Organization for Standardization, 2009). These also implied that both AgNPs and Rutin@AgNPs had reliable cytocompatibility. The concentration of Rutin@AgNPs below 100 mg/L was selected to use in further experiments.

Effect of Rutin@AgNPs on Coagulation *in vivo*

Coagulation time is an intuitive assay for the anticoagulant activity evaluation. In this study, the *in vivo* aPTT and PT were tested after 1 h intravenous injection of Rutin@AgNPs in a mouse model. The aPTT and PT in the saline control group were 38.9 and 12.8 s, respectively, as shown in **Figure 7**. Comparing the coagulation time of two groups, the saline and the AgNPs, limited differences in aPTT or PT results were found. This implied that the AgNPs exhibited low anticoagulant activity. The aPTT and PT results of the rutin group were 75.3 s ($p < 0.01$) and 22.45 ($p < 0.05$), respectively. In comparison with the saline group, results of the rutin group increased by 1.9- and 1.7- fold, for aPTT and PT results, respectively. These findings indicated that the rutin had good anticoagulant activity and could prevent coagulation in both intrinsic and extrinsic clotting pathways. The aPTT and PT results of two rutin@AgNPs groups were longer than the saline group and AgNPs group. This implied the rutin@AgNPs was a promising anticoagulant, as it maintained the anticoagulation activity of rutin. Comparing two Rutin@AgNPs groups, the coagulation time raised when the dose increased. This inferred the coagulation time of the Rutin@AgNPs was dose-dependent. The results of the Rutin@AgNPs (600 μg/kg) showed a significant increase in the coagulation time ($p < 0.01$). This statistical analysis results also indicated that the coagulation time of the Rutin@AgNPs (600 μg/kg) group was competitive to the rutin group and heparin group. So, the Rutin@AgNPs (600 μg/kg) was selected to use in the further *in vivo* experiments.

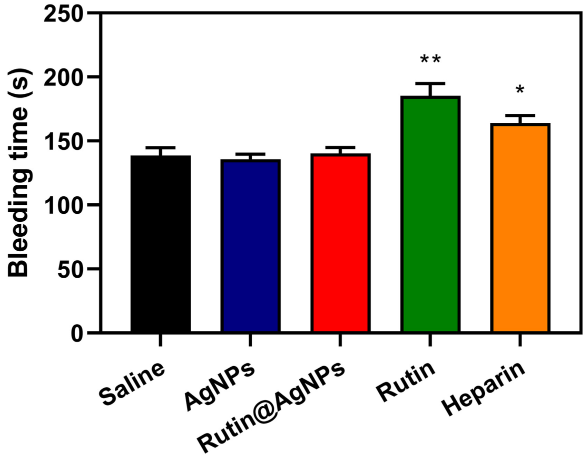

FIGURE 9 | Effect of Rutin@AgNPs on bleeding time in mice. Each value is expressed as mean SD (n 6). *p 0.05, **p 0.01 as compared to values in the saline control by one-way ANOVA post hoc tests.

Antithrombus Formation

The carrageenan-induced venous thrombosis model in mouse was used in this study. This model was built by activating the Hageman (XII) factor, which was the cause of the platelet activation and aggregation, through intraperitoneal injection of carrageenan. The thrombus length that appeared on the mouse tails was used for evaluating the antithrombotic formation results. The results of 24 h and 48 h after injection were shown in **Figure 8**. For the results of 24 h after injection (**Figure 8A**), the thrombus length of the saline group and AgNPs group were similar, which were 3.7 and 3.5 cm, respectively. On the contrary, the thrombus length of the other three groups, Rutin@AgNPs, rutin, and heparin, were shorter, which were 2.4, 1.5, and 2.2 cm ($p < 0.01$), respectively. By comparing these results with the saline group and the AgNPs group, the thrombus formation of these three groups was inhibited. Here, the rutin group was the most effective. This was because rutin effectively targets the PDI and inhibits its activity, thus the platelet accumulation and fibrin generation can be blocked. Moreover, rutin is a kind of flavonoid, which contains antioxidation and anti-inflammatory activities. These activities reduced the inflammation which was caused by carrageenan, and decreased thrombus formation. For the results of after 48 h injections, the thrombus lengths of all the groups were increased, except the Rutin@AgNPs group (thrombus length = 2.6 cm, $p < 0.05$). The rutin group and heparin group, which showed promising results at the first 24 h, had their thrombus lengths increased greatly in the second 24 h. We inferred that the heparin and rutin had relatively shorter half-life limitation, and could degrade or metabolize *in vivo*, so their activities were lost over time. The Rutin@AgNPs inhibited thrombus formation for relatively longer in time, as it could sustainably release the rutin. This made up the fast degradation of the heparin and rutin. Note that, the rutin dose in the Rutin@AgNPs group was 169.8 μg/kg, which was lower than the dose in the rutin group. These findings indicated that

Rutin@AgNPs can make up the half-life limitation of rutin, also increase its overall activities. This further implied that the Rutin@AgNPs had the potential to be used as a long-term antithrombotic agent.

Bleeding Time Evaluation

Bleeding is one of the severe complications of the anticoagulants in clinical trials, and the bleed time is commonly used as a safety evaluation parameter. A mouse tail-transection model was used to determine the bleeding time of Rutin@AgNPs in this study. The bleeding times of five injection sample groups (after 1 h) were illustrated in **Figure 9**. The saline and AgNPs groups' results were similar at about 138.7 s. This was because the AgNPs had limited influence on the coagulation function (see section "Effect of Rutin@AgNPs on Coagulation *in vivo*"). The bleeding times of the rutin group and heparin group were 185.3 s ($p < 0.01$) and 164.2 s ($p < 0.05$), respectively, which were longer than the saline group. This implied that the rutin and heparin caused bleeding complications of anticoagulation, which lead to coagulation inhibitor disorder potentially. The bleeding time of the Rutin@AgNPs group was 140.3 s, which was slightly longer than that of the saline group. But the increment was not statistically significant ($p > 0.5$). Therefore, the Rutin@AgNPs had a limited effect on the normal coagulant function when it was used under a specific dose. From the above, we can infer that the sustained release property of the Rutin@AgNPs controlled the dose of the rutin in the blood. So, the long-term antithrombotic activity can be achieved, and the bleeding risk can be minimized.

CONCLUSION

In this paper, we proposed a new NP, Rutin@AgNPs, which loaded rutin (calculated as 28.3%) on the surface of AgNPs, to control rutin release over time. This NP showed good serum stability, satisfiable hemocompatibility, and cytocompatibility, when concentration below 100 mg/L. The rutin was loaded through a dynamic boronate ester bond, which was glucose-sensitive. This assisted a sustained rutin release in the physiological environment. *In vivo* evaluations showed that Rutin@AgNPs maintained the anticoagulant function of rutin, prolonged the coagulation time in both intrinsic and extrinsic pathways. Comparing with rutin, Rutin@AgNPs not only inhibited the mouse tail thrombosis with a longer time, and solved the short half-life problem of rutin, but minimized bleeding risk as well. These were valid proof that the Rutin@AgNPs had satisfiable biocompatibility, and had a promising future in long-term antithrombotic therapy.

DATA AVAILABILITY STATEMENT

The original contributions presented in the study are included in the article/supplementary material, further inquiries can be directed to the corresponding author/s.

ETHICS STATEMENT

The animal study was reviewed and approved by the Institutional Animal Care and Use Committee of Jiangnan University.

AUTHOR CONTRIBUTIONS

HW developed the main study. MS and HJ helped to complete the animal experiments. XL and PW took part in the preparation and analysis. JXC and JHC drafted the manuscript and developed the study design. All authors have given final approval for this manuscript to be published.

FUNDING

This work was supported by the National Natural Science Foundation of China (51973084, 21978114), Fundamental Research Funds for the Central Universities (JUSRP22022), Opening Project of Key Laboratory of Biomedical Polymers of Ministry of Education at Wuhan University (20200103) and National First-Class Discipline Program of Light Industry Technology and Engineering (LITE2018-20).

REFERENCES

Ansell, J., Hirsh, J., Hylek, E., Jacobson, A., Crowther, M., and Palareti, G. (2008). Pharmacology and management of the vitamin K antagonists. *Chest* 133, 160S–198S. doi: 10.1378/chest.08-0670

Bell, E. J., Folsom, A. R., Lutsey, P. L., Selvin, E., Zakai, N. A., Cushman, M., et al. (2016). Diabetes mellitus and venous thromboembolism: a systematic review and meta-analysis. *Diabetes Res. Clin. Pract.* 111, 10–18. doi: 10.1016/j.diabres.2015.10.019

Chaaban, H., Ioannou, I., Chebil, L., Slimane, M., Gerardin, C., Paris, C., et al. (2017). Effect of heat processing on thermal stability and antioxidant activity of six flavonoids. *J. Food Process. Preserv.* 41:e13203. doi: 10.1111/jfpp.13203

Chen, C., Li, S., Liu, K., Ma, G., and Yan, X. (2016). Co-assembly of heparin and polypeptide hybrid nanoparticles for biomimetic delivery and anti-thrombus therapy. *Small* 12, 4719–4725. doi: 10.1002/smll.201600328

Chen, J.-X., Shi, Y., Zhang, Y.-R., Teng, L.-P., and Chen, J.-H. (2016). One-pot construction of boronate ester based pH-responsive micelle for combined cancer therapy. *Colloids Surf. B Biointerfaces* 143, 285–292. doi: 10.1016/j.colsurfb.2016.03.053

Choi, J.-H., Kim, D.-W., Park, S.-E., Lee, H.-J., Kim, K.-M., Kim, K.-J., et al. (2015). Anti-thrombotic effect of rutin isolated from Dendropanax morbifera Leveille. *J. Biosci. Bioeng.* 120, 181–186. doi: 10.1016/j.jbiosc.2014.12.012

da Costa, E. M., Barbosa, J. M., do Nascimento, T. G., and Macedo, R. O. (2002). Thermal characterization of the quercetin and rutin flavonoids. *Thermochim. Acta* 392, 79–84. doi: 10.1016/s0040-6031(02)00087-4

Dakin, S. G. (2019). Resolving deep vein thrombosis. *Sci. Transl. Med.* 11:eaay7696. doi: 10.1126/scitranslmed.aay7696

Danaei, M., Dehghankhold, M., Ataei, S., Davarani, F. H., Javanmard, R., Dokhani, A., et al. (2018). Impact of particle size and polydispersity index on the clinical applications of lipidic nanocarrier systems. *Pharmaceutics* 10:57. doi: 10.3390/pharmaceutics10020057

Dejana, E., Villa, S., and de Gaetano, G. (1982). Bleeding time in rats: a comparison of different experimental conditions. *Thromb. Haemost* 48, 108–111. doi: 10.1055/s-0038-1657230

Flaumenhaft, R. (2013). Protein disulfide isomerase as an antithrombotic target. *Trends Cardiovasc. Med.* 23, 264–268. doi: 10.1016/j.tcm.2013.03.001

Furie, B., and Flaumenhaft, R. (2014). Thiol Isomerases in Thrombus Formation. *Circ. Res.* 114, 1162–1173. doi: 10.1161/circresaha.114.301808

Gorog, D. A., Fayad, Z. A., and Fuster, V. (2017). Arterial thrombus stability: does it matter and can we detect it? *J. Am. Coll. Cardiol.* 70, 2036–2047. doi: 10.1016/j.jacc.2017.08.065

Gullon, B., Lu-Chau, T. A., Moreira, M. T., Lema, J. M., and Eibes, G. (2017). Rutin: a review on extraction, identification and purification methods, biological activities and approaches to enhance its bioavailability. *Trends Food Sci. Technol.* 67, 220–235. doi: 10.1016/j.tifs.2017.07.008

Hagimori, M., Kamiya, S., Yamaguchi, Y., and Arakawa, M. (2009). Improving frequency of thrombosis by altering blood flow in the carrageenan-induced rat tail thrombosis model. *Pharmacol. Res.* 60, 320–323. doi: 10.1016/j.phrs.2009.04.010

Hirsh, J., Anand, S. S., Halperin, J. L., and Fuster, V. (2001a). Guide to anticoagulant therapy: heparin : a statement for healthcare professionals from the American Heart Association. *Circulation* 103, 2994–3018. doi: 10.1161/01.cir.103.24.2994

Hirsh, J., Anand, S. S., Halperin, J. L., and Fuster, V. (2001b). Mechanism of action and pharmacology of unfractionated heparin. *Arterioscler. Thromb. Vasc. Biol.* 21, 1094–1096. doi: 10.1161/hq0701.093686

Ilinskaya, A. N., and Dobrovolskaia, M. A. (2013a). Nanoparticles and the blood coagulation system. Part I: benefits of nanotechnology. *Nanomedicine (Lond.)* 8, 773–784. doi: 10.2217/nnm.13.48

Ilinskaya, A. N., and Dobrovolskaia, M. A. (2013b). Nanoparticles and the blood coagulation system. Part II: safety concerns. *Nanomedicine (Lond.)* 8, 969–981. doi: 10.2217/nnm.13.49

International Organization for Standardization (2009). *ISO 10993-5:2009. Biological evaluation of medical devices - Part 5: Tests for in vitro cytotoxicity*. Geneva: International Organization for Standardization.

International Organization for Standardization (2017). *ISO 10993-4:2017. Biological evaluation of medical devices - Part 4: Selection of tests for interactions with blood*. Geneva: International Organization for Standardization.

Jasuja, R., Passam, F. H., Kennedy, D. R., Kim, S. H., van Hessem, L., Lin, L., et al. (2011). Protein disulfide isomerase inhibitors: a new class of antithrombotic agents. *Blood* 118:172. doi: 10.1182/blood.V118.21.369.369

Jasuja, R., Passam, F. H., Kennedy, D. R., Kim, S. H., van Hessem, L., Lin, L., et al. (2012). Protein disulfide isomerase inhibitors constitute a new class of antithrombotic agents. *J. Clin. Invest.* 122, 2104–2113. doi: 10.1172/jci61228

Kargl, R., and Kleinschek, K. S. (2020). How can we understand the influence of nanoparticles on the coagulation of blood? *Nanomedicine (Lond.)* 15, 1923–1926. doi: 10.2217/nnm-2020-0177

Kennedy, D. R., Nag, P. P., Galinski, C. N., Bowley, S., Bekendam, R. H., Dilks, J. R., et al. (2013). Development of second generation thiol isomerase inhibitors to prevent thrombus formation. *Blood* 122:926. doi: 10.1182/blood.V122.21.926.926

Kyrle, P. A., Minar, E., Bialonczyk, C., Hirschl, M., Weltermann, A., and Eichinger, S. (2004). The risk of recurrent venous thromboembolism in men and women. *N. Engl. J. Med.* 350, 2558–2563. doi: 10.1056/NEJMoa032959

Lin, L., Gopal, S., Sharda, A., Passam, F., Bowley, S. R., Stopa, J., et al. (2015). Quercetin-3-rutinoside inhibits protein disulfide isomerase by binding to its b'x domain. *J. Biol. Chem.* 290, 23543–23552. doi: 10.1074/jbc.M115.666180

Lippi, G., Franchini, M., and Targher, G. (2011). Arterial thrombus formation in cardiovascular disease. *Nat. Rev. Cardiol.* 8, 502–512. doi: 10.1038/nrcardio.2011.91

Mackman, N. (2008). Triggers, targets and treatments for thrombosis. *Nature* 451, 914–918. doi: 10.1038/nature06797

Piazza, G., Goldhaber, S. Z., Kroll, A., Goldberg, R. J., Emery, C., and Spencer, F. A. (2012). Venous thromboembolism in patients with diabetes mellitus. *Am. J. Med.* 125, 709–716. doi: 10.1016/j.amjmed.2011.12.004

Roy, D., and Sumerlin, B. S. (2012). Glucose-sensitivity of boronic acid block copolymers at physiological pH. *ACS Macro Lett.* 1, 529–532. doi: 10.1021/mz300047c

Sharma, S., Ali, A., Ali, J., Sahni, J. K., and Baboota, S. (2013). Rutin: therapeutic potential and recent advances in drug delivery. *Expert Opin. Investig. Drugs* 22, 1063–1079. doi: 10.1517/13543784.2013.805744

Su, M., Dai, Q., Chen, C., Zeng, Y., Chu, C., and Liu, G. (2020). Nano-medicine for thrombosis: a precise diagnosis and treatment strategy. *Nanomicro Lett.* 12:96. doi: 10.1007/s40820-020-00434-0

Tejamaya, M., Roemer, I., Merrifield, R. C., and Lead, J. R. (2012). Stability of citrate, pvp, and peg coated silver nanoparticles in ecotoxicology media. *Environ. Sci. Technol.* 46, 7011–7017. doi: 10.1021/es2038596

Thompson, C. M., Occhialini, G., McCandless, G. T., Alahakoon, S. B., Cameron, V., Nielsen, S. O., et al. (2017). Computational and experimental studies on the effects of monomer planarity on covalent organic framework formation. *J. Am. Chem. Soc.* 139, 10506–10513. doi: 10.1021/jacs.7b05555

Tian, Y., Zhao, Y., Zheng, W., Zhang, W., and Jiang, X. (2014). Antithrombotic functions of small molecule-capped gold nanoparticles. *Nanoscale* 6, 8543–8550. doi: 10.1039/c4nr01937g

Wang, Y., Zhou, C., Sun, L., Yu, B., Cao, M., and Zhong, S. (2015). One-step synthesis of boronic acid group modified silica particles by the aid of epoxy silanes. *Appl. Surf. Sci.* 351, 353–357. doi: 10.1016/j.apsusc.2015.05.120

Zahoor, M., Shafiq, S., Ullah, H., Sadiq, A., and Ullah, F. (2018). Isolation of quercetin and mandelic acid from *Aesculus indica* fruit and their biological activities. *BMC Biochem.* 19:5. doi: 10.1186/s12858-018-0095-7

Zhang, Z., Zhang, X., Xin, Z., Deng, M., Wen, Y., and Song, Y. (2011). Synthesis of monodisperse silver nanoparticles for ink-jet printed flexible electronics. *Nanotechnology* 22:425601. doi: 10.1088/0957-4484/22/42/425601

Zhao, L., Huang, Q., Liu, Y., Wang, Q., Wang, L., Xiao, S., et al. (2017). Boronic acid as glucose-sensitive agent regulates drug delivery for diabetes treatment. *Materials (Basel)* 10:170. doi: 10.3390/ma10020170 doi: 10.3390/ma10020170

Conflict of Interest: The authors declare that the research was conducted in the absence of any commercial or financial relationships that could be construed as a potential conflict of interest.

frontiers
in Molecular Biosciences

ORIGINAL RESEARCH
published: 03 December 2020
doi: 10.3389/fmolb.2020.610084

BSA-Stabilized Mesoporous Organosilica Nanoparticles Reversed Chemotherapy Resistance of Anaplastic Thyroid Cancer by Increasing Drug Uptake and Reducing Cellular Efflux

Xiao Han[1,2†], Xiaoquan Xu[3†], Yuxia Tang[2], Feipeng Zhu[3], Ying Tian[2], Wei Liu[3], Doudou He[3], Guangming Lu[2*], Yunfei Gu[1*] and Shouju Wang[2,3*]

[1] The First School of Clinical Medicine, Nanjing University of Chinese Medicine, Nanjing, China, [2] Department of Radiology, Jinling Hospital, Nanjing Medical University, Nanjing, China, [3] Department of Radiology, The First Affiliated Hospital of Nanjing Medical University, Nanjing, China

OPEN ACCESS

Edited by:
Gang Liu,
Xiamen University, China

Reviewed by:
Amitava Mukherjee,
VIT University, India
Zhaogang Teng,
Nanjing University of Posts and Telecommunications, China

****Correspondence:***
Guangming Lu
cjr.luguangming@vip.163.com
Yunfei Gu
guyunfei_njucm@163.com
Shouju Wang
shouju.wang@gmail.com

† These authors have contributed equally to this work

Specialty section:
This article was submitted to Nanobiotechnology, a section of the journal Frontiers in Molecular Biosciences

Received: *25 September 2020*
Accepted: *12 November 2020*
Published: *03 December 2020*

Citation:
Han X, Xu X, Tang Y, Zhu F, Tian Y, Liu W, He D, Lu G, Gu Y and Wang S (2020) BSA-Stabilized Mesoporous Organosilica Nanoparticles Reversed Chemotherapy Resistance of Anaplastic Thyroid Cancer by Increasing Drug Uptake and Reducing Cellular Efflux. Front. Mol. Biosci. 7:610084. doi: 10.3389/fmolb.2020.610084

Anaplastic thyroid cancer (ATC) is a highly aggressive and the most lethal type of thyroid cancer. The standard-of-care for unresectable ATC is radiotherapy and chemotherapy, usually based on doxorubicin (Dox). However, most patients develop resistance shortly after treatment. To overcome the drug resistance, we synthesized the mesoporous organosilica nanoparticles (MONPs) loaded with Dox and stabilized the nanocomposites by bovine serum albumin (BSA). The surface area and pore volume of MONPs were 612.653 m^2/g and 0.589 cm^3/g. The loading capacity of Dox-MONPs reached 47.02%. Compared to Dox-MONPs and free Dox, BSA-Dox-MONPs had more durable tumor-killing power on both drug-sensitive cell line HTh74 and drug-resistant cell line HTh74R. The cellular uptake of BSA-Dox-MONPs was 28.14 and 65.53% higher than that of Dox-MONP in HTh74 and HTh74R. Furthermore, the BSA coating decreased the efflux rate of nanocomposites in HTh74 (from 38.95 to 33.05%) and HTh74R (from 43.03 to 32.07%). In summary, BSA-Dox-MONPs reversed the chemotherapy resistance of ATC cells via increased drug uptake and inhibited drug efflux, offering a promising platform for the treatment of chemo-resistant ATC.

Keywords: anaplastic thyroid cancer, chemotherapy resistance, bovine serum albumin, drug efflux, organosilica

INTRODUCTION

Anaplastic thyroid cancer (ATC) has lately received considerable attention for reduced median survival rate and high invasion. The median survival of patients is no longer than 5 months, and the two-year survival rate is less than 15% (Molinaro et al., 2017). Combination treatment, including extensive resection and adjuvant chemo-radiotherapy, is recommended (Haddad et al., 2018). Although doxorubicin (Dox) is the only chemo-drug suggested, the resistance to Dox is collective in ATC, leading to a worse prognosis (Haddad et al., 2018). A critical mechanism behind the Dox resistance is the excessive efflux of chemotherapy drugs (Zinzi et al., 2014; Davis et al., 2015).

Thus, developing new strategies to overcome chemoresistance is crucial to improve patients' outcomes with ATC.

Nowadays, mesoporous nanoparticles have attracted extensive interest because their high loading capacity is suitable for drug loading and delivery (Yao et al., 2017; Teng et al., 2018; Chen et al., 2019, 2020). Among these mesoporous materials, considerable attention has been paid to mesoporous organosilica nanocapsules (MONPs) since their excellent biocompatibility, large surface area, adjustable pore volume, and easily modified surface (Tao et al., 2018; Teng et al., 2018; Yao et al., 2020). MONPs are synthesized using organic group-bridged siloxanes as silicon sources, which is different from pure Si-O-Si groups of inorganic mesoporous silica nanoparticles (MSNs) (Chen et al., 2013; Teng et al., 2014b; Croissant et al., 2015). These doped organic groups give MONPs more advantages, including improved hydrothermal stability and dispersibility (Chen et al., 2014). Furthermore, MONPs can be modified more easily than MSNs (Yu et al., 2011; Burglova et al., 2014). By selectively introducing organic groups, the hydrophilicity of the pores can be adjusted for controllable drug loading and release (Chen et al., 2014; Croissant et al., 2014; Wu et al., 2016). Moreover, MONPs have higher blood compatibility due to attenuated interaction between Si-OH and red blood cells. The previous studies have shown that MONPs exhibit significantly lower hemolysis than MSNs (Yu et al., 2011).

Recently, bovine serum albumin (BSA) has been widely applied in the drug delivery system through coupling interaction on account of its low cytotoxicity, minor immunogenicity, and excellent biocompatibility (Liu et al., 2016; Fang et al., 2019; Pan et al., 2020; Wu et al., 2020). Meanwhile, BSA can improve the stealthiness of the nanoparticles in the blood circulation, thereby enhancing tumor-specific accumulation (Fang et al., 2019). Zhang's research showed that drug-loaded MSNs are more stable and can maintain excellent dispersibility in serum after coated with BSA, leading to accumulation in tumor sites by enhanced permeation and retention (EPR) effect (Zhang et al., 2019). Because of the high metabolism rate, cancer cells need more nutrients and internalized a greater amount of proteins (such as BSA) and amino acids than normal cells. Therefore the BSA coating results in increased cancer cell internalization (Deberardinis and Chandel, 2016). Several studies have shown that BSA modified Au-NPs and galactosylated nanoparticles have greater tumor uptake; however, the effect of BSA coating on MONPs has been scarcely reported (Huang et al., 2018; Unnikrishnan et al., 2020). In our research, BSA-stabilized MONPs were studied to be quantified not only for cellular uptake but also for cellular efflux in ATC.

Currently, there are few nanoplatforms developed for drug-resistant ATC (Marano et al., 2016, 2017; Wang et al., 2018). In our previous research, we constructed Dox-loaded melanin nanoparticles to enhance the efficacy of chemotherapy to drug-resistant ATC (Wang et al., 2018). However, the Dox-loading capacity of melanin nanoparticles was less than 20%, which may be related to their limited surface-area-to-volume ratio (Wang et al., 2018). To increase the loading capacity, herein, we synthesized MONPs (Teng et al., 2014a) to replace melanin nanoparticles for Dox loading. The mesoporous structure and Dox-loading capacity of MONPs were characterized. In addition, BSA coating was used to stabilize Dox-MONPs in chemotherapy-resistant ATC research. The therapeutic efficacy, as well as cellular uptake and efflux of BSA-Dox-MONPs, was compared with Dox-MONPs in drug-sensitive and drug-resistant ATC.

MATERIALS AND METHODS

Chemicals and Materials

Cetyltrimethylammonium bromide (CTAB), concentrated aqueous ammonia solution (25–28 wt%), anhydrous ethanol, Dox, and dimethyl sulfoxide (DMSO) were obtained from Aladdin Reagent. Tetraethoxysilane (TEOS), 1,4-Bis(triethoxysilyl)propane tetrasulfide (TESPTS), and 3-(4,5-Dimethylthiazol-2-yl)-2,5-diphenyltetrazolium bromide (MTT) were purchased from Sigma-Aldrich (St. Louis, MO, United States). BSA was supplied by the Biosharp company. Deionized water (Millipore) with a resistivity of 18.2 MΩ·cm was used in all experiments. 4,6-diamino-2-phenyl indole (DAPI) was provided by Nanjing Keygen Biotech. Co., Ltd. (Nanjing, China). Cancer cells were cultured in F-12 medium with 1% amphotericin, 1% 500x penicillin and streptomycin, and 10% fetal bovine serum (FBS), which were offered by Gibco company. Gibco company offered DMEM medium used to culture HaCaT cells and phosphate buffer saline (PBS) for cell experiments. YF488-AnnexinV was purchased from United States Everbright®Inc.

Synthesis of Mesoporous Organosilica Nanoparticles

Mesoporous organosilica nanoparticles (MONPs) were synthesized according to previously reported protocols (Teng et al., 2014a). Briefly, 0.16 g CTAB was dissolved in a mixture of 75 mL deionized water and 30 mL ethanol containing 1 mL concentrated aqueous ammonia solution (25 wt%). After being vortexed vigorously at 35°C for one-hour, a mixture of TEOS (0.1 mL) and TESPTS (0.25 mL) was then quickly added into the solution, and the reaction was allowed to proceed for 24 h. The product was precipitated by centrifugation and washed thrice with ethanol. Then, the product was resuspended in 37% hydrochloric acid solution in ethanol at a ratio of 1:500 (v/v), gently vortexed at 60°C for 3 h, and collected by centrifugation for three times. Finally, the product was rewashed in pure ethanol thrice and dried in a high vacuum.

Loading Dox to MONPs

Mesoporous Organosilica Nanoparticles stock suspension at a final concentration of 1 mg/mL was prepared by adding MONPs powder to deionized water. To load MONPs with Dox, the MONPs stock suspension was mixed with various concentrations of Dox aqueous solution and vortexed vigorously in the dark for 24 h at room temperature. To find the optimal MONPs: Dox ratio that maximizes the loading efficiency and loading capacity, a series of Dox: MONPs suspension with mass ratio from 0.125: 1 to 8: 1 was set. The Dox concentration in the supernatant was determined by measuring the UV absorbance and comparing it to the standard curve. The loading efficiency and loading capacity were calculated based on the free Dox concentration.

Coating BSA on Dox-MONPs

Dox-MONPs aqueous solution with a concentration of 200 μg/mL was added dropwise into the BSA aqueous solution with a concentration of 1 mg/mL, which was gently vortexed at physiological temperature 37°C. After the addition, the mixture was gently vortexed at 37°C for 3 h, followed by centrifugation and redispersion.

Characterization of Nanoparticles

The UV-Vis spectra of MONPs and its modified products were obtained using PerkinElmer Lambda 35 UV-Vis spectrophotometer. Its hydrodynamic size and Zeta potentials were obtained from a Brookhaven Zeta PALS machine. The transmission electron microscope (TEM) photograph was taken by an FEI TECNAI F20s TWIN microscope. A high angle annular dark-field (HAADF) scanning TEM and energy dispersive X-ray (EDX) analyses were performed (FEI TECNAI F20s TWIN) to characterize the morphologies of nanomaterials and the distribution of organic elements. The samples were suspended in

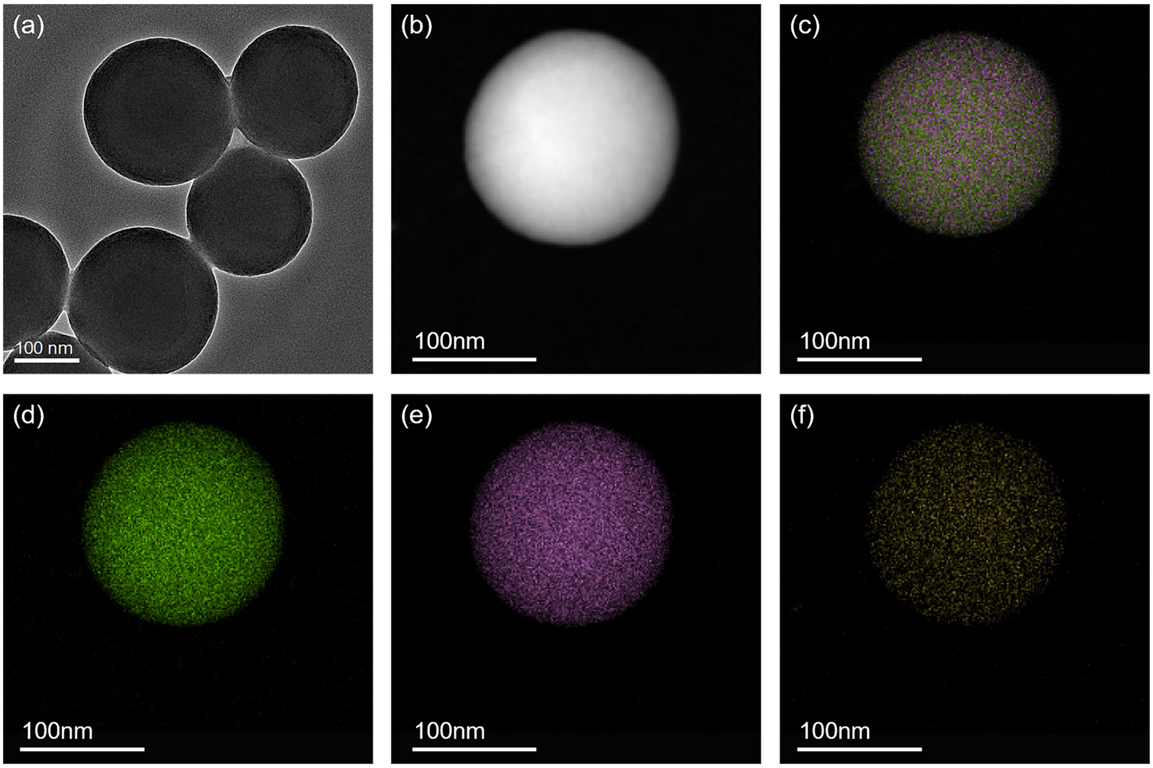

FIGURE 1 | TEM image of **(A)** MONPs and HADDF image of **(B)** MONPs. EDX elemental mapping images of the corresponding MONPs: **(C)** merge of O, Si and S elements, **(D)** oxygen, **(E)** silicon and **(F)** sulfur.

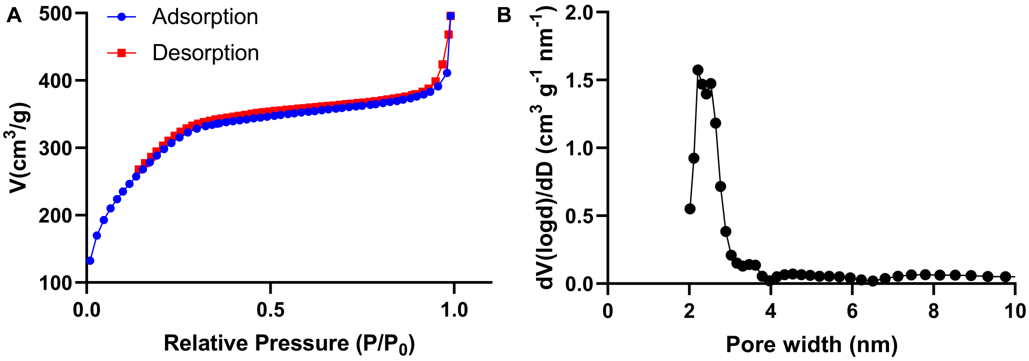

FIGURE 2 | (A) Nitrogen adsorption-desorption isotherms and **(B)** pore-size distribution curves of the MONPs.

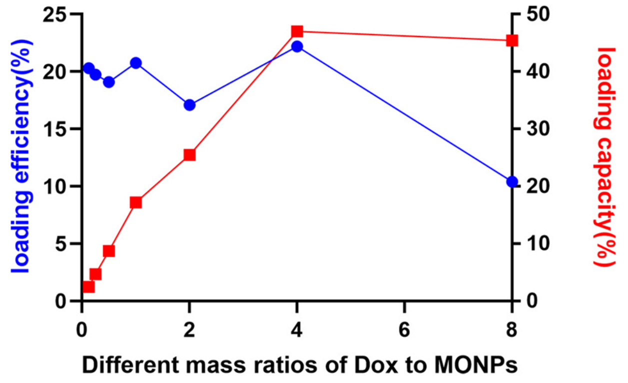

FIGURE 3 | Loading efficiency and loading capacity of Dox-MONPs at different mass ratios of Dox to MONPs.

ethanol ultrasonically and supported onto an ultrathin carbon-coated tinned grid for TEM and EDX measurements. Nitrogen adsorption and desorption experiments were used to measure the pore size and uniformity of MONPs.

MTT Assay

HTh74 and HTh74R cells were routinely cultivated in 25 cm^2 culture flasks at 37°C, 5% CO_2, and 95% humidity, using McCoy F12 medium supplemented with 10% FBS, 1% penicillin and streptomycin. For MTT assay, HTh74 and HTh74R cells at the logarithmic growth phase were seeded in 96-well plates and cultured for 24 h. Different concentrations of free Dox, Dox-MONPs, and BSA-Dox-MONPs were added to 96-well plates and incubated with HTh74 and HTh74R cells for another 24 h. Afterward, the drug-containing culture medium was aspirated and replaced with a complete culture solution containing 0.5% MTT. After 4 h, the formazan produced was dispersed in DMSO and shaken for 10 min to promote sufficient dissolution. Cell viability was quantified by the absorbance at 570 nm with the absorbance at 630 nm as reference. Human Keratinocyte Cells (HaCaT) were cultured in DMEM medium supplemented with 10% FBS, 1% penicillin and streptomycin, at 37°C, 5% CO_2, and 95% humidity. After incubating HaCat with various concentrations of MONPs for 24 h, MTT assays were performed as described above.

Confocal and Fluorescence Microscope Image Analysis

For fluorescence morphology, HTh74 and HTh74R cells were co-incubated with Dox-MONPs and BSA-Dox-MONPs with an equivalent Dox concentration of 25 μg/mL for 6 h and washed gently in cold PBS thrice. Cells obtained were stained by DAPI dye following the instructions and washed twice with PBS. Afterward, the samples were imaged on a confocal laser scanning microscope.

In another experiment, HTh74 and HTh74R cells were first incubated in 12-well plates for 24 h and further incubated with Dox-MONPs and BSA-Dox-MONPs at an equivalent Dox concentration of 25 μg/mL for another 6 h. After incubation, the treated cells were gently washed three times with PBS and further stained with YF488-AnnexinV in the dark according to the instructions. Then the cells obtained were visualized and photographed by fluorescence microscopy.

Flow Cytometry Test

To compare the uptake of Dox-MONPs and BSA-Dox-MONPs, the HTh74 and HTh74R were incubated with Dox-MONPs and BSA-Dox-MONPs containing 25 μg/mL of equivalent effective Dox for 6 h, following with PBS rinses thrice. Then the cells were collected and digested into single cells, subjected to flow cytometry, and the Dox fluorescence signals were measured by Cytoflow cytometer.

In another experiment, HTh74 and HTh74R cells were first cultured in media containing BSA-Dox-MONPs or Dox-MONPs with an equivalent Dox concentration of

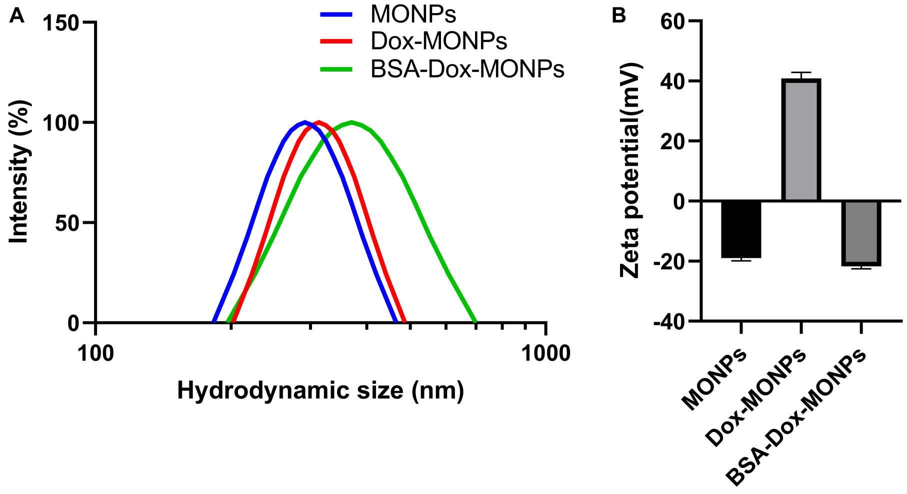

FIGURE 4 | (A) The hydrodynamic size and **(B)** Zeta potential of MONPs, Dox-MONPs and BSA-Dox-MONPs.

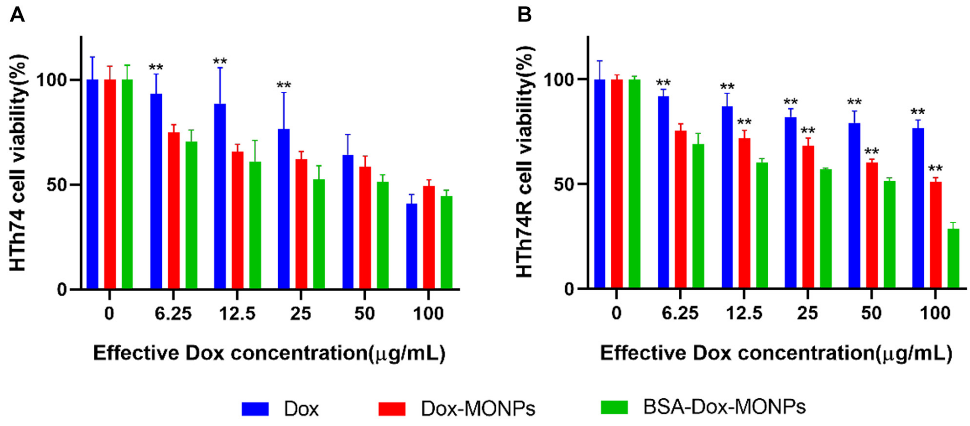

FIGURE 5 | Cell viability of **(A)** HTh74 and **(B)** HTh74R after incubation with various concentrations of MONPs, Dox-MONPs and BSA-Dox-MONPs for 24 h, respectively. *$P < 0.05$, **$P < 0.01$, comparison to BSA-Dox-MONPs.

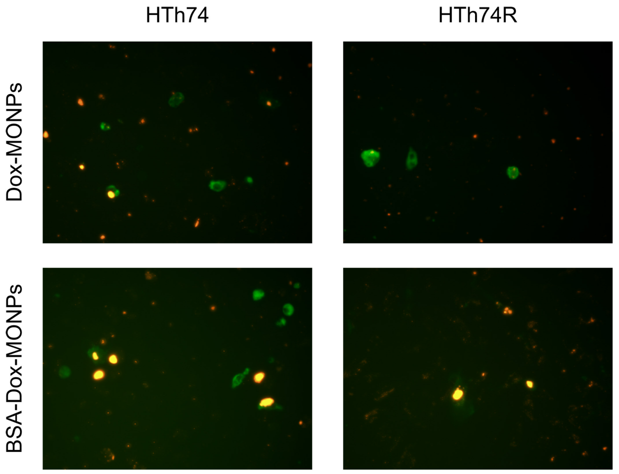

FIGURE 6 | The fluorescence microscope images of YF488-AnnexinV fluorescence staining with HTh74 and HTh74R after incubation with Dox-MONPs and BSA-Dox-MONPs at equivalent Dox concentration of 25 µg/mL for 6 h. The green fluorescence represents early apoptosis and the red fluorescence represents the drug loaded nanoparticles.

25 µg/mL. After 6 h, the nanoparticle-containing media were removed, and the cells were cultured in fresh media for an additional 18 h to allow the efflux of nanoparticles. The cell fluorescence signals before and after culture in fresh media were recorded to evaluate the efflux of nanomaterials. The formula for the efflux ratio of drug-loaded nanoparticles is $(F_1\text{-}F_2)/F_1 \times 100\%$, where F_1 represents the average intracellular fluorescence intensity before culture in fresh media, and F_2 indicates the average intracellular fluorescence intensity after culture in fresh media.

Statistical Analysis

All data were analyzed using Graphpad Prism 7.0 software. All quantitative data are expressed as mean ± SD and analyzed using the one-way ANOVA or *t*-test. The value of 0.05 was defined as a statistically significant threshold.

RESULTS AND DISCUSSION

Mesoporous Organosilica Nanoparticles were successfully synthesized and characterized. TEM image results show that the MONPs are spherical with an average diameter of 224.3 ± 21.2 nm. Notably, the EDX elemental mapping results show that the Si, O, and S elements are uniformly distributed, demonstrating the S elements were successfully doped in the organosilica frameworks (**Figure 1**).

The nitrogen adsorption-desorption isothermal curve conforms to the type IV curve, revealing the typical characteristics of MONPs with uniform mesopore size distribution. The surface area and pore volume of MONPs are 612.653 m^2/g and 0.589 cm^3/g, respectively. The pore size distribution was calculated to be peaked at 2.2 nm according to the NLDFT method (**Figure 2**).

In order to quantitatively evaluate the Dox loading efficiency and capacity of MONPs, a constant amount of MONPs was incubated with various concentrations of Dox. As the Dox-to-MONPs ratio increases, the loading capacity increases and plateaus to about 45% when the mass ratio is equal or greater than four (**Figure 3** and **Supplementary Figures 1**, **2**). However, the Dox loading efficiency fluctuates around 20% and drops when the Dox concentration is high. Taking account of both loading efficiency and capacity, the mass ratio of Dox-to-MONPs was set at 4:1 for the following experiments.

To stabilize MONPs for biomedical applications, the obtained Dox-MONPs were vortexed with BSA solutions. The hydration diameter of MONPs was 291.92 ± 11.85 nm, which was slightly larger than the diameter measured by TEM. Additionally, the hydration diameter of BSA-Dox-MONPs (370.12 ± 3.34 nm) is higher than Dox-MONPs (313.03 ± 4.67 nm), confirming the success of BSA coating (**Figure 4A**). Zeta potential measurements showed that MONPs were negatively charged

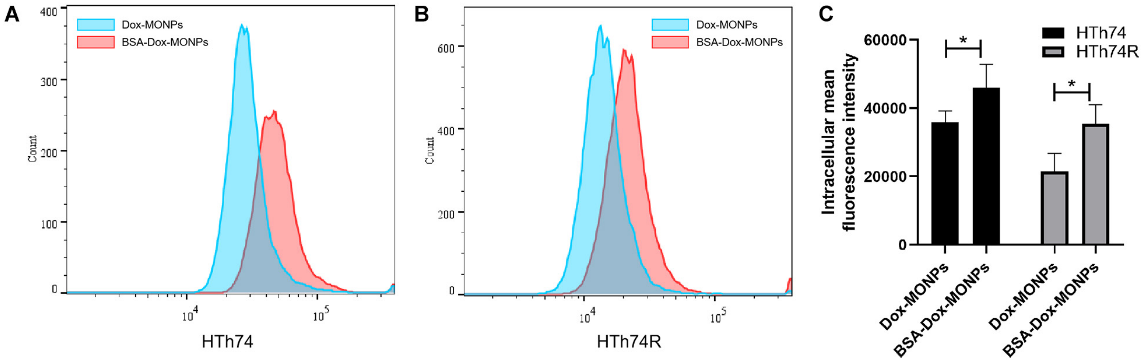

FIGURE 7 | Intracellular Dox fluorescent signal of cells incubated with Dox-MONPs and BSA-Dox-MONPs for 6 h in **(A)** HTh74 and **(B)** HTh74R cells. **(C)** Intracellular fluorescence intensity in HTh74 and HTh74R cells incubated with Dox-MONPs and BSA-Dox-MONPs for 6 h. *$P < 0.05$.

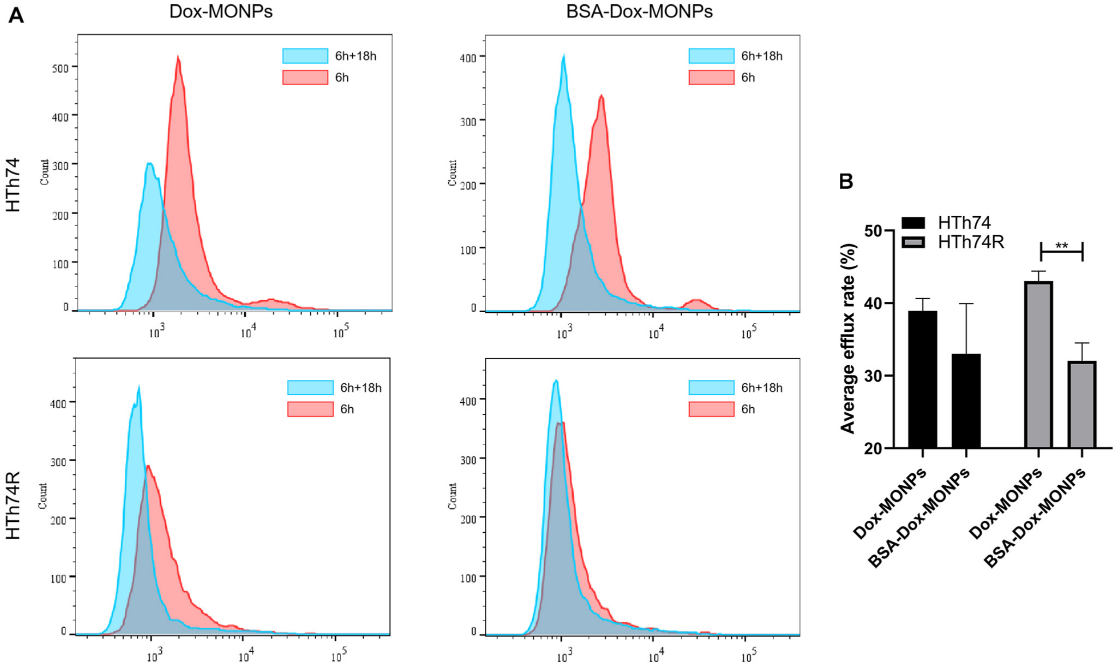

FIGURE 8 | (A) Intracellular Dox fluorescent signal of HTh74 and HTh74R cells incubated with Dox-MONPs and BSA-Dox-MONPs for 6 h and incubated with culture medium for another 18 h, respectively. **(B)** The efflux ratio of drug-loaded nanoparticles. **$P < 0.01$.

(−18.99 ± 0.86 mV) and switched to positive (40.88 ± 1.99 mV) after Dox loading. After BSA coating, the zeta potential of BSA-Dox-MONPs plummeted to −21.70 ± 0.81 mV because the BSA were negatively charged (**Figure 4B**). These results suggested the Dox and BSA was successfully loaded on the MONPs. After being stored for 5 days, BSA-Dox-MONPs' Zeta potential is −22.11 ± 0.96 mV, and the hydration diameter is 368.02 ± 8.90 nm, indicating good stability.

To determine the biocompatibility of MONPs, human keratinocytes HaCaT were incubated with various concentrations of MONPs for 24 h and followed by MTT assays. As shown in **Supplementary Figure 3**, minimal cell death was observed despite the increase of the concentration of MONPs up to 1 mg/mL, indicating the superior biocompatibility of MONPs.

To investigate the impact of MONPs on Dox's therapeutic efficacy, the viability of Dox-MONPs treated and BSA-Dox-MONPs treated ATC cells was compared at equivalent Dox concentration. As shown in **Figure 5** and **Supplementary Figure 4**, at all free Dox concentrations, the viability of HTh74R was significantly lower than HTh74, indicating that HTh74R was drug-resistant. Moreover, the viability of HTh74R at all concentrations and HTh74 at low concentrations treated with Dox-MONPs was substantially lower than with free Dox at equivalent Dox concentration. After coated with BSA, BSA-Dox-MONPs elicited more significant efficacy than Dox-MONPs to HTh74 and HTh74R, suggesting that the BSA coating further improves the therapeutic effect of Dox-MONPs. Furthermore, the modification of MONPs enhanced the efficacy of drug-resistant HTh74R more than that of sensitive HTh74. It is noted that BSA-Dox-MONPs induced significant cell toxicity to HTh74R at a concentration of 100 μg/mL, indicating that BSA stabilization reversed chemotherapy resistance of ATC.

Based on the encouraging results of the above-described MTT assay, fluorescence imaging was used to visualize the anti-tumor effect of Dox-MONPs and BSA-Dox-MONPs. HTh74R cells have weaker red fluorescence than HTh74 cells, which further proves to be drug-resistant cells. Yellow signal, which is the overlap of green and red fluorescent, suggested that the cells that ingested nanoparticles were undergoing apoptosis (**Figure 6**). The overlay image further revealed that drug-loaded nanoparticles promoted early apoptosis of ATC cells. In detail, BSA-Dox-MONPs exhibited stronger yellow fluorescence than Dox-MONPs, suggesting more vital killing ability.

Insufficient intracellular accumulation of drugs due to inefficient drug uptake and enhanced drug efflux is one of the fundamental mechanisms behind the chemo-resistance of ATC. Thus, to explore the mechanism of the enhanced efficacy of BSA-Dox-MONPs, flow cytometry was employed to determine their uptake and efflux. The fluorescence-activated cell sorting (FACS) results showed that HTh74 internalized drug-loaded nanoparticles more effectively than HTh74R, which is in line with the resistance of HTh74R. As shown in **Figure 7**, with Dox loaded and BSA coated, it can be visually observed that the FACS curve shifts to the right, suggesting that both HTh74 and HTh74R internalized the drug-loaded nanoparticles. After covering Dox-MONPs with BSA, the fluorescence intensity in HTh74 and HTh74R cells increased by 28.14 and 65.53%, respectively, indicating that BSA can effectively promote the drug uptake by ATC cells. The fluorescence images of HTh74 and HTh74R cells after incubation were also obtained. The images (**Supplementary Figures 5**, **6**) showed greater intracellular accumulation of Dox for BSA-Dox-MONPs in both HTh74 and HTh74R cells, which further confirmed the observation from FACS. Based on the above results, the BSA-stabilized MONPs killed cancer cells more effectively than Dox-MONPs, which may be partly attributed to the enhanced Dox internalization in drug-resistant ATC cells (Yu et al., 2011).

To quantify the efflux of the drug, HTh74 and HTh74R were incubated with Dox-MONPs and BSA-Dox-MONPs for 6 h and cultured in fresh medium for another 18 h to allow drug efflux. The efflux rate was defined as the ratio of intracellular fluoresce intensity before and after culture in fresh medium. As shown in **Figure 8**, the efflux rates of Dox-MONPs and BSA-Dox-MONPs were 38.95 and 33.05% in HTh74 cells and 43.03 and 32.07% in HTh74R cells. It is worth noting that the BSA coating reduced the efflux rate of MONPs, especially in drug-resistant HTh74R. Taken together, these results indicated BSA-Dox-MONPs reversed the resistance of HTh74R cells by enhancing drug uptake and inhibiting drug efflux.

CONCLUSION

In summary, we have constructed a BSA-coated MONPs as Dox carrier with high loading efficiency and capacity. The BSA-Dox-MONPs showed stronger cancer-killing power than free Dox and Dox-MONPs, especially for drug-resistant HTh74R cells. This improved therapeutic efficacy can be attributed to enhanced drug uptake and reduced drug efflux of drug-resistant ATC cells. In brief, BSA-Dox-MONPs increased the intracellular accumulation of Dox in drug-resistant ATC cells and thus reversed their chemotherapy resistance via increased drug uptake and inhibited drug efflux, offering a promising platform for the treatment of chemo-resistant ATC.

DATA AVAILABILITY STATEMENT

The original contributions presented in the study are included in the article/**Supplementary Material**, further inquiries can be directed to the corresponding author/s.

AUTHOR CONTRIBUTIONS

SW presented the initial idea for the research and provided financial support. XH conducted experiments and wrote most of the article. XX analyzed most of the experimental data and wrote part of the article. YTa guided material synthesis and characterization experiments. FZ and YTi gave support on cell experiments and advice on fluorescence imaging. WL and DH analyzed some of the experimental data and helped with the flow cytometry test. SW, GL, and YG reviewed the data and the results of the experiment and gave valuable suggestions for revising the article. All authors contributed to the article and agreed with the submission version.

FUNDING

This work was supported by the National Natural Science Foundation of China (81871420 and 31930020) and Postgraduate Research & Practice Innovation Program of Jiangsu Province (Grant No. KYCX19_1199).

SUPPLEMENTARY MATERIAL

The Supplementary Material for this article can be found online at: https://www.frontiersin.org/articles/10.3389/fmolb.2020.610084/full#supplementary-material

REFERENCES

Burglova, K., Noureddine, A., Hodacova, J., Toquer, G., Cattoen, X., and Man, M. W. C. (2014). A General Method for Preparing Bridged Organosilanes with Pendant Functional Groups and Functional Mesoporous Organosilicas. *Chem. Eur. J.* 20, 10371–10382. doi: 10.1002/chem.201403136

Chen, F., Zhang, H., Jiang, L., Wei, W., Liu, C., and Cang, S. (2019). Enhancing the cytotoxic efficacy of combined effect of doxorubicin and Cyclosporin encapsulated photoluminescent graphene dotted mesoporous nanoparticles against lung cancer cell-specific drug targeting for the nursing care of cancer patients. *J. Photochem. Photobiol. B Biol.* 198:111578. doi: 10.1016/j.jphotobiol.2019.111578

Chen, Y., Li, X., Wang, M., Peng, L., Yu, Z., Peng, X., et al. (2020). Virus-Inspired Deformable Mesoporous Nanocomposites for High Efficiency Drug Delivery. *Small* 16:1906028. doi: 10.1002/smll.201906028

Chen, Y., Meng, Q., Wu, M., Wang, S., Xu, P., Chen, H., et al. (2014). Hollow mesoporous organosilica nanoparticles: a generic intelligent framework-hybridization approach for biomedicine. *J. Am. Chem. Soc.* 136, 16326–16334. doi: 10.1021/ja508721y

Chen, Y., Xu, P., Chen, H., Li, Y., Bu, W., Shu, Z., et al. (2013). Colloidal HPMO Nanoparticles: Silica-Etching Chemistry Tailoring. Topological Transformation, and Nano-Biomedical Applications. *Adv. Mater.* 25, 3100–3105. doi: 10.1002/adma.201204685

Croissant, J. G., Cattoen, X., Man, M. W. C., Dieudonne, P., Charnay, C., Raehm, L., et al. (2015). One-Pot Construction of Multipodal Hybrid Periodic Mesoporous Organosilica Nanoparticles with Crystal-Like Architectures. *Adv. Mater.* 27, 145–149. doi: 10.1002/adma.201404226

Croissant, J. G., Cattoen, X., Man, M. W. C., Gallud, A., Raehm, L., Trens, P., et al. (2014). Biodegradable Ethylene-Bis(Propyl)Disulfide-Based Periodic Mesoporous Organosilica Nanorods and Nanospheres for Efficient In-Vitro Drug Delivery. *Adv. Mater.* 26, 6174–6180. doi: 10.1002/adma.201401931

Davis, P. J., Incerpi, S., Lin, H. Y., Tang, H. Y., Sudha, T., and Mousa, S. A. (2015). Thyroid Hormone and P-Glycoprotein in Tumor Cells. *BioMed. Res. Int.* 2015, 168427–168427. doi: 10.1155/2015/168427

Deberardinis, R. J., and Chandel, N. S. (2016). Fundamentals of cancer metabolism. *Sci. Adv.* 2:e1600200. doi: 10.1126/sciadv.1600200

Fang, J., Wang, Q., Yang, G., Xiao, X., Li, L., and Yu, T. (2019). Albumin-MnO2 gated hollow mesoporous silica nanosystem for modulating tumor hypoxia and synergetic therapy of cervical carcinoma. *Colloids Surf. B* 179, 250–259. doi: 10.1016/j.colsurfb.2019.03.070

Haddad, R. I., Nasr, C., Bischoff, L., Busaidy, N. L., Byrd, D. R., Callender, G. G., et al. (2018). NCCN Guidelines Insights: Thyroid Carcinoma. Version 2.2018. *J. Natl. Compr. Canc. Network* 16, 1429–1440. doi: 10.6004/jnccn.2018.0089

Huang, Y., Hu, L., Huang, S., Xu, W., Wan, J., Wang, D., et al. (2018). Curcumin-loaded galactosylated BSA nanoparticles as targeted drug delivery carriers inhibit hepatocellular carcinoma cell proliferation and migration. *Int. J. Nanomed.* 13, 8309–8323. doi: 10.2147/IJN.S184379

Liu, C., Guo, Y., Hong, Q., Rao, C., Zhang, H., Dong, Y., et al. (2016). Bovine Serum Albumin Adsorption in Mesoporous Titanium Dioxide: Pore Size and Pore Chemistry Effect. *Langmuir* 32, 3995–4003. doi: 10.1021/acs.langmuir.5b04496

Marano, F., Argenziano, M., Frairia, R., Adamini, A., Bosco, O., Rinella, L., et al. (2016). Doxorubicin-Loaded Nanobubbles Combined with Extracorporeal Shock Waves: Basis for a New Drug Delivery Tool in Anaplastic Thyroid Cancer. *Thyroid* 26, 705–716. doi: 10.1089/thy.2015.0342

Marano, F., Frairia, R., Rinella, L., Argenziano, M., Bussolati, B., Grange, C., et al. (2017). Combining doxorubicin-nanobubbles and shockwaves for anaplastic thyroid cancer treatment: preclinical study in a xenograft mouse model. *Endocr. Relat. Cancer* 24, 275–286. doi: 10.1530/ERC-17-0045

Molinaro, E., Romei, C., Biagini, A., Sabini, E., Agate, L., Mazzeo, S., et al. (2017). Anaplastic thyroid carcinoma: from clinicopathology to genetics and advanced therapies. *Nat. Rev. Endocrinol.* 13, 644–660. doi: 10.1038/nrendo.2017.76

Pan, S., Pei, L., Zhang, A., Zhang, Y., Zhang, C., Huang, M., et al. (2020). Passion fruit-like exosome-PMA/Au-BSA@Ce6 nanovehicles for real-time fluorescence imaging and enhanced targeted photodynamic therapy with deep penetration and superior retention behavior in tumor. *Biomaterials* 230:119606. doi: 10.1016/j.biomaterials.2019.119606

Tao, J., Dang, M., Su, X., Hao, Q., Zhang, J., Ma, X., et al. (2018). Facile synthesis of yolk–shell structured monodisperse mesoporous organosilica nanoparticles by a mild alkalescent etching approach. *J. Colloid Interf. Sci.* 527, 33–39. doi: 10.1016/j.jcis.2018.05.024

Teng, Z., Su, X., Lee, B., Huang, C., Liu, Y., Wang, S., et al. (2014a). Yolk-Shell Structured Mesoporous Nanoparticles with Thioether- Bridged Organosilica Frameworks. *Chem. Mater.* 26, 5980–5987. doi: 10.1021/cm502777e

Teng, Z., Wang, C., Tang, Y., Li, W., Bao, L., Zhang, X., et al. (2018). Deformable Hollow Periodic Mesoporous Organosilica Nanocapsules for Significantly Improved Cellular Uptake. *J. Am. Chem. Soc.* 140, 1385–1393. doi: 10.1021/jacs.7b10694

Teng, Z., Wang, S., Su, X., Chen, G., Liu, Y., Luo, Z., et al. (2014b). Facile Synthesis of Yolk–Shell Structured Inorganic–Organic Hybrid Spheres with Ordered Radial Mesochannels. *Adv. Mater.* 26, 3741–3747. doi: 10.1002/adma.201400136

Unnikrishnan, B. S., Maya, S., Preethi, G. U., Anusree, K. S., Reshma, P. L., Archana, M. G., et al. (2020). Self-assembled drug loaded glycosyl-protein metal nanoconstruct: Detailed synthetic procedure and therapeutic effect in solid tumor treatment. *Colloids Surf. B* 193:111082. doi: 10.1016/j.colsurfb.2020.111082

Wang, K., Wang, S., Chen, K., Zhao, Y., Ma, X., and Wang, L. (2018). Doxorubicin-Loaded Melanin Particles for Enhanced Chemotherapy in Drug-Resistant Anaplastic Thyroid Cancer Cells. *J. Nanomater.* 2018, 1–6. doi: 10.1155/2018/2603712

Wu, J., Niu, S., Bremner, D. H., Nie, W., Fu, Z., Li, D., et al. (2020). A Tumor Microenvironment-Responsive Biodegradable Mesoporous Nanosystem for Anti-Inflammation and Cancer Theranostics. *Adv. Healthc. Mater.* 9:1901307. doi: 10.1002/adhm.201901307

Wu, M., Meng, Q., Chen, Y., Zhang, L., Li, M., Cai, X., et al. (2016). Large Pore-Sized Hollow Mesoporous Organosilica for Redox-Responsive Gene Delivery and Synergistic Cancer Chemotherapy. *Adv. Mater.* 28, 1963–1969. doi: 10.1002/adma.201505524

Yao, X., Ma, S., Peng, S., Zhou, G., Xie, R., Jiang, Q., et al. (2020). Zwitterionic Polymer Coating of Sulfur Dioxide-Releasing Nanosystem Augments Tumor Accumulation and Treatment Efficacy. *Adv. Healthc. Mater.* 9:1901582. doi: 10.1002/adhm.201901582

Yao, X., Niu, X., Ma, K., Huang, P., Grothe, J., Kaskel, S., et al. (2017). Graphene Quantum Dots-Capped Magnetic Mesoporous Silica Nanoparticles as a Multifunctional Platform for Controlled Drug Delivery. Magnetic Hyperthermia, and Photothermal Therapy. *Small* 13:1602225. doi: 10.1002/smll.201602225

Yu, T., Malugin, A., and Ghandehari, H. (2011). Impact of Silica Nanoparticle Design on Cellular Toxicity and Hemolytic Activity. *ACS Nano* 26, 5717–5728. doi: 10.1021/nn2013904

Zhang, J., Shen, B., Chen, L., Chen, L., Meng, Y., and Feng, J. (2019). A dual-sensitive mesoporous silica nanoparticle based drug carrier for cancer synergetic therapy. *Colloids Surf. B* 175, 65–72. doi: 10.1016/j.colsurfb.2018.11.071

Zinzi, L., Capparelli, E., Cantore, M., Contino, M., Leopoldo, M., and Colabufo, N. A. (2014). Small and Innovative Molecules as New Strategy to Revert MDR. *Front. Oncol.* 4:2–2. doi: 10.3389/fonc.2014.00002

Conflict of Interest: The authors declare that the research was conducted in the absence of any commercial or financial relationships that could be construed as a potential conflict of interest.

frontiers
in Molecular Biosciences

ORIGINAL RESEARCH
published: 28 January 2021
doi: 10.3389/fmolb.2020.602282

Baicalin Induces Apoptosis and Suppresses the Cell Cycle Progression of Lung Cancer Cells Through Downregulating Akt/mTOR Signaling Pathway

Xinbing Sui[1,2,3,4]†, Xuemeng Han[2]†, Peng Chen[2]†, Qibiao Wu[4]†, Jiao Feng[2], Ting Duan[2], Xiaying Chen[2], Ting Pan[2], Lili Yan[2], Ting Jin[2], Yu Xiang[2], Quan Gao[2], Chengyong Wen[2], Weirui Ma[2], Wencheng Liu[2], Ruonan Zhang[2,3], Bi Chen[2,3], Mingming Zhang[2], Zuyi Yang[2], Na Kong[2]*, Tian Xie[2,3]* and Xia Ding[1]**

[1] School of Traditional Chinese Medicine, Beijing University of Chinese Medicine, Beijing, China, [2] Department of Medical Oncology, School of Medicine, The Affiliated Hospital of Hangzhou Normal University, College of Pharmacy, Hangzhou Normal University, Hangzhou, China, [3] Key Laboratory of Elemene Class Anti-Cancer Chinese Medicines, Engineering Laboratory of Development and Application of Traditional Chinese Medicine, Collaborative Innovation Center of Traditional Chinese Medicines of Zhejiang Province, Hangzhou Normal University, Hangzhou, China, [4] State Key Laboratory of Quality Research in Chinese Medicines, Faculty of Chinese Medicine, Macau University of Science and Technology, Macau, China

Baicalin, as a natural active ingredient extracted and isolated from the traditional Chinese medicine *Scutellaria baicalensis* Georgi., has been potentially used in various areas for its antioxidative, antitumor, anti-inflammatory, and anti-proliferative activities. Although several studies have reported the antitumor effects of baicalin against various cancer types, its beneficial effects on lung cancer have not yet been elucidated. Therefore, the therapeutic effects and molecular mechanisms of baicalin on lung cancer cell lines H1299 and H1650 were investigated. Here, the results of its antitumor activity were shown. We found that Akt/mTOR pathway inhibition was the essential determinant in baicalin-induced cell cycle arrest. Furthermore, when the Akt Agonist SC79 or Akt plasmid transfection was performed, the antitumor effect of baicalin was significantly abrogated in both H1299 and H1650 cells. In conclusion, we found that baicalin exerted its antitumor activity mainly by inducing Akt-dependent cell cycle arrest and promoting apoptosis, which show great potential for developing a new drug for lung cancer treatment.

Keywords: baicalin, cell cycle, apoptosis, lung cancer, Akt

INTRODUCTION

Lung cancer is still one of the most fatal cancers in the world (Bray et al., 2018). Surgery, chemotherapy, radiotherapy, and molecular target therapy are major treatment options for lung cancer patients (Fiero et al., 2019). Despite recent advances in new antitumor agents and intensity-modulated radiation therapy, the side effects and toxicity of these strategies have produced a bottleneck in clinical lung cancer treatments (Hellmann et al., 2019; Crunkhorn, 2020). Therefore, there is an urgent need to discover alternative reagents or novel therapeutic approaches for lung cancer patients.

Edited by:
Lin Mei,
Sun Yat-sen University, China

Reviewed by:
Jiang Chen,
Zhejiang University, China
Shanming Ruan,
Zhejiang Chinese Medical University, China

****Correspondence:***
Xia Ding
dingx@bucm.edu.cn
Tian Xie
drxiet@aliyun.com
Na Kong
kongna.zju@gmail.com
Xinbing Sui
hzzju@zju.edu.cn

†These authors have contributed equally to this work

Specialty section:
This article was submitted to Nanobiotechnology, a section of the journal Frontiers in Molecular Biosciences

Received: *02 September 2020*
Accepted: *12 October 2020*
Published: *28 January 2021*

Citation:
Sui X, Han X, Chen P, Wu Q, Feng J, Duan T, Chen X, Pan T, Yan L, Jin T, Xiang Y, Gao Q, Wen C, Ma W, Liu W, Zhang R, Chen B, Zhang M, Yang Z, Kong N, Xie T and Ding X (2021) Baicalin Induces Apoptosis and Suppresses the Cell Cycle Progression of Lung Cancer Cells Through Downregulating Akt/mTOR Signaling Pathway. Front. Mol. Biosci. 7:602282. doi: 10.3389/fmolb.2020.602282

Natural compounds have always been one of the most important sources of antitumor drug discovery. Baicalin, which is isolated from the *Scutellaria baicalensis* Georgi (Huang Qin), has been clinically utilized for centuries as a traditional Chinese herbal medicine in China. Baicalin was shown to display various biological properties, including antioxidative, anti-proliferative, anti-inflammatory, antitumor activities, and protective effects against multiple-tissue or organ damage (Chen et al., 2014; Fu et al., 2020; Liu et al., 2020; Song et al., 2020). Recently, few studies have revealed the antitumor action of baicalin in lung cancer cells (Wei et al., 2017; Diao et al., 2019); however, the therapeutic effects and underlying mechanism of baicalin in lung cancer have not been elucidated yet.

In this research, the antitumor activity of baicalin was investigated on the two different lung cancer cells H1299 and H1650, and the results show that baicalin could induce apoptosis as well as cell cycle arrest of lung cancer cells, indicating that baicalin has multiple antitumor mechanisms. According to our study, baicalin was proved for the first time to inhibit the Akt/mTOR pathway, which mainly contributed to the cell arrest and survival inhibition, for its employment in lung cancer treatment. Furthermore, Akt agonist SC79 or Akt overexpression plasmid transfection abrogated the antitumor effect of baicalin in these two lung cancer cells. In a word, our results suggested that baicalin exerted its antitumor activity by promoting apoptosis and inducing Akt-dependent cell cycle arrest in lung cancer cells.

MATERIALS AND METHODS

Cell Culture and Transfection

The human lung cancer H1650 and H1299 cell lines were purchased from ATCC, which were cultured with RPMI-1640 medium containing 10% FBS, 100 units/mL penicillin, and 100 μg/mL streptomycin, which were maintained in the incubator with 5% CO_2 at 37°C. 1×10^6 cells/ml were planted in 6-cm culture plates. Also, the plasmids were transfected into cells using Lipofectamine 2000 (#2173184) (Invitrogen, Carlsbad, CA, United States) according to the manufacturer's instructions.

Reagents and Antibodies

The main reagents and antibodies used in this article are as follows: baicalin (>98%) (#B20570) was purchased from Shanghai Yuanye Biological Co., Ltd. Antibodies against AKT (#4691T), p-AKT (#2853T), CDK2 (#2546), CDK4 (#12790), Cyclin E2 (#4132), Bax (#5023T), Bcl-2 (#4223), and α-tubulin (#2125) were purchased from Cell Signaling Technology.

Cell Viability Assay

The cell viability of H1299 and H1650 with the baicalin treatment was determined using CCK8 (#MA0218) (meilunbio). The 96-well plates were planted were 5×10^4/ml cells per well, which was treated with baicalin (0, 50, and 100 μg/ml) for different times. After treatment, the cell viability was measured at 450 nm wavelength.

Colony-Formation Assay

A density of 3×10^3/ml cells was planted in 10-cm plates. The cells after being treated with baicalin were then maintained for about 2 weeks until they grew to visible colonies. Then, the colonies were fixed with 4% paraformaldehyde and stained with crystal violet.

Cell Cycle Analysis by Flow Cytometry

The 6-cm dish was seeded with 5×10^5 cells then given different treatments for 24 h. Then subsequently, the cells were stained using a cell cycle staining kit (#CCS012) purchased from MultiSciences (Lianke) Biotech Co., Ltd., for 30 min in a dark room.

Apoptosis Assays

The percent of cell apoptosis was assayed using the FITC Annexin V Apoptosis Detection kit according to the instructions (#556547) (BD, United States).

Western Blotting Analysis

The cells from the control and treatment groups were collected and lysed by RIPA. After being centrifuged at a high speed, the supernatant was collected. The protein concentrations were measured, then the total protein was separated by SDS-PAGE (8–12%) and transferred to a PVDF membrane. The PVDF membrane was blocked, and the primary antibody was incubated. Finally, the secondary antibody was incubated and detected by ECL Prime Western Blotting Reagent (#RPN2232) (Amersham).

In vivo Lung Tumor Mouse Model

Female BALB/c-nu mice were purchased and raised for a week to adapt to the environment, then the subcutaneous tumor model was established by subcutaneous injection of tumor cells with the final concentration at 5×10^6/ml and subcutaneous injection in the underarm. After the tumor was formed, mice were randomly divided into four groups: control group (100 μl, 5% DMSO), baicalin group (100 μl, 20 mg/kg baicalin diluted with 5% DMSO), SC79 group, and SC79 combined use of baicalin group. Mice were treated for 16 days, and then the tumors were collected and fixed. The experiment was approved by the Animal Care and Use Committee of Zhejiang University of Traditional Chinese Medicine (approval ID: 11139).

Immunohistochemistry

Tumor tissues were fixed with for 24 h with 10% neutral-buffered formalin. Then, tissues were sectioned (4 μm) and sodium citrate buffer was used for the antigen retrieval of sections. Then, the sections were incubated with 10% normal goat serum and primary antibody for 1 h and overnight, respectively. Next, the biotinylated goat anti-rabbit IgG (Vector Laboratories, Burlingame, CA, United States; catalog # BA-1000; dilution 1:200) was used to incubate the sections for 1 h and subsequently incubate with avidin–biotin-horseradish peroxidase (VECTASTAIN® Elite ABC kit; Vector Laboratories; Burlingame, CA, United States; catalog # PK-4010) for 1 h. Finally, color was detected using DAB substrate kit (Vector Laboratories, catalog # SK-4100).

Statistical Analysis

All tests were performed for three times in all studies unless otherwise stated. All data were expressed as mean ± SD. Student's *t*-test was employed for the significance calculate between different groups.

RESULTS

Baicalin Inhibited the Growth of Lung Cancer Cells

To test the biological function of baicalin in lung cancer, we first analyzed the cytotoxicity and growth inhibition effects of baicalin on lung cancer cells H1299 and H1650. After the treatment with various concentrations of baicalin at three time points, the results indicated that cell viability of lung cancer cells was inhibited by baicalin and the efficacy was positively correlated with drug dose and treatment time (**Figure 1A**). Meanwhile, light microscopy observation also showed that baicalin significantly inhibited the viability of these two lung cancer cells compared with their controls (**Figure 1B**), with more detached and shrunken cells appearing.

Baicalin Triggered Apoptosis, Inhibited Cell Proliferation, and Blocked Cell Cycle G1/S Transition in Lung Cancer Cells

To obtain the effect of baicalin on apoptosis, the cell viability was detected by flow cytometry. As shown in **Figure 2A**, the proportion of apoptotic cells significantly increased in the baicalin treatment group, compared with the control. Colony formation assay was used to determine the anti-proliferation effect of baicalin. Moreover, the colony forming ability was remarkably inhibited by baicalin treatment, even with low concentrations such as 5 μg/ml (**Figure 2B**), indicating that baicalin treatment inhibited cell proliferation of lung cancer. The mechanism in which baicalin inhibited the lung cancer cell proliferation was further investigated via flow cytometry to detect whether baicalin could cause cell cycle arrest. Our data showed that cell cycle was remarkably arrested in the G1/S phase, accompanied with a decreased G2/M phase (**Figure 2C**). Taken together, we found that the cell-cycle arrest and apoptosis induction might be the major antitumor mechanism of baicalin in lung cancer cells.

Furthermore, the results from western blotting in **Figure 3A** show that the protein expression level of Bax was significantly upregulated in a dose-dependent manner, whereas Bcl-2 expression levels were remarkably decreased. The mitochondrial apoptosis proteins Bax and Bcl-2 can be activated by caspase-9 (Venteo et al., 2010); therefore, caspase-9 expression was also detected by western blotting in both baicalin treatment group and control group. Also, the results showed that activated caspase-9 was remarkably upregulated in a dose-dependent manner after baicalin treatment, when compared with their controls (**Figure 3A**).

As we know, cell cycle progression is controlled by a cyclin component and several cyclin-dependent kinases (CDKs), including CDK4/6-cyclin D and CDK2-cyclin E (Phan and Croucher, 2020). The above flow cytometric analysis shows that baicalin treatment could induce G1/S phase arrest. Thus, western blotting was performed to detect whether these cell cycle mediators were regulated by baicalin treatment, and we found

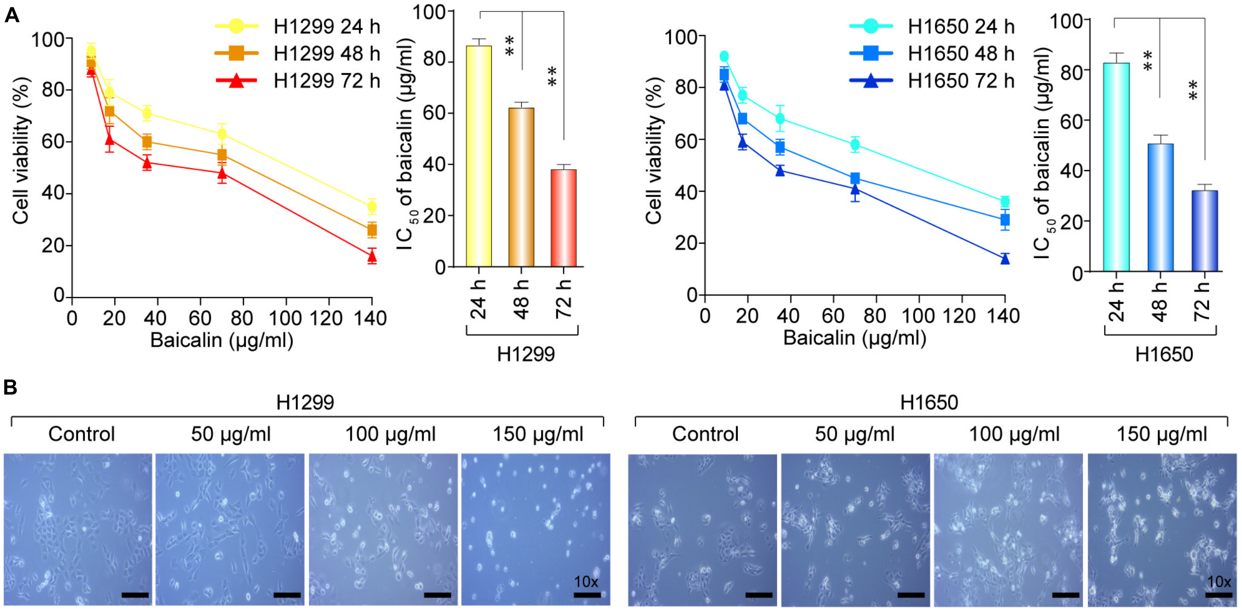

FIGURE 1 | The cell viability of H1299 and H1650 cells was detected after the treatment with baicalin. **(A)** The cell viability was detected with different dose of baicalin treatment for three different time points in H1299 and H1650 lung cancer cells. **(B)** The cell morphological changes were observed by light microscopy with or without treatment of baicalin. The mean ± SD is shown, $^{**}P < 0.01$.

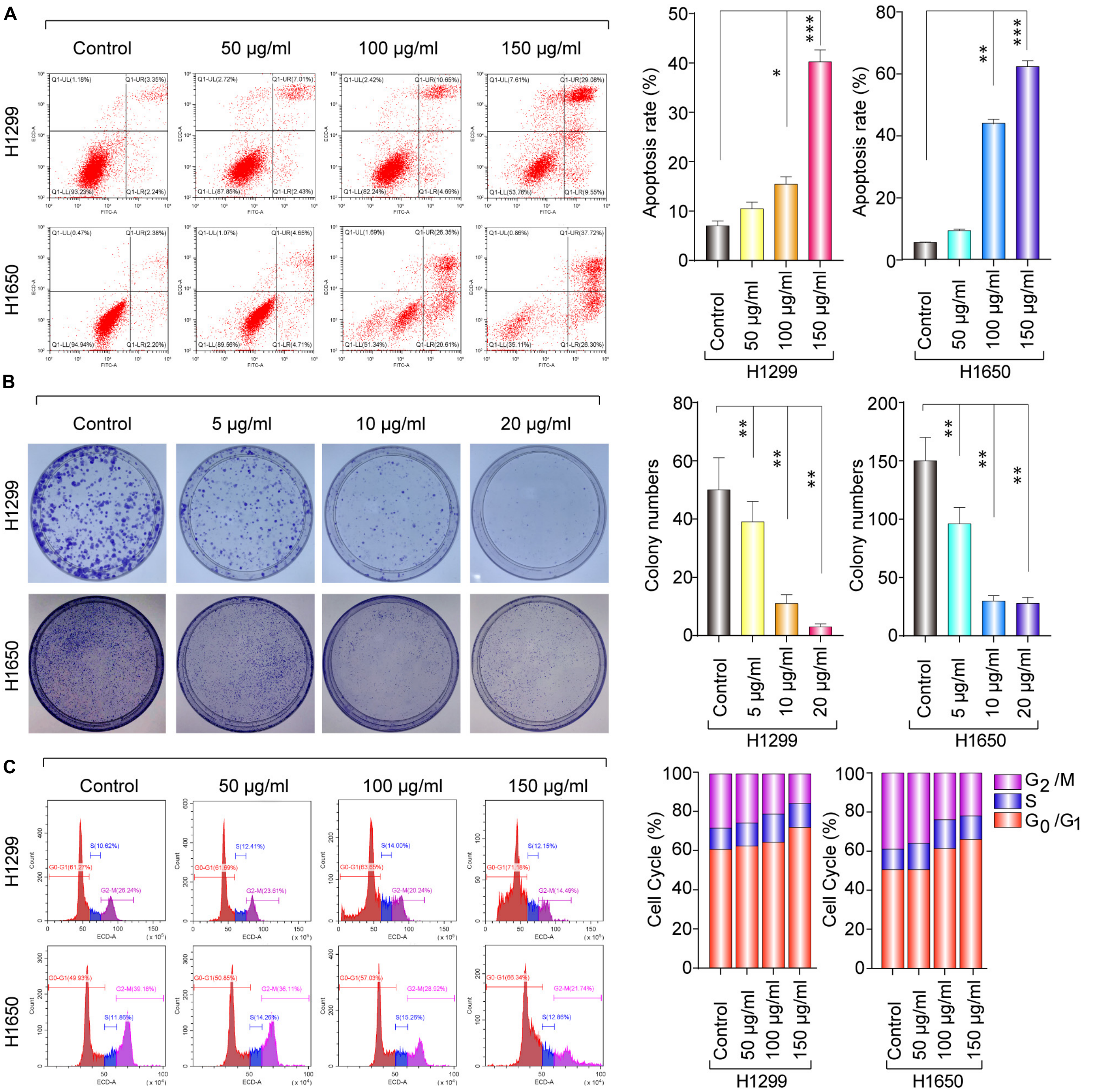

FIGURE 2 | The anticancer effect of baicalin in H1299 and H1650 cells. **(A)** The apoptosis was assayed with or without treatment of baicalin, and representative results were analyzed quantitatively after the treatment. **(B)** The colony-formation assay was performed with or without baicalin treatment, and representative results were analyzed quantitatively. **(C)** The cell cycle was assessed with or without treatment of baicalin by flow cytometry, and representative results were quantitative analyzed. The mean ± SD is shown, $^*P < 0.05$, $^{**}P < 0.01$, $^{***}P < 0.001$.

that the proteins including CDK2, CDK4, and Cyclin E2 were decreased significantly after baicalin treatment (**Figure 3B**).

Akt Signal Was Involved in Baicalin-Induced Cell Cycle Arrest and Apoptosis in Lung Cancer Cells

Akt/mTOR is a classical pathway involved in numerous cellular functions, including cellular proliferation, cell cycle progression, and the development of cancer (American Association for Cancer Research, 2017; Janku et al., 2018). In the Akt/mTOR pathway, protein mTOR can be activated by Akt, which can inhibit cellular apoptosis and promote cell proliferation (Zhang et al., 2017).

Hence, the protein expression in the Akt/mTOR pathway was detected by western blotting. As a result, the expression of p-Akt and p-mTOR was remarkably downregulated after baicalin treatment (**Figure 3C**). To investigate whether the

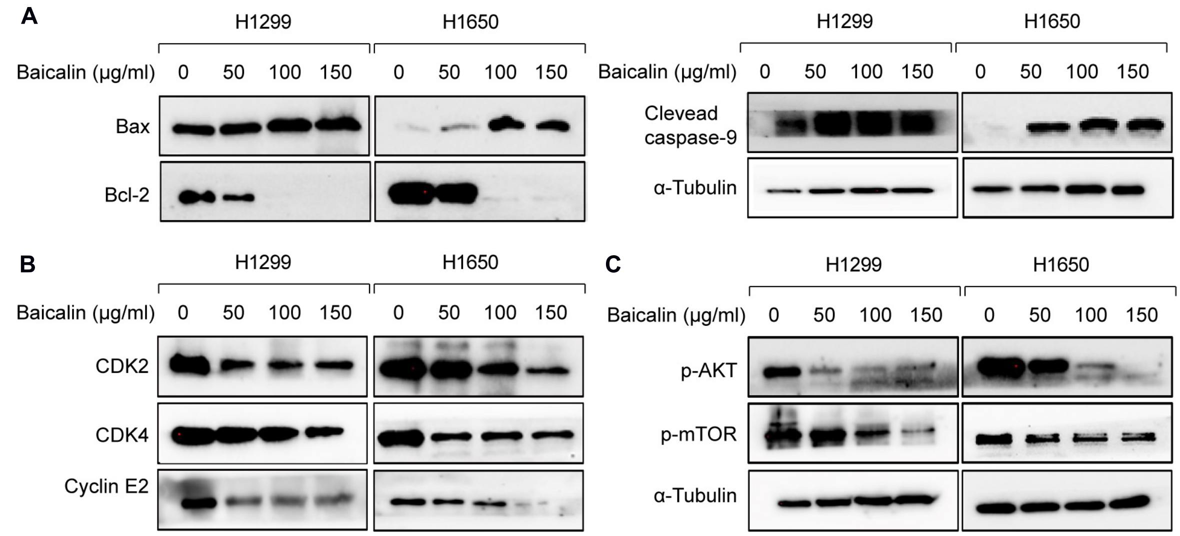

FIGURE 3 | The apoptosis and cell cycle arrest regulatory proteins were analyzed by western blotting. **(A)** The apoptosis-related proteins were analyzed by western blotting in both control and baicalin groups. **(B)** The cell cycle arrest-related proteins were analyzed by western blotting in both control and baicalin groups. **(C)** The protein expressions of Akt and mTOR in lung cancer cells treated with or without baicalin were determined by western blotting.

Akt signal was a key determinant for the antitumor activity of baicalin in lung cancer, we specifically enhanced Akt activation using a pharmacological activator SC79 (5 μM) and the Akt overexpression plasmid. As a result, when the Akt activator SC79 was added to baicalin-treated lung cancer cells, the decreased cell proliferation, increased cell cycle arrest, and increased apoptosis were significantly rescued (**Figures 4A–C**). Next, the Akt overexpression plasmid was used to transfect H1299 and H1650 cells, which was verified by western blotting (**Figure 4D**). This result showed that the antitumor activity of baicalin was remarkably attenuated by Akt overexpression, followed by upregulated phosphorylation of mTOR and expression of cell cycle-related proteins in the G1/S phase including CDK2, CDK4, and Cyclin E2. In conclusion, our results demonstrate that baicalin has antitumor potential via suppressing the Akt/mTOR pathway *in vitro*.

Baicalin Exerted Antitumor Efficacy by Suppressing Akt Activity *in vivo*

The antitumor effect of baicalin was also evaluated *in vivo*. The establishment of the subcutaneous tumor model and drug administration regimen in nude mice is shown in **Figure 5A**. First, BALB/c nude mice were used to establish the subcutaneous tumor model. When xenografts reach 100 mm^3, the mice were, respectively, divided into the control group (DMSO), baicalin group (20 mg/kg), SC79 group, and SC79 combined with baicalin group. The data showed that tumor volume was significantly inhibited by baicalin treatment when compared with the control group (**Figure 5B**). Importantly, there was no significant change in the body weights in four different groups, which indicated that there was no or much lower toxicity when treated with baicalin (**Figure 5C**).

Then, the apoptotic and cell cycle arrest-related proteins from different treatment groups were detected by immunohistochemical staining. As shown in **Figure 6A**, baicalin treatment caused a significant decrease of p-Akt and p-mTOR as well as proteins CDK4 and Cyclin E2. Importantly, these results were also demonstrated by western blotting (**Figure 6B**). In the further study, we found that co-treatment with baicalin and Akt activator SC79 significantly attenuated the decreased tumor size and upregulated the expression of p-Akt, p-mTOR, CDK4, and Cyclin E2, when compared with baicalin treatment alone (**Figures 5**, **6**). These results suggest that baicalin could inhibit tumor growth *in vivo* by suppressing cell cycle progression via inhibiting the Akt signal pathway.

DISCUSSION

Baicalin, as a natural active ingredient derived from the traditional Chinese medicine *Scutellaria baicalensis* Georgi, has great potential to be used for various diseases including cancer. Several studies have reported the role of baicalin in lung cancer. Baicalin might inhibit proliferation of lung cancer cells as a PDZ-binding kinase/T-LAK cell-originated protein kinase (PBK/TOPK) inhibitor both *in vitro* and *in vivo* (Diao et al., 2019). The cell viability, invasion, and metastasis of lung cancer cell A549 and H1299 were detected with the treatment of baicalin by activating the SIRT1/AMPK signaling pathway (You et al., 2018). Baicalin was demonstrated to have cytotoxic and antitumor effects in human chondrosarcoma through inducing apoptotic death and downregulating the phosphoinositide 3-kinase (PI3K)/Akt/mTOR pathway (Zhu et al., 2019). It was also shown that baicalin could suppress cell survival, migration,

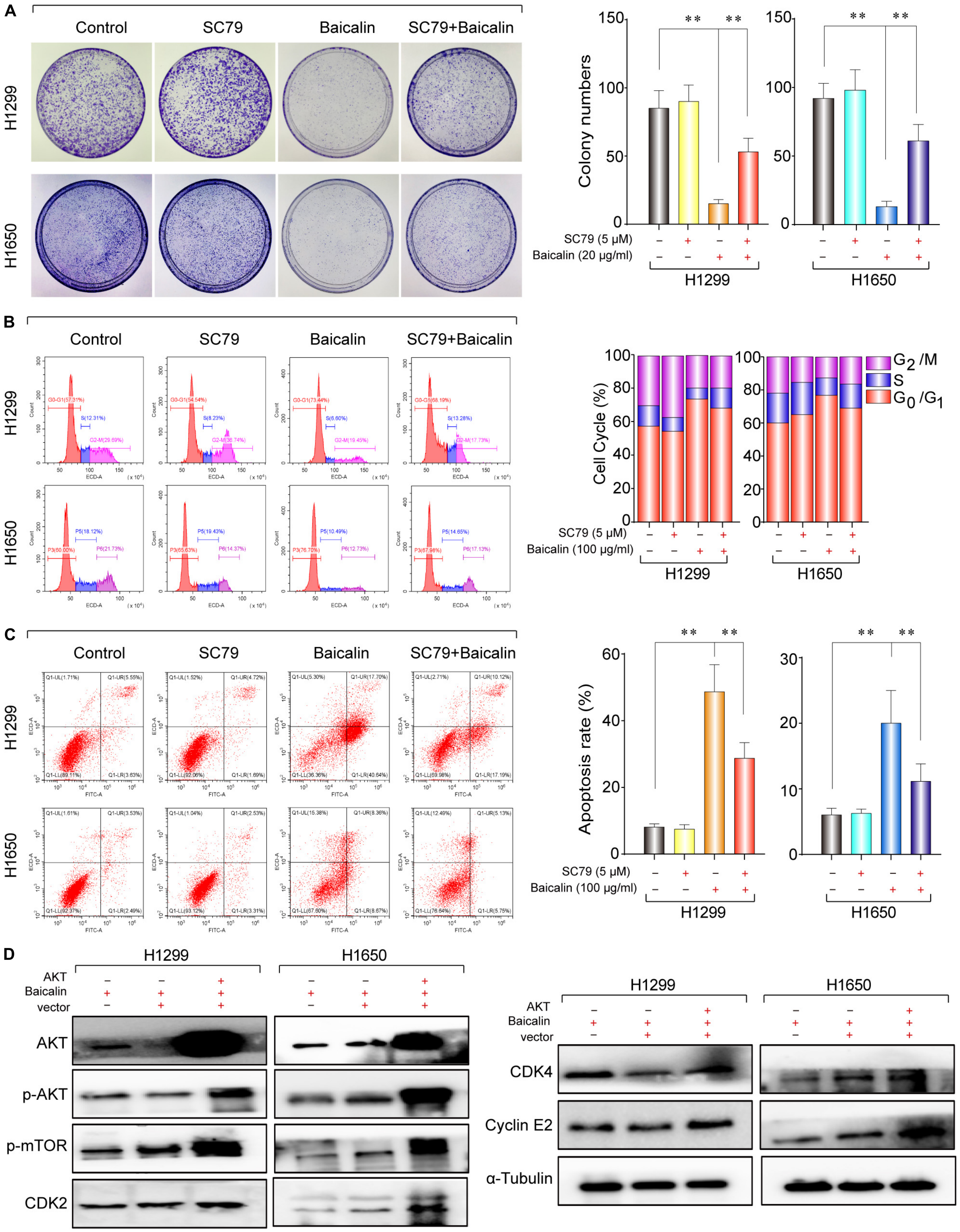

FIGURE 4 | The study of the anticancer mechanism of baicalin in H1299 and H1650 cells. **(A)** The AKT agonist SC79 (5 μM) was used in colony-formation assay to verify the anticancer effect of baicalin, and representative results were analyzed quantitatively after the treatment. **(B)** The AKT agonist SC79 (5 μM) was used to verify the anticancer effect of baicalin by cell cycle assay, and representative results were analyzed quantitatively after the treatment. **(C)** The AKT agonist SC79 (5 μM) was used in apoptosis assay to verify the anticancer effect of baicalin, and representative results were analyzed quantitatively after the treatment. **(D)** The effects of overexpression of AKT on the AKT/mTOR signal pathway and its downstream cell cycle regulatory proteins CDK2, CDK4, and Cyclin E2. The mean ± SD is shown, $^{**}P < 0.01$.

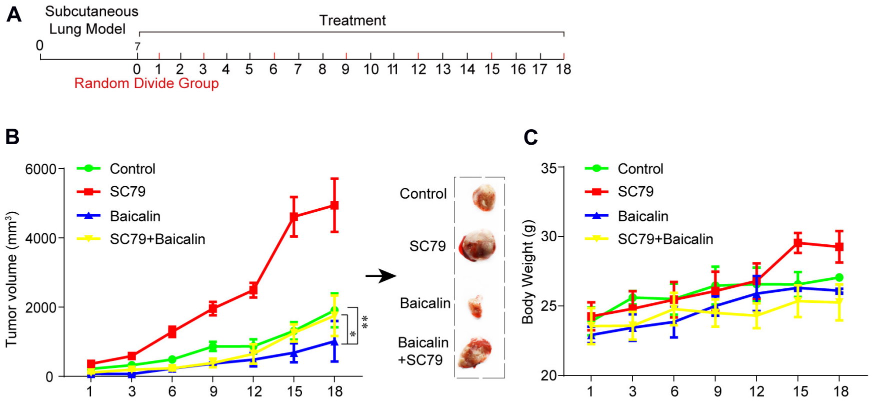

FIGURE 5 | The study of baicalin-suppressed lung cancer growth *in vivo*. **(A)** The scheme of tumor inoculation and systemic injection. **(B)** The tumor volume was monitored in the control group ($n = 4$), SC79 group ($n = 5$), baicalin group ($n = 5$), and SC79 combined use of baicalin group ($n = 5$) to assess the *in vivo* anticancer effect of baicalin. $^{*}P < 0.05$, $^{**}P < 0.01$. **(C)** The body weight was monitored in control group, SC79 group, baicalin group, and SC79 combined use of baicalin group to assess the *in vivo* side effect of the baicalin.

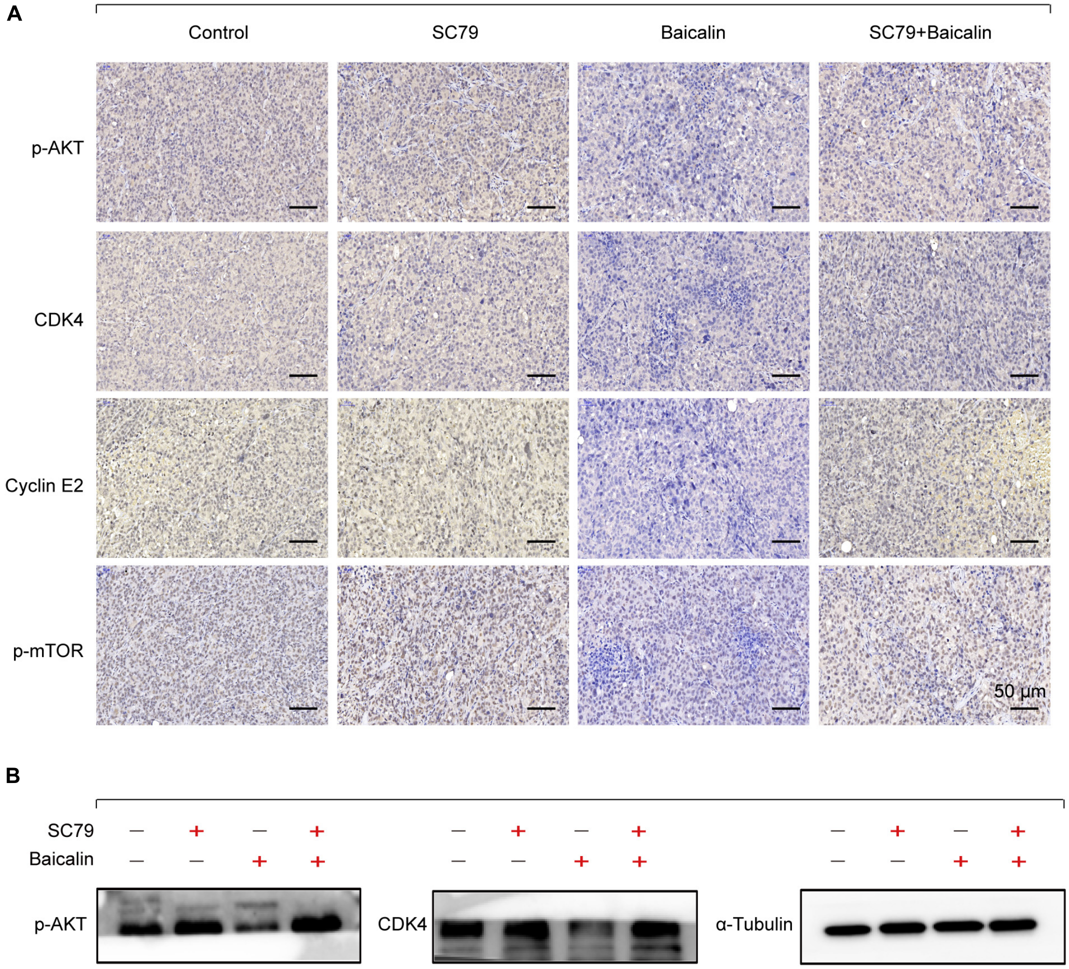

FIGURE 6 | Immunohistochemical staining and western blotting for xenograft tumor sections. **(A)** The immunohistochemistry analysis of the protein expression of p-Akt, p-mTOR, CDK4, and Cyclin E2 in the control group, SC79 group, baicalin group, and SC79 combined use of baicalin group. **(B)** Western blotting was employed to measure the proteins p-Akt and CDK4.

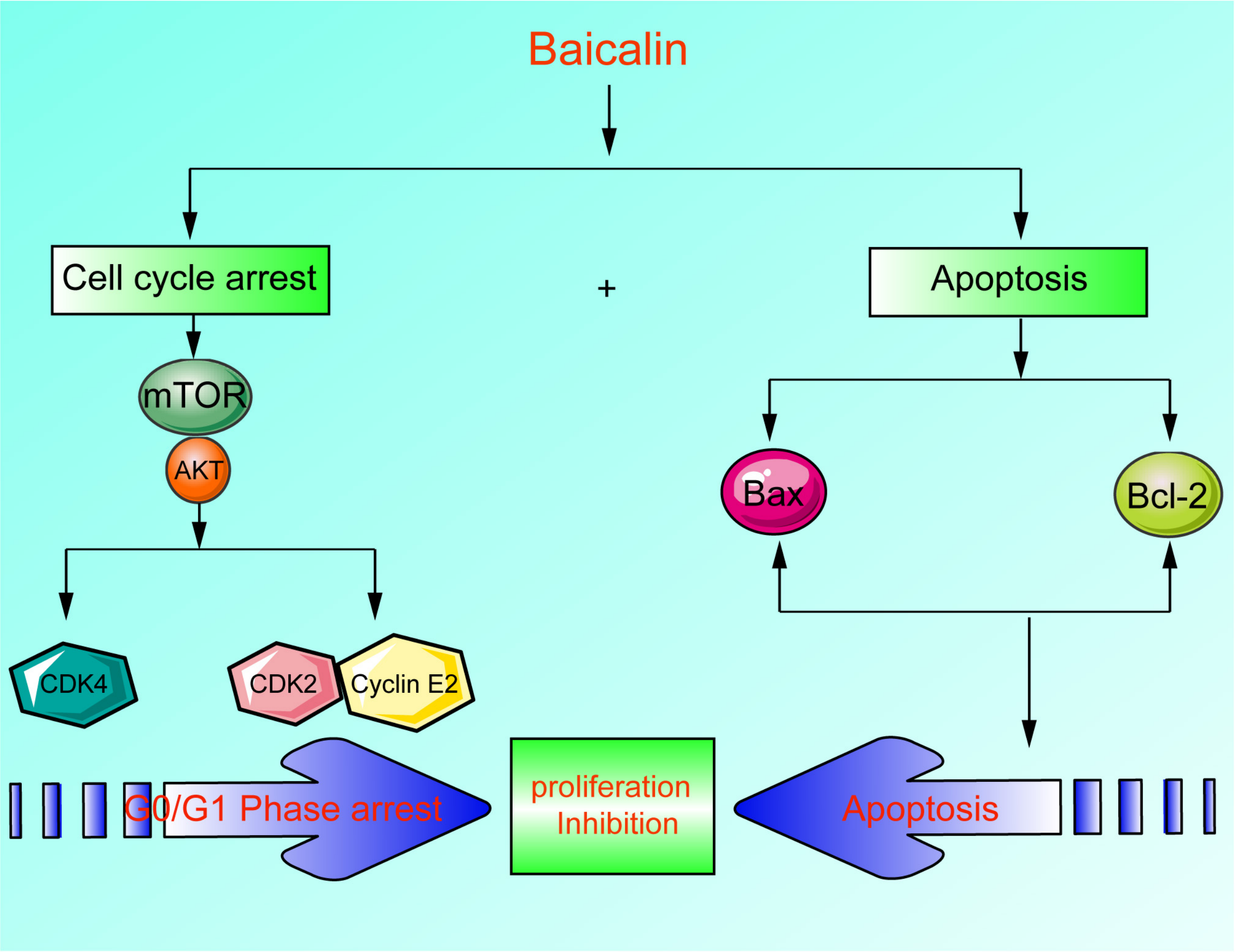

FIGURE 7 | A scheme about the central role of erianin in ferroptosis induction and migration inhibition. Baicalin exerted its anticancer activity through inducing apoptosis, inhibiting cell proliferation, and blocking cell cycle G1-S transition in lung cancer cells in lung cancer cells.

and invasion of mesothelioma cell lines, while sensitizing the cells to chemotherapeutic agents through inhibiting the PI3K/AKT/mTOR signaling pathway (Xu et al., 2019). These studies indicated that baicalin has great potential to be developed as a new anticancer drug; however, its probable antitumor mechanism in lung cancer has not been elucidated, which has become a great obstacle to its clinical application.

In this study, we reported that the antitumor activity of baicalin was proved through inducing apoptosis, inhibiting cell proliferation, and blocking cell cycle G1/S transition in lung cancer cells (**Figure 7**). Currently, it has been found that baicalin has multiple mechanisms to induce apoptosis and inhibit proliferation. However, it has not been reported that baicalin can regulate the Akt/mTOR pathway and G1/S cell cycle pathway in lung cancer cells. Therefore, we investigated the relationship between baicalin-induced anti-proliferation effects in lung cancer cells and the Akt/mTOR pathway. As a result, the Akt/mTOR pathway was significantly inhibited after baicalin treatment, accompanied by the attenuation of G1/S phase-regulated proteins including CDK2, CDK4, and Cyclin E2. Next, we showed that Akt activation by using a pharmacological activator SC79 and overexpressed Akt plasmid attenuated baicalin-induced cell cycle arrest and survival inhibition in both *in vitro* and *in vivo* experiments.

CONCLUSION

Our data suggest that baicalin exerted its antitumor activity mainly by inducing Akt-dependent cell cycle arrest and promoting apoptosis. This novel information partially explained the anti-proliferation property of baicalin on lung cancer cells and would hopefully provide a new natural compound for lung cancer treatment. However, low bioavailability and poor pharmacokinetics have limited the clinical application of baicalin. Thus, improving the bioavailability and pharmacokinetics will be an important issue in the future.

DATA AVAILABILITY STATEMENT

The raw data supporting the conclusions of this article will be made available by the authors, without undue reservation.

ETHICS STATEMENT

The animal study was reviewed and approved by 2020128.

AUTHOR CONTRIBUTIONS

XS, TX, NK, and XD guided and designed the research. XH and PC performed the cell viability assay, western blotting analysis, and *in vivo* experiment. JF, SL, and TD provided major technical supports. XC, TP, LY, TJ, YX, QG, and CW contributed material information gathering and data analysis. WM, WL, MZ, ZY, RZ, and BC collected and sorted the data. XS and PC wrote the manuscript with contributions from the other authors. All authors contributed to the article and approved the submitted version.

FUNDING

This research was supported by grants from National Natural Science Foundation of China (Grant Nos. 81630080, 81874380, 81730108, 81973635, 91129714, and 82022075), Zhejiang Provincial Natural Science Foundation of China for Distinguished Young Scholars (Grant No. LR18H160001), the National Key R&D Program of China (Grant Nos. 2018YFC1704100 and 2018YFC1704106), the Science and Technology Development Fund, Macau SAR (File Nos. 130/2017/A3 and 0099/2018/A3) and Zhejiang province science and technology project of TCM (Grant No. 2019ZZ016).

REFERENCES

American Association for Cancer Research (2017). Pan-cancer analysis pinpoints targets in PI3K pathway. *Cancer Discov.* 7:OF6. doi: 10.1158/2159-8290.CD-NB2017-092

Bray, F., Ferlay, J., Soerjomataram, I., Siegel, R. L., Torre, L. A., and Jemal, A. (2018). Global cancer statistics 2018: globocan estimates of incidence and mortality worldwide for 36 cancers in 185 countries. *CA Cancer J. Clin.* 68, 394–424. doi: 10.3322/caac.21492

Chen, H., Gao, Y., Wu, J., Chen, Y., Chen, B., Hu, J., et al. (2014). Exploring therapeutic potentials of baicalin and its aglycone baicalein for hematological malignancies. *Cancer Lett.* 354, 5–11. doi: 10.1016/j.canlet.2014.08.003

Crunkhorn, S. (2020). Decoy receptor targets lung cancer. *Nat. Rev. Drug Discov.* 19:22. doi: 10.1038/d41573-019-00206-5

Diao, X., Yang, D., Chen, Y., and Liu, W. (2019). Baicalin suppresses lung cancer growth by targeting PDZ-binding kinase/T-LAK cell-originated protein kinase. *Biosci. Rep.* 39:BSR20181692. doi: 10.1042/BSR20181692

Fiero, M. H., Roydhouse, J. K., Vallejo, J., King-Kallimanis, B. L., Kluetz, P. G., and Sridhara, R. (2019). US Food and drug administration review of statistical analysis of patient-reported outcomes in lung cancer clinical trials approved between January, 2008, and December, 2017. *Lancet Oncol.* 20, e582–e589. doi: 10.1016/S1470-2045(19)30335-3

Fu, Y. J., Xu, B., Huang, S. W., Luo, X., Deng, X. L., Luo, S., et al. (2020). Baicalin prevents LPS-induced activation of TLR4/NF-kappaB p65 pathway and inflammation in mice via inhibiting the expression of CD14. *Acta Pharmacol. Sin.* doi: 10.1038/s41401-020-0411-9 [Epub ahead of print].

Hellmann, M. D., Paz-Ares, L., Bernabe Caro, R., Zurawski, B., Kim, S. W., Carcereny Costa, E., et al. (2019). Nivolumab plus Ipilimumab in advanced non-small-cell lung cancer. *N. Engl. J. Med.* 381, 2020–2031. doi: 10.1056/NEJMoa1910231

Janku, F., Yap, T. A., and Meric-Bernstam, F. (2018). Targeting the PI3K pathway in cancer: are we making headway? *Nat. Rev. Clin. Oncol.* 15, 273–291. doi: 10.1038/nrclinonc.2018.28

Liu, J., Zhang, T., Wang, Y., Si, C., Wang, X., Wang, R. T., et al. (2020). Baicalin ameliorates neuropathology in repeated cerebral ischemia-reperfusion injury model mice by remodeling the gut microbiota. *Aging* 12, 3791–3806. doi: 10.18632/aging.102846

Phan, T. G., and Croucher, P. I. (2020). The dormant cancer cell life cycle. *Nat. Rev. Cancer* 20, 398–411. doi: 10.1038/s41568-020-0263-0

Song, X., Gong, Z., Liu, K., Kou, J., Liu, B., and Liu, K. (2020). Baicalin combats glutamate excitotoxicity via protecting glutamine synthetase from ROS-induced 20S proteasomal degradation. *Redox Biol.* 34:101559. doi: 10.1016/j.redox.2020.101559

Venteo, L., Bourlet, T., Renois, F., Douche-Aourik, F., Mosnier, J. F., Maison, G. L., et al. (2010). Enterovirus-related activation of the cardiomyocyte mitochondrial apoptotic pathway in patients with acute myocarditis. *Eur. Heart J.* 31, 728–736. doi: 10.1093/eurheartj/ehp489

Wei, Y., Liang, J., Zheng, X., Pi, C., Liu, H., Yang, H., et al. (2017). Lung-targeting drug delivery system of baicalin-loaded nanoliposomes: development, biodistribution in rabbits, and pharmacodynamics in nude mice bearing orthotopic human lung cancer. *Int. J. Nanomed.* 12, 251–261. doi: 10.2147/ijn.S119895

Xu, W. F., Liu, F., Ma, Y. C., Qian, Z. R., Shi, L., Mu, H., et al. (2019). Baicalin regulates proliferation, apoptosis, migration, and invasion in mesothelioma. *Med. Sci. Monit.* 25, 8172–8180. doi: 10.12659/MSM.919872

You, J., Cheng, J., Yu, B., Duan, C., and Peng, J. (2018). Baicalin, a Chinese herbal medicine, inhibits the proliferation and migration of human non-small cell lung carcinoma (NSCLC) cells, A549 and H1299, by activating the SIRT1/AMPK signaling pathway. *Med. Sci. Monit.* 24, 2126–2133. doi: 10.12659/msm.909627

Zhang, Y., Ng, P., Kucherlapati, M., Chen, F., Liu, Y., Tsang, Y. H., et al. (2017). A pan-cancer proteogenomic atlas of PI3K/AKT/mTOR pathway alterations. *Cancer Cell* 31, 820.e3–832.e3. doi: 10.1016/j.ccell.2017.04.013

Zhu, M., Ying, J., Lin, C., Wang, Y., Huang, K., Zhou, Y., et al. (2019). Baicalin induces apoptotic death of human chondrosarcoma cells through mitochondrial dysfunction and downregulation of the PI3K/Akt/mTOR pathway. *Planta Med.* 85, 360–369. doi: 10.1055/a-0791-1049

Conflict of Interest: The authors declare that the research was conducted in the absence of any commercial or financial relationships that could be construed as a potential conflict of interest.

frontiers
in Bioengineering and Biotechnology

MINI REVIEW
published: 26 February 2021
doi: 10.3389/fbioe.2021.598050

Formation Mechanism and Biomedical Applications of Protease-Manipulated Peptide Assemblies

Tianyue Jiang*[1], *Chendan Liu*[1], *Xiao Xu*[2], *Bingfang He*[1]* and *Ran Mo*[2]

[1] School of Pharmaceutical Sciences, Nanjing Tech University, Nanjing, China, [2] State Key Laboratory of Natural Medicines, Jiangsu Key Laboratory of Drug Discovery for Metabolic Diseases, Center of Advanced Pharmaceuticals and Biomaterials, School of Life Science and Technology, China Pharmaceutical University, Nanjing, China

Edited by:
Lin Mei,
Sun Yat-sen University, China

Reviewed by:
Huaimin Wang,
Westlake University, China
Francesca Taraballi,
Center for Musculoskeletal Regeneration, Houston Methodist Research Institute, United States
Zhiqiang Yu,
Southern Medical University, China

***Correspondence:**
Ran Mo
rmo@cpu.edu.cn
Bingfang He
bingfanghe@njtech.edu.cn

Specialty section:
This article was submitted to Nanobiotechnology, a section of the journal Frontiers in Bioengineering and Biotechnology

Received: *23 August 2020*
Accepted: *04 February 2021*
Published: *26 February 2021*

Citation:
Jiang T, Liu C, Xu X, He B and Mo R (2021) Formation Mechanism and Biomedical Applications of Protease-Manipulated Peptide Assemblies.
Front. Bioeng. Biotechnol. 9:598050.
doi: 10.3389/fbioe.2021.598050

Exploiting enzyme-catalyzed reactions to manipulate molecular assembly has been considered as an attractive bottom-up nanofabrication approach to developing a variety of nano-, micro-, and macroscale structures. Upon enzymatic catalysis, peptides and their derivatives transform to assemblable building blocks that form ordered architecture by non-covalent interactions. The peptide assemblies with unique characteristics have great potential for applications in bionanotechnology and biomedicine. In this mini review, we describe typical mechanisms of the protease-instructed peptide assembly *via* bond-cleaving or bond-forming reactions, and outline biomedical applications of the peptide assemblies, such as drug depot, sustained release, controlled release, gelation-regulated cytotoxicity, and matrix construction.

Keywords: protease, self-assembly, mechanism, peptide assemblies, biomedical application

INTRODUCTION

Bottom-up fabrication is related to a precise control and generation of structures with desired shapes and characteristics starting from smaller dimensions by the self-assembly of atoms or molecules. Bottom-up fabrication approach presents a novel direction to achieve well-defined and functional nano-, micro-, and macroscale structures (Um et al., 2006; Hauser and Zhang, 2010; Chen and Liang, 2012; Yu et al., 2015). Oligopeptides are fascinating backbone of building blocks for self-assembly due to their rich chemistry, ease of synthesis, high biocompatibility, and good biodegradability (Restu et al., 2018; Ma et al., 2020). The peptide assembly is often driven by manifold physical and chemical stimuli, such as temperature (Draper et al., 2017; Lampel et al., 2017), pH (Ghosh et al., 2012), light (Haines et al., 2005), metal ions (Zou et al., 2015), and salinity (Ozbas et al., 2004). Enzyme-mediated reactions as selective biological stimuli, including protease (Toledano et al., 2006; Xu et al., 2014), phosphatase (Tian et al., 2014; Feng et al., 2018; Wang et al., 2018), and carboxylesterases (Li et al., 2015; Zhang et al., 2019), are considered as a preferential approach to induce self-assembly, which has numerous advantages of unique chemo-, regio-, and enantio-selectivity (Sakurai et al., 1988), and mild reaction conditions.

Proteases as a large class of enzymes possess catalytic function to hydrolyze proteins and peptide, which are extensively found in animal offal, plant stems and leaves, fruits, and microorganisms. In the human body, proteases are involved in the occurrence and development of various physiological/pathological activities (Coughlin, 2000; Visse and Nagase, 2003;

Lopez-Otin and Bond, 2008), such as food digestion and absorption, blood coagulation, cell differentiation and autolysis, aging, cancer progression, and metastasis. The protease catalysis approach for peptide synthesis and assembly has attracted considerable attentions over the past few decades (Morihara and Oka, 1981; Ulijn et al., 2002). Under the catalysis of protease, the peptides and their derivatives experience biochemical reactions accompanied by structural changes, and subsequently produce nanosized supramolecular building blocks, which arrange spatially and form specific architecture such as nanofibers *via* intermolecular non-covalent interactions. The assembling nanofibers would further undergo transformation in macroscopic aspect. For example, a sol-gel transition leads to formation of a macroscale hydrogel. In this mini review, we describe typical mechanisms of the protease-instructed peptide assembly, and outline biomedical application of the peptide assemblies.

PROTEASE-INSTRUCTED ASSEMBLY MECHANISM

The mode of the protease-manipulated self-assembly generally involves a combination of covalent and non-covalent interactions. The non-assembling precursors converse into building blocks by protease-catalyzed bond-cleaving or bond-formation reactions, which self-assemble into specific architecture *via* non-covalent interactions mediated by molecular recognition including hydrophobic interaction, hydrogen bonds, π−π stacking, and β-sheet interaction (Loo et al., 2012; Fichman and Gazit, 2014). According to the types of proteases and their specific substrates, both bond cleavage and bond formation are feasible in the protease-manipulated self-assembling systems (**Figure 1A**). A summary of the commonly used proteases with the corresponding precursors and gelators is listed in **Table 1**.

Assembly by Bond-Cleaving Reactions

Protease-catalyzed bond-cleaving reactions prevail in biological processes. A host of proteases with specific catalytic activities in human body have been applied as stimuli to obtain peptide-based building blocks for self-assembly of ordered structures, such as matrix metalloproteinase (MMP), thrombin, and chymotrypsin. For example, MMP can degrade specific amino acid sequences, and each member of the MMP family has certain substrate specificity (Turk et al., 2001; Ratnikov et al., 2014). The non-assembling precursor often consists of building block, hydrophilic moiety, and protease-recognizing linker. The protease-catalyzed hydrolysis of the precursor often leads to removal of hydrophilic moieties and generation of molecular building block that self-assembles by ordered arrangement *via* non-covalent interactions.

Yang et al. (2009) exploited the hydrolytic function of MMP-9 to converse peptide precursors into gelators that could self-assemble into microstructured hydrogels. The designed precursors consisted of short peptides with the amino acid sequence of FFFFCGLDD. The FFFF peptide served as an effective gel factor with a critical gelation concentration of 0.4% (w:v) in water. The cleavage site for MMP-9 is theoretically between G and L. The integrated LDD sequence increased the aqueous solubility of the precursor. The hydrogel was formed after the precursors were incubated with MMP-9 for 45 min, and 2-h incubation brought about 52.8% of FFFFCGLDD, 31.8% of FFFFCG, and 15.4% of FFFF, indicating that MMP-9 could cause the hydrolysis of the FFFFCGLDD peptide and subsequent hydrogel formation *via* the intermolecular non-covalent interactions between the peptide hydrolyzates.

Soellner and colleagues developed a tunable protease-responsive precursor containing three parts: (1) a solubilizing factor, PEG_4-$_D R_D R_D$SP composed of oligo(ethylene glycol), three D-type amino acids with proteolytic resistance and a proline; (2) a gelation factor, PABA-F_5Phe-Phe-NH_2 (PABA: *p*-aminobenzoic acid, F_5Phe: pentafluorophenylalanine); and (3) a protease-recognizing tetrapeptide that links the *C*-terminus of the solubilizing factor and the *N*-terminus of the gelation factor (Bremmer et al., 2012). For different proteases, corresponding specific precursors were synthesized by changing the tetrapeptide linkers. The LTPR, AAPF, and DAFE tetrapeptides were designed for thrombin, chymotrypsin, and GLU-C, respectively. After adding the corresponding protease to the precursor solution, the hydrogel formation was observed within hours. Such protease-triggered self-assembly system was suitable for most serine proteases, resulting in no residue left on the *N*-terminus. However, for matrix protease, specific residues are needed on both sides of the cleavable bond, and the leftover residues connecting to the end of the gelation factor might significantly impede the gelation process. Accordingly, they proposed a dual-enzyme-catalyzed self-assembly strategy to avoid the negative effect of the remaining residues on gelation using the matrix protease alone (Bremmer et al., 2014). The precursor was synthesized by introducing the MMP-9-degradable GPKGLKGA peptide linker. MMP-9 and aminopeptidase M (AP-M) were used simultaneously to trigger the assembly of the precursor. AP-M could indiscriminately cleave the remaining amino acid residues from the termini of peptides (Drag et al., 2010) after the MMP-9-mediated peptide degradation, thereby supporting efficient gelation and achieving stable hydrogel.

Assembly by Bond-Forming Reactions

Proteases have been validated able to exert reverse hydrolysis under non-physiological conditions, such as in organic medium (Xu et al., 2013; Zhu et al., 2018) and at solid/liquid interface (Ulijn et al., 2002). Integrating protease-catalyzed peptide condensation with self-assembly is an appealing approach to shift hydrolysis toward condensation in aqueous medium. Thermolysin and α-chymotrypsin are the mostly used proteases for bond-forming reactions. Ulijn and coworkers first reported the application of protease to selectively instruct assembly of short peptides *via* reverse hydrolysis in 2006 (Toledano et al., 2006), and further characterized this protease-assisted self-assembly under thermodynamic control (Williams et al., 2009). Thermolysin, an endo-protease, was chosen as a model protease and utilized in the reverse hydrolysis reactions, which has a substrate preference for hydrophobic/aromatic residues on the *N*-terminal peptide bonds. Under the catalysis of thermolysin,

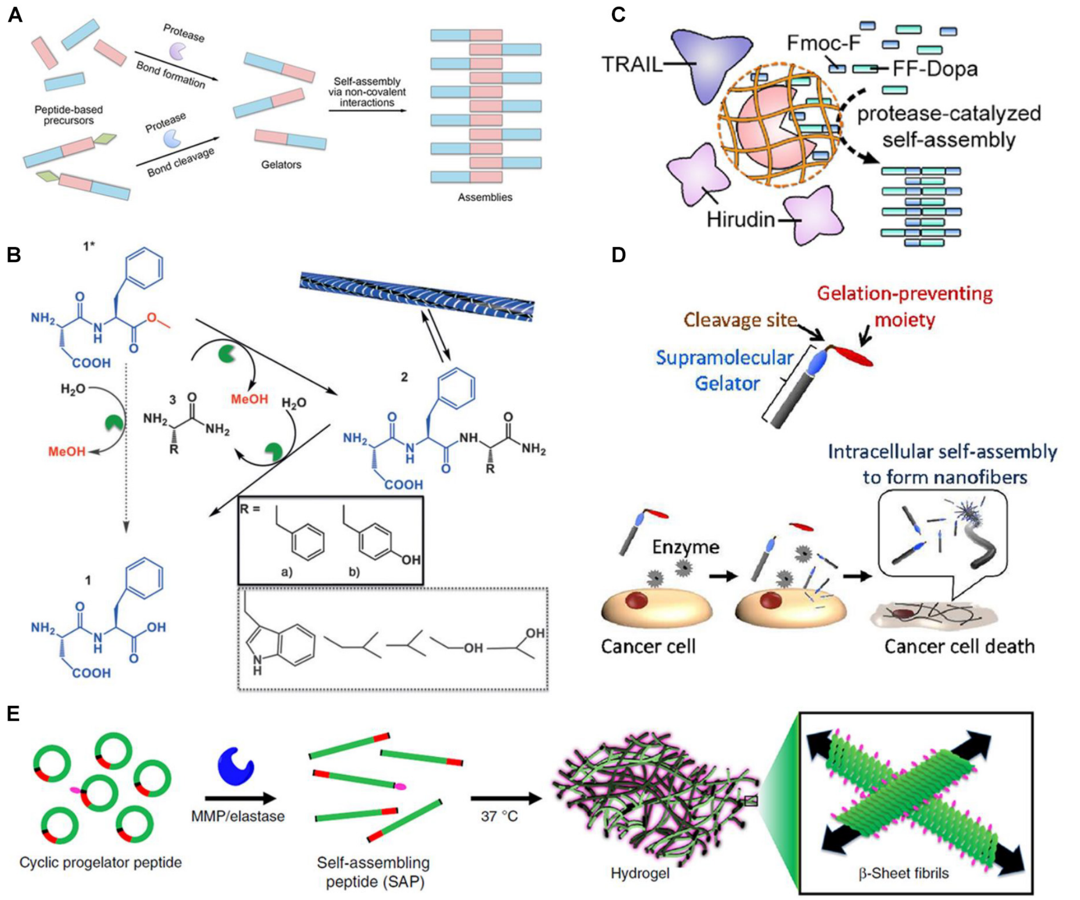

FIGURE 1 | (A) Schematic of protease-triggered bond-formation or bond-cleavage reaction followed by self-assembly. **(B)** Transient hydrogel based on the peptide nanofiber assembly triggered by *a*-chymotrypsin under kinetic control (reprinted with permission from *Angew. Chem. Int. Ed. 2015, 54, 8119–8123*). **(C)** Schematic of substrate-selective protease-assisted self-assembly of the peptide hydrogel for protein delivery (reprinted with permission from *Nano Lett. 2017, 17, 7447–7454*). **(D)** Schematic of selective cytotoxicity of endogenous MMP-7-triggered *in situ* formed peptide assemblies against cancer cells (reprinted with permission from *J. Am. Chem. Soc. 2015, 137, 770–775*). **(E)** Schematic of endogenous enzymatic conversion of cyclic peptides into linear peptides for *in situ* hydrogel formation (reprinted with permission from *Nat. Commun. 2019, 10, 1735*).

two non-gelling precursors, *N*-(fluorenylmethoxycarbonyl) (Fmoc)-capped non-polar amino acids (Fmoc-G, Fmoc-L, Fmoc-F, or Fmoc-T) and nucleophiles (GG, FF, LL, or L-OMe, F-OMe esters), resulted in synthesis of Fmoc-peptide gelators and subsequent assembly of nanofibrous structures driven by $\pi-\pi$ stacking. The assembled nanofibers with a diameter of $\sim$10–20 nm became physically entangled and spontaneously formed hydrogel above a critical concentration. It is worth noting that the free energy variation involved in the peptide self-assembly is enough to reverse the hydrolytic reaction, although the gelator synthesis is not thermodynamically favored in itself. Self-correction, component-selection, and spatiotemporal confinement of this reversible self-assembly under thermodynamic control was investigated. Incubating both L-OMe and F-OMe with Fmoc-T simultaneously in the presence of protease generated Fmoc-TF-OMe as the main product with a yield of 82%. Furthermore, the production of Fmoc-TF-OMe prevailed in the reaction, although Fmoc-T was pre-incubated with L-OMe followed by adding of F-OMe. This protease-instructed self-assembly process was validated to be equilibrium-driven and completely reversible, which rendered self-correction of assembly defects in a spatially confined manner.

Thermodynamically and kinetically controlled techniques have been exploited for the protease-catalyzed peptide synthesis. In general, the reaction controlled by kinetics has faster rates than that controlled by thermodynamics. The peptide containing an activated ester as an acyl donor is often required for the kinetically controlled syntheses (Salam et al., 2005). Gross and colleagues reported an α-chymotrypsin-triggered hydrogelation *via* self-assembly of alternating peptide under kinetic control (Qin et al., 2013). The gel formation was observed in the KL-OEt solution (pH 8.5) within less than 10 s after addition of enzyme. The oligomerization of the "dipeptide lego" manipulated by chymotrypsin resulted in mixed chain oligomers $(KL)_x$ with the average polymerized product $(KL)_{4.7}$, which self-assembled into the β-sheet structures and triggered a sol–gel transition. Chymotrypsin immobilized on the polyethyleneimine/tannic

TABLE 1 | Summary of commonly-used proteases with their corresponding precursors and gelators.

Enzymes	Precursors		Gelators	References
MMP-9	FFFFCGLDD		FFFFCG/FFFF	Yang et al., 2009
Thrombin	PEG$_4$- $_D$R$_D$R$_D$SP-LTPR-PABA-F$_5$Phe-Phe-NH$_2$		PABA-F$_5$Phe-Phe-NH$_2$	Bremmer et al., 2012
Chymotrypsin	PEG$_4$-$_D$R$_D$R$_D$SP-AAPF-PABA-F$_5$Phe-Phe-NH$_2$			
Glu-C	PEG$_4$-$_D$R$_D$R$_D$SP-DAFE-PABA-F$_5$Phe-Phe-NH$_2$			
Thermolysin	Fmoc-A	FF	Fmoc-AFF	Toledano et al., 2006
	Fmoc-V		Fmoc-VFF	
	Fmoc-L		Fmoc-LFF	
	Fmoc-F		Fmoc-FFF	
Thermolysin	Fmoc-F	FF	Fmoc-FFF	Williams et al., 2009
	Fmoc-L	LL	Fmoc-LLLLL/Fmoc-LLL	
	Fmoc-T	L-OMe	Fmoc-TL-OMe	
	Fmoc-T	F-OMe	Fmoc-TF-OMe	
α-Chymotrypsin	KL-OEt		(KL)$_x$	Qin et al., 2013
α-Chymotrypsin	DF-OMe	F-NH$_2$	DFF-NH$_2$	Pappas et al., 2015
		Y-NH$_2$	DFY-NH$_2$	
Thermolysin	Fmoc-T	F-NH$_2$	Fmoc-TF-NH$_2$	Conte et al., 2018
Chymotrypsin	DF-OMe		DFF-NH$_2$	
WQ9-2	Fmoc-F	FF-Dopa	Fmoc-FFF-Dopa	Jiang et al., 2018
MMP-9	PhAc-FFAGLDD		PhAc-FFAGL	Kalafatovic et al., 2016
	GFFLGLDD		GFFLGL	
MMP-7	Palmitoyl-GGGHGPLGLARK		Palmitoyl-GGGHGPLG	Tanaka et al., 2015
MMP-9	NH$_2$-*C(KLDL)$_3$PLGLAGC*-NH$_2$ $_{Cyclic}$		H$_2$N-LAGC-C(NH$_2$) (KLDL)$_3$PLG-OH	Carlini et al., 2019
	NH$_2$-*C(KFDF)$_3$PLGLAGC*-NH$_2$ $_{Cyclic}$		H$_2$N-LAGC-C(NH$_2$) (KFDF)$_3$PLG-OH	
Elastase	NH$_2$-*C(KLDL)$_3$PLGLAGC*-NH$_2$ $_{Cyclic}$		H$_2$N-GC-C(NH$_2$) (KLDL)$_3$PLGLA-OH	
	NH$_2$-*C(KFDF)$_3$PLGLAGC*-NH$_2$ $_{Cyclic}$		H$_2$N-GC-C(NH$_2$) (KFDF)$_3$PLGLA-OH	
Thermolysin	Fmoc-T	L-NH$_2$	Fmoc-TL-NH$_2$	Wang et al., 2020
	Fmoc-Y		Fmoc-YL-NH$_2$	
Thermolysin	Fmoc-L	LL	Fmoc-LLL	Williams et al., 2011

*PABA, p-aminobenzoic acid; F$_5$Phe, pentafluorophenylalanine; *represents a disulfide bond between two cysteines.*

acid membrane generated the mixed product [(KL)$_x$, x = 2–7], which self-assembled to form an entangled nanofibrillar network at the interface (Vigiercarriere et al., 2017). For this enzyme immobilization approach, there was a lag time prior to the beginning of self-assembly, which could be tuned by changing the surface density of chymotrypsin and the concentration of KL-OEt.

Pappas et al. (2015) also reported a transient hydrogel based on the peptide nanofiber assembly that was kinetically controlled but thermodynamically unfavored under certain conditions (**Figure 1B**). The DF-OMe precursor could react with either F-NH$_2$ or Y-NH$_2$ to achieve the tripeptide amide gelators, DFF-NH$_2$ or DFY-NH$_2$ through α-chymotrypsin-catalyzed transacylation. When the concentration of the synthesized tripeptide amide gelators was temporarily higher than the critical gelation concentration, a transient gelation initiated, although the amide hydrolysis was thermodynamically favored. The nanostructure that was formed by the gelation collapsed until the competing hydrolysis was dominant. More importantly, during this enzyme-catalyzed synthesis process, the main product was the kinetically favored DFY-NH$_2$ rather than the thermodynamically favored and more stable DFF-NH$_2$, suggesting that the kinetic control was dominant within this transient formation of nanostructures. Conte et al. (2018) further significantly increased the lifetime of the transiently formed hydrogel in a non-equilibrium system by immobilizing α-chymotrypsin on magnetic nanoparticles. The percentage of gelator remained as high as 80% after 1 month using the immobilized enzyme, while that dropped to 10% after 72 h using the free enzyme. Upon an external magnetic field, nearly all the tripeptide gelators assembled into the nanofibers due to a local high concentration. The immobilization of enzyme also markedly hampered its hydrolytic activity on the tripeptide-based building blocks. Accordingly, the degradation of the self-assembled fibers was noticeably delayed and the lifetime of the hydrogel was dramatically prolonged.

BIOMEDICAL APPLICATIONS

The self-assembly of small-molecule peptides leads to the formation of entangled nanofibers on the microscopic level which can entrap water to form hydrogel on the macroscopic level. The hydrogel possesses unique characteristics, such as high water content, highly porous architecture, tunable flexibility, and structural similarity to natural extracellular matrices, which has been considered as an ideal reservoir for drug delivery as well as a superior scaffold for tissue engineering (Jiang et al., 2018; Li et al., 2019; Gao et al., 2020). Moreover, the *in situ* self-assembly of nanofibers in response to endogenous proteases in the tissue or cellular microenvironments as a potential strategy achieves site-specific retention and even generates selective cytotoxicity toward cancer cells.

Jiang et al. (2017) reported a substrate-selective protease-catalysis strategy to trigger formation of a short peptide-based hydrogel for localized delivery of protein therapeutics (**Figure 1C**). WQ9-2, a metalloprotease, was used as a model protease in the reverse hydrolytic reaction (Xu et al., 2013), which could catalyze the Fmoc-F and FF-Dopa precursors to converse into the Fmoc-FFF-Dopa gelator that self-assembled into the nanofibrous hydrogel. However, WQ9-2 would degrade the encapsulated proteins rapidly, such as tumor necrosis factor-related apoptosis-inducing ligand (TRAIL) and hirudin. To solve this issue, WQ9-2 was encapsulated into a single-protein nanocapsule by weaving a polymeric shell around. The nanocapsule allowed permeation of the small-molecule precursors and maintained the catalytic activity of WQ9-2, but suppressed the proteolytic effect of WQ9-2 on the loaded macromolecular proteins due to spatial hindrance provided by the polymeric sheath. The TRAIL and hirudin co-loaded hydrogel using the WQ9-2 nanocapsule-mediated assembly strategy exhibited synergistic tumor-inhibiting effects on the breast tumor mouse model after a single-dose intratumoral injection. Jiang et al. (2018) also used the WQ9-2-manipulated oligopeptide hydrogel for topical delivery of paclitaxel that was loaded in cell-penetrating peptide (CPP)-modified transfersomes (PTX-CTs). The transfersome was composed of phospholipid and surfactants such as Tween 80 and sodium deoxycholate. The flexible and deformable transfersome could efficiently penetrate the stratum coreum through the intercellular gaps into the epidermis. Meanwhile, the incorporated surfactants and CPP also play significant roles in enhancing the transdermal efficiency of the transfersome. The PTX-CTs embedded hydrogel (PTX-CTs/Gel) was topically painted as a drug depot, which enhanced the skin retention of PTX-CTs. The released PTX-CTs from the hydrogel promoted the skin and tumor penetration of PTX and led to increased cytotoxicity against melanoma cells. PTX-CTs/Gel served as an adjuvant treatment combined with the systemic chemotherapy to efficiently inhibit the melanoma growth on the mouse model.

Kalafatovic et al. (2016) proposed the *in situ* self-assembly strategy manipulated by MMP-9 to increase the cytotoxic activity of chemotherapeutic drugs. Two MMP-9-cleavable peptides, PhAc-FFAGLDD and GFFLGLDD, were synthesized, both of which could assemble into micelles to encapsulate the small-molecule anticancer drug, doxorubicin. Interestingly, they found that PhAc-FFAGLDD and GFFLGLDD converted mainly into PhAc-FFAGL and GFFLGL under the catalysis of MMP-9, respectively, which was different from the expected proteolytic cleavage site between G and L. After intravenous injection, the peptide-based micelles accumulated in the tumor tissue. MMP-9 that was highly expressed in the tumor microenvironment could hydrolyze the micelles, leading to a micelle-to-nanofiber transformation. The formed nanofibers showed prolonged intratumor retention than the original micelles, and acted as a drug reservoir with sustainable release of doxorubicin, resulting in higher effect on inhibiting tumor growth of the triple negative breast tumor mouse model. In contrast, the doxorubicin-loaded D-type peptide-assembled micelles could not be degraded by MMP-9 and converse into nanofibers, which had no effect on tumor growth inhibition.

Tanaka et al. (2015) synthesized a palmitoyl-modified peptide, C16-GGGHGPLGLARK for the *in situ* self-assembly in response to MMP-7 (**Figure 1D**). In the structure of the lipid peptide, the C16 alkyl chain served as a hydrophobic moiety; GGGH provided hydrogen bonds; PLGL was an MMP-7-degradable moiety with the cleavage site between G and L; RK was incorporated as cationic heads. In the absence of MMP-7, the lipid peptide precursor could not be gelled due to the electrostatic repulsion between the cationic RK moieties, while it was converted into the C16-GGGHGPLG gelator and formed nanofibers in the presence of MMP-7. The *in vitro* cytotoxicity studies showed that treatment with C16-GGGHGPLGLARK caused high cytotoxic activity against five different cancer cell models, such as MCF-7, SKBR3, MIAPaCaII, HeLa, and A431 cells, but low cytotoxicity on normal cell models, such as MvE and PE cells. The cytotoxicity was mainly attributed to the vital stress on the cancer cells caused by the intracellularly formed nanofibers. Moreover, the cytotoxicity induced by the peptide was positively correlated with the expression level of MMP-7 within the cancer cells.

In addition to cancer therapy, Carlini et al. (2019) reported the *in situ* peptide assembly approach as a promising hydrogel delivery strategy for cardiovascular disease (**Figure 1E**). Two cyclic peptide precursors, KLDL_{Cyclic} (NH_2-C(KLDL)$_3$PLGLAGC-CONH_2) and KFDF_{Cyclic} (NH_2-C(KFDF)$_3$PLGLAGC-CONH_2), were developed. Under the catalysis of MMP-9, the precursor transformed into a linear peptide with self-assembly ability, and subsequently formed a hydrogel. The precursor solution with favorable fluidity could flow freely through a syringe without clogging and cytotoxicity, and gelate at the site of myocardial infarction with a high level of MMP-9 expression on the rat model.

Wang et al. (2020) used thermolysin to trigger the self-assembly of short peptides in the pores of anodic aluminum oxide (AAO) template for cell culture. The AAO templates with highly-ordered porous structures, high-density pore distribution, and tunable channels offered an ideal confined environment for precise control of peptide assembly. Fmoc-threonine/tyrosine (Fmoc-T/Y) and amide-modified leucine (L-NH_2) were condensed by thermolysin to form Fmoc-T/YL-NH_2. The formed Fmoc-T/YL-NH_2 molecules could self-assemble into fibers that are perpendicular to the channel walls of the AAO templates. The length of fibers was only determined by the pore size of templates rather than the depth. Meanwhile, the precursor concentration had notable effect on the formation of fibers. Higher concentration resulted in denser and thicker fiber networks. The cell morphology and extension of the fibroblasts cultured on the template were obviously affected by the assembled peptide fibers, but no significant impact on the cell viability was observed.

Williams et al. (2011) reported a protease-instructed peptide hydrogel for localized delivery of laminin, an extracellular matrix protein to the damaged tissue on a zebrafish model of muscular dystrophy. The hydrogel was formed by the immobilized thermolysin-mediated self-assembly of Fmoc-LLL *via* π-stacking interactions, which was loaded with laminin and locally injected into a dystrophic zebrafish model. The laminin-loaded hydrogel showed enhanced stability and prolonged persistence within the target tissue *in vivo*, and was demonstrated to be a promising drug delivery system for treatment of diseases caused by structural failure of the extracellular matrix.

CONCLUSION AND FUTURE PERSPECTIVES

Considerable efforts have been increasingly made to pursue biomimic strategies to precisely regulate and control the bottom-up nanofabrication process for production of ordered architecture. We and other researchers have identified that the protease-manipulated self-assembly approach may be suitable for well-defined nanofabrication under thermodynamic or kinetic control. Increasing attention on kinetic regulation allows for creating controllable and tunable structures which do not represent thermodynamic equilibrium. Protease screening and engineering as well as rational design of substrate repertoire can be tuned to generate asymmetric, dynamic, and multicomponent structures with superb functions. The macroscale peptide-based hydrogel formed by the protease-instructed self-assembly can serve as reservoir for drug delivery as well as scaffold for tissue engineering. The *in situ* self-assembly of peptides in response to endogenous protease in the physiological or pathological microenvironment can be used to achieve site-specific retention in the targeted tissue and even to induce cytotoxicity toward cancer cells. However, several challenges still remain in spite of significant achievements in the field of protease-instructed peptide assemblies. The macroscale hydrogel formed by the short peptide often has a relatively lower mechanical strength. Moreover, the *in vivo* behaviors of the peptide assemblies should be comprehensively evaluated and investigated prior to clinical translation, such as metabolism, excretion, and safety, although the peptide-based materials are regarded to possess good biocompatibility and biodegradability. In addition to the peptide self-assembly, enzymes have also been widely exploited to control the assembly of polymers (Teixeira et al., 2012), deoxyribonucleic acids (Park et al., 2009), and nanoparticles (Yang et al., 2018). In a word, the protease-instructed self-assembly supports abundant production of unique nanostructures with desired functions for potential applications in bionanotechnology and biomedicine.

AUTHOR CONTRIBUTIONS

TJ, BH, and RM conceived the idea and organized this mini review. All authors contributed to writing, editing, and literature review.

FUNDING

We acknowledge the support from the National Key Research and Development Program of China (2019YFA0905200), the National Natural Science Foundation of China (81971730 and 81503012), the Natural Science Foundation of Jiangsu Province of China for Excellent Young Scholars (BK20190084), the Young Elite Scientists Sponsorship Program by CAST, and the Fok Ying-Tong Education Foundation for Young Teachers in the Higher Education Institutions of China (171028).

REFERENCES

Bremmer, S. C., Chen, J., Mcneil, A. J., and Soellner, M. B. (2012). A general method for detecting protease activity via gelation and its application to artificial clotting. *Chem. Commun.* 48, 5482–5484. doi: 10.1039/c2cc31537h

Bremmer, S. C., Mcneil, A. J., and Soellner, M. B. (2014). Enzyme-triggered gelation: targeting proteases with internal cleavage sites. *Chem. Commun.* 50, 1691–1693. doi: 10.1039/c3cc48132h

Carlini, A. S., Gaetani, R., Braden, R. L., Luo, C., Christman, K. L., and Gianneschi, N. C. (2019). Enzyme-responsive progelator cyclic peptides for minimally invasive delivery to the heart post-myocardial infarction. *Nat. Commun.* 10:1735. doi: 10.1038/s41467-019-09587-y

Chen, Y., and Liang, G. (2012). Enzymatic self-assembly of nanostructures for theranostics. *Theranostics* 2, 139–147. doi: 10.7150/thno.3696

Conte, M. P., Sahoo, J. K., Abul-Haija, Y. M., Lau, K. H. A., and Ulijn, R. V. (2018). Biocatalytic self-assembly on magnetic nanoparticles. *ACS Appl. Mater. Interfaces* 10, 3069–3075. doi: 10.1021/acsami.7b15456

Coughlin, S. R. (2000). Thrombin signalling and protease-activated receptors. *Nature* 407, 258–264. doi: 10.1038/35025229

Drag, M., Bogyo, M., Ellman, J. A., and Salvesen, G. S. (2010). Aminopeptidase fingerprints, an integrated approach for identification of good substrates and optimal inhibitors. *J. Biol. Chem.* 285, 3310–3318. doi: 10.1074/jbc.M109.060418

Draper, E. R., Su, H., Brasnett, C., Poole, R. J., Rogers, S., Cui, H., et al. (2017). Opening a can of worm (-like micelle) s: the effect of temperature of solutions of functionalized dipeptides. *Angew. Chem. Int. Ed.* 56, 10467–10470. doi: 10.1002/anie.201705604

Feng, Z., Wang, H., Wang, S., Zhang, Q., Zhang, X., Rodal, A. A., et al. (2018). Enzymatic assemblies disrupt the membrane and target endoplasmic reticulum for selective cancer cell death. *J. Am. Chem. Soc.* 140, 9566–9573. doi: 10.1021/jacs.8b04641

Fichman, G., and Gazit, E. (2014). Self-assembly of short peptides to form hydrogels: design of building blocks, physical properties and technological applications. *Acta Biomater.* 10, 1671–1682. doi: 10.1016/j.actbio.2013.08.013

Gao, J., Zhan, J., and Yang, Z. (2020). Enzyme-instructed self-assembly (EISA) and hydrogelation of peptides. *Adv. Mater.* 32:e1805798. doi: 10.1002/adma.201805798

Ghosh, A., Haverick, M., Stump, K., Yang, X., Tweedle, M. F., and Goldberger, J. E. (2012). Fine-tuning the pH trigger of self-assembly. *J. Am. Chem. Soc.* 134, 3647–3650. doi: 10.1021/ja211113n

Haines, L. A., Rajagopal, K., Ozbas, B., Salick, D. A., Pochan, D. J., and Schneider, J. P. (2005). Light-activated hydrogel formation via the triggered folding and self-assembly of a designed peptide. *J. Am. Chem. Soc.* 127, 17025–17029. doi: 10.1021/ja054719o

Hauser, C. A., and Zhang, S. (2010). Designer self-assembling peptide nanofiber biological materials. *Chem. Soc. Rev.* 39, 2780–2790. doi: 10.1039/b921448h

Jiang, T., Shen, S., Wang, T., Li, M., He, B., and Mo, R. (2017). A substrate-selective enzyme-catalysis assembly strategy for oligopeptide hydrogel-assisted combinatorial protein delivery. *Nano. Lett.* 17, 7447–7454. doi: 10.1021/acs.nanolett.7b03371

Jiang, T., Wang, T., Li, T., Ma, Y., Shen, S., He, B., et al. (2018). Enhanced transdermal drug delivery by transfersome-embedded oligopeptide hydrogel for topical chemotherapy of melanoma. *ACS Nano* 12, 9693–9701. doi: 10.1021/acsnano.8b03800

Kalafatovic, D., Nobis, M., Son, J., Anderson, K. I., and Ulijn, R. V. (2016). MMP-9 triggered self-assembly of doxorubicin nanofiber depots halts tumor growth. *Biomaterials* 98, 192–202. doi: 10.1016/j.biomaterials.2016.04.039

Lampel, A., Mcphee, S. A., Park, H. A., Scott, G. G., Humagain, S., Hekstra, D. R., et al. (2017). Polymeric peptide pigments with sequence-encoded properties. *Science* 356, 1064–1068. doi: 10.1126/science.aal5005

Li, J., Kuang, Y., Shi, J., Zhou, J., Medina, J. E., Zhou, R., et al. (2015). Enzyme-instructed intracellular molecular self-assembly to boost activity of cisplatin against drug-resistant ovarian cancer cells. *Angew. Chem. Int. Ed.* 54, 13307–13311. doi: 10.1002/anie.201507157

Li, J., Xing, R., Bai, S., and Yan, X. (2019). Recent advances of self-assembling peptide-based hydrogels for biomedical applications. *Soft Matter.* 15, 1704–1715. doi: 10.1039/c8sm02573h

Loo, Y., Zhang, S., and Hauser, C. A. (2012). From short peptides to nanofibers to macromolecular assemblies in biomedicine. *Biotechnol. Adv.* 30, 593–603. doi: 10.1016/j.biotechadv.2011.10.004

Lopez-Otin, C., and Bond, J. S. (2008). Proteases: multifunctional enzymes in life and disease. *J. Biol. Chem.* 283, 30433–30437. doi: 10.1074/jbc.R800035200

Ma, W., Sha, S. N., Chen, P. L., Yu, M., Chen, J. J., Huang, C. B., et al. (2020). A cell membrane-targeting self-delivery chimeric peptide for enhanced photodynamic therapy and in situ therapeutic feedback. *Adv. Healthc. Mater.* 9:e1901100. doi: 10.1002/adhm.201901100

Morihara, K., and Oka, T. (1981). Peptide bond synthesis catalyzed by subtilisin, papain, and pepsin. *J. Biochem.* 89, 385–395. doi: 10.1093/oxfordjournals.jbchem.a133213

Ozbas, B., Kretsinger, J., Rajagopal, K., Schneider, J. P., and Pochan, D. J. (2004). Salt-triggered peptide folding and consequent self-assembly into hydrogels with tunable modulus. *Macromolecules* 37, 7331–7337. doi: 10.1021/ma0491762

Pappas, C. G., Sasselli, I. R., and Ulijn, R. V. (2015). Biocatalytic pathway selection in transient tripeptide nanostructures. *Angew. Chem. Int. Ed.* 54, 8119–8123. doi: 10.1002/anie.201500867

Park, N., Um, S. H., Funabashi, H., Xu, J., and Luo, D. (2009). A cell-free protein-producing gel. *Nat. Mater.* 8, 432–437. doi: 10.1038/nmat2419

Qin, X., Xie, W., Tian, S., Cai, J., Yuan, H., Yu, Z., et al. (2013). Enzyme-triggered hydrogelation via self-assembly of alternating peptides. *Chem. Commun.* 49, 4839–4841. doi: 10.1039/c3cc41794h

Ratnikov, B. I., Cieplak, P., Gramatikoff, K., Pierce, J., Eroshkin, A., Igarashi, Y., et al. (2014). Basis for substrate recognition and distinction by matrix metalloproteinases. *Proc. Natl. Acad. Sci. U.S.A.* 111, E4148–E4155. doi: 10.1073/pnas.1406134111

Restu, W. K., Nishida, Y., Yamamoto, S., Ishii, J., and Maruyama, T. (2018). Short oligopeptides for biocompatible and biodegradable supramolecular hydrogels. *Langmuir* 34, 8065–8074. doi: 10.1021/acs.langmuir.8b00362

Sakurai, T., Margolin, A. L., Russell, A. J., and Klibanov, A. M. (1988). Control of enzyme enantioselectivity by the reaction medium. *J. Am. Chem. Soc.* 110, 7236–7237. doi: 10.1021/ja00229a061

Salam, S. M. A., Kagawa, K., and Kawashiro, K. (2005). α-chymotrypsin-catalyzed peptide synthesis using N-protected d-amino acid carbamoylmethyl esters as acyl donors. *Biotechnol. Lett.* 27, 1199–1203. doi: 10.1007/s10529-005-0018-8

Tanaka, A., Fukuoka, Y., Morimoto, Y., Honjo, T., Koda, D., Goto, M., et al. (2015). Cancer cell death induced by the intracellular self-assembly of an enzyme-responsive supramolecular gelator. *J. Am. Chem. Soc.* 137, 770–775. doi: 10.1021/ja510156v

Teixeira, L. S., Feijen, J., Van Blitterswijk, C. A., Dijkstra, P. J., and Karperien, M. (2012). Enzyme-catalyzed crosslinkable hydrogels: emerging strategies for tissue engineering. *Biomaterials* 33, 1281–1290. doi: 10.1016/j.biomaterials.2011.10.067

Tian, Y., Wang, H., Liu, Y., Mao, L., Chen, W., Zhu, Z., et al. (2014). A peptide-based nanofibrous hydrogel as a promising DNA nanovector for optimizing the efficacy of HIV vaccine. *Nano Lett.* 14, 1439–1445. doi: 10.1021/nl404560v

Toledano, S., Williams, R. J., Jayawarna, V., and Ulijn, R. V. (2006). Enzyme-triggered self-assembly of peptide hydrogels via reversed hydrolysis. *J. Am. Chem. Soc.* 128, 1070–1071. doi: 10.1021/ja056549l

Turk, B. E., Huang, L. L., Piro, E. T., and Cantley, L. C. (2001). Determination of protease cleavage site motifs using mixture-based oriented peptide libraries. *Nat. Biotechnol.* 19, 661–667. doi: 10.1038/90273

Ulijn, R. V., Baragana, B., Halling, P. J., and Flitsch, S. L. (2002). Protease-catalyzed peptide synthesis on solid support. *J. Am. Chem. Soc.* 124, 10988–10989. doi: 10.1021/ja026912d

Um, S. H., Lee, J. B., Park, N., Kwon, S. Y., Umbach, C. C., and Luo, D. (2006). Enzyme-catalysed assembly of DNA hydrogel. *Nat. Mater.* 5, 797–801. doi: 10.1038/nmat1741

Vigiercarriere, C., Wagner, D., Chaumont, A., Durr, B., Lupattelli, P., Lambour, C., et al. (2017). Control of surface-localized, enzyme-assisted self-assembly of peptides through catalyzed oligomerization. *Langmuir* 33, 8267–8276. doi: 10.1021/acs.langmuir.7b01532

Visse, R., and Nagase, H. (2003). Matrix metalloproteinases and tissue inhibitors of metalloproteinases: structure, function, and biochemistry. *Circ. Res.* 92, 827–839. doi: 10.1161/01.RES.0000070112.80711.3D

Wang, M., Wang, A., Li, J., Li, Q., and Bai, S. (2020). Thermolysin-triggered short peptides self-assembly in confined space and application in cell culturing. *Colloids Surf. A Physicochem. Eng. Asp.* 603:125213. doi: 10.1016/j.colsurfa.2020.125213

Wang, Z., Liang, C., Shang, Y., He, S., Wang, L., and Yang, Z. (2018). Narrowing the diversification of supramolecular assemblies by preorganization. *Chem. Commun.* 54, 2751–2754. doi: 10.1039/c8cc01082j

Williams, R. J., Hall, T. E., Glattauer, V., White, J., Pasic, P. J., Sorensen, A. B., et al. (2011). The in vivo performance of an enzyme-assisted self-assembled peptide/protein hydrogel. *Biomaterials* 32, 5304–5310. doi: 10.1016/j.biomaterials.2011.03.078

Williams, R. J., Smith, A. M., Collins, R., Hodson, N., Das, A. K., and Ulijn, R. V. (2009). Enzyme-assisted self-assembly under thermodynamic control. *Nat. Nanotechnol.* 4, 19–24. doi: 10.1038/nnano.2008.378

Xu, J., Sun, H., He, X., Bai, Z., and He, B. (2013). Highly efficient synthesis of endomorphin-2 under thermodynamic control catalyzed by organic solvent stable proteases with in situ product removal. *Bioresour. Technol.* 129, 663–666. doi: 10.1016/j.biortech.2012.12.036

Xu, J. X., Zhou, Z., Wu, B., and He, B. F. (2014). Enzymatic formation of a novel cell-adhesive hydrogel based on small peptides with a laterally grafted l-3,4-dihydroxyphenylalanine group. *Nanoscale* 6, 1277–1280. doi: 10.1039/c3nr04528e

Yang, S., Yao, D., Wang, Y., Yang, W., Zhang, B., and Wang, D. (2018). Enzyme-triggered self-assembly of gold nanoparticles for enhanced retention effects and photothermal therapy of prostate cancer. *Chem. Commun.* 54, 9841–9844. doi: 10.1039/c8cc05136d

Yang, Z., Ma, M., and Xu, B. (2009). Using matrix metalloprotease-9 (MMP-9) to trigger supramolecular hydrogelation. *Soft Matter.* 5, 2546–2548. doi: 10.1039/B908206A

Yu, Z., Xu, Q., Dong, C., Lee, S. S., Gao, L., Li, Y., et al. (2015). Self-assembling peptide nanofibrous hydrogel as a versatile drug delivery platform. *Curr. Pharm. Des.* 21, 4342–4354. doi: 10.2174/1381612821666150901104821

Zhang, S., Hu, X., Mang, D., Sasaki, T., and Zhang, Y. (2019). Self-delivery of N-hydroxylethyl peptide assemblies to the cytosol inducing endoplasmic reticulum dilation in cancer cells. *Chem. Commun.* 55, 7474–7477. doi: 10.1039/c9cc03460a

Zhu, F., Jiang, T., Wu, B., and He, B. (2018). Enhancement of Z-aspartame synthesis by rational engineering of metalloprotease. *Food Chem.* 253, 30–36. doi: 10.1016/j.foodchem.2018.01.108

Zou, R., Wang, Q., Wu, J., Wu, J., Schmuck, C., and Tian, H. (2015). Peptide self-assembly triggered by metal ions. *Chem. Soc. Rev.* 44, 5200–5219. doi: 10.1039/c5cs00234f

Conflict of Interest: The authors declare that the research was conducted in the absence of any commercial or financial relationships that could be construed as a potential conflict of interest.

Advantages of publishing in Frontiers

OPEN ACCESS
Articles are free to read
for greatest visibility
and readership

FAST PUBLICATION
Around 90 days
from submission
to decision

HIGH QUALITY PEER-REVIEW
Rigorous, collaborative,
and constructive
peer-review

TRANSPARENT PEER-REVIEW
Editors and reviewers
acknowledged by name
on published articles

Frontiers
Avenue du Tribunal-Fédéral 34
1005 Lausanne | Switzerland

Visit us: www.frontiersin.org
Contact us: frontiersin.org/about/contact

REPRODUCIBILITY OF RESEARCH
Support open data
and methods to enhance
research reproducibility

DIGITAL PUBLISHING
Articles designed
for optimal readership
across devices

FOLLOW US
@frontiersin

IMPACT METRICS
Advanced article metrics
track visibility across
digital media

EXTENSIVE PROMOTION
Marketing
and promotion
of impactful research

LOOP RESEARCH NETWORK
Our network
increases your
article's readership